ΕΘΝΙΚΟ ΜΕΤΣΟΒΙΟ ΠΟΛΥΤΕΧΝΕΙΟ

ΣΧΟΛΗ ΜΗΧΑΝΟΛΟΓΩΝ ΜΗΧΑΝΙΚΩΝ

ΤΟΜΕΑΣ ΘΕΡΜΟΤΗΤΑΣ

ΕΡΓΑΣΤΗΡΙΟ ΑΤΜΟΚΙΝΗΤΗΡΩΝ & ΛΕΒΗΤΩΝ

Διδακτορική Διατριβή

ΜΕΛΕΤΗ ΚΑΙ ΜΟΝΤΕΛΟΠΟΙΗΣΗ ΔΙΕΡΓΑΣΙΩΝ ΠΟΛΥΦΑΣΙΚΩΝ ΡΟΩΝ ΜΕ ΕΦΑΡΜΟΓΗ ΣΤΙΣ ΡΕΥΣΤΟΠΟΙΗΜΕΝΕΣ ΚΛΙΝΕΣ ΓΙΑ ΤΗ ΔΕΣΜΕΥΣΗ ΡΥΠΑΝΤΩΝ

Αριστείδης Π. Νικολόπουλος
Διπλ. Μηχανολόγος Μηχανικός Ε.Μ.Π.

Επιβλέπων Καθηγητής: Εμμ. Κακαράς

Αθήνα, 2014

Στην οικογένειά μου

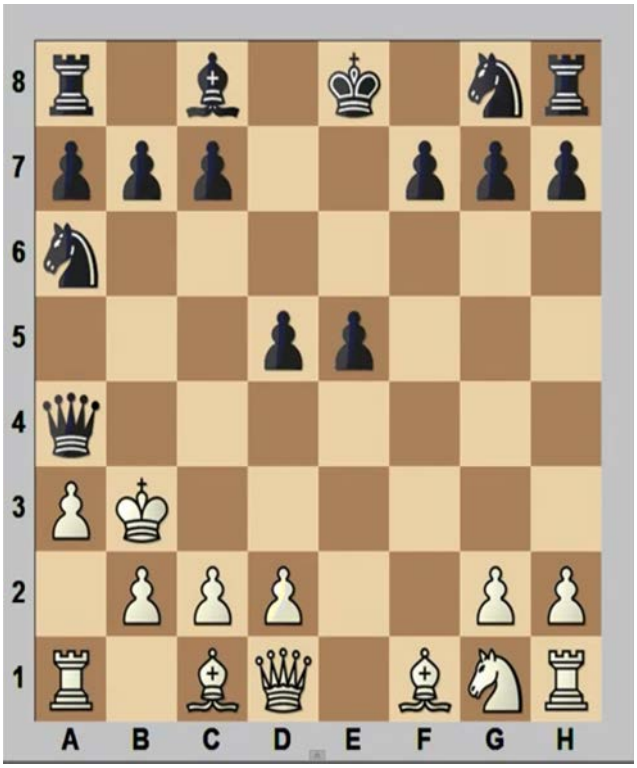

White to move! The Immortal Draw: Carl Hamppe vs Philipp Meitner, Vienna 1872

1.e4 e5 2.Nc3 Bc5 3.Na4 Bxf2+ 4.Kxf2 Qh4+ 5.Ke3 Qf4+ 6.Kd3 d5 7.Kc3 Qxe4 8.Kb3 Na6 9.a3 Qxa4+ (picture)10.Kxa4 Nc5+ 11.Kb4 a5+ 12.Kxc5 Ne7 13.Bb5+ Kd8 14.Bc6 [14.Nf3 b6#] 14...b6+ 15.Kb5 Nxc6 16.Kxc6 [16.Ka4 Nd4 17.Qf1 Bd7+ 18.Qb5 Bxb5#] 16...Bb7+ 17.Kb5 Ba6+ 18.Kc6 Bb7+ ½--½

- « Συχνά νομίζουμε ότι επειδή μελετήσαμε το 'ένα' γνωρίζουμε τα πάντα για το 'δύο', διότι 'ένα και ένα κάνουν δύο'. Ξεχάσαμε να μελετήσουμε το 'και' »

- « Often we think that because we studied "one" we know everything about "two", just because "one plus one equals two". We forgot to study "plus" »

Bertalanffy (Engelhardt, 1989)

Ευχαριστίες

Η παρούσα διατριβή εκπονήθηκε στο Εργαστήριο Ατμοκινητήρων και Λεβήτων του Τμήματος Μηχανολόγων Μηχανικών του ΕΜΠ στα πλαίσια της ερευνητικής μου ενασχόλησης από τον Οκτώβριο του 2008 έως το Σεπτέμβρη του 2013.

Πρώτα από όλα θα ήθελα να ευχαριστήσω τον καθηγητή κ. Εμμ. Κακαρά για την ανάθεση της εργασίας, τη δυνατότητα που μου έδωσε να συνεργαστώ με ερευνητικές ομάδες του εξωτερικού στα πλαίσια της ερευνητικής μου δραστηριότητας και τη συνεχή υποστήριξη και εμπιστοσύνη που έδειξε στο πρόσωπό μου όλα αυτά τα χρόνια.

Είμαι ακόμη υπόχρεος στο Δρ. Π. Γραμμέλη για τη συνεχή και συστηματική καθοδήγησή του, αλλά και την υποστήριξη και τη βοήθειά του σε οποιαδήποτε δυσκολία αντιμετώπισα.

Στους συναδέλφους Δρ. Νίκο Νικολόπουλο Δρ. Γρηγόρη Ίτσκο, Δρ. Μιχάλη Αγρανιώτη και Μανώλη Καραμπίνη είμαι επίσης ευγνώμων για τα ουσιαστικά σχόλια και τις παρατηρήσεις τους πάνω στο κείμενο.

Θα ήθελα επιπλέον να ευχαριστήσω όλα τα μέλη του Εργαστηρίου Ατμοπαραγωγών και ιδιαίτερα την κ. Προκόπου Μ. καθώς και τα μέλη του (πρώην) Ινστιτούτου Τεχνολογίας και Εφαρμογών Στερεών Καυσίμων (ΕΚΕΤΑ/ ΙΤΕΣΚ), και κυρίως την κ. Διάφα Α. και το Δρ. Ραμπίδη Η. για τη συνεργασία τους και την έμπρακτη συμπαράστασή τους στις δραστηριότητές μου.

Ευχαριστώ ακόμη θερμά τα υπόλοιπα μέλη της τριμελούς συμβουλευτικής επιτροπής κ. Κ. Αντωνόπουλο και κ. Κ. Ρακόπουλο για τις παρατηρήσεις τους με στόχο τη βελτίωση της παρούσας εργασίας.

Στους Έλληνες και ξένους συναδέλφους, με τους οποίους συνεργάστηκα στα πλαίσια της ερευνητικής μου εργασίας οφείλω επίσης θερμές ευχαριστίες. Θα ήθελα να ευχαριστήσω, ξεχωριστά το διδάκτορα του IFK, Χαρίτο Α. και τον κ. καθ. του, Scheffknecht, G, καθώς και τον κ. καθ. Leithner R. για τη βοήθειά τους με τα πειραματικά δεδομένα.

Επίσης, θα ήθελα να ευχαριστήσω θερμά τους διπλωματικούς φοιτητές Παπαφωτίου Δ., Ατσόνιο Κ., Μαλγαρινό Η., Βαρβέρη Ν. και τη Ζενέλη Μ. για την αγαστή συνεργασία μας.

Τέλος, οφείλω αρκετά στην οικογένειά μου και τη Βίβιαν Ξυνού για την αμέριστη συμπαράστασή τους σε όλες τις στιγμές της πολυετούς αυτής προσπάθειας μου.

Νικολόπουλος Αριστείδης

Αθήνα, Φεβρουάριος 2014

Σύμφωνα με απόφαση της ΓΣΕΣ στις (/ /20) της Σχολής Μηχανολόγων Μηχανικών του ΕΜΠ η παρούσα Διατριβή γίνεται αποδεκτή στην Αγγλική γλώσσα. Έχει επιπλέον προστεθεί ελληνική περίληψη με έκταση ίση περίπου με τον ένα τρίτο της έκτασης του αγγλικού κειμένου.

Η έγκριση της Διδακτορική Διατριβής από τη Σχολή Μηχανολόγων Μηχανικών του Εθνικού Μετσόβιου Πολυτεχνείου δεν υποδηλώνει αποδοχή των γνωμών του συγγραφέα (Ν. 5343/ 1932, Άρθρο 202)

Επιβλέπων Καθηγητής

Δρ. Εμμ. Κακαράς
Καθηγητής ΕΜΠ

Τριμελής Συμβουλευτική Επιτροπή

Δρ. Κ. Αντωνόπουλος
Καθηγητής ΕΜΠ

Δρ. Κ. Ρακόπουλος
Καθηγητής ΕΜΠ

Δρ. Εμμ. Κακαράς
Καθηγητής ΕΜΠ

Επταμελής Εξεταστική Επιτροπή

Δρ. Εμμ. Κακαράς
Καθηγητής ΕΜΠ

Δρ. Κ. Αντωνόπουλος
Καθηγητής ΕΜΠ

Δρ. Κ. Ρακόπουλος
Καθηγητής ΕΜΠ

Δρ. Π. Γραμμέλης
Ερευνητής Β΄ ΕΚΕΤΑ/ΙΔΕΠ

Δρ. Κ. Χ. Γιαννάκογλου
Καθηγητής ΕΜΠ

Δρ. Σ. Βουτσινάς
Αναπληρωτής Καθηγητής ΕΜΠ

Δρ. Ν. Νικολόπουλος
Ερευνητής Γ΄ ΕΚΕΤΑ/ΙΔΕΠ

Summary

Scope of the present thesis is to develop efficient in terms of computational cost and accurate Computational Fluid Dynamics (CFD) models for the simulation of Circulating Fluidized Beds (CFBs) in order to facilitate with emissions reduction. Therefore, the hydrodynamics as well as combustion and pollutants formation mechanisms are examined for CFB combustion. Moreover, the decarbonization of the energy production industry through the novel Calcium looping CO_2 capture process is investigated.

The fluidized bed reactors are well-known for their inherent efficient mixing, isothermal conditions and low emissions. However, they are governed by complicated multi – phase phenomena. Thus, their up – scaling and design optimization is difficult. CFD modeling can help towards these goals.

CFD modeling of CFBs is not trivial. The main difficulty arises from the fact that particles tend to clog and aggregate under fluidization conditions, and form meso – scale structures which significantly affect the induced drag force. In this thesis, proper incorporation of their effect in the numerical model is investigated. Moreover, except for the examination of the hydrodynamic phenomena, in this work reacting flows are investigated emphasizing on combustion emissions and carbon dioxide capture.

In this thesis, the state – of – the –art pure Eulerian approach is followed for the simulation of the multi – phase flow. In this numerical formulation the novelties of this work are integrated.

Initially, proper simulation of fluidized bed hydrodynamics is investigated. For the simulation of the sub – grid particulate structures an advanced drag scheme is formulated on the notion of the Energy Minimization Multi – Scale (EMMS) theory. The 3 – D model is validated against experimental data, in a simulation of the isothermal flow inside the riser of a 1.2 MW_{th} CFB combustor.

The combusting flow inside the aforementioned riser is also simulated, using the isothermal model as a platform that combustion and pollutants formation mechanisms are integrated. The developed CFD model is one of the first attempts to simulate the combusting flow inside fluidized beds. The results of the model were found to be in good agreement with experimental data for major species (O_2 and CO_2) and mean bed temperature.

Except for the simulation of the combusting flow inside the CFB unit, the NO_x / N_2O formation and destruction mechanisms are numerically investigated through a novel decoupled 3 – D model. Five species are tracked, i.e. NO_x, N_2O, CO, CNO and HCN, and the respective reaction kinetics are retrieved from literature. Two different reaction networks are investigated in order to conclude on whether HCN is released during char combustion or not. The result of the model that assumes no HCN release during char combustion agreed well with the experimental data for NO_x / N_2O. Therefore, this computational effective model can be used for minimization of large scale CFB NO_x / N_2O emissions.

Drastic CO_2 emissions reduction is a challenging task and carbon capture and storage commercially available technologies are expensive. Calcium looping is a promising post – combustion CO_2 capture technology that utilizes two coupled fluidized beds, i.e. the carbonator and the calciner. The carbonator is a novel CFB reactor in which CaO particles capture carbon dioxide.

In this work the flow inside a carbonator reactor is investigated. Initially the hydrodynamics of a small scale CFB cold model carbonator are simulated in a full – loop simulation using the validated EMMS drag scheme and a new stress model for the recirculation system. In the latter area of the loop, the particle loading is high and interparticle

friction forces prevail. A new stress model is formulated for this plastic regime, based on the Pitman-Schaeffer-Gray-Stiles yield criterion, and validated against a repose angle experiment prior to its implementation in the full loop simulation. The developed model for the full loop simulation of the carbonator succeeded in reproducing highly accurate results. The pressure distribution along the loop is predicted with a mean error less than 10%, while the error in the recirculation flux is less than 2%.

The carbonation reaction is also investigated through the simulation of a 10 kW_{th} CFB carbonator. However, for this unit, at the moment, there are no experimental data available for proper validation of a CFD model. Therefore, typical operating conditions are assumed while the actual geometry of the installation is respected. The results of the model agree, at least qualitatively with the observations of the experimenters.

In this thesis a lot of novelties were introduced. An EMMS scheme is formulated, meticulously tested and validated. This thesis is not the first to propose the multi – scale drag schemes, but one of the first attempts to formulate and implement it. Nowadays, the success of these efforts established these models as a *sine qua non* for proper simulation of FBs. Moreover, other researchers pointed out the importance of full – loop simulation but in this thesis for the first time the full – loop simulation was conducted with a theoretically sound stress model for the recirculation system. This stress model is formulated and validated in this thesis. Moreover, this thesis presents one of the few attempts to model combusting flow inside CFBs through CFD techniques. It also proposes a new, computationally effective approach for simulating the NO_x/N_2O. Finally, in this thesis, for the first time a carbonator CFB reactor is simulated.

Concluding, the CFD models developed and validated in this thesis are expected to comprise a useful and powerful tool for efficient scale – up and design optimization of CFB reactors towards emissions reduction and environmental friendly fossil fuels combustion.

Σύνοψη

Ο σκοπός αυτής της διατριβής είναι η ανάπτυξη τριδιάστατων υπολογιστικών μοντέλων υπολογιστικής ρευστοδυναμικής για τη μοντελοποίηση ρευστοποιημένων κλινών ανακυκλοφορίας με σκοπό την εφαρμογή τους για τη μείωση των εκπομπών από αυτές τις εγκαταστάσεις. Υπό αυτό το πρίσμα μελετήθηκε η υδροδυναμική καθώς και η καύση ορυκτών καυσίμων σε τέτοιες μονάδες. Επιπροσθέτως, μελετήθηκε και η δέσμευση του CO_2 μέσω της τεχνολογίας κύκλων ενανθράκωσης / ασβεστοποίησης (Calcium looping).

Οι αντιδραστήρες ρευστοποιημένης κλίνης προσφέρουν αποδοτική ανάμιξη των αντιδρώντων, ομοιόμορφο πεδίο θερμοκρασιών και χαμηλές εκπομπές ρύπων. Ωστόσο, η πολυπλοκότητα των πολυφασικών ροών δυσκολεύει το σχεδιασμό μονάδων μεγάλης κλίμακας και τη βελτιστοποίηση της λειτουργίας τους. Τα μοντέλα υπολογιστικής ρευστοδυναμικής μπορούν να αντιμετωπίσουν αυτό το πρόβλημα.

Η μοντελοποίηση των ρευστοποιημένων κλινών ανακυκλοφορίας δεν είναι εύκολη. Η βασική δυσκολία έγκειται στο φαινόμενο του σχηματισμού σωματιδιακών συμπλεγμάτων, τα οποία είναι δομές μεσο – κλίμακας που επηρεάζουν σημαντικά την οπισθέλκουσα δύναμη. Σε αυτή τη διατριβή, εξετάστηκε η μοντελοποίηση της επίδρασης τέτοιων δομών μέσω κατάλληλων υποπλεγματικών μοντέλων. Επίσης, πλην της υδροδυναμικής, διερευνήθηκε και η μοντελοποίηση της μεταφοράς θερμότητας και των χημικών αντιδράσεων εντός των κλινών δίνοντας έμφαση στο σχηματισμό ρυπαντών και τη δέσμευση του CO_2.

Αρχικά, διερευνήθηκε η ορθή μοντελοποίηση της υδροδυναμικής των μονάδων ρευστοποιημένης κλίνης. Για τη μοντελοποίηση των υποπλεγματικών σωματιδιακών δομών μεσο – κλίμακας αναπτύχθηκε ένα εξελιγμένο μοντέλο Ελαχιστοποίησης Ενέργειας Μέσο – Κλιμάκων (Energy Minimization Multi – Scale, EMMS). Το τριδιάστατο μοντέλο επαληθεύτηκε μέσω πειραματικών δεδομένων για την ισοθερμοκρασιακή ροή εντός του αγωγού ανόδου μιας μονάδας ρευστοποιημένης κλίνης ανακυκλοφορίας καύσης 1.2 MW_{th} CFB.

Επίσης, σε αυτή τη διατριβή μοντελοποιήθηκε η καύση λιγνίτη στην προαναφερθείσα μονάδα. Οι μηχανισμοί της καύσης και τις μεταφοράς θερμότητας όπως και βασικές χημικές αντιδράσεις ενσωματώθηκαν στο υδροδυναμικό μοντέλο. Το μοντέλο που αναπτύχθηκε, είναι μια από τις πρώτες προσπάθειες διεθνώς για την τριδιάστατη μοντελοποίηση της καύσης εντός ρευστοποιημένης κλίνης με τεχνικές υπολογιστικής ρευστοδυναμικής. Τα αποτελέσματα του μοντέλου επέδειξαν καλή συμφωνία με τα πειραματικά δεδομένα για τη συγκέντρωση του O_2 και του CO_2 και για τη μέση θερμοκρασία λειτουργίας της κλίνης.

Εκτός από τη μοντελοποίηση της καύσης στη ρευστοποιημένη κλίνη μοντελοποιήθηκαν και οι εκπομπές NO_x / N_2O μέσω κατάλληλου τριδιάστατου απεπλεγμένου μοντέλου. Πέντε στοιχεία μοντελοποιήθηκαν, NO_x, N_2O, CO, CNO και HCN, και οι αντίστοιχοι ρυθμοί των αντιδράσεων βρέθηκαν από τη βιβλιογραφία. Εξετάστηκαν δύο δίκτυα αντιδράσεων που διαφοροποιούνται στην απελευθέρωση HCN κατά τη διάρκεια της καύσης του εξανθρακώματος. Τα αποτελέσματα του μοντέλου που δεν υποθέτει απελευθέρωση HCN κατά τη διάρκεια της καύσης του εξανθρακώματος επέδειξε καλή συμφωνία με τις πειραματικές μετρήσεις για τα NO_x / N_2O. Ως εκ τούτου, αυτό το επαληθευμένο μοντέλο με το μικρό υπολογιστικό κόστος μπορεί να χρησιμοποιηθεί για την ελαχιστοποίηση των εκπομπών αυτών των αερίων από μεγάλης κλίμακας εγκαταστάσεις.

Η δραστική μείωση των εκπομπών CO_2 είναι αρκετά δύσκολή και οι εμπορικά διαθέσιμες τεχνολογίες δέσμευσης και αποθήκευσης είναι κοστοβόρες. Η τεχνολογία κύκλων ενανθράκωσης / ασβεστοποίησης που χρησιμοποιεί συζυγείς κλίνες, τον ενανθρακωτή και τον ασβεστοποιητή, είναι μια πολλά υποσχόμενη νέα τεχνολογία δέσμευσης. Ο

αντιδραστήρας ενανθράκωσης είναι ένας νέος αντιδραστήρας εντός του οποίου δεσμεύεται το CO_2 από σωματίδια CaO.

Σε αυτή τη διατριβή διερευνήθηκε η ροή εντός του ενανθρακωτή. Αρχικά η υδροδυναμική ενός κρύου μοντέλου μοντελοποιήθηκε λαμβάνοντας υπ' όψη το σύστημα ανακυκλοφορίας και εφαρμόζοντας το μοντέλο οπισθέλκουσας EMMS και ένα νέο μοντέλο για την κοκκώδη συνεκτικότητα που εφαρμόστηκε στο σύστημα ανακυκλοφορίας. Στο σύστημα ανακυκλοφορίας, οι ενδο-σωματιδιακες δυνάμεις τριβής κυριαρχούν. Ένα νέο μοντέλο αναπτύχθηκε, βασιζόμενο στο κριτήριο διαρροής των Pitman-Schaeffer-Gray-Stiles, και επαληθεύτηκε μέσω της μοντελοποίησης ενός πειράματος μέτρησης της γωνίας απόθεσης κοκκώδους υλικού. Τα αποτελέσματα του μοντέλου που αναπτύχθηκε για την πλήρη μοντελοποίηση της υδροδυναμικής του ενανθρακωτή αποδείχτηκαν μεγάλης ακρίβειας. Η κατανομή της πίεσης προλέχθηκε με μέσο σφάλμα μικρότερο του 10%, ενώ το σφάλμα στην ανακυκλοφορία είναι μικρότερο του 2%.

Η αντίδραση ενανθράκωσης διερευνήθηκε μέσω της μοντελοποίησης ενός αντιδραστήρα ρευστοποιημένης κλίνης ενανθράκωσης 10 kW_{th}. Ωστόσο, για αυτή τη μονάδα δεν υπάρχουν διαθέσιμα πειραματικά δεδομένα κατάλληλα για την επαλήθευση ενός μοντέλου υπολογιστικής ρευστοδυναμικής. Ως εκ τούτου, για τη μοντελοποίηση της μονάδας αν και η πραγματική γεωμετρία ελήφθη υπ' όψη, για τις συνθήκες λειτουργίας θεωρήθηκαν τυπικές τιμές που αναφέρονται στη βιβλιογραφία. Τα αποτελέσματα του μοντέλου συμφωνούν ποιοτικά με τις παρατηρήσεις των πειραματιστών.

Σε αυτή τη διατριβή διατυπώθηκαν και διερευνήθηκαν μια σειρά από καινοτομίες. Αν και αυτή δεν είναι η πρώτη φορά που ένα μοντέλο EMMS διαμορφώθηκε και διερευνήθηκε, αλλά μια από τις πρώτες εφαρμογές του, η επιτυχία τέτοιων εφαρμογών οδήγησε στην καθιέρωση αυτής της μεθοδολογίας. Επίσης, αν και άλλοι ερευνητές είχαν ασχοληθεί με τη μοντελοποίηση του συστήματος ανακυκλοφορίας των ρευστοποιημένων κλινών, σε αυτή τη διατριβή για πρώτη φορά διερευνήθηκε η ορθή μοντελοποίηση αυτής της περιοχής με κατάλληλο μοντέλο για τη κοκκώδη συνεκτικότητα. Επίσης, η μοντελοποίηση της καύσης που πραγματοποιήθηκε, είναι μια από τις λίγες δημοσιευμένες προσπάθειες μοντελοποίησης τέτοιων εγκαταστάσεων μέσω τεχνικών CFD. Επιπροσθέτως, στην παρούσα διατριβή διατυπώθηκε μια απεπλεγμένη μεθοδολογία για τη μοντελοποίηση των εκπομπών NO_x/N_2O. Τέλος, σε αυτή την εργασία μοντελοποιήθηκε για πρώτη φορά ένας ενανθρακωτής.

Κλείνοντας, τα μοντέλα υπολογιστικής ρευστοδυναμικής που αναπτύχθησαν και επαληθεύτηκαν σε αυτή τη διατριβή μπορούν να χρησιμοποιηθούν για τον καλύτερο σχεδιασμό ρευστοποιημένων κλινών ανακυκλοφορίας και τη μείωση των εκπομπών από την καύση ορυκτών καυσίμων.

PREFACE

My name is Aristeidis Nikolopoulos and I studied Mechanical Engineering in the National Technical University of Athens (NTUA) and currently I am a PhD candidate of NTUA. My major field of expertise is the numerical investigation of Circulating Fluidized Beds (CFBs), and Computational Fluid Dynamics (CFD) in general.

My diploma thesis in NTUA was undertaken in collaboration with IFK (University of Stuttgart, USTUTT) and focused on experimental investigation of fluidized bed. The hydrodynamics of Dual Fluidized Bed were studied through plexi – glass models and special focus was given on the fluidization phenomena in the returning system of these units and in the efficient coupling of Fluidized Beds. Non mechanical valves (e.g. L-valve) were experimentally tested, in transparent cold models, and the complicated nature of particles fluidization was investigated.

In 2006, I started working as a research mechanical engineer in Centre for Research and Technology Hellas / Institute of Solid Fuels Technology and Applications (CERTH/ISFTA). Initially, I worked in the EU Funded project CFB800 (contract: RFCR-CT-2005-00009) that dealt with pure Eulerian CFD modeling of large scale CFB boilers. While undertaking this CFD task, I understood that conventional CFD models clearly fail to capture the governing mechanisms of fluidization when coarse meshes are applied.

After this realization, I was one of the forerunners in the development of advanced sub – grid models. At that time, Energy Minimization Multi – Scale (EMMS) models were a promising solution for accurate simulations when coarse grids are applied. In collaboration with diploma thesis students an advanced EMMS scheme was formulated and successfully implemented for an iso - thermal simulation of a 1.2 MW_{th} CFB combustor (CFBC). The success of the EMMS scheme developed in this thesis and the EMMS schemes developed by other authors, made their implementation a *sine qua non* for effective simulation of CFB risers.

The aforementioned iso – thermal model was coupled with simple combustion and pollutants formation / destruction mechanisms. The integrated model was implemented in the simulation of the combusting flow of the 1.2 MW_{th} CFBC unit. For the NO_x / N_2O simulation, a decoupled approach was adopted and a model was formulated based on published reaction kinetics data.

After the successful implementation of EMMS theory, the scientific community of CFB modeling turned its attention to full – loop simulation. At that time, I started working in a European Union (EU) funded project for CO_2 capture with calcium looping process that utilizes two interconnected fluidized bed (CAL-Mod, contract: RFCS-CT-2010-0013). The coupling of Fluidized Beds (FBs) was my diploma thesis theme, and I was aware of the complicate nature of governing physics inside the re-circulation system. In collaboration with a diploma thesis student, a sophisticated stress model was formulated and validated for multi – phase flows with very high particle loading. This model, along with the EMMS scheme developed, was applied in a full – loop simulation of IFK's CFB carbonator cold model. Not only was the full – loop of a CFB unit modeled but also, for the first time, the model was validated with available experimental data for the pneumatic valve.

Concluding, this work succeeded in developing a comprehensive 3-D CFD model for full – loop iso - thermal simulations and in developing combusting / reacting flow models for CFBs. Such models can be used for CFB design optimization and emissions reduction.

At different stages of this work, results were published in journals and conferences. A list of publications, that are relevant with this thesis, is given below:

Book Chapters

1. CFD Applications in Steam Boilers, Engineering Applications of Computational Fluid Dynamics, International Energy and Environment Foundation. N. Nikolopoulos, A. Nikolopoulos, E. Karampinis, M. Agraniotis, P. Grammelis, E. Kakaras, 2011, ISBN-13: 978-1466231061, ISBN-10: 1466231068, Vol 1, pp. 23-83.

International Journals

1. A. Nikolopoulos, D. Papafotiou, N. Nikolopoulos, P. Grammelis, E. Kakaras. An advanced EMMS scheme for the prediction of drag coefficient under a 1.2 MW_{th} CFBC isothermal flow—Part I Numerical formulation. Chemical Engineering Science 65, 4080–4088, 2010. (cited: *29* times)

2. A. Nikolopoulos, K. Atsonios, N. Nikolopoulos, P. Grammelis, E. Kakaras. An advanced EMMS scheme for the prediction of drag coefficient under a 1.2 MW_{th} CFBC isothermal flow—Part II Numerical implementation. Chemical Engineering Science 65, 4089–4099, 2010. (cited: *17* times)

3. Atsonios, K., Nikolopoulos, A., Karellas, S., Nikolopoulos, N., Grammelis, P., Kakaras, E. Numerical investigation of the grid spatial resolution and the anisotropic character of EMMS in CFB multiphase flow. Chemical Engineering Science 66, 3979-3990, 2011.(cited: 6 times)

4. A. Nikolopoulos, N. Nikolopoulos, N. Varveris, S. Karellas, P. Grammelis, E. Kakaras. Investigation of proper modeling of very dense granular flows in the recirculation system of CFBs. Particuology 10 (6), pp 699-709, 2012 (cited: *4* times)

5. A. Nikolopoulos, N. Nikolopoulos, , A. Charitos, P. Grammelis, E. Kakaras, A. R. Bidwe, G. Varela. High-resolution 3-D full - loop simulation of a CFB carbonator cold model. Chemical Engineering Science 90, pp 137-150, 2013 (cited: *7* times)

6. A. Nikolopoulos, I. Malgarinos, N. Nikolopoulos, P. Grammelis, S. Karrelas, E. Kakaras. A decoupled approach for NO_x–N_2O 3-D CFD modeling in CFB plants. Fuel 115, pp 401-415, 2014 (cited: 0 times)

Conferences and workshops

1. A. Nikolopoulos, I. Rampidis, N. Nikolopoulos, P. Grammelis, E. Kakaras. Numerical investigation of 3-D transient combusting flow in a 1.2MW_{th} pilot power plant. 20th International Conference on Fluidized Bed Combustion, Xi'an China, 839-845, 2009. (cited: 7 times)
2. A. Nikolopoulos, N. Nikolopoulos, N. Varveris, S. Karellas, E. Kakaras. Investigation of appropriate modeling of the internal friction of very dense particle flows in circulating fluidized bed systems, 7th National Congress on “Fluid Flow Phenomena" Conference, Thessaloniki, 117-124, 2010.
3. A. Nikolopoulos, I. Rampidis, N. Nikolopoulos, P. Grammelis, E. Kakaras. CFD modeling of NO_x formation in a pilot CFBC power plant. Global Conference on Global Warming 2009. Turkey July 8-9, Paper No: GCGW-09-581, 2009.
4. A. Nikolopoulos, D. Papafotiou, K. Atsonios, N. Nikolopoulos, P. Grammelis, E. Kakaras. EMMS Model Development and Application Coupled with CFD Techniques in a 1.2 MW_{th} CFBC Isothermal Flow. Efficient and clean coal technologies, Moscow Russia October 2009.

5. Rampidis, I., Nikolopoulos, A., Koukouzas, N., Grammelis, P., Kakaras, E. Optimization of computational performance and accuracy in 3-D transient CFD model for CFB hydrodynamics predictions (2007) AIP Conference Proceedings, 936, pp. 452-455.
6. A. Nikolopoulos, I. Rampidis, P. Grammelis, E. Kakaras. Simulation of the multiphase flow in Circulating Fluidized Beds and investigation of grid density effect on accuracy. 6th National Congress on “Fluid Flow Phenomena" Conference, Kozani, 2008.
7. A. Nikolopoulos, N. Nikolopoulos, E. Karampinis, P. Grammelis, E. Kakaras. A Comprehensive Numerical Approach of CFB Units Modeling By Means Of CFD, in ICAE, Suzhou, China 2012, pp 2648-2657.
8. A. Nikolopoulos, N., Nikolopoulos, A., Charitos, P. Grammelis, E. Kakaras, A.R. Bidwe, G. Varela, M. Zieba, G. Scheffknecht. Numerical Investigation and Experimental Validation of an Isothermal CFD Model Developed for a CFB Carbonator, in the proceedings of the 21st international conference on Fluidized Bed Combustion, pp 1042-1049
9. A. Nikolopoulos, N. Nikolopoulos, P. Grammelis, E. Kakaras. PSD incorporation in full - loop CFD modeling of CFBs in the proceedings of the 21st international conference on Fluidized Bed Combustion, pp 875-882
10. A. Nikolopoulos, K. Atsonios, N. Nikolopoulos, P. Grammelis, E. Kakaras An advanced thermodynamic model for the simulation of the Calcium Looping Process coupled with CFD model in 2nd International Conference on Chemical Looping, 26-28 September 2012, Darmstadt, Germany
11. K. Atsonios, I. Vorrias, A. Nikolopoulos, N. Nikolopoulos, P. Grammelis, E. Kakaras. Calcium Looping for CO_2 capture from a Lignite fired Power Plant. Presented in the 9th European Conference on Coal Research & its Applications (ECCRIA 9), September 10-12, 2012, University of Nottingham
12. A. Nikolopoulos, N. Nikolopoulos, K. Atsonios, P. Grammelis, E. Kakaras. Coupling of fluid dynamics and thermodynamic tools for the simulation of the Calcium Looping process for CO_2 capture in the 37th International Technical Conference on Clean Coal & Fuel Systems. 3-7 June 2012, Clearwater, FL, USA.
13. A. Nikolopoulos, First results from the full-loop 3D simulation of a CFB carbonator of IFK (Stuttgart) presented in the 61st IEA-FBC workshop in Salerno (Italy), October, 2010. (iea-fbc.org)
14. A. Nikolopoulos. 3-D CFD simulation of a CFB carbonator cold model, presented in the 64th IEA-FBC workshop in Naples (Italy), June 2012. (iea-fbc.org)

In 2012, I became an alternative member of the International Energy Agency – Fluidized Bed Conversion (IEA-FBC) executive committee, representing Greece.

Table of Contents

1. INTRODUCTION

1.1 State – of – the – art in Fluidized Bed Technology

This work focuses on CFD (Computational Fluid Dynamics) simulation of CFB (Circulating Fluidized Bed) units. CFB technology has been rapidly developing in the last decades. The main application of CFB technology is in power generation industry. In this combustion mode except for air and fuel, sand – like inert – material is introduced to the chamber. The elevated volume fraction of inert – material facilitates with achieving homogeneous conditions inside the bed, low temperature combustion and elevated residence time for the fuel. Therefore CFB boilers (Figure 1.1), in contrast to Pulverized Fuel (PF) boilers, present fuel flexibility, high efficiency and plant availability. Moreover, in light of cost efficient and reliable emissions reduction, CFB technology presents inherently low NO_x and in situ desulphuration. For these reasons, one of the most important applications of Fluidized Bed (FB) technology, is the combustion of fossil fuels. The effective design of new generation advanced Circulating Fluidized Bed combustors (CFBC) necessitates the development of new design and optimization tools.

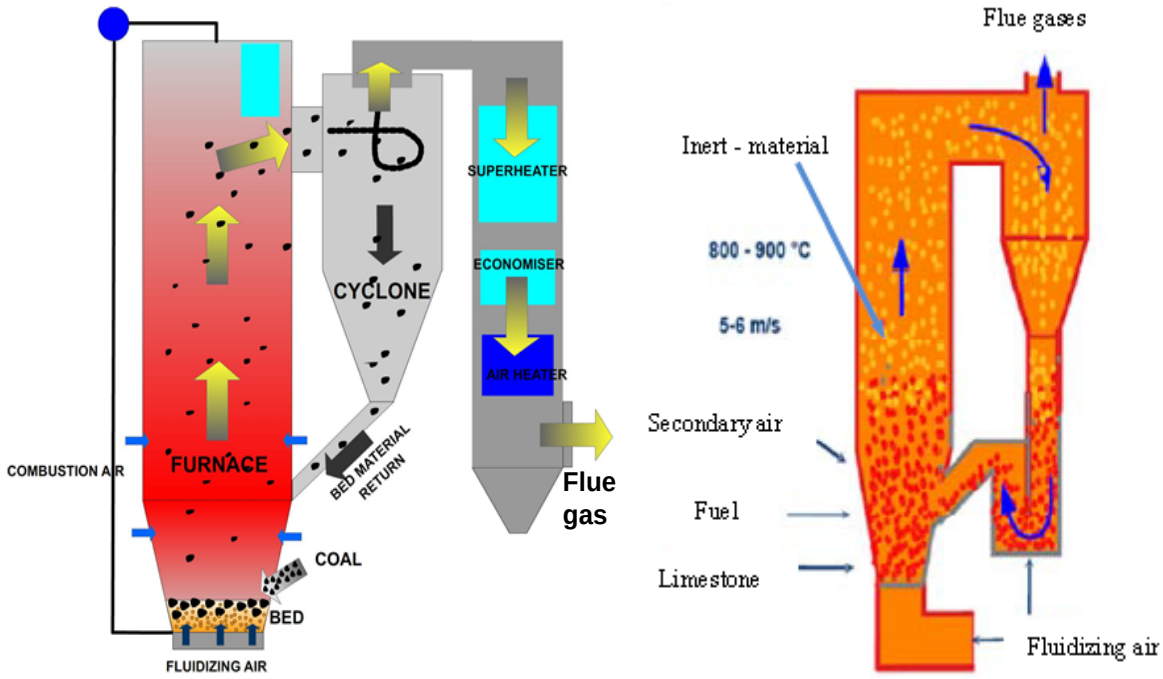

Figure 1.1 CFB combustion technology

Fluidized Bed (FB) technology is not only utilized for fossil fuels combustion. Fluid Catalytic Cracking (FCC) is the most known application of FBs except after CFBCs. Moreover, FBs are currently used in novel processes for the drastic reduction of worldwide CO_2 emissions. Post-combustion, calcium looping (CaL) CO_2 capture technology (Figure 1.2) is a potential solution for CO_2 mitigation, applicable in both new and existing power plants. This technology, proposed by Shimizu et al., 1999, utilizes a Dual Fluidized Bed (DFB) system. Two CFB reactors are inter-connected in this process; i.e. a carbonator and a calciner that both typically operate under the Fast Fluidization (FF) regime. The carbonator is a novel reactor and proper up-scaling to industrial scale will face a lot of difficulties since there is no relative previous experience. Specific technical issues, such as solid mixing in an industrial scale carbonator can hinder the up-scaling procedure and their experimental investigation is of high cost.

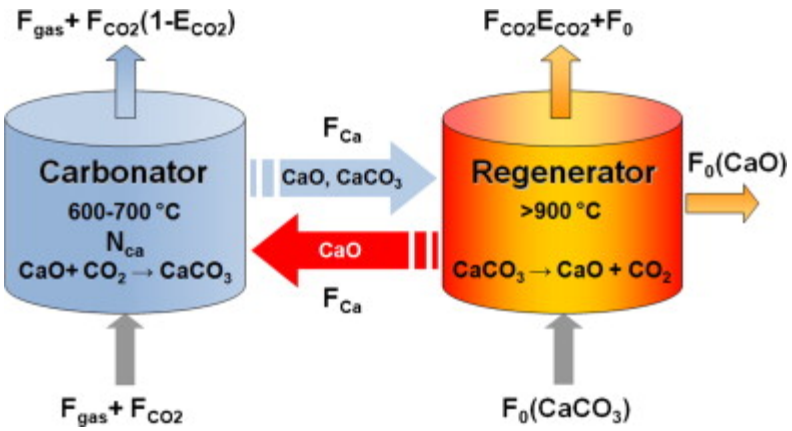

Figure 1.2 Calcium looping process (Charitos et al., 2010[a])

Nowadays trend to scale up CFB boilers (Figure 1.3) and the necessity of deeper understanding of fluidization mechanisms brings forward new challenges regarding the accurate numerical simulation of the hydrodynamic and reacting flow behavior of the fluidized material. CFD modeling can play a very significant role in the design optimization of such CFB reactors, since it can predict the complicated flow characteristics that govern their operation, with the minimum economic cost. This is attributed to their inherent ability to meticulously address complicated issues, such as inert material local concentration, reactants mixing efficiency and temperature distribution. Therefore, the numerical investigation of the multi – phase flow is a *sine qua non* for efficient, in terms of CPU cost, and effective, with respect to accuracy, design optimization of CFB reactors.

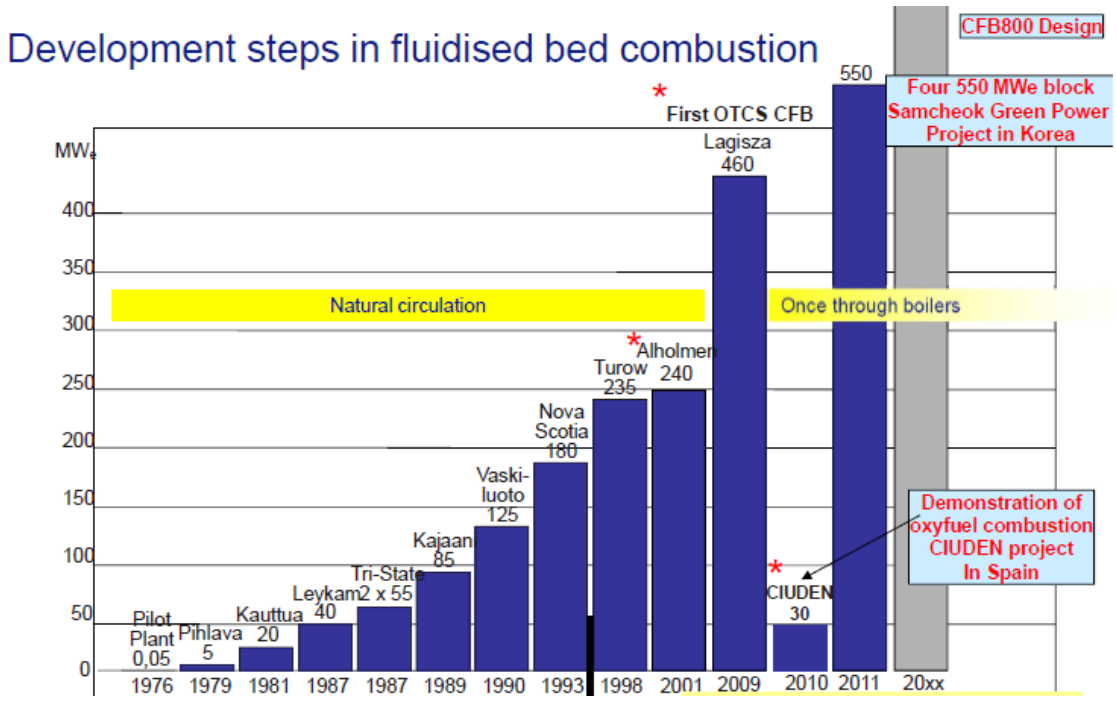

Figure 1.3 Scale – up of CFBC units (Hämäläinen, 2011)

1.2 State – of – the – art of CFD modeling of CFBs

There is a variety of simulation techniques for CFB modeling. The most known is the Two – Fluid –Model (TFM) that treats gas and solids as interpenetrating continua. This pure Eulerian approach, has been investigated a lot and has proved its superiority over the

conventional particle in cell methodologies that treat particles in a Lagrangian fashion. The main reason behind this is that in CFBs, particle loading is high and the Lagrangian formulation proved to be less efficient in the accurate simulation of particle - particle interactions.

The Lagrangian approach is not yet fully abolished. The new, Multi - Phase Particle - In - Cell (MP-PIC) methodology, see Patankar and Joseph, 2001 and Andrews and O'Rourke, 1996, tracks particles in a Lagrangian frame but incorporates some features of the TFM approach (Sundaresan, 2011). Nowadays, the MP-PIC formulation is gaining ground and it is also available in CPFD® and Fluent® platforms. Such models can easily handle Particle Size Distribution (PSD), can track a lot of particle parcels, rare events can be studied and boundary conditions in the wall region can be easily derived and straightforwardly applied (Sundaresan, 2011). On the other hand the Two – Fluid - Model (TFM) formulation has been thoroughly examined and it is still considered the state-of-the-art methodology for CFBs modeling. Nonetheless, the accuracy of the TFM and its high computational cost should be evaluated and optimized.

Most of the numerical studies of CFB's multiphase flow in the recent literature adopt the Eulerian TFM. However, except for MP-PIC, an alternative option is the Direct Numerical Simulation (DNS, Ma et al., 2009), where solid phase is treated separately by equations of classical mechanics and fluid's motion is simulated using Navier - Stokes equations. However, due to the fact that the number of solid particles in a reactor is of an order of magnitude of trillion, this methodology is extremely CPU expensive. Hence, DNS currently can nowadays be applied only in cases, where the solid particles are an order of magnitude of 10^3 and not 10^{12} as reported by Ma et al., 2006.

The majority, of published research activities focused in CFD modeling of CFBs, investigates isothermal flows. However, there are some exceptions; (Gungor, 2008[a, b], 2010; Gungor and Eskin, 2008[a, b]) with their CFD model that incorporates some semi – empirical characteristics and Zhou et al., 2011 as well as Nikolopoulos et al., 2009 with their purely CFD models, simulated the combusting flow inside CFB boilers, using isothermal models as a platform where energy and species equations as well as reaction rates are introduced.

The research activities are still focusing on isothermal TFM modeling, because of the complicated hydrodynamics of the multiphase (gas and inert - material) flow inside CFBs. Thus, even isothermal modeling of CFBs is not trivial. Ge et al., 2008 and Wang et al., 2008, reported that the major difficulties are correlated with the proper modeling of the momentum exchange between the co-existing phases (gas and inert material).

The main source of numerical inaccuracy originates from the closure models used for the calculation of drag force induced to solid particles by the fluidizing gas. Ge et al., 2008 report that conventional drag models (e.g. Gidaspow's (Gidaspow, 1994), or Wen and Yu (Wen and Yu, 1966)) assume homogeneous conditions inside a control volume, which in general, does not represent the actual conditions. The main reason is that solid particles under FF conditions tend to clog and aggregate, forming the so called "clusters" (Gu and Chen, 1998). Particle clusters are characterized as meso – scale structures (Wang and Li, 2007), because their size is bigger than the micro – scale which is correlated with particle diameter and the macro – scale that is correlated with the basic geometrical features of the CFB unit (see Table 1.1).

The physical quantity, mostly affected by the existence of such complex structures in the case of fluidized beds, is the momentum exchange between the gas and solid phases. The drag force induced by the fluidizing gas to particles is severely lowered if particles are clogged when compared with the drag force induced to the same particles being homogeneously dispersed (Zhang et al., 2011). Thus, the assumption of homogeneous conditions inside a

control volume, that every conventional drag model makes, may result in significant numerical error as stated by Ge et al., 2008; Wang et al., 2008 and Hartge et al., 2009, if meso – scale structures exist.

	Micro - scale[a]	Meso - scale[b]	Macro - scale
Length	Mean free path for particles l_p $l_p = \frac{1}{6\sqrt{2}}\left(\frac{d_p}{\varepsilon_s}\right)$ - 3 mm, for ε_s = 0.01; - 0.3 mm, for ε_s = 0.1;	Mean cluster diameter d_{cl} $d_{cl} = d_p + (0.027 - 10d_p)\varepsilon_s + 32\varepsilon_s^6$ - 0.5 mm, for ε_s = 0.01; - 2.7 mm, for ε_s = 0.1;	Apparatus characteristic Length (or diameter). - 0.1 ~ 1 m for lab scale - order of meters for industrial scale
Velocity	Fluctuation velocity $\sqrt{3\Theta_s}$ range: 0.01 ~ 1 m/s	Cluster velocity around 1 m/s	Superficial gas velocity. For CFB, around 5 m/s
Time or frequency	Particles collision frequency $f_c = 6.77\left(\frac{d_p}{\varepsilon_s}\right)\sqrt{\Theta_s}$ range: 10 ~ 1000 Hz	Cluster breakup frequency, around 20 Hz	Mean residence time t_{res} for gas (~ seconds) $t_{res} = L_H / U_o$ for solid (~ minutes) $t_{res} = TSI / G_s$

[a] Calculations made via kinetic theory correlations (Gidaspow, 1994), [b] (Gu and Chen, 1998)

Table 1.1 Characteristic scales (Wang and Li, 2007) for circulating fluidized bed particles (d_p = 250, ρ_s = 2500 kg / m^3)

Ge et al., 2008 as well as Zhang and VanderHeyden, 2001 reported that these problems may be resolved with the application of dense grids. The proper dimensionless grid size, l_r (equivalent cell length to particle diameter) has been reported to be estimated around 20 (Nikolopoulos et al., 2010[a]). However, this statement is not yet proved and new research activities brought forward evidence that contradict such statement. Lu et al., 2009 showed that for a doubly periodic 2-D domain the conventional drag scheme (Gidaspow's) reached grid independency for l_r of 10 as depicted in Figure 1.4. Moreover, in this novel work, the EMMS scheme was tested and found to be grid independent for larger cells. It's interesting that the grid independent solutions of the two drag models do not coincide. Although this work was conducted in two dimensions, simplification that is questionable in a CFB unit simulation (Myöhänen et al., 2006; Nikolopoulos et al., 2010[a]; Sundaresan, 2011), the main conclusions can be extrapolated in the three-dimensional space. Of course, specific values for the l_r ratio e.g. 10 or 20 cannot be that easily extrapolated for 3-D simulations, even if it is proved that they provide grid independent solutions in a 2-D case. These values may be smaller in a 3-D

case but the fact that a grid independent solution can be achieved by the two models seems to be valid. This is due to the fact that the induced meso – scale structures present the same qualitative trends both for 2-D and 3-D simulations. It is interesting that the same kind of speculations have been reported for MP-PIC methodology (Benyahia and Sundaresan).

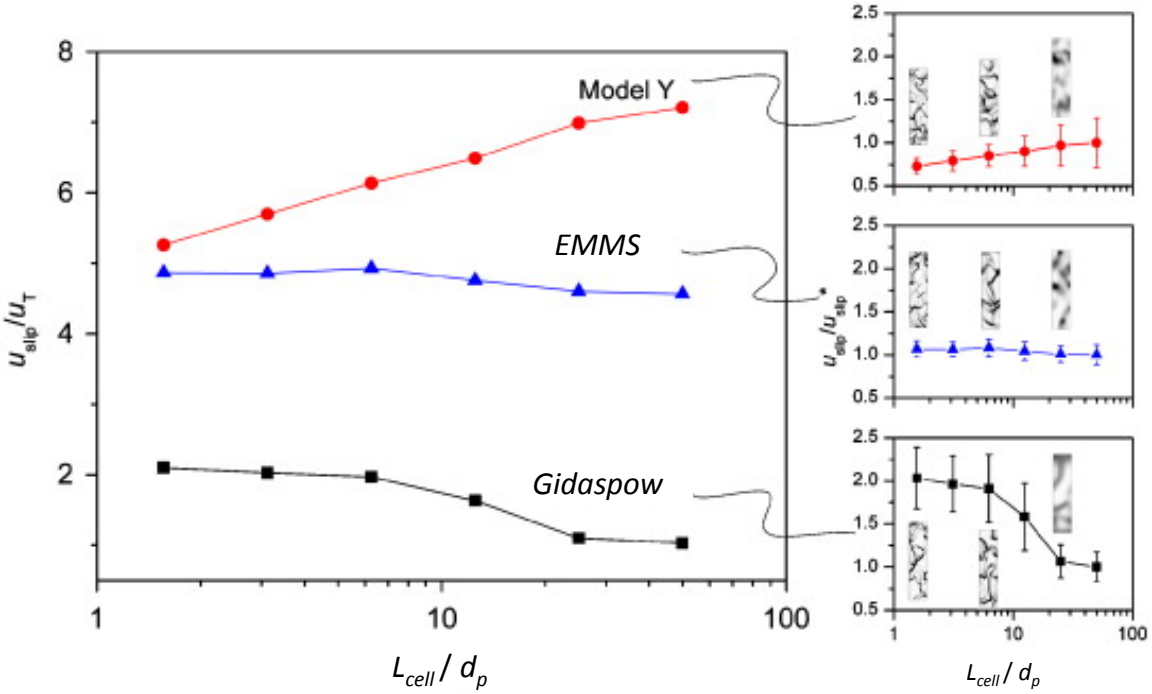

Figure 1.4 Grid independency under various drag schemes (Lu et al., 2009)

On the other hand, the validity of high resolution simulations with ratios less than 10 has been questioned (Sundaresan, 2011). The fine structures that these grid resolutions reproduce may not correspond to the underlying physical reality but are a consequence of the continuum treatment of solids (Sundaresan 2011).

Indeed, the non-continuum character of solid particles may put a barrier to high resolution simulations in the Eulerian frame. Additional difficulties are present since the geometrical features of granules put further limitations. In a hypothetical cubic control volume with edge smaller than the particle diameter the volume fraction of particles in it should be able to reach up to 1. However, in the TFM approach the packing limit correctly puts a barrier in the densification with particles of the control volume. This is an extra reason for the author of this work to believe that the TFM may not be valid in very small control volumes.

The CFD simulations adopting high grid resolution present high theoretical interest. However, the technological interest lies in the other edge, of the very coarse numerical cells. In this case, the characteristic of the EMMS scheme to achieve grid independent solution under coarser grid resolutions (Lu et al., 2009) is of high importance, since dense numerical grids cannot be implemented in large scale installations, due to the existing limitations in the affordable computational resources. Therefore, conventional drag models, such as that by Gidaspow, 1994, are regarded as insufficient for the prediction of large scale CFB.

1.3 Conventional TFM modeling of large scale CFBs

The term “conventional TFM modeling” refers to TFM CFD modeling of a CFB riser under the TFM formulation and simple drag models, such as Gidaspow, 1994 and Wen and Yu, 1966 that do not incorporate particle clustering effects. Such models are mainly tested in small or semi-industrial CFBs and the respective results exhibit adequate accuracy when high

resolution numerical grids are applied (Zhang and VanderHeyden, 2001). However, studies that confirm the latter statement were performed in 2-D.

High – resolution numerical grids, though, cannot be applied to industrial scale CFBs since their application dramatically increases the computation cost and RAM needs to an excessive level that cannot be efficiently copped with state-of-the-art processing equipment. A very good example of conventional TFM modeling of a large scale unit is found in Zhao et al., 1997. Another example is the CFD simulation of CFB800 performed in the frame of this thesis. CFB800 is an 800 MW_{th} supercritical CFBC designed from Foster Wheeler. The volume of this enormous, under design, boiler is more than 20.000 m^3, and it is the bigger CFB unit ever designed. The applied isothermal CFD model that deals with the hydrodynamic behavior of the sand – like inert material, is identical to the one reported by Rampidis et al., 2007, while the conventional drag scheme of Gidaspow was used.

The developed model was efficiently parallelized, and in order to further reduce computational cost, only half of the riser was modeled as CFB800 riser is symmetric. Nevertheless, if the proposed by Ge et al., 2008 and Nikolopoulos et al., 2010[a] grid density is applied on CFB800 (l_r = 20), the produced grid will have more than 30 billion cells. The computational cost for such grid is prohibitive. Thus, the grid resolution for CFB800 modeling was significantly lower. Three different unstructured grids were constructed with full respect to the actual geometry. Initially a very coarse grid with 446,724 elements (l_r = 833), was tested in order to obtain an initial solution. Moreover, two denser grids, with 1.36 (l_r = 572) and 2.91 (l_r = 444) million cells respectively, were constructed to obtain a more accurate solution and estimate grid density effect.

After reaching inventory dynamic equilibrium, proper period time for averaging was evaluated using power spectrum analysis. Twenty seconds was found to be an adequate time period for averaging, as also reported by Kallio, 2006. In generally the developed CFD model captured typical CFB patterns such as core-annulus flow pattern and clusters movement. These patterns were captured at least qualitatively even when the coarser grid was used. In Figure 1.5 a comparison of the results derived with the three different grids are compared for a height of 1 m.

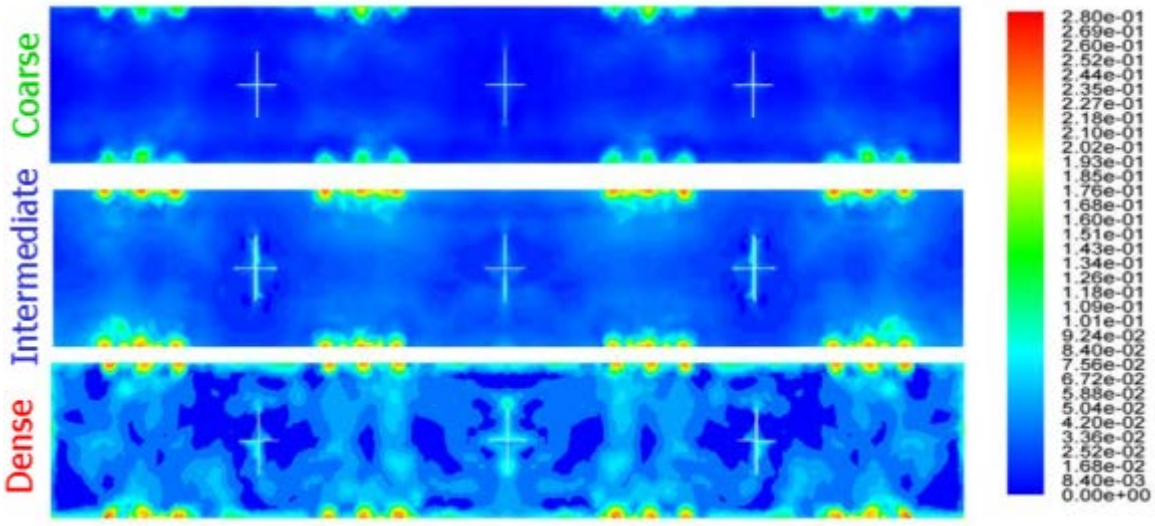

Figure 1.5 Inert material time averaged volume fraction predictions for 1m height of CFB800 under three different grid resolutions.

In each contour of Figure 1.5, inert-material mean volume fraction (averaged for 20 seconds) is depicted. Figure 1.5 points out that, albeit coarse grid qualitatively captures the main flow patterns in the bed, clearly under predicts inert material volume fraction. The prediction of the denser grid, having an averaged cell size that corresponds to l_r = 444, is considered to be more accurate than the coarser grids results, as Foster Wheeler's classified data imply. However, grid independency was not achieved, and further densification of the applied grid will most likely reproduce significantly different results than the dense grid.

Not reaching a grid independent solution is raising questions about results trustworthiness. Moreover, even if the results of the denser grid are considered reliable, it should be underlined that the computational cost for such simulation is of around 8 months in an 8 – core, 8 GB RAM SunV40 Server. The deviations of the coarser grids from the results of the denser grid are so large that make them inappropriate for simulating CFB800. The inert-material volume fraction underestimation is mainly caused by the assumption of homogeneous conditions in such large cells that results in overestimating the average gas-solid drag force and underestimating the average slip velocity.

By the CFB800 paradigm, it is clear that, new advanced models that will be able to enhance the accuracy of the calculations under coarse grids are necessary for simulation of large scale CFB units. It should be underlined that the main source of inaccuracy when coarse grids are applied, originates from the drag model.

1.4 Novelties addressed in this work

This work deals with the TFM CFD simulation of CFBs. It mainly focuses on: 1) the proper simulation of the momentum exchange coefficient (β); 2) the complexities of full – loop simulation, and on 3) the simulation of reacting flows in FBs.

As the conventional drag schemes were found inappropriate for the efficient simulation of the multi – phase flow inside CFB units, the scientific community focused on the development of advanced drag models that do not assume homogeneous conditions inside the control volumes. The EMMS scheme is a sub –grid model that takes under account the multi – phase flow heterogeneity and after the pioneer work of Wang and Li, 2007, the author along with other scientists worldwide (Hartge et al., 2009; Wang et al., 2008; Zhang et al., 2008) worked as a forerunner for EMMS schemes formulation.

A way to enhance the precision of the calculations regarding the momentum exchange coefficient under coarse grid conditions is the implementation of more sophisticated models accounting for the meso-scale particle structures. The driving force of particles clustering is the tendency of particles to clog and aggregate in order to minimize the energy inter - exchanged between the co-existing gas and solid phases. The EMMS analysis (Atsonios et al., 2011; Ge et al., 2011; Hartge et al., 2009; Naren et al., 2007; Nikolopoulos et al., 2010[a]; Nikolopoulos et al., 2010[b]; Wang et al., 2008; Wang and Li, 2007; Zhang et al., 2011) is an advanced methodology, which can be coupled with CFD simulations, capable of overcoming the aforementioned drawbacks of conventional models.

The EMMS scheme shouldn't be misinterpreted as a correction of the Gidaspow's (Gidaspow, 1994) or Wen and Yu (Wen and Yu, 1966) correlation. The latter, conventional models have been developed based on experimental conditions under homogeneous conditions inside a control volume. The EMMS scheme is a drag model that calculates the force induced to the particles as a sum of the respective drag forces to the diluted particles and the particles aggregates.

Micro- and meso- scale complications in fluidization mechanics modeling were analyzed above. However, in the case of CFBs macro-scale phenomena are present with significant

impact on the flow field. The most famous is the core-annulus flow pattern. Nikolopoulos et al., 2010[a] claimed that the optimum grid density distribution in a riser is the uniform. To explain this result they assumed that if in any region of the bed a coarser grid is applied, this accuracy "discount" will have negative effect in the overall accuracy of the model. This behavior can be explained through macro-scale phenomena that play a dominant role in the fluidization regime. Another indirect example of such a behavior is reported by Nikolopoulos et al., 2010[a], regarding the difficult to model bottom zone of a CFB riser. Mass accumulation in this region is not a result of local conditions only, but of the internal re-circulation of particles in the riser. Thus, the accurate simulation of the whole riser is a *sine qua non* for accurate predictions for the pressure drop in the bottom zone.

In this light, the full – loop simulation of CFB units gains ground because this sophisticated modeling approach takes into account all the macro-scale phenomena in the loop. For this reason, it is considered of higher accuracy and sophistication (Zhang et al., 2008) when compared to the sole CFB riser simulation. The number of numerical works adopting the full – loop approach increases (Ge et al., 2011; Shuai et al., 2011[a]; Wang et al., 2011) but the theoretical difficulties also increase. The full CFB loop (riser – cyclone - down-comer – pneumatic valve – joining pipes) simulation should for example focus on proper representation of the friction inter-particle forces (Nikolopoulos et al., 2012[c]) in the returning system, where the particle loading is significantly higher than the respective one inside the CFB riser.

The second novelty of this work is related with the full – loop simulation of CFB units. Full – loop refers to the simulation of the whole CFB unit (riser – cyclone – dipleg – pneumatic valve) and not of only the riser. The scientific essays (Ge et al., 2011; Shuai et al., 2011[a]; Wang et al., 2011) that incorporate this more sophisticated approach increases. However, the appropriate modeling of the returning system is not studied. In this work, for the first time this issue is meticulously studied and a new stress tensor for granular material is formulated for the case of high particle loading where friction forces prevail. This stress model is validated against a repose angle experiment and tested with very good results in a full – loop simulation of a CFB carbonator cold model.

Most of the recent studies, such as the work of Zhang et al., 2008 and Shuai et al., 2011[a], use the same governing equations for the recirculation system with those developed for the CFB riser. However, the fact that in this CFB part the granular phase is much denser than in the other operating parts (e.g. CFB riser) results in quite different governing physical mechanisms. In other words, the recirculation system of CFB does not operate in the fast fluidization regime, as CFB risers do. Thus, a more sophisticated approach for an accurate simulation of the returning system in CFB units is necessary.

The difficulties in the full - loop approach arise from the fact that most of the TFM models, cannot effectively simulate the inter-particle friction forces in the recirculation system, since the standard used stress tensor does not incorporate for the so called "pseudo" compressibility flow effects (Dartevelle, 2003). Consequently, the induced normal and shear stresses are not modeled appropriately during the flow of the granular phase in the CFB recirculation system. This is owed to the fact that conventional models use an insufficient expression for the yield criterion, the von - Misses / Coulomb one, for the calculation of the friction inter-particle forces. Additional difficulties relate to proper modeling of the kinetic, frictional and collisional shear viscosity. In order to overcome the aforementioned difficulties, Nikolopoulos et al., 2012[c] proposes the adoption of an alternative yield function, i.e. the Pitman-Schaeffer-Gray-Stiles yield one. This model proved to simulate the temporal deformation of the solid granular phase in a more accurate way than the standard of von Misses / Coulomb.

Another novelty of this work is the development of the necessary theory for PSD incorporation in the full loop TFM approach. Indeed, the Kinetic Theory of Granular Flows (KTGF) is reformulated in order to account for different size particles collisions in contrast to the mono - sized approach where all particles are of the same size. The CPU cost of this model is high, as in nowadays desktop PCs the calculations may last more than two years for a small scale unit. However, this work is considered important as the model developed may be implemented in the following years, as CPU availability increases, and reveal the accuracy of the mono - sized approach, simplification used almost by every author.

In this work, for the first time a CFB carbonator is simulated. This 10 KW_{th} novel reactor is a part of a DFB pilot unit, used for CO_2 capture. The full – loop of this reactor is simulated and both the advanced EMMS scheme and the new stress model are applied. The carbonation reaction is simulated with published reaction kinetics that are reformulated in order to be applicable is CFD simulations.

Finally, the abovementioned iso – thermal models are used as platforms for reacting flow mechanisms incorporation, In this light, a combusting flow model is formulated for the simulation of a 1.2 MW_{th} pilot CFBC. Simplified reaction mechanisms are used and only major species are tracked. The multi – phase flow in this case comprises of three pure Eulerian phases: 1) the primary gas phase; ii) inert – material and iii) fuel phase. The coupling between these three phases is difficult and there is limited relative information in literature. Additionally, NO_x and N_2O emissions are simulated with a decoupled approach that is formulated within this thesis. NO_x/N_2O reactions network is formulated from published experimental work. In this network, HCN and CNO are considered as intermediate species in NO_x/N_2O path. Simulation results for temperature, major species and NO_x/N_2O are compared with the available experimental data.

This thesis has eight chapters. In the second chapter, at first, the basic fluidization mechanics are summarized. In the same chapter, the TFM approximation is analyzed. In the third chapter, an advanced EMMS scheme is formulated. Moreover, the theoretical complications regarding the proper formulation of the granular stress tensor, for full – loop simulation are addressed in the same chapter, along with proper incorporation of PSD in TFM modeling. In chapters 4 to 7, the developed, in chapter 3, models are tested through simulations of CFB units.

In this light, in chapter 4 the formulated EMMS scheme is utilized for the simulation of a 1.2 MW_{th} CFBC riser. The recirculation system of the unit is excluded from simulations in order to focus on fluidization phenomena inside the riser and deal with proper modeling of gas – particles interaction. This CFBC unit is selected for testing the EMMS scheme developed in this work, due to the following facts: a) isothermal conditions experimental data are available; b) the wall effects in this unit are not severely affecting the bed hydrodynamics since the cross section of the riser is not too low; c) the medium scale of the unit does not put a computational cost barrier. In chapter 5, a reacting flow model is applied for the simulation of the combusting flow of the 1.2 MW_{th} CFBC riser. The iso – thermal model is used as a platform for proper integration of reactions and heat transfer mechanisms. The theoretical background and proper incorporation of these mechanisms in the CFD model are presented in chapter 3.

EMMS scheme validation in terms of effectively reproducing FB hydrodynamics is a milestone for this PhD. The next step is to address the full – loop simulation of a CFBC unit. In this light, a small scale CFB, plexi –glass cold model of a carbonator, is modeled in chapter 6. This unit was built, as a part of a DFB CaL system, by IFK, in order to experimentally investigate the hydrodynamic aspects of such configuration (DFB). Therefore a lot of experimental data are available both for the CFB riser and for the recirculation system.

Moreover, visual observations were recorded and are available for comparison with the numerical predictions. The latter fact is very important especially for the recirculation system of the unit since a numerical model should at least qualitatively capture the granular flow properties in this region.

Finally, in chapter 7 a 10 kW_{th} CFB carbonator is modeled. As far as the hydrodynamics of the CFB unit are concerned, the same models as the ones tested in chapter 6 are applied. The simulation takes into account the carbonation reaction and CO_2, N_2 and CaO, $CaCO_3$ species are tracked within the gas and solid phases respectively.

2. MODELING OF GRANULAR FLOWS

In this theoretical chapter the basic measures of fluidization are summarized. The mean particle size, the particle's sphericity and loading, the minimum fluidization velocity and the terminal velocity are defined. Geldart's particles classification and the fluidization regimes are also presented. Moreover the state – of – the – art modeling strategies are discussed. The aforementioned theoretical background is essential for the comprehension of this thesis, with respect to hydrodynamics. In this thesis, FB hydrodynamics are simulated with the Euler – Euler approach. The Euler / Euler equations, the respective closure equations and the Kinetic Theory for Granular Flows (KTGF) are also presented. The meticulous examination and understanding of these theories is of high importance since they are the core of the conventional CFD modeling of FBs. The iso – thermal CFD models are the platform to which more sophisticated models, such as reacting flow mechanisms, are integrated.

2.1 Fluidization Hydrodynamics

2.1.1 Mean particle size

In a mixture of solids, all particles don't have the same size. So, there is need to obtain the mean particle size of the mixture. For that purpose the size distribution functions Q and q are defined. Q is the volume fraction of particles of size smaller than d_p and q is the volume fraction of particles of size between d_p and $d_p + d(d_p)$. The relationship, between q and Q can be formulated by directly considering particles of any particular size, d_{p1} (Kunii and Levenspiel, 1991).

$$q_1 = \left(\frac{dQ}{d(d_p)} \right)_1 \; and \; Q_1 = \int_o^{d_{p1}} q d(d_p) \qquad \text{Eq. 2.1}$$

For a discrete distribution of particles, the above correlations are rearranged to:

$$q_i = \left(\frac{\Delta Q}{\Delta(d_p)} \right)_i \; and \; Q_i = \sum_1^i (q \Delta d_p)_i = \sum_1^i y_i \qquad \text{Eq. 2.2}$$

In the above correlation, y_i is the fraction of material in size interval i. Particle diameter (d_p) for a discrete distribution can be calculated by the following equation:

$$d_p = \frac{1}{\sum_{all\ i} (y / d_p)_i} \qquad \text{Eq. 2.3}$$

2.1.2 Sphericity - Voidage

Since in a FB, particles are not spherical there is a necessity to quantify how different the shape of the particles is from a perfect sphere. In this light, the measure φ_i (sphericity) is defined as:

$$\varphi_i = \left(\frac{surface\, of\ sphere}{surface\, of\ particle} \right)_{of\ the\ same\ volume} \qquad \text{Eq. 2.4}$$

Consequently $\varphi_i = 1$ for spheres and $0 < \varphi_i < 1$ for all other particle shapes. Voidage (ε or ε_g), is a measure that represents the fraction of the volume that doesn't have particles, in a control volume. Moreover, ε_s indicates the respective volume fraction of solids. Thus in a gas - solid multiphase flow $\varepsilon_g + \varepsilon_s = 1$. Some typical values for voidage, in a fast fluidization reactor are: 0.8 for the dense region, 0.01 - 0.001 for the upper part (freeboard). For a bubbling bed and a fixed bed typical values are 0.6 and 0.4 respectively (Kunii and Levenspiel, 1991). Moreover some characteristic values of voidage is ε_{mf} that represents the voidage under minimum fluidization conditions and ε^{max} which is the packing limit of a granular material, representing the voidage maximum achievable value with no permanent deformation of particulates. Typical values of these measures are 0.5 and 0.35 respectively. The same quantities but for solid phase ($\varepsilon_{s,mf}$ and ε_s^{max}) are 0.5 and 0.65.

It should be underlined that in multiphase flows, two different velocities can be defined, i.e. the actual and the superficial one. When a gas volume flows through a cross section that is partially blocked by particles with a specific volume fraction ($\varepsilon_s = 1 - \varepsilon_g$), the gas flows through the available cross section. The actual gas velocity (u) is the true velocity of gas phase that is calculated based on equation 2.5 that takes into account particles blockage.

$$u = \frac{\dot{V}}{\varepsilon_g A} \qquad \text{Eq. 2.5}$$

The superficial gas velocity (U, eq. 2.6) is rather an artificial measure and not a physical quantity. This measure corresponds to the velocity that gas would have, for the same volume flow, if there were no particles.

$$U = \frac{\dot{V}}{A_c} \qquad \text{Eq. 2.6}$$

Superficial and actual gas velocity interrelate (eq. 2.7). Of course, the actual velocity is always bigger than the superficial one.

$$U = \varepsilon_g \cdot u \qquad \text{Eq. 2.7}$$

2.1.3 Fluidization regimes

Introduction of gas from the bottom of a column containing solid particles through a distributor will have as a result one of the patterns shown in the following figure. Increasing gas velocity or inventory one can change the regime. As fluidizing velocity increases, there are fixed bed, bubbling fluidization, slugging fluidization, turbulent fluidization, fast fluidization and dilute pneumatic conveying regime (Kunii and Levenspiel, 1991).

In fixed bed regime the gas velocity is low enough that particles do not move. The gas can travel upwards in the column through the void formed by the packed particles. As the gas velocity increases the void is not enough and gas starts to move and rearrange particles. In this regime gas mainly travels upwards through bubbles. Therefore, this regime is called "bubbling". If the bed is deep (bed height to column diameter ratio greater than 3) the diameter of the bubbles can increase up to column diameter, causing slugging.

In bubbling regime particles are moving but are not entrained because the gas velocity is not high enough. If the gas velocity is further increased particles are entrained but only a small fraction of them (mainly the smaller particles) achieve in reaching the exit of the column. This regime is called "turbulent" regime. An even further increase of gas fluidizing velocity can achieve significant entrainment which should be recirculated back to the bottom

of the column. This, Fast Fluidization regime, is the most interesting in terms of industrial applications since CFBs operate under it. It should be mentioned that the bottom of the column presents relatively high particles loading (ε_s around 0.2) and that in the upper part of the column (freeboard) particles mainly travel upwards but near the walls down-falling can be observed (Kunii and Levenspiel, 1991). The latter flow patterns is usually called core – annulus.

Further increase of gas velocity results in all particles moving upwards and neither dense bottom zone nor particles down-falling can be observed. This, pneumatic transport, regime is mainly used in industrial application for particles transportation.

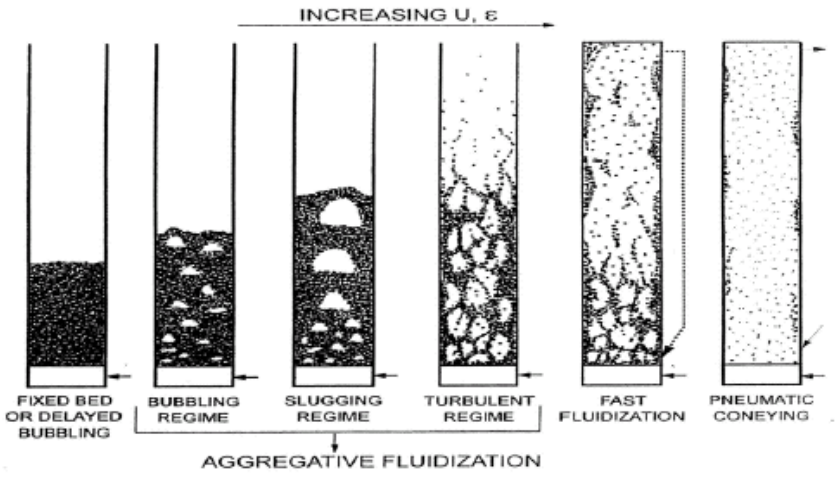

Figure 2.1 Fluidization Regimes

2.1.4 Minimum fluidizing Velocity

The minimum fluidizing velocity U_{mf} is a superficial velocity that corresponds to the lowest gas velocity in which all the particle are suspended by the fluidizing gas. The "classical", Wen and Yu (Wen and Yu, 1966) correlation, can be used to calculate this characteristic velocity:

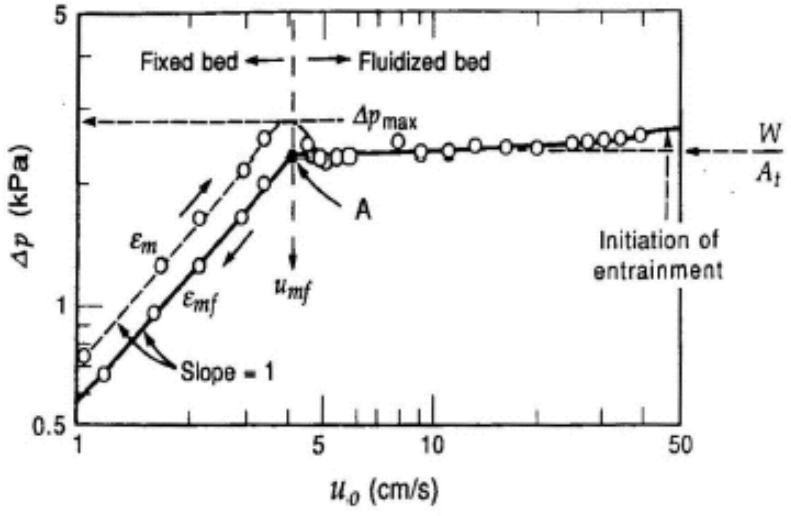

Figure 2.2 Experimental measurement of U_{mf} (Kunii and Levenspiel, 1991)

$$\mathrm{Re}_{mf} = \left[c_1^{\,2} + c_2 Ar \right]^{\frac{1}{2}} - c_1 \qquad \text{Eq. 2.8}$$

$\mathrm{Re}_{mf}\left(=\frac{U_{mf}\rho_g d_p}{\mu}\right)$ is the Reynolds's number for the minimum fluidizing velocity (based on particle size), and $Ar=\frac{d_p^3 g\rho_g(\rho_s-\rho_g)}{\mu^2}$, the Archimedes number. For coarse particles c_1=28.7 and c_2=0.0494, and for fine particles c_1 = 33.7 and c_2 = 0.0408. Nevertheless, U_{mf} can be also estimated experimentally. Figure 2.2 presents the pressure drop in a bed (sand, d_p =160μm) versus the superficial fluidizing velocity.

At relatively low velocity (fixed bed) the pressure drop is described by the famous Ergun's equation (2.9). This equation is in general valid up to a superficial velocity equal to U_{mf} and up to porosity equal to ε_{mf}.

$$\frac{\Delta P}{H_{Bed}}=150\frac{(1-\varepsilon_{mf})^2}{\varepsilon_{mf}^3}\frac{\mu\, U_o}{(\varphi d_p)^2}+1.75\frac{1-\varepsilon_{mf}}{\varepsilon_{mf}^3}\frac{\rho_g U_o^{\,2}}{\varphi d_p} \qquad \text{Eq. 2.9}$$

Increasing the aeration results up to a point in which pressure drop (ΔP) reaches a maximum value. This value is slightly greater than the static pressure of the bed as given by the following equation:

$$\frac{\Delta P}{H_{Bed}}=(1-\varepsilon_{mf})(\rho_s-\rho_g)g \qquad \text{Eq. 2.10}$$

U_{mf} is the velocity in which this change occurs. In this situation the drag force induced by the upward moving gas is equal with the weight of the particles. Therefore, creating this graph from experimental data yields the minimum fluidization velocity.

2.1.5 Terminal velocity

Terminal velocity is the maximum slip velocity that can be achieved between the moving gas and the (moving or immobile) individual solid particles. (Kunii and Levenspiel, 1991) suggests the following methodology for calculating the terminal velocity.

$$U_t^*=\left[\frac{18}{(d_p^*)^2}+\frac{2.335-1.744\phi}{(d_p^*)^5}\right]^{-1} \qquad 0.5<\phi<1 \qquad \text{Eq. 2.11}$$

$$d_p^*=d_p\left[\frac{\rho_g(\rho_s-\rho_g)g}{\mu^2}\right]^{\frac{1}{3}} \qquad \text{Eq. 2.12}$$

After calculating the above measures, the terminal velocity can be derived from the following equation:

$$U_t^*=U_t\left[\frac{\rho_g^2}{\mu(\rho_s-\rho_g)g}\right]^{\frac{1}{3}} \qquad \text{Eq. 2.13}$$

However, in the work of (Geldart, 1986) suggests a different methodology for calculating U_t. It should be underlined that U_t is a physical slip velocity constrain only for individual particles and not for particle structures (clusters) or neighboring particles.

2.1.6 Geldart's Classification of particles

The characteristics and behavior of a fluidized bed are strongly dependent on gas and solid properties. By carefully observing the fluidization of all sorts of sizes and solids, (Geldart, 1973) came up with four clearly recognizable kinds of particle behavior. For smallest to larger particles they are as follows:

- Group A: aeratable, or materials having a small mean particle size and/ or low particle density (up to 1400 kg/m^3).These solids fluidize easily, with smooth fluidization at low gas velocity (bubble free) and controlled bubbling with small bubbles at higher gas velocity. FCC catalyst is representative of these Groups.
- Group B: sand-like, most particles of size 40< d_p <500 and density 1400-4000 kg/m^3. These solids fluidize well with vigorous bubbling action and bubbles grow large.
- Group C: cohesive or very fine powders. Normal fluidization is extremely difficult for these solids because inter-particle forces are greater than those resulting from the action of gas. They tend to rise as a plug of solids or form channels from the distributor to the bed surface.
- Group D: spoutable, or large and/or dense particles Deep beds of these solids are difficult to fluidize. They give large exploding bubbles or severe channeling, or spouting behavior if the gas distribution is uneven.

Geldart's classification, for fluidizing gas ambient air, is shown in the following figure:

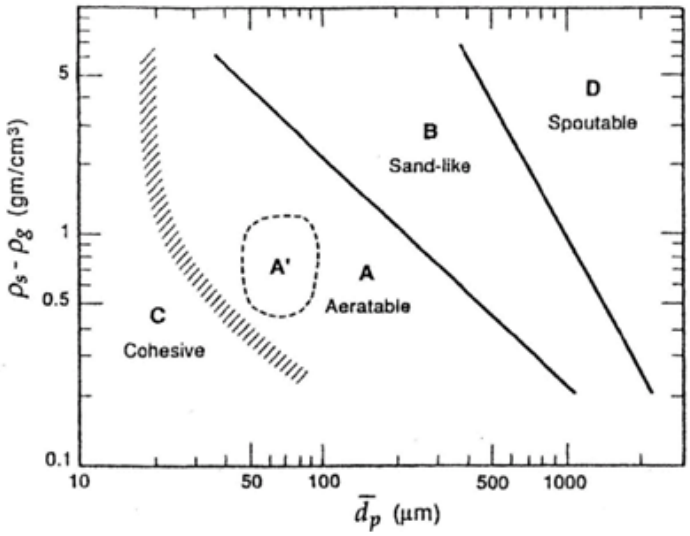

Figure 2.1 Geldart's classification of particles

2.1.7 Particle meso - scale structures (clusters)

Spatiotemporal multi-scale structures play a significant role in the time evolution of various multiphase flows (Liu et al., 1996). Gas-particle flow in CFBs is also dominated by such structures (Ge et al., 2008). Both experimental works as Zou et al., 1994 and Harris et al., 2002 and numerical analysis by Ma et al., 2006 revealed that particles tend to clog and aggregate under fluidized bed conditions forming larger structures called "clusters". The driving force of these mechanisms is the tendency of particles to clog and aggregate in order to minimize the energy interexchanged between the co-existing gas and solid phases. Clusters size varies a lot (Wang and Li, 2007), whilst it has been proposed that their size is proportional to the particles diameter. In addition, numerical results by Zhang and VanderHeyden, 2001 indicated that clusters size may be affected by gas velocity. This impact is described and taken into consideration for the determination of clusters diameter by Wang

and Li, 2007, Wang et al., 2008 and Naren et al., 2007. The highly non-linear and unstable formation of such structures raises significant barriers in the accuracy of numerical simulations for such units. The physical quantity, mostly affected by the existence of such complex structures in the case of fluidized beds, is the momentum exchange between the gas and inert material. The complexity of phenomena related to the drag force acting onto the solid particles and the in-depth understanding of the governing mechanisms, proved to be a major problem for the accurate modeling of industrial CFB applications as reported by Sundaresan, 2000 and Ge et al., 2008.

2.2 Governing equations

In order to decide on the most suitable governing equations in the case of CFB units, one should take into account that these units are operating under the fast fluidization regime (Kunii and Levenspiel, 1991). The large amount of fluidized particles inside them and their high volume and mass loading in the surrounding primary gas phase, make the Eulerian description of the solid phase a reasonable choice. Thus, most of the numerical approaches for the simulation of multiphase flows inside CFB units, in the recent literature, utilize the Eulerian Two – Fluid - Method (TFM). This type of models simulates gas and solid phases as inter-penetrating continua, and in literature are mentioned as pure Eulerian, Euler – Euler or TFM models.

2.2.1 Euler - Euler Equations

In order to simulate the transient, purely 3-D bed hydrodynamics of CFBs the Eulerian equations can be used. These Euler (for the gas) – Euler (for the solid phase) description consists of mass and momentum conservation equations. Additionally, if a reacting flow is simulated, the Energy equations for the gas and solid phases are also included in the set of Partial Differential Equations (PDEs). Usually, the elevated computational cost of such models renders the consideration of solid particles as mono-sized unavoidable. As a result of this simplification, one Eulerian solid phase, with a diameter equal to the mean diameter of particles, represents the whole granular mixture. Thus, generally in CFB units, gas and solids are modeled as two discrete interacting Euler phases. The continuity equation for gas and solids respectively is given in equation 2.14. The mass conservation is expressed via volume percentages (ε_g and ε_s) of each phase. By definition $\varepsilon_g + \varepsilon_s = 1$.

$$\begin{cases} \dfrac{\partial}{\partial t}\left(\varepsilon_g \rho_g\right) + \nabla \cdot \left(\varepsilon_g \rho_g \vec{u_g}\right) = 0 \\ \dfrac{\partial}{\partial t}\left(\varepsilon_s \rho_s\right) + \nabla \cdot \left(\varepsilon_s \rho_s \vec{u_s}\right) = 0 \end{cases} \qquad \text{Eq. 2.14}$$

Equation 2.15 is the momentum equations for gas and solids. The main idea behind the TFM approach is that the solid phase is simulated as a pseudo - fluid with elevated density. Thus the momentum equation of particles resembles the respective for the gas.

$$\begin{cases} \dfrac{\partial}{\partial t}\left(\varepsilon_g \rho_g \vec{u_g}\right) + \nabla \cdot \left(\varepsilon_g \rho_g \vec{u_g}\vec{u_g}\right) = -\varepsilon_g \nabla p + \nabla \cdot \overline{\overline{\tau_g}} + \varepsilon_g \rho_g \vec{g} + \beta\left(\vec{u_s} - \vec{u_g}\right) \\ \dfrac{\partial}{\partial t}\left(\varepsilon_s \rho_s \vec{u_s}\right) + \nabla \cdot \left(\varepsilon_s \rho_s \vec{u_s}\vec{u_s}\right) = -\varepsilon_s \nabla p - \nabla p_s + \nabla \cdot \overline{\overline{\tau_s}} + \varepsilon_s \rho_s \vec{g} + \beta\left(\vec{u_g} - \vec{u_s}\right) \end{cases} \qquad \text{Eq. 2.15}$$

It should be underlined that the partial differential equations (eq. 2.14 - 2.15) for particles are hyperbolic and for the gas phase elliptic (Tsuo and Gidaspow, 1990). The idea of a solid

phase to be simulated as a pseudo – fluid allows the beneficial Eulerian description of the particulates, but an obvious question arises. Do granular pressure and viscosity, involved in equation 2.15, have a physical meaning and how can they be calculated? Einstein, 1906 formulated a theory for the calculation of granular viscosity for sparse particulates inside fluids but only Lun et al., 1984 many years later managed to formulate an integrated theory for the calculation of both granular pressure and viscosity. Their theory is based on the kinetic theory of dense gases applied to granular fluids.

2.2.2 Kinetic theory for granular flows

In the Kinetic Theory of Granular Fluids (KTGF), particles and their fluctuation velocity resemble molecules and their fluctuation velocity, respectively. Thus a granular temperature (Θ_s) can be defined (eq. 2.16), in accordance to the definition of gas temperature.

$$\Theta_s = \frac{1}{3}\left\langle \vec{c}^{\,2} \right\rangle \qquad \text{Eq. 2.16}$$

It can be seen through equation 2.16 that the ratio of the respective "Boltzmann" constant to granulate mass is assumed to be one. Moreover, the solid particles fluctuations are considered as random and isotropic and the respective velocity spectrum is assumed to follow the Maxwell – Boltzmann distribution. The random movement is caused by the viscous dissipation of particles to the surrounding gas (Dartevelle, 2003).

Moreover, in accordance to the energy conservation equation that involved gas temperature, a respective correlation (equation 2.17) can be easily developed for granular temperature. However, the latter equation can be simplified, following the work of (Van Wachem et al., 2001) to an algebraic correlation. This algebraic form (equation 2.18), used with success by many authors (Nikolopoulos et al., 2010[a]; Van Wachem et al., 2001), was developed from the respective partial differential equation 2.17, if the diffusive and convective terms are neglected. In equation 2.18 the first term is the production of granular energy due to shear stresses, the second is the dissipation due to the inelastic collisions (Jung et al, 2009).

$$\frac{3}{2}\left[\frac{\partial}{\partial t}\left(\varepsilon_s \rho_s \Theta_s\right) + \nabla\cdot\left(\varepsilon_s \rho_s \vec{u}_s \Theta_s\right)\right] = \left(-p_s I + \bar{\bar{\tau}}_s\right) : \nabla \vec{u}_s + \nabla\cdot\left(k_{\Theta_s}\nabla\Theta_s\right) - \gamma_{\Theta_s} - 3\beta\Theta_s \qquad \text{Eq. 2.17}$$

$$\left(-p_s \bar{\bar{I}} + \bar{\bar{\tau}}_s\right) : \nabla\overrightarrow{u_s} - \gamma_{\Theta_s} - 3\beta\Theta_s = 0 \qquad \text{Eq. 2.18}$$

Solid pressure (p_s) and stresses can be expressed via the application of the kinetic theory of gases in granular flows in order to capture the governing physics. Granular pressure is defined through an equation of state. In equation 2.19, the first term is similar with the well - know equation of state for the ideal gas, while the second term simulates the effect of particles collisions.

$$p_s = \varepsilon_s \rho_s \Theta_s + 2\rho_s (1+e_{ss})\varepsilon_s^2 g_{o,ss}\Theta_s \qquad \text{Eq. 2.19}$$

In equation 2.19, the restitution coefficient (e_{ss}) quantifies the amount of kinetic energy lost through particle – particle collisions. It is defined as the ratio of outcoming to incoming velocity or alternatively (Chalermsinsuwan et al., 2009[a]) final to initial velocity. It is not constant and depends on granulates properties (e.g. hardness, Hussainova et al., 1999), impact velocity and diameter of colliding particles. For an elastic collision the restitution coefficient is equal to one and smaller values indicate plastic collisions. A value of zero for the restitution

coefficient corresponds to fully plastic collision that results in agglomeration of the colliding particles.

It should be denoted that $e_{s,wall}$ can be also defined for particle – wall surface collisions and that this coefficient is typically used in the boundary condition for granular temperature at the wall surfaces. Most of numerical studies for CFB units seem to arbitrarily select a value for the restitution coefficient. This is due to the limited experimental data available for this coefficient. Moreover, most of experimental data refer to glass or plastic particles that are not similar to ash or sand particles that are the typical inert – material in CFB installations. Table 2.1 summarizes the values used by authors. Through this table, it can be seen that the inter–particle collisions of smaller (Geldart A) particles are considered as almost elastic (e_{ss} ~ 0.99) while collisions between bigger (Geldart B) particles are considered as inelastic (e_{ss} ~ 0.9).

CFD study	Particle Type	Restitution coefficient
(Shuyan et al., 2008)	Geldart A	0.99
(Zhang et al., 2008)	Geldart A	0.99
(Shuyan et al., 2008)	Geldart A	0.99
(Almuttahar and Taghipour, 2008)	Geldart A	0.99
(Benyahia et al., 2000)	Geldart A	0.95
(Hussainova et al., 1999)	Geldart A	0.95
(Lu et al., 2009)	Geldart A	0.90
(Liu and Lu, 2009)	Geldart B	0.90
(Wang et al., 2008)	Geldart A & B	0.95
(Mathiesen et al., 2000)	Geldart B	0.99
(Van Wachem et al., 2001)	Geldart B	0.90
(Hartge et al., 2009)	Geldart B	0.90 & 0.99
(Ibsen et al., 2004)	Geldart B	0.97
(Basu and Fraser, 1991)	Geldart B	0.85, 0.90 & 0.95
(Helland et al., 2002)	Geldart B	0.90

Table 2.1 Restitution coefficient for different simulation studies

The shear part of the stress tensors for gas and solid phase is given by equation 2.20.

$$\begin{cases} \overline{\overline{\tau}}_g = \varepsilon_g \mu_g \left(\nabla \overrightarrow{u_g} + \nabla \overrightarrow{u_g}^T \right) - \left(\varepsilon_g \lambda_g - \frac{2}{3} \varepsilon_g \mu_g \right) \left(\nabla \cdot \overrightarrow{u_g} \right) \overline{\overline{I}} \\ \overline{\overline{\tau}}_s = \varepsilon_s \mu_s \left(\nabla \overrightarrow{u_s} + \nabla \overrightarrow{u_s}^T \right) - \left(\varepsilon_s \lambda_s - \frac{2}{3} \varepsilon_s \mu_s \right) \left(\nabla \cdot \overrightarrow{u_s} \right) \overline{\overline{I}} \end{cases} \quad \text{Eq. 2.20}$$

Equations 2.19 and 2.20, can be used as closure equations of Euler – Euler set of partial differential equations (2.14, 2.15 and 2.17 or 2.18). However, Sundaresan, 2011 correctly underlined that KTGF inherently assumes that there is a clear separation of the scales of random particle motion ($\langle \vec{c} \rangle$) and mean particulate velocity. The validity of this assumption

has not been meticulously studied, despite the fact that the whole TFM approximation depends on this assumption. The theoretical difficulties in examining the contingency of this assumption along with the successful implementation of TFM in numerous simulations of granular flows (Chalermsinsuwan et al., 2009[a, b]; Gidaspow, 1994; Nikolopoulos et al., 2010[a]; Shuai et al., 2011[b]; Zhang and VanderHeyden, 2001) made most of the authors to accept the contingency of TFM without dealing with the validity of the aforementioned assumption.

In equation 2.20, solid shear and bulk viscosity is needed for the calculation of shear and normal stresses. For the calculation of these terms, the KTGF is not sufficient and the plastic theory is also used for the calculation of frictional stresses that prevail when particle loading is very high. In such dense situations, KTGF collapses since random particle motion does not occur anymore. The described above reasoning is depicted in Figure 2.4, and results in the expression of solids shear viscosity as a sum of a kinetic, a collisional and a frictional part ($\mu_s = \mu_{s,kin} + \mu_{s,col} + \mu_{s,fr}$). The frictional term should be taken into account only in the case of a very dense control volume (typically $\varepsilon_s > \varepsilon_{s,fr} = 0.5$) where the kinetic theory is not valid and a plastic-frictional theory should be applied.

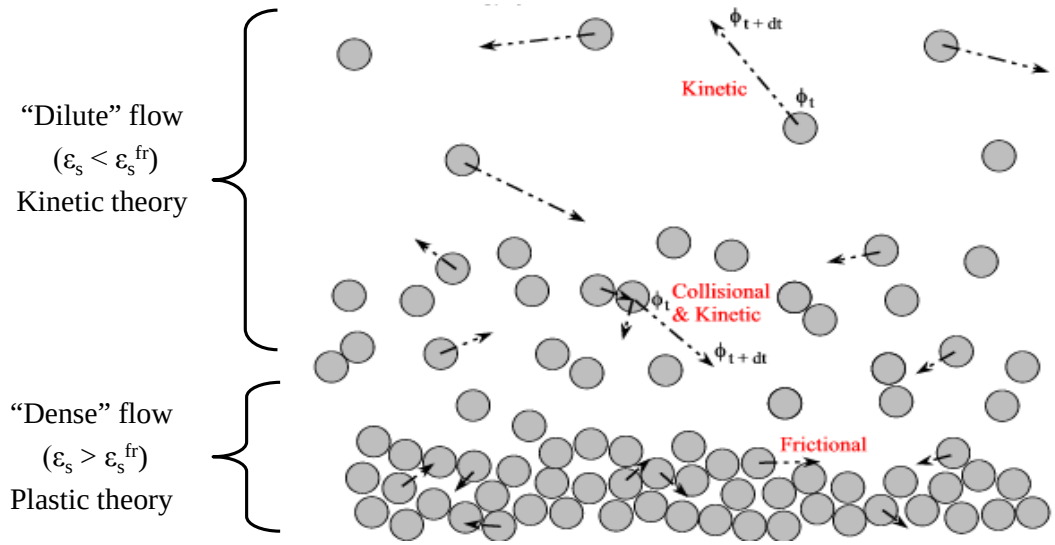

Figure 2.4 Rheological analysis of kinetic and plastic regime (Dartevelle, 2003)

Equations 2.21 (Gidaspow et al., 1992), 2.22 (Gidaspow et al., 1992) and 2.23 (Schaeffer, 1987 or Johnson and Jackson, 1987 - depending on the equation used for the calculation of the frictional pressure) depict correlation utilized for the calculation of the kinetic, collisional and frictional shear viscosity.

$$\mu_{s,kin} = \frac{10\rho_s d_s \sqrt{\Theta_s \pi}}{96\varepsilon_s (1+e_{ss}) g_o} \cdot [1 + \frac{4}{5} g_o \varepsilon_s (1+e_{ss})]^2 \qquad \text{Eq. 2.21}$$

$$\mu_{s,col} = \frac{4}{5}\varepsilon_s \rho_s d_s g_{o,ss} (1+e_{ss}) \sqrt{\frac{\Theta_s}{\pi}} \qquad \text{Eq. 2.22}$$

$$\mu_{s,fr} = \frac{p_s \sin\phi}{2\varepsilon_s \sqrt{\mathrm{II}_{dD}}} \qquad \text{Eq. 2.23}$$

In equation 2.23, that is enabled in the plastic regime the granular pressure can be approximated via equation 2.19 or by an alternative correlation for frictional pressure such as the one proposed by Johnson and Jackson, 1987. It should be underlined that if the latter

approximation is used for the frictional term of shear viscosity, the same approximation must be used for the calculation of p_s in equation 2.15.

In the above equations, $g_{o,ss}$ is the radial distribution function. This scalar is a correction factor that modifies the probability of collisions between grains when the solid granular phase becomes dense. This function may also be interpreted as the non-dimensional distance between spheres.

$$g_{o,ss} = \frac{gr_d + d_p}{gr_d} \qquad \text{Eq. 2.24}$$

$$g_{o,ss} = \left[1 - \left(\frac{\varepsilon_s}{\varepsilon_s^{\max}} \right)^{1/3} \right]^{-1} \qquad \text{Eq. 2.25}$$

Equation 2.24 depicts the definition of radial distribution function (gr_d is the distance between grains). There are a lot of semi-empirical equations developed for this scalar. Equation 2.25 is the most well know, developed by Ogawa et al., 1980. Alternatively, the correlation (eq. 2.26) reported by Lun et al., 1984 can be used.

$$g_{o,ss} = \left[1 - \left(\frac{\varepsilon_s}{\varepsilon_s^{\max}} \right) \right]^{-2.5\varepsilon_s^{\max}} \qquad \text{Eq. 2.26}$$

Moreover, due to variations of the effective density, a granular bulk viscosity should be incorporated as well. Equation 2.27 illustrates such a correlation (Lun et al., 1984).

$$\lambda_s = \frac{4}{3}\varepsilon_s \rho_s d_s g_{0,ss} (1 + e_{ss}) \left(\frac{\Theta_s}{\pi} \right)^{1/2} \qquad \text{Eq. 2.27}$$

Equations 2.21 to 2.23 and 2.27 efficiently capture the granular character of particles flow inside a CFB riser. However, there is one more difficulty in TFM formulation, i.e. the proper simulation of the momentum interexchange coefficient. This coefficient (β) can be conventionally simulated according to Gidaspow's scheme (eq. 2.28), which incorporates both the Wen and Yu (Wen and Yu, 1966) and Ergun (Ergun, 1952) equations.

$$\beta = \begin{cases} \frac{3}{4} C_D \frac{\rho_g \varepsilon_g \varepsilon_s \left| \overrightarrow{u_g} - \overrightarrow{u_s} \right|}{d_s} \varepsilon_g^{-2.65}, & \varepsilon_s \le 0.2 \\ 150 \frac{\varepsilon_s^2 \mu_g}{\varepsilon_g d_s^2} + 1.75 \frac{\rho_g \varepsilon_s \left| \overrightarrow{u_g} - \overrightarrow{u_s} \right|}{d_s}, & \varepsilon_s > 0.2 \end{cases} \qquad \text{Eq. 2.28}$$

However, this coefficient has a strong multi-scale character. Ge et al., 2008 and Wang and Li, 2007 proposed that Wen and Yu correlation is only reliable when the particles are homogeneously dispersed inside a control volume.

2.2.2 Wall Boundary Conditions for Particles

The interaction of particles with wall surfaces has been studied a lot and three models have been formulated: i) the no – slip; ii) the free slip and iii) the partial slip boundary conditions. The no slip condition implies that the velocity of solids at the wall is zero while the free slip condition assumes that no kinetic energy of solids is lost through particle – wall interaction. Johnson and Jackson, 1987 developed the partial – slip boundary condition that implies that a part of particles momentum is lost during their interaction with the solid

boundary. To formulate their model, they considered the force balance in the normal to the wall direction. Of course, this balance takes into account forces acting in particulates. Three terms are incorporated, i.e. the particles stress component normal to the wall (first term in equation 2.29), momentum transportation per m^2 (second term) and the tangential component of friction force (third term).

$$\frac{\left(u_s-u_{wall}\right)\left(\vec{\sigma}_{col}+\vec{\sigma}_{fr}\right)\vec{n}_w}{\left|u_s-u_{wall}\right|}+\frac{\varphi^*\sqrt{3}\pi\rho_g\varepsilon_s\Theta_s^{1/2}\left|\left(u_s-u_{wall}\right)\right|}{6\varepsilon_{s,\max}\left[1-\left(\frac{\varepsilon_s}{\varepsilon_{s,\max}}\right)^{1/3}\right]}+\mathrm{N}_f\tan\delta=0 \qquad \text{Eq. 2.29}$$

Johnson and Jackson, 1987, in their work, neglected the third term of the above equation and developed equation 2.30, that can be used as a boundary condition for wall surfaces in granular flows simulation. Their model is also called the "J-J" model, based on the initial letter of authors' names. This equation is a 3rd type (Robin or Cauchy, Chung, 2002) boundary condition.

$$\mu_s\left.\frac{\partial u_s}{\partial n}\right|_{wall}+\frac{\varphi^*\sqrt{3}\pi\rho_g\varepsilon_s\Theta_s^{1/2}}{6\varepsilon_{s,\max}\left[1-\left(\frac{\varepsilon_s}{\varepsilon_{s,\max}}\right)^{1/3}\right]}u_s\big|_{wall}=0 \qquad \text{Eq. 2.30}$$

It is interesting to investigate which of the three boundary conditions is more suitable for CFBs. As Tsuo and Gidaspow, 1990 underline, a small particle will probably stick to the wall and a big one will self-rotate along the wall surface. In the first case no slip condition seems as the most appropriate, whilst in the second case particles are slipping along the wall, but this movement is hindered by the friction forces between particles and the wall. In the latter case the partial slip boundary condition is the only type of boundary condition that has the necessary sophistication.

The J-J model that Johnson and Jackson, 1987 developed, incorporates the specularity coefficient (φ^*) as a parameter. This normalized parameter quantifies the reflectivity of wall surfaces and its value is bounded between zero and one. In general, $\varphi^* = 0.6$ is selected in most published works (Basu and Fraser, 1991; Johnson and Jackson, 1987; Zhang et al., 2008) as the most suitable value. Almuttahar and Taghipour, 2008 parametrically investigated this parameter in a CFB unit with high re-circulation flux. They tested values between 0.5 and 1, and found that setting the specularity coefficient equal to one resulted in severe deviation from experimental data. Moreover, lower values of this coefficient resulted in higher particle loading close to wall boundaries.

2.2.3 Drag force

Whenever a single particle is within a stream of gas, drag force is induced on the particle. This force depends on the drag coefficient and the relative velocity of the particle and air (or, in other words, the slip velocity $u_{slip} = u_g - u_s$). This force can be conventionally calculated, in the case of FB, by using the following correlation (Wen and Yu, 1966).

$$F=F_{Wen,Yu}=\frac{3}{4}\cdot C_D\cdot\frac{\rho_g\varepsilon_g\varepsilon_s\cdot\left|u_g-u_s\right|\cdot\left(u_g-u_s\right)}{d_p}\cdot\varepsilon_g^{-2.65} \qquad \text{Eq. 2.31}$$

The abovementioned correlation contains the particle's drag coefficient, calculated as:

$$C_D = \begin{cases} (24/\mathrm{Re})\left(1+0.15\,\mathrm{Re}^{0.687}\right), & \mathrm{Re} < 1000 \\ 0.44, & \mathrm{Re} \geq 1000 \end{cases}, \qquad \mathrm{Re} = \frac{\rho_g \varepsilon_g d_p \left|\vec{u_g} - \vec{u_s}\right|}{\mu_g} \qquad \text{Eq. 2.32}$$

This correlation is highly accurate for homogeneously distributed particles. It has been reported by Ge et al., 2008, that Wen & Yu correlation can be implemented with high accuracy only for sparse particles. On the contrary, as solid concentration increases and due to formation of complicated solid structures (clusters), Wen & Yu correlation becomes inaccurate (Ge et al., 2008).

2.2.4 Grid density

Conventional drag models as described by Gidaspow's (Tsuo and Gidaspow, 1990 eq. 2.28), or Syamlal and O'Brein (Syamlal et al., 1993) and Wen and Yu (Wen and Yu, 1966) assume homogeneous conditions inside a control volume, which is far from reality. The main reason is that the formation of clusters is a controlling parameter for the governing physics of such complex two-phase flow system.

Ge et al., 2008 and Wang et al., 2008 reported that standard CFD models, adopting conventional grad schemes, require quite dense computational grids for the accurate prediction of the induced flow. In addition, the numerical error is considerable as stated by Wang et al., 2008 and Hartge et al., 2009 when coarse grids are applied and can only be confronted with very dense computational grids (Ge et al., 2008 as well as Zhang and VanderHeyden, 2001). The density of a computational grid can be expressed via the mean volume of computational cells. However, in the case of granular mediums simulation through the pure Eulerian formulation, the former value is not representative. The level of densification of a numerical grid, should be directly related to the ability of explicit modeling of clusters, whose dimensions are analog to particle diameter (Gu and Chen, 1998; Harris et al., 2002). Thus a representative non – dimensionless measure of grid density can be defined as the ratio of length of cell to particle diameter (l_r). This parameter is defined in Figure 2.5.

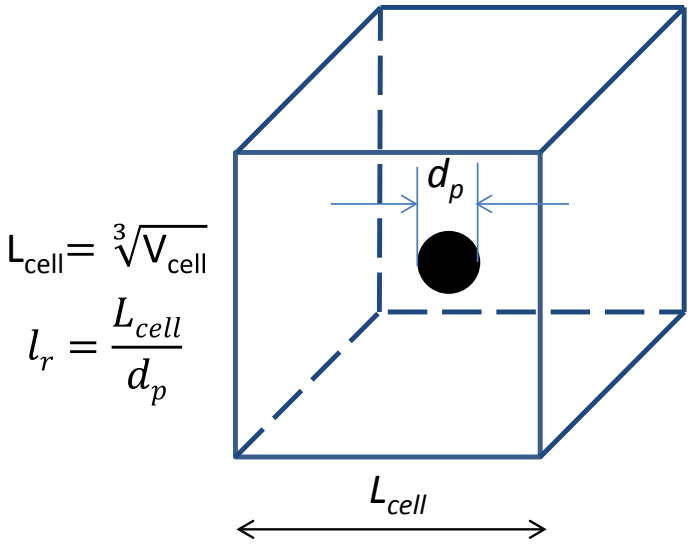

Figure 2.5 Particle to cell length ratio definition

Currently applied grids with low resolution along with the inherent characteristic of current CFD models to assume homogeneous conditions in each computing cell is a significant source of numerical inaccuracy. The multi-scale structures of particles inside the CFB make the accurate modeling of the momentum exchange between the coupled phases (gas and inert material) difficult (Ge et al., 2008). The assumption of homogeneous conditions

result in the underestimation of the average slip velocity between the phases because of the respective overestimation of the average gas–solid drag force as reported by Myöhänen et al., 2006. The accuracy of the Gidaspow's (Gidaspow, 1994) model is increasing with the minimization of the equivalent size of the computational cell, as reported by Ge et al., 2008 as well as Zhang and VanderHeyden, 2001. The accuracy of the homogeneity assumption is increasing for smaller control volume. Theoretically, it has been reported by Ge et al., 2008, that an equivalent cell size of at most 20 times the mean diameter of particles is necessary for a conventional drag model (Gidaspow's equation) to produce highly accurate results. However, grid independent results for a three dimensional numerical simulation of a CFB riser has not yet been achieved and the abovementioned value (~ 20) has been questioned (Lu et al., 2009). However, increasing the grid density severely increases the CPU cost. Therefore, due to increased computational cost, CFD models adopting the TFM approach are not yet applicable to large scale units (Rampidis et al., 2007). In order to understand the severity of the computational cost problem, an example may be useful. For a typical case of isothermal simulation of a 1MW boiler, one would need 800 Gb of RAM and 10 years of real time continuous calculation (serial solver) if the l_r ratio is kept below 20. The reproduced results using the aforementioned grid density will be of relatively high accuracy but it is not certain if the results will also be grid independent. Lu et al., 2009 in a 2-D numerical investigation showed that an l_r ratio less than 10 is necessary for grid independency if conventional drag models such as Gidaspow's are implemented.

Grid independent results for 3-D simulation of CFBs have not been obtained yet. However, even if grid dependent results of higher accuracy are needed, the computational cost of the conventional CFD models is extremely high even for semi – industrial units. Obviously, the CPU and RAM requirements increase to unacceptable limits for larger units, since the volume of the unit increases but the particle diameter does not increase because CFB units operate only with Geldart B particles.

3. BEYOND THE STATE – OF – THE - ART

In this chapter the theoretical novelties of this work are presented. This novelties deal with: a) the momentum exchange coefficient (β); b) the formulation of an alternative stress tensor of solid phase for highly particle loaded control volumes; c) the incorporation of a Particle Size Distribution (PSD) in the CFD model, and d) the formulation of a CFD model incorporating chemical reactions as well as heat and mass transfer mechanisms. Specifically:

a) An EMMS (Energy Minimization Multi-Scale) scheme is developed to address the accurate simulation of the momentum exchange coefficient (β). The accurate representation of this coefficient is of high importance since the low accuracy of the conventional TFM models is mainly induced by the low sophistication of the conventional drag models.

b) A new stress tensor model is formulated based on the Pitman – Schaeffer – Gray - Stiles yield criterion, in order to properly address inter – particle friction forces that dominate the multiphase flow within the recirculation system of CFBs.

c) The PSD incorporation in the TFM approach is not trivial. The KTGF should be reformulated in order to account for different size particles collisions in contrast to the mono - sized approach where all particles are of the same size.

d) A simple reacting flow model is integrated in the isothermal model described in chapter 2. Such type of models can be used for the simulation of the combusting flow within CFBs. Moreover, a decoupled model for the nitric and nitrous oxides simulation and a correlation suitable for the calculation of the carbonation reaction rate in CFD codes, are developed.

It should be underlined that the theory behind these novelties is in line with the TFM formulation and KTGF. This compliance is intended, because these theoretical novelties and the corresponding models emerging from them will be introduced to the state-of-the-art TFM platform.

3.1 EMMS scheme

The EMMS model was originally developed by Liu et al., 1996. In their work, Liu et al., 1996 conceived a thermodynamic-like description of the time-averaged state of fluidization. However, nowadays, the EMMS analysis is being used as an advanced drag model (Wang et al., 2008; Zhang et al., 2008 and Hartge et al., 2009), which can be coupled with CFD simulations to overcome the drawbacks of conventional drag models. In this model, the effect of spatiotemporal particle structures is taken under account explicitly via a sub grid 1-D model. The final result of such an effort can be incorporated in any TFM CFD model through the Heterogeneity index (H_d) introduced in the correlation of β:

$$\beta = \frac{3}{4} C_D \frac{\rho_g \varepsilon_g \varepsilon_s \left| \vec{u_g} - \vec{u_s} \right|}{d_s H_d} \varepsilon_g^{-2.65} \qquad \text{Eq. 3.1}$$

The above equation seems as an alternation of Wen and Yu correlation. This is not valid since the new variable (H_d) incorporates the effect of granulates flow heterogeneity in the calculation of the drag coefficient, and equation 3.1 is a totally new drag model as it will be explained in a following section.

EMMS analysis should be conducted for a control volume taking under account that the multiphase flow under CFB conditions is locally heterogeneous (Wang et al., 2008) and that various regions can be identified inside a control volume. Regions of the control volume in

which particles have an elevated volume fraction of solid phase form the dense phase of the cell (clusters). On the other hand, all solid particles that are rather homogenously dispersed inside the gas phase represent the dilute phase. Figure 3.1 represents the various regions with the corresponding main velocities, which can be found in such a two – phase flow system, similar to the one of a CFB. Dilute phase, is gas dominated while inside the dense phase the flow is generally particle dominated. The dense phase itself (clusters) is a meso – scale structure that arises out of particles and gas compromising (Liu et al., 1996).

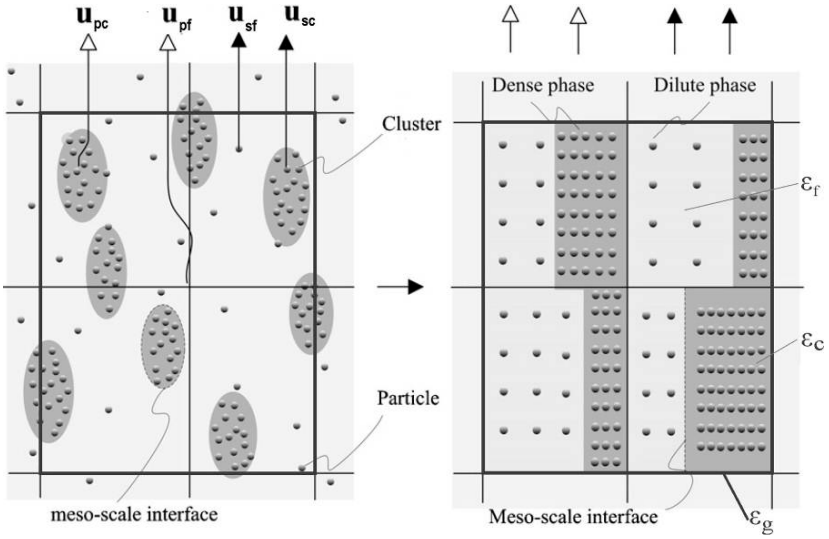

Figure 3.1 Flow phases inside a control volume (Dong et al., 2008).

Although the two phases are clearly defined, there are cases that the particles inside a control volume cannot be grouped in one of the aforementioned phases, i.e. too sparse to be part of the dense phase and too dense to be part of dilute phase. To address this difficulty, the volume percentage of particles packed into structures and resembling clusters is considered as the dense phase. On the contrary, dilute phase is assumed to be consisted of discrete, uniformly dispersed particles of uniform size (d_p), which is in consistency with the approach of Naren et al., 2007.

$U_g = u_g \cdot \varepsilon_g$	$U_s = u_s \cdot \left(1-\varepsilon_g\right)$
$U_{sc} = \varepsilon_c \cdot u_{sc}$	$U_{sf} = \varepsilon_f \cdot u_{sf}$
$U_{si} = \left(1-f\right)\cdot \varepsilon_f \cdot u_{si}$	$U_{pf} = \left(1-\varepsilon_f\right)\cdot u_{sf}$
$U_{pc} = \left(1-\varepsilon_c\right)\cdot u_{sc}$	$U_c = \varepsilon_c \cdot u_c$
$U_f = \varepsilon_f \cdot u_f$	

Table 3.1 Superficial and actual velocity interrelation

The three different (dense, inter - phase and dilute) flow structures involved in the sub – grid 1-D EMMS analysis are characterized by the respective velocities. These vectors are defined in Figure 3.2 along with the respective slip velocities. In this figure, the actual and not the superficial velocities are described. The interrelation of actual (u) and superficial (U) velocity of phases is depicted in Table 3.1 (Papafotiou, 2009). Moreover, Table 3.2 summarizes important closure equations for each flow phase and the equations for calculating the drag force applied to each flow structure (Wang et al., 2008). It should be underlined, that

the famous Wen and Yu correlation (Wen and Yu, 1966) is used for the calculation of the effective drag force within the dilute and dense phase. The assumption of homogeneous conditions is more valid for these structures than for the whole control volume. It is worth mentioning that the characteristic length of inter-phase structure is the diameter of clusters.

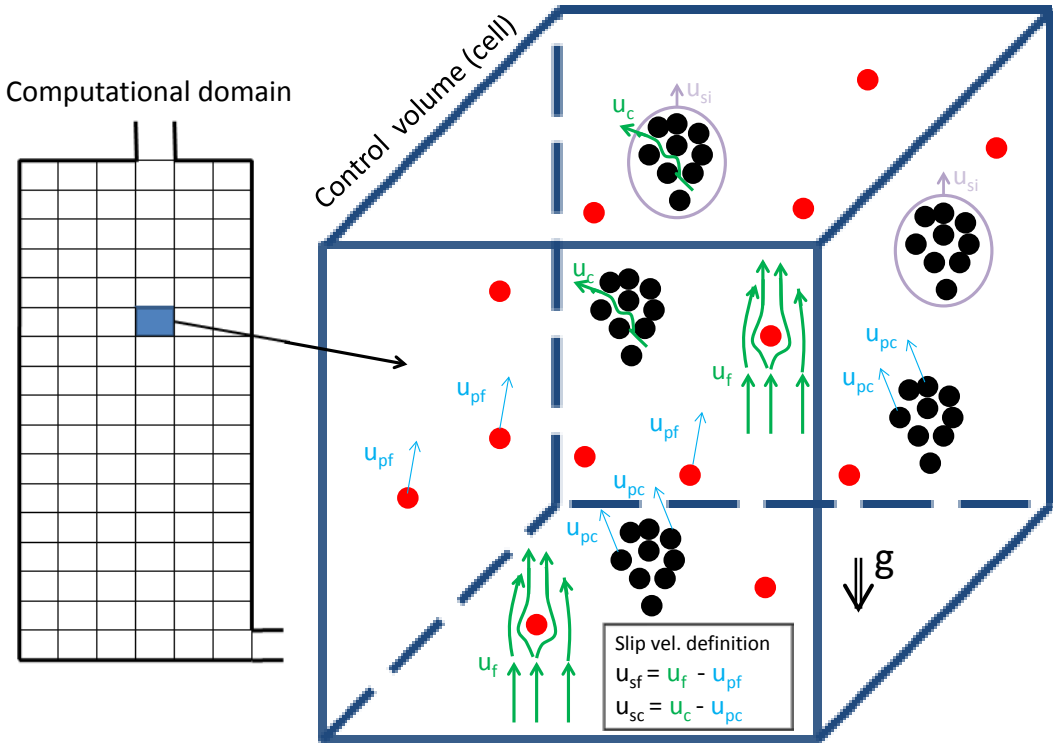

Figure 3.2 Velocity definition inside a control volume for the EMMS scheme. The red color represents dilute phase, black color the dense phase and magenta color the inter-phase. Green represents gas and light blue solids.

The force balance for the clusters and dilute phase in a unit volume of the suspension is given by equations 3.2 and 3.3 respectively, whilst equation 3.4 represents the pressure drop balance between the clusters and the dilute phase (Wang et al., 2008; Yang et al., 2003).

$$\frac{3}{4}\cdot C_{dc}\frac{f\left(1-\varepsilon_c\right)}{d_p}\rho_g U_{sc}\left|U_{sc}\right|+\frac{3}{4}\cdot C_{di}\frac{f\rho_g}{d_{cl}}U_{si}\left|U_{si}\right|=f\left(1-\varepsilon_c\right)\cdot\left(\rho_s-\rho_g\right)\left(g+a_c\right) \quad \text{Eq. 3.2}$$

$$\frac{3}{4}C_{df}\frac{\left(1-f\right)\left(1-\varepsilon_f\right)\cdot\rho_g}{d_p}U_{sf}\left|U_{sf}\right|=\left(1-f\right)\left(1-\varepsilon_f\right)\left(\rho_s-\rho_g\right)\left(g-a_f\right) \quad \text{Eq. 3.3}$$

$$C_{df}\frac{\left(1-\varepsilon_f\right)\cdot\rho_g}{d_p}U_{sf}\left|U_{sf}\right|+\frac{f}{1-f}C_{di}\frac{\rho_g}{d_{cl}}U_{si}\left|U_{si}\right|=C_{dc}\frac{\left(1-\varepsilon_c\right)\cdot\rho_g}{d_p}U_{sc}\left|U_{sc}\right| \quad \text{Eq. 3.4}$$

Additionally, mass conservation for the dilute, the dense and the definition of mean voidage in the control volume are given by equations 3.5, 3.6 and 3.7 respectively.

$$U_f\left(1-f\right)+U_c f=u_g\cdot\varepsilon_g \quad \text{Eq. 3.5}$$

$$U_{pf}\left(1-f\right)+U_{pc}f=u_s\left(1-\varepsilon_g\right) \quad \text{Eq. 3.6}$$

$$\varepsilon_g=f\cdot\varepsilon_c+\left(1-f\right)\cdot\varepsilon_f \quad \text{Eq. 3.7}$$

	Dense phase	Dilute Phase	Inter-phase
Effective drag coefficient	$C_{dc} = C_{d0}\varepsilon_c^{-4.65}$	$C_{df} = C_{d0f}\varepsilon_f^{-4.65}$	$C_{Di} = C_{Doi}(1-f)^{-4.65}$
Standard drag coefficient	$C_{d0c} = \frac{24}{\mathrm{Re}_c} + \frac{3.6}{\mathrm{Re}_c^{0.313}}$	$C_{d0f} = \frac{24}{\mathrm{Re}_f} + \frac{3.6}{\mathrm{Re}_f^{0.313}}$	$C_{d0i} = \frac{24}{\mathrm{Re}_i} + \frac{3.6}{\mathrm{Re}_i^{0.313}}$
Characteristic Reynolds number	$\mathrm{Re}_c = \frac{\rho_g d_p}{\mu_g}\lvert U_{sc}\rvert$	$\mathrm{Re}_f = \frac{\rho_g d_p}{\mu_g}\lvert U_{sf}\rvert$	$\mathrm{Re}_i = \frac{\rho_g d_{cl}}{\mu_g}\lvert U_{si}\rvert$
Superficial slip velocity	$U_{sc} = U_c - \frac{\varepsilon_c \cdot U_{pc}}{1-\varepsilon_c}$	$U_{sf} = U_f - \frac{\varepsilon_f \cdot U_{pf}}{1-\varepsilon_f}$	$U_{si} = (1-f)\cdot\left(U_f - \frac{\varepsilon_f \cdot U_{pc}}{1-\varepsilon_c}\right)$
Drag force per particle or cluster	$F_c = C_{dc}\frac{\pi d_p^{\,2}}{4}\cdot\frac{\rho_g}{2}\cdot U_{sc}\cdot\lvert U_{sc}\rvert$	$F_f = C_{df}\frac{\pi d_p^{\,2}}{4}\cdot\frac{\rho_g}{2}\cdot U_{sf}\cdot\lvert U_{sf}\rvert$	$F_i = C_{di}\frac{\pi d_{cl}^{\,2}}{4}\cdot\frac{\rho_g}{2}\cdot U_{si}\cdot\lvert U_{si}\rvert$
Numbers of particles or clusters in unit volume	$m_c = \frac{f\cdot(1-\varepsilon_c)}{\frac{\pi d_p^{\,3}}{6}}$	$m_f = \frac{(1-f)\cdot(1-\varepsilon_f)}{\frac{\pi d_p^{\,3}}{6}}$	$m_i = \frac{f}{\frac{\pi d_{cl}^{\,3}}{6}}$

Table 3.2 EMMS closure equations.

The formation and dynamic evolution of clusters result in a fluctuations of local volume fraction of solids. An expression for the voidage of the dense phase can be reached, based on the thorough analysis conducted by Wang et al., 2008. In this analysis, clusters are defined as any particle aggregate whose local instantaneous solid concentration is greater than the time-mean local solid concentration by at least *n* times its standard deviation σ_ε. The analysis of Wang et al., 2008 is based on the assumption that volume fraction time – series follow a Poisson distribution. Atsonios et al., 2011 numerically investigated this assumption and found that close to wall regions the Poisson distribution is not a good approximation of the phenomenon and that an Exponential distribution seems more appropriate. However, in this region except for the drag force wall friction forces act on particles dynamics and since the latter forces are not incorporated in the 1 - D EMMS scheme, the assumption of Poisson distribution is applied. Thus, dense phase voidage standard deviation is calculated using equation 3.8 (Wang et al., 2008).

$$\sigma_\varepsilon = \varepsilon_s\sqrt{\frac{(1-\varepsilon_s)^4}{1+4\varepsilon_s+4\varepsilon_s^{\,2}-4\varepsilon_s^{\,3}+\varepsilon_s^{\,4}}} \qquad \text{Eq. 3.8}$$

Following the above reasoning, the volume fraction of gas inside the dense phase (ε_c) can be approximated by the following equation:

$$\varepsilon_c = \varepsilon_g - n\cdot\sigma_\varepsilon \qquad \text{Eq. 3.9}$$

The value of *n* can be chosen with some degree of arbitrariness (Wang et al., 2008). A value of *n*=3 is reported by Soong et al., 1994 and Soong et al., 1995. However, a value of *n* =2 was adopted by Liu, 2005; Sharma et al., 2000 and Tuzla et al., 1998, while Gu and Chen, 1998 assumed a value of *n* =2.5. Manyele et al., 2002; Qi et al., 2005 and Yan et al., 2002 set *n* =1. In contrast to these researchers, Wang and Li, 2007 defined ε_c as a free variable.

Another important scalar in EMMS scheme is the cluster diameter (d_{cl}). This measure expresses the mean meso-scale characteristic length and it is assumed that these structures are spherical. Experimental (Gu and Chen, 1998; Harris et al., 2002; Zou et al., 1994) or theoretical work (Naren et al., 2007; Subbarao, 2010) yielded expressions for the calculation of clusters diameter. However, analytic equations for Geldart B particles such as the one reported by Wang and Li, 2007 or Naren et al., 2007 are the only well-established relations since the respective empirical equations are mainly fed with experimental data concerning Geldart A particles. Nevertheless, in the work of Wang and Li, 2007 the use of the aforementioned analytic expression results in an overestimation of the clusters volume fraction (f =0.4) in the dilute region (voidage > 0.99). In order to overcome this problem, the present work adopted an empirical equation for clusters diameter proposed by (Gu and Chen, 1998).

The latter empirical equation provides almost identical results for the clusters diameter as the one by Harris et al., 2002 as stated by Wang et al., 2008. Harris et al., 2002 using data mainly for Geldart A particles and Geldart B particles proposed an arithmetic expression for the clusters diameter. However, the aforementioned expression for solid volume fraction ε_s less than 0.01, predicts that the clusters diameter is smaller than the diameter of a single particle ($d_{cl} < d_p$), whereas the predicted clusters diameter is negative for solid volume fraction ε_s greater than 0.44 ($\varepsilon_s > 0.44$). These problems are confronted using Gu and Chen (Gu and Chen, 1998) correlation (eq. 3.10), which provides almost identical results for the clusters diameter as the one by Harris et al., 2002.

$$d_{cl} = d_p + \left(0.027 - 10 \cdot d_p\right) \cdot \varepsilon_s + 32 \cdot \varepsilon_s^{\,6} \qquad \text{Eq. 3.10}$$

Moreover, the following constraints (equations 3.11 - 3.13) depict the corresponding physical limits as far as the dense and/or dilute regions are concerned.

$\varepsilon_{mf} \leq \varepsilon_c$ (Naren et al., 2007; Wang and Li, 2007; Yang et al., 2003) Eq. 3.11

$\varepsilon_f \leq 0.9997$ (Wang et al., 2008; Wang and Li, 2007; Yang et al., 2003) Eq. 3.12

$$\varepsilon_c < \varepsilon_g < \varepsilon_f \qquad \text{Eq. 3.13}$$

Within this work the following constraint applicable to the slip velocity in the dilute phase is also proposed. Constraint 3.14, describes the fact that a single particle in dilute phase cannot have a slip velocity greater than its corresponding terminal one.

$$U_{sf}/\varepsilon_f < U_t \qquad \text{Eq. 3.14}$$

The latter constraint refers to the slip velocity of the dilute phase and is not valid for dense phases (Naren et al., 2007). As Kunii and Levenspiel, (1991) denote, terminal velocity is an exponential function of the respective diameter of the structure. Therefore, large structures like clusters have a terminal velocity considerably greater than the terminal velocity of sole particles (Yerushalmi et al., 1976).

The system of all the above equations (3.2 to 3.14) can be solved through the minimization of the energy N_{st}, which is inter - exchanged between gas and solid particles for the suspension and transportation of the particles within a cell (Naren et al., 2007; Wang et al., 2008):

$$N_{st} = \left| \frac{1}{\left(1-\varepsilon_g\right)\cdot\rho_s} \left[m_f \cdot F_f \cdot U_f + m_c \cdot F_c \cdot U_c + m_i \cdot F_i \cdot U_f \cdot \left(1-f\right) \right] \right| \rightarrow \min imum \qquad \text{Eq. 3.15}$$

Concluding, the correlation of the drag force, based on the EMMS model is defined as:

$$F_{EMMS} = \varepsilon_g \cdot \left[f \cdot \left(1-\varepsilon_c\right) \cdot \left(g + a_c\right) + \left(1-f\right) \cdot \left(1-\varepsilon_f\right) \cdot \left(g + a_f\right) \right] \cdot \left(\rho_s - \rho_g\right) \qquad \text{Eq. 3.16}$$

Equation 3.16 is always applied for the calculation of the induced drag force when an EMMS scheme is applied. However, this force is not straightforwardly applied for numerical reasons. Instead, the heterogeneity index is defined. This index is calculated as the ratio of the drag force calculated by the conventional model of Wen and Yu (Wen and Yu, 1966) to the respective force calculated by the proposed EMMS scheme, as depicted in equation 3.17. Equation 3.1 is applied for the calculation of the momentum exchange between gas and solids.

$$H_d = \frac{F_{Wen,Yu}}{F_{Emms}} \qquad \text{Eq. 3.17}$$

3.2 Stress tensor of a granular medium in CFB recirculation system

Recent studies, such as the work of Nguyen et al.; Zhang et al., 2008 and Shuai et al., 2011[a] simulate all parts of the CFD installation including the riser, the cyclone, the down-comer and the pneumatic valve. The authors of those works applied the governing equations developed for the CFB risers, also in the recirculation system. However, particle loading is much higher in the recirculation system and the governing physical mechanisms are quite different.

A more rigorous investigation of the multiphase flow inside common pneumatic valves concludes that the hydrodynamic characteristics of the induced flow are quite different from the fast fluidization regime, which dominates CFB risers. The valves used in CFB installations are mainly the L-valve (Arena et al., 1998; Geldart and Jones, 1991; Yang and Knowlton, 1993) the loop-seal (Basu and Cheng, 2000; Cheng and Basu, 1999; Kim and Kim, 2002) and the seal pot (Kunii and Levenspiel, 1991).

L-valve operation is an excellent example of the complicated nature of granular flows (Yang and Knowlton, 1993), as depicted in Figure 3.3. Three regions can be identified based on the flow patterns induced, i.e. the upper and the lower part of the horizontal leg and the vertical leg. In the upper part of the horizontal leg the pneumatic transport regime is predominant, while in the vertical pipe a fixed bed can be observed. In the lower part of the horizontal leg, depending on the aeration rate, a slug flow with non-fluidized particles may also be identified, as reported by Yang and Knowlton, 1993. The volume fraction of solids inside the valve can reach up to ε_s^{max}, indicating that there are regions of the CFB loop where the flow is very dense.

The loop-seal can be operated in two different modes (Figure 3.4), i.e. as a pass-through device and as a regulator of the circulation flux. The flow inside a loop-seal, operated as a pass-through device, is much simpler, as it is hydro-dynamically governed by the in depth investigated bubbling regime (Basu and Cheng, 2000). Although the flow is dense ($\varepsilon_s = \varepsilon_s^{mf}$), particles move with non-negligible velocity. This is attributed to the drag forces induced by the fluidizing gas resulting in particle velocity in the range of 0.1 to 1 m/s. However, loop-seal can be also utilized as a regulator of the mass flow re-circulating within the unit. In this

case (Basu and Cheng, 2000; Cheng and Basu, 1999; Kim and Kim, 2002) the volume fraction of solids within the down-comer is very high, reaching values up to ε_s^{max}.

Sophisticated simulation of these devices is considered essential for valid full-loop simulations of CFB units. Since the complicated flow field of the riser is modeled in an Eulerian fashion, the same approach should be used for the recirculation system. Conventional TFM models incorporate a stress tensor for the particle phase that is formulated on the basis of kinetic theory for granular solids with volume fraction lower than a limit (ε_s^{fr}). For denser flows, the plastic-frictional theory is used. It should be underlined that virtually all theories consider the granular flows as non-cohesive (zero normal stresses are equivalent with zero shear stresses), as reported by Christakis et al., 2006; Dartevelle, 2003.

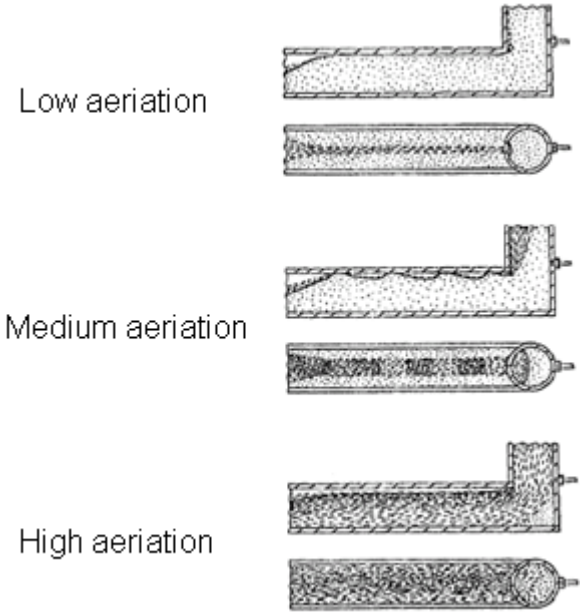

Figure 3.3 L-valve operation (Yang and Knowlton, 1993)

The plastic theory requires a suitable yield criterion and an appropriate flow rule. The yield criterion should obey to the five rules reported by Gray et al., 1991. The yield criterion plotted in the principal stresses / rate of strain frame should be: i) a convex surface; ii) symmetric with respect to the hydrodynamic axis; iii) a closed surface with the two vertexes along the hydrodynamic axis; iv) a nested surface that its radius is proportional to the normal stress; v) dissipative ($D_i : \sigma_i \geq 0$).

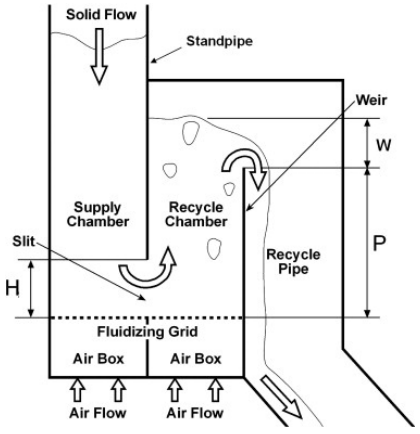

Figure 3.4 Loop-seal operation (Vun et al., 2010)

The extended von Misses Yield criterion is generally used in CFB risers simulation (Nikolopoulos et al., 2010[a]; Nikolopoulos et al., 2010[b]; Tsuo and Gidaspow, 1990; Zhang and VanderHeyden, 2001; Zhang et al., 2008) along with the associated flow rule of Levy-von Misses (Nikolopoulos et al., 2012[c]). The Yield function is depicted in equation 3.18 and the respective geometrical surface in Figure 3.5. Equation 3.19 described the associated flow rule that ensures the normality condition (D_i is a vector perpendicular to the yield surface, in the principal stress frame (Dartevelle, 2003)). In equation 3.19, ξ is the plastic multiplier and it is correlated with solids viscosity. A Yield criterion and a flow rule, along with mathematical manipulation (Dartevelle, 2003) can be used for the formulation of correlations for granular viscosity in the plastic regime.

$$Y = II_{dT} + \langle \sigma \rangle^2 \sin^2 \varphi = 0 \qquad \text{Eq. 3.18}$$

$$D_i = \xi \frac{\partial Y}{\partial \sigma_i} \qquad \text{Eq. 3.19}$$

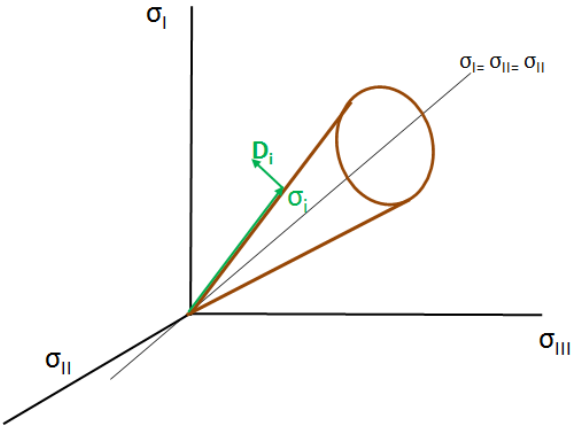

Figure 3.5 von – Misses yield criterion (Dartevelle, 2003)

In Figure 3.5 the von Misses Yield criterion is depicted. Inside, the volume that is bounded by the von – Misses surface, elastic / rigid body mechanics apply. At the surface, yield starts and plastic deformation of the granular material occurs. It can be seen that the von – Misses Yield criterion is a convex, symmetric and nested surface but it is not a closed surface. Additionally, the rate of strain and the stress vectors are perpendicular; therefore, the dissipation of energy is always zero. Moreover, the aforementioned criterion does not take into account the granular material hardening. Control volumes denser in particulates have higher resistance to yield. This phenomenon is not incorporated in the von Misses criterion since the bulk density or the volume function of the material is not incorporated in the developed correlation.

These characteristics along with scientific essays on storage silo of granular materials (Christakis et al., 2006; Christakis et al., 2002; Goodey and Brown, 2004; Goodey et al., 2003) as well as geophysical granular flows (Dartevelle, 2003; Dartevelle, 2004; Dartevelle et al., 2004) have shown that the aforementioned yield criterion is not appropriate for numerical simulation of dense granular flows. Indeed, as reported by Dartevelle, 2003, this yield criterion and the associated Levy-von Misses flow rule, can properly simulate dilatancy of a control volume but not consolidation. Recently, some researchers of the CFB field (Nikolopoulos et al., 2012[c]; Vun et al., 2010), have also abandoned the von Misses criterion and incorporated more sophisticated models. The main drawback of the von – Misses criterion, which results in severe underestimation of the frictional viscous forces, is the fact

that it does not take into account consolidation. This phenomenon can be properly addressed by the yield criterion of Pitman-Schaeffer-Gray-Stiles (eq. 3.20).

$$Y = II_{dT} + \sin^2\varphi\left[\left(\langle\sigma\rangle - P\right)^2 - P^2\right] = 0, \qquad \text{Eq. 3.20}$$

$$\langle\sigma\rangle = P - \lambda\nabla\cdot\vec{u}_s. \qquad \text{Eq. 3.21}$$

Figure 3.6 illustrates the sophisticated Yield criterion of Pitman-Schaeffer-Gray-Stiles. This criterion is not a single surface but a group of surfaces. Changes in the bulk density alter the shape of the surface. This feature is driven by the solids velocity divergence in equation 3.21. This divergence quantifies the change of particle loading in a control volume. This divergence influences the stress applied to solids, since densification of a control volume results in augmented stresses when compared with the respective stresses calculated by the von – Misses yield criterion.

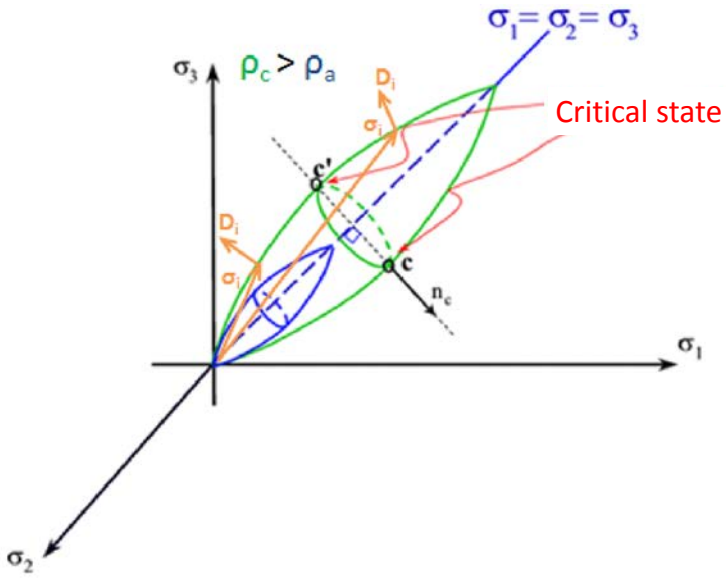

Figure 3.6 Pitman - Schaeffer - Gray – Stiles Yield criterion (Dartevelle, 2003)

It should be underlined that the Pitman - Schaeffer - Gray – Stiles Yield criterion is a convex, symmetric, closed and nested surface and the dissipation of energy is not always zero. In fact the energy dissipation is positive ($D_i \cdot \sigma_i > 0$) for all cases except for the critical state. In this state, the granular material under tension is not plastically deformed but orthogonally the effective density is changed. Moreover, the Pitman - Schaeffer - Gray – Stiles criterion takes into account the granular material hardening. This phenomenon is integrated in their theory (Gray et al., 1991) through the changes of the effective density incorporated in equation 3.21.

It can be observed that the yield criterion of von - Misses/Coulomb can be reached by equation 3.20, should for the stresses term only normal pressure be taken into account, i.e. $\langle\sigma\rangle = P$. Thus, the von - Misses criterion does not take into account the effect of compressibility phenomena (changes of bulk density) occurring during the operation of CFB units. In other words, the sophisticated Pitman - Schaeffer - Gray – Stiles yield criterion does not make the simplification that the time derivative of effective density of particles is zero, i.e. $\frac{\partial}{\partial t}(\varepsilon_s\rho_s) \neq 0$. A detailed overview on the compressibility effects regarding granular flows, can be found in the work of Tardos, 1997. Moreover, in the work of Elaskar et al., 2000 all

the up-to-date available yield criteria are synopsized. Furthermore, an alternative yield criterion, the Drucker- Prager, has been utilized in the modeling of granular material storage silo within a mixture multiphase model by Christakis et al., 2006 with very good results.

Since frictional forces are the most important factor in dense granular flows, it should be underlined that the repose angle is the most representative particle characteristic induced by these forces. In this work, a stress model for the recirculation system of CFBs is developed based on the Pitman - Schaeffer - Gray – Stiles yield criterion. This model is firstly tested for validation purposes in a simulation of a repose angle measurement experiment. Both the new model (based on the Pitman - Schaeffer - Gray – Stiles yield criterion) and the conventional one (based on the von Misses Yield criterion) are tested.

It should be underlined that the present work is a first attempt for the prediction of the repose angle of a granular material, adopting the TFM pure Eulerian approach. Earlier works (Sitharam and Vinod, 2009; Yuu and Umekage, 2008; Zhou et al., 2002) have been conducted with DEM (Discrete Elements Model) methodology. The rotation of particles can be explicitly introduced in the latter methodology and, as reported by Zhou et al., 2002, this characteristic is very important when simulating the repose angle of a granular material. It is denoted that TFM approaches cannot explicitly model this characteristic. However, Shuyan et al., 2008 have tried to implicitly model the effect of rotation through an alternation of the partial differential equation of granular temperature. Despite the fact that DEM methodology generally presents higher accuracy when compared to the TFM one, the TFM is considered as more applicable in the case of a CFB unit. This is owed to the high computational cost the DEM exhibits because of the billion-scale number of particles that should be simulated. Thus, the application of DEM is prohibitive for the simulation of the returning systems in industrial fluidized beds.

3.2.1 Repose angle experiment - Simulation Methodology

In order to investigate the accuracy of the modeling of the frictional inter-particle forces, in the case of very dense granular flows, a typical experiment of angle of repose measurement for a granular material is selected for simulation. Figure 3.7 depicts the slope that is formed whenever a granular material is poured in a flat surface.

The experiment was conducted in the installations of IFK (Stuttgart University) by Nikolopoulos, 2006. The geometry of the installation comprises of two connected simple cylindrical pipes, each of which has a diameter equal to 40 mm. The length of each pipe is 2 m and the two pipes are connected forming a geometry that resembles the letter L, Figure 3.8. In the vertical pipe sand-like material was poured. The material used had a mean diameter of approximately 462 μm, while its density was equal to 2600 kg/m^3.

Figure 3.7 Definition of repose angle of a granular material

The experimental setup included the free-falling motion of an unmeasured batch of material from the top of the vertical pipe. This mass was uniformly poured from its top while at the end of the experiment it stopped moving, after hitting the junction of the two pipes, thus forming an angle of repose. This value (φ) was found to be 36.03^o.

The numerical tests undertaken, focus on the numerical simulation of the prescribed experiment, by implementing two different models for the calculation of shear (kinetic, collisional and frictional term) and normal stresses (kinetic and frictional term) i.e the standard in literature and the proposed / developed one. The experimental procedure is simulated in two dimensions and not three, only for simplification purposes and less CPU requirements.

The coefficient of momentum interexchange (β) between gas and solid phases was simulated with the correlation (eq. 2.28) of Gidaspow (Ding and Gidaspow, 1990), since in very dense granular flows the assumption of homogeneous conditions inside a control volume is accurate enough (Nikolopoulos et al., 2010[a]; Zhang et al., 2008). The differential transport equation of granular temperature is not incorporated in the model. Instead of this, the respective algebraic equation (Syamlal et al., 1993) is used for simplicity. Moreover, the particles are modeled as mono - sized and spherical (φ_i equal to 1) in order to decrease the computational cost and to avoid the numerical complexities that arise from PSD incorporation. Finally, a typical simplification made by most of published works, followed also in this study, is that the effect of moisture is not included in the CFD model. Elevated moisture content increases the angle of repose (Wang et al., 2010[b]).

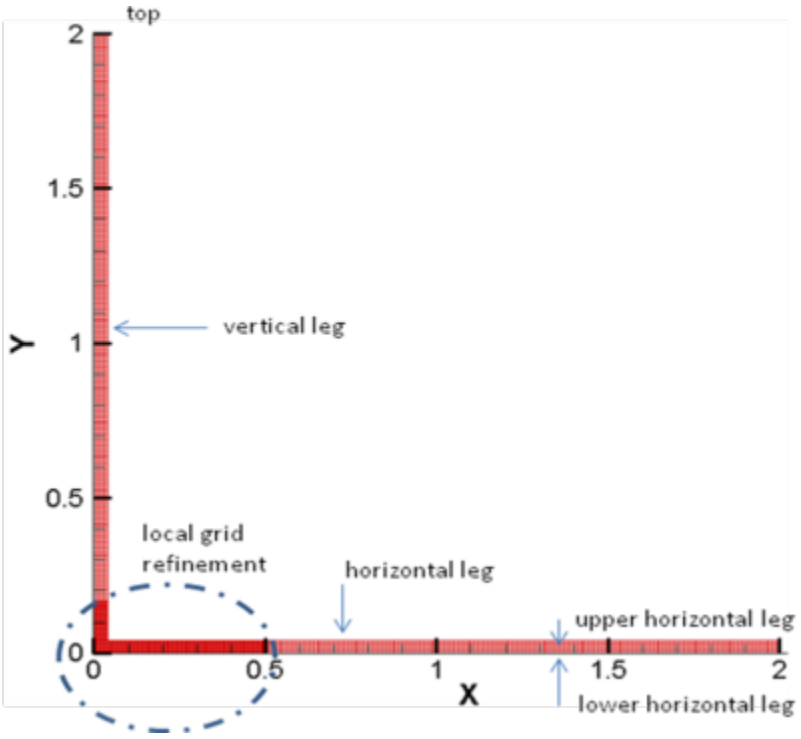

Figure 3.8 Computational domain

The numerical grid consists of 2352 quadratic elements. One level of local refinement is implemented in order to increase numerical accuracy, especially in the region of interest (junction of L-valve),. The lower grid resolution is 10^{-4} m^2/cell while the increased resolution is 2.5 10^{-5} m^2/cell. The equations that describe the hydrodynamics of the multi – phase flow (gas and solid phases) are the continuity equation 2.14 and the momentum equation 2.15. The time step of the calculations is set equal to 40 μs, whilst the transport equations of all the variables are discretized using the QUICK 2nd order spatial discretization scheme (Leonard et al., 1990). Two different modeling approaches were implemented for the calculation of shear and normal stresses of the solid phase,. The first one is the conventional model, adopted by most researchers (Atsonios et al., 2011; Nikolopoulos et al., 2010[b]; Tsuo and Gidaspow, 1990; Zhang and VanderHeyden, 2001; Zhang et al., 2008), whilst the second one is the

custom model developed in this work, based on the yield function of Pitman-Schaeffer-Gray-Stiles, (Gray et al., 1991).

3.2.1.1 Conventional stress model (case A)

The von-Misses yield criterion is based on the approximation that stresses are only affected by the normal pressure $\langle\sigma\rangle = P_s$ .The viscous part of the stress tensor of solid phase is calculated based on the following closure equations (eq. 3.22 to 3.25):

$$\bar{\bar{\tau}}_s = \varepsilon_s \mu\left(\nabla\vec{u}_s + \nabla\vec{u}_s{}^T\right) + \varepsilon_s\left(\lambda - \frac{2}{3}\mu\right)\nabla\cdot\vec{u}_s I \qquad \text{Eq. 3.22}$$

$$\lambda = \begin{cases} \varepsilon_s < \varepsilon_{fr} \Rightarrow \frac{4}{3}\varepsilon_s\rho_s d_s g_o\left(1+e_{ss}\right)\left(\frac{\Theta_s}{\pi}\right)^{\frac{1}{2}} \\ \varepsilon_s \geq \varepsilon_{fr} \Rightarrow \lambda_{fr} \end{cases} \qquad \text{Eq. 3.23}$$

$$P_s = \begin{cases} \varepsilon_s < \varepsilon_s^{fr} \Rightarrow P_{kin} = \varepsilon_s\rho_s\Theta_s + 2\rho_s(1+e_{ss})\varepsilon_s^2 g_o\Theta_s \\ \varepsilon_s \geq \varepsilon_s^{fr} \Rightarrow P_{fr} = 0.1\varepsilon_s\frac{\left(\varepsilon_s - \varepsilon_s^{fr}\right)^2}{\left(\varepsilon_s^{\max} - \varepsilon_s\right)^5} \end{cases} \qquad \text{Eq. 3.24}$$

(Johnson and Jackson, 1987)

$$\mu = \begin{cases} \varepsilon_s < \varepsilon_s^{fr} \Rightarrow \mu_{kin} + \mu_{col} \\ \varepsilon_s \geq \varepsilon_s^{fr} \Rightarrow \mu_{kin} + \mu_{col} + \mu_{fr} \end{cases} \qquad \text{Eq. 3.25}$$

, where

$$\mu_{kin} = \frac{10\rho_s d_s\sqrt{\Theta_s\pi}}{96\varepsilon_s(1+e_{ss})g_o}\cdot\left[1+\frac{4}{5}g_o\varepsilon_s(1+e_{ss})\right]^2 \qquad \text{Eq. 3.26}$$

(Gidaspow et al., 1992)

$$\mu_{col} = \frac{4}{5}\varepsilon_s\rho_s d_s g_o(1+e_{ss})\sqrt{\left(\frac{\Theta_s}{\pi}\right)} \qquad \text{Eq. 3.27}$$

(Gidaspow et al., 1992)

$$\mu_{fr} = \frac{P_s\sin\phi}{2\varepsilon_s\sqrt{II_{dD}}} \qquad \text{Eq. 3.28}$$

(Johnson and Jackson, 1987)

$$\lambda_{fr} = 0 \qquad \text{Eq. 3.29}$$

$$g_o = \left[1-\left(\frac{\varepsilon_s}{\varepsilon_s^{\max}}\right)^{\frac{1}{3}}\right]^{-1} \text{ (Ogawa et al., 1980)} \qquad \text{Eq. 3.30}$$

It should be underlined that shear and bulk viscosity in correlations 3.22, 3.23 and 3.25 to 3.29 are not the effective ones but the empirical viscosity of the pure phase *s*. The effective viscosity can be obtained through multiplication with the volume fraction of solids.

3.2.1.2 Pitman - Schaeffer – Gray - Stiles yield criterion and viscous forces (cases B and C)

The aforementioned conventional model is developed in accordance with the kinetic theory of gases, and it incorporates kinetic as well as collisional contributions to the particle energy destruction. Based on this theory, the solid particles are treated as colliding molecules in dense gases and, hence, the particle-particle interactions are assumed to arise mainly from the kinetic-collisional stresses. Researchers have realized the importance of particle frictional stresses when simulating dense granular flows, and this is the main reason for the addition of the μ_{fr} term in the stress tensor for solid volume fractions above ε_s^{fr}. As a result the aforementioned model has a serious drawback when employed at the intermediate gas-solid flow conditions, such as the ones in bubbling beds. The Pitman- Schaeffer- Gray-Stiles yield criterion is based on the notion that stresses term is linked not only with the normal pressure, but also with the viscous normal stresses, i.e. $\langle\sigma\rangle = P - \lambda\nabla\cdot\vec{u}_s$.

Apart from the incorporation of the Pitman – Schaeffer – Gray – Stiles yield criterion, the proposed model is differentiated because it incorporates an additional term representing the frictional viscosity for solid volume fraction lower than the friction limit. This was proposed in the work of Makkawi et al., 2006, in which the frictional stresses were found to play a significant role, in almost the entire range of the volume fraction of solids. In addition, this approach allows for a smooth transition for the shear stresses between the rapid-intermediate flow and the slow frictional one. As it can be seen in equation 3.28, the calculation of the frictional shear stress involves P_s. The term derived by the pressure expression (P_{kin}) is taken into account for the rapid-intermediate flow, whilst the sum of pressures by Syamlal et al., 1993 (P_{kin}) and frictional pressure (P_{fr}) is considered for the slow frictional one,. This modeling approach, where the particulate phase stress tensor constitutes of the kinetic, collisional and the frictional one, is as well demonstrated in the work of (Patil et al., 2005) and ensure shear stress continuity for ε_s equal to the friction limit.

The basic question, arising from the aforementioned argument, is that expressions should be used for the description of the friction stress tensor in the whole range. These forces are caused by the sustained and/or multi-particle contacts and deformations. The present investigation presents two different approaches for the calculation of the stress tensor, based on the Pitman- Schaeffer- Gray-Stiles yield. Both models are incorporated in the CFD commercial package Fluent (2006) through custom-built UDF subroutines.

Initially the Standard Pitman- Schaeffer- Gray-Stiles yield criterion with a smooth transition (case B) is presented. The numerical model adopted in case B, is described from equations 3.31 to 3.37. The model adopts the sophisticated Pitman- Schaeffer- Gray-Stiles yield criterion for the determination of frictional shear and bulk stresses. Moreover frictional forces are applied for any particle loading and the kinetic and collisional parts of shear viscosity are calculated based on the equations of Gevrin et al., 2008.

$$\lambda = \begin{cases} \varepsilon_s < \varepsilon_{fr} \Rightarrow \dfrac{4}{3}\varepsilon_s\rho_s d_s g_o\left(1+e_{ss}\right)\left(\dfrac{\Theta_s}{\pi}\right)^{\frac{1}{2}} \\ \varepsilon_s \geq \varepsilon_{fr} \Rightarrow \dfrac{P_s}{\varepsilon_s\sqrt{4\sin^2\varphi\cdot II_{dD} + (\nabla\cdot\vec{u}_s)^2}} \end{cases} \text{(Dartevelle, 2003; Lun et al., 1984)} \qquad \text{Eq. 3.31}$$

$$P_s = \begin{cases} \varepsilon_s < \varepsilon_s^{fr} \Rightarrow P_{kin} = \varepsilon_s \rho_s \Theta_s + 2\rho_s (1+e_{ss}) \varepsilon_s^2 g_o \Theta_s \\ \varepsilon_s \geq \varepsilon_s^{fr} \Rightarrow P_{kin} + P_{fr} \end{cases} \quad \text{Eq. 3.32}$$

(Johnson and Jackson, 1987; Syamlal et al., 1993)

$$P_{fr} = \begin{cases} \varepsilon_s < 0.59 \Rightarrow 0.05 \dfrac{\left(\varepsilon_s - \varepsilon_s^{fr}\right)^2}{\left(\varepsilon_s^{\max} - \varepsilon_s\right)^3} \\ \varepsilon_s \geq 0.59 \Rightarrow 10^{25} \left(\varepsilon_s - 0.59\right)^{10} \end{cases} \quad \text{Eq. 3.33}$$

Princeton model, (Srivastava and Sundaresan, 2003; Reuge et al., 2008)

$$\mu = \mu_{kin} + \mu_{col} + \mu_{fr} \quad \text{Eq. 3.34}$$

, where (Gevrin et al., 2008; Dartevelle, 2003):

$$\mu_{kin} = \frac{\sqrt{\pi \Theta_s} \dfrac{d_s \rho_s}{24 \varepsilon_s g_o} \dfrac{\left(5 + 2\varepsilon_s g_o (1+e_{ss})(3e_{ss}-1)\right)}{(1+e_{ss})(3-e_{ss})}}{\left(1 + \dfrac{45\mu_g}{6\varepsilon_s g_o d_s \rho_s \sqrt{\dfrac{\Theta_s}{\pi}} (1+e_{ss})(3e_{ss}-1)}\right)} \quad \text{Eq. 3.35}$$

$$\mu_{col} = \frac{4}{5} \varepsilon_s \rho_s g_o (1+e_{ss}) \left(\frac{\mu_{kin}}{\rho_s} + d_s \sqrt{\frac{\Theta_s}{\pi}} \right) \quad \text{Eq. 3.36}$$

$$\mu_{fr} = \frac{P_s \sin^2 \varphi}{\varepsilon_s \sqrt{4 \sin^2 \varphi \cdot \mathrm{II}_{dD} + (\nabla \cdot \vec{u}_s)^2}} \quad \text{Eq. 3.37}$$

The radial distribution function is calculated through equation 3.30.

An alternative new model is also tested. This model incorporated the Standard Pitman-Schaeffer- Gray-Stiles yield criterion with a smooth transition, based on Laux correlation (case C). Laux, 1998 tested several models from the field of soil mechanics to incorporate long term particle contacts. It was demonstrated that certain frictional models should be included in order to improve the description of phenomena such as heap formation. The frictional stress model that gave the best results is given by μ_{Laux} (eq. 3.38) proposed by Laux, 1998. This expression is used for the calculation of frictional viscosity in this test case (C), instead of equation 3.37, whilst all the other sub-models are kept the same with the previous case (B). It should be noted that for the calculation of the bulk viscosity for particle loading greater than the friction limit, eq. 3.31 is used that is based on the Pitman- Schaeffer- Gray-Stiles yield criterion. The numerical results indicate that the values as calculated by Laux, 1998 and Dartevelle, 2003 expressions are of the same magnitude for solid volume fractions below 0.5, whilst, Laux, 1998 expression is almost ten times higher than the corresponding by (Dartevelle, 2003) for fractions higher than 0.55.

$$\mu_{fr} = \mu_{Laux} = \frac{6 \sin \varphi}{9 - \sin^2 \varphi} \frac{3 |\lambda \nabla \cdot \vec{u}_s - \dfrac{P_s}{\varepsilon_s}|}{2\sqrt{3 |\mathrm{II}_{2D}|}} \quad \text{Eq. 3.38}$$

For all scenarios examined, the isotropic/ hydrostatic pressure P is approximated with the well-known correlation of Johnson and Jackson, 1987. However, alternative options also exist (Gray et al., 1991). Table 3.3 summarizes the most important parameters of the adopted

multiphase model. The restitution coefficient was set equal to 0.9. This is a typical value, as reported by Ding and Gidaspow, 1990 as well as Hartge et al., 2009 for Geldart B particles. Moreover, regarding the boundary conditions, severe difficulties in the correct modeling of the wall effects on solid particles (Boutreux et al., 1997) exist. Generally, in CFB risers the no slip, the free slip and the partial slip boundary conditions (Johnson and Jackson, 1987) have been implemented in the recent literature. Most of the works (Hartge et al., 2009; Zhang et al., 2008) report the partial slip of particles on wall surfaces as the most appropriate boundary condition for the numerical simulation of the riser of a CFB unit. However, in CFB risers the multiphase flow is not very dense and the volume fraction of solids is generally less than ε_{fr}. Therefore, the wall boundary condition is parametrically investigated both for the horizontal and for the vertical leg, by implementing either partial or no slip conditions. Regarding the boundary condition for granular temperature (Θ_s) a Dirichlet (1st type) condition is applied (Θ_s= 0.0001 m^2 / s^2).

e_{ss}	0.9 (Ding and Gidaspow, 1990; Hartge et al., 2009)
ε_s^{max}	0.65
ε_s^{fr}	0.5 (Gidaspow et al., 1992)
ρ_g	1.225
μ_g	$1.8\ 10^{-5}$
ρ_s	2600
d_p	462 μm

Table 3.3 Model parameters.

Case	Model	Mass	Vertical Tube	Horizontal Tube
A	von-Misses/ Coulomb yield criterion	1.04	no-slip	no-slip
B	Pitman- Schaeffer- Gray-Stiles yield criterion	1.04	no-slip	no-slip
C	Pitman- Schaeffer- Gray-Stiles yield criterion (Laux Theory)	1.04	no-slip	no-slip
D	Pitman- Schaeffer- Gray-Stiles yield criterion	1.04	partial-slip	partial –slip
E	Pitman- Schaeffer- Gray-Stiles yield criterion (Laux Theory)	1.04	partial -slip	partial -slip
F	Pitman- Schaeffer- Gray-Stiles yield criterion	2.08	no-slip	no-slip

Table 3.4 Initial and boundary conditions of all cases examined.

As abovementioned, the mass of particles was not experimentally measured. However, this value has no effect on the repose angle of the material, as it is later shown. Thus, an arbitrary value of 1.04 kg/s and velocity of 2 m/s for a time period of 0.4 s was chosen. It should be mentioned that the solid phase was injected at the inlet of the vertical pipe uniformly and that at t = 0 s the solid mass within the domain is zero. Therefore, the mass that entered the solution domain after 0.4 s equals to 0.416 kg. This procedure is preferred against the alternative approach of patching to the solution domain this mass. Moreover, smaller values of solid flux would increase the computational time while higher values would result

in choking (Basu and Fraser, 1991) of the flow in the down-comer. The respective gas flow for the same time period is set to zero, while the initial velocity of the gas at t = 0 s for the whole domain is set to zero. After 0.4 sec the solid mass input is set to zero. After this initial period of 0.4 s the batch of 0.416 kg that entered the solution domain continued to perform a free-fall in the vertical pipe. The numerical cases presented in the following paragraphs, lasted around 5 days each, in a single core 2.4 GHz PC with 4 GM Ram memory.

3.2.2 Numerical predictions by the implementation of the two yield - criteria

The numerically investigated cases are shown in Table 3.4. The simulated geometry and the corresponding computational grid are depicted in Figure 3.8. The two model approaches, i.e. the conventional one (case A) and the proposed ones (cases B and C), are applied in the commercial code Fluent®, so as to numerically simulate the temporal evolution of the experimental procedure. Cases D to F are tested in order to parametrically examine the effect of wall boundary conditions and initial mass on the numerical simulation of the phenomenon. The corresponding numerical results regarding the evolution of the phenomenon, as predicted by the three approaches are shown in Figure 3.9, Figure 3.10 and Figure 3.12 for cases A, B and C respectively. In these cases the no - slip boundary condition is applied for the walls.

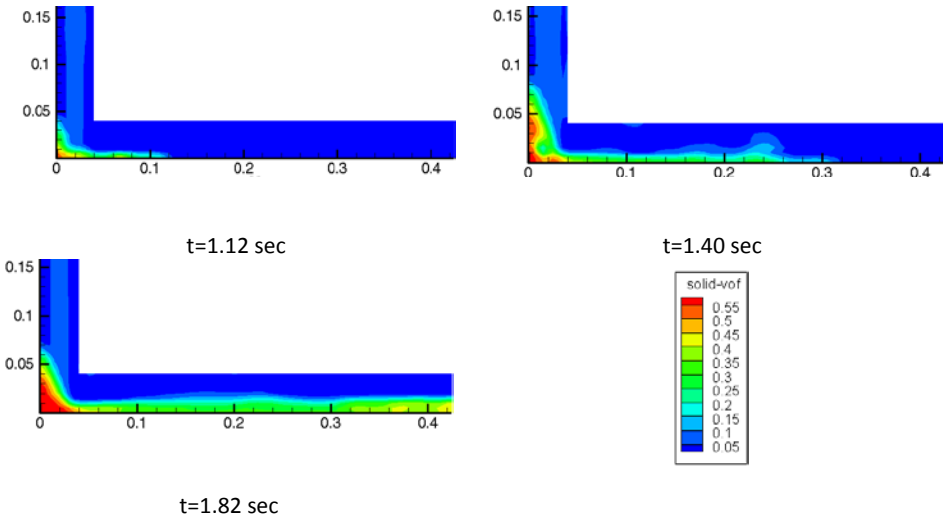

Figure 3.9 Temporal evolution of solid volume fraction for case A.

The inability of the conventional model (case A) to properly simulate the consolidation of the dense solid phase (Dartevelle, 2003) results in the severe underestimation of both the internal frictional viscous forces within the solid phase. Thus, the solid phase is flowing continuously without ever reaching a static angle of repose. Figure 3.9 clearly shows this trend, since the repose angle at t = 1.82 s is almost equal to zero. The experiments revealed that the solid phase stopped flowing within the horizontal pipe, reaching a final repose angle equal to around $\varphi = 36.03^{o}$, behavior that strongly contradicts with the numerical predictions of the conventional model. The yield criterion and the associated Levy-von Misses flow rule, adopted in model A, properly simulate dilatancy but not consolidation of the dense solid phase. The outcome of this drawback is the severe underestimation of both frictional viscous forces of granulates and of the friction forces between particles and the boundary walls, resulting in its continuous flow without ever reaching a static angle of repose.

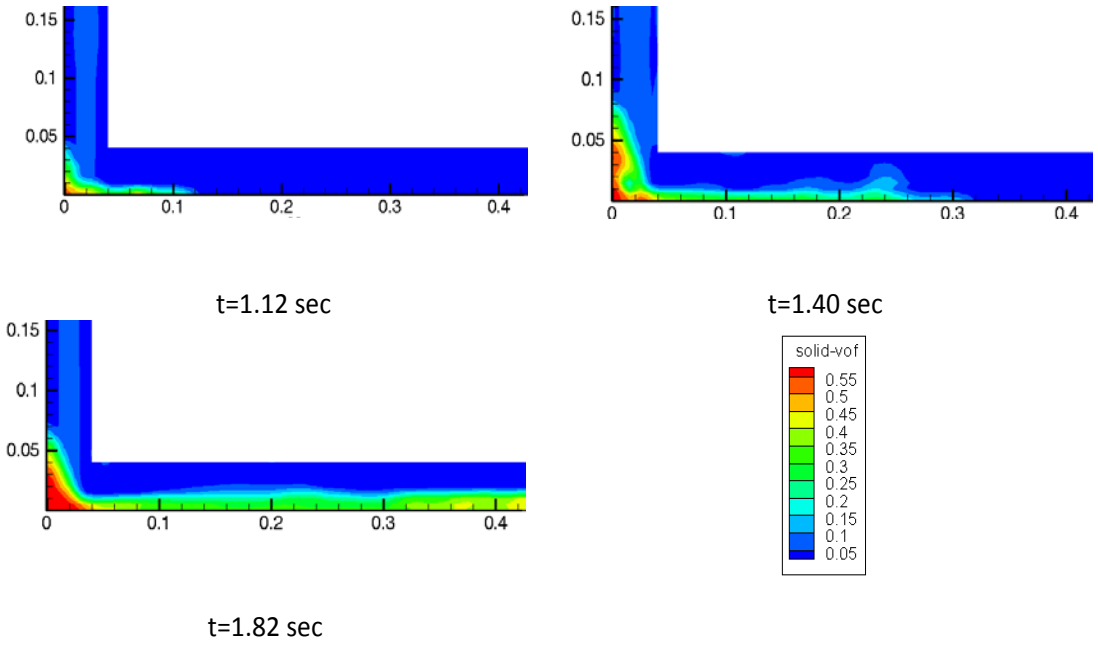

Figure 3.10 Temporal evolution of solid volume fraction for case B.

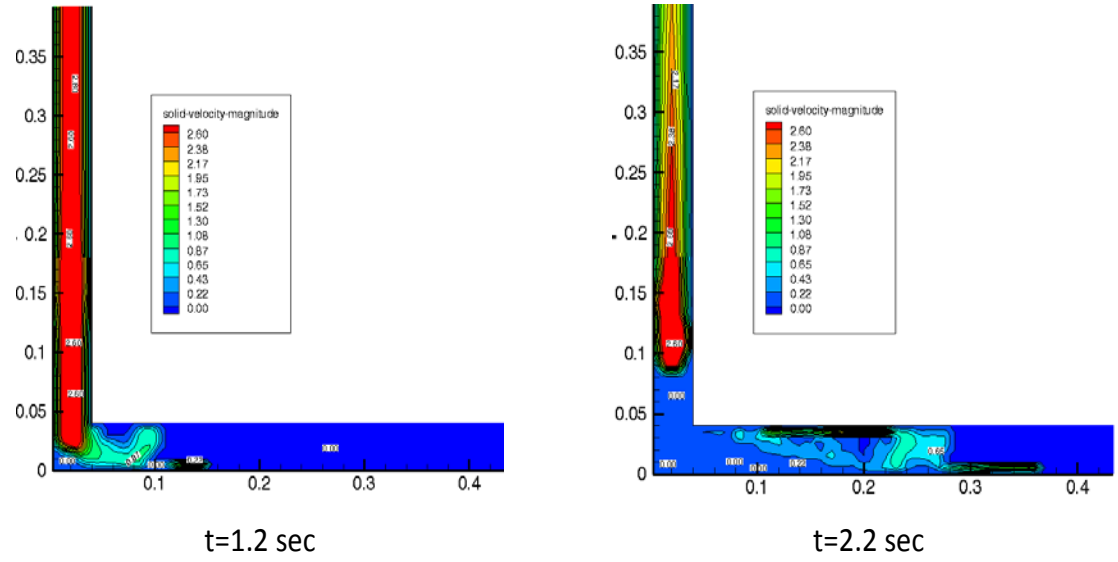

Figure 3.11 Temporal evolution of solid velocity for case B.

The time evolution of the same phenomenon adopting approach B is depicted in Figure 3.10. It should be underlined that the color-map of Figure 3.9 also applies for Figure 3.10 and Figure 3.12. Unlike to the conventional model, the dense granular flow stops flowing in the horizontal pipe, reaching a final static state with a repose angle approximately equal to φ = 21.0^{o}, Figure 3.10, t = 2.20sec. At this time instant, the velocity field within the solid phase is equal to zero, Figure 3.11, t = 2.20sec. At the interface region of solid and gas phases, the solid velocity magnitude is not zero due to the drag force induced by the gas phase and the inherent numerical diffusion of Eulerian formulation. However, this force action is incoherent with the actual physical situation, where the solid phase should have already ceased moving. This model behavior is the result of the arithmetic diffusion caused by the QUICK discretization scheme of the solids volume fraction equation.

As the time period of simulation increases the solid phase velocity magnitude decreases, reaching an almost zero value in the whole solid mass, at t = 2.2sec, Figure 3.11. The predicted repose angle agrees quite well with the corresponding experimentally measured one. To sum up, although the repose angle is much smaller than the experimentally measured one, it is of high technological importance that the solid phase stops moving. To the author's best knowledge this has not ever before achieved by a pure Eulerian approach.

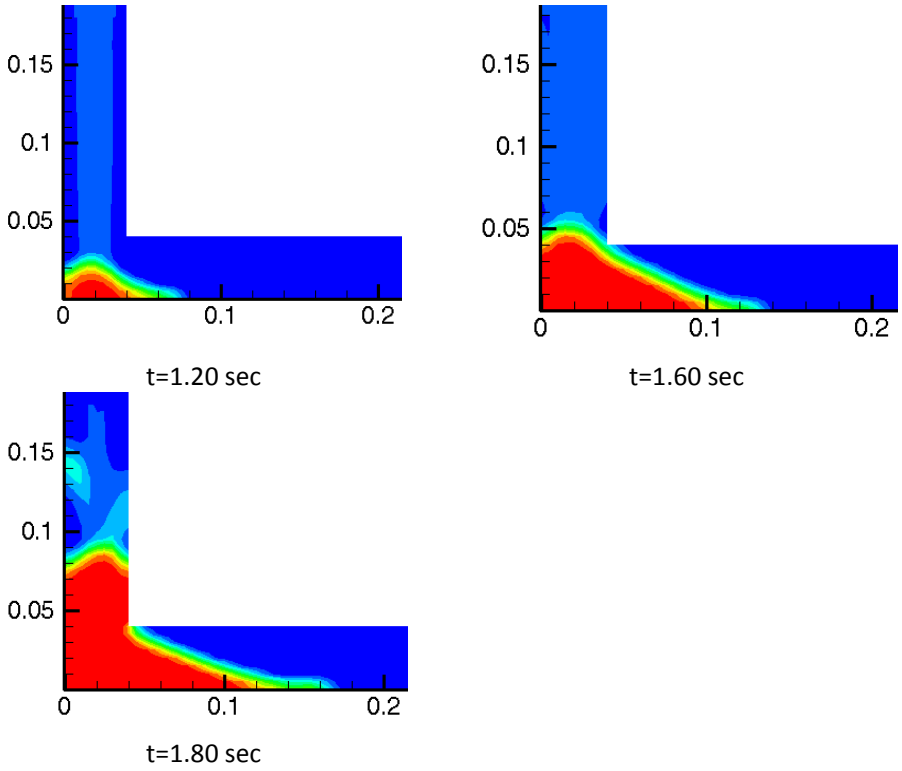

Figure 3.12 Temporal evolution of solid volume fraction for case C.

To overcome the aforementioned difficulties and deviations from the experiment, the model described in section 2.4.1 was extended by applying the Laux, 1998 correlation for the calculation of the frictional shear stress as analyzed in section 3.2.1. Figure 3.12 depicts the temporal evolution of solid volume fraction for case C. The dense granular flow stops flowing in the horizontal pipe, reaching a final static state with a repose angle approximately equal to $\varphi = 29.5^{o}$, Figure 3.12, t = 1.80sec. In comparison to the previous model, the solid has already ceased moving, due to the higher frictional forces exerted to the solid phase by the implementation of Laux, 1998 equation, Figure 3.12, t = 1.2sec. This fact is verified by the solid velocity magnitude presented at Figure 3.13 for the aforementioned time instants. Although the predicted repose angle is smaller than the experimental one, it is of high interest that a sizeable repose angle is achieved. This confirms that the application of the Pitman-Schaeffer- Gray-Stiles yield criterion associated with Laux, 1998 frictional force is an approach towards the correct direction for the simulation of dense granular flow characteristics within the Eulerian approach.

Figure 3.13a, b, and c show the spatial distribution of viscosity at t = 1.20 sec for cases A, B and C respectively, depicting the large differences in the predictions of the standard model and the proposed ones. This variation explains the difference in the temporal evolution of the phenomenon, as predicted by all models.

Aiming to investigate the effect of the boundary wall conditions on the evolution of the phenomenon, cases B and C are both examined with a different boundary condition (partial slip) in the horizontal and vertical pipes. The parametric study revealed that a higher spread of

granulates is observed for cases D and E in comparison to cases B and C. In the latter cases a smaller repose angle is predicted (case D: 15.5°, E: 17.5°). Figure 3.14 and Figure 3.15 depict the time evolution of the phenomenon for cases D and E respectively. In all cases, the partial slip boundary wall condition with a typical specularity coefficient (0.6) results in the continuous flow of the dense phase in the horizontal pipe, although the Pitman- Schaeffer-Gray-Stiles yield criterion is adopted. This is owed to the inability of standard partial-slip condition to describe the friction exhibited by the dense solid granular phase, when in contact with the solid wall. Therefore, high values of particles velocity near boundary wall (around to 0.22 m/s, Figure 3.16, t = 1.80) are induced when this type of boundary condition is applied.

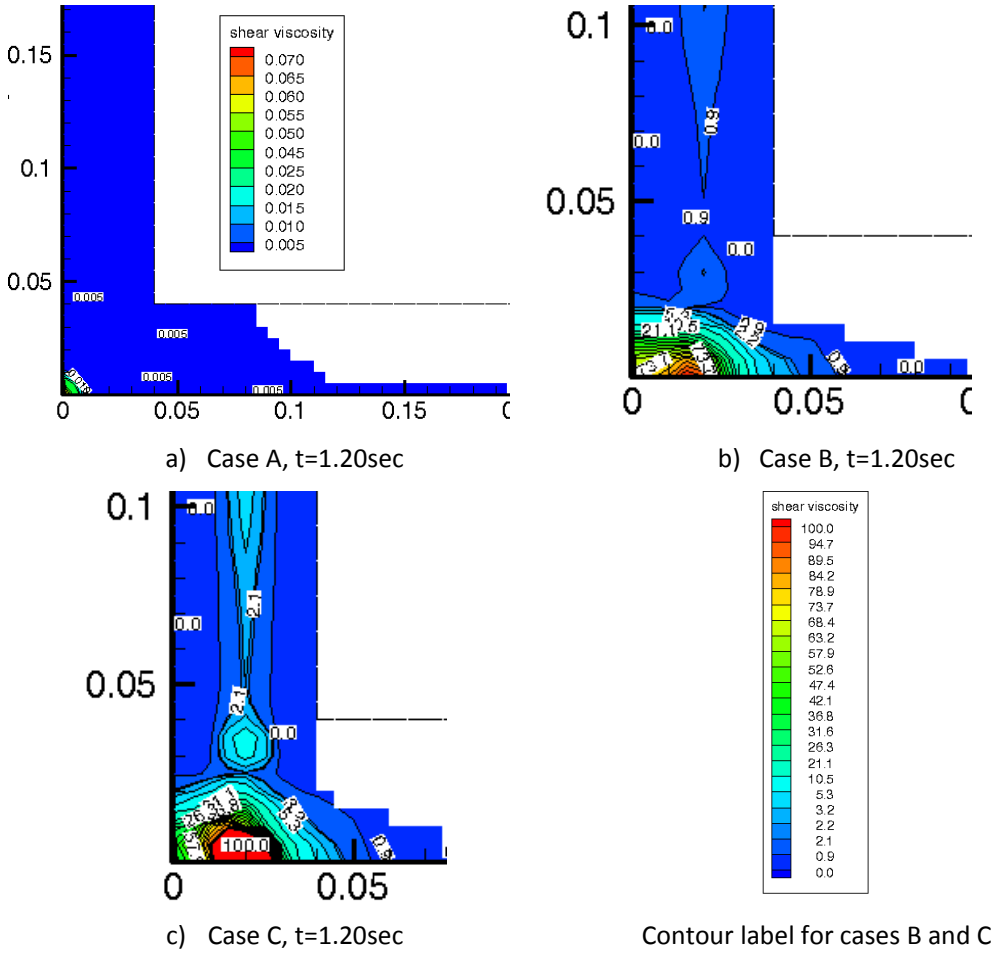

Figure 3.13 Shear viscosity (μ_s) magnitude for case A, B and C at t=1.20sec

The main reason for this failing is the inadequacy of the standard wall boundary conditions (no slip, free slips and partial slip) to consider the effect of adhesion forces between the solid phase particles and the wall. However, a more sophisticated correlation based on the extrapolation of the granulates stress tensor to the wall surfaces is difficult to be derived, since the governing physical mechanisms during the contact of these two different solid phases is quite complicated and not yet fully known (Boutreux et al., 1997).

Initial mass is another parameter that could influence the numerical results. In order to investigate this issue, an initial batch of particles equal to 2.08 kg was also simulated for cases B and C (case F, G). The wall boundary conditions in this case are identical to those in cases B and C, as depicted in Table 3.4.

Figure 3.17 and Figure 3.18 present the temporal evolution of the granular phase for the corresponding cases F and G. From Figure 3.10 and Figure 3.17, it is depicted that the temporal evolution of the phenomenon is not affected by the initial solid mass. The same argument stands for cases C and G, as depicted in Figure 3.12 and Figure 3.18, for which it is deduced that neither the angle of repose nor the final state depend on the initial solid mass. In case F the predicted repose angle is equal to that of case B, where a repose angle of 21^o is predicted. In cases G and C the corresponding values are φ = 29.5^o and 29.7^o.

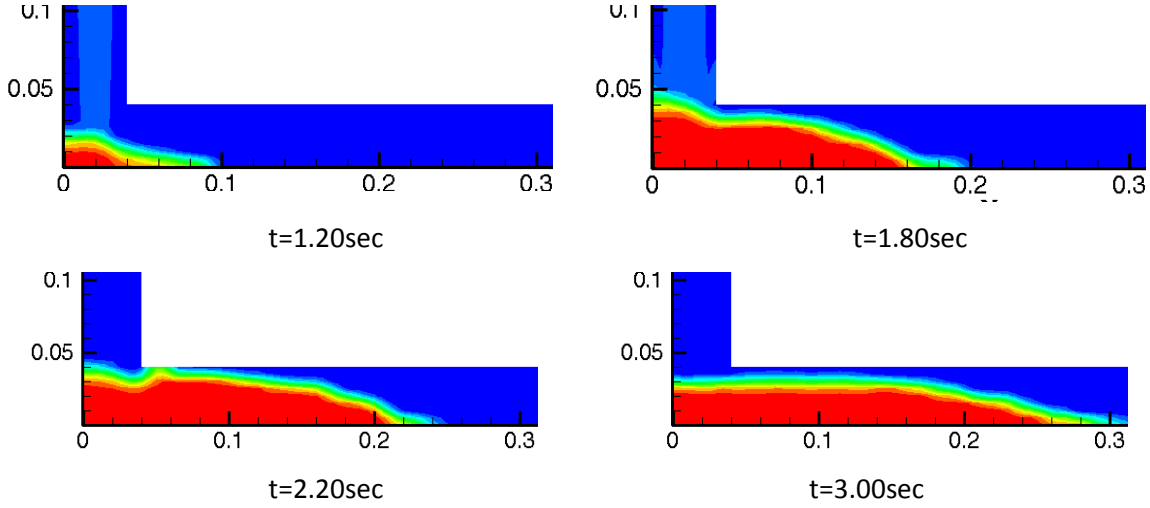

Figure 3.14 Temporal evolution of solid volume fraction for case D.

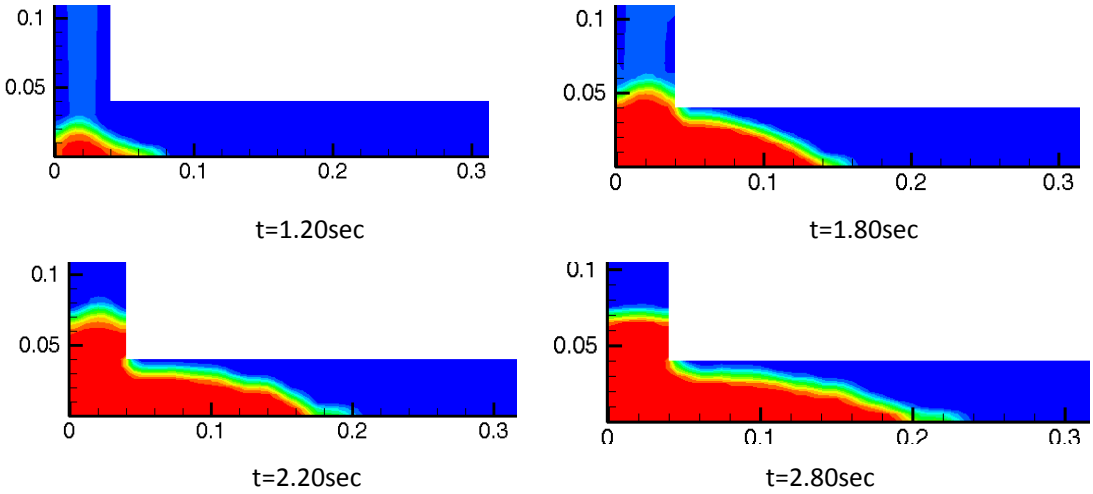

Figure 3.15 Temporal evolution of solid volume fraction for case E.

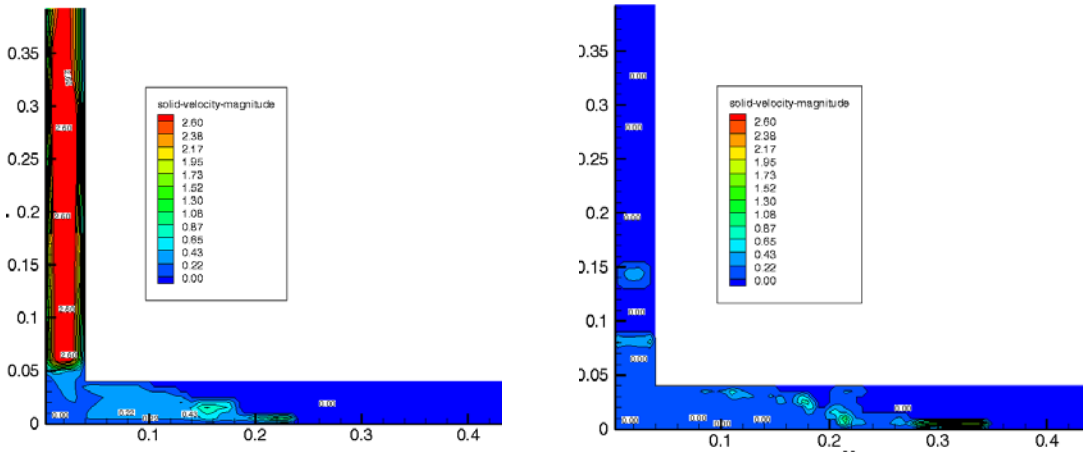

Figure 3.16 Temporal evolution of solid velocity for case E.

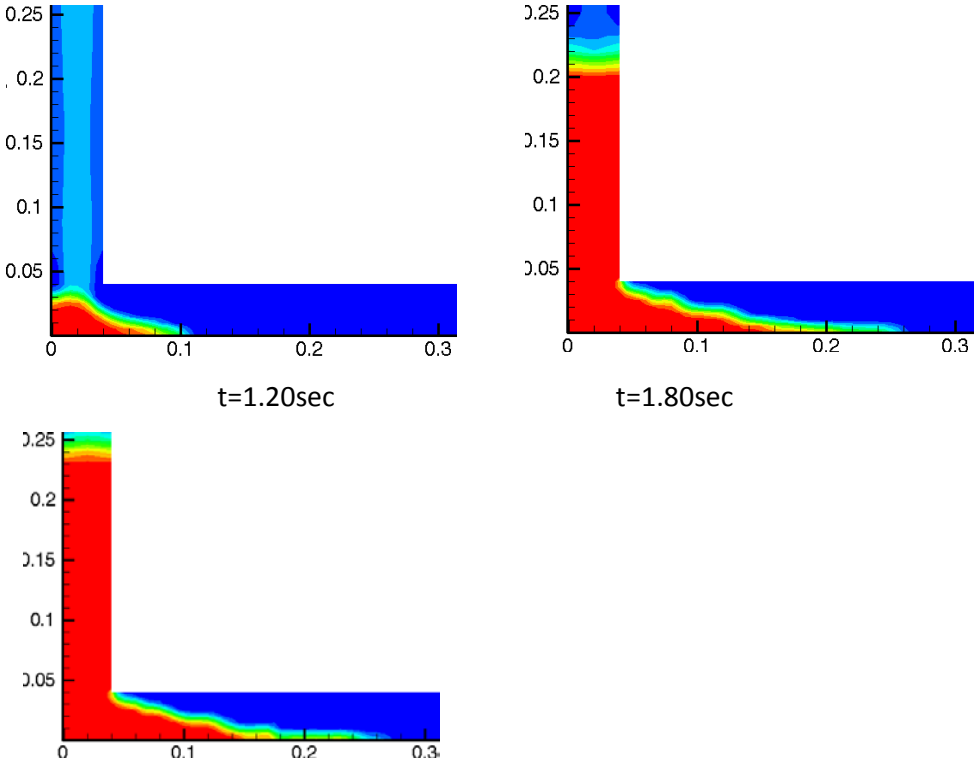

Figure 3.17 Temporal evolution of solid velocity for case F.

This numerical prediction is in line with the well-known fact that the repose angle of a granular material only changes as a function of the physical properties of the material, of the surrounding gas and of wall surface characteristics; it does not depend on the amount of the granular material. Therefore, the fact that the repose angle does not significantly change between Cases B and F illustrates that the proposed model is in line with the governing physics of the phenomenon. A negligible difference observed in the repose angle values between the two aforementioned cases may be attributed to the different levels of numerical diffusion, that any TFM methodology exhibits, owed to the different particle loading.

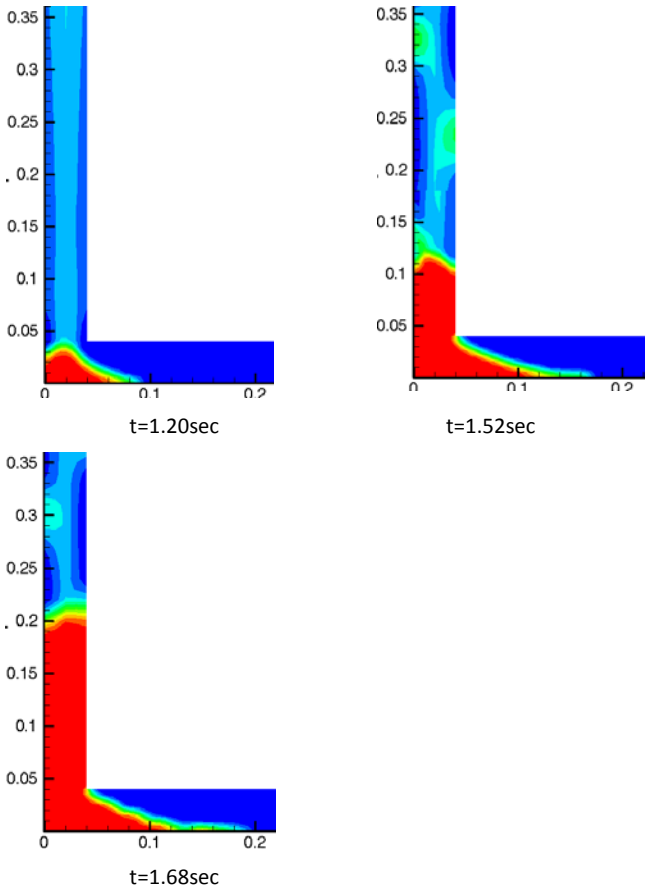

Figure 3.18 Temporal evolution of solid velocity for case G.

3.3 Introduction of Particle Size Distribution in kinetic theory

Full – loop TFM (Two Fluid Model) modeling of fluidized beds (Zhang et al., 2008) is considered the state-of-the-art simulation approach. However, its accuracy has been questioned (Nikolopoulos et al., 2010[a, b]; Wang et al., 2008; Zhang et al., 2008), since the meso-scale structures induced under fluidization regimes, cannot be sufficiently considered. To improve its validity, sophisticated sub-grid models have been developed for the calculation of the drag force acting on particles, such as EMMS (Ge et al., 2008). Yet, another possible source of inaccuracy is the mono - sized approximation, used in the majority of TFM CFD works (Nikolopoulos et al., 2010[a, b]; Shuai et al., 2011[a, b , c]; Wang et al., 2008; Zhang et al., 2008). PSD incorporation in TFM presents very high computational cost in contrast to recently developed simulation techniques that straightforwardly apply PSD.

A new, competitive to TFM, modeling approach is the Multi – Phase Particle – In – Cell (MP-PIC) proposed by Patankar and Joseph, 2001. This methodology is based on the Discrete Particle Method (DPM) under which particles are modeled in a Lagrangian fashion. This methodology makes the application of PSD straightforward. However, TFM formulation proved to be more efficient than conventional DPM, as reported by Sundaresan, 2011, due to the application of the kinetic theory developed by (Lun et al., 1984). The disadvantages of DPM were spotted and under this light the Multi – Phase Particle – In – Cell (MP-PIC) was proposed by Patankar and Joseph, 2001. In this sophisticated particle in cell methodology, the Lagrangian frame is utilized for particle tracking but the volume fraction of particles is also incorporated.

Within this section the methodology for incorporating the PSD of the granular material in the TFM approach is described. In poly-disperse TFM modeling, each of the particle diameters is simulated as a discrete Eulerian phase. This is because the momentum equations of each diameter should be separately solved in order to account for the granules segregation. The number of the Eulerian solid phases is denoted as *N*, resulting in the solution of $N + 1$ Eulerian phases (*N* granular and one gas phase) in terms of mass and momentum conservation. Unfortunately, this formulation increases severely the computational cost, but it is very interesting to compare the results of this computational expensive approach with the common mono-sized simplification. In the mono-sized approach, *N* equals to 1 and the only particle phase solved corresponds to the mean solid particle diameter.

The state-of-the-art simulation approach of CFB units is the full – loop TFM. This modeling technique is not simulating only the riser of a CFB but also the returning system (cyclone – down-comer – pneumatic valve) of the unit. Most of the recent studies, such as the work of Zhang et al., 2008 and Shuai et al., 2011[a], use the same governing equations for the recirculation system with those developed for the CFB riser as discussed in a previous section. However, the impotence of von – Misses yield criterion and the corresponding correlations for granular viscosity to efficiently address inter – particle friction forces makes the utilization of Pitman - Schaeffer – Gray - Stiles yield criterion necessary. Thus, within this chapter a poly – disperse TFM model is developed for both yield criteria and generally for the two stress models described in section 3.2.

The closure equations for viscous granular stresses that have been developed by Gidaspow et al., 1992; Johnson and Jackson, 1987; Lun et al., 1984 and Ogawa et al., 1980 for the mono - sized approximation, as a first approach, could be also used for poly - dispersed cases. Indeed Gao et al., 2008 incorporated this approach in their CFD study. A straightforward application of these correlations, in a poly – dispersed case, is to calculate the granular stress tensor components of each solid phase based on the aforementioned equations and taking into account the volume fraction and diameter of the solid phase that is investigated. However, Benyahia, 2008 correctly pointed out that the correlations for the poly - dispersed case should be consistent with the mono-sized correlations. The latter requirement is not fulfilled and in order to properly formulate correlations for granular pressure and stresses, the way that the corresponding mono - sized correlations were developed should be examined.

Lun et al., 1984 developed the theory for calculating the stress tensor for the pseudo-fluid granular phase by applying the kinetic theory. Their idea was that these phenomena could be simulated through the kinetic theory of dense gases. The kinetic theory of gases correlates the thermodynamic temperature with the fluctuating velocity of molecules. In granular flows instead of molecules there are particles, and in correspondence with temperature, a granular temperature (Θ) can be defined. The kinetic theory has been successfully applied to the case of the mono-sized approach for the formulation of equations for granular pressure, bulk and shear stresses. However, the mono-sized analysis takes into account only particles of the same diameter.

On the other hand, in a poly - dispersed case, the kinetic analysis should take into account the collision of particles of different size. In this light, Mathiesen et al., 2000 developed such correlations in their novel work. Regarding the solid pressure, the correlation reported in the work of Mathiesen et al., 2000 has two terms (eq. 3.39). The first term, as expected, corresponds to the ideal gas equation of state and the second term describes the contribution of inelastic collisions between particles.

$$P_s = \varepsilon_s \rho_s \theta_s + \sum_{n=1}^{N} P_{c,sn} \qquad \text{Eq. 3.39}$$

The second term is calculated from equation 3.40

$$P_{c,sn} = \frac{\pi}{3}(1+e_{sn}) d_{sn}^3 g_{sn} n_s n_n m_o \left\{ \frac{\theta_s \theta_n}{\frac{m_s}{m_n}\theta_s + \frac{m_n}{m_s}\theta_n} \right\} \left\{ \frac{\left(m_o / m_s\right)^2 \theta_s \theta_n}{\left[\theta_s + \left(m_n / m_s\right)^2 \theta_n\right](\theta_s + \theta_n)} \right\}^{3/2} \qquad \text{Eq. 3.40}$$

The subscripts *s* and *n* denote two different solid phases that are involved in a random collision. Thus e_{sn} is the restitution coefficient for collisions between particles of phases *s* and *n*, in contrast to e_{ss} which is the restitution coefficient for collisions between identical particles of phase *s*. Restitution coefficient is an important parameter quantifying the percentage energy loss from particle–particle collisions. Previous studies (Almuttahar and Taghipour, 2008; Hartge et al., 2009; Wang et al., 2008; Wen and Yu, 1966; Zhang et al., 2008) report a restitution coefficient of solids ranging from 0.9 to 0.99, in the case of CFB installations for particles of the same size. A typical value for e_{ss} is 0.9 as proposed for Geldart B particles by Hartge et al., 2009; Helland et al., 2002; Liu and Lu, 2009 and Wen and Yu, 1966 while a value of 0.99 seems more appropriate for smaller (Geldart A) particles (Almuttahar and Taghipour, 2008; Ibsen et al., 2004; Wang et al., 2008; Zhang et al., 2008). For simplicity reasons, the effect of different particle size on the amount of energy lost due to collisions can be neglected. Thus e_{sn} can be set equal to a constant value for all particle phases based on the mean particle diameter; i.e. 0.9 for Geldart B particle mixtures or 0.99 for Geldart A particle mixtures. Moreover, in order to be able to calculate $P_{c,sn}$, scalars, such as m_o, m_s, d_{sn} and n_s, involved in equation 3.40 should be defined. Therefore, the following correlations are used:

$$d_{sn} = \frac{1}{2}(d_s + d_n), m_o = m_s + m_n, n_s = \frac{6\varepsilon_s}{\pi d_s^3}, m_s = \frac{\pi d_s^3 \rho_s}{6} \qquad \text{Eq. 3.41}$$

It should be underlined that equation 3.39 for $N = 1$ results in the standard equation of solid pressure (eq. 3.24, FLUENT, 2006; Lun et al., 1984). Moreover, for a binary mixture ($N = 2$) consisting of particles of the same diameter, the sum of the two granular pressures calculated from equation 3.39 equals to the corresponding granular pressure calculated by equation 3.24, considering the granular medium as mono - sized. The latter illustrate the consistency of equation 3.39. Moreover, following the same reasoning all the equations described below, are consistent with the respective mono – sized ones.

The radial distribution for two solid phases ($g_{o,sn}$) can be calculated by the following correlation reported by (Mathiesen et al., 2000). The radial distribution function of the granular material (g_o) is calculated by the correlation developed by Lun et al., 1984. This correlation should take into account all the granular material in a control volume and for this reason the total volume fraction of solids is used in it.

$$g_{o,sn} = \frac{N}{2}\frac{g_o}{1-\varepsilon_g}(\varepsilon_s + \varepsilon_n), g_o = \left[1 - \frac{(1-\varepsilon_g)}{\varepsilon_s^{\max}}\right]^{-2.5\varepsilon_s^{\max}} \qquad \text{Eq. 3.42}$$

Another problem is that, in equation 3.42, the packing limit of a mixture of particles should be calculated. The packing limit is strongly dependent on particles mean diameter, (Liu and Ha, 2002). Indeed, packed particles of small size leave less unoccupied space than

larger particles. In this light, the packing limit of each solid phase should depend on the particle diameter of the corresponding solid phase. Moreover, in an arbitrary control volume of the flow-field inside a CFB riser, the particle size distribution is varying and depends upon the induced flow field. The packing limit of the granular mixture in a control volume should be a function of the volume fraction of each particulate phase and of their respective packing limit. Although, such correlations exist in literature (Liu and Ha, 2002; Zou et al., 1999), the complexity of these correlations along with the fact that Fluent® platform does not provide a way to apply them, render their application to the developed model infeasible. Thus, packing limit is considered to be equal to the packing limit of the mean particle size for all particulate phases and for their mixtures.

The frictional granular pressure, which is applied when the friction limit is exceeded, is calculated by equation 3.43. The author believes that the friction limit should be variable depending on the mixture composition. Thus, friction limit should be treated the same way with the packing limit. However, this is not yet possible because of the high number of complexities involved in applying a not constant friction limit and the lack of appropriate correlations available in literature. In addition, a varying friction limit may also result in numerical instabilities since as reported by Makkawi et al., 2006 the smooth transition of stresses from the kinetic controlled regime to the frictional regime (controlled by the visco-plastic theory) is of high importance regarding solver's robustness. Concluding, ε_{fr} is considered constant, equal to the typical value of 0.5.

$$P_{fr,s} = \begin{cases} 0 \quad , \; for \sum_{n=1}^{N} \varepsilon_n < 0.5 \\ 0.1\varepsilon_s \dfrac{\sum_{n=1}^{N} \varepsilon_n - \varepsilon^{fr}}{\varepsilon^{\max} - \sum_{n=1}^{N} \varepsilon_n}, \; for \sum_{n=1}^{N} \varepsilon_n > 0.5 \end{cases} \qquad \text{Eq. 3.43}$$

As far as the bulk viscosity is concerned, the standard equation (eq. 3.23) in the case of a mono - sized granular medium is reformulated (eq. 3.44) for a polydispersed granular mixture by Mathiesen et al., 2000.

$$\lambda_s = \frac{1}{\varepsilon_s} \sum_{n=1}^{N} P_{c,sn} \frac{d_{sn}}{3} (\theta_s + \frac{m_n}{m_s} \theta_n) \sqrt{\frac{2}{\pi \theta_s \theta_n (\theta_s + \left(\frac{m_n}{m_s} \right)^2 \theta_n)}} \qquad \text{Eq. 3.44}$$

Regarding the kinetic and collisional granular viscosity, suitable correlations were developed for a poly - dispersed case by Mathiesen et al., 2000. These correlations, equations 3.45 to 3.48 and the proposed equation 3.48 for the frictional viscosity, were formulated by the application of the KTGF for collisions of particles of different sizes, and are in accordance with the conventional correlations depicted in 3.36, 3.35 and 2.23 respectively.

$$\mu_{col} = \frac{1}{\varepsilon_s} \sum_{n=1}^{N} P_{c,sn} \frac{d_{sn}}{5} (\theta_s + \frac{m_n}{m_s} \theta_n) \sqrt{\frac{2}{\pi \theta_s \theta_n (\theta_s + \left(\frac{m_n}{m_s} \right)^2 \theta_n)}} \qquad \text{Eq. 3.45}$$

$$\mu_{kin} = \frac{2\mu_{dil,s}}{\frac{1}{N} \varepsilon_s \sum_{n=1}^{N} (1 + e_{sn}) g_{sn}} \left\{ 1 + \frac{4}{5} \sum_{n=1}^{N} g_{sn} \varepsilon_n (1 + e_{sn}) \right\}^2 \qquad \text{Eq. 3.46}$$

where, the shear viscosity under dilute conditions is calculated by the following equation. Conventional frictional models that are based on the von – Misses yield criterion result in the following description of shear and bulk viscosity.

$$\mu_{dil,s} = \frac{5}{16 d_s^2}\sqrt{\frac{m_s \theta_{s,av}}{\pi}}$$

$$\theta_{s,av} = \frac{2 m_s \theta_s}{\left\{\sum_{n=1}^{N} \frac{n_n}{n_s}\left(\frac{d_{sn}}{d_s}\right)^2 \sqrt{\frac{\left(m_o/m_s\right)^2 \theta_n}{\left(\theta_s + \left(m_n/m_s\right)^2 \theta_n\right)}}\left(\frac{\left(m_o/m_s\right)^2 \theta_s \theta_n}{\left(\theta_s + \left(m_n/m_s\right)^2 \theta_n\right)\left(\theta_s + \theta_n\right)}\right)^{3/2}\right\}^2} \qquad \text{Eq. 3.47}$$

$$\mu_{fr,s} = \frac{P_{fr}\sin\varphi}{2\varepsilon_s \sqrt{\mathrm{II}_{dD,s}}}, \lambda_{fr,s} = 0 \qquad \text{Eq. 3.48}$$

The above equations (equations 3.39 to 3.48) can be used for the formulation of the granular stress tensor in polydispersed CFD modeling of a CFB riser. However, in the returning system of a CFB unit neither the conventional correlations for the mono - sized case nor the corresponding correlations for the polydispersed case can be used. The reason is that in this region friction forces, which prevail over the kinetic and collisional ones, are not described in a proper way by the aforementioned equations as depicted in the previous section where the validity of von – Misses Yield criterion was tested for very dense granular flows.

To solve this problem, the sophisticated Pitman- Schaeffer- Gray-Stiles yield should be alternatively used in the returning system. The equations for the polydispersed case based on the mono - sized correlations proposed by chapter 3.2 of this PhD, are:

$$\mu_{fr,s} = \frac{P_{fr}\sin^2\varphi}{\varepsilon_s\sqrt{4\sin^2\varphi\cdot \mathrm{II}_{dD,s} + (\nabla\cdot\vec{u}_s)^2}}, \lambda_{fr,s} = \frac{P_{fr}\sin\varphi}{\varepsilon_s\sqrt{4\sin^2\varphi\cdot \mathrm{II}_{dD,s} + (\nabla\cdot\vec{u}_s)^2}} \qquad \text{Eq. 3.49}$$

Moreover, for the determination of kinetic and collisional viscosity in the returning system, the following correlations 3.50 and 3.51 should be used, instead of equations 3.45 and 3.46 respectively. These correlations are developed within this work, based on the respective mono - sized correlations developed by Boelle et al., 1995 and Gevrin et al., 2008.

To sum up, this section presents a group of equations, which could be used for a poly - dispersed granular material simulation, all of which are consistent with the corresponding mono-sized correlations found in the recent literature when their average diameter is considered.

$$\mu_{kin,2} = \frac{4\mu_{dil,s}\left[1+\frac{2}{5}\sum_{n=1}^{N} g_{sn}\varepsilon_n\left(3e_{sn}-1\right)\left(1+e_{sn}\right)\right]}{\frac{1}{N}\varepsilon_s\sum_{n=1}^{N}\left(1+e_{sn}\right)\left(3-e_{sn}\right)g_{sn}}\left[1+\frac{3\mu_g\varepsilon_s}{\sum_{n=1}^{N} P_{c,sn}\frac{d_{sn}}{5}\left(\Theta_s+\frac{m_n}{m_s}\Theta_n\right)\sqrt{\frac{2}{\pi\Theta_s\Theta_n\left(\Theta_s+\left(\frac{m_n}{m_s}\right)^2\Theta_n\right)}}}\right]^{-1} \qquad \text{Eq. 3.50}$$

$$\mu_{col,2}=\frac{1}{5}\frac{\dfrac{4\mu_{dil,s}\left[1+\dfrac{2}{5}\sum_{n=1}^{N}g_{sn}\varepsilon_{\mathrm{n}}\left(3e_{sn}-1\right)\left(1+e_{sn}\right)\right]}{\dfrac{1}{N}\varepsilon_{\mathrm{s}}\rho_{s}\sum_{n=1}^{N}\left(1+e_{sn}\right)\left(3-e_{sn}\right)g_{sn}}\sum_{n=1}^{N}\dfrac{\pi}{3}\left(1+e_{sn}\right)d_{sn}^{3}g_{sn}n_{s}n_{n}m_{o}}{1+\dfrac{3\mu_{g}\varepsilon_{\mathrm{s}}}{\sum_{n=1}^{N}P_{c,sn}\dfrac{d_{sn}}{5}\left(\Theta_{\mathrm{s}}+\dfrac{m_{\mathrm{n}}}{m_{\mathrm{s}}}\Theta_{\mathrm{n}}\right)\sqrt{\dfrac{2}{\pi\Theta_{\mathrm{s}}\Theta_{\mathrm{n}}\left(\Theta_{\mathrm{s}}+\left(\dfrac{m_{\mathrm{n}}}{m_{\mathrm{s}}}\right)^{2}\Theta_{\mathrm{n}}\right)}}}}$$

$$+\frac{1}{\varepsilon_{\mathrm{s}}}\sum_{n=1}^{N}P_{c,sn}\frac{d_{sn}}{5}\left(\Theta_{\mathrm{s}}+\frac{m_{\mathrm{n}}}{m_{\mathrm{s}}}\Theta_{\mathrm{n}}\right)\sqrt{\frac{2}{\pi\Theta_{\mathrm{s}}\Theta_{\mathrm{n}}\left(\Theta_{\mathrm{s}}+\left(\dfrac{m_{\mathrm{n}}}{m_{\mathrm{s}}}\right)^{2}\Theta_{\mathrm{n}}\right)}}$$

Eq. 3.51

3.4 Reacting flows in CFBs

The numerical simulation of the reacting flows in CFBs is a challenging task. Such a task incorporates the simulation of granulates hydrodynamics, that were discussed above, as well as homogeneous and heterogeneous chemical reactions and in most of the cases heat transfer mechanisms. There are not too many published papers that incorporate such mechanisms as most of them focus on FBs' hydrodynamics. Therefore, appropriate closure equations and / or simulation techniques should be developed in order to address reacting flows simulation. In this thesis, such work is undertaken for: a) simulation of solid fuels CFB combustion; b) simulation of the CO_2 capture with CaO inside CFB carbonators, and c) simulation of nitrous oxides emissions.

3.4.1 Combustion modeling in CFBC

The numerical simulation of the isothermal granular flow within CFB risers is not trivial but as reported above there are a lot of published papers dealing with this issue and since early 90s significant progress has been achieved. On the contrary, limited literature is available for the proper simulation of the combustion (Gungor and Eskin, 2008[a, b]). Moreover the few published studies that incorporate combustion mechanisms, approach the complicated physics, which dominate the operation of CFB combustor, in a two-dimensional way (Gungor, 2008[a, b]; Gungor and Eskin, 2008[a, b]; Zhou et al., 2011), disregarding that the flow within FB is purely three dimensional (Myöhänen et al., 2006). This section focuses on the development of a three-dimensional model, taking into account fuel particle combustion mechanisms in a CFBC riser. The basis for the incorporation of chemistry and heat transfer models is the conventional isothermal model, described in chapter 2 and in Rampidis et al., 2007.

The simulation of combusting flow within FBs with the TFM formulation is difficult. The main difficulties are the computational cost and the proper simulation of the momentum and heat exchange coefficients between solids (inert-material and fuel). As concerns proper modeling of momentum and heat exchange coefficients, little information is reported in the literature. Even in the simpler case of gas – solid momentum exchange, it is worth noticing that models which are based on the assumption of homogeneous conditions for each computational cell, fail to predict the governing physics of such processes, under certain conditions (Ge et al., 2008; Ge et al., 2011; Hartge et al., 2009; Nikolopoulos et al., 2010[b]; Zhang et al., 2011). This failure was the driving force for the development and

implementation of the novel EMMS schemes. However, EMMS implementation in combusting flow is not straightforward because gas density and viscosity is not constant and the mechanisms of particle clogging should take into account that fuel and inert – material particles have different properties. Moreover, the changes of gas properties increase the complexity of EMMS implementation in CFD codes. Additionally, the mechanisms of particle clogging in polydispersed granular flows are not known yet.

Currently, EMMS schemes cannot be applied to combusting granular flows without questionable simplifications:

1. Gas properties that are a function of temperature should be considered constant. The assumption of isothermal conditions inside CFB risers is generally reasonable due to the high heat transfer coefficient experienced in such units (Kunii and Levenspiel, 1991).
2. Fuel and inert – material particles are identical and they are both represented by the mean diameter of their binary mixture, or by the mean diameter of the inert – material, which has greater particle loading. This is a rough simplification that may result in inaccurate simulation of the FB hydrodynamics.

Therefore, the selection of a conventional drag model, such as Gidaspow seems to be the only theoretically sound choice. The drawbacks of such models has been thoroughly discussed in chapter 2, but it has been stated by Ge et al., 2008 that for industrial purposes such correlations may be utilized under proper grid density (Ge et al., 2008; Zhang and VanderHeyden, 2001). The description of multiphase flow as interpenetrating continua incorporates the concept of phase's volume fractions, denoted by ε_q. The continuity equation for phase q is:

$$\frac{\partial}{\partial t}(\varepsilon_q \rho_q) + \nabla \cdot (\varepsilon_q \rho_q \vec{u}_q) = S_q \qquad \text{Eq. 3.52}$$

S_q represents the mass source terms for q^{th} phase. As far as gases are concerned, the momentum equation is:

$$\frac{\partial}{\partial t}(\varepsilon_q \rho_q \vec{u}_q) + \nabla \cdot (\varepsilon_q \rho_q \vec{u}_q \vec{u}_q) = -\varepsilon_q \nabla p_g + \nabla \cdot \bar{\bar{\tau}}_q + \varepsilon_q \rho_q \vec{g} + \sum_{l=1}^{n} \left[\beta (\vec{u}_l - \vec{u}_q) + \dot{m}_{lq} \vec{u}_{lq} - \dot{m}_{ql} \vec{u}_{ql} \right] \qquad \text{Eq. 3.53}$$

while for the for the q^{th} solid phase the following equation is proposed:

$$\frac{\partial}{\partial t}(\varepsilon_q \rho_q \vec{u}_q) + \nabla \cdot (\varepsilon_q \rho_q \vec{u}_q \vec{u}_q) = -\varepsilon_q \nabla p_g - \nabla p_q + \nabla \cdot \bar{\bar{\tau}}_q + \varepsilon_q \rho_q \vec{g} + \sum_{l=1}^{n} \left[\beta (\vec{u}_l - \vec{u}_q) + \dot{m}_{lq} \vec{u}_{lq} - \dot{m}_{ql} \vec{u}_{ql} \right] \qquad \text{Eq. 3.54}$$

The above equation is applied for the two solid phases i.e. inert material and fuel. In equations 3.53 and 3.54 the two last terms in the right hand side describe the momentum transfer between q^{th} and l^{th} phases due to mass transfer ($\dot{m}_{lq}$) caused by reactions. $\vec{u}_{lq}$ is the interphase velocity, defined as follows. If $\dot{m}_{lq} > 0$ (i.e., phase p mass is being transferred to phase q), $\vec{u}_{lq} = \vec{u}_p$; if $\dot{m}_{lq} < 0$ (i.e., phase q mass is being transferred to phase p), $\vec{u}_{lq} = \vec{u}_q$. Likewise, if $\dot{m}_{lp} > 0$ then $\vec{u}_{lp} = \vec{u}_q$; if $\dot{m}_{ql} < 0$ then $\vec{u}_{ql} = \vec{u}_l$.

The enthalpy equation for each phase is:

$$\frac{\partial}{\partial t}\left(\varepsilon_q \rho_q H_q\right) + \nabla \cdot \left(\varepsilon_q \rho_q \vec{u}_q H_q\right) = \varepsilon_q \frac{\partial P_q}{\partial t} + \bar{\bar{\tau}}_q : \nabla \vec{u}_q - \nabla \cdot \vec{q}_q + S_q + \sum_{l=1}^{n} Q_{lq} \qquad \text{Eq. 3.55}$$

The heat transfer between the primary gas phase and the two Eulerian solid phases (inert – material and fuel), is calculated as follows (Gunn, 1978):

$$\dot{Q}_{qg} = h_{qg} \cdot (T_q - T_g) \quad \text{Eq. 3.56}$$

$$h_{qg} = \frac{6 \cdot K_g \cdot \varepsilon_q \cdot \varepsilon_g \cdot Nu_g}{d_f^2} \quad \text{Eq. 3.57}$$

For the calculation of *Nu* number, (Gunn 1978) proposed the following equation.

$$Nu_g = \left(7 - 10\varepsilon_g + 5\varepsilon_g^2\right)\left(1 + 0.7\,\mathrm{Re}_q^{0.2}\,\mathrm{Pr}^{1/3}\right) + \left(1.33 - 2.4\varepsilon_g + 1.2\varepsilon_g^2\right)\mathrm{Re}_q^{0.7}\,\mathrm{Pr}^{1/3} \quad \text{Eq. 3.58}$$

This equation is valid for particle loading from 0 to 65 %, and Re up to 10^5 and its applicable for heat transfer between a gas and a granular material. Prandtl and Reynolds numbers in equation 3.58 are calculated as follows:

$$\mathrm{Pr} = \frac{c_{p_g}\mu_g}{K_g} \quad \text{Eq. 3.59}$$

$$\mathrm{Re}_q = \frac{\left|\vec{u}_q - \vec{u}_g\right|\rho_g d_q}{\mu_g} \quad \text{Eq. 3.60}$$

Since species are tracked within gas and fuel phases, the respective generic transport equation for multiphase flows is solved for each species except for one in each phase. Equation 3.87 depicts such an equation for a gaseous species. For the calculation of heat transfer between granular phases, i.e. inert – material and fuel a comprehensive model is not available in the respective literature (Zhou et al., 2011). However, equations 3.57 to 3.60 that comprise Gunn's model (Gunn, 1978) can be used for heat transfer between solid phases (Nikolopoulos et al., 2009). In equations 3.61 to 3.64, *q* index refer to inert – material that is treated as a "pseudo" gas phase. This assumption is supported by the KTGF that treats granular materials as gases.

$$h_{qf} = \frac{6 \cdot K_q \cdot \varepsilon_q \cdot \varepsilon_f \cdot Nu_q}{d_f^2} \quad \text{Eq. 3.61}$$

$$\mathrm{Pr} = \frac{c_{p_q}\mu_q}{K_q} \quad \text{Eq. 3.62}$$

$$\mathrm{Re}_q = \frac{\left|\vec{u}_q - \vec{u}_f\right|\rho_q d_f}{\mu_q} \quad \text{Eq. 3.63}$$

Heat and momentum exchange coefficients between solids phases and gas were modeled using the models of Gunn, 1978 and Gidaspow's (eq. 2.28) respectively. Although Gunn's model generally refers to gas – solid interaction, in this work is also used for the thermal interaction between the two solid phases since the information for their thermal interaction which is reported in the literature is very limited. Although this approximation may look oversimplified, the numerical results presented in chapter 5 agree quite well with the corresponding experimental data. Additionally the symmetric model of Syamlal, 1987 is used for the simulation of the momentum exchange coefficient between solid phases (fuel and inert-material).

$$Nu_q = \left(7 - 10\varepsilon_q + 5\varepsilon_q^2\right)\left(1 + 0.7\,\mathrm{Re}_q^{0.2}\,\mathrm{Pr}^{1/3}\right) + \left(1.33 - 2.4\varepsilon_q + 1.2\varepsilon_q^2\right)\mathrm{Re}_q^{0.7}\,\mathrm{Pr}^{1/3} \quad \text{Eq. 3.64}$$

As far as the effect of turbulence is concerned, albeit in bed hydrodynamics seemed to have a small influence it was found to be important in combusting flows (Nikolopoulos et al., 2009; Rampidis et al., 2007; Wang and Li, 2007). In order to simulate in a realistic way the

homogeneous reactions rates, values of k^t and ε^t are needed as inputs for the Finite Rate/Eddy dissipation concept.

The fuel conversion comprises of three heterogeneous reactions. The first one is depicted in eq. 3.65 and refers to moisture evaporation / boiling. The second heterogeneous reactions, depicted in equation 3.66 describes the volatiles release (devolatilization). The third one is the char combustion.

$$H_2O(s) \xrightarrow{boiling} H_2O(g) \qquad \text{Eq. 3.65}$$

$$vol.(s) \xrightarrow{devolatilization} vol.(g) \qquad \text{Eq. 3.66}$$

Moreover, three homogeneous reactions are defined, referring to combustion of CH_4 (Gungor and Eskin, 2008[b]), H_2 and CO (Zhao et al., 2007). Homogeneous reactions are described via equations 3.67 to 3.69 along with reaction rates expressions. The constants of these reactions are summarized in Table 3.5. Reaction rate (R) units are Kmol $[m^3_{gas}s]^{-1}$ and the universal gas constant R_u units in these equations are J[Kmol K]$^{-1}$.

$$CH_4 + \frac{3}{2}O_2 \longrightarrow CO + 2H_2O,\ R = Ae^{-\frac{E}{R_u T_g}} \left[C_{CH_4}\right]^{0.7} \left[C_{O_2}\right]^{0.8} \qquad \text{Eq. 3.67}$$

$$H_2 + \frac{1}{2}O_2 \longrightarrow H_2O,\ R = Ae^{-\frac{E}{R_u T_g}} \left[C_{H_2}\right]\left[C_{O_2}\right]^{0.5} \qquad \text{Eq. 3.68}$$

$$CO + \frac{1}{2}O_2 \longrightarrow CO_2,\ R = Ae^{-\frac{E}{R_u T_g}} \left[C_{CO}\right]\left[C_{O_2}\right]^{0.25} \left[C_{H_2O}\right]^{0.5} \qquad \text{Eq. 3.69}$$

Reactions	A (varying units)	E (J/Kmol)
Eq. 3.67(CH_4)	$5.012\ 10^{11}$	$2\ 10^8$
Eq. 3.68(H_2)	$9.87\ 10^{15}$	$3.1\ 10^7$
Eq. 3.69(CO)	$2.239\ 10^{12}$	$1.7\ 10^8$

Table 3.5 Homogeneous reaction constants (FLUENT, 2010; Zhao et al., 2007)

The reactions rates depicted in equations 3.67 to 3.69 refer to the pure kinetics of the reactions and are accurate only if the respective reactants are fully mixed. Species mixing is controlled by turbulence and the effect of mixing on reaction rates is incorporated in the CFD model through the Eddy dissipation model (Magnussen and Hjertager, 1976). In this model, the rate of production of species i due to reaction r, ($R_{i,r}$) is given by the smaller of the two expressions below (equations 3.70 and 3.71). The empirical constants A_E and B_E, involved in these equations, are set equal to 4 and 0.5 respectively. The reaction rate introduced in the CFD model is the minimum predicted by the finite rate- and the eddy dissipation-model.

$$R_{i,r} = \nu'_{i,r} M_{w,i} A_E \rho_g \frac{\varepsilon_g^t}{k_g^t} \min_R \left(\frac{Y_R}{\nu'_{R,r} M_{w,R}} \right) \qquad \text{Eq. 3.70}$$

$$R_{i,r} = v'_{i,r} M_{w,i} A_E \mathrm{B}_E \rho_g \frac{\varepsilon_g^t}{k_g^t} \frac{\sum_{PR} Y_{PR}}{\sum_j^N v''_{j,r} M_{w,j}} \quad \text{Eq. 3.71}$$

As seen in equations 3.70 and 3.71, k_g^t and ε_g^t are required as inputs in order to be able to calculate the reaction rates through the Eddy dissipation model. Therefore, an appropriate turbulence model should be incorporated in the CFD model in order to efficiently and accurately calculate the effect of turbulent mixing on reaction rates.

The dispersed turbulence model is the appropriate model when the concentrations of the secondary phases are dilute. Fluctuating quantities of the secondary phases can therefore be given in terms of the mean characteristics of the primary phase and the ratio of the particle relaxation time and eddy-particle interaction time. The model is applicable when there is clearly one primary continuous phase and the rest are dispersed dilute secondary phases. Turbulence predictions are obtained from the modified k – ε model:

$$\frac{\partial}{\partial t}\left(\varepsilon_g \rho_g k_g^t\right) + \nabla \cdot \left(\varepsilon_g \rho_g \vec{u}_g k_g^t\right) = \nabla \cdot \left(\varepsilon_g \frac{\mu_g^t}{\sigma_{k_g^t}} \nabla k_g^t \right) + \varepsilon_g G_{k,g} - \varepsilon_g \rho_g \varepsilon_g^t + \varepsilon_g \rho_g \Pi_{k_g^t} \quad \text{Eq. 3.72}$$

$$\frac{\partial}{\partial t}\left(\varepsilon_g \rho_g \varepsilon_g^t\right) + \nabla \cdot \left(\varepsilon_g \rho_g \vec{u}_g \varepsilon_g^t\right) = \\ = \nabla \cdot \left(\varepsilon_g \frac{\mu_g^t}{\sigma_{\varepsilon_g^t}} \nabla \varepsilon_g^t \right) + \varepsilon_g \frac{\varepsilon_g^t}{k_g^t} \left(C_{1\varepsilon_g^t} G_{k,g} - C_{2\varepsilon_g^t} \varepsilon_g \rho_g \right) - \varepsilon_g \rho_g \varepsilon_g^t + \varepsilon_g \rho_g \Pi_{\varepsilon_g^t} \quad \text{Eq. 3.73}$$

The effect of particulates on gas turbulence is calculated through an algebraic sub-model. More information on k – ε dispersed turbulence model can be found in (FLUENT, 2010). The k – ε dispersed turbulence model is appropriate for dilute granular flows. However, in FBs the multi – phase flow is rather denser. Theoretically, in FBs the "per phase" or the "Reynolds stresses" turbulence models are more appropriate (Rampidis et al., 2007). The "per phase" turbulence model adds two more PDEs, per granular phase, in the problem. These additional equations describe k – ε of granular phases. The Reynolds stresses adds six more PDEs per Eulerian phase. The computational cost increment due to those additional equations makes their application difficult especially on combusting flow simulations of CFBCs, because the computational cost of such simulations is very high and any further increase should be avoided. Therefore, Rampidis et al., 2007 and Zhou et al., 2011, have used the k – ε dispersed turbulence model in CFBC CFD simulations. The results of these studies depicted that this simplified turbulence model could be used in FBs modeling.

Except for the homogeneous reactions described above, inside a CFBC heterogeneous reactions, i.e. moisture evaporation, devolatilization and char combustion, take place as well. The moisture evaporation / boiling rate is calculated through equation 3.74 as reported by Tullin et al., 1993. It is enabled for temperature greater than 373 K as long as there is moisture in the solid phase. The first term within brackets in the right hand side represents the number of fuel particles in the control volume. The second term represents the moisture evaporation rate per particle. It should be underlined that due to the Eulerian formulation, all fuel particles within a specific control volume share the same properties. Moreover, it should be underlined that the necessary heat for reaction 3.65 is provided by the gas phase.

$$\dot{m}_f^w = \left(\frac{6 \cdot m_f}{\pi \cdot \rho_f \cdot d_p^{\,3}}\right)\left(-\pi \cdot d_p \cdot Nu_p \cdot \frac{K_{ps}}{c_{p_{ps}}} \cdot \ln\left(1+\frac{c_{p_{ps}} \cdot (T_g - T_{ps})}{1 - L_w}\right)\right) \qquad \text{Eq. 3.74}$$

In equation 3.74, the thermal conductivity (K_{ps}) and heat capacity ($c_{p_{ps}}$) for the water at the surface of the particle are calculated for temperature equal to $T_{ps}=T_f+1/3(T_g-T_f)$ (Sofialidis et al., 2005) through proper temperature polynomials (FLUENT, 2006). *Nu* number in equation 3.74 is calculated as $Nu_p=2+0.5Re^{0.5}$. L_w is the latent heat of water at temperature T_{ps}.

Regarding reaction 3.66, the change in mass of the solid phase in each computational cell, due to devolatilization, is calculated by a simple one step reaction model according to equation 3.75. As regards reaction constants, A_{vol} (492000 s^{-1}) is the pre-exponential factor, and E_{vol} (7.4×10^7 J/kmol) (Leithner et al., 1993) is the corresponding activation energy of the devolatilization reaction.

$$\dot{m}_{devol} = \frac{6 \cdot m_f}{\pi \cdot \rho_f \cdot d_f^{\,3}} \cdot A_{vol} \cdot e^{-E_{vol}/(R_u T_f)} \cdot Y_{vol} \qquad \text{Eq. 3.75}$$

The most important reaction in CFBCs is the char combustion (eq. 3.76) that incorporates the oxidation of char to carbon monoxide and dioxide (Basu, 1999). Char combustion comprises of three mechanisms (Models I-III), depicted in Figure 3.19, and φ_c is the controlling parameter. This parameter controls the char conversion to carbon dioxide and carbon monoxide.

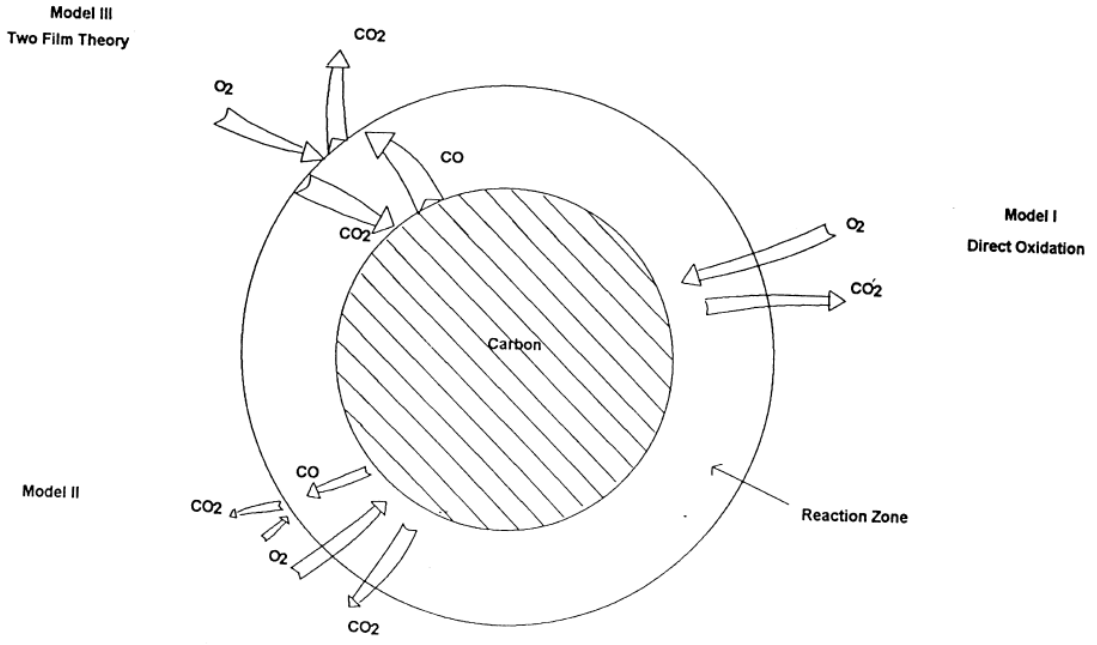

Figure 3.19 Modeling of char combustion (Basu, 1999)

Model I: The first mechanism refers to oxygen dilution on carbon surface and partial oxidation of CO. Carbon monoxide further oxidation takes place in the gas phase. This homogeneous reaction is considered to take place so close to the char surface that CO_2 is the primary combustion product. This combustion mechanism is dominating for low Reynolds numbers, large char particles (~ 1 mm) or at high temperatures (900 – 1300^{o}C).

Model II: Under this model the combustion products are CO and CO_2 on the carbon surface. Carbon monoxide and carbon dioxide dilute away from the carbon surface. CO

oxidation is achieved away from the particle surface (Basu, 1999). This combustion regime prevails for low temperature or small particle size.

Model III: In this model, oxygen cannot reach the carbon surface. It reacts with the CO in a gas-phase reaction away from the carbon surface. One part of the CO2 formed dilutes back to the carbon surface to be reduced to CO (two-film theory, Basu, 1999).

All these models can be summarized in the following equation:

$$C(s)+\frac{1}{\phi_c}\mathrm{O}_2(g)\longrightarrow\left(2-\frac{2}{\phi_c}\right)CO_2+\left(\frac{2}{\phi_c}-1\right)CO \qquad \text{Eq. 3.76}$$

The φ_c parameter is reported as a function of particle size (Leithner et al., 1993) and ranges from 1 to 2.

In contrast to moisture boiling and devolatilization, char combustion kinetics are more complicated. In the latter reaction, two controlling mechanisms exist. The first is the reaction kinetics and the second is the diffusion of oxygen into particles surface represented by k_c and h_m respectively. Equations 3.77 to 3.82 describe the char combustion mechanism adopted (Basu, 1999).

$$\dot{m}_{char}=(\pi\cdot d_c{}^2)\cdot\frac{P_{O_2(g)}}{1/h_m+1/k_c} \qquad \text{Eq. 3.77}$$

$$h_m=12\phi_c ShD_{O_2(g)}/(d_c R_u T) \qquad \text{Eq. 3.78}$$

In equation 3.78, that describes the diffusion rate constant, the universal gas constant units are kPa m^3 [Kg K]$^{-1}$. Equation 3.79 (Basu, 1999) depicts the kinetic rate. These two rates are combined in equation 3.77. The mechanisms that they represent, oxygen diffusion on particle surface and reaction kinetics are considered that are acting simultaneously (in parallel).

$$k_c=0.0117\exp(-2859/T_p) \qquad \text{Eq. 3.79}$$

$$Sh=\frac{R_c(m/s)d_c}{D_{O_2(g)}}=2\varepsilon_g+0.69\left[\frac{\left|\vec{u}_g-\vec{u}_s\right|\rho_g d_c}{\varepsilon_g\mu_g}\right]^{0.5}Sc^{0.33} \qquad \text{Eq. 3.80}$$

$$Sc=\frac{\mu_g}{\rho_g D_{O_2(g)}} \qquad \text{Eq. 3.81}$$

Regarding the change in fuel particle volume during combustion, the shrinking core approximation is adopted. The shrinking diameter of char (d_c) is calculated through equation 3.82 with the time instant carbon burn-off (U_{fc}), as proposed by Smith, 1982; Field, 1969.

$$\frac{d_c}{d_o}=(1-U_{fc})^{1/3} \qquad \text{Eq. 3.82}$$

The shrinking core model is enabled during char combustion and during this process the fuel density is considered constant. In water evaporation and devolatilization the diameter of the fuel phase is considered constant and fuel density is decreasing proportionally to the respective mass loss. This treatment is based on the assumption that water boiling and devolitilization create pores in the fuel particle. However, when these reactions are finished and char combustion is enabled, the particle density does not further increase but the particle diameter is decreasing.

3.4.2 Simulation of the carbonation reaction

The carbonation reaction (equation 3.83) is a heterogeneous reaction that is very important in the CaL CO_2 capture process. Through experimental tests performed in pilot plants, reaction rates can be developed as the one of Charitos et al., 2010[b] that is depicted in equation 3.84.

$$CaO + CO_2 \rightarrow CaCO_3 + \mathrm{H}eat \quad \text{Eq. 3.83}$$

$$\frac{dX_{carb}}{dt} = \frac{k_s S_o}{1-e_0} \cdot \left(X_{\max} - X_{carb}\right)^{2/3} \left(C_{CO_2} - C_{CO_2,eq}\right) \quad \text{Eq. 3.84}$$

However, the aforementioned correlation cannot be applied to a CFD simulation as it is. The following correlation (equation 3.85) that assumes that each control volume is a continuous stirred-tank reactor (CSTR) is proposed (Nikolopoulos et al., 2012[a]). This means that inside a control volume the mixing of the reactants is considered perfect and the limiting factors are the availability of free CaO and carbon dioxide concentration with respect to the equilibrium of the reaction. Thus, any meso – scale effect on this reaction rate is ignored.

$$R(mol/s) = -N_{Ca}\left(\frac{k_s S_o}{1-e_0}\right) \cdot \left(X_{\max} - X_{carb}\right)^{2/3} \left(C_{CO_2} - C_{CO_2,eq}\right) \quad \text{Eq. 3.85}$$

$$C_{CO_2,eq} = \frac{1.462 \cdot 10^{11}}{T_g} e^{\left[\frac{-19130}{T_g}\right]} \quad \text{Eq. 3.86}$$

In equation 3.85, $C_{CO2,eq}$ is the equilibrium concentration of CO_2 that is a function of the operating conditions and is calculated through equation 3.86 (Charitos et al., 2010[b]). X_{max} and X_{carb} are the maximum $CaCO_3$ and actual $CaCO_3$ to Ca mole fractions respectively. The X_{max} does not equal to one due to sintering (Rodriguez et al., 2011) that particles suffer due to the repeated calcination steps that are performed in high temperatures. Constants k_s, S_0 and e_0 are sorbent characteristics i.e. surface carbonation rate constant, initial CaO surface area and particles porosity respectively. N_{Ca} is the total moles of Ca inside the control volume.

3.4.3 NO_x / N_2O simulation methodology

The decoupled approach is proposed for the calculation of NO_x / N_2O concentrations. According to this technique, the concentration of nitrogen oxides produced in a combustion system is generally very low, that the chemistry of nitric species and their interaction with other gases in the combustion chamber has minimal effect on the concentrations of the main products of combustion and on the estimated flow field and temperature distribution (FLUENT, 2010). Thus, NO_x calculation can be decoupled from the combustion modeling.

The NO_x decoupled approach has been adopted in previous simulations concerning NO_x modeling in PF boilers (Nikolopoulos et al., 2011; Li et al., 2004; Le Bris et al., 2007). It is considered a widely approved method for predicting nitrogen oxide emissions.

However, this technique has not yet been applied in fluidized bed reactor simulations. In previously published papers concerning CFB plants, NO_x numerical investigation is performed coupled with combustion simulation (Gungor and Eskin, 2008[b]; Desroches-Ducarne et al., 1998; Liu and Gibbs, 2002; Afacan et al., 2007; Mukadi et al., 2000). In this work, the decoupled approach is selected in order to minimize the computational cost and determine if it can be used in CFB boilers. The generic transport equation for multiphase flow is solved for 5 species, i.e. NO, HCN, CNO, N_2O and CO.

$$\frac{\partial \varepsilon_g \rho_g \mathrm{Y}^{sp}}{\partial t} + \nabla \cdot \left(\varepsilon_g \rho_g \vec{u}_g \mathrm{Y}^{sp} \right) - \nabla \cdot (\varepsilon_g \Gamma \nabla Y^{sp}) = S \qquad \text{Eq. 3.87}$$

The diffusion term Γ for turbulent flows is given as:

$$\Gamma = \rho_g D_{iff} + \frac{\mu_t}{Sc} \qquad \text{Eq. 3.88}$$

Where *Sc* = 0.7 (Versteeg and Malalasekera, 2007) and the turbulent viscosity is calculated as shown below:

$$\mu_t = 0.09 \rho_g \frac{k^{t^2}}{\varepsilon^t} \qquad \text{Eq. 3.89}$$

In equations 3.87 to 3.89, ρ_g, ε_g, $\vec{u}_g$, k^t and ε^t are "frozen" variables, equal to the respective combustion model results for each control volume. Through the NO_x – N_2O modeling procedure these values do not change. *S* (mg of species per cubic meter per second), represents the source terms that reflect the network of reactions that each species participate.

Reaction rates for all five species were incorporated in the source term of each equation using User Defined Functions (UDFs). For example, if the intermediate gaseous species CNO is involved in 3 reactions, I, II and III, with corresponding reaction rates, RI, RII and RIII respectively, and in reaction I CNO is a product while in II and III is a reactant, the source term which will be incorporated in the transport equation of CNO is: $\mathrm{S_{CNO}} = \mathrm{R_I} - \mathrm{R_{II}} - \mathrm{R_{III}}$. This modeling approach is not supported by Fluent platform and therefore NO_x / N_2O decoupled model is incorporated in the commercial package via User Defined Scalars (UDS).

3.5 Conclusions

In this chapter, the theoretical novelties of this thesis are presented along with their theoretical background. These are: a) the advanced drag model (EMMS) that takes into account particle aggregates via sub – grid resolution of particles clustering; b) the new stress tensor developed for the recirculation system that can be used in full – loop simulations; c) the development of proper stress models for full – loop TFM poly – dispersed simulations; d) the development of a CFD model for the simulation of the combusting / reacting flow inside FBs; e) the development of a decoupled approach for the simulation of NO_x / N_2O. All these novelties were developed under the TFM formulation, since this is the state – of – the – art modeling technique for FBs.

As regards the simulation of the drag simulation, in this work an advanced EMMS scheme is developed for the investigation of the multi-scale structures induced in a CFBs multiphase flow. This 1-D sub – grid model was initially proposed by Wang and Li, 2007 and has been widely accepted as a better drag model than the conventional ones. Because of its success it is further investigated by a lot of authors worldwide.

In order to formulate such a model denser and diluter in particles regions of a control volume should be defined along with the respective momentum and mass balance equations for the dilute and the dense phase as well as for their inter – phase. Except for these correlations, empirical correlations can be used as regards the characteristic length and the particle loading of the dense phase. Moreover, in the system of equations describing the EMMS, constrains are introduced reflecting physical restrictions. In contrast with literature, in this work, an additional constrain is introduced regarding the terminal velocity. The system of equations is solved as a non - linear optimization problem through the minimization of the

energy exchange between gas and particles. The model developed is tested and validated in chapter 4 of this thesis.

A new modeling approach for the calculation of the shear and normal granular stresses suitable for the simulation of dense granular flows in a CFB recirculation system is developed. The proposed model adopts the Pitman-Schaeffer-Gray-Stiles yield criterion, in contrast to the conventional von - Misses / Coulomb one, for the formulation of the granular stress tensor. Since such a model has never been applied before in CFD simulations of CFBs, its validity is tested in a much simpler case. The accuracy of the proposed model is tested against a simple experiment of a batch of sand-like granular material poured inside an L-valve. In contrast to the conventional model of von - Misses/Coulomb, which is used in less dense flows, the proposed model is capable of describing more consistently the frictional forces and, thus, predicting more accurately both the flow immobility after a time period as well as the value of the repose angle. Optimum results were achieved with the adoption of a no-slip boundary condition for the vertical and the horizontal leg. Although the suggested model was proved to be better for CFB recirculation systems, the conventional approach is still considered more appropriate for the less dense flows in CFB risers, as several existing works (Zhang et al., 2008; Hartge et al., 2009; Atsonios, 2010) have demonstrated. An optimal full-loop simulation of a CFB system should therefore combine both models, i.e. von - Misses / Coulomb criterion for the riser and the cyclone, and the Pitman-Schaeffer-Gray-Stiles yield criterion for simulating the down-comer and the pneumatic valve of the recirculation system.

In this work the kinetic theory is applied for the formulation of all the necessary closure equations, when a full – loop TFM poly - dispersed CFD simulation of CFBs is performed. These equations are developed in order to simultaneously take under account the PSD and the inter-particle friction forces within the dense in the returning system. These correlations offer an integrated approach for the formulation of the stress tensor of the granular medium. The new poly – dispersed correlations were developed from the respective mono – sized correlations, using the KTGF, taking into account collisions of particles of different size. The poly – dispersed correlations proposed and / or developed in this work are consistent with the respective mono – sized ones. Finally, a poly – dispersed TFM numerical simulation may be of high computational cost and not easily applied currently, but PSD incorporation is a prerequisite for the prediction of particles segregation in CFBs that is of high industrial and theoretical importance. As the computational resources increase with time, the poly – dispersed model developed in this work could be used for full – loop TFM poly – dispersed simulations in the future.

Except for the theoretical work undertaken in granulates hydrodynamics, in this chapter proper models for the reacting flows inside FB are as well formulated. At first a comprehensive numerical model that incorporates combustion mechanisms is developed including both homogeneous and heterogeneous reactions. Three Eulerian phases are defined (gas, inert material and fuel) and their momentum and heat interaction is simulated through appropriate source terms in the respective partial differential equations of each phase. As far as the heat transfer between the two solid phases, no suitable model was found in literature. Therefore, Gunn's model that was originally developed for gas and solid phases heat transfer was reformulated in order to simulate solid phase to solid phase heat transfer. In this light, the inert – material is considered as a "pseudo - gas" with characteristics, e.g. coefficients of heat conduction and convection, that resemble solids.

In each phase, species are defined and tracked. In gas phase only major species are tracked and the reactions between them are simulated with the Finite rate / Eddy dissipation concept. Finite rate constants are retrieved from literature while turbulence characteristics are

retrieved through the solution of k – ε dispersed model. On the other hand, heterogeneous conditions are more difficult to simulate, especially under the TFM approach. Evaporation and devolatilization reactions are simulated through well-known expressions. Char combustion is simulated with the shrinking core model that takes into account the respective kinetics as well as the oxygen and carbon dioxide diffusion in the surface of fuel particles.

Finally, a decoupled approach was formulated for the simulation of NO_x / N_2O in CFBCs. Such an approach, that is a well-established technique in PF simulations, requires the solution of the combusting flow. Temperature and major species spatial distribution are retrieved from the solution of the combusting flow. The advantage if this approach is the significantly low CPU cost.

The aforementioned novelties are tested in simulating FBs in the following chapters. In order to be able to draw safe conclusions for each of them, in each chapter only one new model is tested. In chapter 4, the EMMS scheme is applied to an iso - thermal simulation of a CFBC riser and its results are compared with experimental data. In chapter 5, the combusting flow model is applied and its results are compared with experimental data for temperature and O_2, CO_2 measurements for validation purposes. Moreover, in the same chapter NO_x / N_2O decoupled approach is tested. In chapter 6, the validated in chapter 4, EMMS model is used in a full – loop simulation along with the stress model developed for the recirculation system. Finally, in chapter 7 a hot CFB carbonator is modeled using the same models as in chapter 6 for granulates hydrodynamics and the model developed for the carbonation reaction. It should be mentioned that whenever possible, conventional models are also applied, in order to evaluate the new models through results comparison.

4. ISOTHERMAL MODELING OF A CFB RISER

As far as large scale units are concerned, experience and reliable CFD models can play a significant role in the design optimization of CFB power plants. Their inherent ability to thoroughly address complicated issues such as inert material spatial distribution, fuel mixing efficiency and temperature distribution makes them a very powerful tool for this scope.

Several efforts have been made in CFD modeling of CFBs in the past and after the pioneer work of Gidaspow (Gidaspow, 1994), simulations on this area of interest flourished. The majority of CFD works focuses on 2D simulations (Benyahia et al., 2000; Chalermsinsuwan et al., 2009[a]; Mathiesen et al., 2000; Tsuo and Gidaspow, 1990; Wang and Li, 2007; Yang et al., 2003) but the developing CPU technology contributed to the realization of 3D simulations.

Except for some few resent CFD studies (Nikolopoulos et al., 2009; Zhou et al., 2011), the majority of published works focuses on isothermal modeling of CFB units. Isothermal modeling incorporates neither the energy conservation equation and heat transfer mechanisms nor chemical reactions. However, the importance of these models is high since they are the platform on which thermo-chemical mechanisms are integrated in order for a comprehensive CFD model for reacting granular flows to be formulated (Nikolopoulos et al., 2009). The importance of efficient, accurate and with low computational cost TFM isothermal models (Ge et al., 2008) led in extensive numerical and theoretical studies in the past decade.

The complexity of formulating accurate correlations for the momentum coefficient (β) in equation 2.15, resulted in a lot of research effort about this coefficient. Zhang and VanderHeyden, 2001 in their 3-D work used Wen and Yu's approximation (eq. 2.31) for the calculation of the drag force between the co-existing phases (Wen and Yu, 1966) in contrast to Gidaspow's equation (eq. 2.28, (Ibsen et al., 2004; Tsuo and Gidaspow, 1990)). However, these models of low sophistication, adopt the assumption of homogeneous conditions inside each control volume. The induced, by this assumption, numerical error has been reported to be huge when low grid resolution is applied (Ge et al., 2008).

In this light, new sub –grid drag models were developed that take into account the sub grid particulate structures. The EMMS schemes take into account flow heterogeneity inside a control volume via consideration of particles clustering mechanisms. This is achieved through a number of equations and constrains applied to a sub-grid level (Ge et al., 2008), among which the most important is the minimization function of the energy interexchanged between the co-existing gas and solid phases. This analysis may be conducted for the whole spectrum of particle loading, or for only the relatively diluter. Wang et al., 2008 that used the EMMS analysis in order to calculate the drag coefficient in the case of a 2-D simulation, for dense conditions (ε_s > 0.35), calculated the drag coefficient through Ergun's relation (eq. 2.9) assuming homogeneous conditions. Contrarily, Zhang et al., 2008 didn't use Ergun's equation in their 3D simulation utilizing an EMMS scheme (Wang and Li, 2007) for all possible particle loadings. This approach is also adopted in this work. It should be denoted that Ergun equation predicts a drag force on particles significantly higher than the corresponding one of the EMMS scheme (Nikolopoulos et al., 2010[b]).

In this chapter, the developed, in chapter 3, EMMS models is applied and validated. The theoretical novelties developed in this work, regarding isothermal TFM modeling, are: i) the custom built advanced EMMS drag scheme; ii) the new stress model for dense in particles conditions; and iii) the poly - dispersed stress model. The sequential investigation is preferred, in order to check the validity of each model separately.

Initially, within this chapter, the advanced EMMS scheme is tested in a simulation of a CFB riser. The stress tensor applied in this case, is the conventional one (equations 3.22 to 3.30) and the recirculation system of this unit is excluded from the simulation for simplification purposes. Moreover, numerical and theoretical complexities related with the simulation of the recirculation system are preferred to be examined in a later stage of this work, after the investigation of EMMS scheme is finished.

4.1 The 1.2 MW_{th} CFBC pilot plant

The 1.2MW_{th} pilot plant simulated in this section is illustrated in Figure 4.1. It is selected for its moderate size (semi – industrial scale) and the experimental data available regarding isothermal conditions (Leithner et al., 1993). Isothermal data can be used for validation of isothermal CFD models. In Leithner et al., 1993, geometrical and experimental data as well as operating conditions are available only for the CFB riser; data for the recirculation system are not considered essential at this stage. This is because, in this numerical investigation, the EMMS scheme developed should be examined in a simplified case where secondary modeling factors effect on results is minimized. In this way, conclusions on the momentum interexchange coefficient (β) modeling can be drawn easier.

The isothermal CFD model developed, is implemented in Fluent's 6.3.26 (FLUENT, 2006) version applying user defined functions (UDF) module, for the calculation of drag coefficient. These are fabricated in house subroutines, which exchange data with the main code algorithm and in this case their final result is the momentum exchange coefficient (β).

The corresponding boundary conditions are taken from the experimental work of Leithner et al., 1993, which was conducted under isothermal conditions (T=825^{o}C). The installation has a 9.5m height and a mean cross section of 0.4 m^2. The combustion chamber of the rig consists of two sections. The lower part (furnace's hopper) has a height of 3.15m. It is totally refractory lined and the cross section increases linear from 0.39x0.45m^2 at the distributor plate to 0.54x0.81m^2 at the top of the hopper. The upper part (the rectangular freeboard) has a height of about 6.35m. Secondary air is fed through five inlets along the height of the combustion chamber. Figure 4.1 presents the geometry of the furnace. It should be mentioned that the returning system of the unit has been excluded from the present simulation. There are some scientific essays that consider the influence of the returning system simulation on the flow in the riser as low (Benyahia et al., 2000; Hussain et al., 2005; Koksal and Hamdullahpur, 2005). Additionally, bed inventory is considered as an unknown quantity since the corresponding experimental value is not known, while solids recirculation flow rate is available from experimental work.

Mesh	Computational Cells	L_{cell}	l_r
Coarse	5,724 (9x6x106)	86.0 mm	330
Dense	45,576 (12x18x211)	43.0 mm	165

Table 4.1 Features of numerical grids.

In this pilot installation air staging is applied. The primary aeration is 86% of the total air entering the riser, whilst the rest is supplied through openings along the height of the riser (Figure 4.1). Table 4.1 summarizes important characteristics of the used uniform meshes, whereas in Table 4.2 the main gas/solid properties are presented. In order to simulate the transient, purely 3-D bed hydrodynamics (Myöhänen et al., 2006), the numerical grids constructed are three dimensional. These grids fully respect the actual geometry of the riser.

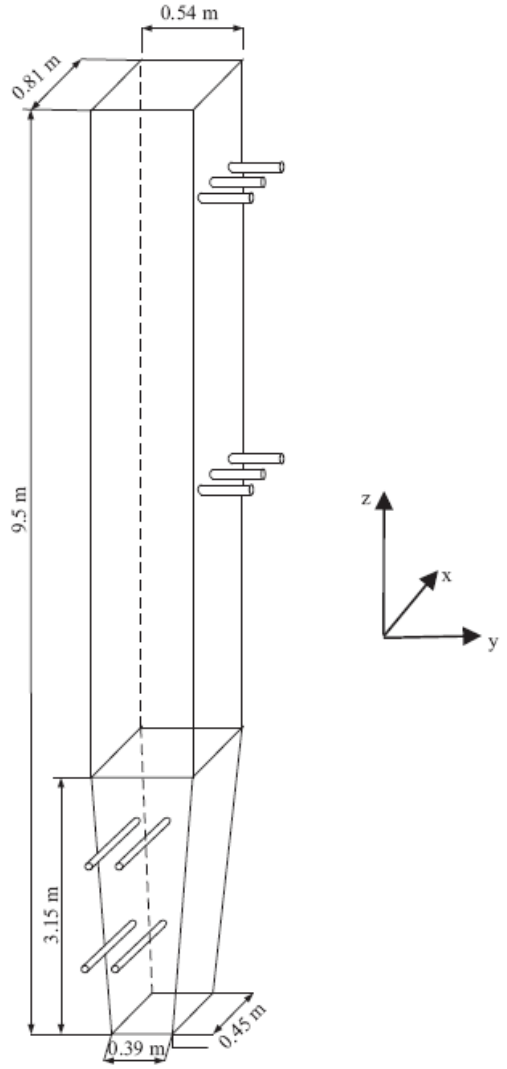

Figure 4.1 1.2 MW_{th} CFBC pilot plant (Leithner et al., 1993)

In this study both a conventional drag model and the new EMMS scheme developed in chapter 3 are tested. As it can be seen in Table 4.2, the CFBC unit operates with Geldart B particles. It should be mentioned that an EMMS scheme for Geldart B particles have not been investigated a lot (Wang et al., 2008) in contrast to the majority of the published research papers who investigated Geldart A particles (Chalermsinsuwan et al., 2009[a, b]; Naren et al., 2007; Wang et al., 2008; Wang and Li, 2007; Yan et al., 2002; Zhang et al., 2008). As far as granular model closure equations are concerned, in this study, typical models used in the majority of the relevant published works (Benyahia et al., 2000; Hartge et al., 2009; Wang et al., 2008; Wang and Li, 2007; Yang et al., 2003; Zhang et al., 2008) are used.

The set of partial differential equations comprises of equations 2.14 and 2.15. Regarding closure equations, the stress tensor is calculated through equation 2.20 and granular pressure through equation 2.19. The bulk and shear viscosity coefficients are calculated through equations 2.21 to 2.23 and 2.27 respectively. The momentum interexchange coefficient is modeled with either Gidaspow model (equation 2.28) or the EMMS scheme (equation 3.1). Granular temperature is modeled with the simplified algebraic equation 2.18

For the momentum and volume fraction equations, second and third order spatial discretization schemes (Table 4.3) are applied, whilst the respective time discretization of equations is conducted by a first order implicit scheme. The Finite Volume Method (FVM) is applied for the solution of the set of PDEs while the flux through the surfaces of the control volumes is expressed via Finite Difference Equations (FDE). The pressured based solver is used that means that the non - conservative form of Reynolds averaged Navier – Stokes is solved (Chung, 2002).

particle diameter	260μm (Geldart B particles).
particle density	2600 kg/m^3
gas density	0.3068 kg/m^3
gas viscosity	4.2277 10^{-5} kg/(ms)
e_{ss}	0.9
Packing Limit	0.63
Friction Limit	0.61
Minimum Fluidization Voidage (ε_{mf})	0.55

Table 4.2 Gas and solid basic properties.

Frictional viscosity	(Schaeffer, 1987)
Radial distribution	(Lun et al., 1984)
Solid pressure	(Lun et al., 1984)
Granular temperature	(Syamlal et al., 1993)
frictional pressure	(Ding and Gidaspow, 1990)
Drag coefficient	EMMS scheme / Gidaspow model
Scalars phase value	Green-Gauss Cell Based
Unsteady formulation	1st Order - Implicit
Pressure-velocity coupling	Phase coupled SIMPLE
Momentum discretization	Third-Order MUSCL
Volume fraction discretization	QUICK

Table 4.3 Parameters of the simulation.

In order to study the effect of the grid density on the numerical results, two different uniform grids are implemented. This parametric study is undertaken with the simultaneous examination of the proper simulation of the momentum interexchange coefficient. The coarse grid consists of 9 x 6 x 106 (5,724) hexahedral cells, whilst the denser grid consists of 18 x 12 x 211 (45,576) cells, which is two times denser than the coarse one. The ratio of the cell size to the particle's diameter (l_r) is 330 for the coarse grid and 165 for the dense one. These values are significantly higher than the theoretical maximum allowable value of 20, proposed by Ge et al., 2008 for an accurate modeling of the flow field by conventional models. For the coarse grid, the time step is set to be 0.5 and 1msec implementing either EMMS or Gidaspow's schemes respectively, while in the case of the dense grid the respective time step is set to 0.02 msec for the EMMS scheme and 0.33 msec for the case of Gidaspow's model. In each case, the corresponding time-step was selected in order to have a convergent solution for each time step, satisfying the CFL criterion. Boundary conditions for gas and particles are given in Table 4.4. It should be denoted that regarding the exit of the riser a boundary

condition for particulates is not applicable due to the hyperbolic nature of the partial differential equations governing particles hydrodynamics.

	height z (m)	gas phase	solid phase
distributor of the riser	0	$\|u_g\|$=5.724 m/s (primary air) Volume flow 1.005 m^3/s	$\varepsilon_s = 0$
Five secondary gas inlets and one for solids re-circulation (z=0.7m)	0.5	$\|u_g\|$=12.743 m/s	$\varepsilon_s = 0$
	0.7	$\|u_g\|$=5.287157 m/s	$\|u_s\|$=5.287157m/s Mass flow (5.03 Kg/sec) ε_s = 0.009145104
Total secondary gas volume flow: 0.164 m^3/s	2.15	$\|u_g\|$=15.501 m/s	$\varepsilon_s = 0$
	2.8	$\|u_g\|$=2.05 m/s	$\varepsilon_s = 0$
	5.6	$\|u_g\|$=2.178 m/s	$\varepsilon_s = 0$
	7.6	$\|u_g\|$=2.306 m/s	$\varepsilon_s = 0$
ceiling	9.3	$\|u_g\|$=0 m/s	no slip condition
lateral walls	n.a.	$\|u_g\|$=0 m/s	no slip condition
exit of the riser	9.5	P=0	n.a.

Table 4.4 Boundary conditions

Gas and inert-material are modeled as two discrete interacting Euler phases. The Eulerian description is essential for the simulation of inert-material phase due to its high volume and mass loading in the surrounding primary gas phase. Computational cost is high; therefore inert material particles are considered and modeled as mono-sized, simplification which is expected to have an impact on the most precise description of the induced flow field.

4.2 Drag scheme

Gidaspow and EMMS schemes, described by equations 2.28 and 3.1 respectively, are the conventional and the advanced approach for the simulation of the momentum interexchange coefficient. By comparing the two equations, it can be seen that the only differentiation is the introduction of H_d. This observation may lead in the false conclusion that the EMMS model is a simple alternation of the Gidaspow model. However, the EMMS scheme is a totally new model and the H_d factor is not a simple correction factor. This factor is used for numerical reasons and it implicitly applies equation 3.16 for the calculation of the drag force.

4.2.1 The H_d function

The calculation of the momentum exchange coefficient, with the advanced EMMS scheme requires the solution of the minimization problem described in section 3.1 (Nikolopoulos et al., 2010[b]). The commercial GAMS - General Algebraic Modeling System, (http://www.gams.com/) - package is selected to solve the nonlinear optimization mathematical problem. This program is a high-level modeling program for solving optimization problems, described by a number of equalities and/or inequalities constraints.

The set of equations comprising the EMMS scheme, analytically are: a) equations 3.2 to 3.7; b) constraints 3.11 to 3.14; c) closure equations 3.8 to 3.10 and the ones depicted in Table 3.2. The system is solved through the minimization of equation 3.15 for any triplet of u_g, u_s and ε_g, and for the operational conditions of the experiment selected for modeling (Leithner et al., 1993). For every triplet, once the abovementioned set of equations is solved, the H_d index can be calculated through equation 3.17. To implement the EMMS scheme the H_d index function should be calculated for every case, for any possible triplet.

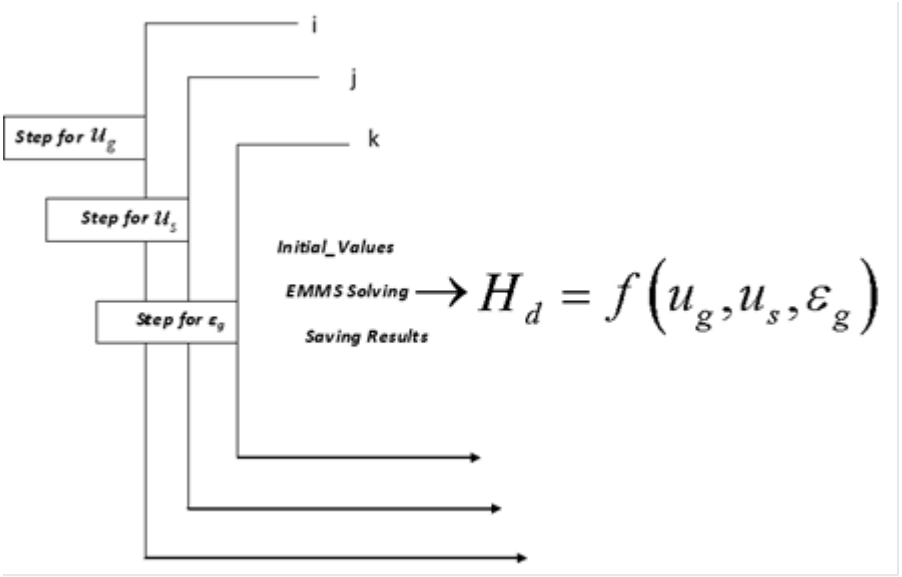

Figure 4.2 Schematic of solution procedure

The system of equations describing the EMMS scheme is a Discontinuous Derivatives Nonlinear Problem (DNLP, http://www.gams.com/). This category of problems require the maximization or minimization of a function *f(x)*, that is subjected to constraints (*g(x)* ¢ 0, where ¢ is a set of inequality and equality operators). The vector of variables (*x*), that are continuous real numbers, can be also subjected to inequalities ($L_o \leq x \leq U_{up}$). DNPL is similar to NLP, except that non-smooth functions (abs, min, max) can be involved in *f(x)* and *g(x).* For solving the DNLP problem the CONOPT solver is used. This is a feasible path solver based on the generalized reduced gradient method (http://www.gams.com/).

The solution procedure followed in GAMS software is depicted in Figure 4.2. The GAMS software succeeded in solving the problem for the operating conditions described in Table 4.2 for all triplets. Although the EMMS scheme needs these triplets as input, the obtained results revealed that the H_d index is a function both of ε_g and of the absolute velocity difference of the gas and solid phase $|(u_g-u_s)|$, which is also confirmed by Zhang et al., 2008. Plotting the values of H_d as a function of ε_g for a specific set of values (u_g=2.5 m/sec, u_s=1 m/sec and u_{slip}=1.5 m/sec), distributions as the one depicted in Figure 4.3 are produced. Each distribution can be split up in three main areas A, B and C. Area A refers to dilute conditions ($0.95 \leq \varepsilon_g < \varepsilon^*$), while area B to rather denser conditions ($0.82 \leq \varepsilon_g < 0.95$). The physical difference between areas A and B is small. Nevertheless these areas are examined separately since the numerical fitting of the EMMS results is conducted separately for these two areas, in order to achieve higher accuracy. In area C, on the other hand, a significant change occurs; clusters voidage (ε_c) stops increasing and remains constant and equal to ε_{mf}. This phenomenon will be explained in a following paragraph.

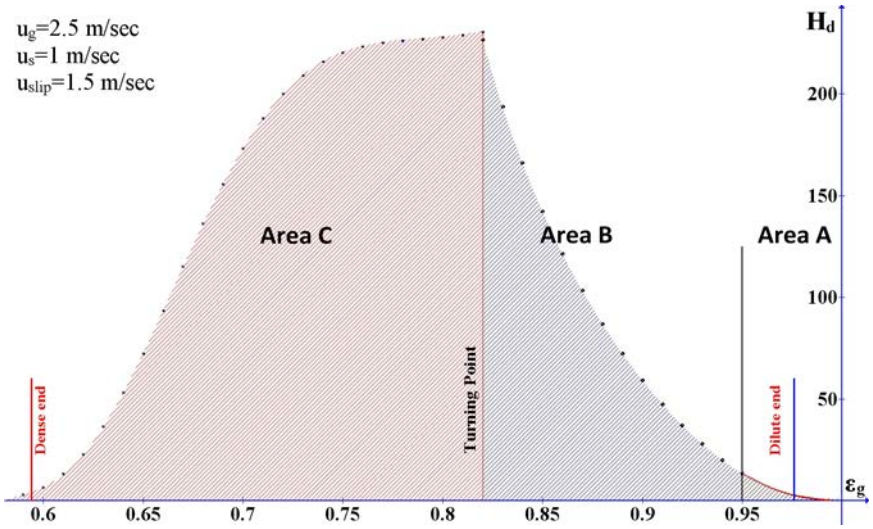

Figure 4.3 The $H_d(\varepsilon_g)$ function for u_{slip}=1.5m/sec.

For each of these areas (A, B and C), different mathematical expressions $H_d = f\left(|u_{slip}|, \varepsilon_g\right)$ are used for interpolation purposes. Area A is mathematically bounded by $0.95 \le \varepsilon_g \le \varepsilon^*$, where ε^* denotes the limiting value of ε_g above which H_d is equal to 1. This value is not considered constant, as in the work of Wang and Li, 2007, but as a function of slip velocity (Nikolopoulos et al., 2010[b]; Papafotiou, 2009). This novelty is believed to have an impact in the accuracy of the CFD model since in a significant proportion of a riser the volume fraction values are close to this "dilute end" region (Atsonios, 2010).

For Area A, the following expression is used for H_d fitting:

$$H_d = \sum_{i=1}^{4} 10^{\alpha_i \cdot \left[1000 \cdot \left(\varepsilon_g - 0.95\right)\right]^i} \qquad \text{Eq. 4.1}$$

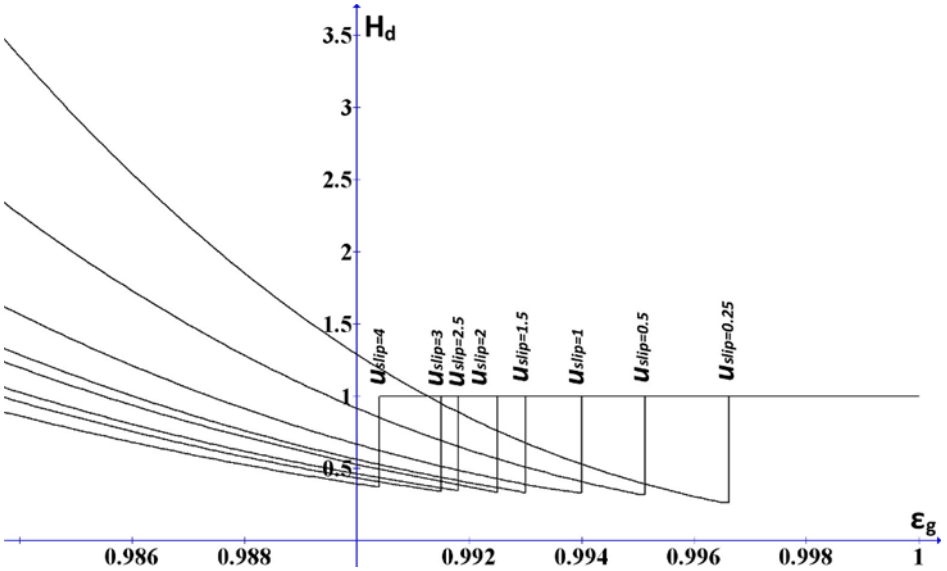

Figure 4.4 The $H_d(\varepsilon_g)$ function for u_{slip} = 1.5 m/sec (zoom in the dilute region).

For area B that is mathematically bounded by $0.82 \le \varepsilon_g \le 0.95$, the following expression is used:

$$H_d = \sum_{i=1}^{4} a_i \varepsilon_g{}^i \qquad \text{Eq. 4.2}$$

For area C that is mathematically bounded by $\varepsilon_{mf}(=0.55) \le \varepsilon_g \le 0.82$, the heterogeneity index is expressed by

$$H_d = \sum_{i=1}^{6} a_i \varepsilon_g{}^i \qquad \text{Eq. 4.3}$$

It should also be mentioned that since the problem is solved for specific values of u_{slip}, a linear interpolation method is used for obtaining the corresponding value of H_d for every slip velocity.

$$w = \frac{u_{slip}^{+} - u_{slip}}{u_{slip}^{+} - u_{slip}^{-}} \qquad \text{Eq. 4.4}$$

$$H_d\left(u_{slip}\right) = (1-w)\cdot H_d\left(u_{slip}^{+}\right) + w \cdot H_d\left(u_{slip}^{-}\right) \qquad \text{Eq. 4.5}$$

Although linear interpolation is the least accurate approach, it is the most computationally efficient. Additionally, more accurate interpolation schemes (Lagrange polynomials and splines) were tested (Atsonios, 2010) with no significant improvement in interpolation accuracy.

4.2.2 Description of the EMMS Results

The results presented in the following paragraphs are indicative for the specific operational conditions of the 1.2 MW_{th} unit; therefore, they cannot be regarded as universal and used for any other case. All EMMS parameters are calculated for various slip velocities and a wide range of control volume voidage (ε_g). Flow heterogeneity is predicted for a region expanding from ε_g maximum value of ε^* (the dilute limit above which H_d = 1), close to the dilute end area, as well as through A, B and C areas and ending at the dense end or bubbling end, which is equal to around $\varepsilon_g = \varepsilon_{mf} = 0.55$.

In general, the formation of dense flow phase is controlled by two separate mechanisms. On one hand, it is the mass enlargement of clusters through the addition of new particles followed by the increment of their volume, without any further densification of the dense phase; this mechanism can be characterized as extensive cluster growth. On the other hand, the addition of new particles in the control volume can alternatively lead to denser clusters without any change in clusters size. This will be achieved if new particles cause a rearrangement of the interior of the dense phase, reaching a more compact set of solid particles. This pattern can be characterized as intensive growth of cluster. These two different mechanisms can be regarded as the main causes due to which clusters are increasing in mass. The understanding of which of the two patterns dominate the formation of a cluster plays a significant role in the physical interpretation of the EMMS numerical results. In advance, it must be denoted that intensive growth mechanism is dominant for Areas A and B, whereas clusters grow only extensively in Area C. Moreover, the importance of the physical constraint mathematically expressed by equation 3.11 should be underlined, since it differentiates area B from C. A critical value of ε_g equal to around 0.82 is predicted, separating area B from C and taking into account that ε_{mf} is equal to 0.55 for the geometrical characteristics of the particles investigated. A more thorough and meticulous analysis for each area is provided below.

4.2.2.1 Characteristics of Area A

In this area, mathematically bounded by the inequality $0.95 < \varepsilon_g < \varepsilon^*$, the control volume is considered to be very dilute in particles. This flow characteristic decreases the robustness of the solving procedure and a good solution initialization was found to be of great importance. Not only, was the solver initialized from the solution of the previous triplet (e_g, u_g, u_s), but

also a very small calculation step for ε_g ($\delta\varepsilon_g$ = 0.000125) was adopted. It is noticeable that dilute flow conditions (Area A) represent a large proportion of a typical flow field within a CFB riser. Hence, proper modeling of the drag coefficient within this region is very important for the overall accuracy of the CFD model. The heterogeneity index H_d varies significantly, whilst it equals to one for extremely high values of ε_g (approximately ε_g >0.994). In this region where f=0. (Figure 4.5, $\varepsilon_g \geq \varepsilon^*$), Wen and Yu's (Wen and Yu, 1966) correlation predictions coincide with those of EMMS.

From a physical point of view, the flow regime in this region is rather sparse and the overall slip velocity inside the control volume is high or comparable to the corresponding terminal velocity. Additionally, structures such as clusters cannot be developed in adequate quantities in order to increase the slip velocity of the dense phase. Since the overall slip velocity is a weighted average of the corresponding values of the two co-existing phases (gas and inert material), the aforementioned mechanism results in a high slip velocity for the dilute phase. Thus, the constraint, defined by equation 3.14, cannot be satisfied, and it is not included in the implementation of the model for this region. This exclusion doesn't lack of physical interpretation, whereas the aforementioned constraint is mostly valid only for fully developed flows. Moreover, a sharp transition for H_d can be observed in the extremely dilute area (0.994 < ε_g < 0.995). It should be underlined that all measures monitored are continuous around the critical point of $\varepsilon_g = \varepsilon^*$, while their derivatives with respect to ε_g are discontinuous. This transition has also been confirmed by (Zhang et al., 2008). Nevertheless, in this work, ε^* is considered as a function of u_{slip} (Figure 4.4) and not constant as assumed by (Wang and Li, 2007). ε^* is fitted with respect to overall u_{slip}.

Moving within area A, towards denser flows and up to ε_g = 0.95, the present model predicts a steadily rising volume fraction of cluster phase (Figure 4.5). Such high values of f, predicted also by Wang and Li, 2007 may not realistically represent the governing physics, since the flow is rather dilute in order to have such big percentage of its volume occupied by clusters. However, as Wang and Li, 2007 correctly pointed out, in this region flow heterogeneity does exist, but instead of being attributed to particles clustering mechanism, it can be attributed to the interaction of the gas phase with the moderate sparsely scattered solid particles. EMMS scheme integrates such phenomena caused by neighboring of particles, but arithmetically considers them as structures resembling clusters.

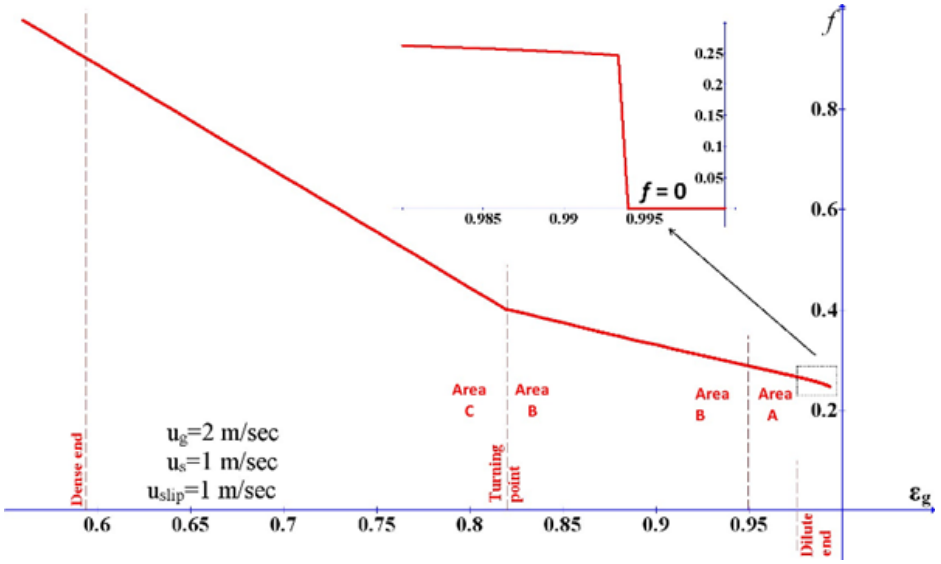

Figure 4.5 Dense phase volume percentage (f).

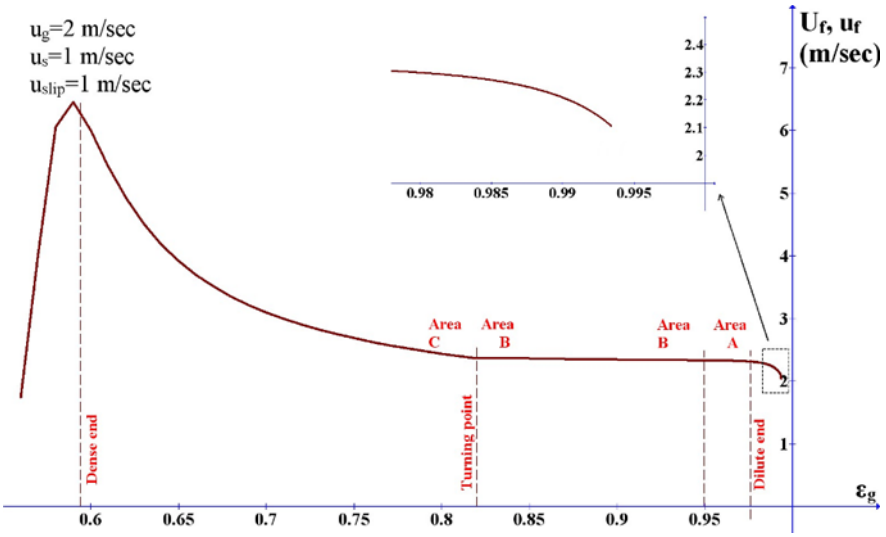

Figure 4.6 Gas velocity within dilute phase

Regarding the gas phase characteristics outside the cluster structure (Figure 4.6), it is clear that the increase of clusters volume fraction forces the gas phase to flow around the clusters rather than to penetrate into them. Thus, the gas phase velocity outside the cluster u_f is increasing and simultaneously the corresponding one inside the cluster u_c (Figure 4.7) is decreasing. It should be denoted that u_f (Figure 4.6) and u_c (Figure 4.7) in the dilute end region tend to the overall gas velocity (u_g = 2 m/sec) and the gas dominates over the particles. Hence, for very dilute phases (ε_g close to ε*), gas velocity is not considerably affected by the low inertia of particles.

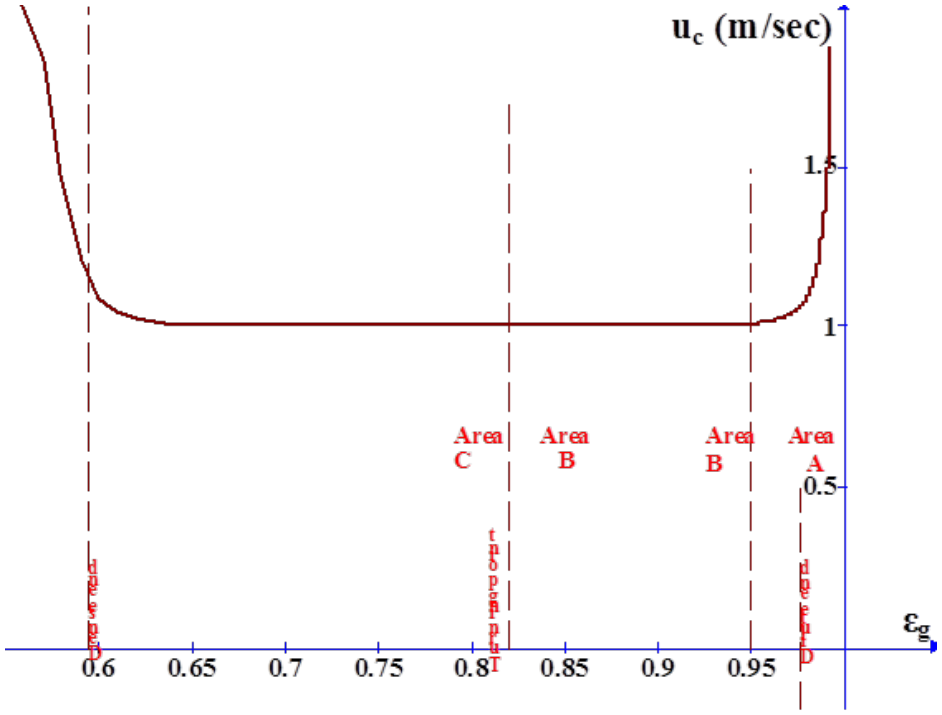

Figure 4.7 Gas velocity within dense phase

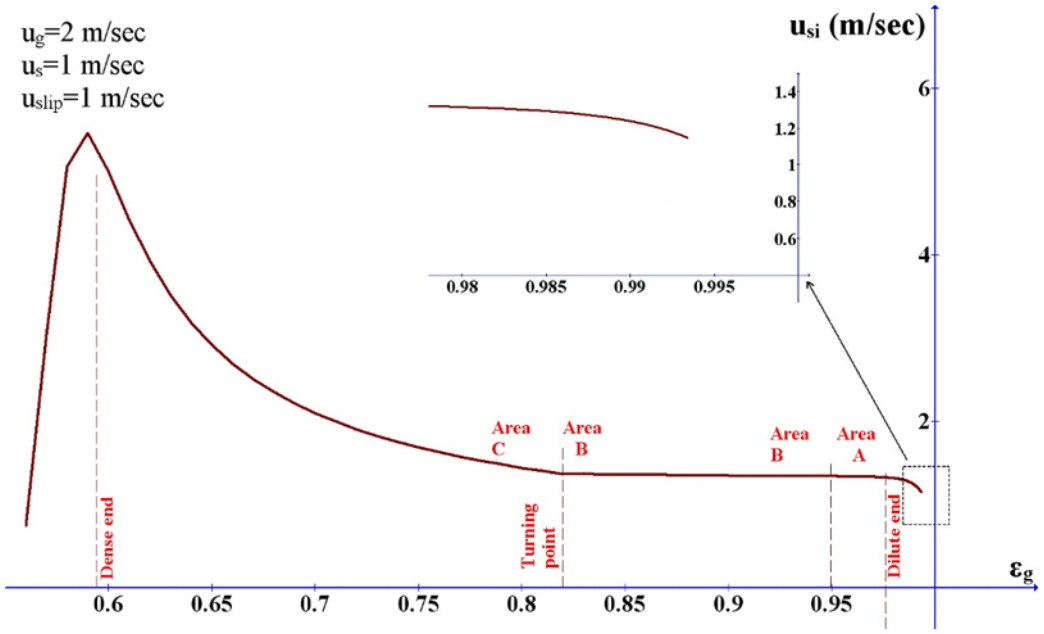

Figure 4.8 Actual slip velocity of inter-phase u_{si}.

Additionally, close to the dilute end region (ε^*), the slip velocity of cluster's interface u_{si}, is increasing rapidly (from 1. to 1.2 m/sec) with the increase of the clusters volume fraction. It reaches an almost constant value of 20% higher than u_{slip} (Figure 4.8), since the development of clusters contributes to the development of larger slip velocity.

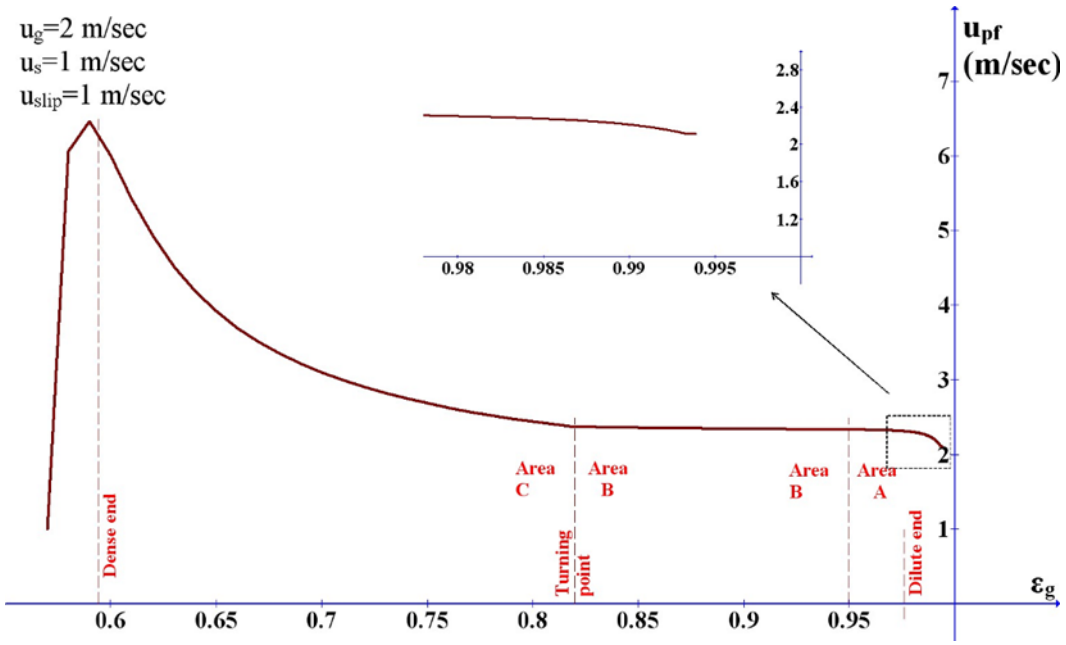

Figure 4.9 Particles velocity in dilute phase.

The velocity of the corresponding dilute phase outside the cluster structure is approximately equal to $u_{f,}$ since the gas drifts the particles, because area A is characterized by extremely small volume fraction of particles (Figure 4.9).

As far as the particle velocity inside the cluster (u_{pc}) is concerned, this remains almost constant equal to u_s = 1 m/sec and thus Figure 4.10 presenting the slip velocity of gas and particles inside the cluster is of the same trend as indicated in Figure 4.7. Therefore, inside

clusters, the velocity of particles (u_{pc}) decelerates the gas one, as the volume fraction of the particles increases.

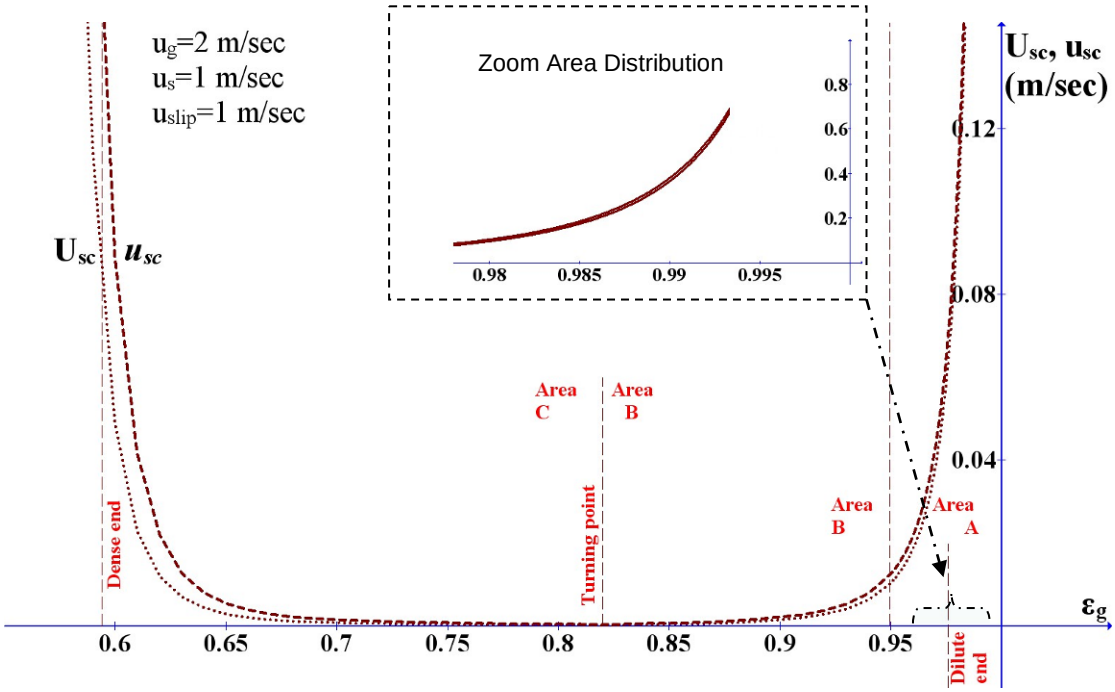

Figure 4.10 Actual and superficial slip velocity within dense phase.

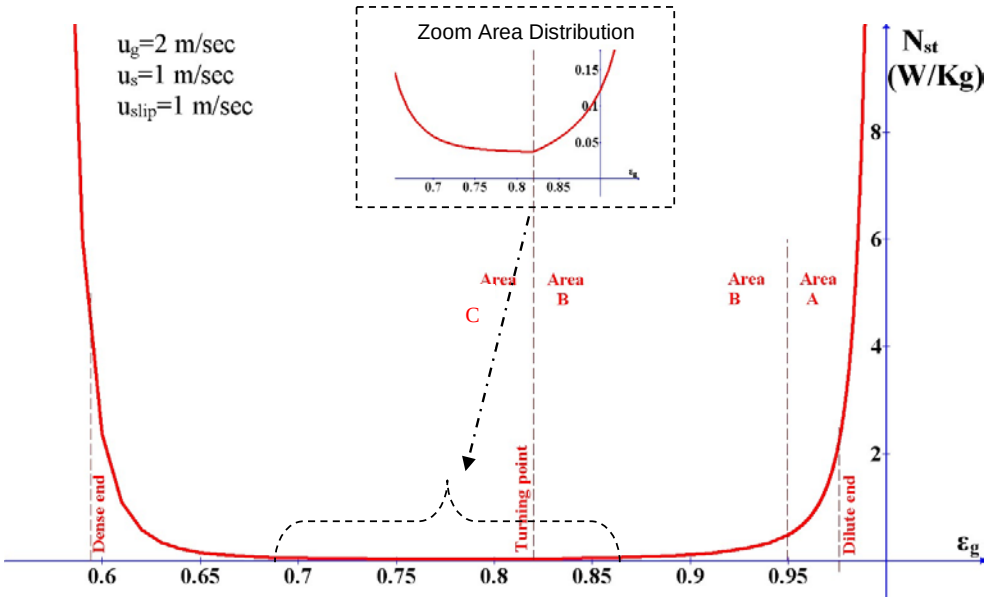

Figure 4.11 Energy exchange between phases (N_{st}).

Since particle aggregation mechanisms are not very dominant within region A, energy exchanged per unit of particle mass (N_{st}) is very large close to ε^* as depicted in Figure 4.11. However, since this variable expresses the energy exchange between gas and particles reduced to the overall particle mass, N_{st} decreases as dense phase is growing. In addition, dilute phase acceleration $(a_f + g)$ is almost equal to zero, as also predicted by Wang and Li, 2007. Particles acceleration inside the cluster shares the same trend with the energy exchange due to the decrease of slip velocity depicted in Figure 4.10 and the decrease of the forces exerted (Table 3.2). It is important that the EMMS scheme developed in this work, predicts

values of α_c (Figure 4.12) that have a better physical interpretation than those calculated by the corresponding scheme of Wang and Li, 2007.

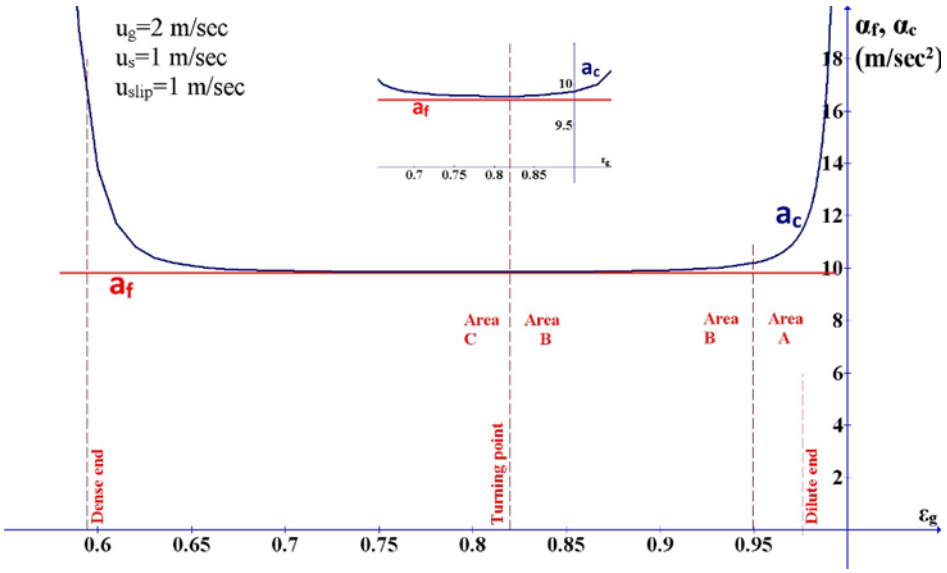

Figure 4.12 Dilute and dense phase acceleration.

4.2.2.2 Characteristics of Area B.

In area B, the same mechanisms governing area A are present. Since particles' clustering mechanism is more intense in this region, the energy interexchange reduced to the overall particle mass (N_{st}) is very low (Figure 4.11). An increase of solid concentration in a control volume results in an increase in the volume fraction of the dense phase. In addition, clusters diameter, as it is shown in Figure 4.13, doesn't increase much and the intensive growth of clusters remains the dominant mechanism of clusters enlargement.

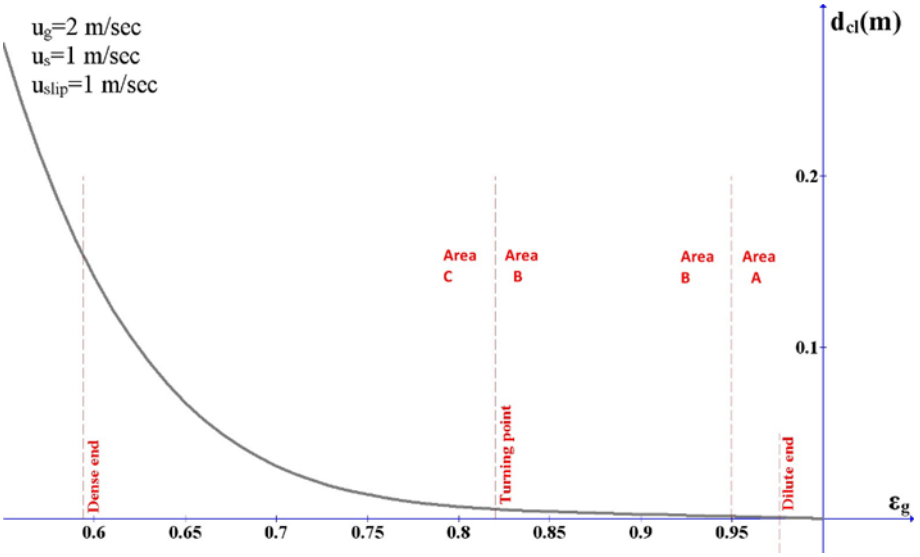

Figure 4.13 Cluster's diameter evolution.

Similarly to area A, the slip velocity of clusters (u_{si}) is larger than the overall slip velocity u_{slip} (Figure 4.8). However, slip velocity inside dilute and dense phases (u_{sf} and u_{sc} respectively) is rather small. Outside the cluster structure, the gas domination over particles is

again predicted as explained in area A. On the other hand inside the clusters (within area B), the respective domination of particles over the gas phase is enhanced compared to the area A, as it is shown in Figure 4.10 ($0.82 < \varepsilon_g < 0.95$, $u_c = u_{pc}$ and $u_{pf} = u_f$). As in area A, the developed model predicts more realistic values of α_c than Wang and Li, 2007 and thus small values for N_{st} are predicted. To sum up, there is not a significant physical distinction between areas A and B. However, from an arithmetic point of view, it is more efficient and numerically more accurate to fit H_d by different polynomial fittings for each area.

4.2.2.3 Characteristics of Area C.

Area's C bounds are described by a maximum value of ε_g equal to 0.82 and minimum value of ε_{mf}, for which constraint described by 3.11, also used by Wang and Li, 2007 as well as by Yang et al., 2003, is enabled. This constraint proved to have a significant impact on EMMS scheme results. Its significance relies on the prevention of clusters further densification, because their voidage (ε_c) cannot be smaller than the minimum fluidization voidage (ε_{mf}). Thus, clusters in Area C increase in mass only due to their respective diameter increase since no further densification can be achieved. Dense phase volume fraction curve (Figure 4.5), presents an increase in its slope at the turning point from area B to C. Since the solids volume fraction in the dense flow region cannot be further increased, the added mass in the control volume leads to a larger increase of the volume occupied by the dense flow phase. Such a tendency, also predicted by Wang and Li, 2007, imposes an upper limit of H_d for every value of slip velocity. The maximum value of the heterogeneity index is spotted in the turning point, reflecting the overall minimum of N_{st} curve (Figure 4.11) at the same spot.

As far as the respective gas velocity in dilute phase (u_f) is concerned, there is an increase in its magnitude (Figure 4.6), since the available free area for the gas phase is reducing because of the respective increase of dense phase volume fraction (Figure 4.5). Following the increase of gas phase velocity, the dispersed particles velocity is increased (Figure 4.9). The particles velocity inside the clusters (u_{pc}) is not altered with a velocity magnitude equal to around 1m/sec.

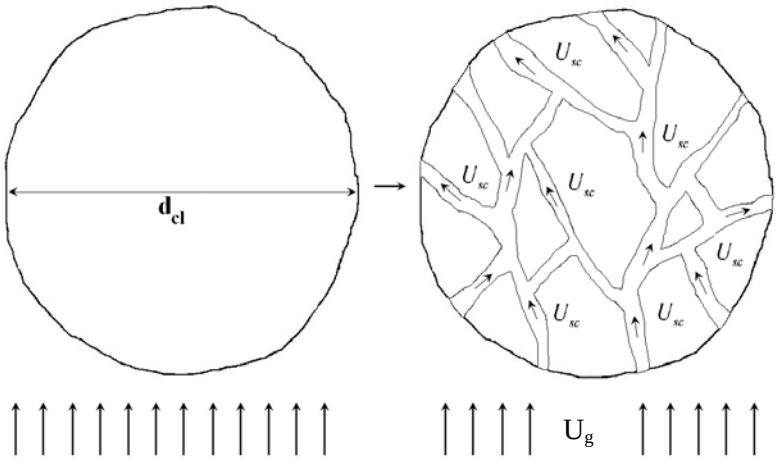

Figure 4.14 Collapse of the uniform structure of clusters.

For larger particle concentration (ε_g<0.59 or ε_s>0.41), the flow should resemble the emulsion phase of bubbling fluidization (Yang et al., 2003). This tendency is also predicted by the developed EMMS model. It is achieved numerically despite the utilization of the empirical equation 3.10 for the diameter of clusters, which implies a monotonically increase of clusters diameter as a function of ε_s. As a matter of fact, this equation predicts clusters with an unnatural size of 20 cm for great values of ε_s*=0.45*. In the recent literature, such empirical correlations (like eq. 3.10) describing the evolution of clusters diameter were developed (Gu

and Chen, 1998; Harris et al., 2002; Zou et al., 1994) through experimental campaigns with a focus on the flow region of $\varepsilon_g>0.7$. Due to the increase of clusters diameter (Figure 4.13), gas phase is penetrating into clusters, increasing the slip velocity magnitude, u_{sc}, between the phases (Figure 4.10). As a result, clusters as a single structure are no longer valid (Figure 4.14) and its slip velocity defined at its interface is decreasing (Figure 4.8).

Another result of clusters "collapse" as a single structure is that N_{st} increases since the slip velocity magnitude between the phases is increasing. At the same time, α_c (Figure 4.12) increases. In the very dense region, where ε_g equal to ε_{mf}, u_f and u_c equal to the overall gas velocity (u_g), whilst the same is observed for the particles velocity (u_{pf} equals to u_{pc} and u_s). Moreover, the slip velocity of clusters (u_{si}) equals to the overall slip velocity. At this point the EMMS scheme indicates that a regime of flow homogeneity inside the control volume is reached.

The presented evolution of physical mechanisms governing the size and characteristics of clusters are in a good agreement with relevant observations and predictions by other researchers in the recent literature, despite the stiff expression of d_{cl}. It should be mentioned that Wang and Li, 2007 also predicted the value of H_d equal to 1 for ε_g *equal to* ε_{mf}, confirming the results of the present work.

4.2.2.4 Slip velocity effect

The slip velocity between the gas and the particle phase is also affecting EMMS results. The importance of this effect has been reported even by authors that neglect it (Chalermsinsuwan et al.). In Figure 4.15 the energy exchange between phases (N_{st}) is plotted against u_{slip} for various volume fractions of solid phase. It is clear that small values of slip velocity promote the minimization of the energy exchange, whilst increased slip velocity render cluster structures relatively unstable. The correlation depicted in Figure 4.15 reveals that H_d (high N_{st} implies small H_d) and u_{slip} are inversely proportional. The sensitivity of meso – scale structures to the amplitude of gas velocity is implicitly confirmed by Zhang and VanderHeyden, 2001, who modeled a CFB unit using a conventional drag model in a relatively dense grid, under various operational conditions.

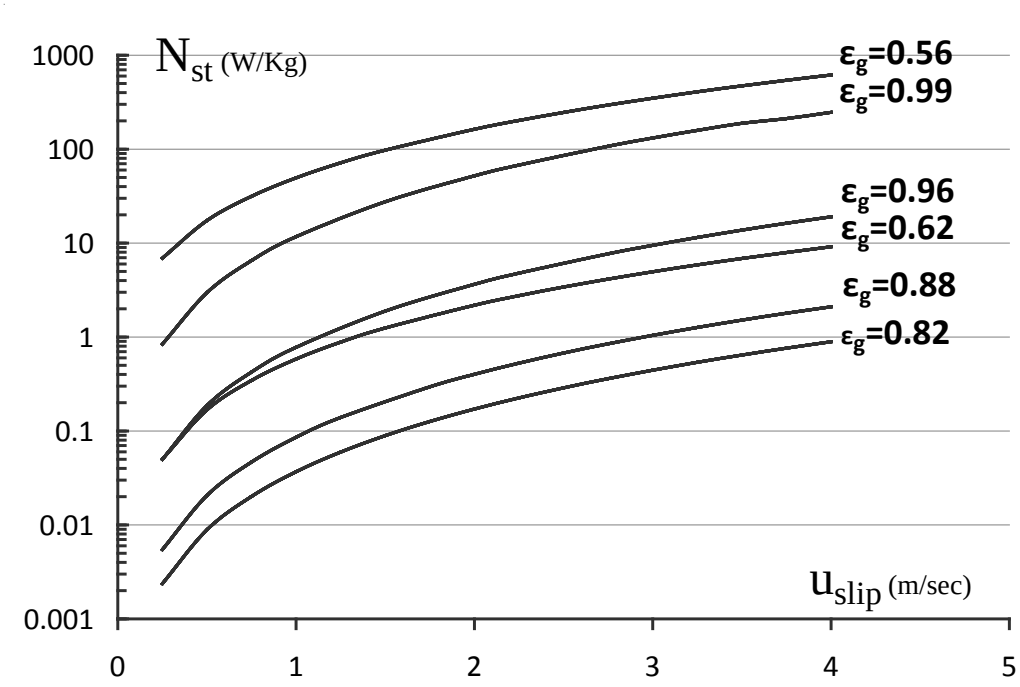

Figure 4.15 The objective function

4.3 Assumptions of the CFD model

The simplifications made in the case of the 1.2 MW_{th} CFBC isothermal modeling are summarized below. The assumptions (1 to 11) refer to the simulations undertaken with the EMMS scheme.

1) The returning system of the CFB does not affect riser's operation except for the mass flux delivered to the riser (Benyahia et al., 2000; Hussain et al., 2005; Koksal and Hamdullahpur, 2005). This flux is considered constant, equal to the experimentally measured value.

2) Particles are considered mono – sized. The PSD is ignored and the mean diameter represents the granulate mixture. Moreover, attrition or other thermochemical phenomena that affects the temporal evolution of PSD are neglected.

3) Clusters are considered as spherical and it is assumed that in each control volume they all have the same properties.

4) The temporal evolution of clusters is ignored. Thus, the heterogeneity index is only a function of local slip velocity and voidage. Moreover, the status of neighboring control volumes is not taken into account. This assumption is crucial for the straightforward implementation of the EMMS scheme. However, more complicated models that will incorporate the temporal evolution of heterogeneity may be formulated in the future, probably via suitable differential equations.

5) All wall surfaces are considered flat. This is not true for the freeboard of the CFBC where tube walls exist, but is valid for the hopper region that is refractory lined.

6) The flow is isothermal. There is no spatial or temporal differentiation in temperature. The experiment (Leithner et al., 1993) was conducted in iso – thermal conditions but temporal and / or spatial variations may have occurred.

7) Turbulence effect is neglected (Rampidis et al., 2007). This assumption is based on the well-known fact that the presence of a secondary phase, e.g. a granular phase, dumps down the turbulence effect.

8) For the calculation of granular temperature the diffusion and convective terms are neglected.

9) Uniform velocity profiles are considered at the inlets for gas and solids.

10) Secondary forces are neglected (added mass force, electrostatic forces, lift, buoyancy). Added mass force is very small compared to the drag force. The lift force is neglected because all particles are considered spherical. Electrostatic forces importance is very low for high temperatures (Bi, 2011) and can be neglected in the case of the isothermal modeling of the 1.2 MW_{th} CFBC riser since the temperature is over 800^{o} Celsius.

11) Particles self – rotation is neglected.

4.4 CFD simulation of the CFBC riser

Four different models are tested (Table 4.5). The effect of both grid density and drag modeling on numerical results is investigated. UDFs for the evaluation of the momentum inter-exchange coefficient through the aforementioned EMMS scheme are developed and incorporated in Fluent platform. The solution field was initialized and after around 100 solution seconds an almost equilibrium state was reached for all cases (from I to IV, see Table 4.5).

Representative mean values of scalars were derived via averaging the instantaneous values for a proper time period of around 20 sec (Kallio, 2006; Rampidis et al., 2007). Since

the application of EMMS scheme lowered the applied drag force to particles, the mass inventory in the riser increased from around 110 kg (as Gidaspow's model predicted) to approximately 170 kg. Respectively, in the case of the dense grid, Gidaspow's model reached equilibrium at around 270 kg (case III), whereas using EMMS scheme the solids inventory in the riser was approximately 310 kg (case IV). This increase in solids inventory is reflected in Figure 4.16. This figure presents the spatial distribution of the average static pressure along Z-axis (height of the furnace). Unfortunately, the only experimental data, which are available from the experimental campaign, under the simulated operating conditions, are the three values of static pressure presented.

Drag scheme / Grid density	Gidaspow	EMMS
Coarse grid	Case I	Case II
Dense grid	Case III	Case IV

Table 4.5 Definition of test cases examined

As far as the grid density effect is concerned, the numerical results obtained by the application of the dense grid using either EMMS or Gidaspow model are more accurate than the respective ones using the coarse grid. Figure 4.16 presents the pressure distribution along the bed, where the coarse grid significantly under predicts the experimental value of pressure at the height of Z=0.5m, which is equal to around 5800 Pa. Another, important observation is that the EMMS scheme results are also grid dependent. The reason behind this grid dependency is not yet fully known. It may be attributed to the fact that inside a control volume the size and particle loading of clusters is considered uniform.

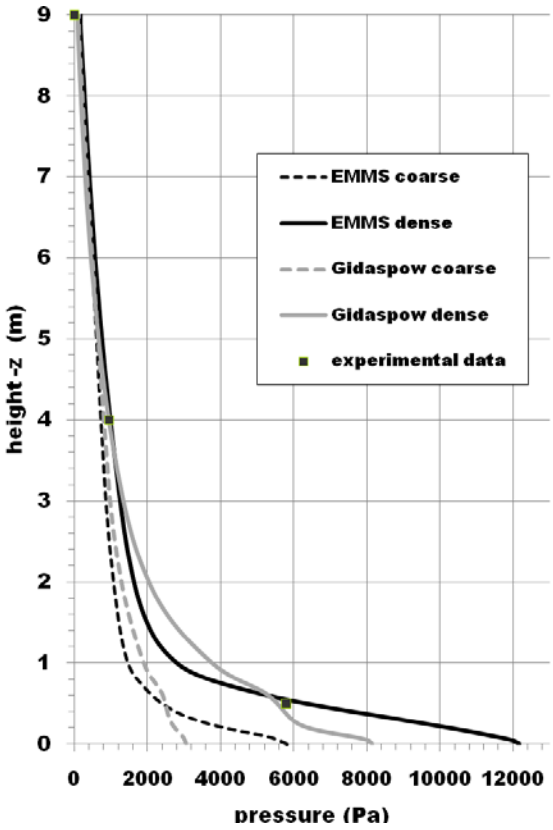

Figure 4.16 Pressure profile along the bed.

The comparison of the results for the cases III and IV, which use a dense grid, depicts the better description of the governing physical mechanisms by EMMS approach, especially at the low region of the bed. Even in the coarse grid case, the numerical results obtained by the EMMS approach (case II), are much closer to the corresponding experimental data than the predictions of Gidaspow's approximation. The differentiation of EMMS and Gidaspow schemes in the denser grid as concerns the pressure distribution predictions is spotted in the region of Z<0.5 (lower part of the furnace hopper). Unfortunately there are no experimental values for the abovementioned region in order to evaluate the EMMS model, and its ability to reproduce the governing physics.

Figure 4.17 and Figure 4.18 present the time averaged mean solid volume fraction and slip velocity distributions at the middle of the cross-section along the height of the riser for all cases. The aforementioned figures indicate that the bed hydrodynamics main differences are spotted in the bottom dense region, where the governing physical mechanisms are more complicated. Therefore the necessity for sophisticated drag models such as EMMS is underlined. Supporting the advantages of EMMS over convectional models a typical S-shape (Kunii and Levenspiel, 1991) curve with a value equal to around to 0.2 for solids volume fraction in the bottom zone is predicted with the EMMS. This is valid regardless of the grid density used in the numerical simulations.

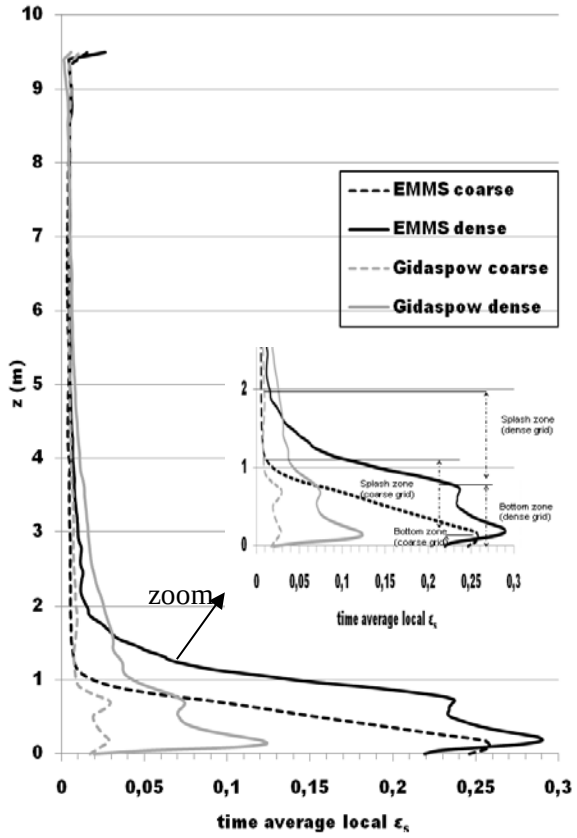

Figure 4.17 Time averaged mean local solid volume fraction, at the middle of the cross-section along the height of the riser (ε_s).

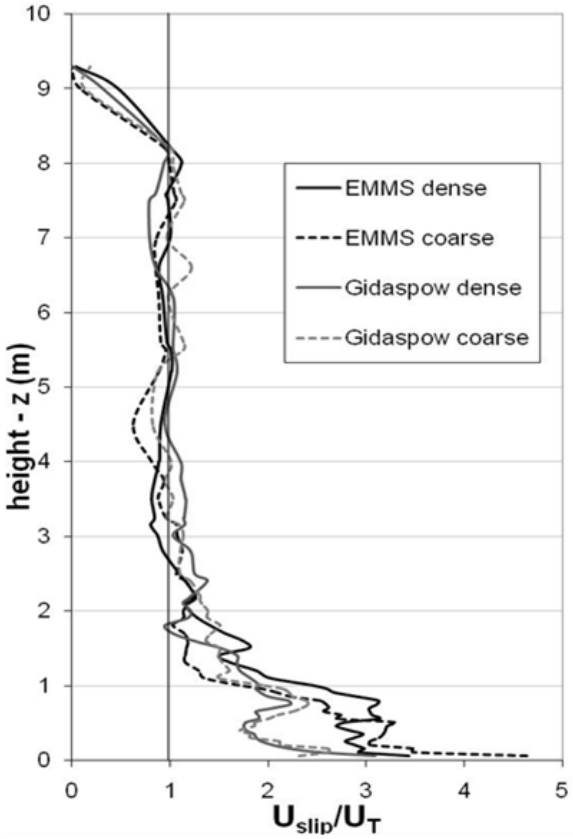

Figure 4.18 Time and spatial (for each cross-section) averaged mean slip velocity, dimensioned with the terminal velocity of particles, along the height of the riser.

As it was previously stated, EMMS efficiently captures the S-shape distribution even under coarse grid conditions where Gidaspow's correlation clearly fails (Wang et al., 2008; Zhang et al., 2008). This can be attributed both to the calculated lower drag forces especially

in the denser bottom region and to the more accurate modeling of the internal recirculation within the riser (core-annulus flow). Moreover, in the case of the dense grid, both drag models predict larger bottom and splash zones than the respective coarse grid (Figure 4.17). Nevertheless, in the upper region of the bed (freeboard) the differences are small and cannot be easily distinguished in Figure 4.17 and Figure 4.18. However these differences cannot be regarded as insignificant and in general they affect the induced flow field in the bottom region as well, due to the internal recirculation.

In the bottom region, with the implementation of the EMMS scheme for the calculation of the drag coefficient (case II and IV), the slip velocity is increasing due to the decrease of the free-path cross-section available for the gas phase (Figure 4.18). However, in the freeboard, Gidapow's drag model predicts considerably higher slip velocity. This difference can be attributed to the low values of H_d (Figure 4.19). Solids volume fraction in that area is close to its respective value at the dilute end region, an area in which the proposed EMMS scheme (Nikolopoulos et al., 2010[b]) predicts that the gas-inert material force is greater than the force predicted by Wen and Yu (Wen and Yu, 1966) correlation ($F_{EMMS} > F_{WEN,YU}$).

As the freeboard region is concerned, the flow in this area is rather dilute in particles and particle structures that could elevate the slip velocity above the U_t is highly unlikely to exist. Thus, the slip velocity should generally not exceed its physical constraint. Despite the fact that in general, EMMS and Gidaspow's results do not have strong differences in this region, it is of importance that EMMS model respects the aforementioned constraint.

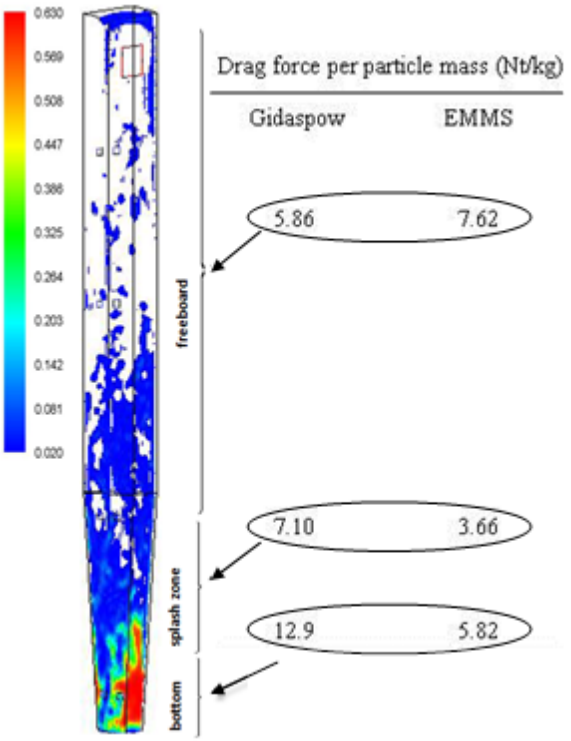

Figure 4.19 Solids volume fraction and the respective drag force distribution within the three zones of the bed, in the case of the dense grid.

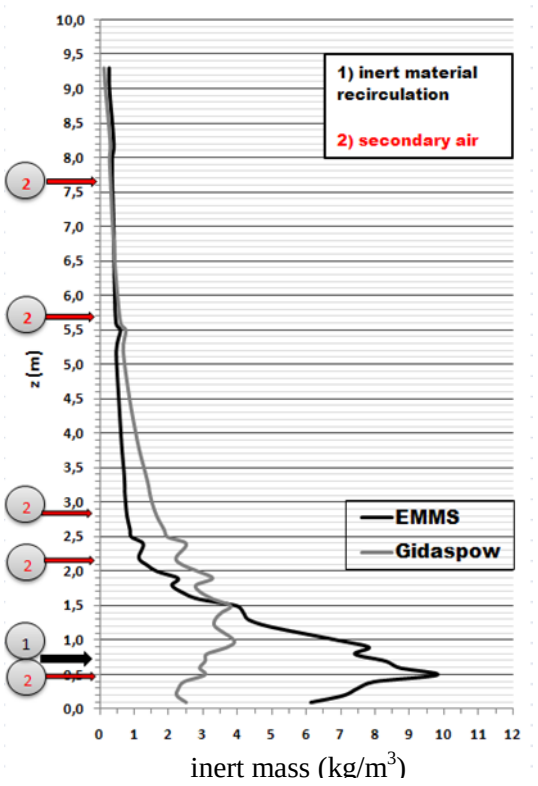

Figure 4.20 Time average inert mass distribution in the case of the dense grid.

Figure 4.19 depicts a volume integral of the drag force per particles mass for the flow field as predicted in case IV. This is calculated for the three regions of the riser (bottom,

splash and freeboard), either with Gidaspow or EMMS approximation. At the bottom zone, EMMS mean calculated drag force is lower than the respective one by Gidaspow's model since almost 3/4 of the volume of this region has an H_d greater than 1; thus, solid particles have higher residence time in this region. As a consequence, an elevated volume fraction is observed in this region (Figure 4.17). Higher particle loading further enhances clusters formation and inherently decreases the corresponding drag force per particle mass.

Regarding the splash zone, the volume percentage with a larger drag force acting on particles ($F_{EMMS} > F_{Gidaspow}$, H_d <1) is increasing (around to 21%) in contrast to the bottom zone. Nevertheless from Figure 4.19 it seems that the overall drag force calculated by EMMS is smaller than the Gidaspow's corresponding one. In addition, u_{slip} calculated via Gidaspow is a little lower in comparison with the one calculated by EMMS, because of the different total mass inside this area (mass calculated by EMMS is greater than the respective one calculated by Gidaspow's model, as depicted in Figure 4.20.

Finally, for the greatest volume of the bed, i.e. the freeboard, EMMS scheme plays a less significant role in the time evolution of the phenomenon. This is attributed to the fact that the H_d is mostly equal to 1 in this region.

Another important aspect of the multiphase flow inside a CFB riser is depicted in Figure 4.21. This figure depicts the distribution of the time averaged particle volume fraction. Dilute conditions are the most commonly observed. Thus, the polynomial described in equation 4.1 is the one applied most of the times. This fact underlines the significance of proper formulation of equation 4.1. The coefficients of the polynomials should be calculated with high accuracy. In this light it is important to treat the dilute end not as constant but as a function of slip velocity. It is also interesting that the H_d index applied is mainly low. In only a small fraction (lower than 10%) of the bed the H_d values applied are high. Although, large values of heterogeneity index are applied only to a small portion of the bed, and in almost half of the bed the Wen and Yu correlation is applied, the differentiation of the results observed in Figure 4.16 underline the significance of the low values of H_d and their proper determination through the EMMS scheme.

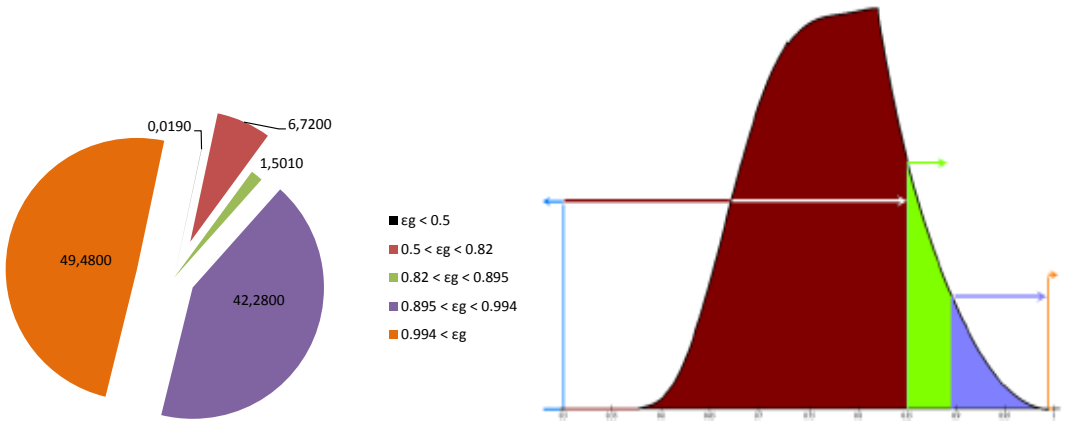

Figure 4.21 Effect of each polynomial (eq. 4.1 to 4.3) to the H_d function in (case IV)

Getting a further insight into the results of the dense grid, Gidaspow's model (Figure 4.20) predicts an almost uniform distribution of solid particles along the bed. On the other hand, EMMS predicts a dense bottom region; a prediction that agrees better with common experience in CFB (Hartge et al., 2009). Moreover using both models, the maximum solids concentration is spotted close to solids recirculation inlet (Figure 4.20, z=0.5m). However, in the case of the EMMS model the maximum solids concentration is much larger than in the

case of Gidaspow's model (10 kg/m^3 in contrast to 3 kg/m^3). It is also interesting to point out that the aforementioned local increase in the case of EMMS is rather sharp. On the other hand, the same model predicts slightly smaller solids concentration in the freeboard region. To sum up, EMMS model implementation increased the solids concentration in the bottom region of the riser in contrast to Gidaspow's model. This additional mass may be attributed to two factors; the overall increase of solids inventory prediction (310 in case IV, compared to 270 kg in case III) and the lower particle loading in the freeboard.

Grid density also plays a significant role in the aforementioned characteristics of the induced flow field. A denser spatial discretization results in more accurate simulations because small solids structures within a control volume are more accurately simulated (Figure 4.23). From Figure 4.22, it is evident that the solids volume fraction is predicted to be higher close to the wall region than in the core region either using denser grid or EMMS formulation. This is due to the small values of gas velocity characterizing the region close to the boundary walls in contrast to the neighboring core region. Using a coarse grid and Gidaspow's approximation for the drag force a rather small mean typical value of ε_s is predicted in the core of the bottom region (about 0.005, Figure 4.22).

Figure 4.24 and Figure 4.25 describing the spatial evolution of the solids volume fraction distribution and its corresponding velocity indicate that the standard core annulus flow pattern apparent in CFBs risers is successfully predicted by using the EMMS scheme in the dense grid. The aforementioned profiles are representative of such a flow pattern, as it was also depicted in previously published works (Zhang et al., 2008). In detail, the solids volume fraction follows an almost parabolic shape, with the corresponding mean value decreasing along the height of the riser. On the other hand the respective gradients of the ε_s inside the annulus region increase is bigger at the Z=1.5 plane (splash region). The opposite is occurring for the velocity field evolution of particles. For both of these variables the most inhomogeneous conditions are observed for the slice passing from the gas and solids inlet boundary conditions (Z=0.5m). Furthermore, it is very interesting to observe that solids tend to accumulate at the four corners of the riser. In this region the maximum down – falling velocity of solids towards the bottom region is observed. Figure 4.24 and Figure 4.25 describe a main recirculation zone induced by the solid particles in the vertical direction (Z-axis) of the riser.

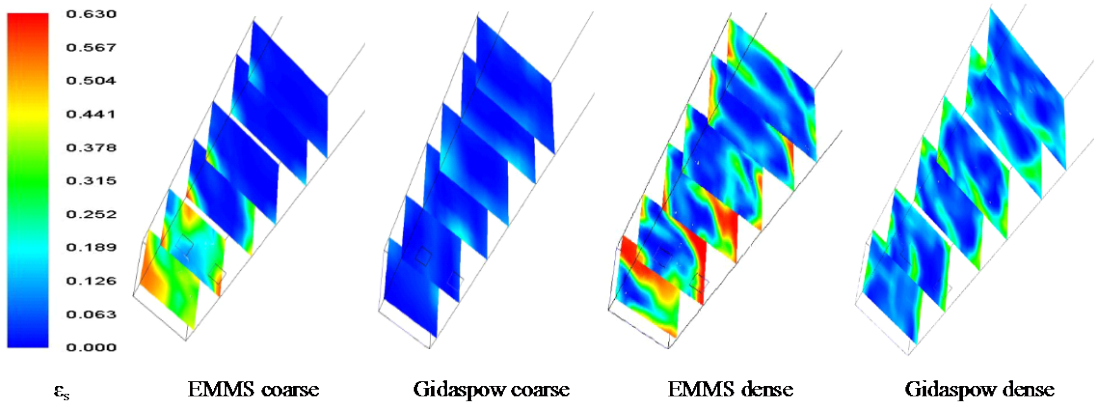

Figure 4.22 Instantaneous solid volume fraction distribution at various heights of the bed for the examined cases (I-IV).

In addition, complying with the common experience on CFB's (Kunii and Levenspiel, 1991) the width promotion of the annulus zone against the core one at the bottom zone is predicted (Figure 4.26-a). Moreover, a neck mechanism is observed for the induced flow field

at a plane passing from the gas and solids feeding system. This mechanism increases locally the velocity of the gas and solid phases. This phenomenon is of industrial interest since it plays a significant role in the penetration, the mixing and the residence time of the fuel or any other reacting solid that is inserted into a bed through similar ports. Moreover, the high solid velocity is expected to play a negative role, as concerns the attrition of the granulates within the CFB riser.

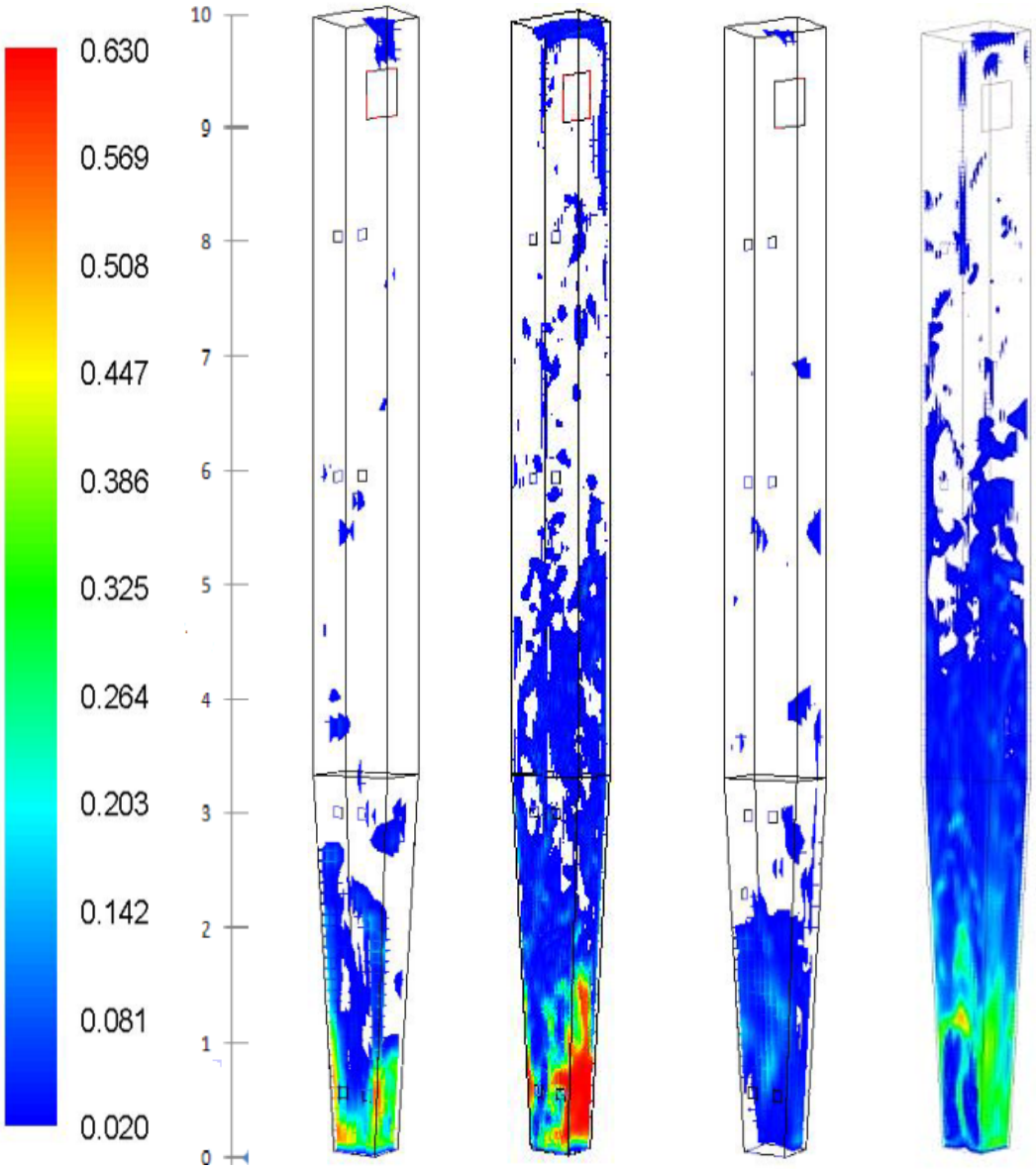

Figure 4.23 Instantaneous Solids volume fraction (0.02-0.63)

The fluctuations of solid volume fraction are also affected by grid density. Since these fluctuations reflect the volume of clusters passing through, it is expected that dense grid implementation would result in sharper fluctuations. This was confirmed, not only for Gidaspow's model but also for EMMS scheme. Figure 4.27 illustrates ε_s time series at the center of the cross-section for Z=5m. It is obvious that the dense grid simulation has a

significant advantage in the accuracy of the numerical results, since it is able to explicitly simulate smaller clusters.

Grid independency, in this specific numerical investigation is not achieved for both schemes (EMMS or Gidaspow). Wang et al., 2008 state that the required grid resolution, at least for two dimensional simulations, should correspond to a L_{cell} to d_p ratio equal to around 95 (five times lower grid density than the one proposed by Ge et al., 2008. However, this lower grid density would result in a grid consisting of $4 \cdot 10^5$ cells. Such a grid is not applicable due to the high computational cost.

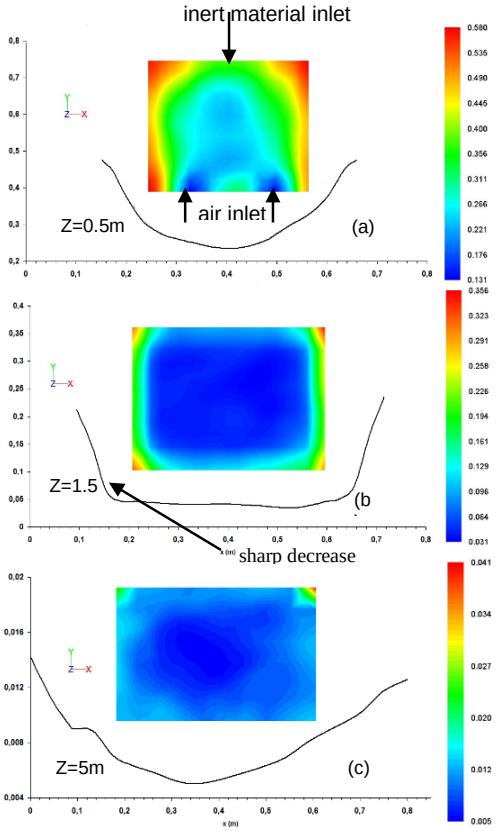

Figure 4.24 Time averaged solids volume fraction at the representative horizontal slices of the three important zones: (a) Z=0.5m (bottom zone), (b) Z=1.5m (splash zone) and (c) Z=5m (freeboard zone).

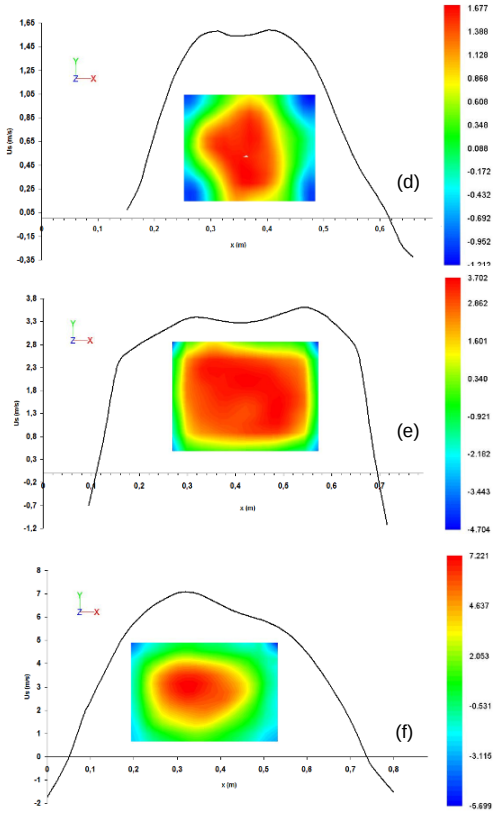

Figure 4.25 Time averaged solids Z-velocity at the representative horizontal slices of the three important zones: (d) Z=0.5m (bottom zone), (e) Z=1.5m (splash zone) and (f) Z=5m (freeboard zone).

Nevertheless, EMMS implementation for the calculation of the drag force between the co-existing phases significantly improves the numerical results. Therefore the required grid density to achieve independent solution is estimated to be lower compared to the theoretical reported value in the case of conventional drag schemes. This statement is also supported by the findings of Lu et al., 2009.

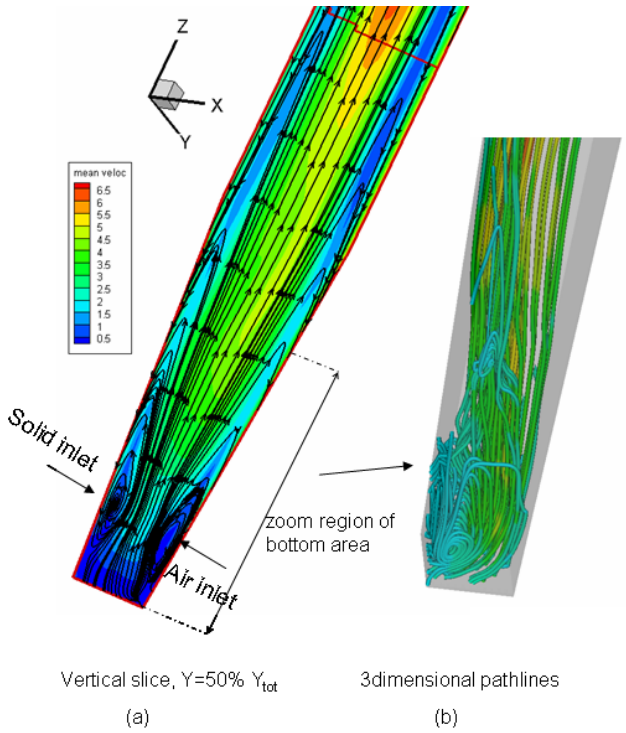

Figure 4.26 (a) Kidney vortex close to the inlet and (b) 3-D path-lines in the bottom zone.

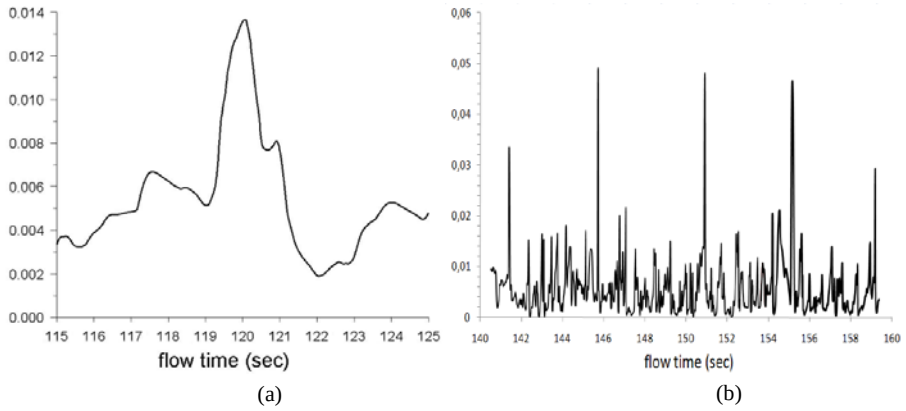

Figure 4.27 Instantaneous solids volume fraction in the cross section center at height z = 5 m for coarse and dense grid for EMMS application in the case of (a) coarse and (b) dense grid.

4.5 Conclusions

The EMMS scheme, developed in chapter 3, was successfully applied to a 3 – D CFD numerical simulation of the hydrodynamics of a CFB riser. The EMMS equations comprise a nonlinear optimization problem that incorporates equality and inequality constraints and an objective function, referring to the energy exchange between flow phases. This optimization problem was solved, for the operating conditions of the CFB unit examined, with the GAMS package prior to CFD simulations. The result of the optimization problem revealed that albeit an empirical equation for clusters diameter was implemented in order to simplify the EMMS matrix solution, the numerical results within the dense phase indicated that the developed model efficiently captured the inhomogeneous physical mechanisms governing the induced flow field.

Moreover, the consideration of acceleration of each phase as a free variable with the prescribed constraints adopted in the present work predicted more reasonable results for the

acceleration of solid particles in contrast to other works (Wang and Li, 2007). Additionally, the developed model predicted more realistic values for the clusters volume fraction (*f*) in comparison with the work of Wang and Li, 2007 as concerns the dilute region of area A. Nevertheless, the EMMS model takes into account the effect of particle neighboring on the momentum exchange coefficient between the phases in this area in an implicit manner. Therefore, an extended experimental and numerical investigation on this area should be conducted, which may lead to an alternation of EMMS model approximation for this area. From a qualitative point of view, EMMS results agreed well with other available data in the recent literature, whilst heterogeneity index (H_d) quantifying the flow heterogeneity of each control volume was proved to be only a function of u_{slip} and ε_g. Finally, a proper interpolation scheme for the H_d index is applied, in order to directly couple the EMMS scheme with a CFD Eulerian TFM code.

The EMMS scheme results, as the H_d index is concerned, were incorporated to the CFD code via UDFs in order to simulate the isothermal flow of the $1.2MW_{th}$ CFBC unit. Gidaspow's conventional drag model was also applied, in order to be able to compare the two models with respect to experimental data for pressure distribution. Gidaspow's explicit inability to simulate the effect of clusters that have dimensions smaller than the equivalent size of the computational cell, necessitated the simultaneous investigation of the grid density and its effect on simulation accuracy in conjunction with the drag modeling approach. Moreover, grid density was investigated because the coarseness of the meshes used is a *sine qua* non for realizable modeling of large scale units. EMMS scheme application proved to considerably increase the accuracy of the numerical results in contrast to Gidaspow's approximation. However, the actual calculation time, for the same grid density, is larger compared to conventional drag schemes, since the applied time step for the EMMS case was smaller compared to the respective time step of the Gidaspow case. Additionally, EMMS model clearly increased the accuracy of the results in the dense bottom zone, predicting more realistic values for the solid concentration and pressure distribution. This area is the most challenging among the others (splash and freeboard), due to its high solids concentration which results in strong flow heterogeneity. In addition, this region is strongly affected by the internal circulation of solids, induced by the core – annulus flow pattern, which is more precisely modeled by the proposed EMMS scheme.

EMMS scheme was found to simulate better the complicated patterns of the CFB. The well-known S – shape profile of particles loading is predicted with the advanced EMMS scheme even for the coarse grid simulation. Moreover, the results of the CFD models that adopt the EMMS drag scheme seem to respect the terminal velocity of particles in the freeboard. Even though such a behavior has not been investigated experimentally, the dilute conditions in the freeboard imply that at least large cluster should not be present in this region. Therefore, in general the mean gas – particles slip velocity should not exceed the terminal velocity of single particles. Thus, the EMMS drag model seems to prevail over Gidaspow's, as far as the S - shape profile and the slip velocity predictions are concerned.

The numerical investigation undertaken in this chapter validated the EMMS model developed in this thesis. Moreover, it revealed that the EMMS scheme can achieve more accurate results with the same grid density in comparison with the Gidaspow model. Since conventional drag models are supposed to need extremely dense computational grids, for highly accurate simulations, it is very important that the EMMS scheme can increase the accuracy without implementing a denser grid. This advantage of the EMMS scheme is very important as concerns the future simulations of CFBs because it suppresses the required computational needs at lower levels.

5. SIMULATION OF COMBUSTION AND POLLUTANTS FORMATION MECHANISMS

Technological applications of Circulating Fluidized Bed Combustors have been developed rapidly in the power generation industry as they combine fuel flexibility and high efficiency especially for biomass co-combustion. At the same time as the applications of CFB technology scale up, an 800 MW_e CFBC unit is already under design process as reported by Wu et al., 2004, new challenges arise in the field of the numerical prediction of their hydrodynamic behavior and their combustion and emissions performance. Reliable 3-D models are essential for the optimization of large scale units' design, as they can predict inert material concentration in bed, fuel mixing efficiency and temperature profiles. Simulation with the aid of CFD may be regarded as one of the most sophisticated approaches for the prediction of critical parameters controlling the efficient operation of such installations. CFD techniques are expected to substitute empirical or semi-empirical models in large scale CFBC designing.

The majority of the CFD studies on CFBs have been focused on isothermal modeling of CFBCs (Kallio, 2006; Rampidis et al., 2007; Wang et al., 2008). Such numerical approaches constitute the basis onto which combustion and pollutants formation models can be incorporated, in order to develop a validated and reliable tool for the simulation of CFBCs. However, even for the cold flow simulation, the uncertainty behind a substantial number of parameters is significant. The most important parameter as reported by Wang et al., 2008 is the momentum exchange coefficient between gas and inert material (Ge et al., 2008).

Regarding the numerical simulation of CFB combusting / reacting flows, limited data are available in literature, especially for combustion mechanisms (Gungor, 2008[b]; Gungor and Eskin, 2008[b]). Moreover the majority of these studies, approach the complicated physics, which dominate the operation of a CFB combustor, in a two-dimensional way (Gungor, 2008[b]; Gungor and Eskin, 2008[b]), overlooking their three dimensional character (Myöhänen et al., 2006). This chapter focuses on the application of a three-dimensional model, taking into account the conversion mechanisms of fuel particles, as drying, devolatilization and char combustion. The basis for the incorporation of chemistry and heat transfer models is an already developed isothermal model (Rampidis et al., 2007).

As concerns proper modeling of momentum and heat exchange coefficients between solids (inert-material and fuel), little information is reported in the literature. Even in the simpler case of cold flow modeling, it is worth noticing that models which are based on the assumption of homogeneous conditions for each computational cell, fail to predict the governing physics of such processes, under certain conditions (Ge et al., 2008). However, it has been stated by Ge et al., 2008 that for industrial purposes simplified equations may be utilized under proper grid density (Ge et al., 2008; Zhang and VanderHeyden, 2001).

A key characteristic of fluidized bed combustion is low and uniform operating temperature, usually in the range of 1025 - 1200 K, in contrast to conventional pulverized coal-fired boilers, which is approximately 1600K (Nikolopoulos et al., 2011). Under PF (Pulverized Fuel) combustion conditions, the temperature distribution is far from uniform. Hot spots can be spotted with temperatures up to 2000K. In such conditions, air nitrogen is oxidized and leads to the formation of thermal-NO_x (Thomas, 1997; Hayhurst and Lawrence, 1996). A local increase of just 100K can lead to a doubling of the local thermal NO_x formation rate (Nikolopoulos et al., 2011). Nonetheless, under fluidized bed combustion conditions (low and uniform temperature), the formation of thermal-NO_x is minimized which

results in low NO_x emissions, as nitric oxides are formed almost entirely from fuel nitrogen (Hayhurst and Lawrence, 1996; Armesto et al., 2003; Thomas, 1997).

However, low combustion temperature enhances the formation of nitrous oxide (N_2O), emissions of which range from 15 to 200 ppm (Chen et al., 2001; Wójtowicz et al., 1993; Mann et al., 1992) in comparison to lower levels observed in pulverized coal combustion boilers (<20ppm Chen et al., 2001; Wójtowicz et al., 1993; Mann et al., 1992; Thomas, 1997; Blair et al., 1977). Nitrous oxide (N_2O) is known to be involved in both the greenhouse effect and the depletion of the ozone layer (Wójtowicz et al., 1993). CFD modeling offers a reliable way of investigating the chemical mechanisms that govern the formation of nitrogen oxides and control the final NO/N_2O emissions. Prediction of gaseous emissions from a CFB plant can be achieved with the assistance of CFD modeling, which may be used for the design optimization of industrial scale units.

This chapter is divided in two sections: a) CFD modeling of combustion mechanisms; b) NO_x and N_2O decoupled simulation. In the first section, full 3-D simulation of the combusting flow inside a 1.2 MW_{th} CFBC is performed, in order to describe in a more precise and detailed way the induced flow and heat transfer effects in the CFB riser. In the second section a decoupled NO_x / N_2O model is applied using the solution of the combustion model as input and NO_x / N_2O emissions are investigated.

Reaction kinetics are essential for the incorporation of reactions in the model. A review in literature concerning reaction rates is also carried out, in order to conclude to a chemical reaction network which reflects better the most important reactions taking place in a fluidized bed.

5.1 Combusting flow simulation of a 1.2 MW_{th} CFBC

As industrial Circulating Fluidized bed Combustors (CFBCs) tend to be scaled up, numerous design and operating problems emerge. At the same time uncertainties which concern hydrodynamics, combustion and pollutants formation mechanisms, come in to sight. Along with experience, CFD analysis can play a crucial role providing further insight on the complex multiphase combusting flow of CFBCs. This section aims to present a methodology for CFBCs comprehensive modeling, taking into consideration the coupling of hydrodynamics – heat transfer – chemical phenomena that take place in the bed.

Computational cost is an important drawback of CFD modeling of CFBC. In previous chapters, it was demonstrated that the computational cost is high even for CFD simulation of the isothermal flow in a CFB riser. The addition of combustion and pollutants formation mechanisms in such simulations severely increases both the complexity and the computational cost of such models. Therefore, a combination of acceptable accuracy with high computational efficiency is an objective.

For this purpose, simple combustion mechanisms are integrated in an isothermal model and applied for the simulation of a 1.2 MW_{th} pilot plant. In this comprehensive model gas, inert-material and fuel are taken into consideration, as three discrete, pure Eulerian phases, as it can be seen in Figure 5.1. Major gaseous chemical components such as O_2, CO_2. H_2O, N_2, volatiles, CO, CH_4, H_2 are defined for combustion simulation and HCN for NO_x / N_2O decoupled simulation. Species are also defined within the fuel Eulerian phase i.e ash, water, volatiles and char.

It is worth mentioning that the commercial software (Fluent® V6.4) used in this work is not equipped with combusting or reacting flow sub –models under the TFM pure Eulerian frame. Therefore, the reaction rates of the involved reactions are coded and incorporated in Fluent® platform through proper UDFs.

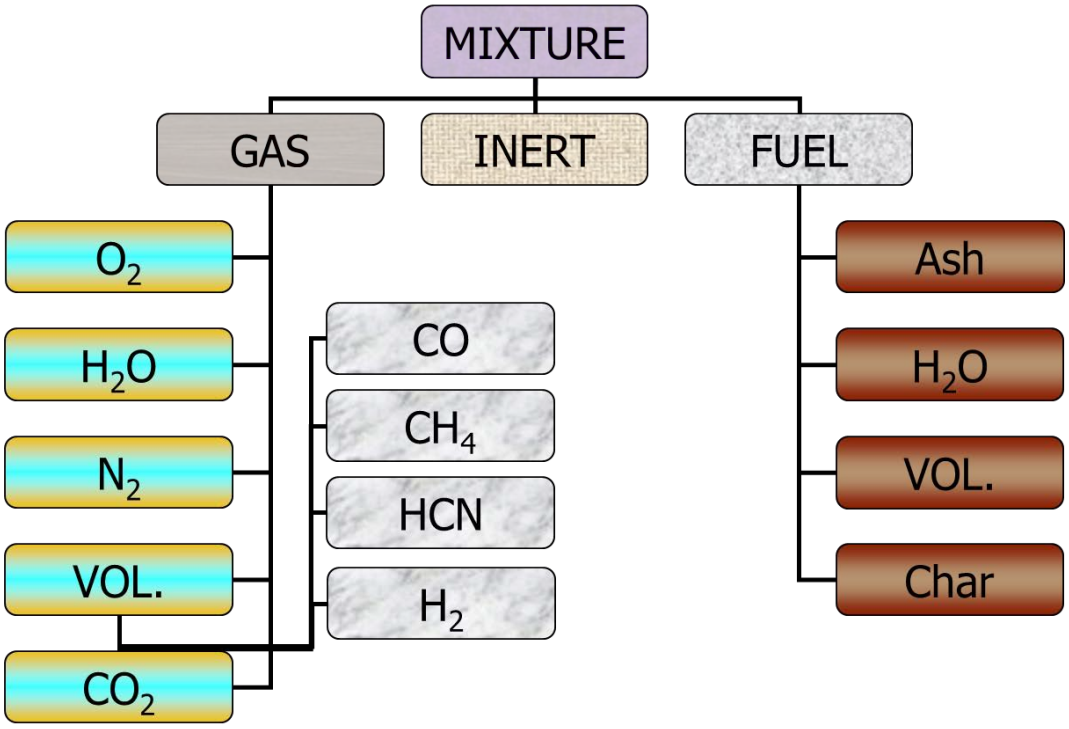

Figure 5.1 Eulerian phases and species incorporated in the CFD model of CFBC

5.1.1 Unit Description and Combustion simulation

In this chapter the 1.2MW_{th} pilot plant examined in chapter 4 is simulated. However, in chapter 4, an experiment conducted under isothermal conditions was simulated, while in this chapter the typical operation of the CFBC is considered. This unit is described in Leithner et al., 1993. The installation has 9.5 m height and 0.4 m^2 mean cross section (Figure 4.1). The combustion chamber of the rig consists of two sections. The lower part (the furnace hopper) is totally refractory lined. Three out of the four freeboard walls are refractory lined. The temperature of the one that is not refractory lined is 610 K. This temperature refers to the outer surface of the tubes that is facing the bed. Combustion air is fed as primary air through the distributor plate, while additional primary air is fed into the bottom region of the furnace hopper with the fuel and the recirculated bed material. Secondary air is fed through five inlets along the height of the combustion chamber. The ratio of primary to secondary aeration is 86% to 14%. The computational grid consists of 5,724 hexahedral, structured and uniform cells, with a mesh resolution of 9 cm distance per computational cell. The returning system has been excluded from the simulation for simplicity.

Particle Size Distribution introduction for fuel phase in the Eulerian approach is not easily feasible in terms of computational cost. Therefore, fuel particles were considered and modeled as mono - sized, simplification which is expected to have an impact on the most precise description of the induced flow field and on heterogeneous reactions that are affected by particle surface. The shrinking core model is adopted for the combustion of char. According to this model, which is adopted by many authors investigating fluidized bed simulation cases (Goel et al., 1996[b]; Desroches-Ducarne et al., 1998; Gungor and Eskin, 2008[b]; Kilpinen et al., 2002). It is assumed that during char combustion the particle diameter decreases. The fuel which was used for the experiments is Rhenish lignite. Proximate analysis conducted by (Leithner et al., 1993) is presented in Table 5.1. It is worth mentioning that the sampling ports for the gas concentration measurements are located at four levels along the height of the riser (at 1.15, 2.15, 5.2 and 8.3 m respectively). The air fuel ratio (lambda) is

1.15 while the fuel enters the riser with a flow rate of 0.14 kg/s at a temperature of 373 K. The combustion air in this unit is introduced through the distributer and the secondary air inlets. The respective flows are depicted in table 5.2.

Proximate Analysis		Ultimate Analysis	
moisture	57.00w%	C	27.1
volatiles	21.63w%	H	1.92
char	19.07w%	O	11.18
ash	2.30w%	N	0.33
mean fuel diameter	1500μm	S	0.17
Heating value (a.r.)	8560 MJ/Kg	ash	2.3
Density (a.r.)	2400 kg/m^3	Water	57

Table 5.1 Rhenish lignite properties

Inlet	Volume flow [m^3/h]	Port Height (z)
Distributer	828 @ 501K	0
Solid (inert – material and fuel) feed port	202 @ 501K	0.7
Secondary air 1	199 @ 501K	0.5
Ignition burner	121 @ 501K	2.15
Secondary air 2	32 @ 501K	2.8
Secondary air 3	34 @ 501K	5.6
Secondary air 4	36 @ 501K	7.6

Table 5.2 Air staging

As far hydrodynamics are concerned, the model presented in chapter 4 is used with the adoption of the conventional drag scheme since, as discussed in section 3.4, the adoption of the advanced EMMS scheme is not straightforward in the case of combusting flows. Moreover, the equations 3.52 to 3.57 are used for the heat transfer and reactions mechanisms simulation.

5.1.2 Results and discussion

A set of 25 partial differential equations governing the phenomenon, is solved. The prescribed set of equations, presented a very stiff numerical behavior. Therefore an efficient coupling among phases is found crucial in terms of numerical stability. In general, the comprehensive combustion model proved to be much more computational expensive than the isothermal flow model, but certainly not prohibitive for application in pilot scale CFBC units.

The flow field inside the CFB riser was initialized from the solution of the corresponding isothermal case, in order to reduce the computational cost for reaching solids inventory and temperature stabilization. Unfortunately, the quantity of inert material in the riser started to decrease rapidly, moving away from the equilibrium state. Reaching equilibrium again was proved to be time consuming.

The numerical methodology is validated with experimental data form Leithner et al., 1993. In the experimental campaign, mean CO_2 and O_2 concentration were measured in the four different heights mentioned above. These measurements, along with the numerical predictions for these species profiles along the height of the combustor, averaged at each height, are illustrated in Figure 5.2 and Figure 5.3.

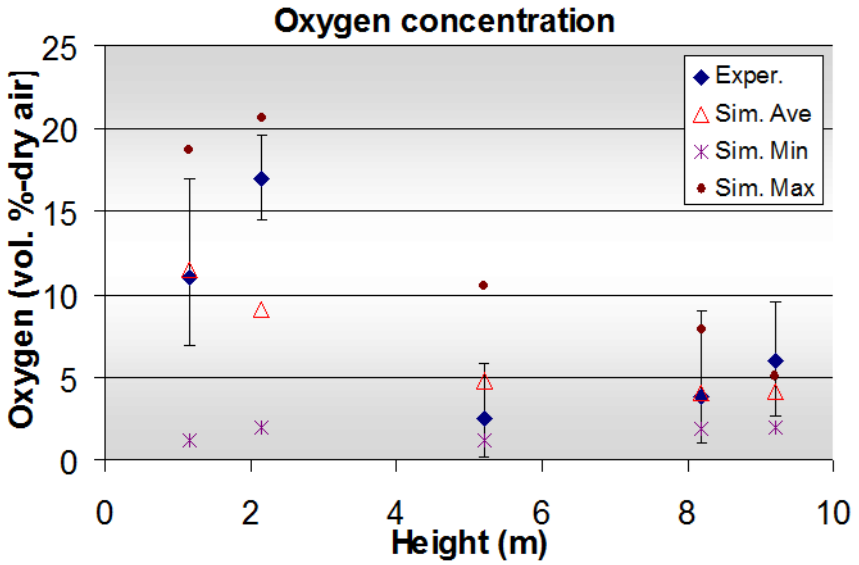

Figure 5.2 Time averaged volumetric (% dry) O_2 concentration along the bed (simulated and experimental values).

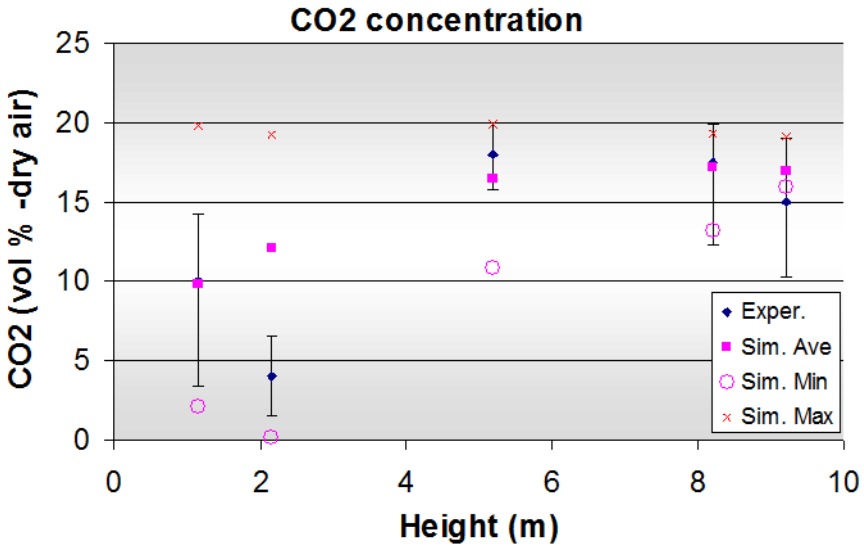

Figure 5.3 Time averaged volumetric (% dry) CO_2 concentration along the bed (simulated and experimental values).

The minimum, maximum and mean experimental values are presented. In each height there were 9 available experimental measurements in different locations, across each slice. An exception is the measurements conducted for the height of 2.15 meters where only two measurements are available. Unfortunately it is not clear by the report of Leithner et al., 1993, at which exact point of each slice (X,Y coordinates) these measurements were conducted. Figure 5.2 and Figure 5.3 depict that the agreement with the experimental data is very good, except for the predictions for the height of 2.15. Concerning this cross-section depicted in

Figure 5.4, the numerical approach presented in this study predicts O_2 and CO_2 concentrations with values close to the experimental data at certain regions of this area.

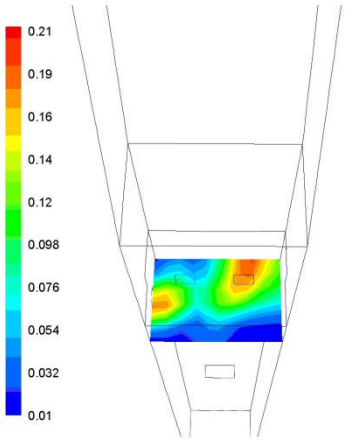

Figure 5.4 Time Averaged dry volumetric (%) concentration of O_2 for height 2.15m.

Nevertheless, it should be noted that for this height, the area weighted averaging of these quantities disagree with the corresponding experimental mean value. Nonetheless, the experimental measurements that were used for deriving the mean value of the abovementioned height are only two. The experimentally observed increase of mean oxygen concentration from Z=1.1m to Z=2.15m, should be further investigated, since there is no secondary air opening placed between these two cross-sections. Therefore an increase of oxygen concentration between these two cross sections is highly unlikely to occur since all reactions involved in lignite combustion do not produce oxygen. In this light, it is believed that either the two experimental values are not representative for this height or the two aforementioned experimental measurements were not properly conducted.

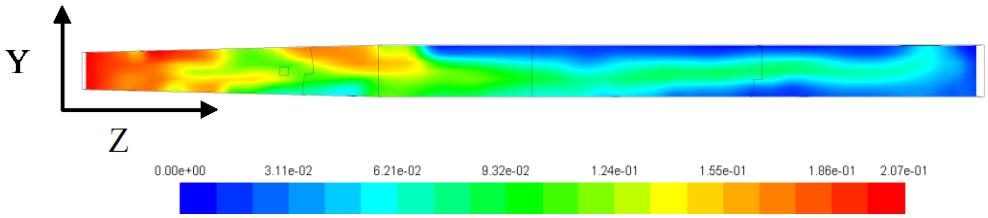

Figure 5.5 Time Averaged dry volumetric (%) concentration of O_2 for X=0.405m.

In general the developed model predicts that O_2 is consumed faster close to walls where fuel concentration is higher (in the annulus region), than in the core region of the bed (Figure 5.5). Additionally in the core region O_2 values are generally higher, which is consistent with literature (Zhao et al., 1997).

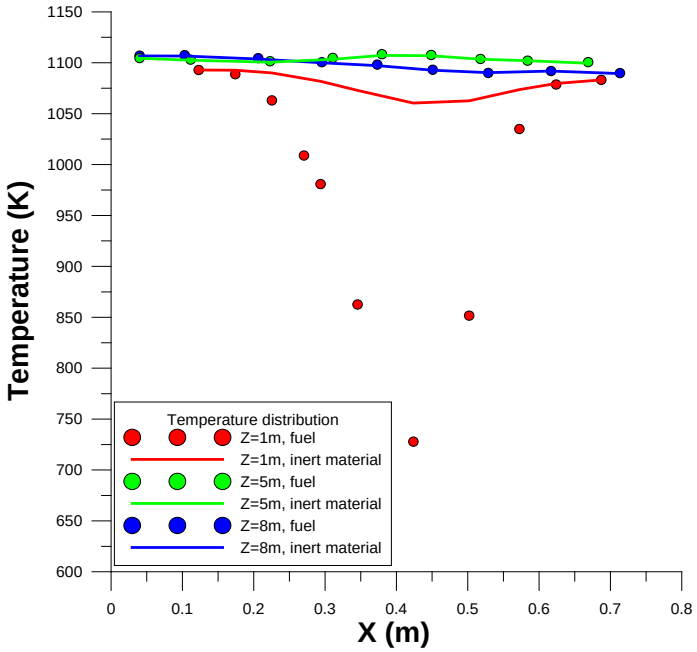

Figure 5.6 Temperature profiles along X (Y=0.27) axis,
for inert-material and fuel for different heights.

The mean temperature inside the riser is accurately predicted. A mean value of 1095 K is predicted, while the experimental data report 1100 K (Leithner et al., 1993). The predicted temperature field clearly shows uniformity. Gas, inert-material and fuel phase temperature values are very close to each other, indicating the efficient heat transfer in the bed. Figure 5.6 presents temperature profiles along the height of the bed for inert and fuel phases. Fuel phase generally is found to have a slightly higher temperature than the other phases at 5K maximum, in general. Nonetheless, at height Z=1m where the fuel enters the bed, there is a temperature difference between fuel and inert phase which takes a maximum value of 350K. This is expected, since the fuel at that point has just entered the reactor and has high moisture content (57%). Additionally near the riser exit a temperature difference of 80K is predicted, which is attributed to further local char combustion and results in fuel temperature increase. The increased char combustion is caused by the mixing of oxygen rich core region gasses with the fuel rich annulus region solids that takes place in the exit area. At the same time, inert material at this height of the riser has very low volume fraction which leads to a decreased heat transfer coefficient and high temperature difference with the fuel phase. The considerable reaction rate of char combustion at the exit pipe is also verified experimentally (Leithner et al., 1993).

5.2 NO_x – N_2O CFD modeling

In this section, a 3-D CFD model for the formation of NO_x and N_2O is applied to the combustion field of the 1.2 MW_{th} CFBC, and its results are compared with experimental data. In order to minimize the computational cost, NO_x modeling is decoupled from combustion modeling. NO_x decoupled method has been successfully incorporated in PF modeling, reproducing accurate results. In this section, a first approach to the incorporation of NO_x decoupled method in CFBC modeling is tested. However, a decoupled approach requires the simulation of the combusting flow prior to NO_x modeling. For this reason, the combusting flow of the 1.2 MW_{th} simulated in section 5.1 is used.

Reaction kinetics, retrieved from literature, are used in the numerical model. Literature is reviewed focusing on reaction rates, in order to conclude to a network of chemical reactions which efficiently reproduce NO_x and N_2O formation and destruction mechanisms.

5.2.1 Investigation of NO_x / N_2O formation-destruction mechanisms

Combustion of coal is separated into two stages, the initial stage of devolatilization, and the subsequent burning of the char (Hayhurst and Lawrence, 1996). During devolatilization, hydrocarbon species (C_xH_y), hydrogen (H_2), water vapor (H_2O), carbon monoxide, carbon dioxide (CO, CO_2) and tars are released, while the ring structures containing nitrogen decompose, and as a result, nitrogen is released in the form of HCN, NH_3, N_2 and tar-bounded nitrogen (Blair et al., 1977; Nelson et al., 1992).

Devolatilization takes place on the lower parts of the bed, particularly around fuel insertion area. Fuel particles, as soon as they enter the combustion chamber, are heated with high rates by the much hotter particles of the bed, due to good mixing conditions and temperature uniformity. Devolatilization is followed by the stage of char combustion, which lasts much longer and concern the burning of the residual fuel.

Fuel nitrogen follows the same path. One part is released in volatiles, while the rest remains in the char. As proposed by Goel et al., 1996[a], the distribution of the initial fuel nitrogen (fuel-N) in volatile nitrogen (volatile-N) and char nitrogen (char-N) strongly influences the final emissions of nitrogen oxides. This distribution depends greatly on fuel type. According to Wójtowicz et al., 1993, for coal combustion, approximately 60% of the initial fuel-N remains in the char. Due to lack of experimental data for the ratio of volatile-N to char-N of the fuel investigated, it was assumed that 43% of the initial N is released in volatiles, a value which is obtained from the work of Fine et al., 1974, who examined this ratio as a function of operating temperature. This value is also in line with the work of Wójtowicz et al., 1993. Likewise, the ratio of hydrogen cyanide (HCN) to ammonia (NH_3) released in volatiles is of great importance (Kilpinen et al., 2002), as concerns the final NO/N_2O emissions because these species are considered precursors of nitrogen oxides. In modeling studies, a simplistic empirical methodology is used for setting this ratio that defines the N – products of devolatilization. This simplification depends on the fuel. For example, species volatile ratio of HCN : NH_3 for bituminous coal is usually 9 to 1 (Winter et al., 1996), while for biomass, 1 to 9 (Liu and Gibbs, 2002). Hayhurst and Lawrence, 1996 propose that during coal combustion, the main product of devolatilization is hydrogen cyanide (HCN). In this work, it was assumed that volatile nitrogen appeared only in the form of hydrogen cyanide, because the ammonia concentration observed during the experiments was too low (Leithner et al., 1993).

Nitrogen oxides are formed during both char and volatiles combustion. All reactions taking place inside the bed and concern the nitrogen path, are summarized in Figure 5.7 and consist of four main mechanisms:

- ✓ NO/N_2O formation via homogenous reactions
- ✓ NO/N_2O destruction via homogenous reactions
- ✓ NO/N_2O formation via heterogeneous reactions
- ✓ NO/N_2O destruction via heterogeneous reactions

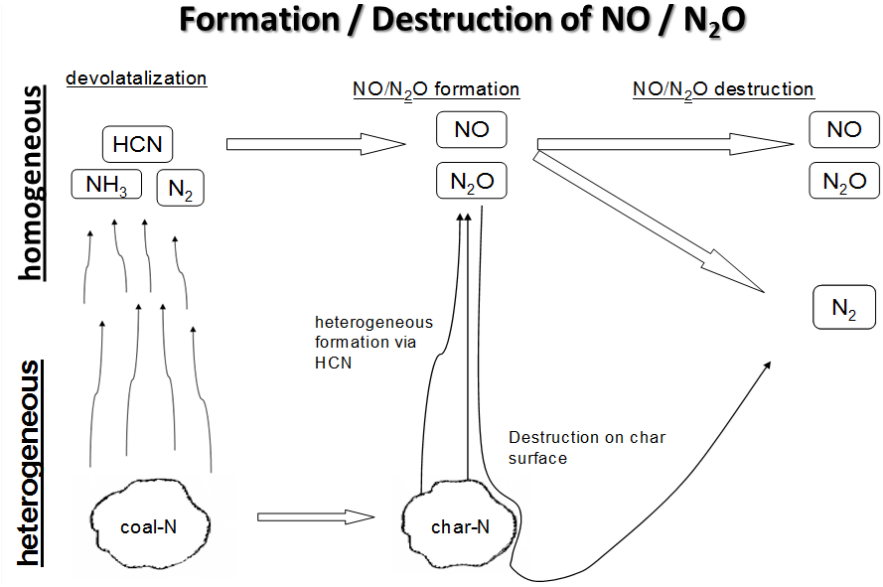

Figure 5.7 Mechanism of NO / N_2O formation in fluidized bed combustion of coal.

5.2.2 Reaction Network

In Table 5.3 the main reactions of the scheme shown in Figure 5.7 are presented along with reaction rates, constants and model parameters. Two different reaction networks are tested, simply entitled model 1 and model 2. The differentiations between the two models will be discussed latter in this section.

For the fuel investigated, in a dry ash free base, the Nitrogen to carbon molar ratio (*N/C*) was measured equal to 0.84584% for the fuel tested in the 1.2 MW_{th} CFBC plant. Nitrogen fraction released with volatiles was not experimentally measured. This important parameter is calculated through the work of Fine et al., 1974 that experimentally measured, under pyrolysis conditions, this fraction, for a wide range of fossil fuels, and they concluded that this fraction is a function of operating temperature. Based on this work and taking into account the operating temperature of the CFBC unit numerically investigated (822 ^{o}C), the fraction of Nitrogen released with volatiles is set equal to 43% of the initial Nitrogen content of the raw fuel. The rest of fuel Nitrogen is considered as char bounded. However, this nitrogen fraction can undergo two different reaction paths as well. The fraction of char bounded Nitrogen directly oxidized to NO_x and N_2O is estimated, and not measured, by Leithner et al., 1993 to be equal to 30%. The rest (70%), during char combustion, is released in the gas phase as HCN.

In order to calculate the rate of a lot of heterogeneous reactions, in the reactions network, the number of fuel particles (N_p) should be calculated, in order to calculate the effective surface area ($N_p \pi d^2$). In a Lagrangian frame, this measure is easily calculated because particles or parcels of particles are tracked. However, in an Eulerian frame, as the one used in this work in order to simulate particulates, N_p cannot be straightforwardly calculated. Usually, the effective surface area is calculated as the ratio of the volume of the Eulerian phase in each cell to the volume of a single particle based on its initial diameter (d_o). However, this treatment over predicts the surface area. Therefore, an alternative approach is adopted. The number of particles is calculated for the diameter of the Eulerian phase (d_o), but the active surface area is calculated using d_c.

$$N_p \pi d_c^2 = \frac{6 \varepsilon_f V_{cell}}{d_o^3} d_c^2 \qquad \text{Eq. 5.1}$$

No.	Reaction	Parameters	Rate Expression (mol/m^3_{gas}*s)	Reference	Usage	
					Model 1	Model 2
			Homogenous formation			
I	$HCN + \frac{1}{2}O_2 \rightarrow CNO + H$	$k^{I} = 2{,}14 \cdot 10^{5} \cdot \exp(-10000/T)$	$k^{I} \cdot C_{O_2} \cdot C_{HCN}$	¥, £, ç	Yes	Yes
II	$CNO + \frac{1}{2}O_2 \rightarrow NO + CO$	$\frac{k_2^{II}}{k_1^{II}} = 1{,}02 \cdot 10^{9} \cdot \exp(-25460/T)$	$k^{I} \cdot C_{O_2} \cdot C_{HCN} \cdot (\frac{k_1^{II}}{k_1^{II} + k_2^{II} \cdot C_{NO}})$	¥, £, ç	Yes	Yes
III	$CNO + NO \rightarrow N_2O + CO$		$k^{I} \cdot C_{O_2} \cdot C_{HCN} \cdot (\frac{k_2^{II} \cdot C_{NO}}{k_1^{II} + k_2^{II} \cdot C_{NO}})$	¥, £, ç	Yes	Yes
IV	$NH_3 + \frac{5}{4}O_2 \rightarrow NO + \frac{3}{2}H_2O$	$k^{IV} = 2{,}73 \cdot 10^{14} \cdot \exp(-38160/T)$	$k^{IV} \cdot C_{NH_3} \cdot C_{O_2}$	£, ç, ß	No	No
			Homogenous destruction			
V	$NH_3 + 3/4\,O_2 \rightarrow 1/2\,N_2 + 3/2\,H_2O$	$k^{V} = 3{,}38 \cdot 10^{7} \cdot \exp(-10000/T)$	$k^{V} \cdot \frac{C_{NH_3} \cdot C_{O_2}}{C_{O_2} + 0.054}$	¥, £	No	No
VI	$NO + NH_3 + \frac{1}{2}O_2 \rightarrow N_2 + \frac{3}{2}H_2O$	$k^{VI} = 1{,}11 \cdot 10^{12} \cdot \exp(-29400/T)$	$k^{VI} \cdot (C_{O_2} \cdot C_{NH_3} \cdot C_{NO})^{0,5}$	¥ , £, ç, Б	No	No
VII	$N_2O + \frac{1}{2}O_2 \rightarrow N_2 + O_2$	$k^{VII} = 1{,}75 \cdot 10^{8} \cdot \exp(-23800/T)$	$k^{VII} \cdot C_{N_2O}$	Þ	Yes	No
		$k^{VII}\ 5{,}7 \cdot 10^{9} \cdot \exp(-27000/T)$	$k^{VII} \cdot C_{N_2O}$	ç	No	Yes
VIII	$N_2O + CO \rightarrow 2N_2 + CO_2$	$k^{VIII} = 2{,}51 \cdot 10^{11} \cdot \exp(-23180/T)$	$k^{VIII} \cdot C_{N_2O} \cdot C_{CO}$	Þ	No	No
		$k^{VIII} = 50{,}1 \cdot \exp(-5292/T)$	$k^{VIII} \cdot C_{N_2O} \cdot C_{CO}$	£	No	Yes

No.	Reaction	Parameters	Rate Expression (mol/m^3_{gas}*s)	Reference	Usage	
					Model 1	Model 2
			Heterogeneous formation			
IX	$\text{char} - \text{N} + \frac{1}{2}\text{O}_2 \rightarrow (-\text{CNO})$				Yes	Yes
X	$(-\text{CNO}) + \frac{1}{2}\text{O}_2 \rightarrow \text{NO} + (-\text{CO})$	$\frac{k_2^X}{k_1^X} = 4{,}86 \cdot 10^{-5} \cdot \exp(14999/T)$	$f_c \frac{N}{C} \cdot R_C \cdot (\frac{k_1^X}{k_1^X + k_2^X \cdot C_{NO}})$	¿	Yes	Yes
XI	$(-\text{CNO}) + \text{NO} \rightarrow \text{N}_2\text{O} + (-\text{CO})$		$f_c \frac{N}{C} \cdot R_C \cdot (\frac{k_2^X \cdot C_{NO}}{k_1^X + k_2^X \cdot C_{NO}})$	¿	Yes	Yes
			Heterogeneous destruction			
XII	$\text{NO} + (-\text{C}) \rightarrow \frac{1}{2}\text{N}_2 + \text{CO}$	$k_a^{XII} = 1{,}3 \cdot 10^5 \cdot \exp(17111/T)$	$k_a^{XII} \cdot N_p \cdot \pi \cdot d_c^2 \cdot C_{NO}$ (mol/s)	£	Yes	No
		$k_b^{XII} = 1{,}17 \cdot 10^8 \cdot \exp(-13221/T)$	$k_b^{XII} \cdot C_{NO}$ (mol/m^3-fuel*s)	¿	No	Yes
XIII	$NO + (-CO) \rightarrow \frac{1}{2} N_2 + CO_2$	$k^{XIII} = 9{,}6 \cdot 10^4 \cdot \exp(-10000/T)$	$k^{XIII} \cdot C_{NO} \cdot C_{CO}$	¥	Yes	Yes
XIV	$\text{N}_2\text{O} + (-\text{C}) \rightarrow \text{N}_2 + \text{CO}$	$k^{XIV} = 2{,}9 \cdot 10^9 \cdot \exp(-16983/T)$	$k^{XIV} \cdot N_p \cdot \pi \cdot d_c^2 \cdot C_{N_2O}$ (mol/s)	£	No	No
			$k^{XIV} \cdot C_{N_2O}$ (mol/m^3-fuel*s)	¥	No	Yes

No.	Reaction	Parameters	Rate Expression (mol/m^3_{gas}*s)	Reference	Usage	
					Model 1	Model 2
			Thermal NO_x			
XV	$N_2 + O_2 \rightarrow 2NO$		based on Ω	ø	Yes	Yes
			Fuel nitrogen			
XVI	$N - volatiles \xrightarrow{devol} HCN$		R_{vol}		Yes	Yes
XVII	$N - char \rightarrow HCN$		$(1 - f_c)\frac{N}{C} \cdot R_c$		Yes	No

Table 5.3 Reaction Network for the modeling of NO and N_2O formation from coal combustion

Concentrations in Table 5.3 are in mol per cubic meter of gas phase and the universal gas constant (R_u) is KJ[mol K]$^{-1}$.

References for Table 5.3:

- ¥ (Desroches-Ducarne et al., 1998)
- £ (Gungor and Eskin, 2008[b])
- ¿ (Kilpinen et al., 2002)
- Þ (Chen et al., 2001)
- ß (Afacan et al., 2007)
- ø (FLUENT, 2006)
- ç (Liu and Gibbs, 2002)
- Б (Jensen et al., 1995)
- Ω Zeldovich mechanism (FLUENT, 2010)

Products of fuel devolatilization, hydrogen cyanide (HCN) and ammonia (NH_3) play an important role acting as gas-phase precursors for both NO and N_2O and these homogeneous reaction pathways have been extensively studied. HCN is oxidized to form an intermediate species, NCO, which can yield either NO or N_2O ((Kilpinen and Hupa, 1991) reactions I, II, III). As far as this scheme is concerned, authors (Desroches-Ducarne et al., 1998; Kilpinen et al., 2002 as well as Liu and Gibbs, 2002) have reached to an agreement about the reaction rates.

Nitric oxide (NO) is also formed by the oxidation of NH_3 (reaction IV), while hardly any N_2O is formed from ammonia-based fuel nitrogen radicals (NH_i). This conclusion was made by experiments carried out by Kilpinen and Hupa, 1991 and Kramlich et al., 1989 who injected ammonia and hydrogen cyanide in fuel-lean flue gas from burning coal and natural gas respectively. The researchers concluded that N_2O was preferentially formed from cyanide species, whereas very little N_2O was released during NH_3 injection.

For reactions IV, V, VI containing ammonia, many researchers (Desroches-Ducarne et al., 1998; Liu and Gibbs, 2002; Afacan et al., 2007; Jensen et al., 1995) agree on reaction rate expressions. Most authors use the expressions derived from the work of Jensen et al., 1995, with slight modifications. It should be underlined that reactions IV and V are catalyzed by the presence of char particles and inert bed material.

The homogenous reactions concerning the reduction of nitric oxide are not important under fluidized bed operating conditions, as it is extracted from previous works (Wójtowicz et al., 1993; Desroches-Ducarne et al., 1998; Liu and Gibbs, 2002; Jensen et al., 1995). The only reaction mentioned by Jensen et al., 1995 and is adopted by Desroches-Ducarne et al., 1998; Gungor and Eskin, 2008[b] and Liu and Gibbs, 2002, is the homogeneous destruction of NO in the presence of ammonia and oxygen (reaction VI).

The homogenous reduction of N_2O is temperature dependent (Hayhurst and Lawrence, 1996). At low combustion temperatures (~1000-1200 K), i.e. typical fluidized bed operating conditions, the homogenous destruction mechanisms are not drastic. On the contrary, for temperatures higher than 1200 K, N_2O is rapidly decomposing (immediately after its generation) by O, OH, H radicals. The most important reactions concerning the homogenous destruction of N_2O are presented in Table 5.3 (reactions VII, VIII).

Reaction rates for homogenous N_2O decomposition (reaction VII) were found in the work of Chen et al., 2001; Liu and Gibbs, 2002; Gungor and Eskin, 2008[b] and Mukadi et al., 2000. The reaction rate expressions suggested by the authors are all in the same order of magnitude, with the only exception of the expression proposed by Gungor and Eskin, 2008[b]. The reaction rate proposed by Gungor and Eskin, 2008[b] was found to be higher than the others by 4 orders of magnitude. Nitrous oxide reduction after reaction with carbon monoxide (CO) was reported in the work of Mukadi et al., 2000; Chen et al., 2001 and Gungor and Eskin, 2008[b]).

Plenty of research has been carried out on heterogeneous reactions, due to the complexity of their nature. In fluidized bed combustion, due to the presence of solid inert and fuel particles, heterogeneous reactions are of utmost importance to the formation and destruction of nitrogen oxides.

According to literature, nitrogen oxides are heterogeneously formed following two different paths: a) char-N oxidation and b) oxidation of HCN (Reaction XVII).

- As concerns path a), it is proposed by Chen et al., 2001; Goel et al., 1996[a, b], and adopted by other researchers (Kilpinen et al., 2002; Liu and Gibbs, 2002) that oxygen breaks the nitrogen containing aromatic rings bound to the char surface and then reacts with the free nitrogen atoms to form an active intermediate, such as –CNO, still bounded on the char surface. This active intermediate decomposes to form NO, or reacts with NO to form N_2O (reactions IX, X, XI). This theory which was proposed for the heterogeneous formation

of nitrogen oxides by the oxidation of the active intermediate –CNO is similar to the homogenous destruction of gaseous intermediate CNO. The reaction rate adopted in this work was developed by Kilpinen et al., 2002 who estimated new expressions for the constants and compared them to the previous ones given by Goel et al., 1996[a, b]. Tullin et al., 1993 proposed that the nitrogen (N) and carbon are oxidized at relative rates that are in proportion to the nitrogen/carbon atomic ratio (N/C) in the char. For this reason, the rate of heterogeneous formation of nitrogen oxides is proportional to the char combustion rate, as shown in Table 5.3.

- As concerns path b), it is observed that HCN is also released during char combustion (Kilpinen and Hupa, 1991; Winter et al., 1996). This process is called slow or secondary devolatilization. Hydrogen cyanide can then undergo homogenous oxidation to form either NO or N_2O as discussed above. However, in their work, Goel et al., 1996[b] showed, after series of experiments, that cyanide species are not released in significant amounts during char combustion and that the formation of nitric and nitrous oxides derive almost entirely from the oxidation of char-N. The fuel which they used for the experiments was Newland coal. The contribution of HCN released during char combustion to the final NO/N_2O emissions may depend on the fuel.

In this work, 2 different models are adopted (Table 5.3). In model 1, it is assumed that 30% of char-N is oxidized directly to form NO or N_2O, as estimated by Leithner et al., 1993, while the rest is released in the form of HCN. This value was used in a previous simulation which was carried out in the frame of the experimental report (Leithner et al., 1993). In model 2, the assumption of Goel et al., 1996[b] is adopted, according to which 100% of char-N is oxidized to form NO and N_2O.

Nitric oxides can be also formed via a series of catalytic reactions on the surface of other solid particles present in the combustion chamber, except char particles. However, these reactions exceed the purpose of this work and therefore are not included in the simulation models. Heterogeneous reduction of nitrogen oxides on char surface, as authors suggest (Gulyurtlu et al., 1994; Goel et al., 1996[a]), is one of the most important reactions in a fluidized bed reactor, which in fact influences the total amount of NO_x-N_2O emissions. Bonn et al., 1995 proposed that almost 60% of the total N_2O formed in a fluidized bed is decomposed on char surface.

Reaction XII, NO reduction on char surface, describes the absorption of one molecule of nitric oxide (NO) from an active site of the char (-C) in order to form molecular nitrogen. Reaction XIV is similar with reaction XII and concerns the reduction of nitrous oxide (N_2O) on char surface. However, after thorough examination of previous works, a general disagreement in reaction rate expressions for these reactions is observed. It is suggested that the difference between rate expressions can be attributed to the different fuels which were used for the estimation of the kinetic parameters. Reaction rates for reactions XII, XIV can be found in previous works (Chen et al., 2001; Desroches-Ducarne et al., 1998; Gungor and Eskin, 2008[b]; Kilpinen et al., 2002; Liu and Gibbs, 2002; Mukadi et al., 2000).

In reaction XIII, one NO molecule binds to the surface of char forming the intermediate active compound (-NO), which reacts with the intermediate (-CO) respectively to form molecular nitrogen (N_2). Whenever NO and CO molecules are present near the surface of char, reaction XIII is catalyzed. (Jensen et al., 1995) indicate that this reaction is also catalyzed by solid particles of the bed. Reactions rate expressions for reaction XIII are found in the work of Chen et al., 2001; Desroches-Ducarne et al., 1998; Gungor and Eskin, 2008[b]; Kilpinen et al., 2002; Liu and Gibbs, 2002; Afacan et al., 2007 and Jensen et al., 1995.

As shown in Table 5.3, not all reactions are used in the two models which were tested. Specifically, reactions IV, V and VI containing ammonia (NH_3) were not included because as it was dictated from the experimental data (Leithner et al., 1993), that the main product of fuel

devolatilization was hydrogen cyanide (HCN) while ammonia (NH_3) was produced in small negligible concentrations, as mentioned before.

In Model 1, reactions VIII and XIV are not incorporated, due to the under prediction of nitrous oxide formation as it is discussed in the results section. Finally, reaction XV (thermal NO_x), is incorporated in the chemical reaction network in order to demonstrate its expected low contribution to the formation of NO_x.

5.2.3 NO_x / N_2O simulation methodology

Zero initial concentration is assumed for all five gases within the bed, except for carbon monoxide (CO). The initial concentration of CO is obtained from the solution of the combustion model, because it is a product of combustion process and therefore its formation cannot be simulated with one reaction rate. Thus, it is assumed that the amount of CO released during combustion is independent of the CO released by chemical reactions involved in the NO_x – N_2O scheme depicted in Table 5.3. In CO transport equation, the mass flux function (the convectional term) is set to zero, in order to retain the CO concentration profile of the combustion simulation. Transport equations are solved using the implicit method, with time step of $\Delta t = 10$ μs.

Diffusion coefficient (D_{iff}) is different for each gas. However, because of limited data published for the diffusion of chemical species during combustion in fluidized bed, D_{iff} is set equal to 6.8 10^{-6} m^2s^{-1} for all species solved. This approach was also adopted by Kilpinen et al., 2002. However, in this work other values for this coefficient are also tested. A value of 10^{-04}, proposed by Tullin et al., 1993 is also applied, but no difference is observed in the results. This can be attributed to the high gas velocity in the bed (approximately 5 - 15 ms^{-1} on the main z – axis). Therefore, for the species transport equation it is concluded that the convective term is dominating over the diffusion term.

As the decoupled approach is adopted, profiles of temperature (T), char combustion rate (R_c), volatile release rate (R_{vol}), char diameter (d_c) and O_2 concentration inside the bed are obtained from the solution of the combustion simulation (chapter 5.1).

5.2.4 NO_x/N_2O Results and discussion

Results of the simulation for both models against the experimental data are presented in the following figures. Figure 5.8 depicts the concentration of NO_x across the height of the bed. In this figure, the mass-weighted average, minimum and maximum of NO_x concentration are presented for every surface across the height of the bed.

Results seem to be in good agreement with the experimental data for both Models, especially near the distributor plate and the outlet. However, the transition from the second to the third point (from 2.25 to 5.2 m) does not appear as sharp as measured during the experimental procedure. This small increase which is predicted by the simulation, can be probably attributed to the addition of secondary air at the height of 5.6 m, which dilutes the flue-gas and therefore leads to the decrease of NO_x concentration. Model 2 results seem to agree better with the experimental data. Therefore, the results of Model 2 simulation will be mainly investigated in this section.

Figure 5.9 shows the role of reactions II and X in the net formation of NO. Reaction XV, formation of thermal-NO, proved to be negligible, with a maximum of 2.45E^{-19} Kmol $[m^3s]^{-1}$ and is not depicted in Figure 5.9. This result agrees well with the expected behavior since the combustion temperature is low (Chen et al., 2001).

Through thorough examination of the numerical model results, it is clear that gas-phase formation of NO from HCN (Reactions I + II) is the most important pathway on the lower section of the bed, where HCN is released in high rates during devolatilization. Devolatilization takes

place around fuel injection area. Fuel particles, after entering the combustion chamber, are instantaneously heated by the much hotter particles of the bed due to good mixing conditions and temperature uniformity.

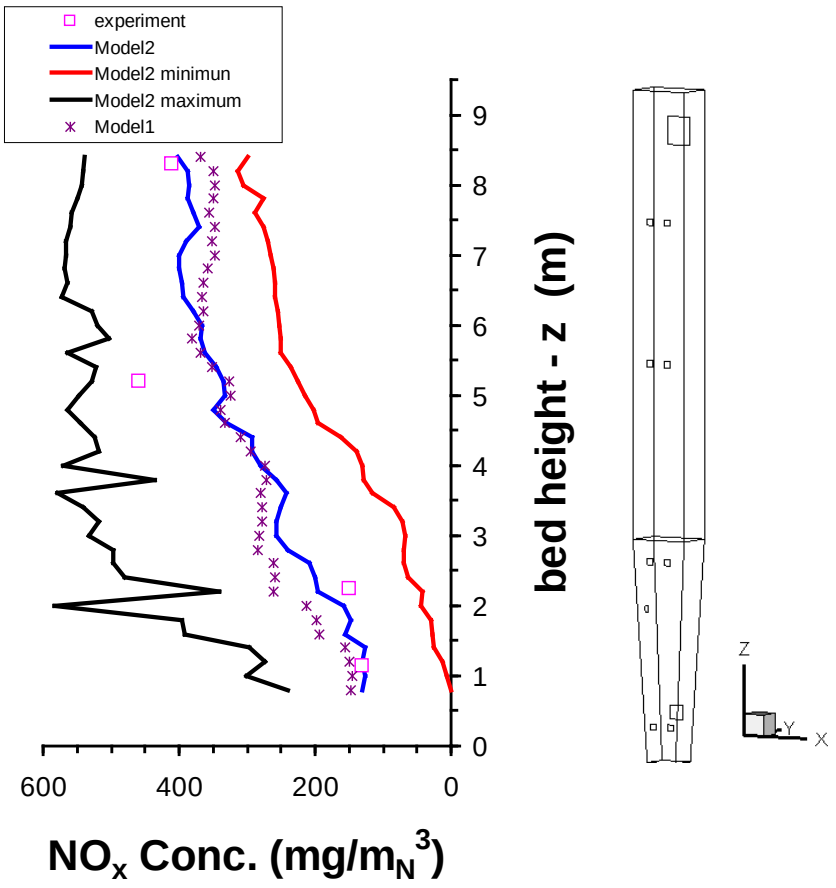

Figure 5.8 Concentration of NO_x plotted against the height of the bed

The mean concentration of HCN along the riser is shown in Figure 5.10. A spike is observed on the lower section due to large quantities of volatile-HCN, which is consumed at the upper parts. The outlet concentration of hydrogen cyanide is very small, as expected.

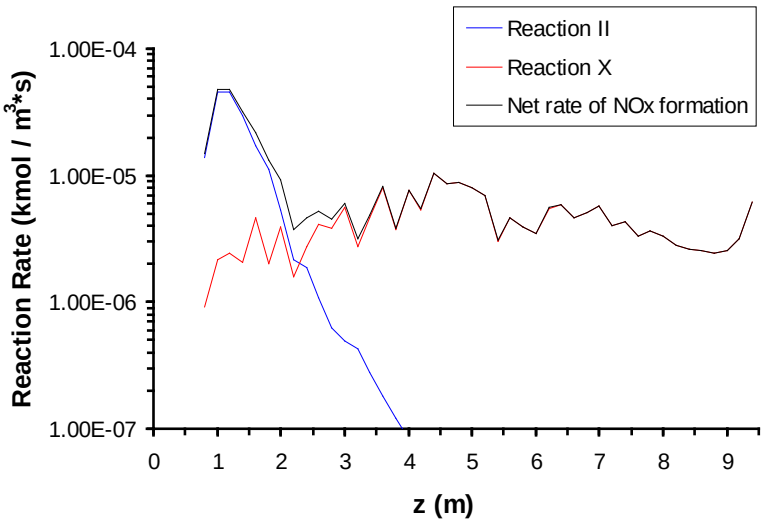

Figure 5.9 Contribution of reactions RII and RX to the NO net formation (log scale)

However, when Model 1 is adopted, very high concentration of HCN is observed on the bed outlet in combination with very low N_2O concentration. The extremely high concentration of HCN which is even greater than the one of nitrous oxide dictated that the assumption for HCN release during char combustion is not appropriate with respect to the fuel used and reaction rates available. Due to the relatively low rate at which hydrogen cyanide forms NO and N_2O (RI – RIII in Table 5.3), a large amount of HCN released from the char, does not form nitrogen oxides and therefore is transferred to the outlet of the riser.

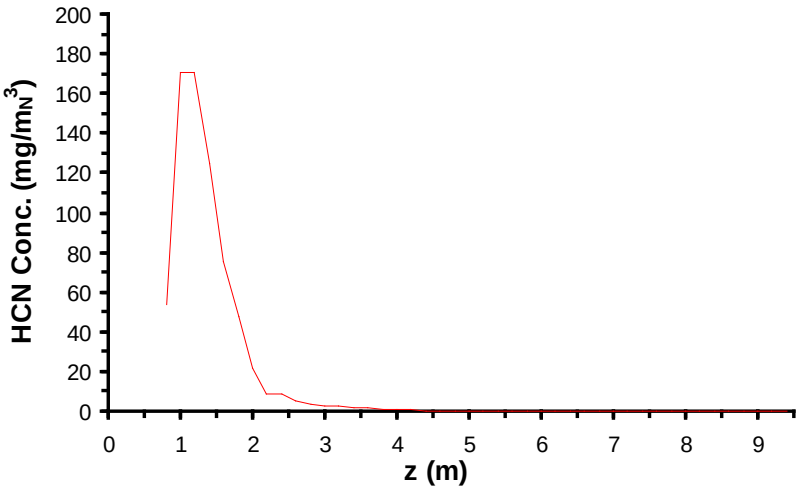

Figure 5.10 HCN concentration along reactor (Model 2)

Heterogeneous NO formation (Reaction X) has a more homogenous trend along the height of the bed (Figure 5.9). This is because the reaction rate depends on char combustion rate R_c (Table 5.3). The investigation of the combustion model results depicted the uniformity of combustion rate along the bed height. Higher R_c values were observed near the walls due to the higher concentration of inert bed material and fuel particles (fast fluidization regime). Fuel particles are evenly distributed inside the volume of the bed due to the very good mixing conditions. However, they are not in the same combustion phase, due to internal and external recirculation. Thus, at the same time, at relatively close range, a particle may have consumed 90% of char, and another particle may be on the stage of devolatilization.

Figure 5.11 shows the rates of all reactions involved in the destruction of NO_x as predicted via model 2. The rate of reaction III is not presented in Figure 5.11 because its contribution proved to be negligible when compared to the net destruction of NO_x (in the range of 10^{-10}). As it is shown in Figure 5.11, the reaction of NO with carbon monoxide complex (-CO), i.e. reaction XIII, is predicted to be the most important NO_x reduction reaction. The presence of carbon monoxide, which is a product of both combustion process and reactions II and III, at relatively high concentrations, enhances this reaction.

NO reduction on char surface (reaction XII) has a more homogenous trend along the riser. Reaction rate depends on the local concentration of fuel particles inside the bed (number of particles) and the local NO concentration. Since the reactor operates in the fast fluidization regime, large amounts of solid particles are concentrated on the lower part of the bed, while the upper part (freeboard) is more dilute.

For reactions III and XI, both of which destruct NO_x and form nitrous oxide, it is worth mentioning that the heterogeneous destruction of NO (Reaction XI) is much more drastic than the corresponding gas-phase reduction (Reaction III). The reason is that nitrous oxide, given the reaction rates available in Table 5.3, is preferentially formed via the heterogeneous mechanism (Reaction XI) rather than the homogenous mechanism (Reaction III). In order to conceive the

difference between homogenous and heterogeneous N_2O formation, in Figure 5.12 and Figure 5.13, the distribution of NO and N_2O formation from the intermediates NCO (homogenous formation) and –CNO (heterogeneous formation) respectively is presented against typical values of NO concentration in fluidized bed reactors.

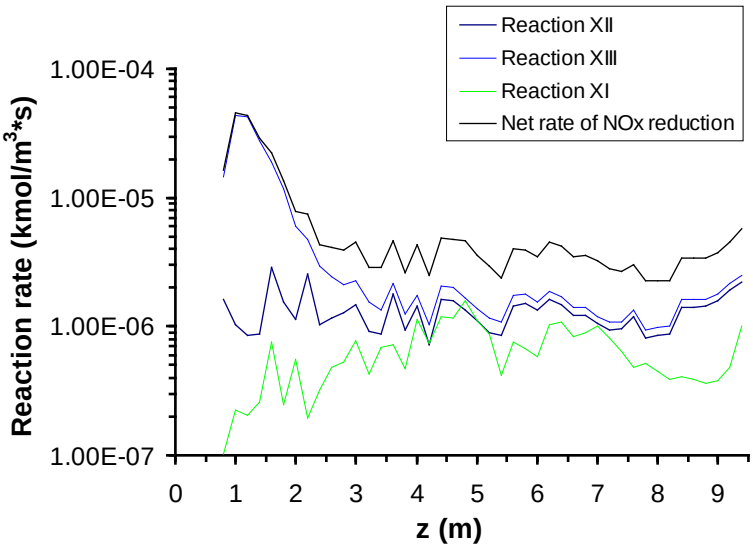

Figure 5.11 Contribution of reactions XI, XII and XIII to the net reduction of NO (log scale)

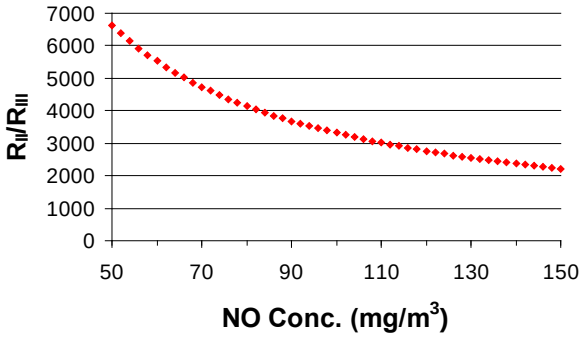

Figure 5.12 NO/N_2O mole formation from the homogenous oxidation of –CNO

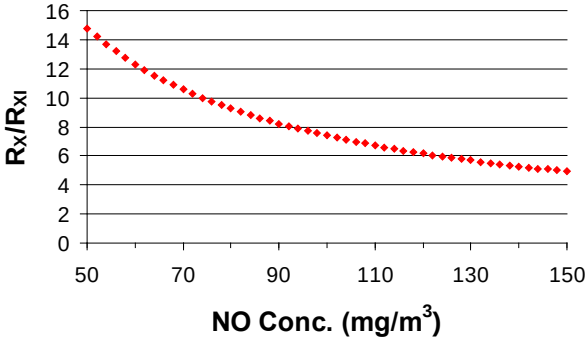

Figure 5.13 NO/N_2O mole formation from the heterogeneous oxidation of active –CNO

It is worth mentioning that for every mole of N_2O which is formed from the heterogeneous mechanism, approximately 6 to 14 moles of NO are formed, whereas for the homogenous mechanism, 4,000 NO moles are generated. Therefore, when Model 1 is adopted, 70% of char nitrogen is released as HCN during char combustion stage which then results in the low formation of nitrous oxide. On the other hand, when Model 2 is adopted, much more N_2O is produced. In this light, model 2 simulates better the NO_x / N_2O reaction network inside the bed.

Nitrous oxide, as mentioned before, is only formed via Reactions III and XI and its formation depends on the local NO concentration (Table 5.3, Figure 5.12 and Figure 5.13). In both N_2O formation reactions, one molecule of NO is required. Nitric oxide's presence is therefore obligatory for N_2O generation. In fact, (Hayhurst and Lawrence, 1996) found that the total number of moles of fuel nitrogen that contribute to the creation of nitrogen oxides is approximately constant. What really changes with temperature is the NO / N_2O ratio. Thus, for high temperatures, the mechanisms leading to the formation of nitric oxide (NO) are favored, and most of the nitrous oxide (N_2O) which is created, is rapidly decomposed. At lower temperatures, however, the path for the formation of nitrous oxide is relatively favored.

In Figure 5.14, the results of N_2O concentration using Models 1 and 2 are presented. Model 1 simulation results seem to under predict nitrous oxide formation in the fluidized bed. This is because of the assumption that HCN is released from the char, as discussed above.

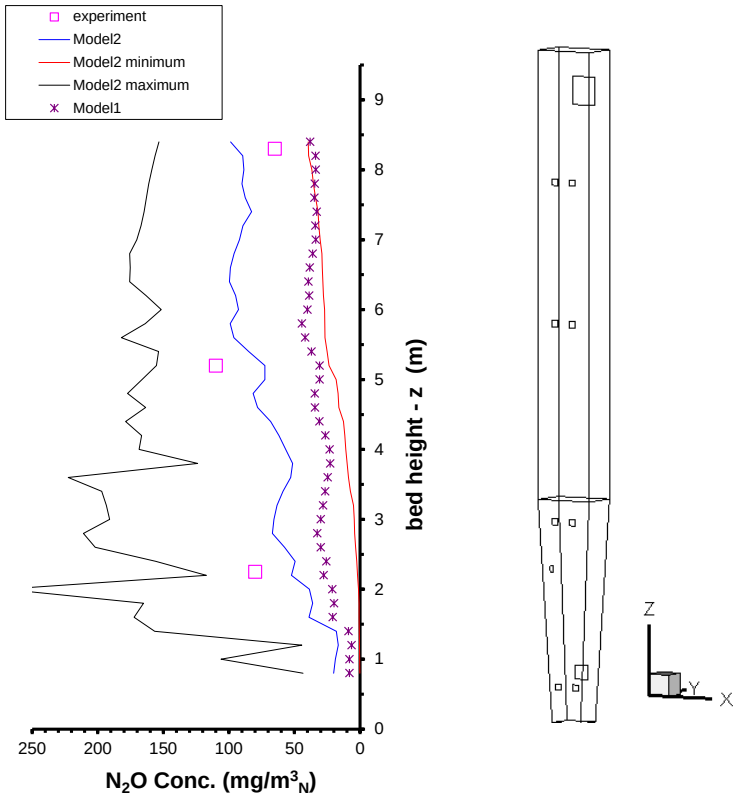

Figure 5.14 Concentration of N_2O plotted against the height of the bed.

Results of Model 2 seem to agree better with the measured data. However, the simulated values do not coincide with the experimental ones. It is worth mentioning that for the Height z=1.15 the value 350 mg per normal cubic meter was measured (Leithner et al., 1993). This value is not included in Figure 5.14 since it is considered highly unrealistic. This enormous value of N_2O on the lower section of the bed can be attributed to limited sample point measurements. NO is needed for the formation of N_2O, and NO formation rate is high on the lower section (Figure 5.9). However, NO concentration is low (Figure 5.8), due to convection phenomena induced by the high gas velocity in the bottom bed and thus N_2O formation rate is low. Moreover, Desroches-Ducarne et al., 1998 and Mukadi et al., 2000 report that N_2O concentration, in general, increases with height as CFD results and all experimental data except the one for z=1.15 indicate.

Even though, in Model 1 there is no N_2O destruction reaction incorporated, the N_2O concentration is still under predicted. On the contrary, in Model 2, three N_2O destruction reactions are incorporated (reactions VII, VIII and XIV). The rate of homogenous decomposition of N_2O (reaction VII), as shown in Table 5.3, depends only on the local concentration of nitrous oxide. The homogeneous destruction of nitrous oxide due to carbon monoxide (reaction VIII) is stronger on the lower section of the bed (Figure 5.15) due to the release of large quantities of carbon monoxide by volatile hydrocarbons combustion.

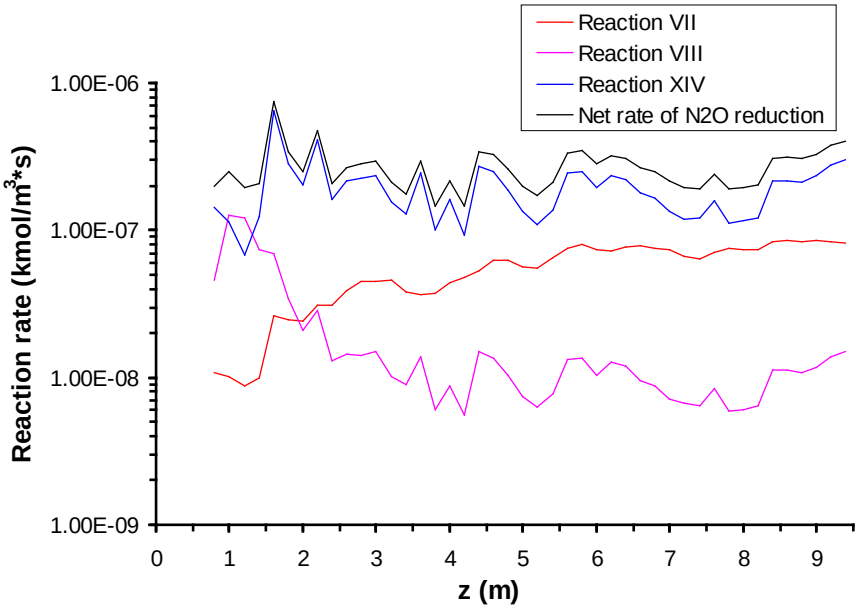

Figure 5.15 Contribution of reactions VII, VIII and XIV to the net N_2O reduction (log. Scale)

The heterogeneous destruction of N_2O on char surface (reaction XIV) is presented in literature as the most significant N_2O reduction reaction. The significance of this reaction is confirmed by the simulation (Figure 5.15). The rate of N_2O destruction on the surface of the char has a relatively homogenous trend along the height of the bed, as it depends on fuel particle concentration. The similarity between this reaction and the heterogeneous destruction of NO on char surface is obvious.

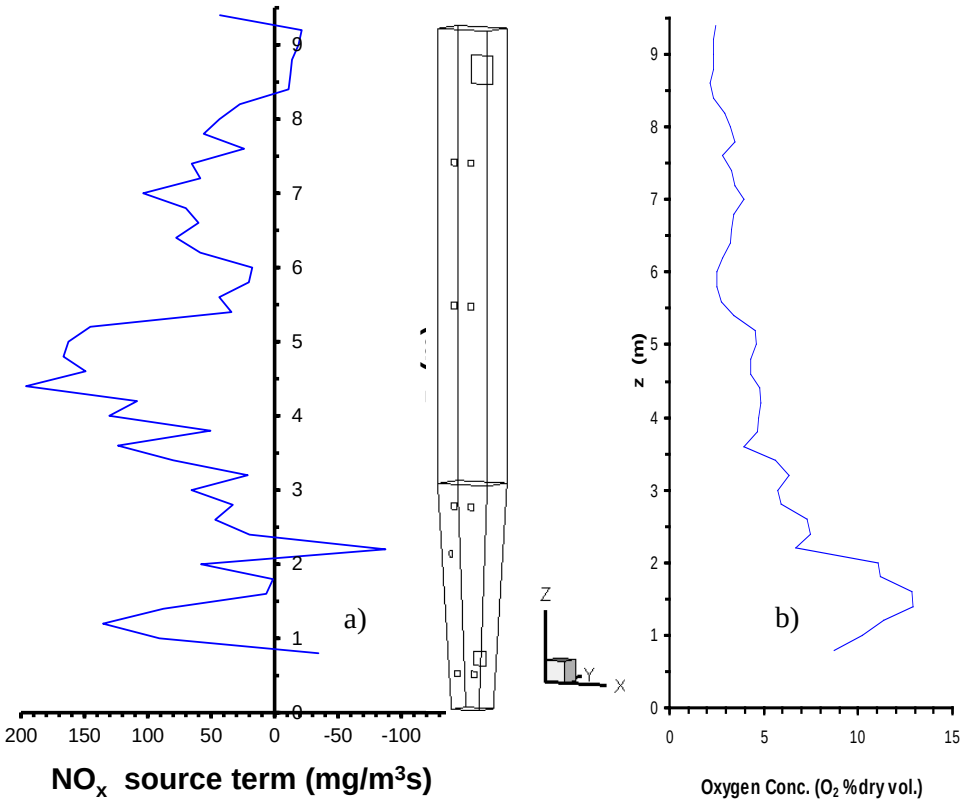

Figure 5.16 a) NO_x Source term plotted against the height of the bed; b) Average oxygen concentration plotted against the height of the bed

Finally, the NO_x formed at each computational cell, is described by the source term in NO_x transport equation. Figure 5.16a depicts the profile of NO_x source term plotted against the height of the bed, while in Figure 5.16b the mean oxygen concentration is presented. From Figure 5.16a, intense NO_x formation is observed on the lower part of the bed, mainly due to the presence of gaseous volatiles that are released instantaneously after fuel insertion at z = 0.7m, and due to oxidizing conditions. Then, a sharp decrease in NO_x formation is observed, which is attributed to the sharp decrease in oxygen levels. Oxygen is consumed for the oxidation of volatile species. Above the insertion of secondary air at 2.15m and especially at 2.8m, there is enough oxygen to enhance the formation of NO_x from homogenous (volatiles that are not consumed and they are transferred from the lower part) and heterogeneous mechanisms (char oxidation). This increment in NO_x formation is observed in Figure 5.16a. However, the oxygen level drops once more due to combustion. At 5.6m and above, NO_x formation mechanisms are favored due to the new insertion of secondary air. NO_x is now formed almost entirely from char oxidation (as seen in Figure 5.9). The same trend is observed along the riser. Between secondary air inlets, NO_x are formed at a relatively high rate. When oxygen decreases, destruction reactions are enhanced, thus NO_x formation rates decrease. Therefore it can be concluded that air staging ports, separate the combustion chamber in different zones in which the same pattern in NO_x formation is observed.

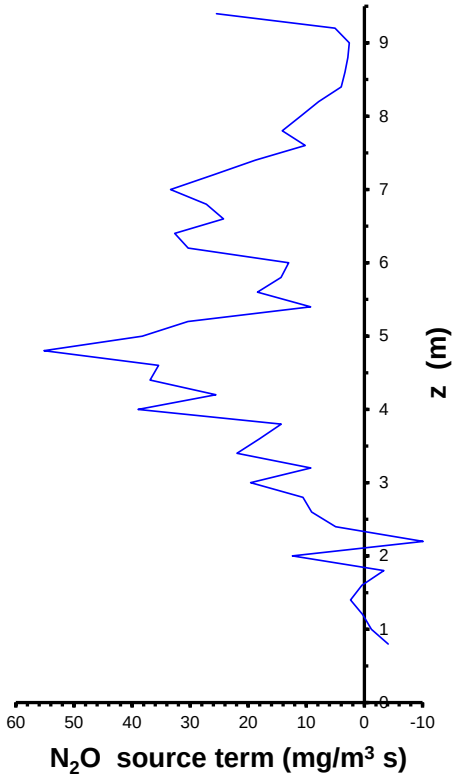

Figure 5.17 N_2O Source term plotted against the height of the bed

The respective source term of N_2O is plotted in Figure 5.17 against the bed height. Through comparison of Figure 5.17 and Figure 5.16a depicting the NO formation rate, the same trends are observed. This is attributed to the fact that the air staging influences N_2O formation in the same way as it affects NO_x formation. However, on the lower section of the bed, where high NO_x formation rates are observed, N_2O formation rates are not similarly high for two reasons. Firstly, the formation of nitrous oxide from volatile HCN is a rather "slow" reaction, as already discussed before, and secondly, the creation of N_2O depends on the concentration of NO, which is low on the lower section (Figure 5.8).

5.3 Conclusions

A three dimensional simulation of a combusting flow in a CFBC is presented. Despite the numerous assumptions of the model and the uncertainties that may entail, good agreement between experimental data and numerical results is achieved. Oxygen and CO_2 profiles are well predicted except for the height of Z=2.15m. At this height the deviations from the experimental data are attributed to the incomplete set of experimental data in combination with the non-uniform distribution of the oxygen in this height. Moreover, the mean temperature in the bed, as well as the increased difference between the fuel and inert material temperature at the exit of the combustion chamber are well predicted. As the proper modeling of heat exchange between fuel and inert-material is concerned, Gunn's equation gives qualitatively correct results. Nevertheless, more sophisticated models should be developed, taking into consideration flow heterogeneity in each computational cell. The developed CFD model is capable of efficiently modeling a CFBC. However in order to further increase accuracy, improved closure equations are needed. The computational cost for such modeling was found extremely high but not prohibitive for large scale CFBC simulations.

A decoupled 3-D simulation for the formation of NO_x-N_2O in the 1.2 MW_{th} CFB plant was also performed. The results of this approach seem to have good accuracy while the computational cost is low. However, the combustion field must be simulated in advance. An additional problem is the difficulty in finding appropriate reaction rate constants in literature. Different reaction rate expressions were found for the same reactions, differences which reflect the fact that different fuels have different behavior especially as concerns the heterogeneous reactions. The adoption of the Eulerian approach for the description of the multiphase flow also makes the simulation of heterogeneous reactions more difficult since the number of particles and the effective char surface in each computational cell cannot be straightforwardly calculated. The results of the simulation suggest that nitric oxides are formed homogenously on the lower section of the bed from the oxidation of HCN, while on the upper stages, heterogeneous formation is the dominant mechanism. N_2O is formed mainly through the heterogeneous mechanism. The main reaction for the reduction of nitrous oxide was found to be the heterogeneous reduction on char surface, fact that agrees with literature. It was found that the main product of fuel devolatilization that led to the formation of nitric oxides was HCN, while no HCN was released during char combustion. With the assumption of HCN release during both devolatilization and char combustion (Model 1), HCN concentration on the outlet was too high. Therefore, Model 2 which does not assume HCN release during char combustion, but direct oxidation of char – bounded nitrogen seems to be more accurate. However, such a behavior may be fuel specific and more experimental and simulation work is needed before drawing final and universal conclusions.

As far as the air staging is concerned, simulation showed that the insertion of secondary air separates the formation of nitrogen oxides in different zones. On the lower part of those zones oxygen is abundant due to secondary air inlets, and NO_x formation is favored which is then followed by the formation of N_2O. On the upper part of those zones, large amounts of oxygen have been consumed, which reflects to the gradual reduction in NO_x and N_2O formation (Figures Figure 5.16 and Figure 5.17 respectively).

The developed model achieved in predicting NO_x and N_2O with good accuracy, especially close to furnace exit and can be used for CFBC design optimization. The decoupled approach followed is computationally inexpensive, allowing the efficient simulation of NO_x and N_2O even of large scale units. However, for such simulations the combusting flow field is a prerequisite. These data can be either obtained by CFD, which is computationally expensive or by semi – empirical models that are computational inexpensive but rely on empirical correlations.

6. FULL – LOOP MODELLING OF A CFB COLD MODEL CARBONATOR

In the previous chapter the CFD simulation of the combusting flow inside a CFB boiler was investigated along with pollutants formation and in situ destruction mechanisms. Such a model can help in designing FBCs with lower emissions with respect to CO, NO_x, N_2O and SO_x. However, nowadays there is alos a need for drastic CO_2 reduction that cannot be conducted in situ in conventional fossil fuel combustors.

Post-combustion, calcium looping (CaL) CO_2 capture is regarded as a promising solution applicable to both new and existing power plants. This technology, theoretically proposed by Shimizu et al., 1999, utilizes a dual fluidized bed (DFB) system that couples two FB reactors; the carbonator and the calciner. In the carbonator the CO_2 is captured by CaO particles while in the calciner the sorbent is regenerated. Charitos et al., 2010[b] examined the process under realistic conditions in IFK (Institut fur Feuerungs und Kraftwerkstechnik, Institute of Combustion and Power Plant Technology). The cold model of this DFB installation comprises of a Circulating fluidized Bed carbonator and a Bubbling Fluidized Bed (BFB) calciner. The presently modeled carbonator reactor is a novel one and its up-scaling to an industrial scale confronts difficulties, due to lack of experience and the associated high cost of experimental campaigns. Therefore, it is of interest to develop CFD models for this new type of reactor and help in its up – scaling and design optimization.

CFD modeling can predict the complicated flow characteristics governing CFB operation, with the minimum economic cost. This is attributed to their inherent ability to meticulously address complicated issues, such as inert material concentration in the bed, reactants mixing efficiency and temperature distribution, with a reduced cost when compared to experimental campaigns.

The TFM approximation, coupled with the EMMS scheme was tested in chapter 4. Although the EMMS scheme properly addresses the micro- and meso- scale characteristics of the flow, the additional influence of macro-scale characteristics, such as the core-annulus flow pattern and the pulsing behavior of a Loop – Seal (Larsson et al., 2011), should be also taken into consideration. In this light, the application of the EMMS scheme with the simultaneous modeling of the full CFB loop is considered as the most accurate numerical approach (Zhang et al., 2008), when compared to the sole CFB riser simulation. Therefore, the number of numerical works adopting the full – loop increases (Ge et al., 2011; Shuai et al., 2011[a]; Wang et al., 2011). The full CFB loop (riser – cyclone – downcomer – pneumatic valve – joining pipes) simulation should for example focus on proper representation of the friction inter-particle forces (Nikolopoulos et al., 2012[c]) in the returning system.

In this section, the full loop of a transparent cold model CFB of a 10kW Carbonator is simulated. Since the unit is rather small, in this 3-D numerical investigation, a very dense numerical grid is applied with an l_r of about 21. To the best of the author's knowledge this is the highest grid density ever applied for 3-D CFD simulation of CFBs. Both Gidapsow's and EMMS drag schemes are tested and evaluated against experimental data for the pressure profile of the whole loop and for the particles entrainment. It should be underlined that this is the first time that the predictions of a TFM model are straightforwardly compared with pressure experimental data for the pneumatic valve of a CFB unit.

6.1 EMMS Scheme Formulation

As in chapter 4, the EMMS scheme is formulated for the specific operating conditions of USTUTT's CFB carbonator cold model. It should be underlined that the interpolation equations 4.1 to 4.3 cannot be used, since the polynomial coefficients depend on the operating conditions of the CFB unit under consideration. Thus, these coefficients should be calculated from scratch for the simulation of any CFB unit. The numerical procedure for the development and the implementation of EMMS scheme is as follows:

- The first step is to solve the set of the equations for every possible value of gas, solid velocities and solid volume fraction, requiring the minimization of the objective function, which reflects the energy exchange between gas and solid particles inside a control volume.
- The second step is to couple the EMMS scheme with the CFD model simulating the flow patterns of the governing phases (gas and solid). It should be underlined that for each particular combination of CFB unit and operating conditions, the model has to be solved from the beginning.

The EMMS scheme is integrated to the state-of-the-art TFM modeling technique. This advanced sub-grid model is used for the calculation of the momentum interexchange coefficient (β) between the interacting gas and solid phases. The conventional model by (Gidaspow, 1994) correlates the (Wen and Yu, 1966) and Ergun (Ergun, 1952) equations for drag calculation, depending on the solid phase fraction in a control volume, according to the equation 2.28.

More information on the numerical formulation of the EMMS scheme, adopted in the present section of this PhD can be found in chapter 3 or in (Nikolopoulos et al., 2010[b]). Briefly, equations 3.2 to 3.4 represent the force balance for the clusters and the dilute phases in a suspension unit volume, respectively. The latter correlation (eq. 3.4) represents the pressure drop balance between the clusters and the dilute phase (Wang et al., 2008). Dense phase voidage standard deviation is calculated using equation 3.8 (Wang et al., 2008). The latter is symbolized as ε_c and is approximated by equation 3.9. In this equation the constant n is involved.

The value of n in the abovementioned equation can be chosen with some degree of arbitrariness (Wang et al., 2008). A value of $n = 1$ is proposed by Yan et al., 2002; Manyele et al., 2002 and Qi et al., 2005 while $n = 2$ was proposed by Liu, 2005; Sharma et al., 2000; Tuzla et al., 1998 and Gu and Chen, 1998 proposed $n = 2.5$. Finally $n = 3$ is proposed by Soong et al., 1995 and Soong et al., 1994. In the present investigation a value of $n = 2$ is adopted, as most of the authors propose, for the EMMS development for the CFB model of USTUTT. The mean cluster diameter is calculated according to Gu and Chen, 1998 correlation (eq. 3.10), as explained in the work of (Nikolopoulos et al., 2010[b].

Concluding, the mathematical expression for the estimation of the drag force, based on the EMMS model is given in equation 3.16. The force calculated by this correlation is in fact applied to the CFD model when the EMMS scheme is adopted. However, this force is indirectly applied to the CFD model through equation 3.1 that is an alternation of equation 2.28 that contains the heterogeneity index H_d. As described in equation 3.17, this index is defined as the ratio of the drag force calculated by the conventional model of Wen and Yu to the respective force calculated by the proposed EMMS scheme (Nikolopoulos et al., 2010[a]).

The nonlinear optimization mathematical problem is solved, for any triplet of u_g, u_s and ε_g, and for the specific operational conditions of the small sized model unit of USTUTT. The basic design parameters under which this unit is operated, are given in the following Table 6.1 Particle – gas properties for USTUTT small sized model tests (ρ_g, μ_g, ρ_s, d_p, ε_{mf}). These operational conditions were defined by USTUTT's experimental team members (Table 6.1).

d_p (particle diameter)	142 μm
ρ_s (particle density)	5700 kg m^{-3}
ρ_g (gas density)	1.225 kg m^{-3}
μ_g (gas viscosity)	1.7894 10^{-5} kg $[ms]^{-1}$
ε_{mf} (minimum Fluidization Voidage)	0.55

Table 6.1 Particle – gas properties for USTUTT small sized model tests

The set of equations is solved for the aforementioned operating conditions using the commercial optimization package GAMS® (http://www.gams.com/). The arithmetic results satisfy the physical condition that the heterogeneity index (H_d) depends on both the slip velocity and the gas volume fraction (u_{slip}, ε_g) in accordance with the findings of (Nikolopoulos et al., 2010[a]). Figure 6.1 presents the variation of H_d as a function of gas volume fraction for a specific slip velocity (u_{slip} = 2 m/sec). Similar functions are calculated for a wide range of slip velocities, whilst for intermediate velocity values an interpolation procedure is followed.

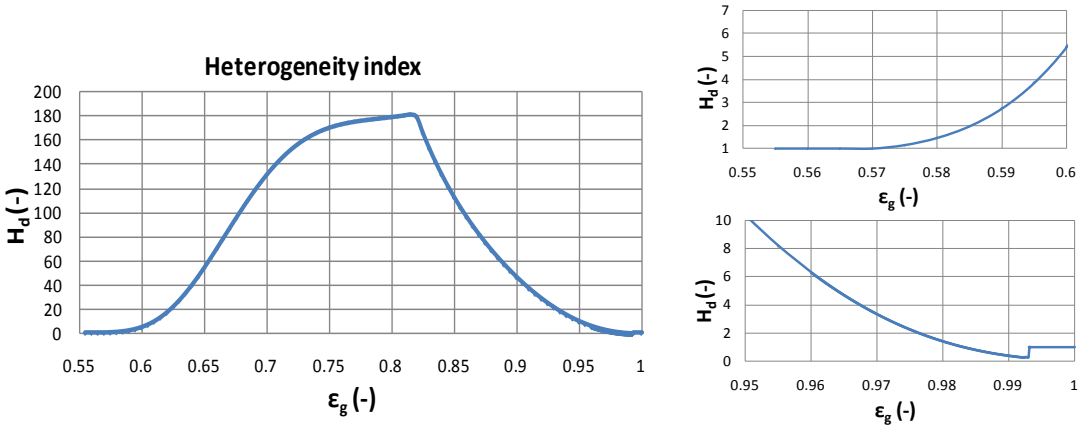

(a) (b)

Figure 6.1 (a) The $H_d(\varepsilon_g)$ function for u_{slip}=2 m/sec. (b) dense and dilute end zoom in areas.

Mathematical expressions in the form of $H_d=f(|u_{slip}|, \varepsilon_g)$ are, as a next step, developed in order to efficiently interpolate the results of the EMMS scheme for its more efficient implementation in the CFD model. It should be stated that for highly dense conditions (ε_g < 0.6), the flow is predicted, by the EMMS, as homogeneous and therefore H_d is considered equal to 1 (Nikolopoulos et al., 2010[a]).

6.2 Addressing Friction Forces in the Returning System

The components for particles circulation and gas sealing used in CFB installations are mainly the L-valve (Geldart and Jones, 1991; Arena et al., 1998; Yang and Knowlton, 1993), the loop-seal (Basu and Cheng, 2000; Cheng and Basu, 1999 and Kim and Kim, 2002) and the seal pot (Kunii and Levenspiel, 1991). In the case of USTUTT's cold model carbonator, which is simulated in this chapter, a loop-seal is used.

The flow inside a Loop-seal is hydrodynamically governed by the well investigated bubbling regime (Basu and Cheng, 2000). Although the flow is dense (ε_s equals to $\varepsilon_{s,mf}$), particles move with non-negligible velocity in the range of 0.1 to 1 m/s, due to the drag force induced by the fluidizing gas. When the Loop – seal is operated in this mode it is a pass – through device.

However, Loop – Seal can be also utilized as a regulator of the flow rate of re-circulating particles. The Loop – Seal of USTUTT's installation is operated under this second mode. In this case (Basu and Cheng, 2000; Cheng and Basu, 1999 and Kim and Kim, 2002), the volume fraction of solids within the down-comer is very high, reaching values up to $\varepsilon_{s,max}$.

Variable	Standard models (riser)	New models (CFB returning system)
μ_{kin}	$\frac{10\rho_s d_s\sqrt{\Theta_s\pi}}{96\varepsilon_s(1+e_{ss})g_o} \times [1+\frac{4}{5}g_o\varepsilon_s(1+e_{ss})]^2$ (Gidaspow et al., 1992)	$\frac{\sqrt{\pi\Theta_s}\frac{d_s\rho_s}{24\varepsilon_s g_o}\frac{\left(5+2\varepsilon_s g_o(1+e_{ss})(3e_{ss}-1)\right)}{(1+e_{ss})(3-e_{ss})}}{\left(1+\frac{45\mu_g}{6\varepsilon_s g_o d_s\rho_s\sqrt{\frac{\Theta_s}{\pi}}(1+e_{ss})(3e_{ss}-1)}\right)}$ (Boelle et al., 1995), (Gevrin et al., 2008)
μ_{col}	$\frac{4}{5}\varepsilon_s\rho_s d_s g_o(1+e_{ss})\sqrt{\left(\frac{\Theta_s}{\pi}\right)}$ (Gidaspow et al., 1992)	$\frac{4}{5}\varepsilon_s\rho_s g_o(1+e_{ss})\left(\frac{\mu_{kin}}{\rho_s}+d_s\sqrt{\frac{\Theta_s}{\pi}}\right)$ (Boelle et al., 1995), (Gevrin et al., 2008)
μ_{fr}	$\frac{P_{fr}\sin\phi}{2\varepsilon_s\sqrt{II_{dD}}}$ (Johnson and Jackson, 1987)	$\frac{P_s\sin^2\varphi}{\varepsilon_s\sqrt{4\sin^2\varphi\cdot II_{dD}+(\nabla\cdot\vec{u}_s)^2}}$ (Dartevelle, 2003)
λ_{fr}	0	$\frac{P_s}{\varepsilon_s\sqrt{4\sin^2\varphi\cdot II_{dD}+(\nabla\cdot\vec{u}_s)^2}}$ (Dartevelle, 2003)
μ	$\varepsilon_s<\varepsilon_s^{fr}\Rightarrow\mu_{kin}+\mu_{col}$ $\varepsilon_s\geq\varepsilon_s^{fr}\Rightarrow\mu_{kin}+\mu_{col}+\mu_{fr}$	$\mu=\mu_{\text{kin}}+\mu_{\text{col}}+\mu_{\text{fr}}$ (Makkawi et al., 2006)
P_s	$\varepsilon_s<\varepsilon_s^{\text{fr}}\Rightarrow P_{\text{kin}}$ $\varepsilon_s\geq\varepsilon_s^{\text{fr}}\Rightarrow P_{\text{fr}}$	$\varepsilon_s<\varepsilon_s^{\text{fr}}\Rightarrow P_{\text{kin}}$ $\varepsilon_s\geq\varepsilon_s^{\text{fr}}\Rightarrow P_{\text{kin}}+P_{\text{fr}}$
g_o	$\left[1-\left(\frac{\varepsilon_s}{\varepsilon_s^{\max}}\right)^{\frac{1}{3}}\right]^{-1}$ (Ogawa et al., 1980)	$\left[1-\left(\frac{\varepsilon_s}{\varepsilon_s^{\max}}\right)\right]^{-2.5\varepsilon_s^{\max}}$ (Lun et al., 1984)

Table 6.2 Mathematical expressions for the calculation of granular material viscous stresses in the CFB riser and in the returning system (Nikolopoulos et al., 2012[c])

In standard TFM models the stress tensor for the particle phase is formulated on the basis of granular kinetic theory for solids volume fraction lower than the friction limit (ε_s^{fr}). In the case of denser flows, the plastic-frictional theory is used with a suitable yield criterion and an appropriate flow rule. The criterion that is commonly used in recent literature is the von Misses / Coulomb yield criterion (Nikolopoulos et al., 2010[a, b]; Zhang and VanderHeyden, 2001; Tsuo and

Gidaspow, 1990 and Zhang et al., 2008). However, as discussed in chapter 3, researches of other fields of interesting working on granules simulation (Christakis et al., 2002; Goodey and Brown, 2004; Goodey et al., 2003; Christakis et al., 2006; Dartevelle, 2003; Dartevelle, 2004 and Dartevelle et al., 2004) revealed that the von Misses/ Coulomb yield criterion is not appropriate for the numerical simulation of dense flows. The reason is that, as reported by Dartevelle, 2003, the von Misses/ Coulomb and the Levy-von Misses flow rule, can properly simulate dilatancy but not consolidation. Thus, the standard yield criterion cannot model the effect of the "compressibility" phenomena (changes of bulk density) occurring in the returning system of CFB units, resulting in severe underestimation of the frictional viscous forces. This drawback can be overcome by the use of the more sophisticated yield criterion of Pitman-Schaeffer-Gray-Stiles depicted by equations 3.20 and 3.21.

For all the aforementioned reasons, the Pitman- Schaeffer- Gray-Stiles yield criterion is adopted and the respective stress tensor is incorporated in the CFD commercial package Fluent (FLUENT, 2010) for the returning system, with the use of custom-built User Defined Functions (UDF). The goal is to simulate with high accuracy the flow characteristics of a granular material in the recirculation system of a CFB unit.

For the calculation of the viscous part of the stress tensor of solid and gas phase, equation 2.20 is used. The calculation of shear and normal stresses of the solid phase in the returning system is based on the yield function of Pitman- Schaeffer- Gray-Stiles. Table 6.2 summarizes the formulas used for the calculation of viscous forces (kinetic, collisional and frictional) for the CFB riser and for the returning system. The isotropic/ hydrostatic pressure P is approximated with the well-known correlation of Johnson and Jackson, 1987. The values of important model parameters are presented in Table 6.3.

The proposed model for the recirculation system, which was validated in chapter 3, incorporates frictional viscosity even for solid volume fraction lower than the friction limit. This approach is reported in the work of Makkawi et al., 2006. The idea behind this is that: a) frictional stresses were found to play a significant role in almost the whole range of particles loading, and b) this approach allows for a smooth transition for the shear stresses between the rapid-intermediate flow and the slow frictional one. This modeling approach, where the granulates stress tensor constitutes of a kinetic, a collisional and a frictional term over the whole range of particle loading, is as well demonstrated in the work of Patil et al., 2005 and ensure shear stress continuity for ε_s equal to the friction limit. The same technique is used for the calculation of granular pressure in the recirculation system.

e_{ss}	0.9 (Ding and Gidaspow, 1990; Hartge et al., 2009)
ε_s^{max}	0.65
ε_s^{fr}	0.5 (Gidaspow et al., 1992)

Table 6.3 Model parameters

6.3 Numerical Grid Density

The spatial discretization is a very important aspect of every numerical simulation. Ge et al., 2008 and Zhang and VanderHeyden, 2001 report that the simulation of meso – scale structures can be explicitly resolved with the application of dense grids. The necessary dimensionless grid size, l_r (equivalent cell length to particle diameter) has been reported to be around to 20 (Nikolopoulos et al., 2010[a]), but this has not yet fully proved and new research activities disagree with this statement, i.e. Lu et al., 2009; Wang et al., 2010[a] showed that for a doubly periodic 2-D domain the application of the Gidaspow scheme has achieved a grid independent solution for l_r

equal to around 10. On the other hand, the EMMS scheme was found to reproduce grid independent numerical results for coarser grids. It is very important that this study depicted that the grid independent results of the EMMS and Gidaspow's models do not coincide.

Although, Lu et al., 2009 and Wang et al., 2010[a] performed numerical runs in two dimensions, similar conclusions can be extrapolated for three-dimensional runs. Of course, unambiguous values for the l_r ratio e.g. 10 or 20 cannot be easily extrapolated to 3-D simulations, for which lower values might be expected. However, Sundaresan, 2011 reports that for the TFM approach, the validity of simulations with l_r ratios less than 10 is as well under question. Indeed, the non-continuum character of solid particles puts a barrier to high resolution simulations in the frame of Eulerian descriptions. Moreover, there are additional difficulties since the geometrical features of granules put further limitations. In a hypothetical cubic control volume with edges smaller than the particle diameter, the volume fraction of particles should be able to reach 1. However, in the TFM approach the packing limit is correctly setting a barrier in the densification with particles of the control volume. This is an extra reason for the author of this work to believe that the TFM equations may not be valid in very small control volumes. The same kind of speculations have been also reported for MP-PIC methodology (Benyahia and Galvin, 2010).

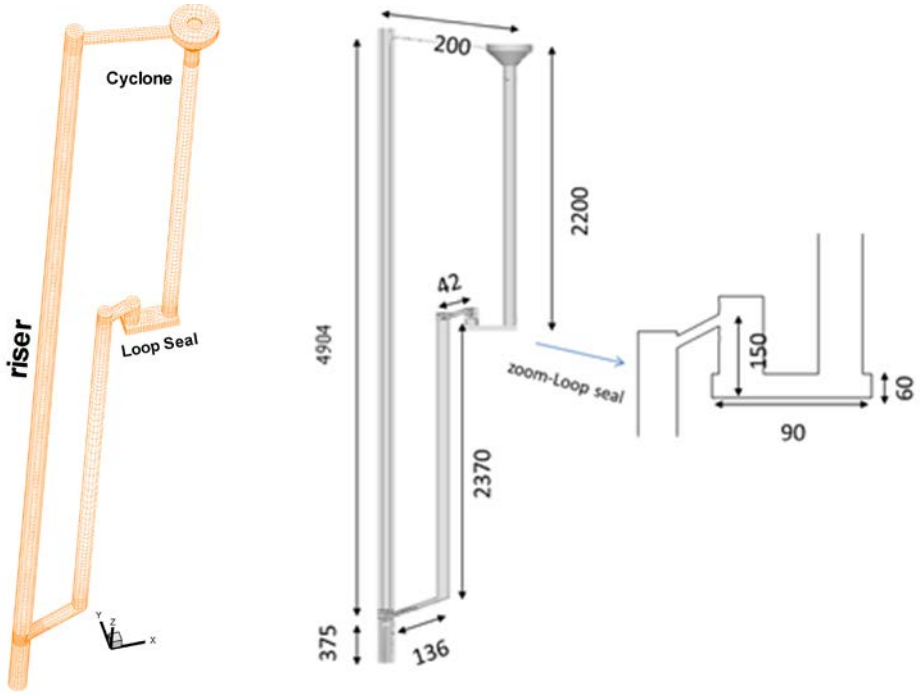

Figure 6.2 Wireframe and basic dimensions (mm) of the USTUTT plexi-glass CFB.

In this context, for the full loop geometry of USTUTT the mean ratio of the equivalent cell size to particles diameter is set equal to 21. This small sized cold model is fully discretized with minor simplifications regarding the cyclone shape. The l_r factor is kept strictly constant for the hexahedral cells discretizing the CFB riser and the mixture of the hexahedral and tetrahedral elements for the returning system. The fact that such a high grid density is applied, allows for important conclusions to be drawn on the validity of Gidapspow's and EMMS drag model.

Figure 6.2 presents the geometrical configuration of the small model unit. The CFB loop is discretized by 286,753 elements. The volume of the computational cells is strictly kept uniform in the riser, so as to increase the numerical accuracy of the calculations (Atsonios et al., 2011). Initially a coarser grid was applied (l_r ~33) with relatively good results regarding Gidaspow scheme. However, when the EMMS scheme was applied, the bottom zone of the riser became very dense and numerical problems and errors arose. The source of this failure is attributed to the

complicated flow patterns the fluidizing gas is following in order to overcome solid particles resistance; patterns those cannot be easily described by the application of coarse grid resolutions. Additionally, the aforementioned flow patterns changed rapidly in time and in certain time steps the mass conservation equation couldn't converge. It is believed, that such problems will not occur in simulations of larger CFBs where the riser diameter to particle diameter ratio is significantly lower. This ratio, in the small sized model is equal to around 200 (the diameter of the riser is 30 mm).

6.4 Boundary and Operating Conditions

The wall boundary conditions for gas and solid phase are set individually. The no slip condition is used for the gas phase for all walls in the computational domain. The partial slip condition (Johnson and Jackson, 1987) is used for the wall surfaces of the riser adopting a specularity coefficient (φ^*) of 0.6 (Almuttahar and Taghipour, 2008; Atsonios et al., 2011; Benyahia et al., 2000; Zhang and VanderHeyden, 2001). In the regions of the downcomer and of the Loop – Seal, the no slip condition is applied for the solid phase. Regarding the spatial discretization schemes for the momentum and volume fraction equations, the second order QUICK scheme is used. The restitution coefficient (e_{ss}) is set to 0.9 (Atsonios et al., 2011) as the particles in USTUTT installation (ambient conditions) are categorized as Geldart B (Geldart, 1973). In the transient calculations, the time step is set to 20 μs and a bounded second order implicit (FLUENT, 2010) time discretization scheme is applied. The phase coupled SIMPLE algorithm is used for pressure–velocity coupling, whilst for the determination of scalars facet values the Green-Gauss node based approximation is adopted. The superficial gas velocity in the carbonator distributor is set to 2.87 m/s and in the bottom aeration of Loop-seal equal to 0.106 m/s. The air flow rate is 8.95 kg/h and 1.5 kg/h respectively.

Full loop simulation (Shuai et al., 2011[a]; Zhang et al., 2008) is a new more sophisticated approach in CFD modeling of CFB units. More published approaches include the simulation of only the CFB riser and exclude the recirculation system (cyclone – downcomer – pneumatic valve – joining pipe, Koksal and Hamdullahpur, 2005; Benyahia et al., 2000; Abbasi and Arastoopour, 2011 and Shuai et al., 2011[b]). The main drawback of this formulation is that either the solid inventory of the riser or the recirculation rate should be a known quantity. However, both quantities are difficult to be experimentally determined. Although the recirculation rate can be simply measured with a diversion valve, this is an invasive technique of low accuracy, because of the high temporal fluctuations of the recirculation rate. As far as the solid inventory is concerned, this is also a function of time and shouldn't be straightforwardly calculated through pressure drop in the riser at least for small scale units.

For the full loop simulation, the total solid inventory (TSI) in the unit should be a known quantity and the recirculation rate an unknown one. In a typical CFB unit, the TSI can be measured easily and with high accuracy prior to the experimental investigation. Unfortunately, since the small scale CFB is a part of the DFB cold model of USTUTT (Charitos et al., 2010[a]) this value was not measured for the CFB loop. However, since the calciner's cold model operates under the bubbling regime and the total mass in the dual installation is measured, the CFB TSI is easily calculated to around 1.5 kg.

6.5 Assumptions of the full – loop CFD model

The simplifications made in the case of the full – loop isothermal modeling of the small scale CFB carbonator cold model are summarized below. The assumptions (1 to 8) refer to the simulations undertaken with the EMMS scheme. The assumptions made in chapter 4, are mainly

also adopted for this simulation. However, the returning system is not neglected in this case study and the wall surfaces are exactly represented by the numerical grid since there are no tube walls.

1) Particles are considered mono – sized.

2) Clusters are considered as spherical and it is assumed that in each control volume they all have the same properties. Moreover, the temporal evolution of clusters is ignored.

3) The flow is isothermal. There is no spatial or temporal differentiation in temperature.

5) Turbulence effect is neglected (Rampidis et al., 2007).

6) For the calculation of granular temperature the diffusion and convective terms are neglected.

7) Secondary forces are neglected (added mass force, electrostatic forces, lift, buoyancy). For ambient conditions, electrostatic forces may be not negligible (Bi, 2011) but cannot be introduced in the CFD model, since there is no approximation for them available in the literature

8) Particles self – rotation is neglected.

6.6 CFB Pressure Profile

The numerical simulation started with the initialization of the volume fraction of solids. In this light, the TSI of 1.5 kg is evenly split between the riser and the down-comer. The CFD simulations of USTUTT's small sized model started by implementing the simpler Gidaspow's drag scheme.

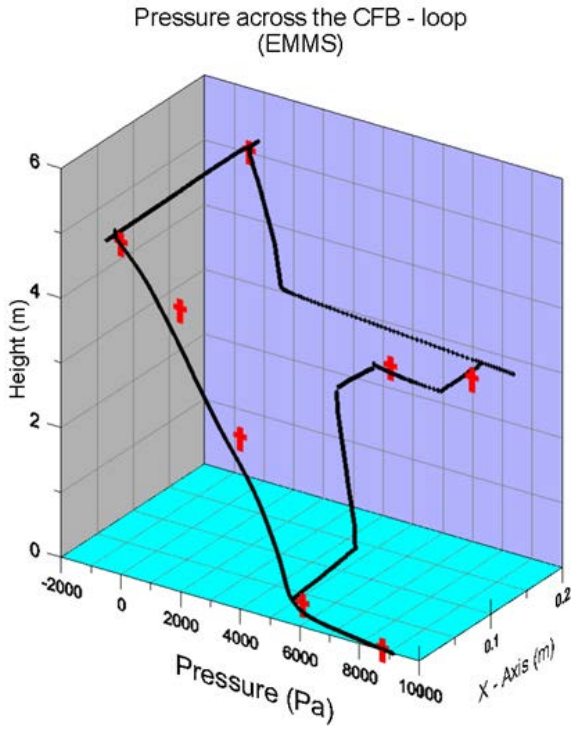

Figure 6.3 Comparison of experimental (red crosses) and numerical predictions (continuous black line) of the EMMS model regarding the pressure profile across the loop.

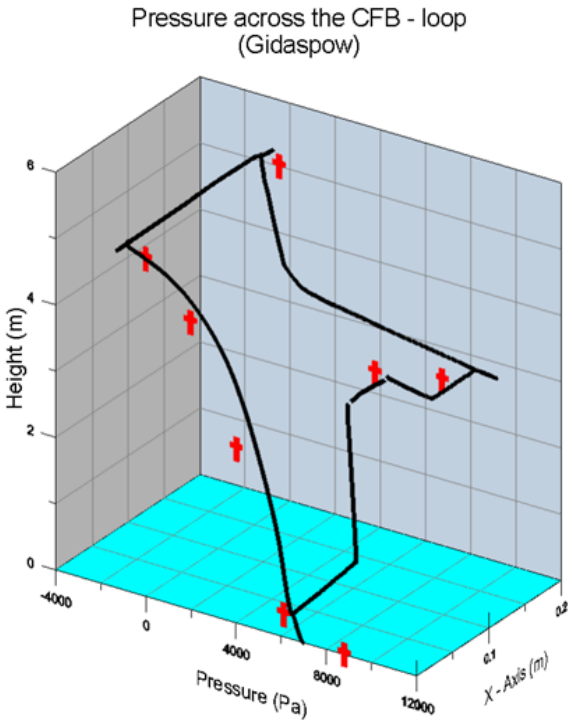

Figure 6.4 Comparison of experimental (red crosses) and numerical predictions (contin. Black line) of the Gidaspow model regarding the pressure profile across the loop.

To reach a dynamic equilibrium for the mass in the riser and the returning system, a time period of around 35 seconds is required. This value can be compared with the average value of 100 sec, which is reported as adequate for similar simulations that exclude the returning system (Nikolopoulos et al., 2010[a]). However, the adequate time period for averaging and obtaining

representative mean values for important scalars (e.g. pressure), is found to be significantly higher than the period of 15 - 20 seconds commonly used for only the riser simulations (Nikolopoulos et al., 2010[a]). After achieving equilibrium, the sampling of time instant values is performed for a period of 120 sec (t = 35 – 155 sec). The same solution procedure is adopted for the EMMS simulation, as well.

Figure 6.3 and Figure 6.4 depict the time averaged pressure profile along the CFB loop as derived by the implementation of both the EMMS and Gidaspow's model respectively in comparison with the corresponding experimental values measured by USTUTT. While the Gidaspow's drag model clearly fails to predict the pressure at the carbonator bottom, the accuracy of the EMMS scheme is high and the mean error is less than 10%. The EMMS results almost coincide with the experimental data. The small deviations from the experimental data can be attributed to the mono - sized approach and the small uncertainty in the total solids inventory of the CFB loop.

Regarding, the Loop – Seal simulation, pressure predictions agree quite well with the experimental values for both drag models. This fact shows the validity of the proposed solid stress model for this highly dense in particles region. It should be underlined that this is the first time that the accuracy of a CFD model is tested against experimental values of pressure inside a pneumatic valve.

It should be stated that the conventional stress model, described in Table 6.2, is also tested in the recirculation system, but with bad results. As a matter of fact, the underestimation of solid stresses in this case is so big, that the seal broke. As a result the fluidization gas of the riser bypassed the Loop – seal and entered the cyclone through the downcomer. This incorrect prediction is observed even for zero aeration in the Loop – Seal. Other full loop CFD studies (Nguyen et al.; Zhang et al., 2008) have not reported such a behavior. This contradiction may be related to the special USTUTT CFB loop geometry, as far as the re-circulation system is concerned. Since, the CFB is a part of a DFB installation, the Loop – seal of the CFB is almost 3 meters higher than the distributor of the riser. This special geometrical feature is not observed in typical CFBs (Zhang et al., 2008), and plays an important role in the induced pressure difference that the Loop – seal has to overcome in order to efficiently transfer particles from a low pressure region (downcomer) to a high pressure one (bottom zone of riser).

The accuracy of the two drag schemes should be as well studied under the light of the applied high grid resolution. Although a value of l_r equal to around 21 is considered as low enough for Gidaspow's predictions to be of high accuracy, this was not achieved. This observation coupled with the conclusion of Lu et al., 2009 that the two schemes converge to different solutions questions the Gidaspow's correlation validity. A clear answer to this issue can be given by the implementation of a denser grid (l_r around to 10), but this is not yet feasible due to the current computational cost limits. Nevertheless, this work depicts that EMMS scheme is more valid than the Gidaspow one, for the same grid resolution.

6.7 Solids Mass Flux Time Series

Another important variable, affected by the proper simulation of the drag coefficient and the pneumatic valve is the re – circulation flux. USTUTT measured this quantity to be around 63 kg/h. This variable along with the numerically predicted time series of particulates mass entering and exiting the riser are plotted in Figure 6.5.

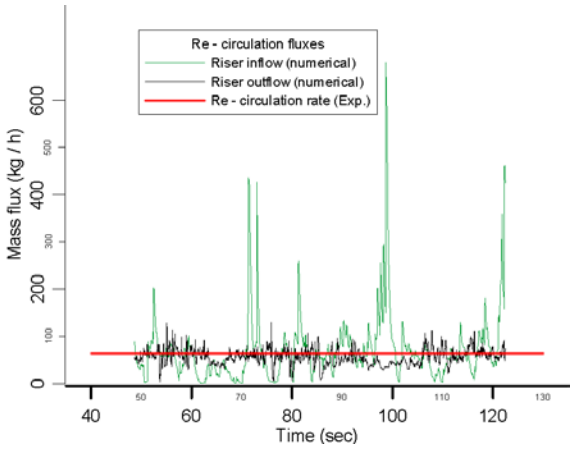

Figure 6.5 Comparison of the experimental recirculation flux and predicted time series for the mass entering (green) and exiting (black) the riser.

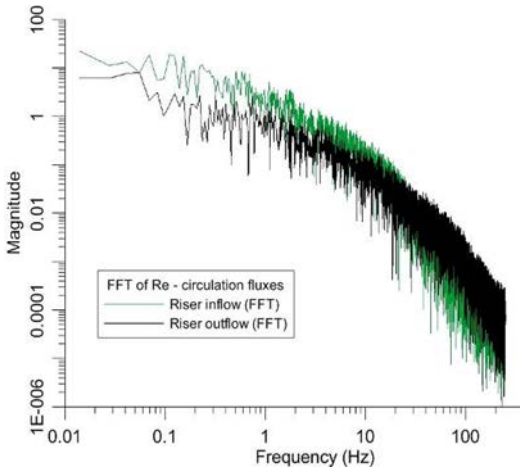

Figure 6.6 Power Spectral Density of the inlet and outlet mass flux time series (120 sec data, sampled with 500 Hz).

The numerical results refer to the CFD model that incorporates the EMMS scheme for the calculation of the drag force. Although, the two time series differ a lot, their mean values almost coincide. Moreover, the experimental value is reproduced with high accuracy (error <2%). The CFD model incorporating the Gidaspow approach overestimated this value with an error of around 10%, although the Loop – seal pressure distribution is accurately predicted (Figure 6.4).

It is interesting to notice that the Loop – seal delivers particles in the riser through pulses. This pulsing behavior was also confirmed by optical observations of the experimentalists that carried out the experimental campaign in the transparent plexi – glass small sized unit. Moreover, regarding the hydrodynamics of the CFB riser it is very interesting that these high amplitude and low frequency pulses are dumped down within the riser (Figure 6.6).

Concluding, the EMMS scheme for the momentum exchange coefficient along with the application of Pitman – Schaffer – Gray – Stiles yield criterion in the re – circulation system succeed in capturing the complicated hydrodynamic behavior of the full loop CFB unit. Regarding the implementation of the Pitman- Schaeffer- Gray-Stiles yield criterion in contrast to the standard one of von- Misses / Coulomb, the proposed model is found to be able to describe more consistently the exerted frictional forces within the granular phase in the Loop - Seal.

6.8 Flow Characteristics of the CFB

The results of the CFD model incorporating the EMMS scheme are meticulously studied since this model is relatively new and the hydrodynamics of a CFB carbonator have never been studied before. The figures of this passage are plotted with X to Z axis ratio equal to 0.3 for reasons of figure clearanceness, while the X to Y ratio is equal to 1. For all variables the time-averaged values are plotted and the velocity vectors are plotted as uniform (their length is not a function of velocity magnitude), except for the figures otherwise denoted.

Figure 6.7 depicts the spatial distribution both of the pressure and the solids volume fraction as distributed during the CFB small sized model operation. Pressure values are given in Pa. From Figure 6.7 it is clear that the EMMS model, predicts high solid concentrations at the bottom and the exit region of the riser, which is in agreement with the optical observations. It is of high technological interest the fact that the exit shape is quite steep, opposing to the easy outflow of the particles from the riser towards the cyclone. This effect should be cared of in the design of larger units, since it induces unnecessary pressure drop and high attrition rates at this area. At this

point, it should be mentioned that the solid phase in the top area of the riser is not motionless. Regarding the Loop-Seal solid phase volume fraction distribution is a typical one, resembling a fixed bed column, in the down-comer, characterized by a high particle loading. This is desirable because it ensures the gas sealing.

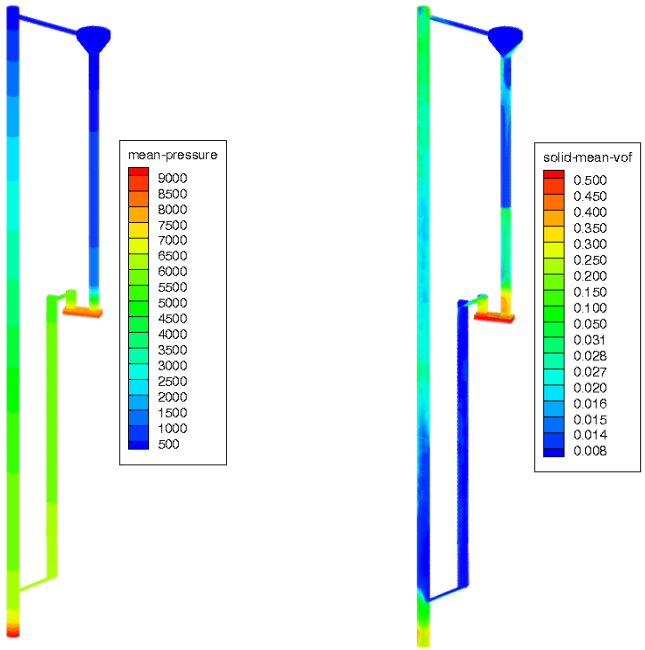

Figure 6.7 Time Averaged pressure and solids volume fraction for the USTUTT plexi-glass small sized CFB.

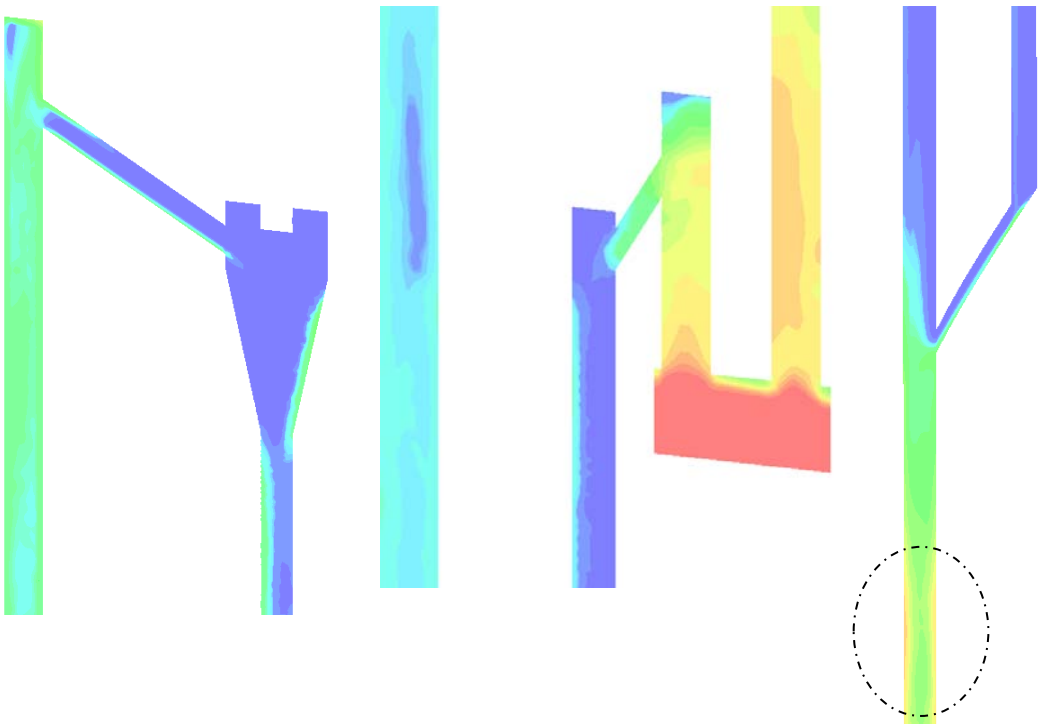

Figure 6.8 Average mean solids volume fraction for a) the cyclone (Y=0.0)

b) the Loop-seal (Y=0.0)

c) the bottom zone (X/Z axis ratio=1) (Y=0.0)

Figure 6.8 depicts the solid volume fraction in the areas of technological interest i.e. the cyclone, the pneumatic valve and the dense bottom zone of the riser. The solid volume fraction is becoming denser moving upwards the riser close to its exit. In the smaller diameter pipe that leads to the cyclone, the flow is characterized by a steep gradient of solid concentration and the induced flow field is characterized by a chute motion of particles. The similar pattern is observed in the joining pipe. In addition, close to the riser distributor, the solid phase is getting so dense that it prevents the free flow of gas phase, thus inducing a high pressure gradient, as depicted in Figure 6.7.

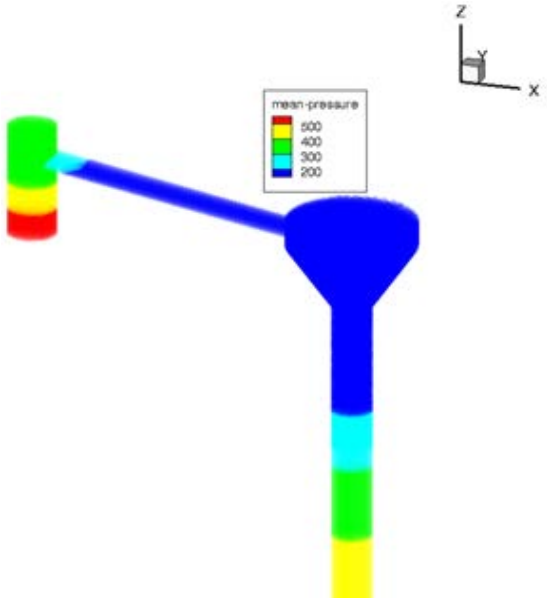

Figure 6.9 Pressure drop at the exit region.

Figure 6.10 presents the velocity fields of gas and solid phases, undimensionilized with the gas inlet velocity at the riser (U_o=2.89 m/s). Throughout the small sized model the gas phase is characterized by more- than- twice higher velocity than the solid one. The interesting fact is that both velocity fields have the greatest values in the region of the pipe that connects the riser exit with the cyclone. This is due to the fact that the diameter of this pipe is much smaller to the riser one, imposing a high pressure gradient in this area, Figure 6.9. Moreover, the riser is characterized by higher velocity than the rest of the loop, because the Loop-Seal, opposes to the free flow of gas phase.

The most important fact, revealed from the solid velocity spatial distribution is related to the exit of the joining pipe at the riser (area A). Figure 6.11 depicts the velocity vector field and its corresponding magnitude at this area of high technological interest. From this figure, it is easily deduced that the momentum of solid particles is higher than the momentum of the gas phase flowing perpendicular to it, thus allowing the solid particles to hit the opposite wall of the riser. This behavior has also been visually observed in the experimental campaign. This results in high attrition rates and consequently the operational cost is increased (Charitos et al., 2009).

Furthermore, the induced vector field reveals that the region below level A is not refreshed, at least with high rates, with new material. In other words it may be claimed that this geometry configuration coupled with the specific operating conditions impose a cushion for the solid particles.

As far as the cyclone area is concerned, Figure 6.12a presents the induced solid velocity vector field. According to this, the solid particles exiting the riser towards the cyclone are those which travel from that side, whilst the rest in the opposite side hit the ceiling and then travel downwards back to lower regions of the riser. From this fact, it is clear that the design of this

region plays a significant role in the particles recycling and should be investigated in depth as a design parameter.

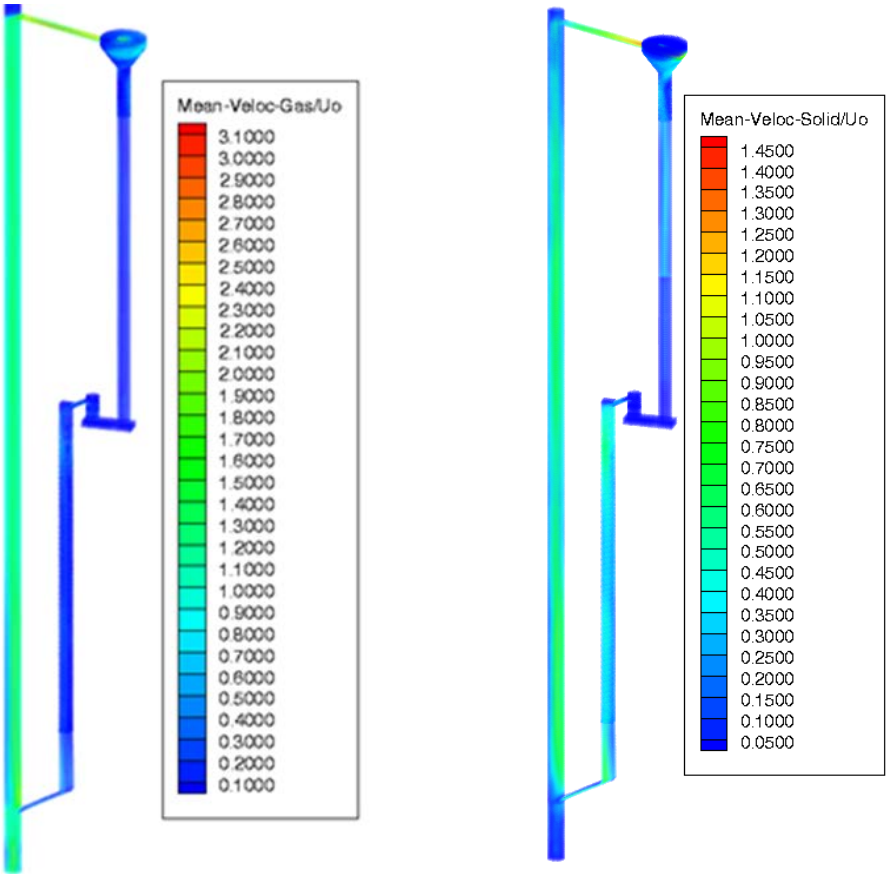

Figure 6.10 Average mean velocity field of the a) gas phase (Y=0.0) b) the solid phase (Y=0.0)

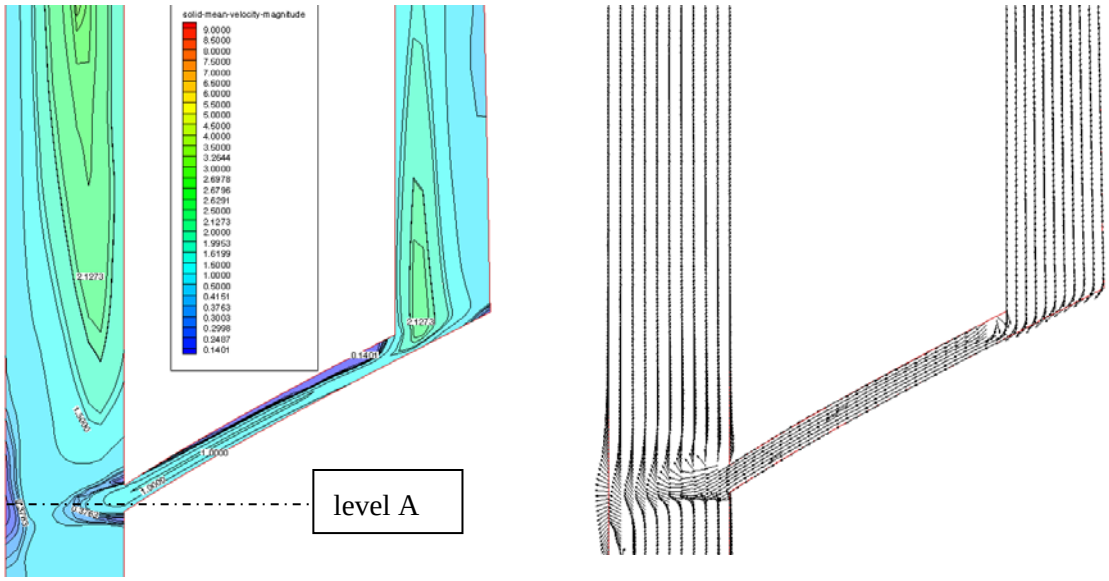

Figure 6.11 Average mean velocity of the solid phase at the joining pipe a) contour field (Y=0.0) b) vector field (uniform vectors) (Y=0.0)

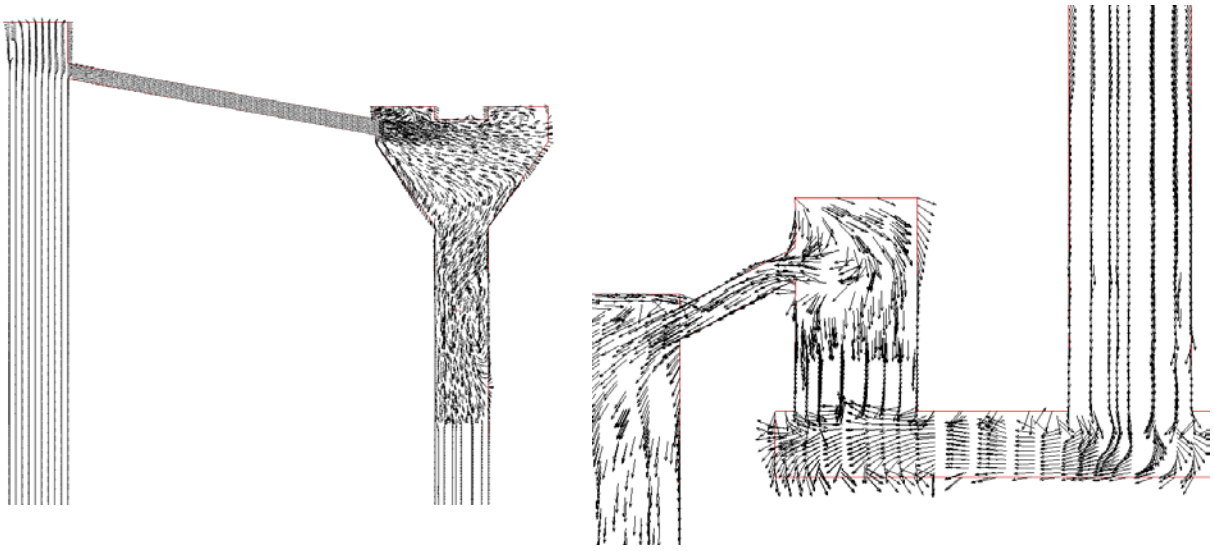

Figure 6.12a) Average mean velocity vector field of the solid phase at the a) cyclone (uniform vectors) (Y=0.0) b) the Loop-seal (uniform vectors) (Y=0.0)

Figure 6.12b presents the induced solid flow field in the region of the Loop-seal. In this region the solid particles are entering the Loop - Seal having formed an almost fixed-bed flow regime. It should be mentioned that this figure presents time-averaged values. Figure 6.13 presents the same with Figure 6.12b, but the length of the vectors are drawn as a function of the velocity magnitude. This is done in order to show that a motion towards the outlet of the Loop-seal is induced on the solid particles, and the magnitude of this velocity is increasing with its distance from the Loop-seal bottom. This resembles the formation of a boundary layer within the solid phase and should be further investigated.

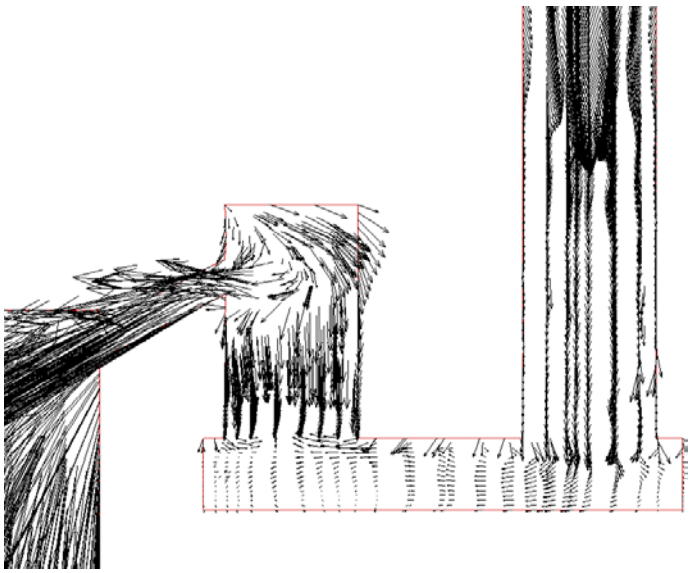

Figure 6.13 Average mean velocity vector field of the solid phase at the Loop-seal (vectors as a function of velocity magnitude) (Y=0.0)

As far as the gas phase is concerned, Figure 6.14 depicts its main characteristics in: a) the joining pipe and b) the Loop – Seal. In the Loop-Seal, although the gas phase is entering perpendicular to the Loop – Seal distributor, due to the motion of the solid phase towards the exit of the Loop-Seal, it begins moving horizontally as well. In addition, in the exit region of the Loop – Seal the solid phase accelerates.

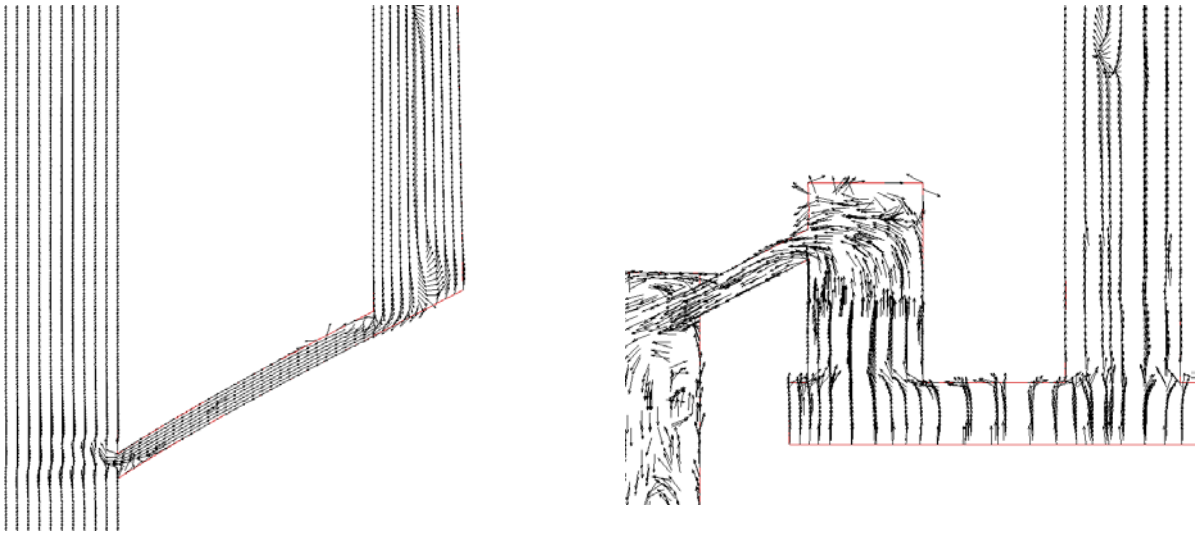

Figure 6.14 Average mean gas phase velocity vector field at the a) joining pipe (uniform vectors) (Y=0.0) b) the Loop-seal (uniform vectors) (Y=0.0)

6.9 Conclusions

The hydrodynamics of a full loop CFB carbonator are numerically investigated. The innovative character of this work is the adoption of the full-loop modelling approach. The implementation of the EMMS scheme for the calculation of the drag coefficient and of the Pitman-Schaeffer-Stiles yield criterion in the Loop - Seal, proved to be crucial factors for the accurate simulation of the carbonator unit.

As far as the EMMS model is concerned, it should be underlined that it succeeded in reproducing highly accurate results. This fact, enhances the conclusions drawn in chapter 4. The EMMS model used in the full – loop simulation is exactly the same as the one applied to the 1.2 MW_{th} CFBC isothermal simulation, fact that further enhances its validity and more important its universality. In the simulation of the small scale CFB full – loop the time – step is the same for both EMMS and Gidaspow schemes in contrast to the simulation of the 1.2 MW_{th} CFB performed in chapter 4. This means that maybe lower time – steps are not needed for implementing EMMS schemes, a fact that enhances the computational cost effectiveness of this model.

The conventional drag model accuracy is rather good, except for the dense bottom zone. In general, high accuracy was expected (Ge et al., 2008) since grid density is rather high. However, in the dense bottom zone the Gidaspow scheme clearly fails to capture the hydrodynamics of this region. It should be underlined that this region plays a significant role in a lot of processes using CFB technology. This is also valid for CFB carbonators since the majority of the CO_2 capture takes place in this region (Charitos et al., 2011; Rodriguez et al., 2011).

The full – loop simulation performed, allowed the investigation of the proper modeling of the returning system. The big difference between the recirculation system and the riser is that the pneumatic valve is rather denser in particles, in order to achieve sealing for the fluidization gas of the riser. In such elevated particle loadings, inter - particle friction forces prevail and their accurate simulation is a *sine qua non* for the simulation of the CFB loop. As discussed in chapter 3 of this thesis, conventional stress models that are usually applied to CFB risers severely under predict the friction forces. This conclusion was verified in this chapter as well. When these models were applied in the Loop – Seal the under prediction of the friction forces is so high that the particles cannot prevent the gas of the riser from entering the Loop – Seal and reaching the cyclone through the downcomer. Breaking the seal makes the unit no longer operational, and such a behavior was predicted from the conventional stress model even for zero aeration in the Loop Seal. This prediction strongly contradicts to the CFB technology experience and the experimental

data, fact that illustrates that conventional stress models should not be applied in the returning system of CFBs.

The new stress model formulated in this thesis based on the Pitman-Schaeffer-Stiles yield criterion and the work of Dartevelle, 2003 and was validated in chapter 3 of this thesis was tested in the full – loop simulation of the CFB cold model carbonator. Not only it succeeded in not letting riser gases to break the seal, but also succeeded in simulating with high accuracy the pressure drop in the Loop – Seal. This was achieved for both drag models tested, fact that indicates that particle – particle friction is the most important force in this region of the CFB loop.

Except for the comparison with the experimental data for pressure and the recirculation flux the CFD results were also compared with visual observations. The CFD model developed captured the pulsing behavior of the Loop – Seal, the lower particle loading in the higher part of the weir of the Loop –Seal and the penetration of the recirculating stream in the riser. This qualitative agreement strengthens the validity of the model. Concluding, the agreement of numerical results with the experimental data is high, even for the difficult-to-model dense bottom zone of the riser. Apart from pressure measurements, the mass circulation in the CFB loop is also predicted with an error less than 2%.

7. SIMULATION OF A 10 KW_{th} CARBONATOR

Directives for drastic reduction of worldwide CO_2 emissions introduce the necessity for novel and high efficient CO_2 capture technologies. Post-combustion, calcium looping (CaL) CO_2 capture is regarded as a promising solution applicable to both new and existing power plants. This technology, first theoretically proposed by Shimizu et al., 1999, utilizes a Dual Fluidized Bed (DFB) system that continuously loops CaO particles to capture CO_2 in the form of $CaCO_3$ within the carbonator and subsequently to the regenerator where the $CaCO_3$ is calcined and the CO_2 is released in a concentrated form ready for storage. Abanades et al., 2007 performed an economic analysis of this process, while Charitos et al., 2010[a, b] and Charitos et al., 2011 first examined the process under realistic conditions in IFK. This DFB installation comprises of a Circulating fluidized Bed carbonator and a Bubbling Fluidized Bed (BFB) calciner. The presently modeled carbonator reactor is a novel one and its up - scaling to an industrial scale confronts difficulties, due to lack of experience and the high cost of the respective experimental campaigns. Therefore, it is of interest to develop CFD models for this new type of reactor and help in its up – scaling and design optimization.

The efficient design of large scale units is challenging: a) the efficiency of the mixing is not as high as in the smaller scales and it is strongly affected by the number and location of the feeding ports and b) the heat removal from the carbonator is difficult because in large scale units the available surfaces for heat extraction are not sufficient. Both aspects can be investigated through CFD models, and help in process design optimization, with a reduced cost. It is worth mentioning that especially the efficiency of mixing is very difficult to be investigated with experiments at this scale. Thus, the only realistic approach is to develop accurate and efficient numerical models that can tackle this problem.

In the previous chapter the hydrodynamics of a CFB carbonator were investigated. The proposed CFD model efficiently captured bed hydrodynamics. In this chapter, the carbonation reaction will be as well investigated. This is the first time that such a reaction will be investigated by CFD. The models successfully applied in the case of the cold model will be also applied in the case of the hot installation (DIVA reactor). Unfortunately, up to this point there are no experimental and / or operational data available for validating the CFD model. However, the model is developed and applied to USTUTT's installation for typical operating conditions.

7.1 Unit description

The 10 KW_{th} DIVA carbonator is a part of a DFB pilot installation constructed in USTUTT Stuttgart. This reactor is a typical CFB except for the interconnection with the calcination reactor. The solid material inside the full – loop of the CFB carbonator is a mixture of calcium oxide and calcium carbonated, while the flue gases are a mixture of nitrogen and carbon dioxide. The calcined material enters the CFB carbonator in the riser at a height of 1.5 m. In the Loop – Seal of the CFB carbonator there is an exit that leads to the calciner. The mass flux through this exit is controlled by an oscillating cone valve. The opening of this valve controls the recirculation between the two reactors. The concept of such DFB operation is analyzed in Nikolopoulos, 2006. The interconnection between the two reactors via pneumatic valves ensures the sealing of gasses between the two reactors.

In this work, only the CFB carbonator is simulated, including its recirculation system. The calciner is not simulated but the effect of its operation on carbonation efficiency is taken into account through: a) the composition (X_{calc}) of the solid flux that is entering the riser of the

carbonator, and b) the maximum available CaO that is available for fast carbonation (X_{max}) and not deactivated due to sintering.

Reactor height	L	m	12.292
Riser diameter	D	m	0.071
Solids in the CFB system	TSI	kg	6.5
Flue gas molar flow	F_{FG}	kmol/s	$2.802 \cdot 10^{-4}$
CO_2 molar concentration in the flue gas	y_{CO2}	kmol/kmol	0.114
Calcium looping ratio	F_{Ca}/F_{CO2}	kmol/kmol	17.40
Recirculating solids inlet temperature	T_R	^oC	900
Operating temperature	T_g	^oC	650
Calciner conversion	X_{calc}	-	0.0294
Max. carbonation conversion	X_{max}	-	0.0854

Table 7.1 Carbonator geometry and operational conditions

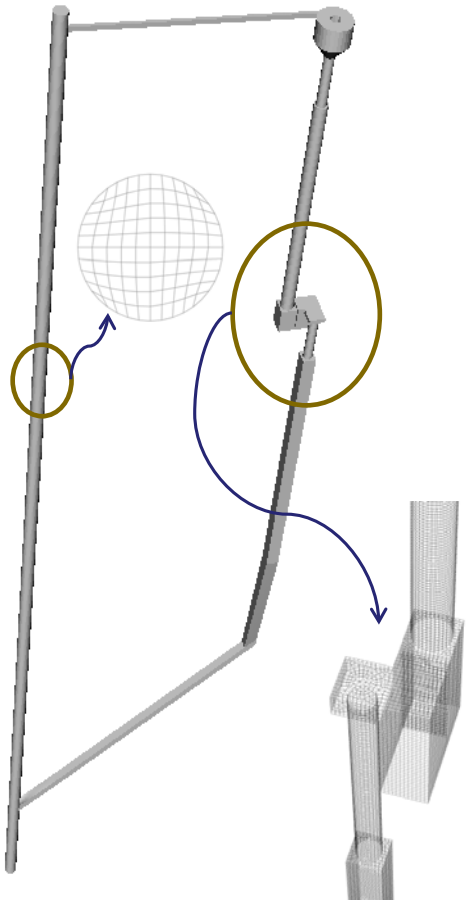

Figure 7.1 Grid constructed for the 10 KW_{th} DIVA carbonator

Table 7.1 summarizes geometrical and typical operation data of the installation. It should be underlined that the grid constructed fully respects the geometrical features of DIVA but the operational data considered for the simulation do not refer to a specific experiment but reflect typical values published in literature (Charitos et al., 2010[b]). The flue-gas composition is adjusted

in order to simulate typical coal combustion off - gasses. The limestone has a maximum capture capacity of X_{max} (maximum $CaCO_3$ molar uptake per mole of Calcium). This value is considerably smaller than unity because after repeated cycles of carbonation / calcination, sintering of particles due to the high temperature of the calciner creates a non-reacting core that carbon dioxide cannot easily reach (Charitos 2013). X_{calc} is the $CaCO_3$ to Calcium molar ratio of the particles exiting the calciner and entering the carbonator. This variable is zero for full calcination inside the calciner but because of the high CO_2 gas concentration in this reactor, full calcination is difficult to be achieved. It should be mentioned that F_{Ca} is the molar flow of calcium that is being recirculated between the reactors and that the product of F_{Ca} with (X_{max}-X_{calc}) depicts the available sorbent for carbon dioxide capture in this reactor.

As mentioned above the 3 – D numerical grid is constructed with full respect to the actual geometry (Figure 7.1). The grid is constructed trying to keep the same non – dimensional grid density as in the case of the small scale cold model simulation presented in chapter 6 (Nikolopoulos et al., 2012[b]). It consists of 392,130 hexahedral cells and l_r equals to 21. Special care is taken in constructing a uniform grid, especially in the riser, as Atsonios et al., 2011 propose.

7.2 Methodology - Assumptions

The numerical model applied in the case of DIVA reactor incorporates granulates hydrodynamics, species tracking and only one heterogeneous reaction. The energy equations of the two phases (gas - solids) is not solved as iso - thermal conditions are assumed in the CFB loop. The gas density and laminar viscosity are calculated by weight averaging of the respective gaseous species properties. The carbonation reaction is simulated through equation 3.85. In fact this chemical reaction is treated as a mass transfer mechanism since the energy equations are not solved. The respective mass source terms are applied to CaO and $CaCO_3$ solid species and CO_2 for the gas phase. The characteristics of the sorbent are not known. However, k_s, S_0 and e_0 are needed for the calculation of the reaction rate according to equation 3.85. For these constants, typical values (k_s = 5.95E^{-10} m^4 [mol s]$^{-1}$, S_0 = 40.E^{+6} m^2 m^{-3} and e_0 = 0.5) are retrieved from literature (Abanades et al., 2004). As regards fluidization hydrodynamics, the approaches adopted in the previous chapter are also followed in this simulation.

An advanced EMMS scheme is developed, using the same formulation as in the case of the small scale cold model CFB, but for the operating conditions of DIVA (Table 7.2). The H_d index is fitted with polynomials of ε_g for different slip velocities, and incorporated in the CFD code through a UDF. For the returning system the stress model described in Table 6.2 is applied, as it was found to be essential for the accurate simulation of the pneumatic valve. As far as model parameters are concerned the parameter reported in the previous chapter (Table 6.3) are applied.

d_p (particle diameter)	350 μm
ρ_s (particle density)	1800 kg m^{-3}
ε_{mf} (minimum Fluidization Voidage)	0.55

Table 7.2 Particle – gas properties for DIVA

The boundary conditions used for gas and solids phases are also identical with the ones adopted in chapter 6, except for the exit in the Loop – Seal that feeds carbonated particles in the calciner. In this exit, the solids molar flow is explicitly defined to be equal to the molar flow delivered to the riser from the calciner through the inlet located at height z=1.5 m of the riser. The molar fraction of the solid species is defined by a Neumann type boundary condition assuming zero gradient of molar fraction in the direction defined by the normal to the exit surface vector.

The simplifications made in the case of this simulation are generally similar with the ones for the simulation of the small scale CFB cold model. The assumptions are listed below (1 to 9).

1) Particles are considered mono – sized.

2) Clusters are considered as spherical and it is assumed that in each control volume they all have the same properties. Moreover, the temporal evolution of clusters is ignored.

3) The flow is considered iso - thermal. There is no spatial or temporal differentiation in temperature. In the DIVA installation, the temperature of the carbonator is controlled via thermal resistances that work in an on / off mode and assure iso – thermal conditions. However, close to the inlet through which particles from the calciner enter the carbonator, higher temperatures may be observed since the temperature of these particles is higher (900 ^{o}C)

4) Turbulence effect is neglected (Rampidis et al., 2007).

5) For the calculation of granular temperature the diffusion and convective terms are neglected.

6) Secondary forces are neglected (added mass force, lift, buoyancy).

7) Particles self – rotation is neglected.

8) Each computational cell is considered as a CSTR as far as carbonation reaction is concerned. Therefore, the meso – scale structures effect on the reaction rate is neglected.

9) The effect of the fluctuating mass flux between the reactors is neglected as the flux is considered constant. This simplification may have an effect on the accuracy of the model, but the only alternative is to simulate the whole DFB installation, since there are no experimental data for this behavior. However, simulating the whole DFB installation almost doubles the computational cost and the simulation of the oscillating cone valve that controls the recirculation between the two reactors is not easy.

As far as the solution initialization is concerned the mass of Calcium particles were evenly distributed between the riser and the pneumatic valve. Moreover the molar fractions of solid species is set according to an initial carbonation conversion of 5% (X_{carb} = 0.05). The time step of the calculations is set to 40 μs. The simulation continued for 80 seconds until the multi – phase flow seemed to be fully developed. However, no averaging is conducted, as this procedure is computational expensive and the final results will not have high added value since there are no experimental data available for comparison.

7.3 Results and discussion

As the operational data of the unit were found in literature and there are no experimental data available for validation, the developed model can only be qualitatively evaluated. Moreover, as no averaging is conducted, the results refer to instantaneous values and not to representative mean values. As expected, the typical CFB hydrodynamic phenomena, i.e. dense bottom zone and core – annulus flow pattern are captured (Figure 7.2a). Moreover, the carbonation reaction is high at the bottom zone region (Figure 7.2b) due to: a) the elevated particle loading of calcium; b) the high CO_2 partial pressure, and c) the reactivated material that is fed close to this region. This trend is observed in experimental works (Charitos et al., 2010[b]; Charitos et al., 2011), that report that the majority of CO_2 capture is performed in the bottom region.

The CO_2 profile along the riser is presented in Figure 7.3. In this figure, it can also be observed that the majority of the CO_2 is captured in the bottom zone, while in the freeboard the rest of CO_2 is captured with smaller rates (Nikolopoulos et al., 2012[a]). The decrease in CO_2 concentration for z = 1.5 m is caused by the two inlets that are located in this area. The first is delivering calcined particles from the calciner. However, before particles can reach the carbonator, they pass through a Loop – Seal that is fluidized with pure nitrogen. Moreover, the

second inlet delivers mass in the riser from the recirculation system of DIVA through the joining pipe. The Loop – Seal of DIVA is also fluidized by nitrogen. Therefore, from both inlets nitrogen is introduced and the flow of CO_2 is locally diluted. It should be denoted that in this figure the carbon dioxide concentration is not averaged in each cross – section.

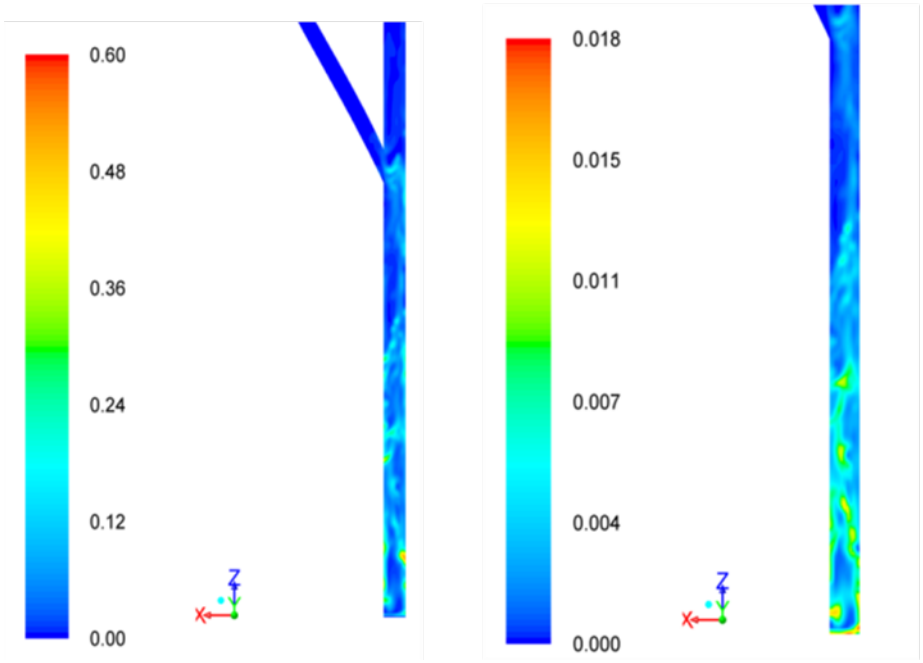

Figure 7.2 a) Instantaneous solids volume fraction; b) carbonation rate [kmol/(m^3 s)]

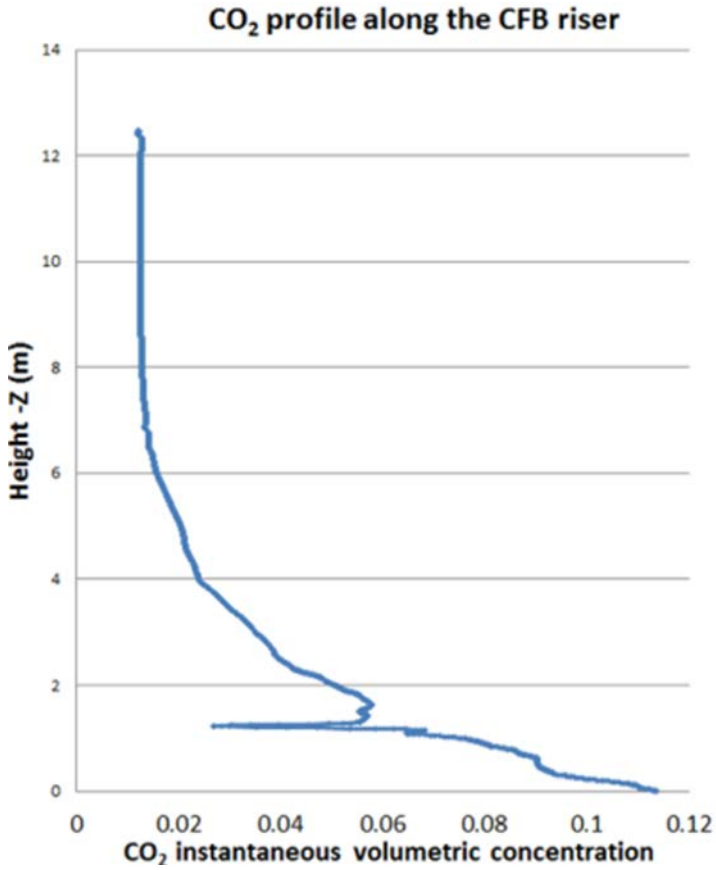

Figure 7.3 Instantaneous CO_2 profile along the axis of the riser

7.4 Conclusions

In this chapter, a 10 KW_{th} CFB carbonator is simulated for the first time. This pilot unit is capturing CO_2 from typical coal flue gasses with CaO particles. The CFD model developed for this reactor is based on the hydrodynamic model that was presented and validated in the previous chapter. Moreover, the carbonation reaction is incorporated into the CFD model as a mass transfer mechanism. The mass transfer rate is defined by a suitable expression developed from a correlation reported in literature and assuming that each control volume is a CSTR. As no experimental data are available for the DIVA reactor, at least for proper validation of a CFD model, the numerical investigation took into account the actual geometry of the full loop of the CFB reactor but the operating conditions were selected by data in literature. This means that the results of the numerical study are only indicative. However, the model effectively captured the trends reported in literature, at least qualitatively. The majority of CO_2 is captured in the dense bottom zone and the overall CO_2 capture in the carbonator is slightly higher than 90%. Both of these trends are reported by experimental works as well (Charitos et al., 2010[b]; Charitos et al., 2011; Rodriguez et al., 2011).

8. CONCLUSIONS

In this thesis, the numerical simulation of CFBs is investigated. Proper modeling of fluidization phenomena is a difficult task and most worldwide efforts focus on granulates hydrodynamics (Atsonios et al., 2011; Gidaspow et al., 1992; Ma et al., 2009; Nikolopoulos et al., 2010[a, b]; Nikolopoulos et al., 2012[b]; Vashisth and Grace, 2011; Wang and Li, 2007). However, there are some few studies on reacting flows (Gungor, 2008[b]; Gungor and Eskin, 2008[b]; Nikolopoulos et al., 2009; Wang et al., 2012[a]; Zhou et al., 2011).

Most of works focusing on FB hydrodynamics, investigate the meso – scale phenomena that severely affect the drag force induced to particles by the fluidization gas (Ge et al., 2008). A proper way to include the effect of the spatio – temporal particulate structures, simply called clusters, in the CFD simulations is via 1 –D subgrid models. As a forerunner, along with other scientist across the world, within this PhD I investigated the EMMS schemes that implicitly resolve sub – grid structures.

In this work, such an advanced EMMS scheme is developed in order to incorporate the effect of the multi-scale structures in the CFD model. This model comprises a set of equality and inequality constraints and an objective function referring to the energy exchange between flow phases. The numerical set was developed using empirical, semi-empirical and analytical equations coupled with physical constraints. Most of these correlations were found in literature except for a few constraints that were proposed by this work. The selection of the correlations to be used in the formulation of the EMMS scheme was based on their physical interpretation at first, and by the produced results of the EMMS optimization problem. Except for the H_d index, the acceleration, slip velocity and voidage of each phase along with clusters volume fraction were examined and evaluated.

The developed model predicted more realistic values for the clusters volume fraction (f) in comparison with the work of Wang and Li, 2007 as concerns the dilute area A. The consideration of the acceleration of each phase as free variables predicted more reasonable results for these variables in contrast to Wang and Li, 2007 model that predicted very high acceleration of clusters. On the other hand, the developed incorporates some empirical equations that their universality is not certain. The most important empirical equation is the one that defines the characteristic length of the meso – scale structures. Such a correlation was used in order to simplify the EMMS matrix solution. Albeit an empirical equation for clusters diameter was implemented, the numerical results in the dense region were found to be accurate, at least qualitatively.

The model predicted that for dense control volumes within the dense phase the slip velocity is high as a significant amount of gas penetrates in the clusters. This fact implies that the “cluster” of particles is no longer a rigid flow structure but it is broken into smaller structures. This prediction of the model is in line with the well-known fact that for high particle loading the flow is rather homogeneous as in the emulsion phase of the bubbling regime.

For control volumes with lower particle loading, close to the dilute end region the results of the developed EMMS model agree well with literature data (Wang and Li, 2007). Nevertheless, in this area, due to the very low volume fraction of solids, clusters may not exist but particle neighboring plays a significant role in the momentum exchange coefficient between the phases. The EMMS model takes into account this phenomenon in an implicit manner, through consideration of very dilute clusters. The accuracy of this approach has not been investigated yet either experimentally and / or numerically. Such works may lead in a finer tuning of the EMMS model for this area.

From a qualitative point of view, EMMS results agreed well with other available data in the recent literature, whilst heterogeneity index (H_d) quantifying the flow heterogeneity of each control volume was proved to be only a function of u_{slip} and ε_g. Finally, a proper interpolation scheme for this index was applied, in order to straightforwardly couple the EMMS scheme with a CFD Eulerian TFM code.

The developed EMMS scheme was initially applied in the simulation of a 1.2 MW_{th} CFBC iso – thermal flow. Except for this advanced scheme, the Gidaspow drag scheme was also applied, in order to be able to evaluate the new model in comparison with the conventional one that assumes homogeneous conditions inside each computational cell. The grid density effect on accuracy was also investigated. A coarse and a dense grid were applied for both the drag schemes. The results of this study revealed that increasing the grid density, the accuracy of the model also increases for both drag models as more meso – scale structures are explicitly resolved. However, for the same grid density the EMMS scheme proved to be more accurate than the Gidaspow scheme, conclusion supported by experimental data. This means that the EMMS model can increase the accuracy of the CFD model without the application of denser grids that increase the computational cost very much. Moreover, the new model captured characteristic flow patterns of CFBs, such as the S – Shape and the core – annulus and respected the terminal velocity of particles in the freeboard, even in the case of the coarse grid. However, EMMS scheme proved to be grid dependent. This result has not been discussed thoroughly in the literature yet. The reason behind this grid dependency is not yet understood. It may be attributed to the fact that inside a control volume the size and particle loading of clusters is considered uniform and that dilute and dense phase are homogeneous. However, even if this is the case, the assumption of homogeneous conditions inside those phases is more valid that the assumption of homogeneous conditions inside the control volume. This may also explain the higher accuracy and superiority of the EMMS model over Gidaspow's correlation.

The combusting flow simulation of the same 1.2 MW_{th} CFBC was also investigated. The CFBC unit is fed with Rheinian Lignite as a fuel. The three phases (gas, inertmaterial and fuel) were simulated in a pure Eulerian frame. Combustion and heat transfer mechanisms were incorporated in the hydrodynamic model and a simplified reaction network was formulated. Homogeneous reaction kinetics were retrieved from literature and were directly applied to the CFD model. Heterogeneous reactions, i.e. moisture evaporation, devolatilization and char combustion were also incorporated in the combusting flow model. The TFM approach does not track fuel particles and therefore the calculation of the number of particles per cell is challenging. Another difficulty is the selection of closure equations for the solid phases heat transfer. The heat transfer mechanism was modeled through an alternation of the Gunn's model while heterogeneous reactions were incorporated via UDFs. The char combustion was approximated with the shrinking core model and the devolatilization and moisture evaporation as single step reactions.

Only major species were considered i.e. O_2, CO_2. H_2O, N_2, volatiles, CO, CH_4, H_2, HCN and char, water, volatiles and ash for the gas and fuel phases respectively. The results of the model agreed well with the available experimental data for oxygen and carbon dioxide. This agreement indicates that both homogeneous and heterogeneous reactions were properly approximated. Through the examination of the oxygen contours it was observed that the core – annulus flow pattern affects the radial distribution of oxygen. Lower concentrations were observed close to the walls in the annulus region, where the volume fraction of the fuel is higher, and in the core of the flow the opposite phenomenon is observed.

Moreover, the mean temperature of the bed was accurately predicted. The simulations predicted a mean value of 1095 K, while the experimental data report 1100 K (Leithner et al., 1993). The temperature of the bed is quite uniform. These fuel particles, when burning, exhibit a

slight temperature increase. Additionally near the exit of the riser temperature differences of 80 K between fuel phase and inertmaterial were observed. These differences, also verified experimentally (Leithner et al., 1993), are attributed to increased local char combustion. This increase in char combustion is happening because in the exit region, the core – annulus flow pattern no longer exist and the higher oxygen concentration of the core region is mixed with the unburnt fuel of the annulus.

As far as the combusting flow in FBs is concerned, the numerical model developed was validated and despite the numerous simplifications and uncertainties it was able to reproduce results of adequate accuracy. However, a severe drawback of this pure Eulerian model is the very high computational cost that makes its application in large scale boilers difficult but not prohibitive.

The solution of the combusting flow by the reacting flow CFD model made the simulation of the NO_x-N_2O feasible. This was performed with a custom built 3 – D decoupled model. This was the first time that such an approach is tested in a simulation of a CFBC unit. The model was successfully validated against experimental data for both NO_x and N_2O. The results of the model, revealed that in general N_2O is formed through the heterogeneous mechanism, which is rather uniform along the height of the bed, as it is proportional to char combustion and NO_x concentration. On the other hand, nitric oxides are formed homogenously on the lower section of the bed due the oxidation of volatiles HCN, while on the upper stages, the oxidation of char bounded nitrogen caused by char combustion is the dominant mechanism. As reported in literature, the reduction of nitrous oxide on char surface was found to be a quite significant reaction.

The release of HCN during char combustion was parametrically investigated. Two models were tested: a) HCN is produced during both devolatilization and char combustion (Model 1) and b) HCN is produced only during devolatilization (Model 2). When model 1 was applied, HCN concentration on the outlet was too high. Therefore, Model 2 which does not assume HCN release during char combustion, but direct oxidation of char – bounded nitrogen seems to be more accurate. This result agrees with the theory of Goel et al., 1996[a, b]. However, final conclusions cannot be drawn since such a behavior may be fuel specific.

The NO_x-N_2O decoupled model simulated nitric and nitrous oxides with good accuracy, especially for the exit of the riser. Therefore, this validated and computationally inexpensive model can be used for the minimization of CFBC emissions, even of large scale units. However, for such simulations the combusting flow field is a prerequisite. These data can be either obtained by combusting flow CFD simulations that are computationally expensive or by semi – empirical models. These models are an attractive alternative since they are computational inexpensive but since they rely on empirical correlations, their universality is questionable.

NO_x-N_2O were not the only pollutants that were studied in this thesis. The challenging CO_2 capture was investigated. In particular, this thesis focused on the numerical simulation of Calcium Looping process. The main component of a CaL plant is the CFB carbonator. This reactor was numerically investigated. At first the hydrodynamic simulation of the CFB loop was performed, through the simulation of an iso – thermal experiment conducted in a small scale CFB cold model. The full-loop simulation is not trivial and up to now only a few researchers (Ge et al., 2011; Shuai et al., 2011[a]; Wang et al., 2011) have performed such an approach. In this work, a new stress model was developed for the recirculation system taking into account that within the pneumatic valve particles bulk density is high and interparticle friction forces prevail. The stress model developed based on an alternative yield criterion, i.e. the Pitman-Schaeffer-Stiles in contrast to the conventional extended von – Misses, was validated prior to its application in a full loop simulation. The validation was performed through the simulation of a repose angle

experiment. It should be mentioned that the conventional stress model clearly underpredicts the frictional forces and failed to capture the repose of the granular medium.

Except for the new granular stress model application within the pneumatic valve, the EMMS scheme developed in this work was applied for the calculation of the drag coefficient. Both of these novel models proved to be crucial factors for the accurate simulation of the full loop CFB unit. As pressure drop predictions are concerned, the accuracy of the model was very high, even for the difficult-to-model dense bottom zone. Apart from pressure measurements, the mass circulation in the CFB loop was reproduced with high accuracy. In fact the mean error for the pressure drop is less than 10% while the error in the flux is less than 2%. It is worth mentioning that for the first time the pressure predictions for a pneumatic valve are compared with experimental data. Except for experimental measurements the CFD model was also verified through visual observations. The model captured at least qualitatively, the pulsing behavior of the Loop – Seal and the penetration of the recirculation flux in the bottom zone of the riser.

As the respective conventional models were also tested useful conclusions can be drawn for them as well. The conventional stress model clearly failed, as it predicted that the gas of the riser bypasses the freeboard and enters the cyclone through the Loop – Seal. The Gidapow model on the other hand, simulated with relatively good accuracy the CFB unit. This result was expected since the grid density applied is very high (~ l_r equal to 21). However, the Gidaspow scheme failed in simulating the dense bottom zone of the riser even for this high grid density. It is not known whether this solution is grid independent, fact that would permanently obsolete the Gidaspow scheme even for dense grid simulations, or even higher grid density (~ l_r << 21) is needed in order to accurately simulate the hydrodynamics of the bottom zone.

Except for the investigation of the cold flow inside a CFB carbonator, the carbonation reaction was also investigated. This investigation was performed through the simulation of a hot 10 kW_{th} CFB carbonator installation. This reactor (DIVA) is operated by IFK, but up to now there are no experimental data available for CFD simulations. Therefore, an initial investigation was undertaken for typical operating conditions and for the actual geometry of DIVA. The carbonation reaction was simulated through a reaction rate developed from published correlations and assuming that each control volume is a CSTR. There are no final results for this model, but the full – loop CFD model developed, predicted that the majority of carbon dioxide is captured in the bottom zone as literature suggests.

The present study focused on the hydrodynamics and reacting flow mechanisms inside CFBs. Emphasis was given on emissions simulation, and the models developed can be used for effective design optimization and for the minimization of combustion emissions. Although, a lot of issues were tackled, especially as concerns the fluidization hydrodynamics, there is still work to be done in order to produce accurate and efficient, in terms of CPU cost, reliable CFD models.

Grid independency is the Holy Grail for the CFD simulation of CFBs. This has not yet achieved for 3 – D simulations. Future work should focus on defining the appropriate grid density in order to reproduce grid independent CFD results. The increment of the CPU resources may help in achieving such a goal in the near future, and also may allow for full loop polydispersed TFM modeling. Moreover, the models developed in this work were tested in small scale units and it would be of interest to apply them in larger scale units in order to investigate the CPU needs and their accuracy. The developed EMMS scheme can be also improved through explicitly taking into account particles neighboring for control volumes of low bulk density and through substitution of the semi – empirical equations by analytical ones, when those become available. Such substitution is expected to enhance the universality of the model.Moreover, the effect of the meso – scale structures on the heterogeneous reaction should be investigated (Wang et al., 2012[b]) as it may significantly affect the respective reaction rates. Finally, as the new MP-PIC

methodology seems to be a promising alternative for the TFM (Chen and Wang, 2013), it would be interesting to test the developed in this thesis models under this lagrangian frame.

NOMENCLATURE

A	pre – exponential reaction constant [varying i.e. s^{-1} , $(mol\ s)^{-1}$]
A_c	cross section [m^2]
A_E	eddy dissipation empirical constant [-]
Ar	Archimedes number [-]
a_c	acceleration of particles in dense phase [m/s^2]
a_f	acceleration of particles in dilute phase [m/s^2]
B_E	eddy dissipation empirical constant [-]
$\vec{c}$	Random granules velocity [m/s]
¢	equality or inequality operator [-]
c	constants [varying dimensions]
c_p	specific heat capacity at constant pressure [J/Kg K]
C	gas concentration [mol/m^3]
C_{dc}	effective drag coefficient in the dense phase [-]
C_{df}	effective drag coefficient in the dilute phase [-]
C_{di}	effective drag coefficient in the inter-phase [-]
d	diameter [m]
d_c	char diameter [m]
d_o	initial diameter [m]
D	Rate of strain tensor [s^{-1}]
D_{iff}	Diffusivity [m^2/s]
$D_{O_2(g)}$	oxygen diffusivity [m^2/s]
e_0	sorbent particle porosity [-]
e_{ss}	restitution coefficient [-]
f	clusters volume fraction [m^3 of clusters / m^3 in control volume]
F	molar flow [mol/s]
$f(x)$	function [-]
F	drag Force [N]
g	gravitational acceleration [m/s^2]
$g(x)$	function [-]
g_o	radial distribution function [-]
gr_d	grains distance [m]
G_s	solids mass flux or feeding rate [kg/s]

h	heat transfer coefficient [W/K m^3]
h_m	diffusion rate coefficients [kg/(m^2 s kPa)]
H	Enthalpy [J/kg]
H_d	heterogeneity index [-]
I	unit tensor [-]
II_{dD}	second invariant of the deviatoric rate-of-strain tensor [s^{-2}]
II_{dT}	second invariant of the deviatoric stress tensor [Pa^2]
k	rate constant [varying, e.g. 1/s, mol/(m^3s)]
k_c	Char combustion rate $\left[\frac{kg}{m^2 \cdot s \cdot kPa}\right]$
k_s	surface carbonation rate constant [m^4/(mol s)]
K	thermal conductivity [W/K m]
k^t	turbulent kinetic energy [m^2/s^2]
$k_{\Theta s}$	diffusion coefficient for granular energy [kg/(ms)]
L_w	latent heat of water [J/kg]
L	length [m]
L_o	lower bound [varying]
L_H	height of reactor [m]
l_p	mean free path for particles [m]
l_r	length ratio [-]
$\dot{m}$	mass transfer between phases [Kg/s m^3]
m_f	mass of fuel in a cell [kg]
$\dot{m}_{ps}^{w}$	moisture evaporation rate [kg/s]
M_w	molecular weight [kg/kmol]
N_{Ca}	Amount of calcium [mol]
N_f	component of friction force, normal to the wall [N]
N_p	number of particles in a control volume [#]
n	constant in the equation of ε_c [-]
$\vec{n}$	unit vector normal to the wall surface [-]
N_{st}	energy interexchanged between flow phases [W/kg]
Nu	Nusselt number [-]
P	normal frictional isotropic/hydrostatic stress [Pa]
$P_{O_2(g)}$	partial pressure of oxygen [kPa]
Pr	Prandtl number [-]

$\vec{q}$ heat flux [W/m^2]

Q volume fraction of particles of size smaller than d_p [-]

$\dot{Q}$ rate of energy transfer between phases [W/m^3]

Q_i volume fraction of particles of size between d_p and d_p+ d(d_p) [-]

R reaction rate $\left[\frac{mol}{m_{gas}^3 \cdot s}\right]$

R_c char combustion reaction rate $\left[\frac{mol_{char}}{m_{gas}^3 \cdot s}\right]$

Re Reynolds [-]

R_{vol} volatile release rate $\left[\frac{mol_{volatiles}}{m_{gas}^3 \cdot s}\right]$

R_u Universal gas constant [(8314.47 kJ/(mol K)]

S Source term [varying units)

Sc Schmidt number [-]

Sh Sherwood number [-]

S_0 initial CaO surface area [m^2/m^3]

t time [s]

T Temperature [K]

t_{res} residence time [s]

$\bar{\bar{\tau}}_s$ viscous stress tensor [Pa]

u_{slip} actual slip velocity in control volume [m/s]

u_{slip}^{+} next calculated value (via GAMS) of actual slip velocity in control volume [m/s]

u_{slip}^{-} previous calculated value (via GAMS) of actual slip velocity in control volume [m/s]

U_c superficial gas velocity in dense phase [m/s]

U_f superficial gas velocity in dilute phase [m/s]

U_{fc} Un burnt carbon percentage [%]

U_{sc} superficial slip velocity in dense phase [m/s]

U_{sf} superficial slip velocity in dilute phase [m/s]

U_{si} superficial slip velocity in interphase [m/s]

U_{pc} superficial particle velocity in dense phase [m/s]

U_{pf} superficial particle velocity in dilute phase [m/s]

U_{up} Upper bound [varying]

U_t terminal velocity [m/s]

$\vec{u}$	actual velocity [m/s]
$\vec{u}_{lq}$	Interphase velocity [m/s]
$\dot{V}$	volume flow [m^3/s]
V	volume [m^3]
w	weight factor [-]
X_{carb}	CaO carbonation conversion [mol%]
X_{calc}	$CaCO_3$ fraction in the outlet of the calciner [mol%]
X_{max}	CaO maximum CO_2 carrying capacity [mol%]
y_i	fraction of solid material in size interval I [-]
y_{CO2}	volumetric percentage of CO_2 in gas [vol.%]
Y	yield function [Pa]
Y_P	mass fraction of any product species
Y_R	mass fraction of a particular reactant
Y^{sp}	species concentration [$mg_{species}$/ kg_{gas}]
Y_{vol}	mass percentage of volatiles in each particle [kg_{vol}/kg_{fuel}]
∇	nabla operator
$:$	double inner product
β	momentum exchange coefficient [kg/(m^3s)]
Γ	diffusion term [kg/(ms)]
$\gamma_{\Theta s}$	the collisional dissipation of energy [kg/(ms^3)]
δ	angle of friction between wall surface and adjusting particles [rad]
E	activation energy [J/kmol]
E_k	Kinetic energy of particles [m^2/s^2]
ε	volume fraction [-]
ε_c	voidage in dense volume [m^3 of gas/m^3 of dense phase]
ε_f	voidage in dilute volume [m^3 of gas/m^3 of dilute phase]
ε^t	rate of turbulent kinetic energy dissipation [m^2/s^3]
Θ	granular temperature [m^2/s^2]
λ	bulk viscosity [Pa·s]
μ	shear viscosity [Pa·s]
μ^t	turbulent viscosity (kg/m/s)
$\nu'_{I,r}$	stoichiometric coefficient for reactant *I* in reaction *r*
$\nu''_{I,r}$	stoichiometric coefficient for product *j* in reaction *r*
ξ	plastic multiplier [$(Pa \cdot s)^{-1}$]

ρ	density [kg/m^3]
$\langle\sigma\rangle$	normal stress (average of the three principal stresses) [Pa]
σ	stress [Pa]
σ_ε	dense phase voidage standard deviation [-]
φ	angle of repose [rad or degrees]
φ_c	char combustion parameter [-]
φ_i	sphericity [-]
φ^*	specularity coefficient [-]

Sub-, Super- scripts

Ca	Calcium
cell	refers to computational cell
cl	cluster
col	collision part
eq	equilibrium
f	fuel index
FG	flue gas
fr	frictional
g	gas
i	species (reactants) index
j	species (products) index
kin	kinetic part
l	index for an Eulerian phase
max	maximum
mf	minimum fluidization
n	solid phase
p	particle
PR	products index
ps	particle surface
q	index for an Eulerian phase
r	reaction index
R	reactants index
s	solid phase
t	terminal
vol	volatiles or devolitilization

ABBREVIATIONS

A.R.	As received
BFB	Bubbling Fluidized Bed
CaL	Calcium Looping
CFB	Circulating Fluidized Bed
CFBC	Circulating Fluidized Bed Combustor
CFL	Courant–Friedrichs–Lewy condition
CPU	Central Processing Unit
CSTR	Continuous Stirred-Tank Reactor
DEM	Discrete Element Model
DFB	Dual Fluidized Bed
EMMS	Energy Minimization Multi - Scale
EU	European Union
FB	Fluidized Bed
FCC	Fluid catalytic cracking
FDE	Finite Difference Equations
FFT	Fast Fourier Transformation
FVM	Finite Volume Method
Gb	Gigabyte
IFK	Institut fur Feuerungs und Kraftwerkstechnik
KTGF	Kinetic Theory of Granular Fluids
MP-PIC	Multi - Phase Particle - In - Cell
MUSCL	Monotonic Upwind Scheme for Conservation Laws
n.a.	not applicable
N-S	Navier – Stokes
PDE	Partial Differential Equation
PSD	Particle Size Distribution
RAM	Random Access Memory
SIMPLE	Semi-Implicit Method for Pressure-Linked Equations
TFM	Two – Fluid – Model
TSI	Total Solids Inventory
UDF	User Defined Function
USTUTT	University of Stuttgart

REFERENCES

Abanades, C.J., Grasa, G., Alonso, M., Rodriguez, N., Anthony E. J., Romeo, L.M., 2007. Cost Structure of a Postcombustion CO_2 Capture System Using CaO. Environ. Sci. Technol. 41, 5523-5527.

Abanades, J.C., Anthony, E.J., Lu, D.Y., Salvador, C., Alvarez, D., 2004. Capture of CO_2 from combustion gases in a fluidized bed of CaO. AIChE Journal 50, 1614-1622.

Abbasi, E., Arastoopour, H., 2011. CFD simulation of CO_2 sorption in a circulating fluidized bed using deactivation kinetic model, in: Knowlton, T.M. (Ed.), Tenth International Conference on Circulating Fluidized Beds and Fluidization Technology, Sunriver, Oregon, pp. 736-743.

Afacan, O., Gogebakan, Y., SelÇUk∗, N., 2007. Modeling of NO_x emissions from Fluidized Bed Combustion of high volatile lignites. Combustion Science and Technology 179, 227-247.

Almuttahar, A., Taghipour, F., 2008. Computational fluid dynamics of a circulating fluidized bed under various fluidization conditions. Chemical Engineering Science 63, 1696-1709.

Andrews, M.J., O'Rourke, P.J., 1996. The multiphase particle-in-cell (MP-PIC) method for dense particulate flows. International Journal of Multiphase Flow 22, 379-402.

Arena, U., Langeli, C.B., Cammarota, A., 1998. L-valve behaviour with solids of different size and density. Powder Technology 98, 231-240.

Armesto, L., Boerrigter, H., Bahillo, A., Otero, J., 2003. N_2O emissions from fluidised bed combustion. The effect of fuel characteristics and operating conditions. Fuel 82, 1845-1850.

Atsonios, K., 2010. Υπολογιστική Διερεύνηση της Ισοθερμοκρασιακής Ροής σε Ρευστοποιημένη Κλίνη Ανακυκλοφορίας, Diplom thesis in Mechanical Engineer. NTUA, Athens.

Atsonios, K., Nikolopoulos, A., Karellas, S., Nikolopoulos, N., Grammelis, P., Kakaras, E., 2011. Numerical investigation of the grid spatial resolution and the anisotropic character of EMMS in CFB multiphase flow. Chemical Engineering Science 66, 3979-3990.

Basu, P., 1999. Combustion of coal in circulating fluidized-bed boilers: a review. Chemical Engineering Science 54, 5547-5557.

Basu, P., Cheng, L., 2000. An Analysis of Loop Seal Operations in a Circulating Fluidized Bed. Chemical Engineering Research and Design 78, 991-998.

Basu, P., Fraser, S., 1991. Circulating fluidized bed boilers: design and operations. Butterworth - Heinemann.

Benyahia, S., 2008. Verification and validation study of some polydisperse kinetic theories. Chemical Engineering Science 63, 5672-5680.

Benyahia, S., Arastoopour, H., Knowlton, T.M., Massah, H., 2000. Simulation of particles and gas flow behavior in the riser section of a circulating fluidized bed using the kinetic theory approach for the particulate phase. Powder Technology 112, 24-33.

Benyahia, S., Galvin, J.E., 2010. Estimation of numerical errors related to some basic assumptions in discrete particle methods. Industrial and Engineering Chemistry Research 49, 10588-10605.

Benyahia, S., Sundaresan, S., Do we need sub-grid scale corrections for both continuum and discrete gas-particle flow models? Powder Technology.

Bi, X.. Electrostatic Phenomena in Fluidized Systems: Present Status of understanding and research needs, in: Knowlton, T.M. (Ed.), Tenth International Conference on Circulating Fluidized Beds and Fluidization Technology - CFB-10, Sunriver, Oregon 2011, USA, pp 41 - 57

Blair, D.W., Wendt, J.O.L., Bartok, W., 1977. Evolution of nitrogen and other species during controlled pyrolysis of coal. 16th Symposium (International) on Combustion, pp 475-489.

Boelle, A., Balzer, G., Simonin, O., 1995. Second-order prediction of the particle-phase stress tensor of inelastic spheres in simple shear dense suspensions. Gas–Particle Flows ASME FED 228, 9-18.

Bonn, B., Pelz, G., Baumann, H., 1995. Formation and decomposition of N_2O in fluidized bed boilers. Fuel 74, 165-171.

Boutreux, T., Raphaël, E., De Gennes, P.G., 1997. Propagation of a pressure step in a granular material: The role of wall friction. Physical Review E - Statistical Physics, Plasmas, Fluids, and Related Interdisciplinary Topics 55, 5759-5773.

Chalermsinsuwan, B., Gidaspow, D., Piumsomboon, P., 2011. Two- and three-dimensional CFD modeling of Geldart A particles in a thin bubbling fluidized bed: Comparison of turbulence and dispersion coefficients. Chemical Engineering Journal 171, 301-313.

Chalermsinsuwan, B., Piumsomboon, P., Gidaspow, D., 2009[a]. Kinetic theory based computation of PSRI riser: Part I—Estimate of mass transfer coefficient. Chemical Engineering Science 64, 1195-1211.

Chalermsinsuwan, B., Piumsomboon, P., Gidaspow, D., 2009[b]. Kinetic theory based computation of PSRI riser: Part II—Computation of mass transfer coefficient with chemical reaction. Chemical Engineering Science 64, 1212-1222.

Charitos, A., Hawthorne, C., Bidwe, A.R., Korovesis, L., Schuster, A., Scheffknecht, G., 2010[a]. Hydrodynamic analysis of a $10kW_{th}$ Calcium Looping Dual Fluidized Bed for post-combustion CO_2 capture. Powder Technology 200, 117-127.

Charitos, A., Hawthorne, C., Bidwe, A.R., Sivalingam, S., Schuster, A., Spliethoff, H., Scheffknecht, G., 2010[b]. Parametric investigation of the calcium looping process for CO_2 capture in a $10kW_{th}$ dual fluidized bed. International Journal of Greenhouse Gas Control 4, 776-784.

Charitos, A., Hawthorne, C.C., Bidwe, A.R., Holz, H., Pfeifer, T., Schulze, A., Schlegel, D., Schuster, A., Scheffknecht, G., 2009. Parametric study on the CO_2 capture efficiency of the carbonate looping process in a 10 kW dual fluidized bed, pp. 583-589.

Charitos, A., Rodríguez, N., Hawthorne, C., Alonso, M., Zieba, M., Arias, B., Kopanakis, G., Scheffknecht, G., Abanades, J.C., 2011. Experimental validation of the calcium looping CO_2 capture process with two circulating fluidized bed carbonator reactors. Industrial and Engineering Chemistry Research 50, 9685-9695.

Charitos, A 2013. Experimental Characterization of the Calcium Looping Process for CO2 Capture. PhD thesis in Von der Fakultät Energie-, Verfahrens- und Biotechnik der Universität Stuttgart.

Chen, X., Wang, J. A comparison of two-fluid model, dense discrete particle model and CFD-DEM method for modeling impinging gas–solid flows.Powder Technology 254, 2014, 94-102

Chen, Z., Lin, M., Ignowski, J., Kelly, B., Linjewile, T.M., Agarwal, P.K., 2001. Mathematical modeling of fluidized bed combustion. 4: N_2O and NO_X emissions from the combustion of char. Fuel 80, 1259-1272.

Cheng, L., Basu, P., 1999. Effect of pressure on loop seal operation for a pressurized circulating fluidized bed. Powder Technology 103, 203-211.

Christakis, N., Chapelle, P., Patel, M.K., 2006. Analysis and modeling of heaping behavior of granular mixtures within a computational mechanics framework. Advanced Powder Technology 17, 383-398.

Christakis, N., Chapelle, P., Patel, M.K., Wang, J., Cross, M., 2002. Mathematical modelling of the behaviour of granular material in a computational fluid dynamics framework using micro- mechanical models, Fifth World Congress on Computational Mechanics, Vienna, Austria.

Chung, T.J., 2002. Computational Fluid Dynamics. Cambridge University Press.

Dartevelle, S., 2003. Numerical and granulometric approaches to geophysical granular flows. Michigan Technological University, USA. .

Dartevelle, S., 2004. Numerical modeling of geophysical granular flows: 1. A comprehensive approach to granular rheologies and geophysical multiphase flows. Geochemistry, Geophysics, Geosystems 5.

Dartevelle, S., Rose, W.I., Stix, J., Kelfoun, K., Vallance, J.W., 2004. Numerical modeling of geophysical granular flows: 2. Computer simulations of plinian clouds and pyroclastic flows and surges. Geochemistry, Geophysics, Geosystems 5.

Desroches-Ducarne, E., Dolignier, J.C., Marty, E., Martin, G., Delfosse, L., 1998. Modelling of gaseous pollutants emissions in circulating fluidized bed combustion of municipal refuse. Fuel 77, 1399-1410.

Ding, J., Gidaspow, D., 1990. A bubbling fluidization model using kinetic theory of granular flow. AIChE Journal 36, 523-538.

Dong, W., Wang, W., Li, J., 2008. A multiscale mass transfer model for gas–solid riser flows: Part 1 — Sub-grid model and simple tests. Chemical Engineering Science 63, 2798-2810.

Einstein, A., 1906. A new method of determinating molecular dimensions. Ann. Phys. Leipzig 19, 289-306.

Elaskar, S.A., Godoy, L.A., Gray, D.D., Stiles, J.M., 2000. A viscoplastic approach to model the flow of granular solids. International Journal of Solids and Structures 37, 2185-2214.

Engelhardt, W., 1989. Cognition of Life Phenomena. Nauka, Moscow.

Ergun, S., 1952. Fluid flow through packed columns. Chemical Engineering Progress 48, 89–94.

Field, M.A., 1969. Rate of combustion of size-graded fractions of char from a low-rank coal between 1,200 K and 2,000 K. Combustion and Flame 13, 237-252.

Fine, D.H., Slater, S.M., Sarofim, A.F., Williams, G.C., 1974. Nitrogen in coal as a source of nitrogen oxide emission from furnaces. Fuel 53, 120-125.

FLUENT, 2006. User Guide.

FLUENT, 2010. Theory Guide.

Gao, J., Chang, J., Lu, C., Xu, C., 2008. Experimental and computational studies on flow behavior of gas–solid fluidized bed with disparately sized binary particles. Particuology 6, 59-71.

Ge, W., Wang, W., Dong, W., Wang, J., Lu, B., Xiong, Q., Li, J., 2008. Meso-scale structure—A challenge of computational fluid dynamics for circulating fluidized bed risers, Proceedings of the 9th International Conference on Circulating Fluidized Beds Hamburg, pp. 19-37.

Ge, W., Wang, W., Yang, N., Li, J., Kwauk, M., Chen, F., Chen, J., Fang, X., Guo, L., He, X., Liu, X., Liu, Y., Lu, B., Wang, J., Wang, J., Wang, L., Wang, X., Xiong, Q., Xu, M., Deng, L., Han, Y., Hou, C., Hua, L., Huang, W., Li, B., Li, C., Li, F., Ren, Y., Xu, J., Zhang, N., Zhang, Y., Zhou, G., Zhou, G., 2011. Meso-scale oriented simulation towards virtual process engineering (VPE)—The EMMS Paradigm. Chemical Engineering Science 66, 4426-4458.

Geldart, D., 1973. Types of gas fluidization. Powder Technology 7, 285-292.

Geldart, D., 1986. Gas fluidization technology. John Wiley & Sons Ltd.

Geldart, D., Jones, P., 1991. The behaviour of L-valves with granular powders. Powder Technology 67, 163-174.

Gevrin, F., Masbernat, O., Simonin, O., 2008. Granular pressure and particle velocity fluctuations prediction in liquid fluidized beds. Chemical Engineering Science 63, 2450-2464.

Gidaspow, D., 1994. Multiphase flow and fluidization: Continuum and kinetic theory descriptions with applications, USA.

Gidaspow, D., Bezburuah, R., Ding, J., 1992. Hydrodynamics of circulating fluidized beds, kinetic theory approach, Fluidization VII, Proceedings of the 7th Engineering Foundation Conference on Fluidization. In O.E. Potter and D.J. Nicklin (Eds.), pp. 75-82.

Goel, S., Sarofim, A., Kilpinen, P., Hupa, M., 1996[a]. Emissions of nitrogen oxides from circulating fluidized-bed combustors: Modeling results using detailed chemistry. Symposium (International) on Combustion 26, 3317-3324.

Goel, S., Zhang, B., Sarofim, A.F., 1996[b]. NO and N_2O formation during Char combustion: Is it HCN or surface attached nitrogen? Combustion and Flame 104, 213-217.

Goodey, R.J., Brown, C.J., 2004. The influence of the base boundary condition in modelling filling of a metal silo. Computers and Structures 82, 567-579.

Goodey, R.J., Brown, C.J., Rotter, J.M., 2003. Verification of a 3-dimensional model for filling pressures in square thin-walled silos. Engineering Structures 25, 1773-1783.

Gray, D.D., Stiles, J.M., Celik, I., 1991. Theoretical and Numerical Studies of Constitutive Relations for Frictional Granular Flow.

Gu, W.K., Chen, J.C.. A model for solid concentration in circulating fluidized beds. L.S. Fan, T.M. Knowlton (Eds.), Fluidization, vol. IX, Engineering Foundation, Durago, Colorado (1998), pp. 501–508

Gulyurtlu, I., Esparteiro, H., Cabrita, I., 1994. N_2O formation during fluidized bed combustion of chars. Fuel 73, 1098-1102.

Gungor, A., 2008[a]. Analysis of combustion efficiency in CFB coal combustors. Fuel 87, 1083-1095.

Gungor, A., 2008[b]. Two-dimensional biomass combustion modeling of CFB. Fuel 87, 1453-1468.

Gungor, A., 2010. Simulation of emission performance and combustion efficiency in biomass fired circulating fluidized bed combustors. Biomass and Bioenergy 34, 506-514.

Gungor, A., Eskin, N., 2008[a]. Effects of operational parameters on emission performance and combustion efficiency in small-scale CFBCs. Journal of the Chinese Institute of Chemical Engineers 39, 541-556.

Gungor, A., Eskin, N., 2008[b]. Two-dimensional coal combustion modeling of CFB. International Journal of Thermal Sciences 47, 157-174.

Gunn, D.J., 1978. Transfer of heat or mass to particles in fixed and fluidised beds. International Journal of Heat and Mass Transfer 21, 467-476.

Hämäläinen, J., 2011. VTT's expertise in Fluidized Bed Combustion of Fossil Fuels and Biomass, BIOCLUS EU project

Harris, A.T., Davidson, J.F., Thorpe, R.B., 2002. The prediction of particle cluster properties in the near wall region of a vertical riser (200157). Powder Technology 127, 128-143.

Hartge, E.-U., Ratschow, L., Wischnewski, R., Werther, J., 2009. CFD-simulation of a circulating fluidized bed riser. Particuology 7, 283-296.

Hayhurst, A.N., Lawrence, A.D., 1996. The amounts of NO_x and N_2O formed in a fluidized bed combustor during the burning of coal volatiles and also of char. Combustion and Flame 105, 341-357.

Helland, E., Occelli, R., Tadrist, L., 2002. Computational study of fluctuating motions and cluster structures in gas-particle flows. International Journal of Multiphase Flow 28, 199-223.

http://www.gams.com/, . GAMS.

Hussain, A., Ani, F.N., Darus, A.N., Mustafa, A., Salema, A.A., 2005. Simulation studies of gas–solid in the riser of a circulating fluidized bed, 18th International Conference on Fluidized Bed Combustion, pp. 201–207.

Hussainova, I., Kubarsepp, J., Shcheglov, I., 1999. Investigation of impact of solid particles against hardmetal and cement targets. Tribology International 32, 337–344.

Ibsen, C.H., Helland, E., Hjertager, B.H., Solberg, T., Tadrist, L., Occelli, R., 2004. Comparison of multifluid and discrete particle modelling in numerical predictions of gas particle flow in circulating fluidised beds. Powder Technology 149, 29-41.

Jensen, A., Johnsson, J.E., Andries, J., Laughlin, K., Read, G., Mayer, M., Baumann, H., Bonn, B., 1995. Formation and reduction of NO_x in pressurized fluidized bed combustion of coal. Fuel 74, 1555-1569.

Johnson, P.C., Jackson, R., 1987. Frictional–collisional constitutive relations for granular materials, with application to plane shearing. Journal of Fluid Mechanics 176, 67-93.

Jung, J., Gidaspow, D., Gamwo, I.K. Design and Understanding of Fluidized-Bed Reactors. VDM Verlag Dr. Muller Aktiengesellschaft & Co. KG 2009.

Kallio, S., 2006. Characteristics of gas and solids mixing in a CFB deternibed from 3D CFD simulations 19th International conference on Fluidized bed Combustion, Austria.

Kilpinen, P., Hupa, M., 1991. Homogeneous N_2O chemistry at fluidized bed combustion conditions: A kinetic modeling study. Combustion and Flame 85, 94-104.

Kilpinen, P., Kallio, S., Konttinen, J., Barišić, V., 2002. Char-nitrogen oxidation under fluidised bed combustion conditions: single particle studies. Fuel 81, 2349-2362.

Kim, S.W., Kim, S.D., 2002. Effects of particle properties on solids recycle in loop-seal of a circulating fluidized bed. Powder Technology 124, 76-84.

Koksal, M., Hamdullahpur, F., 2005. CFD simulation of the gas-solid flow in the riser of a circulating fluidized bed with secondary air injection. Chemical Engineering Communications 192, 1151-1179.

Kramlich, J.C., Cole, J.A., McCarthy, J.M., Lanier, W.S., McSorley, J.A., 1989. Mechanisms of nitrous oxide formation in coal flames. Combustion and Flame 77, 375-384.

Kunii, D., Levenspiel, O., 1991. Fluidization Engineering (2nd Ed.). Boston: Butterworth-Heinemann.

Larsson, A., Seemann, M., Thunman, H., 2011. Temperature of Biomass Volatiles Leaving a Bubbling Fluidized Bed Gasifier, August 28-29 ed, Vienna University of Technology, Austria.

Laux, H., 1998. Modeling of dilute and dense dispersed fluid-particle flow. . NTNU Trondheim, Trondheim, Norway.

Le Bris, T., Cadavid, F., Caillat, S., Pietrzyk, S., Blondin, J., Baudoin, B., 2007. Coal combustion modelling of large power plant, for NO_x abatement. Fuel 86, 2213-2220.

Leithner, R., Müller, H., Müller, J., Schlutz, A., Vorckrodt, S., Wang, J., Papageorgiou, N., Kakaras, E., Ntouros, Z., Carvalho, M., Azevedo, J., Saraiva, P., 1993. Minimization of the formation of air pollutants in the CAFBC by using European fuels and additives

Leonard, B.P., Mokhtari, S., Lewis Research Center. Institute for Computational Mechanics in, P., 1990. ULTRA-SHARP nonoscillatory convection schemes for high-speed steady multidimensional flow. NASA; Institute for Computational Mechanics in Propulsion, NASA Lewis Research Center, Case Western Reserve University ; For sale by the National Technical Information Service, [Washington, D.C.]; [Cleveland, Ohio]; Springfield, Va.

Li, K., Thompson, S., Peng, J., 2004. Modelling and prediction of NOx emission in a coal-fired power generation plant. Control Engineering Practice 12, 707-723.

Liu, D., Kwauk, M., Li, H., 1996. Aggregative and particulate fluidization—The two extremes of a continuous spectrum. Chemical Engineering Science 51, 4045-4063.

Liu, H., Gibbs, B.M., 2002. Modelling of NO and N_2O emissions from biomass-fired circulating fluidized bed combustors. Fuel 81, 271-280.

Liu, H., Lu, H., 2009. Numerical study on the cluster flow behavior in the riser of circulating fluidized beds. Chemical Engineering Journal 150, 374-384.

Liu, S., Ha, Z., 2002. Prediction of random packing limit for multimodal particle mixtures. Powder Technology 126, 283-296.

Liu, X., 2005. Aggregation and lateral transfer behaviour of particles in gas–solid fluidized beds. , Institute of Process Engineering, Chinese Academy of Science, Beijing, PR China.

Lu, B., Wang, W., Li, J., 2009. Searching for a mesh-independent sub-grid model for CFD simulation of gas–solid riser flows. Chemical Engineering Science 64, 3437-3447.

Lun, C.K.K., Savage, S.B., Jeffrey, D.J., Chepurniy, N., 1984. Kinetic theories for granular flow: inelastic particles in Couette flow and slightly inelastic particles in a general flowfield. Journal of Fluid Mechanics 140, 223-256.

Ma, J., Ge, W., Wang, X., Wang, J., Li, J., 2006. High-resolution simulation of gas–solid suspension using macro-scale particle methods. Chemical Engineering Science 61, 7096-7106.

Ma, J., Ge, W., Xiong, Q., Wang, J., Li, J., 2009. Direct numerical simulation of particle clustering in gas–solid flow with a macro-scale particle method. Chemical Engineering Science 64, 43-51.

Magnussen, B.F., Hjertager, B.H., 1976. On mathematical models of turbulent combustion with special emphasis on soot formation and combustion. , 16th Symp. (Int'l.) on Combustion. The Combustion Institute.

Makkawi, Y.T., Wright, P.C., Ocone, R., 2006. The effect of friction and inter-particle cohesive forces on the hydrodynamics of gas–solid flow: A comparative analysis of theoretical predictions and experiments. Powder Technology 163, 69-79.

Mann, M.D., Collings, M.E., Botros, P.E., 1992. Nitrous oxide emissions in fluidized-bed combustion: Fundamental chemistry and combustion testing. Progress in Energy and Combustion Science 18, 447-461.

Manyele, S.V., Pärssinen, J.H., Zhu, J.X., 2002. Characterizing particle aggregates in a high-density and high-flux CFB riser. Chemical Engineering Journal 88, 151-161.

Mathiesen, V., Solberg, T., Hjertager, B.H., 2000. Predictions of gas/particle flow with an Eulerian model including a realistic particle size distribution. Powder Technology 112, 34-45.

Mukadi, L., Guy, C., Legros, R., 2000. Prediction of gas emissions in an internally circulating fluidized bed combustor for treatment of industrial solid wastes. Fuel 79, 1125-1136.

Myöhänen, K., Tanskanen, V., Hyppänen, T., Kurki-Rajamäki, R., Nevalainen, T., 2006. CFD modeling of fluidized bed system, Conference on Simulation and Modelling, Finland.

Naren, P.R., Lali, A.M., Ranade, V.V., 2007. Evaluating EMMS Model for Simulating High Solid Flux Risers. Chemical Engineering Research and Design 85, 1188-1202.

Nelson, P.F., Buckley, A.N., Kelly, M.D., 1992. Functional forms of nitrogen in coals and the release of coal nitrogen as NO_x precursors (HCN and NH_3). Symposium (International) on Combustion 24, 1259-1267.

Nguyen, T.D.B., Seo, M.W., Lim, Y.-I., Song, B.-H., Kim, S.-D., CFD simulation with experiments in a dual circulating fluidized bed gasifier. Computers & amp; Chemical Engineering.

Nikolopoulos, A., 2006. Hydrodynamic study and design of solid circulation devices and configurations for dual fluidised bed system for CO_2 capture. University of Stuttgart.

Nikolopoulos, A., Atsonios, K., Nikolopoulos, N., Grammelis, P., Kakaras, E., 2010[a]. An advanced EMMS scheme for the prediction of drag coefficient under a 1.2 MW_{th} CFBC isothermal flow-Part II: Numerical implementation. Chemical Engineering Science 65, 4089-4099.

Nikolopoulos, A., Atsonios, k., Nikolopoulos, N., Grammelis, P., Kakaras, E., 2012[a]. An advanced thermodynamic model for the simulation of the Calcium Looping Process coupled with CFD model. 2nd International Conference on Chemical Looping, Darmstadt, Germany.

Nikolopoulos, A., Nikolopoulos, N., Charitos, A., Grammelis, P., Kakaras, E., 2012[b]. 3-D TFM Full – Loop CFD simulation of CFBs. Addressing Proper Simulation of the Dense Flow within Pneumatic Valves., 21st International Conference on Fluidized Bed Combustion (FBC 21), Naples, Italy.

Nikolopoulos, A., Nikolopoulos, N., Varveris, N., Grammelis, P., Karellas, S., Kakaras, E., 2012[c] Investigation of proper modeling of very dense granular flows in the recirculation system of CFBs. Particuology 10 (6) pp 699-709.

Nikolopoulos, A., Papafotiou, D., Nikolopoulos, N., Grammelis, P., Kakaras, E., 2010[b]. An advanced EMMS scheme for the prediction of drag coefficient under a 1.2 MW_{th} CFBC isothermal flow-Part I: Numerical formulation. Chemical Engineering Science 65, 4080-4088.

Nikolopoulos, A., Rampidis, I., Nikolopoulos, N., Grammelis, P., Kakaras, E., 2009. Numerical investigation of 3-D transient combusting flow in a 1.2MW_{th} pilot power plant, pp. 839-844.

Nikolopoulos, N., Nikolopoulos, A., Karampinis, E., Grammelis, P., Kakaras, E., 2011. Numerical investigation of the oxy-fuel combustion in large scale boilers adopting the ECO-Scrub technology. Fuel 90, 198-214.

Ogawa, S., Umemura, A., Oshima, N., 1980. On the equations of fully fluidized granular materials. Zeitschrift für angewandte Mathematik und Physik ZAMP 31, 483-493.

Papafotiou, D., 2009. Ανάπτυξη και εφαρμογή μοντέλου EMMS για τη μελέτη της υδροδυναμικής πυκνών διφασικών ροών των ρευστοποιημένων κλινών, Diplom thesis in Mechanical engineering of NTUA, Athens.

Patankar, N.A., Joseph, D.D., 2001. Modeling and numerical simulation of particulate flows by the Eulerian–Lagrangian approach. International Journal of Multiphase Flow 27, 1659-1684.

Patil, D.J., Annaland, M., Kuipers, J., 2005. Critical comparison of hydrodynamic models for gas-solid fluidised beds. Part I: bubbling gas-solid fluidized bed operated with a jet. Chemical Engineering Science 60, 57–72.

Qi, X., Zeng, T., Huang, W., Zhu, J., Shi, Y., 2005. Experimental study of solids holdups inside particle clusters in CFB risers. Journal of Sichuan University 37, 46-50.

Rampidis, I., Nikolopoulos, A., Koukouzas, N., Grammelis, P., Kakaras, E., 2007. Optimization of computational performance and accuracy in 3-D transient CFD model for CFB hydrodynamics predictions, pp. 452-455.

Reuge, N., Cadoreta, L., Coufort-Saudejaud, C., Pannala, S., Syamlal, M., Caussat, B., 2008. Multifluid Eulerian modeling of dense gas–solids fluidized bed hydrodynamics: Influence of the dissipation parameters. Chemical Engineering Science 63, 5540-5551.

Rodriguez, N., Alonso, M., Abanades, J.C., Charitos, A., Hawthorne, C., Scheffknecht, G., Lu, D.Y., Anthony, E.J., 2011. Comparison of experimental results from three dual fluidized bed test facilities capturing CO_2 with CaO, pp. 393-401.

Schaeffer, D.G., 1987. Instability in the evolution equations describing incompressible granular flow. Journal of Differential Equations 66, 19-50.

Sharma, A.K., Tuzla, K., Matsen, J., Chen, J.C., 2000. Parametric effects of particle size and gas velocity on cluster characteristics in fast fluidized beds. Powder Technology 111, 114-122.

Shimizu, T., Hirama, T., Hosoda, H., Kitano, K., Inagaki, M., Tejima, K., 1999. A Twin Fluid-Bed Reactor for Removal of CO_2 from Combustion Processes. Chemical Engineering Research and Design 77, 62-68.

Shuai, W., Guodong, L., Huilin, L., Juhui, C., Yurong, H., Jiaxing, W., 2011[a]. Fluid dynamic simulation in a chemical looping combustion with two interconnected fluidized beds. Fuel Processing Technology 92, 385-393.

Shuai, W., Huilin, L., Guodong, L., Zhiheng, S., Pengfei, X., Gidaspow, D., 2011[b]. Modeling of cluster structure-dependent drag with Eulerian approach for circulating fluidized beds. Powder Technology 208, 98-110.

Shuai, W., Pengfei, X., Huilin, L., Yunchao, Y., Lijie, Y., Jiaxing, W., 2011[c]. Simulation of particles and gas flow behavior in a riser using a filtered two-fluid model. Chemical Engineering Science 66, 593-603.

Shuyan, W., Zhiheng, S., Huilin, L., Long, Y., Wentie, L., Yonlong, D., 2008. Numerical predictions of flow behavior and cluster size of particles in riser with particle rotation model and cluster-based approach. Chemical Engineering Science 63, 4116-4125.

Sitharam, T.G., Vinod, J.S., 2009. Critical state behaviour of granular materials from isotropic and rebounded paths: DEM simulations. Granular Matter 11, 33-42.

Smith, W. 1982. The combustion of coal chars: a review in 19th symposium on combustion. The combustion institute, pp 1045 – 1065.

Sofialidis, D., Faltsi, O., Sardi, K., Skevis, G., Skodras, G., Kaldis, S.P., Sakellaropoulos, G.P., 2005. Modelling low-temperature carbonisation of solid fuels in a heated rotary kiln for clean fuel production. Fuel 84, 2211-2221.

Soong, C.H., Tuzla, K., Chen, J.C., 1994. Identification of particle clusters in circulating fluidized bed, in: Avidan, A.A. (Ed.), Circulating Fluidized Bed Technology, pp. 615-620.

Soong, C.H., Tuzla, K., Chen, J.C., 1995. Experimental determination of cluster size and velocity in circulating fluidized bed., in: J.F. Large, C.L. (Ed.). Engineering Foundation, New York, pp. 219-227.

Srivastava, A., Sundaresan, S., 2003. Analysis of a frictional-kinetic model for gas-particle flow. Powder Technology 129 72–85.

Subbarao, D., 2010. A model for cluster size in risers. Powder Technology 199, 48-54.

Sundaresan, S., 2000. Modeling the hydrodynamics of multiphase flow reactors: Current status and challenges. AIChE Journal 46, 1102-1105.

Sundaresan, S., 2011. Reflections on mathematical models and simulation of gas-particle flows, in: Knowlton, T.M. (Ed.), Tenth International Conference on Circulating Fluidized Beds and Fluidization Technology - CFB-10, Sunriver, Oregon, USA 2011, pp. 21 - 40.

Syamlal, M., 1987. A Review of Granular Stress Constitutive Relations. National Technical Information Service, Springfield, VA.

Syamlal, M., Rogers, W., O'Brien, T.J., 1993. MFIX documentation: Theory guide. Technical Note DOE/METC-94/1004. Morgantown Energy Technology Centre, Morgantown, West Virginia.

Tardos, G.I., 1997. A fluid mechanistic approach to slow, frictional flow of powders. Powder Technology 92, 61-74.

Thomas, K.M., 1997. The release of nitrogen oxides during char combustion. Fuel 76, 457-473.

Tsuo, Y.P., Gidaspow, D., 1990. Computation of flow patterns in circulating fluidized beds. AIChE Journal 36, 885-896.

Tullin, C.J., Goel, S., Morihara, A., Sarofim, A.F., Beer, J.M., 1993. NO and N_2O Formation for Coal Combustion in a Fluidized Bed: Effect of Carbon Conversion and Bed Temperature,. Energy & Fuels 7, 796-802.

Tuzla, K., Sharma, A.K., Chen, J.C., Schiewe, T., Wirth, K.E., Molerus, O., 1998. Transient dynamics of solid concentration in downer fluidized bed. Powder Technology 100, 166-172.

Van Wachem, B.G.M., Schouten, J.C., Van den Bleek, C.M., Krishna, R., Sinclair, J.L., 2001. Comparative analysis of CFD models of dense gas-solid systems. AIChE Journal 47, 1035-1051.

Vashisth, S., Grace, J.R., 2011. Hydrodynamics of a cluster descending at the wall of a CFB riser: numerical study., in: Knowlton, T.M. (Ed.), Tenth International Conference on Circulating Fluidized Beds and Fluidization Technology - CFB-10, Sunriver, Oregon 2011, USA, pp. 553–560.

Versteeg, H.K., Malalasekera, W., 2007. An Introduction to Computational Fluid Dynamics, The Finite Volume Method. Pearson Educatiom Limited.

Vun, S., Naser, J., Witt, P., 2010. Extension of the kinetic theory of granular flow to include dense quasi-static stresses. Powder Technology 204, 11-20.

Wang, J., Ge, W., Li, J., 2008. Eulerian simulation of heterogeneous gas-solid flows in CFB risers: EMMS-based sub-grid scale model with a revised cluster description. Chemical Engineering Science 63, 1553-1571.

Wang, S., Gao, J., Lu, H., Liu, G., Xu, P., Sun, L., 2012[a]. Simulation of flow behavior of particles by cluster structure-dependent drag coefficient model for chemical looping combustion process: Air reactor modeling. Fuel Processing Technology 104, 219-233.

Wang W., Zhang, N., Lu, B., Li, J., 2012[b] Multiscale CFD : a practical approach for simulation of large-scale Fluidized Bed combustors, in 21st International Conference on Fluidized Bed Combustion (FBC 21), Naples, Italy 2012

Wang, W., Li, J., 2007. Simulation of gas–solid two-phase flow by a multi-scale CFD approach—of the EMMS model to the sub-grid level. Chemical Engineering Science 62, 208-231.

Wang, W., Lu, B., Zhang, N., Shi, Z., Li, J., 2010[a]. A review of multiscale CFD for gas–solid CFB modeling. International Journal of Multiphase Flow 36, 109-118.

Wang, W., Zhang, J., Yang, S., Zhang, H., Yang, H., Yue, G., 2010[b]. Experimental study on the angle of repose of pulverized coal. Particuology 8, 482-485.

Wang, X., Jiang, F., Lei, J., Wang, J., Wang, S., Xu, X., Xiao, Y., 2011. A revised drag force model and the application for the gas–solid flow in the high-density circulating fluidized bed. Applied Thermal Engineering 31, 2254-2261.

Wen, C.Y., Yu, Y.H., 1966. Mechanics of fluidization, Chemical Engineering Progress Symposium Series, pp. 100-111.

Winter, F., Wartha, C., Löffler, G., Hofbauer, H., 1996. The NO and N_2O formation mechanism during devolatilization and char combustion under fluidized-bed conditions. Symposium (International) on Combustion 26, 3325-3334.

Wójtowicz, M.A., Pels, J.R., Moulijn, J.A., 1993. Combustion of coal as a source of N_2O emission. Fuel Processing Technology 34, 1-71.

Wu, Y., Lu, J., Zhang, J., Liu, Q., Yue, G., Zhang, Y., 2004. Conceptual design of an 800MW_e supercritical pressure circulating fluidized bed boiler.

Yan, A., Manyele, S.V., Parssinen, J.H., Zhu, J.X., 2002. The interdependence of micro and macro flow structures under a high-flux flow, Proceedings of the Seventh International Circulating Fluidized Beds Conference Canadian Society for Chemical Engineering, Ottawa, pp. 357-364.

Yang, N., Wang, W., Ge, W., Li, J., 2003. Analysis of flow structure and calculation of drag coefficient for concurrent-up gas–solid flow. . Chinese Journal of Chemical Engineering 11, pp. 79–84.

Yang, W.-C., Knowlton, T.M., 1993. L-valve equations. Powder Technology 77, 49-54.

Yerushalmi, J., Turner, D.H., Squires, A.M., 1976. The fast fluidized bed. Industrial and Engineering Chemistry Process Design and Development 15, 47–53.

Yuu, S., Umekage, T., 2008. Constitutive Relations and Computer Simulation of Granular Material. Advanced Powder Technology 19, 203-230.

Zhang, D.Z., VanderHeyden, W.B., 2001. High-resolution three-dimensional numerical simulation of a circulating fluidized bed. Powder Technology 116, 133-141.

Zhang, N., Lu, B., Wang, W., Li, J., 2008. Virtual experimentation through 3D full-loop simulation of a circulating fluidized bed. Particuology 6, 529-539.

Zhang, Y., Ge, W., Wang, X., Yang, C., 2011. Validation of EMMS-based drag model using lattice Boltzmann simulations on GPUs. Particuology 9, 365-373.

Zhao, J., Brereton, C., Grace, J.R., Jim Lim, C., Legros, R., 1997. Gas concentration profiles and NO_x formation in circulating fluidized bed combustion. Fuel 76, 853-860.

Zhao, Y., Kim, H.Y., Yoon, S.S., 2007. Transient group combustion of the pulverized coal particles in spherical cloud. Fuel 86, 1102-1111.

Zhou, W., Zhao, C.S., Duan, L.B., Chen, X.P., Liang, C., 2011. Two-dimensional computational fluid dynamics simulation of nitrogen and sulfur oxides emissions in a circulating fluidized bed combustor. Chemical Engineering Journal 173, 564-573.

Zhou, Y.C., Xu, B.H., Yu, A.B., Zulli, P., 2002. An experimental and numerical study of the angle of repose of coarse spheres. Powder Technology 125, 45-54.

Zou, B., Li, H., Xia, Y., Ma, X., 1994. Cluster structure in a circulating fluidized bed. Powder Technology 78, 173-178.

Zou, R.P., Yu, A.B., Lin, X.Y., 1999. Packing of quaternary mixtures of fibrous particles. Journal of the American Ceramic Society 82, 933-938.

ΕΛΛΗΝΙΚΗ ΕΚΤΕΤΑΜΕΝΗ ΠΕΡΙΛΗΨΗ

1. ΕΙΣΑΓΩΓΗ

1.1 Τεχνολογία ρευστοποιημένων κλινών

Η παρούσα εργασία επικεντρώνεται στην προσομοίωση με τεχνικές υπολογιστικής ρευστοδυναμικής (CFD) ρευστοποιημένων κλινών ανακυκλοφορίας (CFB). Οι ρευστοποιημένες κλίνες ανακυκλοφορίας ως τεχνολογία εξελίχθηκε ραγδαία τις τελευταίες δεκαετίες. Η βασική εφαρμογή αυτών των αντιδραστήρων είναι η χρησιμοποίησή τους ως λεβήτων στην ηλεκτροπαραγωγή. Σε αυτή την εφαρμογή, για την καύση του καυσίμου εκτός του αέρα, εισάγεται και αδρανές υλικό στο λέβητα. Η παρουσία του αδρανούς υλικού σε υψηλές ποσότητες επιτυγχάνει ομοιόμορφο θερμοκρασιακό πεδίο εντός της κλίνης, χαμηλές θερμοκρασίες καύσης και αυξημένο χρόνο παραμονής για τα στερεά. Για αυτούς του λόγους οι λέβητες ρευστοποιημένης κλίνης ανακυκλοφορίας (Εικόνα 1.1) έχουν υψηλή απόδοση και διαθεσιμότητα και μπορούν να κάψουν αποτελεσματικά ένα μεγάλο εύρος καυσίμων. Επίσης, έχουν χαμηλές εκπομπές NO_x και μπορεί να εφαρμοστεί in situ αποθείωση. Ο αποτελεσματικός σχεδιασμός βιομηχανικής κλίμακας λεβήτων αυτής της τεχνολογίας απαιτεί νέα εργαλεία σχεδιασμού και βελτιστοποίησης.

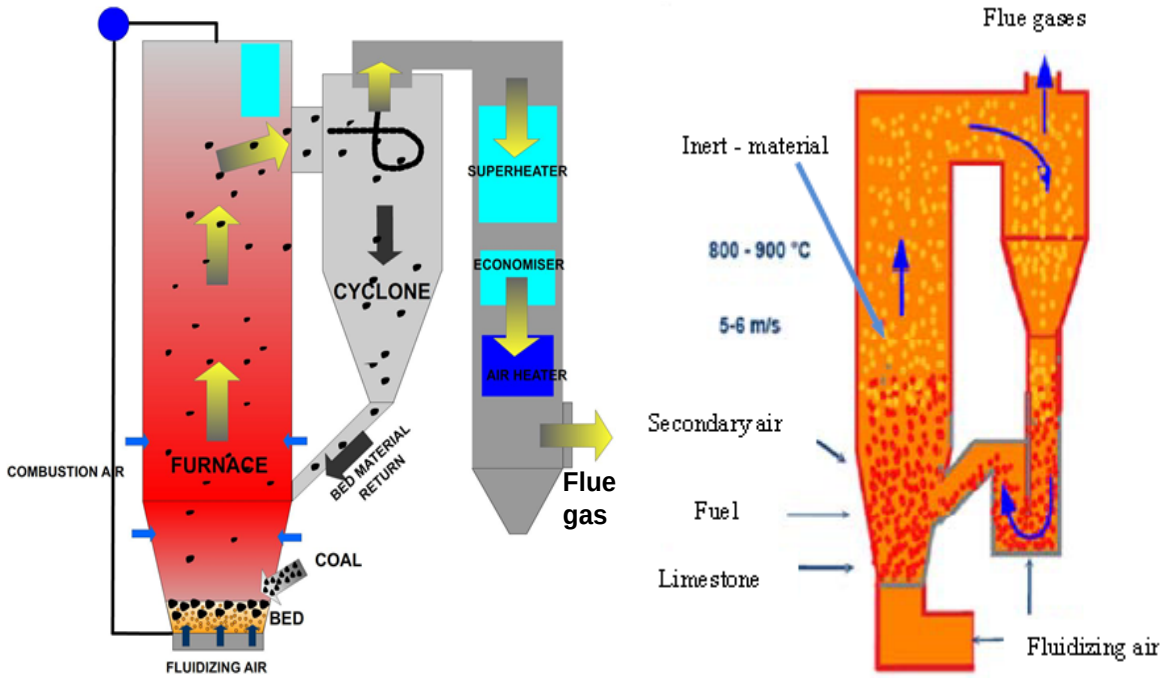

Σχήμα 1.1 Ρευστοποιημένες κλίνες ανακυκλοφορίας καύσης

Η δέσμευση CO_2 με τη διεργασία ενανθράκωσης / ασβεστοποίησης (calcium looping, CaL, εικόνα 1.2) είναι μια καινούργια εφαρμογή της τεχνολογίας ρευστοποιημένων κλινών ανακυκλοφορίας που μπορεί να χρησιμοποιηθεί και σε υφιστάμενες αλλά και σε καινούργιες ηλεκτροπαραγωγικές μονάδες, για τη μείωση των εκπομπών του διοξειδίου του άνθρακα. Αυτή η τεχνολογία αιχμής, προτάθηκε από τους Shimizu et al., 1999, και χρησιμοποιεί δύο υδροδυναμικά συζευγμένους (συζυγείς κλίνες, DFB) αντιδραστήρες ρευστοποιημένης κλίνης ανακυκλοφορίας , τον ενανθρακωτή και τον ασβεστοποιητή. Ο ενανθρακωτής είναι ένας καινούργιος αντιδραστήρας του οποίου ο βιομηχανικός σχεδιασμός θα παρουσιάσει δυσκολίες, αφού δεν υπάρχει αντίστοιχη εμπειρία. Η πειραματική διερεύνηση σημαντικών

τεχνικών ζητημάτων όπως η ανάμιξη των στερεών σε βιομηχανικής κλίμακας μονάδες έχει υψηλό οικονομικό κόστος, και μόνο τα μοντέλα υπολογιστικής ρευστοδυναμικής έχουν το αναγκαίο υπόβαθρο έτσι ώστε να τα διερευνήσουν αποτελεσματικά, και μάλιστα με πολύ μικρό κόστος.

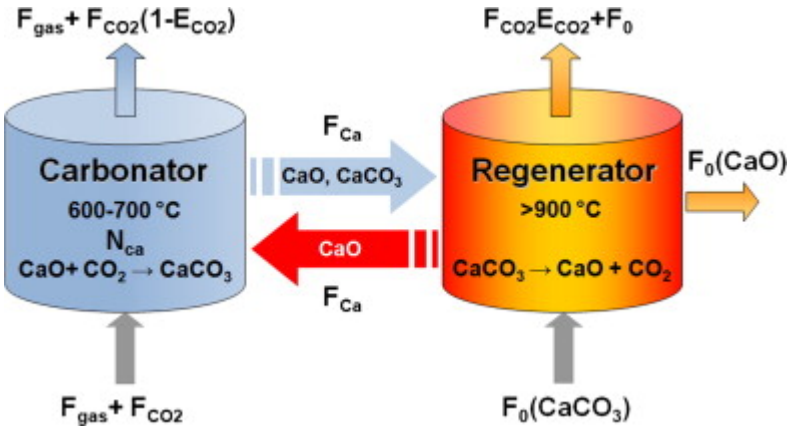

Σχήμα 1.2 Διεργασία κύκλου ενανθράκωσης / ασβεστοποίησης (Charitos et al., 2010[a])

1.2 CFD Μοντελοποίηση ρευστοποιημένων κλινών ανακυκλοφορίας

Ανάμεσα στις τεχνικές μοντελοποίησης ρευστοποιημένων κλινών ανακυκλοφορίας, η πιο συχνά εφαρμοζόμενη είναι η Two – Fluid –Model (TFM). Σε αυτή την προσέγγιση, το αέριο και το στερεό μοντελοποιούνται ως συνεχή αλληλοδιαπερατά μέσα. Αυτή η περιγραφή του φαινομένου με εξισώσεις κατά Euler, έχει διερευνηθεί αρκετά και έχει αποδειχθεί η ανωτερότητά της σε σύγκριση με τα συμβατικά μοντέλα σωματιδίων σε κελιά που χειρίζονται τα σωματίδια με εξισώσεις κατά Lagrange. Η βασική αιτία αυτής της υπεροχής είναι η αυξημένη φόρτιση σε σωματίδια των ρευστοποιημένων κλινών και η δυσκολία μοντελοποίησης των ενδο-σωματιδιακών αλληλεπιδράσεων με εξισώσεις του Lagrange.

Οι εξισώσεις του Lagrange δεν έχουν ακόμη ολοκληρωτικά εγκαταλειφθεί. Η νέα μέθοδος Multi - Phase Particle - In - Cell (MP-PIC) των Patankar and Joseph, 2001 και Andrews and O'Rourke, 1996, μοντελοποιεί τα σωματίδια κατά Lagrange αλλά ενσωματώνει κάποια χαρακτηριστικά της TFM μεθοδολογίας όπως αναφέρει ο Sundaresan, 2011.

Η μεθοδολογία TFM μπορεί να είναι πιο διαδεδομένη αλλά η ακρίβειά της πρέπει να αυξηθεί με ταυτόχρονη μείωση του μεγάλου υπολογιστικού της κόστους. Υπό αυτό το πρίσμα η πλειοψηφία των μελετητών επικεντρώνουν την έρευνά τους στη μοντελοποίηση ισοθερμοκρασιακών ροών. Υπάρχουν κάποιες λίγες εξαιρέσεις όπως οι Gungor, 2008[a, b], 2010 και Gungor and Eskin, 2008[a, b] που με μοντέλα υπολογιστικής ρευστοδυναμικής που χρησιμοποιούν όμως και κάποιες ημι-εμπειρικές σχέσεις καθώς και οι Zhou et al., 2011 και οι Nikolopoulos et al., 2009 με μοντέλα υπολογιστικής ρευστοδυναμικής, μοντελοποιούν ροές σε ρευστοποιημένες κλίνες ανακυκλοφορίας καύσης. Σε αυτά τα μοντέλα οι εξισώσεις ενέργειας και ρυπαντών ενσωματώνονται στο ισοθερμοκρασιακό μοντέλο.

Η κύρια πηγή σφαλμάτων είναι η μοντελοποίηση της οπισθέλκουσας. Οι Ge et al., 2008 αναφέρουν πως τα συμβατικά μοντέλα (π.χ. του Gidaspow, 1994 ή των Wen και Yu, 1966) υποθέτουν ομοιογενείς συνθήκες στον όγκο ελέγχου, υπόθεση που εν γένει δεν ανταποκρίνεται στην πραγματικότητα. Ο βασικός λόγος είναι ότι τα σωματίδια υπό συνθήκες ταχείας ρευστοποίησης σχηματίζουν συμπλέγματα (Gu and Chen, 1998). Τα συμπλέγματα σωματιδίων είναι δομές μέσο – κλίμακας (Wang and Li, 2007), επειδή το μέγεθός τους είναι σημαντικά μεγαλύτερο από τη διάμετρο των σωματιδίων και σημαντικά μικρότερο από τη διάμετρο ή το μήκος της μονάδας (βλέπε πίνακα 1.1).

.

	Μικρό - κλίμακα[a]	Μέσο - κλίμακα[b]	Μάκρο - κλίμακα
Μήκος	Μέση ελεύθερη διαδρομή σωματιδίων l_p $l_p = \frac{1}{6\sqrt{2}}\left(\frac{d_p}{\varepsilon_s}\right)$ - 3 mm, για ε_s = 0.01 - 0.3 mm, για ε_s = 0.1	Μέση διάμετρος σωματιδίων d_{cl} $d_{cl} = d_p + (0.027 - 10d_p)\varepsilon_s + 32\varepsilon_s^6$ - 0.5 mm, για ε_s = 0.01 - 2.7 mm, για ε_s = 0.1	Χαρακτηριστικό μήκος μονάδας (ή διάμετρος). - 0.1 ~ 1 m για εργαστηριακή κλίμακα - αρκετά μέτρα για βιομηχανικές εφαρμογές
Ταχύτητα	Ταχύτητα ταλαντώσεων $\sqrt{3\Theta_s}$ εύρος: 0.01 ~ 1 m/s	Ταχύτητα σωματιδιακών συμπλεγμάτων περίπου 1 m/s	Φαινόμενη ταχύτητα αερίου. για CFB, περίπου 5 m/s
Χρόνος ή συχνότητα	Συχνότητα σύγκρουσης σωματιδίων $f_c = 6.77\left(\frac{d_p}{\varepsilon_s}\right)\sqrt{\Theta_s}$ εύρος: 10 ~ 1000 Hz	Συχνότητα διάλυσης σωματιδιακών συμπλεγμάτων περίπου 20 Hz	Μέσος χρόνος παραμονής t_{res} για αέριο (~ δευτερόλεπτα) $t_{res} = L_H / U_o$ για στερεά (~ λεπτά) $t_{res} = TSI / G_s$

[a] Οι υπολογισμοί έγιναν με την κινητική θεωρία (Gidaspow, 1994), [b] (Gu and Chen, 1998)

Πίνακας 1.1 Χαρακτηριστικές κλίμακες μήκους (Wang and Li, 2007) για τα σωματίδια εντός ρευστοποιημένων κλινών ανακυκλοφορίας (d_p = 250, ρ_s = 2500 kg / m^3)

Σε συνθήκες ταχείας ρευστοποίησης, η αλληλεπίδραση ορμής μεταξύ αερίων και στερεών επηρεάζεται σε μεγάλο βαθμό από τα συμπλέγματα σωματιδίων. Η οπισθέλκουσα μειώνεται σημαντικά όταν τα σωματίδια οργανώνονται σε συμπλέγματα εν αντιθέσει με όταν είναι ομοιόμορφα διασκορπισμένα (Zhang et al., 2011). Συμπερασματικά, η υπόθεση του ομοιόμορφου διασκορπισμού, την οποία υιοθετούν όλα τα συμβατικά μοντέλα, μπορεί να οδηγήσει σε σημαντικά αριθμητικά σφάλματα όπως αναφέρουν και οι Ge et al., 2008, Wang et al., 2008 και Hartge et al., 2009, εάν εντός του όγκου ελέγχου υπάρχουν δομές μέσο – κλίμακας.

Οι Ge et al., 2008 και Zhang and VanderHeyden, 2001 αναφέρουν πως αυτά τα προβλήματα ενδέχεται να επιλυθούν με την εφαρμογή πολύ πυκνών αριθμητικών πλεγμάτων. Η κατάλληλη αδιαστασιοποιημένη πυκνότητα πλέγματος, l_r (ισοδύναμο μήκος κελιού προς μέση διάμετρο σωματιδίων) έχει εκτιμηθεί ότι πρέπει να είναι περίπου 20 (Nikolopoulos et al., 2010[a]). Παρ' όλα αυτά, αυτή η εκτίμηση δεν έχει επιβεβαιωθεί ακόμη και οι Lu et al., 2009 έδειξαν ότι για ένα περιοδικό διδιάστατο όγκο ελέγχου, το συμβατικό μοντέλο του Gidaspow αναπαρήγαγε αποτελέσματα με ανεξαρτησία πλέγματος για l_r 10, όπως φαίνεται και στο σχήμα 1.3. Στην πρωτότυπη εργασία τους, οι προαναφερθέντες ερευνητές μελέτησαν και το μοντέλο EMMS, που είναι ένα υποπλεγματικό μοντέλο που λαμβάνει υπ' όψη τα συμπλέγματα σωματιδίων, και βρήκαν πως αναπαραγάγει αποτελέσματα με ανεξαρτησία πλέγματος για αραιότερα πλέγματα.

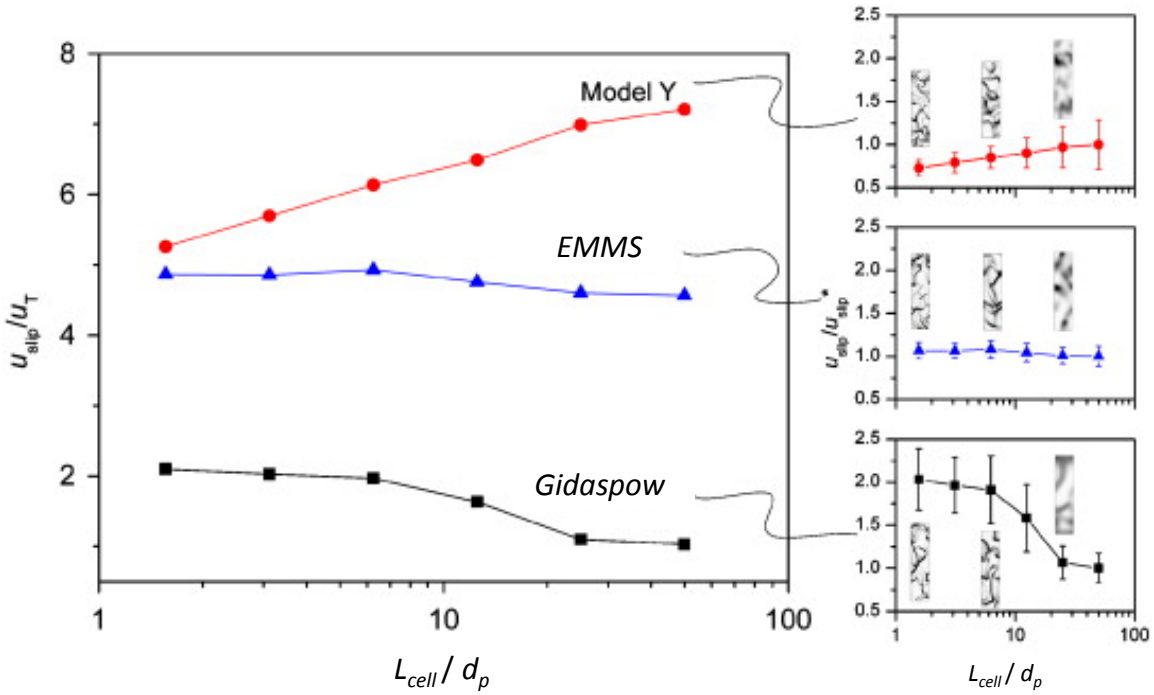

Σχήμα 1.3 Ανεξαρτησία πλέγματος για διάφορα μοντέλα οπισθέλκουσας (Lu et al., 2009)

Η εφαρμογή πολύ πυκνών πλεγμάτων έχει τεράστιο θεωρητικό ενδιαφέρον. Αντιθέτως, τα αραιά πλέγματα έχουν τεχνολογικό ενδιαφέρον, γιατί μόνο αραιά πλέγματα μπορούν να εφαρμοστούν σε βιομηχανικής κλίμακας μονάδες. Σε τέτοιες περιπτώσεις, η ικανότητα του μοντέλου EMMS να επιτυγχάνει ανεξαρτησία πλέγματος για σχετικά αραιά πλέγματα (Lu et al., 2009) είναι πολύ σημαντική, επειδή τα πυκνά πλέγματα λόγω του υπολογιστικού κόστους δεν μπορούν να εφαρμοστούν σε μεγάλης κλίμακας μονάδες. Συμπερασματικά, τα συμβατικά μοντέλα, όπως του Gidaspow, 1994 θεωρούνται ακατάλληλα για τη μοντελοποίηση μεγάλης κλίμακας ρευστοποιημένων κλινών ανακυκλοφορίας.

1.3 Εφαρμογή συμβατικών μοντέλων TFM σε βιομηχανική κλίμακα

Ο όρος συμβατικά μοντέλα αναφέρεται στην μοντελοποίηση του αγωγού ανόδου ρευστοποιημένης κλίνης ανακυκλοφορίας με την μεθοδολογία TFM και απλών μοντέλων οπισθέλκουσας όπως των Gidaspow, 1994 και των Wen and Yu, 1966, οι οποίες δεν λαμβάνουν υπ' όψη τα συμπλέγματα σωματιδίων.

Ένα πολύ καλό παράδειγμα της εφαρμογής συμβατικών μοντέλων σε μεγάλης κλίμακας κλίνες είναι η εργασία των Zhao et al., 1997. Ένα άλλο παράδειγμα είναι η μοντελοποίηση της μονάδας CFB800 που πραγματοποιήθηκε στα πλαίσια αυτής της διατριβής. Η μονάδα CFB800 είναι μια υπό σχεδιασμό 800 MW_{th} υπερκρίσιμη ρευστοποιημένη κλίνη ανακυκλοφορίας καύσης της Foster Wheeler. Ο όγκος του αγωγού ανόδου είναι τεράστιος, περίπου ίσος με 20.000 m^3. Το ισοθερμοκρασιακό μοντέλο που εφαρμόστηκε για την αριθμητική προσομοίωση της προαναφερθείσας μονάδας είναι ίδιο με το μοντέλο που περιγράφεται στην εργασία των Rampidis et al., 2007 ενώ για τον υπολογισμό της οπισθέλκουσας χρησιμοποιήθηκε το μοντέλου του Gidaspow.

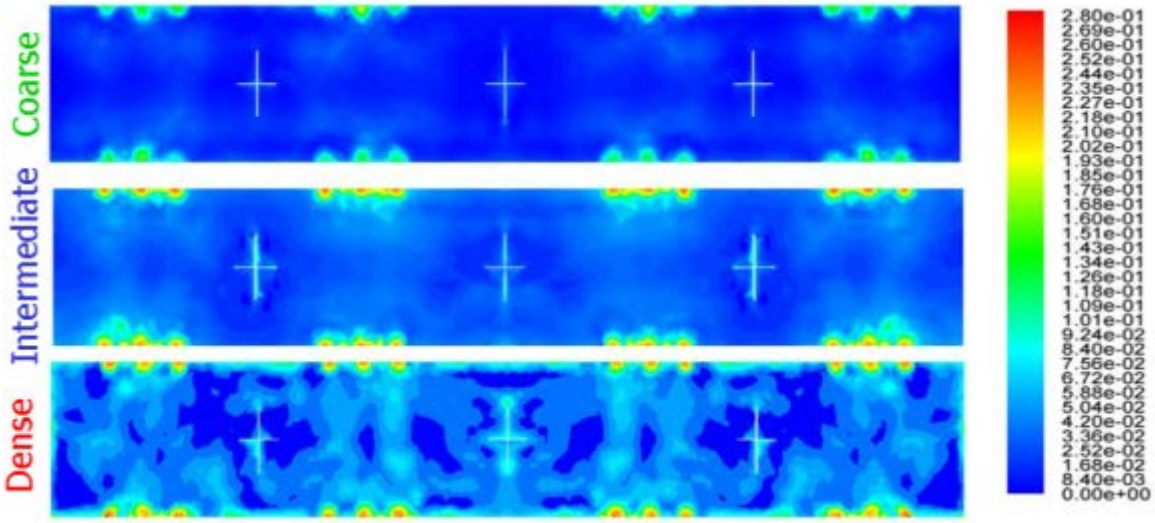

Σχήμα 1.4 Πρόλεξη του χρονικά μέσου ποσοστού όγκου σωματιδίων για ύψος 1 m της CFB800 για τρία διαφορετικά πλέγματα.

Για την εξαγωγή αντιπροσωπευτικών μέσων τιμών, έγινε δειγματοληψία για κατάλληλο χρονικό διάστημα (20 δευτερόλεπτα). Εν γένει, το υπολογιστικό μοντέλο επιτυχώς προέλεξε τυπικά ροϊκά φαινόμενα όπως το δακτύλιος-πυρήνας (core-annulus) και ο σχηματισμός συμπλεγμάτων σωματιδίων. Αυτά τα τυπικά ροϊκά φαινόμενα αναπαρήχθησαν υπολογιστικά ακόμη και υπό το αραιό πλέγμα. Στο σχήμα 1.4 συγκρίνονται τα αποτελέσματα των τριών διαφορετικών πλεγμάτων για ύψος 1 m.

Στο σχήμα 1.4, απεικονίζεται το μέσο (σταθμισμένο για περίοδο 20 δευτερολέπτων) ποσοστό όγκου του αδρανούς υλικού. Παρατηρώντας το σχήμα 1.4 είναι προφανές πως αν και το αραιό πλέγμα αναπαράγει τα κύρια ροϊκά φαινόμενα, εντούτοις υποεκτιμά εντόνως το ποσοστό όγκου των σωματιδίων. Οι προλέξεις του πυκνού πλέγματος (l_r = 444) θεωρούνται οι πιο αξιόπιστες όπως υποδεικνύεται και από διαβαθμισμένα στοιχεία της Foster Wheeler. Παρ' όλα αυτά, δεν επετεύχθη πλεγματική ανεξαρτησία, και είναι ιδιαιτέρως πιθανό περαιτέρω πύκνωση του πλέγματος να οδηγούσε σε διαφορετικά αποτελέσματα.

Τα αποτελέσματα υπολογιστικών μοντέλων που δεν είναι ανεξάρτητα του πλέγματος δεν είναι απολύτως αξιόπιστα. Επίσης, ακόμα και αν τα αποτελέσματα του πυκνού μοντέλου θεωρηθούν ακριβή, πρέπει να υπογραμμιστεί ότι το υπολογιστικό κόστος για μια τέτοια μοντελοποίηση είναι περίπου οχτώ μήνες σε ένα οχτα-πύρινο, 8 GB RAM SunV40 Server. Η μεγάλη διαφοροποίηση των αποτελεσμάτων των αραιότερων πλεγμάτων από τα αποτελέσματα του αντίστοιχου πυκνού τα καθιστά ακατάλληλα για τη μοντελοποίηση της μονάδας CFB800. Η υποεκτίμηση του ποσοστού όγκου των σωματιδίων οφείλεται κυρίως στην υπόθεση ομοιογενών συνθηκών σε τόσο μεγάλα κελιά η οποία οδηγεί στην υπερεκτίμηση της οπισθέλκουσας και την υποεκτίμηση της ταχύτητας ολίσθησης.

Το παράδειγμα της μοντελοποίησης της μονάδας CFB800, αναδεικνύει την ανάγκη για ένα νέο, εξελιγμένο μοντέλο οπισθέλκουσας που θα επιδεικνύει υψηλή ακρίβεια ακόμη και όταν χρησιμοποιούνται αραιά πλέγματα. Θα πρέπει να υπογραμμιστεί πως τα αριθμητικά σφάλματα που παρουσιάζονται στα αραιά πλέγματα πηγάζουν από το μοντέλο οπισθέλκουσας.

1.4 Καινοτομίες της παρούσας εργασίας

Αυτή η εργασία καταπιάνεται με την TFM μοντελοποίηση ρευστοποιημένων κλινών ανακυκλοφορίας και επικεντρώνεται σε: 1) την κατάλληλη μοντελοποίηση του συντελεστή

εναλλαγής ορμής μεταξύ αέριου και σωματιδίων (β), 2) την πλήρη (full – loop) μοντελοποίηση των μονάδων ρευστοποιημένης κλίνης ανακυκλοφορίας συμπεριλαμβανομένου του συστήματος ανακυκλοφορίας, και 3) την μοντελοποίηση αντιδράσεων που λαμβάνουν χώρα σε ρευστοποιημένες κλίνες.

Ένας τρόπος να αυξηθεί η ακρίβεια των μοντελοποιήσεων σε αραιά πλέγματα είναι η εφαρμογή εξελιγμένων μοντέλων για τον προσδιορισμό της οπισθέλκουσας που λαμβάνουν υπ' όψη την επίδραση των συμπλεγματικών σωματιδιακών δομών. Το μοντέλο Ελαχιστοποίησης Ενέργειας Μεσο – Κλιμάκων ή όπως αποκαλείται στην Αγγλική Energy Minimization Multi – Scale (EMMS), είναι ένα τέτοιο μοντέλο, και μπορεί να συζευχθεί με τα μοντέλα υπολογιστικής ρευστομηχανικής για να αντιμετωπίσει το προαναφερθέν πρόβλημα (Atsonios et al., 2011; Ge et al., 2011; Hartge et al., 2009; Naren et al., 2007; Nikolopoulos et al., 2010[a]; Nikolopoulos et al., 2010[b]; Wang et al., 2008; Wang and Li, 2007 και Zhang et al., 2011).

Η επίδραση των μίκρο- και μέσο- κλιμάκων αναλύθηκε παραπάνω. Ωστόσο, στις μονάδες CFB, η επίδραση φαινομένων μάκρο-κλίμακας είναι εξίσου σημαντική. Το πιο γνωστό τέτοιο φαινόμενο είναι το core-annulus. Υπό αυτό το πρίσμα, η πλήρης μοντελοποίηση των μονάδων ρευστοποιημένης κλίνης ανακυκλοφορίας, συμπεριλαμβανομένου του συστήματος ανακυκλοφορίας, κερδίζει έδαφος επειδή λαμβάνει υπ' όψη όλα τα φαινόμενα μάκρο-κλίμακας. Η πλήρης μοντελοποίηση των CFB (αγωγός ανόδου – κυκλώνας – αγωγός καθόδου – πνευματική βαλβίδα – αγωγός επανένωσης) πρέπει να αναπαριστά ορθά τις δυνάμεις τριβής μεταξύ των σωματιδίων στο σύστημα ανακυκλοφορίας (Nikolopoulos et al., 2012[c]) όπου η φόρτιση σε σωματίδια είναι σημαντικά μεγαλύτερη από αυτή του αγωγού ανόδου.

Η δεύτερη καινοτομία αυτής της δουλειάς αναφέρεται στην πλήρη μοντελοποίηση μονάδων CFB. Οι Ge et al., 2011; Shuai et al., 2011[a] και Wang et al., 2011διεξήγαγαν τέτοιες μοντελοποιήσεις αλλά δεν μελέτησαν την ορθή μοντελοποίηση του συστήματος ανακυκλοφορίας. Σε αυτή την εργασία για πρώτη φορά, μελετήθηκε η μοντελοποίηση του συστήματος ανακυκλοφορίας και διαμορφώθηκε κατάλληλος τανυστής των κοκκωδών τάσεων για την περίπτωση υψηλά φορτισμένων σε σωματίδια όγκων ελέγχου. Το νέο μοντέλο επαληθεύτηκε μέσω της μοντελοποίησης πειράματος για τη μέτρηση της γωνίας απόθεσης κοκκώδους υλικού. Σε δεύτερο στάδιο, το μοντέλο εφαρμόστηκε σε μια πλήρη μοντελοποίηση ενός κρύου μοντέλου (cold model) ρευστοποιημένης κλίνης ανακυκλοφορίας ενανθράκωσης.

Επίσης, αναπτύχθηκε κατάλληλο μοντέλο για την εισαγωγή κατανομής διαμέτρων σωματιδίων στην πλήρη TFM μοντελοποίηση. Οι εξισώσεις του μοντέλου που αναπτύχθηκαν στην παρούσα διατριβή έχουν ως αφετηρία την εφαρμογή της Κινητικής Θεωρίας Κοκκωδών Ροών (Kinetic Theory of Granular Flows, KTGF) σε συγκρούσεις σωματιδίων διαφορετικής διαμέτρου, σε αντίθεση με τα μοντέλα που εξετάζουν συγκρούσεις όμοιων σωματιδίων. Το υπολογιστικό κόστος του μοντέλου που αναπτύχθηκε είναι πάρα πολύ μεγάλο, για τους σημερινούς επεξεργαστές, και χρειάζονται πάνω από δύο χρόνια για την μοντελοποίηση μιας μικρής κλίμακας κλίνης. Ωστόσο, το μοντέλο μπορεί να εφαρμοστεί στο μέλλον, εφόσον η ταχύτητα των υπολογιστικών συστημάτων συνεχώς αυξάνεται. Μια τέτοια μοντελοποίηση, θα αναδείξει πόσο μεγάλο είναι το σφάλμα όταν εφαρμόζεται η απλούστευση πως όλα τα σωματίδια έχουν τις ίδιες ιδιότητες.

Σε αυτή την διατριβή, για πρώτη φορά μοντελοποιήθηκε μια μονάδα ρευστοποιημένης κλίνης ανακυκλοφορίας ενανθράκωσης. Η 10 KW_{th} μονάδα που μοντελοποιήθηκε είναι κομμάτι μιας πιλοτικής συζυγούς εγκατάστασης, που μελετά τη δέσμευση CO_2. Όσον αφορά στην υδροδυναμική μοντελοποίηση της μονάδας, εφαρμόστηκε το μοντέλο EMMS και ο νέος τανυστής για το σύστημα ανακυκλοφορίας. Η ενανθράκωση προσομοιώθηκε μέσω

δημοσιευμένων εξισώσεων οι οποίες αναδιατάχθηκαν ούτως ώστε να μπορούν να ενσωματωθούν στο μοντέλο υπολογιστικής ρευστοδυναμικής.

Κλείνοντας, μοντελοποιήθηκε η καύση στερεού καυσίμου (λιγνίτης) σε πιλοτική μονάδα ρευστοποιημένης κλίνης ανακυκλοφορίας καύσης (CFBC) με ισχύ 1.2 MW_{th}. Για αυτή την πολύπλοκη μοντελοποίηση χρησιμοποιήθηκαν απλοποιημένοι χημικοί μηχανισμοί και βασικά χημικά στοιχεία. Το μοντέλο αποτελείται από τρεις φάσεις μοντελοποιούνται με εξισώσεις Euler: 1) η αέρια φάση, ii) το αδρανές υλικό και iii) το καύσιμο. Η μοντελοποίηση της αλληλεπίδραση μεταξύ των φάσεων είναι δύσκολη και δεν υπάρχουν πολλές πληροφορίες στη βιβλιογραφία για αυτή. Επιπροσθέτως, μοντελοποιήθηκαν οι εκπομπές NO_x και N_2O με ένα απεπλεγμένο μοντέλο που αναπτύχθηκε στα πλαίσια αυτής της διατριβής. Το μοντέλο αυτό απεμπλέκει την επίλυση της καύσης από τη μοντελοποίηση των NO_x / N_2O. Το δίκτυο αντιδράσεων των NO_x / N_2O διαμορφώθηκε από διαθέσιμα βιβλιογραφικά δεδομένα. Το HCN και το CNO θεωρήθηκαν ως ενδιάμεσες ενώσεις στο σχηματισμό NO_x/N_2O. Τα αποτελέσματα της μοντελοποίησης συγκρίθηκαν με πειραματικά δεδομένα για τη μέση θερμοκρασία της κλίνης, για τις καθ' ύψος συγκεντρώσεις βασικών αερίων και των NO_x / N_2O.

2. ΜΟΝΤΕΛΟΠΟΙΗΣΗ ΚΟΚΚΩΔΩΝ ΡΟΩΝ

Σε αυτό το κεφάλαιο οι παρουσιάζονται εξισώσεις Euler / Euler, και η κινητική θεωρία των κοκκωδών ροών. Η εξέταση αυτών των εξισώσεων είναι σημαντική γιατί είναι ο πυρήνας της TFM. Σε αυτό το μοντέλο, ενσωματώνονται τα μοντέλα που αναπτύχθηκαν σε αυτή τη διατριβή.

2.1 Εξισώσεις

Οι εξισώσεις του Euler μπορούν να περιγράψουν την μη μόνιμη πολυφασική ροή εντός των ρευστοποιημένων κλινών. Αυτές οι κατά Euler (για το αέριο) – Euler (για το στερεό) μερικές διαφορικές εξισώσεις αναφέρονται στη διατήρηση μάζας και ενέργειας. Επιπροσθέτως, η διατήρηση της ενέργειας μπορεί να χρησιμοποιηθεί για την μοντελοποίηση ροών με θερμοκρασιακές διακυμάνσεις και αντιδράσεις. Συνήθως, εξαιτίας του μεγάλου υπολογιστικού κόστους, όλα τα σωματίδια θεωρούνται ίδιας διαμέτρου, με αποτέλεσμα όλα τα σωματίδια να περιγράφονται από μια εξίσωση που αναφέρεται στη μέση διάμετρο του μείγματος σωματιδίων. Η εξίσωση της συνέχειας για το αέριο και το στερεό (εξίσωση 2.1) εμπλέκει το ποσοστό όγκου των σωματιδίων και του αερίου. Εξ ορισμού, $\varepsilon_g + \varepsilon_s = 1$.

$$\begin{cases} \dfrac{\partial}{\partial t}\left(\varepsilon_g \rho_g\right) + \nabla \cdot \left(\varepsilon_g \rho_g \overrightarrow{u_g}\right) = 0 \\ \dfrac{\partial}{\partial t}\left(\varepsilon_s \rho_s\right) + \nabla \cdot \left(\varepsilon_s \rho_s \overrightarrow{u_s}\right) = 0 \end{cases} \qquad \text{Εξ. 2.1}$$

Η εξίσωση 2.2 περιγράφει τη διατήρηση της ορμής των δύο φάσεων.

$$\begin{cases} \dfrac{\partial}{\partial t}\left(\varepsilon_g \rho_g \overrightarrow{u_g}\right) + \nabla \cdot \left(\varepsilon_g \rho_g \overrightarrow{u_g}\overrightarrow{u_g}\right) = -\varepsilon_g \nabla p + \nabla \cdot \overline{\overline{\tau_g}} + \varepsilon_g \rho_g \vec{g} + \beta\left(\overrightarrow{u_s} - \overrightarrow{u_g}\right) \\ \dfrac{\partial}{\partial t}\left(\varepsilon_s \rho_s \overrightarrow{u_s}\right) + \nabla \cdot \left(\varepsilon_s \rho_s \overrightarrow{u_s}\overrightarrow{u_s}\right) = -\varepsilon_s \nabla p - \nabla p_s + \nabla \cdot \overline{\overline{\tau_s}} + \varepsilon_s \rho_s \vec{g} + \beta\left(\overrightarrow{u_g} - \overrightarrow{u_s}\right) \end{cases} \qquad \text{Εξ. 2.2}$$

Αξίζει να αναφερθεί πως οι εξισώσεις για τα σωματίδια είναι υπερβολικού τύπου ενώ για το αέριο ελλειπτικού (Tsuo and Gidaspow, 1990). Η περιγραφή των σωματιδίων κατά Euler έχει το πλεονέκτημα πως τα δισεκατομμύρια των σωματιδίων εντός της κλίνης περιγράφονται με χωρικές μεταβλητές, αλλά εγείρονται κάποια σημαντικά ερωτήματα. Έχουν η κοκκώδης πίεση και το ιξώδες, που εμπλέκονται στην εξίσωση 2.2, φυσική σημασία και πώς δύναται να υπολογιστούν; Ο Einstein, 1906 δημιούργησε μια θεωρία για τον υπολογισμό της κοκκώδους συνεκτικότητας για μεμονωμένα σωματίδια εντός ρευστού αλλά μόνο έπειτα από πολλά χρόνια οι Lun et al., 1984 κατάφεραν να παραθέσουν μια ολοκληρωμένη θεωρία για τον προσδιορισμό της κοκκώδους συνεκτικότητας και πίεσης. Η θεωρία τους βασίστηκε στην επέκταση της κινητικής θεωρία πυκνών αερίων για κοκκώδεις ροές.

Στην κινητική θεωρία κοκκωδών ροών τα σωματίδια και οι ταλαντώσεις στην ταχύτητά τους παραλληλίζονται με μόρια και με τις ταλαντώσεις τους αντίστοιχα. Συνεπώς η κοκκώδης θερμοκρασία (Θ_s) μπορεί να οριστεί (εξ. 2.3), σε επαλληλία με τον ορισμό της θερμοκρασίας των αερίων.

$$\Theta_s = \frac{1}{3}\left\langle \vec{c}^{\,2} \right\rangle \qquad \text{Εξ. 2.3}$$

Όπως φαίνεται και από την εξίσωση ο λόγος της αντίστοιχης σταθεράς του "Boltzmann" προς τη μάζα του κόκκου θεωρήθηκε ίσος με τη μονάδα. Επιπλέον, οι μίκρο-ταλαντώσεις της σωματιδιακής ταχύτητας θεωρούνται ισότροπες και η διασπορά τους ακολουθεί την κατανομή Maxwell – Boltzmann.

Σε πλήρη αντιστοιχία με την εξίσωση διατήρησης ενέργειας για τα αέρια, μια εξίσωση μπορεί να διατυπωθεί για την κοκκώδη θερμοκρασία (εξ. 2.4). Η εξίσωση αυτή μπορεί να απλουστευθεί εάν αγνοηθούν οι όροι διάχυσης και συναγωγής (Van Wachem et al., 2001). Με αυτή την απλούστευση προκύπτει η αλγεβρική εξίσωση 2.5.

$$\frac{3}{2}\left[\frac{\partial}{\partial t}\left(\varepsilon_s\rho_s\Theta_s\right)+\nabla\cdot\left(\varepsilon_s\rho_s\vec{u}_s\Theta_s\right)\right]=\left(-p_sI+\overline{\overline{\tau}}_s\right):\nabla\vec{u}_s+\nabla\cdot\left(k_{\Theta_s}\nabla\Theta_s\right)-\gamma_{\Theta_s}-3\beta\Theta_s \quad \text{Εξ. 2.4}$$

$$\left(-p_s\overline{\overline{I}}+\overline{\overline{\tau}}_s\right):\nabla\overrightarrow{u_s}-\gamma_{\Theta_s}-3\beta\Theta_s=0 \quad \text{Εξ. 2.5}$$

Η κοκκώδης πίεση (p_s) και οι τάσεις μπορούν να εκφραστούν μέσω της κινητικής θεωρίας. Η κοκκώδης πίεση ορίζεται μέσω καταστατικής εξίσωσης. Μια τέτοια εξίσωση είναι η 2.6, στην οποία ο πρώτος όρος αντιστοιχεί με την καταστατική εξίσωση των τέλειων αερίων, ενώ ο δεύτερος μοντελοποιεί τις ανελαστικές κρούσεις μεταξύ των σωματιδίων.

$$p_s=\varepsilon_s\rho_s\Theta_s+2\rho_s(1+e_{ss})\varepsilon_s^2g_{o,ss}\Theta_s \quad \text{Εξ. 2.6}$$

Οι διατμητικές τάσεις για το αέριο και το στερεό περιγράφονται από τους ακόλουθους τανυστές:

$$\begin{cases}\overline{\overline{\tau}}_g=\varepsilon_g\mu_g\left(\nabla\overrightarrow{u_g}+\nabla\overrightarrow{u_g}^T\right)-\left(\varepsilon_g\lambda_g-\frac{2}{3}\varepsilon_g\mu_g\right)\left(\nabla\cdot\overrightarrow{u_g}\right)\overline{\overline{I}}\\ \overline{\overline{\tau}}_s=\varepsilon_s\mu_s\left(\nabla\overrightarrow{u_s}+\nabla\overrightarrow{u_s}^T\right)-\left(\varepsilon_s\lambda_s-\frac{2}{3}\varepsilon_s\mu_s\right)\left(\nabla\cdot\overrightarrow{u_s}\right)\overline{\overline{I}}\end{cases} \quad \text{Εξ. 2.7}$$

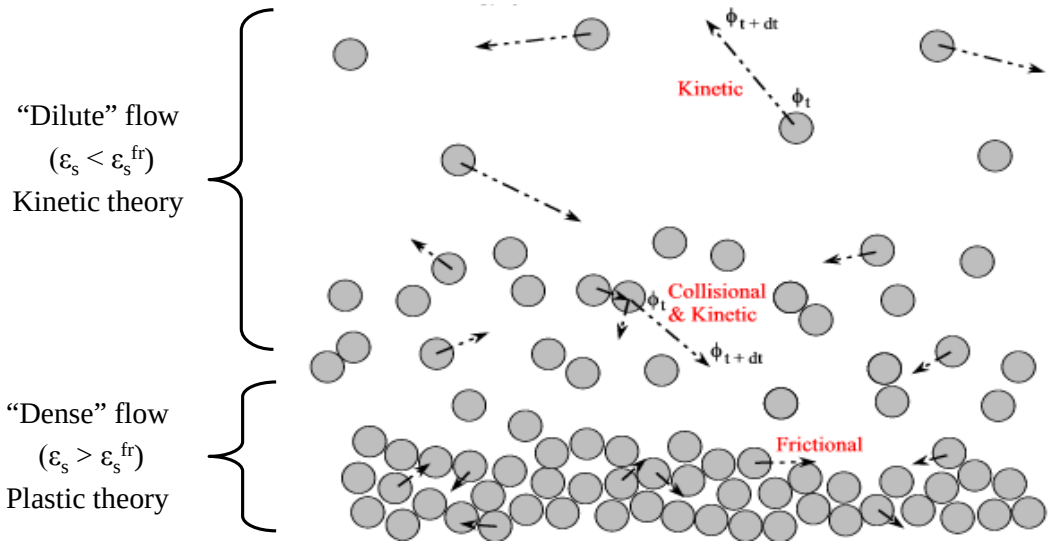

Σχήμα 2.1 Συνεκτικότητα σωματιδιακής φάσης (Dartevelle, 2003)

Για τον υπολογισμό του τανυστή των σωματιδιακών τάσεων χρειάζεται να προσδιοριστεί η διατμητική και η ορθή συνεκτικότητα του στερεού. Για τον υπολογισμό αυτών των όρων, η κινητική θεωρία κοκκωδών ροών δεν επαρκεί και πρέπει να επιστρατευθεί και η πλαστική θεωρία των παραμορφώσιμων στερεών για τις περιπτώσεις που η φόρτιση σε σωματίδια είναι τόσο μεγάλη που υπερισχύουν οι δυνάμεις τριβής μεταξύ των

σωματιδίων (σχήμα 2.1). Η διατμητική συνεκτικότητα υπολογίζεται ως το άθροισμα της κινητικής, προσκρουστικής και τριβικής συνεκτικότητας ($\mu_s = \mu_{s,kin} + \mu_{s,col} + \mu_{s,fr}$). Συνήθως, η συνεκτικότητα τριβής συνυπολογίζεται μόνο για πυκνούς όγκους ελέγχου ($\varepsilon_s > \varepsilon_{s,fr} = 0.5$). Οι εξισώσεις 2.8 (Gidaspow et al., 1992), 2.9 (Gidaspow et al., 1992) and 2.10 ((Schaeffer, 1987) ή (Johnson and Jackson, 1987) δύναται να χρησιμοποιηθούν για τον προσδιορισμό της κινητικής, προσκρουστικής και τριβικής συνεκτικότητας αντίστοιχα.

$$\mu_{s,kin} = \frac{10\rho_s d_s \sqrt{\Theta_s \pi}}{96\varepsilon_s (1+e_{ss}) g_o} \cdot [1+\frac{4}{5} g_o \varepsilon_s (1+e_{ss})]^2 \qquad \text{Εξ. 2.8}$$

$$\mu_{s,col} = \frac{4}{5}\varepsilon_s \rho_s d_s g_{o,ss} (1+e_{ss}) \sqrt{\frac{\Theta_s}{\pi}} \qquad \text{Εξ. 2.9}$$

$$\mu_{s,fr} = \frac{p_s \sin\phi}{2\varepsilon_s \sqrt{\mathrm{II}_{dD}}} \qquad \text{Εξ. 2.10}$$

Στην εξίσωση 2.10 η οποία ενεργοποιείται στην περιοχή της πλαστικής παραμόρφωσης η σωματιδιακή πίεση μπορεί να υπολογιστεί μέσω της εξίσωσης 2.6 ή από την εξίσωση των Johnson and Jackson, 1987 για την κοκκώδη πίεση τριβής. Στις εξισώσεις 2.8 – 2.10 η μεταβλητή $g_{o,ss}$ συμβολίζει τη συνάρτηση ακτινικής διασποράς. Επιπροσθέτως, λόγω μεταβολών του ποσοστού όγκου των σωματιδίων εντός όγκου ελέγχου (ψευδό-συμπιεστότητα), η κοκκώδης ορθή συνεκτικότητα πρέπει να προσδιορισθεί (Lun et al., 1984):

$$\lambda_s = \frac{4}{3}\varepsilon_s \rho_s d_s g_{0,ss} (1+e_{ss}) \left(\frac{\Theta_s}{\pi}\right)^{1/2} \qquad \text{Εξ. 2.11}$$

Επίσης, στην εξίσωση 2.2 εμπλέκεται ο συντελεστής εναλλαγής ορμής (β) μεταξύ των φάσεων. Ο συντελεστής αυτός μπορεί να υπολογιστεί από το συμβατικό μοντέλο του Gidaspow (εξ. 2.12), το οποίο συνδυάζει τις εξισώσεις των Wen and Yu, 1966 και του Ergun, 1952.

$$\beta = \begin{cases} \frac{3}{4} C_D \frac{\rho_g \varepsilon_g \varepsilon_s \left|\overrightarrow{u_g} - \overrightarrow{u_s}\right|}{d_s} \varepsilon_g^{-2.65}, & \varepsilon_s \le 0.2 \\ 150\frac{\varepsilon_s^2 \mu_g}{\varepsilon_g d_s^2} + 1.75 \frac{\rho_g \varepsilon_s \left|\overrightarrow{u_g} - \overrightarrow{u_s}\right|}{d_s}, & \varepsilon_s > 0.2 \end{cases} \qquad \text{Εξ. 2.12}$$

Ωστόσο, η εναλλαγή ορμής επηρεάζεται σημαντικά από φαινόμενα μεσο-κλίμακας (Ge et al., 2008) και οι Wang and Li, 2007 ισχυρίστηκαν πως η εξίσωση του Wen and Yu είναι αξιόπιστη μόνο για ομοιογενώς διασκορπισμένα σωματίδια. Η οπισθέλκουσα δύναμη είναι συνάρτηση του συντελεστή εναλλαγής ορμής και της ταχύτητας ολίσθησης ($u_{slip} = u_g - u_s$). Η δύναμη αυτή μπορεί να υπολογισθεί μέσω της εξίσωσης των Wen and Yu, 1966 ως:

$$F = F_{Wen,Yu} = \frac{3}{4} \cdot C_D \cdot \frac{\rho_g \varepsilon_g \varepsilon_s \cdot \left|u_g - u_s\right| \cdot \left(u_g - u_s\right)}{d_p} \cdot \varepsilon_g^{-2.65} \qquad \text{Εξ. 2.13}$$

$$C_D = \begin{cases} \left(24/\mathrm{Re}\right)\left(1+0.15\,\mathrm{Re}^{0.687}\right), & \mathrm{Re} < 1000 \\ 0.44, & \mathrm{Re} \ge 1000 \end{cases}, \qquad \mathrm{Re} = \frac{\rho_g \varepsilon_g d_p \left|\overrightarrow{u_g} - \overrightarrow{u_s}\right|}{\mu_g} \qquad \text{Εξ. 2.14}$$

2.2 Πυκνότητα πλέγματος

Οι Ge et al., 2008 και οι Wang et al., 2008 ανέφεραν πως τα συμβατικά μοντέλα υπολογιστικής ρευστοδυναμικής χρειάζονται πυκνά πλέγματα για να αναπαράγουν υψηλής ακρίβειας αποτελέσματα. Η πυκνότητα του πλέγματος μπορεί να εκφραστεί αδιάστατα ως ο λόγος του ισοδύναμου μήκους κελιού προς τη διάμετρο των σωματιδίων (l_r), όπως φαίνεται και στο σχήμα 2.2. Θεωρητικά, έχει προταθεί από τους Ge et al., 2008, ότι η πυκνότητα του πλέγματος που χρειάζεται για υψηλής ακρίβειας μοντελοποίηση με τα συμβατικά μοντέλα οπισθέλκουσας (π.χ. του Gidaspow) πρέπει να αντιστοιχεί σε l_r μικρότερο ή ίσο του 20. Βέβαια, η ορθότητα της συγκεκριμένης τιμής έχει αμφισβητηθεί από τα αποτελέσματα των Lu et al., 2009 που προτείνει ότι για πλεγματικά ανεξάρτητα αποτελέσματα το l_r πρέπει να είναι ίσο ή μικρότερο του 10. Τόσο πυκνά πλέγματα είναι δύσκολο να εφαρμοστούν ακόμη και σε μικρής κλίμακας μονάδας λόγω του μεγάλου υπολογιστικού κόστους, και για αυτό το λόγο δεν έχει ακόμη επιτευχθεί πλεγματική ανεξαρτησία σε τρισδιάστατες μοντελοποιήσεις. Προφανώς, το υπολογιστικό κόστος εκτινάσσεται σε μη αποδεκτά επίπεδα όσο το μέγεθος των μονάδων προς μοντελοποίηση μεγαλώνει αφού ο όγκος των μονάδων αυξάνεται αλλά η διάμετρος των σωματιδίων παραμένει περίπου ίδια.

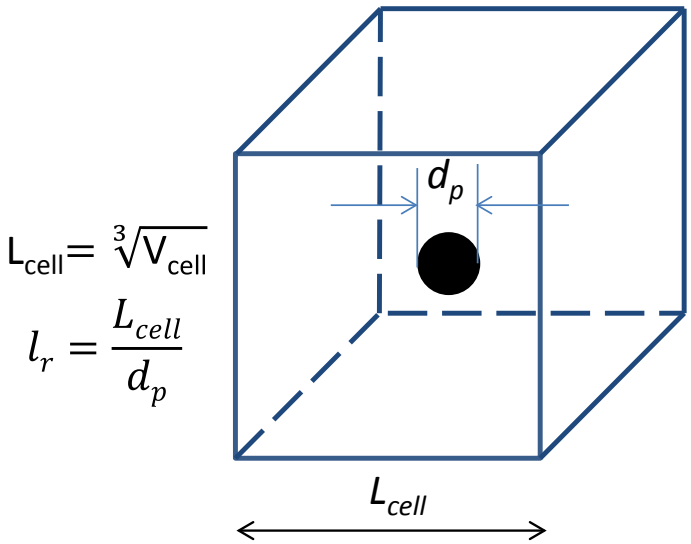

Σχήμα 2.2 Ορισμός του l_r

3. ΑΝΑΠΤΥΞΗ ΜΟΝΤΕΛΩΝ

Σε αυτό το κεφάλαιο παρουσιάζονται οι θεωρητικοί νεωτερισμοί αυτής της μελέτης που σχετίζονται με: α) το συντελεστή εναλλαγής ορμής (*β*), β) την ανάπτυξη ενός εναλλακτικού τανυστή των σωματιδιακών τάσεων για τους υψηλά φορτισμένους σε σωματίδια όγκους ελέγχου, γ) την ενσωμάτωση κατανομής σωματιδίων στη μεθοδολογία TFM, και δ) την ενσωμάτωση μηχανισμών μεταφοράς θερμότητας και μάζας στο υπολογιστικό μοντέλο.

3.1 Μοντέλο EMMS

Τα μοντέλα οπισθέλκουσας που βασίζονται στο μοντέλο EMMS, μπορούν να συζευχθούν με τα μοντέλα υπολογιστικής ρευστοδυναμικής έτσι ώστε να ξεπεραστούν τα προβλήματα που παρουσιάζονται από την επιλογή συμβατικών μοντέλων οπισθέλκουσας. Στα μοντέλα EMMS, η επίδραση των σωματιδιακών δομών μεσο-κλίμακας λαμβάνεται έμμεσα υπ' όψη μέσω υποπλεγματικής ανάλυσης. Τα αποτελέσματα ενός τέτοιου μοντέλου μπορούν να ενσωματωθούν σε κώδικες υπολογιστικής ρευστοδυναμικής μέσω του συντελεστή ετερογένειας (H_d):

$$\beta = \frac{3}{4} C_D \frac{\rho_g \varepsilon_g \varepsilon_s \left| \overrightarrow{u_g} - \overrightarrow{u_s} \right|}{d_s H_d} \varepsilon_g^{-2.65} \qquad \text{Εξ. 3.1}$$

Η ανάλυση EMMS διεξάγεται λαμβάνοντας υπ' όψη την υποπλεγματική ετερογένεια (Wang et al., 2008) και ορίζει δύο περιοχές. Οι περιοχές όπου τα σωματίδια έχουν υψηλό ποσοστό όγκου ορίζονται ως η πυκνή δομή. Αντιθέτως η περιοχή όπου τα σωματίδια είναι αραιά και ομοιογενώς κατανεμημένα ορίζεται ως η αραιή δομή. Το σχήμα 3.1 απεικονίζει τα συμπλέγματα σωματιδίων και τη μοντελοποίηση αυτών μέσω των δύο προαναφερθέντων δομών. Στην αραιή δομή, το αέριο κυριαρχεί έναντι των σωματιδίων, ενώ στην πυκνή δομή συμβαίνει το αντίθετο. Η επιφάνεια επαφής των δύο φάσεων ορίζει τα συμπλέγματα σωματιδίων που είναι μια δομή μεσο-κλίμακας που προκύπτει από το συμβιβασμό των σωματιδίων με τον αέρα (Liu et al., 1996).

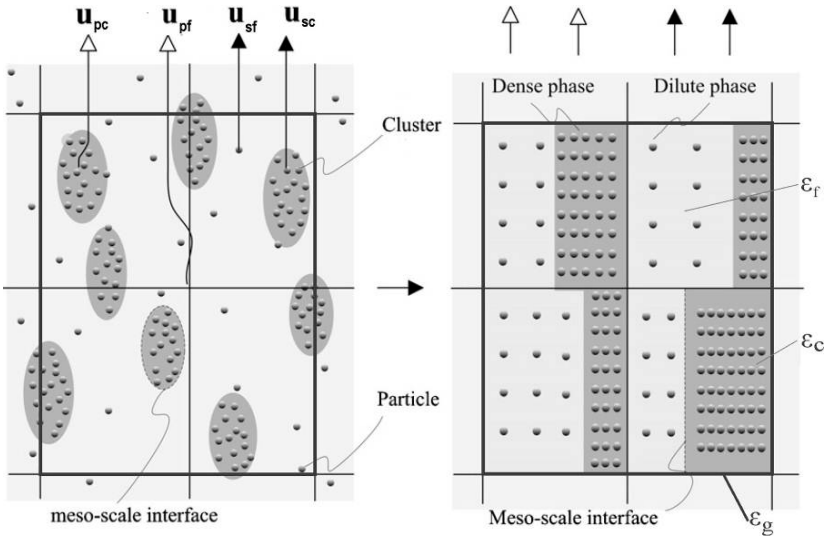

Σχήμα 3.1 Ροϊκές δομές εντός ενός όγκου ελέγχου (Dong et al., 2008).

Οι τρεις ροϊκές δομές (αραιή, πυκνή, επαφή) μαζί με την αλληλεπίδρασή τους χαρακτηρίζονται και από αντίστοιχες ταχύτητες οι οποίες ορίζονται στον πίνακα 3.1

(Papafotiou, 2009). Επίσης, στον πίνακα 3.2 συνοψίζονται σημαντικές εξισώσεις για τον υπολογισμό των συντελεστών οπισθέλκουσας κάθε φάσης (Wang et al., 2008).

$U_g = u_g \cdot \varepsilon_g$	$U_s = u_s \cdot \left(1-\varepsilon_g\right)$
$U_{sc} = \varepsilon_c \cdot u_{sc}$	$U_{sf} = \varepsilon_f \cdot u_{sf}$
$U_{si} = \left(1-f\right)\cdot \varepsilon_f \cdot u_{si}$	$U_{pf} = \left(1-\varepsilon_f\right)\cdot u_{sf}$
$U_{pc} = \left(1-\varepsilon_c\right)\cdot u_{sc}$	$U_c = \varepsilon_c \cdot u_c$
$U_f = \varepsilon_f \cdot u_f$	

Πίνακας 3.1 Φαινόμενες και πραγματικές ταχύτητες

	Πυκνή δομή	Αραιή Δομή	Διεπιφάνεια
Αισθητός συντελεστής οπισθέλκουσας	$C_{dc} = C_{d0}\varepsilon_c^{-4.65}$	$C_{df} = C_{d0f}\varepsilon_f^{-4.65}$	$C_{Di} = C_{Doi}(1-f)^{-4.65}$
Συντελεστής οπισθέλκουσας	$C_{d0c} = \frac{24}{\mathrm{Re}_c} + \frac{3.6}{\mathrm{Re}_c^{0.313}}$	$C_{d0f} = \frac{24}{\mathrm{Re}_f} + \frac{3.6}{\mathrm{Re}_f^{0.313}}$	$C_{d0i} = \frac{24}{\mathrm{Re}_i} + \frac{3.6}{\mathrm{Re}_i^{0.313}}$
Αριθμός Reynolds	$\mathrm{Re}_c = \frac{\rho_g d_p}{\mu_g}\left\|U_{sc}\right\|$	$\mathrm{Re}_f = \frac{\rho_g d_p}{\mu_g}\left\|U_{sf}\right\|$	$\mathrm{Re}_i = \frac{\rho_g d_{cl}}{\mu_g}\left\|U_{si}\right\|$
Φαινόμενη ταχύτητα ολίσθησης	$U_{sc} = U_c - \frac{\varepsilon_c \cdot U_{pc}}{1-\varepsilon_c}$	$U_{sf} = U_f - \frac{\varepsilon_f \cdot U_{pf}}{1-\varepsilon_f}$	$U_{si} = \left(1-f\right)\cdot\left(U_f - \frac{\varepsilon_f \cdot U_{pc}}{1-\varepsilon_c}\right)$
Δύναμη οπισθέλκουσας ανά σωματίδιο ή σύμπλεγμα	$F_c = C_{dc}\frac{\pi d_p^{\,2}}{4}\cdot\frac{\rho_g}{2}\cdot U_{sc}\cdot\left\|U_{sc}\right\|$	$F_f = C_{df}\frac{\pi d_p^{\,2}}{4}\cdot\frac{\rho_g}{2}\cdot U_{sf}\cdot\left\|U_{sf}\right\|$	$F_i = C_{di}\frac{\pi d_{cl}^{\,2}}{4}\cdot\frac{\rho_g}{2}\cdot U_{si}\cdot\left\|U_{si}\right\|$
Αριθμός σωματιδίων ή συμπλεγμάτων ανά όγκο	$m_c = \frac{f\cdot\left(1-\varepsilon_c\right)}{\frac{\pi d_p^{\,3}}{6}}$	$m_f = \frac{\left(1-f\right)\cdot\left(1-\varepsilon_f\right)}{\frac{\pi d_p^{\,3}}{6}}$	$m_i = \frac{f}{\frac{\pi d_{cl}^{\,3}}{6}}$

Πίνακας 3.2 Συντελεστές οπισθέλκουσας υποπλεγματικών δομών (Wang et al., 2008).

Η ισορροπία δυνάμεων για τα συμπλέγματα σωματιδίων και την αραιή δομή δίδονται από τις εξισώσεις 3.2 και 3.3 αντίστοιχα, ενώ η εξίσωση 3.4 αναφέρεται στην πτώση πίεσης εντός του όγκου ελέγχου (Wang et al., 2008; Yang et al., 2003).

$$\frac{3}{4}\cdot C_{dc}\frac{f\left(1-\varepsilon_c\right)}{d_p}\rho_g U_{sc}\left|U_{sc}\right| + \frac{3}{4}\cdot C_{di}\frac{f\rho_g}{d_{cl}}U_{si}\left|U_{si}\right| = f\left(1-\varepsilon_c\right)\cdot\left(\rho_s-\rho_g\right)\left(g+a_c\right) \quad \text{Εξ. 3.2}$$

$$\frac{3}{4}C_{df}\frac{\left(1-f\right)\left(1-\varepsilon_f\right)\cdot\rho_g}{d_p}U_{sf}\left|U_{sf}\right| = \left(1-f\right)\left(1-\varepsilon_f\right)\left(\rho_s-\rho_g\right)\left(g-a_f\right) \quad \text{Εξ. 3.3}$$

$$C_{df}\frac{\left(1-\varepsilon_f\right)\cdot\rho_g}{d_p}U_{sf}\left|U_{sf}\right|+\frac{f}{1-f}C_{di}\frac{\rho_g}{d_{cl}}U_{si}\left|U_{si}\right|=C_{dc}\frac{\left(1-\varepsilon_c\right)\cdot\rho_g}{d_p}U_{sc}\left|U_{sc}\right| \qquad \text{Εξ. 3.4}$$

Επιπροσθέτως, οι εξισώσεις διατήρησης μάζας για την αραιή και την πυκνή δομή και το μέσο κλάσμα όγκου του αέρα περιγράφονται από τις εξισώσεις 3.5, 3.6 και 3.7 αντίστοιχα.

$$U_f\left(1-f\right)+U_c f=u_g\cdot\varepsilon_g \qquad \text{Εξ. 3.5}$$

$$U_{pf}(1-f)+U_{pc}f=u_s(1-\varepsilon_g) \qquad \text{Εξ. 3.6}$$

$$\varepsilon_g=f\cdot\varepsilon_c+\left(1-f\right)\cdot\varepsilon_f \qquad \text{Εξ. 3.7}$$

Η τυπική απόκλιση της διακύμανσης του ποσοστού όγκου του αερίου εντός της πυκνής δομής μπορεί να υπολογιστεί από την εξίσωση 3.8 που ανεπτύχθη από τους Wang et al., 2008.

$$\sigma_\varepsilon=\varepsilon_s\sqrt{\frac{(1-\varepsilon_s)^4}{1+4\varepsilon_s+4{\varepsilon_s}^2-4{\varepsilon_s}^3+{\varepsilon_s}^4}} \qquad \text{Εξ. 3.8}$$

Το κλάσμα αερίου εντός της πυκνής δομής (ε_c) δύναται να προσεγγιστεί ως:

$$\varepsilon_c=\varepsilon_g-n\cdot\sigma_\varepsilon \qquad \text{Εξ. 3.9}$$

Η τιμή του συντελεστή *n* επιλέγεται με κάποιο βαθμό ελευθερίας (Wang et al., 2008). Οι Soong et al., 1994 και Soong et al., 1995 προτείνουν *n*=3 ενώ οι Liu, 2005, Sharma et al., 2000, Tuzla et al., 1998 *n* =2. Οι Gu and Chen, 1998 πρότειναν *n* =2.5 και οι Manyele et al., 2002, Qi et al., 2005 και Yan et al., 2002 *n* =1. Σε αντίθεση με αυτή τη προσέγγιση οι Wang and Li, 2007 όρισαν το ε_c ως ελεύθερη μεταβλητή.

Η διάμετρος των συμπλεγμάτων (d_{cl}) εκφράζει το χαρακτηριστικό μήκος της δομής μεσο-κλίμακας. Πειραματικές (Gu and Chen, 1998; Harris et al., 2002; Zou et al., 1994) ή θεωρητικές (Naren et al., 2007; Subbarao, 2010) εργασίες κατάφεραν να καταστρώσουν εμπειρικές και αναλυτικές εξισώσεις αντίστοιχα, για τον προσδιορισμό αυτού του μήκους. Στην παρούσα εργασία επιλέχθηκε η εξίσωση των Gu and Chen, 1998:

$$d_{cl}=d_p+\left(0.027-10\cdot d_p\right)\cdot\varepsilon_s+32\cdot{\varepsilon_s}^6 \qquad \text{Εξ. 3.10}$$

Επιπροσθέτως οι ακόλουθοι περιορισμοί (3.11 - 3.13) αντικατοπτρίζουν τα φυσικά όρια της αραιής και της πυκνής δομής.

$\varepsilon_{mf}\le\varepsilon_c$ (Naren et al., 2007; Wang and Li, 2007; Yang et al., 2003) Εξ. 3.11

$\varepsilon_f\le 0.9997$ (Wang et al., 2008; Wang and Li, 2007; Yang et al., 2003) Εξ. 3.12

$$\varepsilon_c<\varepsilon_g<\varepsilon_f \qquad \text{Εξ. 3.13}$$

Σε αυτή την εργασία ενσωματώθηκε στο μοντέλο EMMS και ο κάτωθι περιορισμός για την ταχύτητα ολίσθησης εντός της αραιής δομής

$U_{sf}/\varepsilon_f < U_t$ Εξ. 3.14

Το σύστημα των παραπάνω εξισώσεων (3.2 έως 3.14) μπορούν να επιλυθούν μέσω της ελαχιστοποίησης μιας συνάρτησης κόστους. Στο μοντέλο EMMS, επιβάλλεται η

ελαχιστοποίηση της ενέργειας που συναλλάσσεται μεταξύ του αερίου και του στερεού (N_{st}), για την αιώρηση και μεταφορά των σωματιδίων (Naren et al., 2007; Wang et al., 2008):

$$N_{st} = \left| \frac{1}{\left(1-\varepsilon_g\right)\cdot\rho_s} \left[m_f \cdot F_f \cdot U_f + m_c \cdot F_c \cdot U_c + m_i \cdot F_i \cdot U_f \cdot \left(1-f\right) \right] \right| \rightarrow \min imum \qquad \text{Εξ. 3.15}$$

Αν το παραπάνω μη γραμμικό πρόβλημα ελαχιστοποίησης επιλυθεί για δεδομένες συνθήκες εντός του όγκου ελέγχου, η οπισθέλκουσα μπορεί ύστερα να υπολογιστεί ως:

$$F_{EMMS} = \varepsilon_g \cdot \left[f \cdot \left(1-\varepsilon_c\right) \cdot \left(g + a_c\right) + \left(1-f\right) \cdot \left(1-\varepsilon_f\right) \cdot \left(g + a_f\right) \right] \cdot \left(\rho_s - \rho_g\right) \qquad \text{Εξ. 3.16}$$

Ωστόσο, η εξίσωση αυτή δεν επιβάλλεται άμεσα στο μοντέλο υπολογιστικής ρευστοδυναμικής, αλλά έμμεσα μέσω του συντελεστή ετερογένειας που υπολογίζεται μέσω της εξίσωσης 3.17. Στο μοντέλο υπολογιστικής ρευστοδυναμικής εφαρμόζεται η εξίσωση 3.1.

$$H_d = \frac{F_{Wen,Yu}}{F_{Emms}} \qquad \text{Εξ. 3.17}$$

3.2 Τανυστής των κοκκωδών τάσεων για το σύστημα ανακυκλοφορίας

Πρόσφατες υπολογιστικές μελέτες όπως των Nguyen et al.; Zhang et al., 2008 και των Shuai et al., 2011[a] μοντελοποιούν πλήρως (αγωγός ανόδου – κυκλώνας – αγωγός καθόδου – πνευματική βαλβίδα) τις μονάδες ρευστοποιημένης κλίνης ανακυκλοφορίας. Ωστόσο, σε αυτές τις εργασίες τα μοντέλα που εφαρμόζονται στον αγωγό ανόδου εφαρμόζονται και στο σύστημα ανακυκλοφορίας. Το ποσοστό όγκου των σωματιδίων στο σύστημα ανακυκλοφορίας όμως, είναι αρκετά υψηλότερο και οι φυσικοί μηχανισμοί που διέπουν την κοκκώδη ροή αρκετά διαφορετικοί. Τα συμβατικά μοντέλα TFM, όπως αυτά περιγράφτηκαν στο δεύτερο κεφάλαιο χρησιμοποιούν ένα τανυστή σωματιδιακών τάσεων βασισμένο στην κινητική θεωρία των κοκκωδών ροών για ποσοστό σωματιδιακής φόρτισης μικρότερα του ε_s^{fr}. Για πυκνότερες ροές εφαρμόζεται η θεωρία της πλαστικής παραμόρφωσης.

Η θεωρία της πλαστικής παραμόρφωσης χρειάζεται ένα κατάλληλο κριτήριο διαρροής και ένα κριτήριο ροής. Το κριτήριο διαρροής πρέπει να σέβεται τους πέντε κανόνες που παράθεσαν οι Gray et al., 1991. Το κριτήριο διαρροής στο τρισορθογώνιο σύστημα των κύριων τάσεων / ρυθμών παραμόρφωσης πρέπει να είναι: i) κυρτή επιφάνεια, ii) συμμετρικό ως προς τον υδροδυναμικό άξονα, iii) κλειστή επιφάνεια με τα δύο ακραία σημεία επί του υδροστατικού άξονα, iv) με ακτίνα ανάλογη των ορθών τάσεων, v) να έχει μη μηδενικό ρυθμό καταστροφής ενέργειας ($D_i : \sigma_i \geq 0$).

Το κριτήριο διαρροής του von Misses Yield χρησιμοποιείται ως επί των πλείστον στις μοντελοποιήσεις του αγωγού ανόδου (Nikolopoulos et al., 2010[a]; Nikolopoulos et al., 2010[b]; Tsuo and Gidaspow, 1990; Zhang and VanderHeyden, 2001; Zhang et al., 2008) μαζί με το κανόνα ροής των Levy-von Misses (Nikolopoulos et al., 2012[c]). Η εξίσωση του κριτήριου διαρροής είναι η 3.18 και απεικονίζεται στο σχήμα 3.5. Η εξίσωση 3.19 περιγράφει τον κανόνα ροής. Ένα κριτήριο διαρροής και ένας κανόνας ροής μπορούν να χρησιμοποιηθούν για την κατάστρωση εξισώσεων για τον υπολογισμό της τριβικής κοκκώδους συνεκτικότητας (Dartevelle, 2003).

$$Y = II_{\mathrm{dT}} + \left\langle \sigma \right\rangle^2 \sin^2 \varphi = 0 \qquad \text{Εξ. 3.18}$$

$$D_i = \xi \frac{\partial Y}{\partial \sigma_i} \qquad \text{Εξ. 3.19}$$

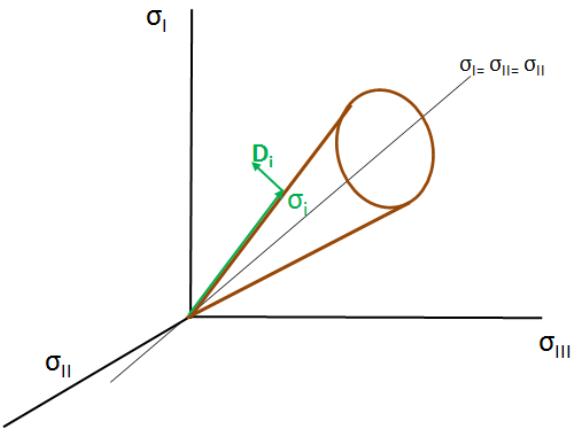

Σχήμα 3.5 Το κριτήριο διαρροής του von – Misses (Dartevelle, 2003)

Το κριτήριο διαρροής του von – Misses είναι μια κυρτή, συμμετρική επιφάνεια με ακτίνα ανάλογη των ορθών τάσεων αλλά δεν είναι κλειστή επιφάνεια. Επίσης, τα διανύσματα του ρυθμού παραμόρφωσης και της τάσης είναι κάθετα με αποτέλεσμα ο ρυθμός καταστροφής ενέργειας να είναι πάντα μηδενικός. Επιπροσθέτως, το προαναφερθέν κριτήριο δεν αντιλαμβάνεται την επιπρόσθετη αντίσταση στην διαρροή κατά την διάρκεια πύκνωσης ενός όγκου ελέγχου.

Αυτές οι αδυναμίες, δύναται να ξεπεραστούν με την εφαρμογή του κριτηρίου διαρροής των Pitman-Schaeffer-Gray-Stiles:

$$Y = II_{\mathrm{dT}} + \sin^2\varphi\left[\left(\langle\sigma\rangle - P\right)^2 - P^2\right] = 0, \qquad \text{Εξ. 3.20}$$

$$\langle\sigma\rangle = P - \lambda\nabla\cdot\vec{u}_{\mathrm{s}}. \qquad \text{Εξ. 3.21}$$

Το σχήμα 3.6 απεικονίζει το εξελιγμένο κριτήριο διαρροής των Pitman-Schaeffer-Gray-Stiles. Το κριτήριο αυτό δεν είναι μια επιφάνεια αλλά ομάδα επιφανειών. Αλλαγές στη φόρτιση του όγκου από σωματίδια μετασχηματίζουν την επιφάνεια του κριτήριου διαρροής.

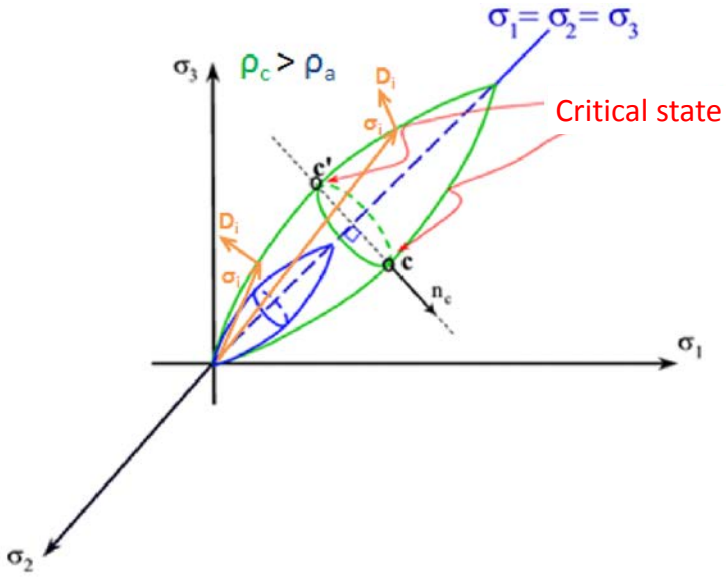

Σχήμα 3.6 Κριτήριο διαρροής των Pitman - Schaeffer - Gray – Stiles (Dartevelle, 2003)

Θα πρέπει να υπογραμμιστεί πως το κριτήριο διαρροής των Pitman - Schaeffer - Gray – Stiles Yield είναι μια κυρτή, συμμετρική, κλειστή επιφάνεια με ακτίνα ανάλογη των ορθών τάσεων. Επιπροσθέτως ο ρυθμός καταστροφής ενέργειας δεν είναι μηδενικός ($D_i : \sigma_i > 0$), με εξαίρεση την κρίσιμη κατάσταση.

Οι δυνάμεις τριβής μεταξύ των σωματιδίων είναι η πιο σημαντική δύναμη για μεγάλα ποσοστά όγκου σωματιδίων. Η γωνία απόθεσης είναι το χαρακτηριστικό των κοκκωδών μειγμάτων που επηρεάζεται περισσότερο από τις προαναφερθείσες δυνάμεις. Στην παρούσα διατριβή, ένας τανυστής αναπτύχθηκε για τις κοκκώδεις τάσεις με βάση το κριτήριο διαρροής των Pitman - Schaeffer - Gray – Stiles. Ο τανυστής αρχικά εξετάστηκε για λόγους επαλήθευσης στη μοντελοποίηση ενός πειράματος μέτρησης της γωνίας απόθεσης κοκκώδους υλικού. Σε αυτή τη διερεύνηση εξετάστηκε και το συμβατικό κριτήριο διαρροής. Θα πρέπει να τονιστεί, ότι αυτή η διερεύνηση διεξάγεται για πρώτη φορά υιοθετώντας την περιγραφή κατά Euler του πεδίου της διφασικής ροής.

3.2.1 Μεθοδολογία μοντελοποίησης γωνίας απόθεσης

Με σκοπό την επαλήθευση του μοντέλου για τις δυνάμεις τριβής μεταξύ των σωματιδίων μοντελοποιήθηκε ένα πείραμα προσδιορισμού της γωνίας απόθεσης κοκκώδους υλικού. Το πείραμα πραγματοποιήθηκε στις εγκαταστάσεις του IFK από το Nikolopoulos, 2006.Η εγκατάσταση αποτελείται από δύο απλούς κυλινδρικούς σωλήνες διαμέτρου 40 mm. Το μήκος των αγωγών είναι 2 m, σχήμα 3.7. Το κοκκώδες υλικό που αποτέθηκε ήταν διαμέτρου 462 μm και πυκνότητας 2600 kg/m^3.

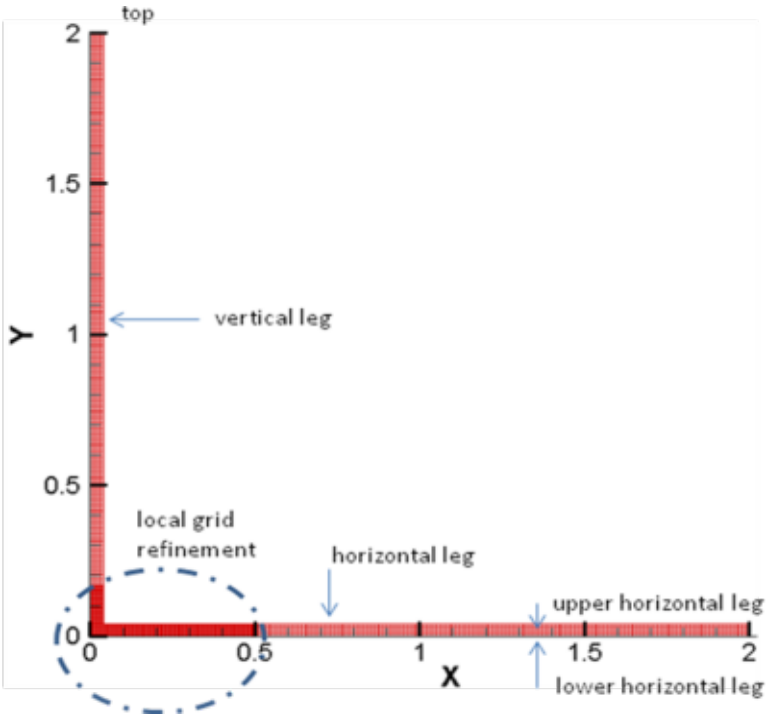

Σχήμα 3.7 Γεωμετρικά χαρακτηριστικά της διάταξης και υπολογιστικό πλέγμα

Το κοκκώδες υλικό εισάγεται από τον κάθετο αγωγό και πραγματοποιεί ελεύθερη πτώση έως ότου φτάσει στον οριζόντιο αγωγό. Εκεί αποτίθεται σχηματίζοντας ένα κώνο του οποίου η γωνία βάσης είναι η γωνία απόθεσης του υλικού (φ). Για το υπό διερεύνηση κοκκώδες υλικό η γωνία αυτή μετρήθηκε 36.03^o.

Η αριθμητική διερεύνηση επικεντρώθηκε στη μοντελοποίηση αυτού του πειράματος με την εφαρμογή δύο διαφορετικών μοντέλων για τον τανυστή της σωματιδιακή φάσης, το συμβατικό και το νέο που βασίζεται στο κριτήριο διαρροής των Pitman - Schaeffer - Gray – Stiles. Η διερεύνηση έγινε σε δύο διαστάσεις για λόγους υπολογιστικού κόστους. Για τον

υπολογισμό του συντελεστή εναλλαγής ορμής (β) χρησιμοποιήθηκε το μοντέλο του Gidaspow (Ding and Gidaspow, 1990). Επίσης χρησιμοποιήθηκε η αλγεβρική έκφραση για την κοκκώδη θερμοκρασία. Τα σωματίδια θεωρήθηκαν σφαιρικά (φ_i ίσο με 1) και αγνοήθηκε η κατανομή διαμέτρων τους.

Ο αριθμητικός κάναβος αποτελείται από 2352 τετραεδρικά στοιχεία. Το χρονικό βήμα των υπολογισμών τέθηκε ίσο με 40 μs, και δεύτερης τάξης σχήματα εφαρμόστηκαν για τη χωρική διακριτοποίηση.

3.2.1.1 Συμβατικό μοντέλο τάσεων (περίπτωση Α)

Για το κριτήριο διαρροής του von-Misses ο τανυστής των σωματιδιακών τάσεων δίνεται από τις εξισώσεις 3.22 έως 3.25:

$$\overline{\overline{\tau}}_s = \varepsilon_s \mu \left(\nabla \vec{u}_s + \nabla \vec{u}_s^{\,T} \right) + \varepsilon_s \left(\lambda - \frac{2}{3}\mu \right) \nabla \cdot \vec{u}_s I \qquad \text{Εξ. 3.22}$$

$$\lambda = \begin{cases} \varepsilon_s < \varepsilon_{fr} \Rightarrow \dfrac{4}{3}\varepsilon_s \rho_s d_s g_o (1+e_{ss}) \left(\dfrac{\Theta_s}{\pi} \right)^{\frac{1}{2}} \\ \varepsilon_s \geq \varepsilon_{fr} \Rightarrow \lambda_{fr} \end{cases} \qquad \text{Εξ. 3.23}$$

$$P_s = \begin{cases} \varepsilon_s < \varepsilon_s^{fr} \Rightarrow P_{kin} = \varepsilon_s \rho_s \Theta_s + 2\rho_s (1+e_{ss}) \varepsilon_s^2 g_o \Theta_s \\ \varepsilon_s \geq \varepsilon_s^{fr} \Rightarrow P_{fr} = 0.1 \varepsilon_s \dfrac{\left(\varepsilon_s - \varepsilon_s^{fr} \right)^2}{\left(\varepsilon_s^{\max} - \varepsilon_s \right)^5} \end{cases} \qquad \text{Εξ. 3.24}$$

(Johnson and Jackson, 1987)

$$\mu = \begin{cases} \varepsilon_s < \varepsilon_s^{fr} \Rightarrow \mu_{kin} + \mu_{col} \\ \varepsilon_s \geq \varepsilon_s^{fr} \Rightarrow \mu_{kin} + \mu_{col} + \mu_{fr} \end{cases} \qquad \text{Εξ. 3.25}$$

$$\mu_{kin} = \frac{10 \rho_s d_s \sqrt{\Theta_s \pi}}{96 \varepsilon_s (1+e_{ss}) g_o} \cdot \left[1 + \frac{4}{5} g_o \varepsilon_s (1+e_{ss}) \right]^2 \qquad \text{Εξ. 3.26}$$

(Gidaspow et al., 1992)

$$\mu_{col} = \frac{4}{5}\varepsilon_s \rho_s d_s g_o (1+e_{ss}) \sqrt{\left(\frac{\Theta_s}{\pi} \right)} \qquad \text{Εξ. 3.27}$$

(Gidaspow et al., 1992)

$$\mu_{fr} = \frac{P_s \sin\phi}{2\varepsilon_s \sqrt{II_{dD}}} \qquad \text{Εξ. 3.28}$$

(Johnson and Jackson, 1987)

$$\lambda_{fr} = 0 \qquad \text{Εξ. 3.29}$$

$$g_o = \left[1 - \left(\frac{\varepsilon_s}{\varepsilon_s^{\max}} \right)^{\frac{1}{3}} \right]^{-1} \text{ (Ogawa et al., 1980)} \qquad \text{Εξ. 3.30}$$

3.2.1.2 Το κριτήριο διαρροής των Pitman - Schaeffer – Gray - Stiles και οι συνεκτικές τάσεις (περιπτώσεις Β και C)

Σε αυτές τις περιπτώσεις εκτός από το εναλλακτικό κριτήριο διαρροής μια επιπλέον διαφοροποίηση είναι η ενσωμάτωση των τριβικών τάσεων και για ποσοστά όγκου

σωματιδίων μικρότερα του ορίου τριβής. Αυτή η προσέγγιση υιοθετήθηκε από τους Makkawi et al., 2006 και επιβεβαιώθηκε πως οι δυνάμεις τριβής παίζουν σημαντικό ρόλο σχεδόν για όλο το εύρος των κλασμάτων όγκου των σωματιδίων. Επιπροσθέτως, αυτή η προσέγγιση επιτρέπει την αριθμητικά ομαλή μετάβαση για τις διατμητικές τάσεις από την ταχεία ροή στην τριβική αργή.

Στην παρούσα αριθμητική διερεύνηση, εξετάστηκαν δύο διαφορετικά μοντέλα που βασίζονται στο κριτήριο των Pitman- Schaeffer- Gray-Stiles για τον προσδιορισμό των σωματιδιακών τάσεων. Αρχικά διερευνήθηκε, το κλασικό κριτήριο διαρροής των Standard Pitman- Schaeffer- Gray-Stiles (περίπτωση B). Οι εξισώσεις του μοντέλου είναι οι 3.31 έως 3.37. Αξίζει να σημειωθεί πως για τον υπολογισμό της κινητικής και προσκρουστικής συνεκτικότητας χρησιμοποιήθηκαν οι σχέσεις των Gevrin et al., 2008.

$$\lambda = \begin{cases} \varepsilon_s < \varepsilon_{fr} \Rightarrow \dfrac{4}{3}\varepsilon_s \rho_s d_s g_o \left(1+e_{ss}\right)\left(\dfrac{\Theta_s}{\pi}\right)^{\frac{1}{2}} \\ \varepsilon_s \geq \varepsilon_{fr} \Rightarrow \dfrac{P_s}{\varepsilon_s \sqrt{4\sin^2\varphi \cdot II_{dD} + (\nabla \cdot \vec{u}_s)^2}} \end{cases}$$ (Dartevelle, 2003; Lun et al., 1984) Εξ. 3.31

$$P_s = \begin{cases} \varepsilon_s < \varepsilon_s^{fr} \Rightarrow P_{kin} = \varepsilon_s \rho_s \Theta_s + 2\rho_s (1+e_{ss}) \varepsilon_s^2 g_o \Theta_s \\ \varepsilon_s \geq \varepsilon_s^{fr} \Rightarrow P_{kin} + P_{fr} \end{cases}$$ Εξ. 3.32

(Johnson and Jackson, 1987; Syamlal et al., 1993)

$$P_{fr} = \begin{cases} \varepsilon_s < 0.59 \Rightarrow 0.05 \dfrac{\left(\varepsilon_s - \varepsilon_s^{fr}\right)^2}{\left(\varepsilon_s^{\max} - \varepsilon_s\right)^3} \\ \varepsilon_s \geq 0.59 \Rightarrow 10^{25}\left(\varepsilon_s - 0.59\right)^{10} \end{cases}$$ Εξ. 3.33

Princeton model, (Srivastava and Sundaresan, 2003; Reuge et al., 2008)

$$\mu = \mu_{kin} + \mu_{col} + \mu_{fr}$$ Εξ. 3.34

, όπου (Gevrin et al., 2008; Dartevelle, 2003):

$$\mu_{kin} = \frac{\sqrt{\pi \Theta_s}\, \dfrac{d_s \rho_s}{24 \varepsilon_s g_o} \dfrac{\left(5 + 2\varepsilon_s g_o \left(1+e_{ss}\right)\left(3e_{ss}-1\right)\right)}{\left(1+e_{ss}\right)\left(3-e_{ss}\right)}}{\left(1 + \dfrac{45\mu_g}{6\varepsilon_s g_o d_s \rho_s \sqrt{\dfrac{\Theta_s}{\pi}}\left(1+e_{ss}\right)\left(3e_{ss}-1\right)}\right)}$$ Εξ. 3.35

$$\mu_{col} = \frac{4}{5}\varepsilon_s \rho_s g_o \left(1+e_{ss}\right)\left(\frac{\mu_{kin}}{\rho_s} + d_s \sqrt{\frac{\Theta_s}{\pi}}\right)$$ Εξ. 3.36

$$\mu_{fr} = \frac{P_s \sin^2\varphi}{\varepsilon_s \sqrt{4\sin^2\varphi \cdot \mathrm{II}_{dD} + (\nabla \cdot \vec{u}_s)^2}}$$ Εξ. 3.37

Η συνάρτηση ακτινικής κατανομής υπολογίστηκε από την εξίσωση 3.30. Ένα άλλο μοντέλο εξετάστηκε επίσης. Το μοντέλο αυτό χρησιμοποιεί το κριτήριο διαρροής των Pitman-Schaeffer- Gray-Stiles με ομαλή μετάβαση χρησιμοποιώντας και την εξίσωση του Laux, 1998 (περίπτωση C) για τον υπολογισμό της τριβικής διατμητικής συνεκτικότητας (εξίσωση 3.38). Στην περίπτωση C η εξίσωση αυτή χρησιμοποιείται αντί της 3.37 (περίπτωση B), ενώ όλα τα άλλα υπομοντέλα είναι ίδια με αυτά της περίπτωσης (B).

$$\mu_{fr} = \mu_{Laux} = \frac{6\sin\varphi}{9-\sin^2\varphi}\frac{3|\lambda\nabla\cdot\vec{u}_s - \frac{P_s}{\varepsilon_s}|}{2\sqrt{3|\mathrm{II}_{2D}|}} \qquad \text{Εξ. 3.38}$$

Σε όλα τα μοντέλα που εξετάστηκαν η υδροστατική πίεση των στερεών προσομοιώθηκε με την εξίσωση των Johnson and Jackson, 1987. Ο πίνακας 3.3 συνοψίζει τις σημαντικές παραμέτρους του προβλήματος. Για την οριακή συνθήκη της κοκκώδους θερμοκρασίας εφαρμόστηκε συνθήκη πρώτου τύπου (Dirichlet) με Θ_s= 0.0001 m^2 / s^2.

e_{ss}	0.9 (Ding and Gidaspow, 1990; Hartge et al., 2009)
ε_s^{max}	0.65
ε_s^{fr}	0.5 (Gidaspow et al., 1992)
ρ_g	1.225
μ_g	$1.8\ 10^{-5}$
ρ_s	2600
d_p	462 μm

Πίνακας 3.3 Παράμετροι προβλήματος

Περίπτωση	**Μοντέλο**	**Μάζα**	**Ο.Σ. Τοιχωμάτων**
A	von-Misses/ Coulomb κριτήριο διαρροής	1.04	μη ολίσθηση
B	Pitman- Schaeffer- Gray-Stiles κριτήριο διαρροής	1.04	μη ολίσθηση
C	Pitman- Schaeffer- Gray-Stiles κριτήριο διαρροής και Laux	1.04	μη ολίσθηση

Πίνακας 3.4 Περιπτώσεις που εξετάστηκαν.

3.2.2 Αποτελέσματα των μοντέλων συνεκτικότητας

Τα αποτελέσματα των μοντέλων A, B και C, παρατίθενται στα σχήματα 3.8, 3.10 και 3.11 αντίστοιχα.

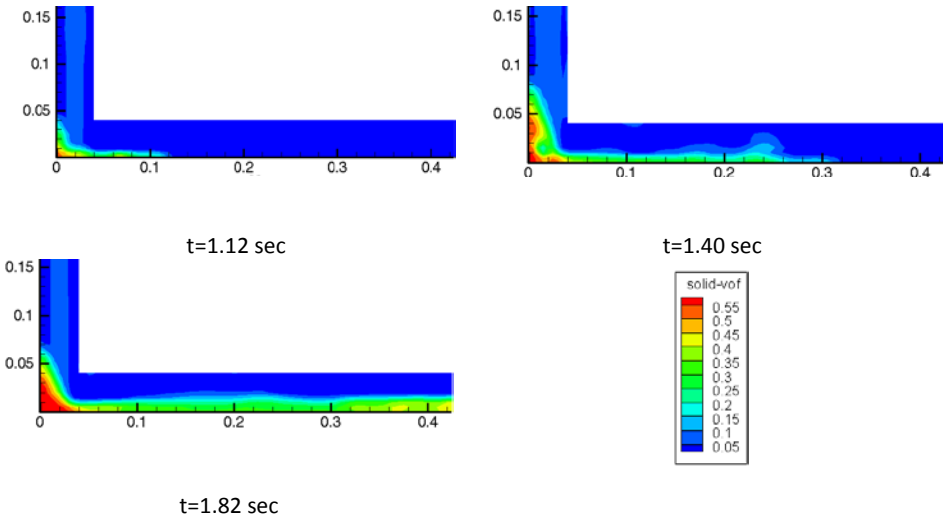

Σχήμα 3.8 Χρονική εξέλιξη του κλάσματος όγκου των στερεών για το μοντέλο A.

Στο σχήμα 3.8 παρατηρείται η αδυναμία του συμβατικού μοντέλου να μοντελοποιήσει την πυκνή ροή των σωματιδίων. Το μοντέλο υποεκτιμά σε μεγάλο βαθμό τις ενδο-σωματιδιακές δυνάμεις τριβής. Έτσι η σωματιδιακή φάση δεν σταματάει ποτέ την κίνηση της.

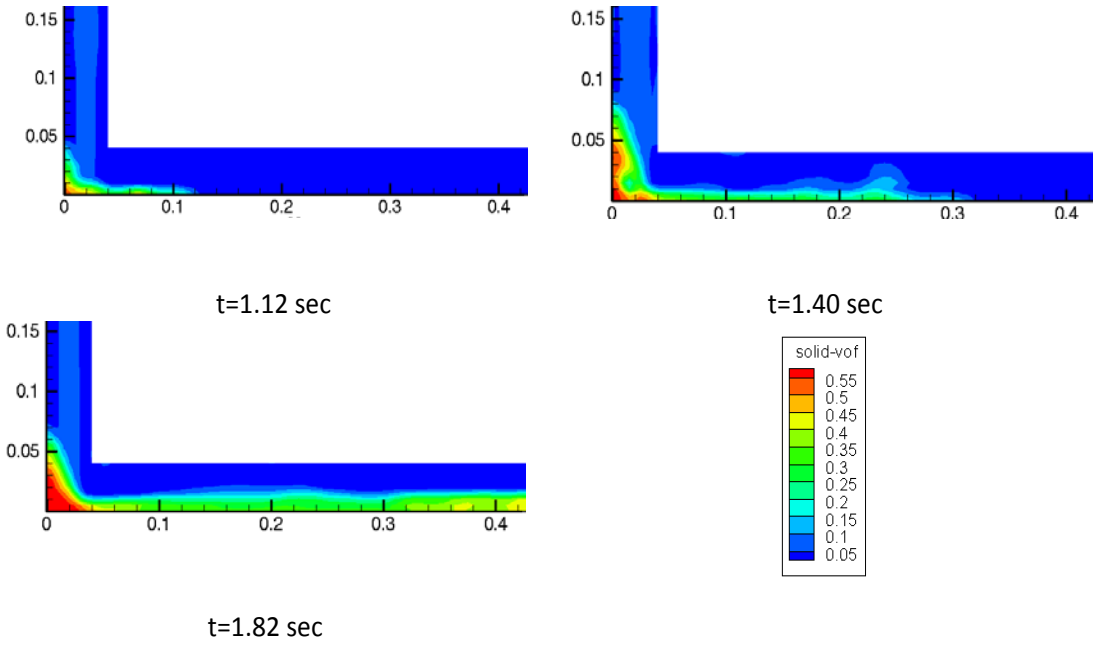

Σχήμα 3.9 Χρονική εξέλιξη του κλάσματος όγκου των στερεών για το μοντέλο Β.

Η χρονική εξέλιξη του ίδιου φαινομένου όπως προλέχθηκε από το μοντέλο Β απεικονίζεται στο σχήμα 3.9. Πρέπει να τονιστεί πως η λεζάντα της αντιστοιχίας χρωμάτων ι τιμών του σχήματος 3.8 ισχύει και για τα σχήματα 3.9 και 3.11. Σε αντίθεση με τις προλέξεις του συμβατικού μοντέλου Α, το μοντέλο Β προβλέπει ορθώς ότι οι κόκκοι σταματούν να κινούνται και σχηματίζουν γωνία απόθεσης φ = 21.0^{o}, σχήμα 3.10, t = 2.20sec. Σε αυτή τη χρονική στιγμή οι ταχύτητες των σωματιδίων είναι σχεδόν μηδενικές, σχήμα 3.10, t = 2.20sec.

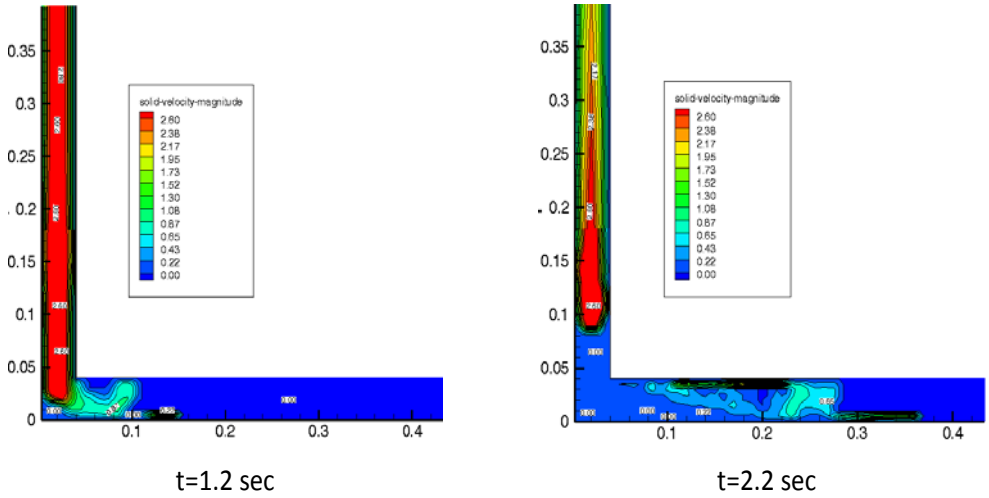

Σχήμα 3.10 Χρονική εξέλιξη της ταχύτητας των κόκκων για το μοντέλο Β.

Συνοψίζοντας, αν και η γωνία απόθεσης που αναπαράγεται υπολογιστικά έχει σημαντική διαφορά με την αντίστοιχη πειραματική είναι σημαντικό πως και με τα δύο μοντέλα που αναπτύχθηκαν (Β και C) το κοκκώδες υλικό σταμάτησε να κινείται. Είναι η πρώτη φορά που κάτι τέτοιο επιτυγχάνεται με τις εξισώσεις κατά Euler.

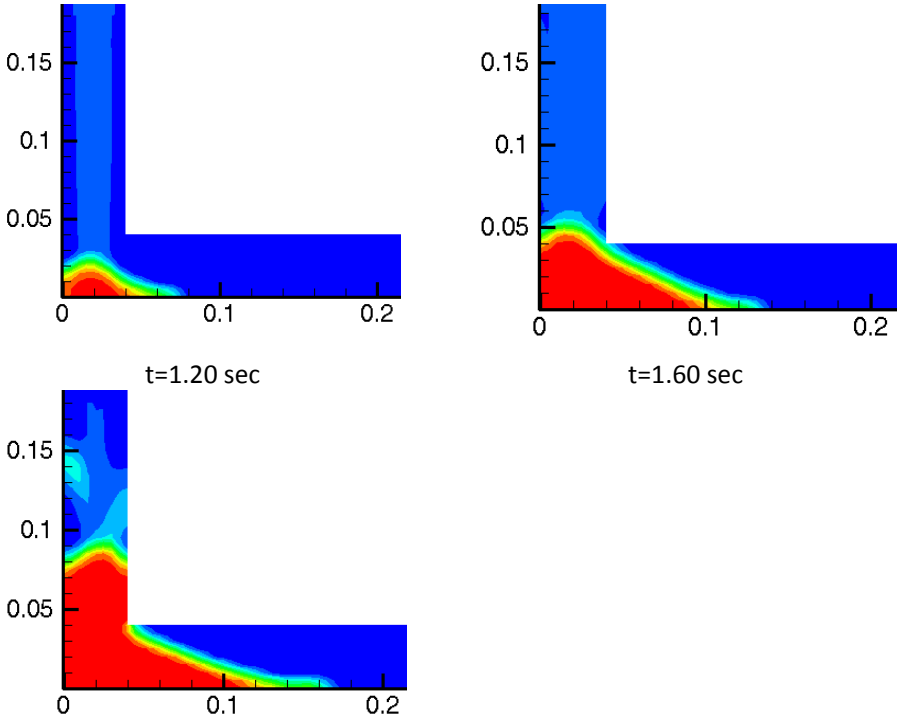

Σχήμα 3.11 Χρονική εξέλιξη του κλάσματος όγκου των στερεών για το μοντέλο C.

Το σχήμα 3.11 αναπαριστά την εξέλιξη του φαινομένου για το μοντέλο C. Και σε αυτή την περίπτωση το υλικό ακινητοποιείται και σχηματίζει γωνία απόθεσης ίση με $\varphi = 29.5^{o}$, τιμή ή οποία είναι ακριβέστερη από αυτή του μοντέλου B.

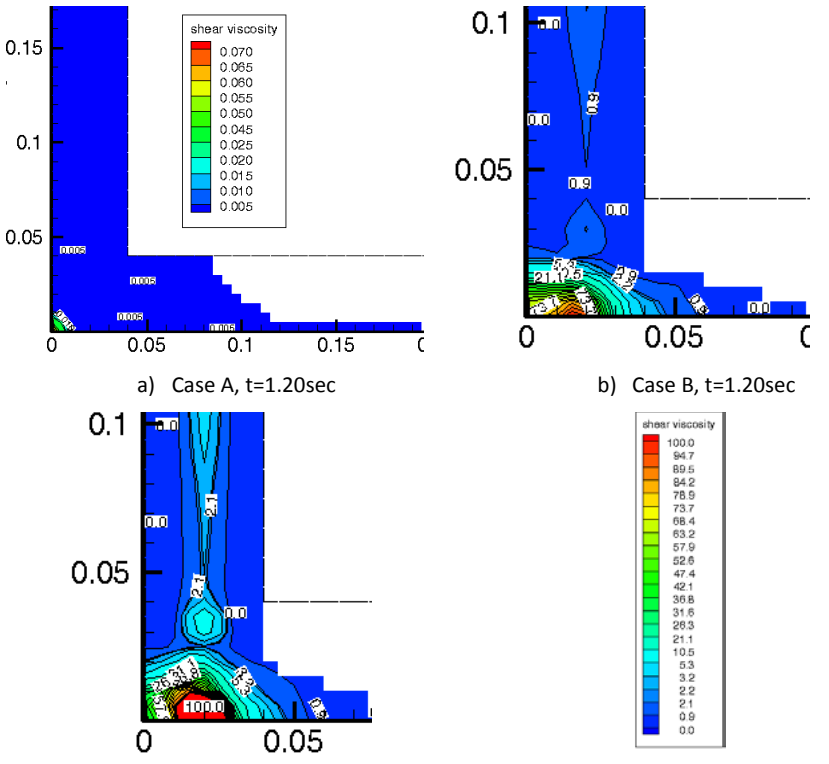

Σχήμα 3.12 Διατμητική συνεκτικότητα (μ_s) για τα μοντέλα A, B και C για t=1.20sec

Το σχήμα 3.12a, b, and c παρουσιάζει τη χωρική κατανομή της σωματιδιακής διατμητικής συνεκτικότητας για t = 1.20 sec για τα μοντέλα A, B και C αντίστοιχα. Οι διαφορές ιδιαίτερα με το συμβατικό μοντέλο είναι μεγάλες και εξηγούν τις μεγάλες διαφορές στην πρόλεξη της γωνία απόθεσης.

3.3 Ενσωμάτωση κατανομή διαμέτρων στην κινητική θεωρία

Μια ακόμη πιθανή πηγή σφαλμάτων, είναι η απλούστευση πως όλα τα σωματίδια είναι ίδια και αντιπροσωπεύονται από τη μέση διάμετρο. Αυτή η απλούστευση υιοθετείται σχεδόν από όλους τους ερευνητές που μοντελοποιούν ρευστοποιημένες κλίνες ανακυκλοφορίας με την TFM μεθοδολογία (Nikolopoulos et al., 2010[a, b]; Shuai et al., 2011[a, b , c]; Wang et al., 2008; Zhang et al., 2008). Η ενσωμάτωση κατανομής διαμέτρων στην TFM αυξάνει πάρα πολύ το υπολογιστικό κόστος.

Στα μοντέλα κατά Euler που ενσωματώνουν την κατανομή διαμέτρων κάθε διάμετρος των σωματιδίων αντιστοιχεί σε μια διακριτή Euler φάση. Ο αριθμός των στερεών φάσεων συμβολίζεται με N, και ο συνολικός αριθμός φάσεων είναι N + 1 (N κοκκώδεις και μια του αερίου). Αν και αυτή η προσέγγιση αυξάνει το κόστος υπερβολικά, η σύγκριση των αποτελεσμάτων της με τα αντίστοιχα μονοδιαμετρικά, θα ήταν πολύ χρήσιμη και θα υποδείκνυε το σφάλμα που επιφέρει αυτή η απλούστευση.

Για την πλήρης μοντελοποίηση των ρευστοποιημένων κλινών ανακυκλοφορίας θα πρέπει να διατυπωθεί ένα μοντέλο κατανομής διαμέτρων που θα χρησιμοποιεί το συμβατικό μοντέλο (με βάση το κριτήριο διαρροής του von - Misses) για τον αγωγό ανόδου και το νέο μοντέλο (με βάση το εναλλακτικό κριτήριο διαρροής) για το σύστημα ανακυκλοφορίας.

Στην περίπτωση της μοντελοποίησης κατανομής διαμέτρων, η κινητική θεωρία των κοκκωδών ροών θα πρέπει να λάβει υπ' όψη τις συγκρούσεις σωματιδίων διαφορετικού μεγέθους για να διατυπώσει ορθές και συνεπείς εξισώσεις για την κοκκώδη πίεση και συνεκτικότητα. Οι Mathiesen et al., 2000 ανέπτυξαν τέτοιες εξισώσεις και η κοκκώδης πίεση μπορεί να υπολογιστεί ως:

$$P_s = \varepsilon_s \rho_s \theta_s + \sum_{n=1}^{N} P_{c,sn} \qquad \text{Εξ. 3.39}$$

$$P_{c,sn} = \frac{\pi}{3}(1+e_{sn}) d_{sn}^3 g_{sn} n_s n_n m_o \left\{ \frac{\theta_s \theta_n}{\frac{m_s}{m_n}\theta_s + \frac{m_n}{m_s}\theta_n} \right\} \left\{ \frac{\left(m_o / m_s\right)^2 \theta_s \theta_n}{\left[\theta_s + \left(m_n / m_s\right)^2 \theta_n\right](\theta_s + \theta_n)} \right\}^{3/2} \qquad \text{Εξ. 3.40}$$

$$d_{sn} = \frac{1}{2}(d_s + d_n), m_o = m_s + m_n, n_s = \frac{6\varepsilon_s}{\pi d_s^3}, m_s = \frac{\pi d_s^3 \rho_s}{6} \qquad \text{Εξ. 3.41}$$

Θα πρέπει να τονιστεί πως η εξίσωση 3.39 είναι συνεπής αφού για N = 1 εκφυλίζεται στην αντίστοιχη εξίσωση για την κοκκώδη πίεση σωματιδίων ιδίου μεγέθους (εξίσωση. 3.24).

Η συνάρτηση ακτινικής κατανομής δύο σωματιδιακών φάσεων ($g_{o,sn}$) μπορεί να υπολογιστεί ως (Mathiesen et al., 2000):

$$g_{o,sn} = \frac{N}{2} \frac{g_o}{1-\varepsilon_g}(\varepsilon_s + \varepsilon_n), g_o = \left[1 - \frac{(1-\varepsilon_g)}{\varepsilon_s^{\max}}\right]^{-2.5\varepsilon_s^{\max}} \qquad \text{Εξ. 3.42}$$

Η τριβική κοκκώδης πίεση μοντελοποιείται με την εξίσωση 3.43.

$$P_{fr,s}=\begin{Bmatrix} 0 \quad , for \sum_{n=1}^{N}\varepsilon_n < 0.5 \\ 0.1\varepsilon_s \dfrac{\sum_{n=1}^{N}\varepsilon_n - \varepsilon^{fr}}{\varepsilon^{\max}-\sum_{n=1}^{N}\varepsilon_n}, for \sum_{n=1}^{N}\varepsilon_n > 0.5 \end{Bmatrix} \quad \text{Εξ. 3.43}$$

Όσων αφορά την ορθή συνεκτικότητα, η συμβατική μονοδιαμετρική εξίσωση 3.23 αντικαθίσταται με την αντίστοιχη της για κατανομή διαμέτρων (εξίσωση 3.44, Mathiesen et al., 2000).

$$\lambda_s=\frac{1}{\varepsilon_s}\sum_{n=1}^{N}P_{c,sn}\frac{d_{sn}}{3}(\theta_s+\frac{m_n}{m_s}\theta_n)\sqrt{\frac{2}{\pi\theta_s\theta_n(\theta_s+\left(\frac{m_n}{m_s}\right)^2\theta_n)}} \quad \text{Εξ. 3.44}$$

Από τους Mathiesen et al., 2000, αναπτύχθηκαν κατάλληλες εξισώσεις και για την κινητική και προσκρουστική συνεκτικότητα. Αυτές οι εξισώσεις (3.48 και 3.45 αντίστοιχα) είναι συνεπείς με τις αντίστοιχες μονοδιαμετρικές. Για την τριβική συνεκτικότητα προτείνεται η εξίσωση 3.48.

$$\mu_{col}=\frac{1}{\varepsilon_s}\sum_{n=1}^{N}P_{c,sn}\frac{d_{sn}}{5}(\theta_s+\frac{m_n}{m_s}\theta_n)\sqrt{\frac{2}{\pi\theta_s\theta_n(\theta_s+\left(\frac{m_n}{m_s}\right)^2\theta_n)}} \quad \text{Εξ. 3.45}$$

$$\mu_{kin}=\frac{2\mu_{dil,s}}{\frac{1}{N}\varepsilon_s\sum_{n=1}^{N}(1+e_{sn})g_{sn}}\left\{1+\frac{4}{5}\sum_{n=1}^{N}g_{sn}\varepsilon_n(1+e_{sn})\right\}^2 \quad \text{Εξ. 3.46}$$

$$\mu_{dil,s}=\frac{5}{16d_s^2}\sqrt{\frac{m_s\theta_{s,av}}{\pi}}$$

$$\theta_{s,av}=\frac{2m_s\theta_s}{\left\{\sum_{n=1}^{N}\frac{n_n}{n_s}\left(\frac{d_{sn}}{d_s}\right)^2\sqrt{\frac{\left(m_o/m_s\right)^2\theta_n}{\left(\theta_s+\left(m_n/m_s\right)^2\theta_n\right)}}\left(\frac{\left(m_o/m_s\right)^2\theta_s\theta_n}{\left(\theta_s+\left(m_n/m_s\right)^2\theta_n\right)\left(\theta_s+\theta_n\right)}\right)^{3/2}\right\}^2} \quad \text{Εξ. 3.47}$$

$$\mu_{fr,s}=\frac{P_{fr}\sin\varphi}{2\varepsilon_s\sqrt{\mathrm{II}_{dD,s}}},\lambda_{fr,s}=0 \quad \text{Εξ. 3.48}$$

Αυτές οι εξισώσεις (3.39 ως 3.48) μπορούν να χρησιμοποιηθούν για τους τανυστές των σωματιδιακών τάσεων στον αγωγό ανόδου. Ωστόσο, όσον αφορά το σύστημα ανακυκλοφορίας, κατάλληλες σχέσεις πρέπει να αναπτυχθούν για την ορθή μοντελοποίηση των ενδο-σωματιδιακών δυνάμεων τριβής, σε αντιστοιχία με τη θεωρητική ανάπτυξη τέτοιων σχέσεων στο υποκεφάλαιο 3.2 για τη μονοδιαμετρική προσέγγιση. Εν ολίγοις, το κριτήριο διαρροής των Pitman- Schaeffer- Gray-Stiles και οι εξισώσεις των Boelle et al., 1995 και Gevrin et al., 2008, για την κινητική και προσκρουστική συνεκτικότητα πρέπει να

ενσωματωθούν στο πολυδιαμερικό μοντέλο. Στην παρούσα εργασία τέτοιες σχέσεις αναπτύχθηκαν για την κινητική, προσκρουστική και τριβική συνεκτικότητα, εξισώσεις 3.49, 3.50 και 3.51 αντίστοιχα.

$$\mu_{kin,2}=\frac{4\mu_{dil,s}\left[1+\frac{2}{5}\sum_{n=1}^{N}g_{sn}\varepsilon_{\mathrm{n}}\left(3e_{sn}-1\right)\left(1+e_{sn}\right)\right]}{\frac{1}{N}\varepsilon_{\mathrm{s}}\sum_{n=1}^{N}\left(1+e_{sn}\right)\left(3-e_{sn}\right)g_{sn}}\left[1+\frac{3\mu_g\varepsilon_{\mathrm{s}}}{\sum_{n=1}^{N}P_{c,sn}\frac{d_{sn}}{5}\left(\Theta_{\mathrm{s}}+\frac{m_{\mathrm{n}}}{m_{\mathrm{s}}}\Theta_{\mathrm{n}}\right)\sqrt{\frac{2}{\pi\Theta_{\mathrm{s}}\Theta_{\mathrm{n}}\left(\Theta_{\mathrm{s}}+\left(\frac{m_{\mathrm{n}}}{m_{\mathrm{s}}}\right)^2\Theta_{\mathrm{n}}\right)}}}\right]^{-1} \quad \text{Εξ. 3.49}$$

$$\mu_{col,2}=\frac{1}{5}\frac{\frac{4\mu_{dil,s}\left[1+\frac{2}{5}\sum_{n=1}^{N}g_{sn}\varepsilon_{\mathrm{n}}\left(3e_{sn}-1\right)\left(1+e_{sn}\right)\right]}{\frac{1}{N}\varepsilon_{\mathrm{s}}\rho_s\sum_{n=1}^{N}\left(1+e_{sn}\right)\left(3-e_{sn}\right)g_{sn}}\sum_{n=1}^{N}\frac{\pi}{3}\left(1+e_{sn}\right)d_{sn}^3g_{sn}n_sn_nm_o}{1+\frac{3\mu_g\varepsilon_{\mathrm{s}}}{\sum_{n=1}^{N}P_{c,sn}\frac{d_{sn}}{5}\left(\Theta_{\mathrm{s}}+\frac{m_{\mathrm{n}}}{m_{\mathrm{s}}}\Theta_{\mathrm{n}}\right)\sqrt{\frac{2}{\pi\Theta_{\mathrm{s}}\Theta_{\mathrm{n}}\left(\Theta_{\mathrm{s}}+\left(\frac{m_{\mathrm{n}}}{m_{\mathrm{s}}}\right)^2\Theta_{\mathrm{n}}\right)}}}+\frac{1}{\varepsilon_{\mathrm{s}}}\sum_{n=1}^{N}P_{c,sn}\frac{d_{sn}}{5}\left(\Theta_{\mathrm{s}}+\frac{m_{\mathrm{n}}}{m_{\mathrm{s}}}\Theta_{\mathrm{n}}\right)\sqrt{\frac{2}{\pi\Theta_{\mathrm{s}}\Theta_{\mathrm{n}}\left(\Theta_{\mathrm{s}}+\left(\frac{m_{\mathrm{n}}}{m_{\mathrm{s}}}\right)^2\Theta_{\mathrm{n}}\right)}}} \quad \text{Εξ. 3.50}$$

$$\mu_{fr,s}=\frac{P_{fr}\sin^2\varphi}{\varepsilon_s\sqrt{4\sin^2\varphi\cdot\mathrm{II}_{dD,s}+\left(\nabla\cdot\vec{u}_s\right)^2}},\lambda_{fr,s}=\frac{P_{fr}\sin\varphi}{\varepsilon_s\sqrt{4\sin^2\varphi\cdot\mathrm{II}_{dD,s}+\left(\nabla\cdot\vec{u}_s\right)^2}} \quad \text{Εξ. 3.51}$$

3.4 Προσομοίωση αντιδράσεων σε CFBs

Η αριθμητική προσομοίωση μηχανισμών μεταφοράς μάζας και ενέργειας και των αντίστοιχων αντιδράσεων στις ρευστοποιημένες κλίνες ανακυκλοφορίας παρουσιάζει δυσκολίες. Μια τέτοια μοντελοποίηση προϋποθέτει την επίλυση της υδροδυναμικής όπως και ομογενών / ετερογενών αντιδράσεων καθώς και μηχανισμών μεταφοράς ενέργειας. Κατάλληλες εξισώσεις πρέπει να αναπτυχθούν για την μοντελοποίηση των αντιδράσεων. Σε αυτή τη διατριβή αναπτύχθηκαν μοντέλα για τη: α) μοντελοποίηση της καύσης στερεού καυσίμου, β) μοντελοποίηση της δέσμευσης CO_2 με σωματίδια CaO εντός ρευστοποιημένης κλίνης ανακυκλοφορίας ενανθράκωσης, και γ) μοντελοποίηση των εκπομπών οξειδίων και υπεροξειδίων του αζώτου.

3.4.1 Μοντελοποίηση καύσης σε ρευστοποιημένες κλίνες

Αυτό το υποκεφάλαιο της διατριβής καταπιάνεται με την ανάπτυξη ενός τρισδιάστατου μοντέλου καύσης το οποίο λαμβάνει υπ' όψη την καύση των σωματιδίων του ορυκτού καυσίμου εντός του αγωγού ανόδου ρευστοποιημένης κλίνης ανακυκλοφορίας. Το μοντέλο όσον αφορά στην υδροδυναμική, υιοθετεί το συμβατικό ισοθερμοκρασιακό μοντέλο που περιγράφεται στο κεφάλαιο 2 της παρούσας διατριβής και στην εργασία των Rampidis et al., 2007.

Οι βασικές δυσκολίες μιας τέτοιας μοντελοποίησης είναι το μεγάλο υπολογιστικό κόστος και η ακριβής μοντελοποίηση της αλληλεπίδρασης μεταξύ των στερεών φάσεων (αδρανούς υλικού και καυσίμου). Για την οπισθέλκουσα, χρησιμοποιείται το μοντέλο του Gidaspow καθώς σε αυτή την περίπτωση η εφαρμογή του EMMS παρουσιάζει θεωρητικές και πρακτικές δυσκολίες.

Οι τρεις φάσεις (αέριο, αδρανές και καύσιμο) περιγράφονται με εξισώσεις κατά Euler. Η εξίσωση της συνέχειας για τη φάση *q* είναι:

$$\frac{\partial}{\partial t}(\varepsilon_q \rho_q) + \nabla \cdot (\varepsilon_q \rho_q \vec{u}_q) = S_q \qquad \text{Εξ. 3.52}$$

Ο όρος S_q, αναπαριστά τον όρο πηγής για τη *q* φάση λόγω αντιδράσεων. Όσων αφορά την εξίσωση ορμής του αερίου:

$$\frac{\partial}{\partial t}(\varepsilon_q \rho_q \vec{u}_q) + \nabla \cdot (\varepsilon_q \rho_q \vec{u}_q \vec{u}_q) = -\varepsilon_q \nabla p_g + \nabla \cdot \bar{\bar{\tau}}_q + \varepsilon_q \rho_q \vec{g} + \sum_{l=1}^{n} \left[\beta \left(\vec{u}_l - \vec{u}_q \right) + \dot{m}_{lq} \vec{u}_{lq} - \dot{m}_{ql} \vec{u}_{ql} \right] \qquad \text{Εξ. 3.53}$$

ενώ η αντίστοιχη εξίσωση για τη q^{th} στερεά φάση είναι:

$$\frac{\partial}{\partial t}(\varepsilon_q \rho_q \vec{u}_q) + \nabla \cdot (\varepsilon_q \rho_q \vec{u}_q \vec{u}_q) = -\varepsilon_q \nabla p_g - \nabla p_q + \nabla \cdot \bar{\bar{\tau}}_q + \varepsilon_q \rho_q \vec{g} + \sum_{l=1}^{n} \left[\beta \left(\vec{u}_l - \vec{u}_q \right) + \dot{m}_{lq} \vec{u}_{lq} - \dot{m}_{ql} \vec{u}_{ql} \right] \qquad \text{Εξ. 3.54}$$

Η εξίσωση ενέργειας για κάθε φάση:

$$\frac{\partial}{\partial t}(\varepsilon_q \rho_q \mathrm{H}_q) + \nabla \cdot (\varepsilon_q \rho_q \vec{u}_q \mathrm{H}_q) = -\varepsilon_q \frac{\partial P_q}{\partial t} + \bar{\bar{\tau}}_q + \nabla \vec{u}_q - \nabla \vec{q}_q + S_q + \sum_{l=1}^{n} (\dot{Q}_{lq}) \qquad \text{Εξ. 3.55}$$

Η μετάδοση θερμότητας μεταξύ του αερίου και των δύο στερεών φάσεων μοντελοποιείται με το μοντέλο του Gunn, 1978:

$$\dot{Q}_{qg} = h_{qg} \cdot (T_q - T_g) \qquad \text{Eq. 3.56}$$

$$h_{qg} = \frac{6 \cdot K_g \cdot \varepsilon_q \cdot \varepsilon_g \cdot Nu_g}{d_f^2} \qquad \text{Eq. 3.57}$$

Για τον υπολογισμό του αριθμού *Nu*, οι Tullin et al., 1993 πρότειναν την ακόλουθη εξίσωση.

$$Nu_g = \left(7 - 10\varepsilon_g + 5\varepsilon_g^2\right)\left(1 + 0.7\,\mathrm{Re}_q^{0.2}\,\mathrm{Pr}^{1/3}\right) + \left(1.33 - 2.4\varepsilon_g + 1.2\varepsilon_g^2\right)\mathrm{Re}_q^{0.7}\,\mathrm{Pr}^{1/3} \qquad \text{Εξ. 3.58}$$

όπου

$$\mathrm{Pr} = \frac{c_{p_g} \mu_g}{K_g} \qquad \text{Εξ. 3.59}$$

$$\mathrm{Re}_q = \frac{\left|\vec{u}_q - \vec{u}_\mathrm{g}\right| \rho_g d_q}{\mu_g} \qquad \text{Εξ. 3.60}$$

Για τον υπολογισμό της μετάδοσης θερμότητας μεταξύ δύο κοκκωδών υλικών δεν έχει αναπτυχθεί κατάλληλο μοντέλο στη βιβλιογραφία (Zhou et al., 2011). Λόγο αυτού του προβλήματος, σε αυτή τη διατριβή αναπτύχθηκε ένα τέτοιο μοντέλο. Οι εξισώσεις 3.57 έως 3.60 που αποτελούν το μοντέλο του Gunn, 1978, θα μπορούσαν να χρησιμοποιηθούν για τη μοντελοποίηση της μετάδοσης θερμότητας μεταξύ κοκκωδών φάσεων (Nikolopoulos et al., 2009). Στις εξισώσεις 3.61 έως 3.64, ο δείκτης *q* αναφέρεται στο αδρανές υλικό που εντός των κλινών είναι πολύ περισσότερο από το καύσιμο. Το αδρανές υλικό σε αυτή την παραλλαγή του μοντέλου του Gunn θεωρείται “ψευδο-” ρευστό, θεώρηση που συμφωνεί με την κοκκώδη κινητική θεωρία.

$$h_{qf} = \frac{6 \cdot K_q \cdot \varepsilon_f \cdot \varepsilon_q \cdot Nu_q}{d_f^2}$$ Εξ. 3.61

$$\mathrm{Pr} = \frac{c_{p_q} \mu_q}{K_q}$$ Εξ. 3.62

$$\mathrm{Re}_q = \frac{\left|\vec{u}_q - \vec{u}_f\right| \rho_q d_f}{\mu_q}$$ Εξ. 3.63

$$Nu_q = \left(7 - 10\varepsilon_q + 5\varepsilon_q^2\right)\left(1 + 0.7\,\mathrm{Re}_q^{0.2}\,\mathrm{Pr}^{1/3}\right) + \left(1.33 - 2.4\varepsilon_q + 1.2\varepsilon_q^2\right)\mathrm{Re}_q^{0.7}\,\mathrm{Pr}^{1/3}$$ Εξ. 3.64

Επιπροσθέτως, το μοντέλο του Syamlal, 1987 (symmetric) μπορεί να μοντελοποιήσει την αλληλεπίδραση ορμής μεταξύ των κόκκων των διαφορετικών φάσεων.

Η τύρβη έχει εν γένει μικρή επίδραση στην υδροδυναμική της κλίνης αλλά φαίνεται να επιδρά σημαντικά στις αντιδράσεις που λαμβάνουν χώρα σε τέτοιες μονάδες (Nikolopoulos et al., 2009; Rampidis et al., 2007; Wang and Li, 2007). Η τύρβη επηρεάζει κυρίως την ανάμειξη των αντιδρώντων και των προϊόντων των ομογενών αντιδράσεων.

Η καύση του καυσίμου συντελείται μέσω τριών διαδοχικών ετερογενών αντιδράσεων. Η πρώτη είναι η εξάτμιση της υγρασίας. Η δεύτερη η απομάκρυνση των πτητικών (εξ. 3.65 και 3.66). Η τρίτη κατά σειρά αντίδραση είναι η καύση του εξανθρακώματος.

$$\mathrm{H_2O}(s) \xrightarrow{boiling} \mathrm{H_2O}(g)$$ Εξ. 3.65

$$vol.(s) \xrightarrow{devolatilization} vol.(g)$$ Εξ. 3.66

Επίσης, τρεις ομογενείς αντιδράσεις ενσωματώνονται στο μοντέλο. Η καύση του μεθανίου (Gungor and Eskin, 2008[b]), του H_2 και του CO (Zhao et al., 2007), εξισώσεις 3.67 έως 3.69, αντίστοιχα.

$$CH_4 + \frac{3}{2}O_2 \longrightarrow CO + 2H_2O,\ R = Ae^{-\frac{E}{R_u T_g}}\left[C_{CH_4}\right]^{0.7}\left[C_{O_2}\right]^{0.8}$$ Eq. 3.67

$$H_2 + \frac{1}{2}O_2 \longrightarrow H_2O,\ R = Ae^{-\frac{E}{R_u T_g}}\left[C_{H_2}\right]\left[C_{O_2}\right]^{0.5}$$ Eq. 3.68

$$CO + \frac{1}{2}O_2 \longrightarrow CO_2,\ R = Ae^{-\frac{E}{R_u T_g}}\left[C_{CO}\right]\left[C_{O_2}\right]^{0.25}\left[C_{H_2O}\right]^{0.5}$$ Eq. 3.69

Αντίδραση	*A* (διάφορες μονάδες)	*E* (J/Kmol)
Eq. 3.67(CH_4)	$5.012\ 10^{11}$	$2\ 10^{8}$
Eq. 3.68(H_2)	$9.87\ 10^{15}$	$3.1\ 10^{7}$
Eq. 3.69(CO)	$2.239\ 10^{12}$	$1.7\ 10^{8}$

Πίνακας 3.5 Σταθερές των ομογενών αντιδράσεων (FLUENT, 2010; Zhao et al., 2007)

Οι κινητικοί ρυθμοί των ομογενών αντιδράσεων είναι ακριβείς μόνο όταν τα αντιδρώντα είναι πλήρως αναμεμειγμένα στον όγκο ελέγχου. Η ανάμειξή τους επηρεάζεται από τα επίπεδα της τύρβης και αυτή η επίδραση λαμβάνεται υπ' όψη μέσω του μοντέλου αντιδράσεων διάχυσης δινών (Eddy dissipation model, Magnussen and Hjertager, 1976):

$$R_{i,r} = \nu'_{i,r} M_{w,i} A_E \rho_g \frac{\varepsilon_g^t}{k_g^t} \min_R \left(\frac{Y_R}{\nu'_{R,r} M_{w,R}} \right) \quad \text{Εξ. 3.70}$$

$$R_{i,r} = \nu'_{i,r} M_{w,i} A_E \mathrm{B}_E \rho_g \frac{\varepsilon_g^t}{k_g^t} \frac{\sum_{PR} Y_{PR}}{\sum_j^N \nu''_{j,r} M_{w,j}} \quad \text{Εξ. 3.71}$$

Όπως φαίνεται στις εξισώσεις 3.70 and 3.71, τα χαρακτηριστικά της τύρβης (k_g^t και ε_g^t) πρέπει να υπολογιστούν για να μπορεί να εφαρμοστεί το μοντέλο διάχυσης δινών. Συνεπώς, η τύρβη πρέπει να μοντελοποιηθεί και αυτό επιτυγχάνεται μέσω του μοντέλου k – ε για πολυφασική ροή διασκορπισμένων σωματιδίων (k – ε dispersed, FLUENT, 2010, Rampidis et al., 2007, Zhou et al., 2011).

Ο ρυθμός της ετερογενούς αντίδρασης απομάκρυνσης της υγρασίας δύναται να προσομοιωθεί από την εξίσωση 3.72 (Tullin et al., 1993) για θερμοκρασίες άνω των 373 K

$$\dot{m}_f^w = \left(\frac{6 \cdot m_f}{\pi \cdot \rho_f \cdot d_p^{\,3}}\right)\left(-\pi \cdot d_p \cdot Nu_p \cdot \frac{K_{ps}}{c_{p_{ps}}} \cdot \ln\left(1 + \frac{c_{p_{ps}} \cdot (T_g - T_{ps})}{1 - L_w}\right)\right) \quad \text{Εξ. 3.72}$$

Για την απελευθέρωση των πτητικών επιστρατεύεται ένα απλοϊκό μοντέλο ενός σταδίου, εξίσωση 3.73. Οι σταθερές, A_{vol} (492000 s^{-1}) και E_{vol} (7.4x10^7 J/kmol, Leithner et al., 1993) , είναι ο προεκθετικός συντελεστής και η ενέργεια ενεργοποίησης.

$$\dot{m}_{devol} = \frac{6 \cdot m_f}{\pi \cdot \rho_f \cdot d_f^{\,3}} \cdot A_{vol} \cdot e^{-E_{vol}/(R_u T_f)} \cdot Y_{vol} \quad \text{Εξ. 3.73}$$

Η πιο σημαντική αντίδραση εντός της κλίνης καύσης, είναι η οξείδωση του εξανθρακώματος (εξ. 3.74) προς σχηματισμό μονοξειδίου και διοξειδίου του άνθρακα (Basu, 1999). Η αναλογία των προϊόντων ελέγχεται από την παράμετρο φ_c. που δύναται να υπολογιστεί μέσω των εξισώσεων που παραθέτουν οι Leithner et al., 1993, και παίρνει τιμές από 1 έως 2.

$$C(s) + \frac{1}{\phi_c} \mathrm{O}_2(g) \longrightarrow \left(2 - \frac{2}{\phi_c}\right) CO_2 + \left(\frac{2}{\phi_c} - 1\right) CO \quad \text{Εξ. 3.74}$$

Η μοντελοποίηση του ρυθμού καύσης είναι αρκετά περίπλοκη καθώς εμπλέκονται κινητικοί παράμετροι και φαινόμενα διάχυσης (k_c και h_m αντίστοιχα). Οι εξισώσεις 3.75 έως 3.80 περιγράφουν το μοντέλο καύσης που υιοθετήθηκε σε αυτή τη διατριβή (Basu, 1999).

$$\dot{m}_{char} = (\pi \cdot d_c^{\,2}) \cdot \frac{P_{O_2(g)}}{1/h_m + 1/k_c} \quad \text{Εξ. 3.75}$$

$$h_m = 12 \phi_c Sh D_{O_2(g)} / (d_c R_u T) \quad \text{Εξ. 3.76}$$

$$k_c = 0.0117 \exp(-2859 / T_p) \quad \text{Εξ. 3.77}$$

$$Sh = \frac{R_c(m/s) d_c}{D_{O_2(g)}} = 2\varepsilon_g + 0.69 \left[\frac{\left|\vec{u}_g - \vec{u}_s\right| \rho_g d_c}{\varepsilon_g \mu_g} \right]^{0.5} Sc^{0.33} \quad \text{Εξ. 3.78}$$

$$Sc = \frac{\mu_g}{\rho_g D_{O_2(g)}} \quad \text{Εξ. 3.79}$$

Όσον αφορά στη μεταβολή του όγκου του καυσίμου κατά τη διάρκεια της καύσης, υιοθετήθηκε η προσέγγιση μοντέλο μειούμενου πυρήνα (shrinking core). Η μειούμενη διάμετρος (d_c) μπορεί να υπολογιστεί από την εξίσωση του Field, 1969.

$$\frac{d_c}{d_o}=(1-U_{fc})^{1/3} \quad \text{Eq. 3.80}$$

3.4.2 Μοντελοποίηση της αντίδρασης ενανθράκωσης

Η ενανθράκωσης (εξίσωση 3.81) είναι μια ετερογενής αντίδραση που είναι πολύ σημαντική για τη διεργασία δέσμευσης CO_2 μέσω κύκλων ενανθράκωσης / ασβεστοποίησης (CaL). Ο ρυθμός αντίδρασης έχει μελετηθεί μέσω πειραματικών μετρήσεων σε πιλοτικές μονάδες. Οι Charitos et al., 2010[b] κατέληξαν στη σχέση 3.82.

$$CaO + CO_2 \rightarrow CaCO_3 + \mathrm{H}eat \quad \text{Εξ. 3.81}$$

$$\frac{dX_{carb}}{dt} = \frac{k_s S_o}{1-e_0} \cdot \left(X_{\max} - X_{carb}\right)^{2/3} \left(C_{CO_2} - C_{CO_2,eq}\right) \quad \text{Εξ. 3.82}$$

Ωστόσο, η εξίσωση δεν μπορεί να χρησιμοποιηθεί σε μοντέλα υπολογιστικής ρευστοδυναμικής. Η ακόλουθη εξίσωση 3.83, βασίζεται στην εξίσωση 3.82 και υιοθετώντας την υπόθεση πως κάθε όγκος ελέγχου προσομοιάζει ένα συνεχώς αναδευόμενο αντιδραστήριο (continuous stirred-tank reactor, CSTR) προτάθηκε από τους Nikolopoulos et al., 2012[a]. Ωστόσο, με αυτή την προσέγγιση η επίδραση των δομών μεσο-κλίμακας αγνοείται.

$$R(mol/s) = -N_{Ca}\left(\frac{k_s S_o}{1-e_0}\right)\cdot\left(X_{\max} - X_{carb}\right)^{2/3}\left(C_{CO_2} - C_{CO_2,eq}\right) \quad \text{Eq. 3.83}$$

$$C_{CO_2,eq} = \frac{1.462\cdot 10^{11}}{T_g} e^{\left[\frac{-19130}{T_g}\right]} \quad \text{Eq. 3.84}$$

3.4.3 Μοντελοποίηση των NO_x / N_2O

Σε αυτή τη διατριβή προτείνεται η απεπλεγμένη μοντελοποίηση για την προσομοίωση των NO_x / N_2O. Σύμφωνα με αυτή την προσέγγιση η μοντελοποίηση οξειδίων του αζώτου απεμπλέκεται από τη μοντελοποίηση της καύσης. Αυτή η απλούστευση βασίζεται στην υπόθεση πως τα οξείδια του αζώτου επηρεάζονται αλλά δεν επηρεάζουν την καύση του καυσίμου και την υδροδυναμική της κλίνης.

Αυτή η μεθοδολογία έχει επιτυχώς εφαρμοστεί σε μοντελοποιήσεις λεβήτων κονιοποιημένου καυσίμου (Nikolopoulos et al., 2011; Li et al., 2004 and Le Bris et al., 2007), και θεωρείται ως κατάλληλη και ακριβής για τη μοντελοποίηση των οξειδίων του αζώτου. Ωστόσο αυτή η τεχνική δεν έχει ακόμα εφαρμοστεί στις ρευστοποιημένες κλίνες (Gungor and Eskin, 2008[b]; Desroches-Ducarne et al., 1998; Liu and Gibbs, 2002; Afacan et al., 2007 και Mukadi et al., 2000). Το κύριο πλεονέκτημα αυτής της μεθοδολογίας είναι το χαμηλό υπολογιστικό κόστος και για αυτό θα διερευνηθεί η υιοθέτησή του για την μοντελοποίηση των εκπομπών NO_x / N_2O από λέβητες ρευστοποιημένης κλίνης ανακυκλοφορίας.

Σε αυτό το μοντέλο, επιλύονται οι εξισώσεις μεταφοράς πέντε αέριων ενώσεων, NO, HCN, CNO, N_2O και CO.

$$\frac{\partial \varepsilon_g \rho_g \mathrm{Y}^{sp}}{\partial t} + \nabla\cdot\left(\varepsilon_g \rho_g \vec{u}_g \mathrm{Y}^{sp}\right) - \nabla\cdot\left(\varepsilon_g \Gamma \nabla Y^{sp}\right) = S \quad \text{Εξ. 3.85}$$

$$\Gamma = \rho_g D_{iff} + \frac{\mu_t}{Sc} \quad \text{Εξ. 3.86}$$

$$\mu_t = 0.09\rho_g \frac{k^{t^2}}{\varepsilon^t}$$ Εξ. 3.87

Στις εξισώσεις 3.85 έως 3.85, οι μεταβλητές ρ_g, ε_g, $\vec{u}_g$, k^t και ε^t είναι "παγωμένες", και ισούνται με την αντίστοιχη τιμή που προέλεξε το μοντέλο καύσης.

4. ΙΣΟΘΕΡΜΟΚΡΑΣΙΑΚΗ ΜΟΝΤΕΛΟΠΟΙΗΣΗ ΑΓΩΓΟΥ ΑΝΟΔΟΥ ΡΕΥΣΤΟΠΟΙΗΜΕΝΗΣ ΚΛΙΝΗΣ

Σε αυτό κεφάλαιο της διδακτορικής διατριβής, μοντελοποιείται ένας αγωγός ανόδου μιας πιλοτικής ρευστοποιημένης κλίνης ανακυκλοφορίας καύσης, ισχύος 1.2MW_{th} υπό ισοθερμοκρασιακές συνθήκες. Σε αυτή τη μοντελοποίηση διερευνήθηκαν μόνο υδροδυναμικά φαινόμενα, και μάλιστα η μελέτη επικεντρώθηκε στα συμπλέγματα σωματιδίων και την επίδρασή τους στην επαγόμενη οπισθέλκουσα δύναμη. Υπό αυτό το πρίσμα, το υποπλεγματικό μοντέλο οπισθέλκουσας EMMS που αναπτύχθηκε σε αυτή τη διατριβή εφαρμόστηκε στην μοντελοποίηση μιας ισοθερμοκρασιακής ροής εντός του αγωγού ανόδου. Επίσης, για λόγους σύγκρισης εφαρμόστηκε και το συμβατικό μοντέλο οπισθέλκουσας του Gidaspow. Σε συνδυασμό και παράλληλα με την αριθμητική διερεύνηση των μοντέλων οπισθέλκουσας διερευνήθηκε και η επίδραση της πυκνότητας πλέγματος στα αποτελέσματα.

4.1 Η μονάδα καύσης 1.2 MW_{th}

Η πιλοτική μονάδα ρευστοποιημένης κλίνης καύσης 1.2MW_{th} που μοντελοποιήθηκε απεικονίζεται στο σχήμα 4.1. Επιλέχθηκε για μοντελοποίηση λόγω του σχετικά μικρού μεγέθους της και της διαθεσιμότητας πειραματικών δεδομένων για ισοθερμοκρασιακές συνθήκες (Leithner et al., 1993).

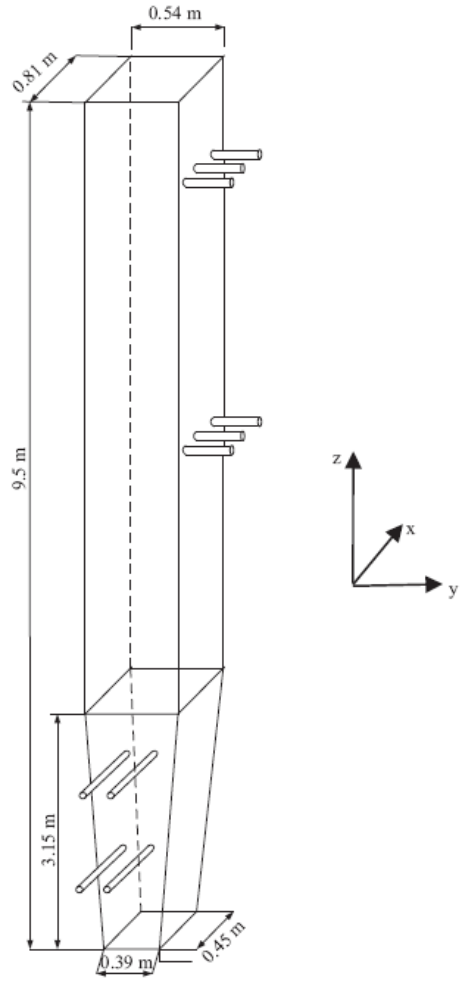

Σχήμα 4.1 Πιλοτική μονάδα 1.2 MW_{th} CFBC (Leithner et al., 1993)

Το ισοθερμοκρασιακό μοντέλο που αναπτύχθηκε ενσωματώθηκε σε εμπορικό πακέτο υπολογιστικής ρευστοδυναμικής (Fluent 6.3.26, FLUENT, 2006) μέσω κατάλληλου κώδικα (User Defined functions, UDFs) όπου αυτό ήταν απαραίτητο. Οι οριακές συνθήκες πάρθηκαν από την πειραματική εργασία των Leithner et al., 1993, που πραγματοποιήθηκε σε σταθερή θερμοκρασία (T =825^{o}C). Η μονάδα έχει 9.5m ύψος και μέση διατομή 0.4 m^2.

Το πρόβλημα μοντελοποιήθηκε ως τρισδιάστατο, καθώς η ροή εντός των κλινών έχει ισχυρά τριδιάστατα χαρακτηριστικά (Myöhänen et al., 2006). Επίσης τα πλέγματα κατασκευάστηκαν σεβόμενα πλήρως την πραγματική γεωμετρία του αγωγού ανόδου. Ο πίνακας 4.1 συνοψίζει τα σημαντικά χαρακτηριστικά των ομοιόμορφων εξαεδρικών αριθμητικών πλεγμάτων, ενώ ο πίνακας 4.2 τις ιδιότητες του αερίου και των στερεών

Πλέγμα	κάναβοι	L_{cell}	l_r
Αραιό	5,724 (9x6x106)	86.0 mm	330
Πυκνό	45,576 (12x18x211)	43.0 mm	165

Πίνακας 4.1 Χαρακτηριστικά των αριθμητικών πλεγμάτων.

διάμετρος σωματιδίων	260μm (Geldart B).
πυκνότητα σωματιδίων	2600 kg/m^3
πυκνότητα αερίου	0.3068 kg/m^3
συνεκτικότητα αερίου	4.2277 10^{-5} kg/(ms)
e_{ss}	0.9

Πίνακας 4.2 Ιδιότητες αέριου και σωματιδίων

Το σύστημα των μερικών διαφορικών εξισώσεων που καταστρώθηκε αποτελείται από τις εξισώσεις 2.1 και 2.2. Για τον υπολογισμό των τανυστών των δύο φάσεων η εξίσωση 2.7 χρησιμοποιήθηκε ενώ για την κοκκώδη πίεση η εξίσωση 2.6. Οι συντελεστές ορθής και διατμητικής συνεκτικότητας προσδιορίστηκαν από τις εξισώσεις 2.8 έως 2.11. Για τον υπολογισμό του συντελεστή εναλλαγής ορμής (β) χρησιμοποιήθηκε κατά περίπτωση το συμβατικό μοντέλο του Gidaspow (εξίσωση 2.12) ή το EMMS (εξίσωση 3.1). Η κοκκώδης θερμοκρασία μοντελοποιήθηκε μέσω της αλγεβρικής εξίσωσης 2.5

4.2 Μοντέλο οπισθέλκουσας

4.2.1 Η συνάρτηση ετερογένειας (H_d)

Η μοντελοποίηση του αγωγού ανόδου με το μοντέλο EMMS προϋποθέτει την επίλυση του μη γραμμικού προβλήματος βελτιστοποίησης που παρουσιάστηκε στο κεφάλαιο 3.1 (Nikolopoulos et al., 2010[b]). Για αυτή την επίλυση χρησιμοποιήθηκε το εμπορικό πακέτο GAMS - General Algebraic Modeling System, (http://www.gams.com/).

Το σύστημα εξισώσεων του EMMS αποτελείται από: α) τις εξισώσεις 3.2 έως 3.7 και 3.8 και 3.10, β) τους περιορισμούς 3.11 έως 3.14, και γ) τις εξισώσεις του πίνακα 3.2. Το σύστημα επιλύεται μέσω της ελαχιστοποίησης της συναλλασσόμενης ενέργειας, που περιγράφεται από την εξίσωση 3.15, για κάθε τριπλέτα u_g, u_s και ε_g, καθώς και για τις συνθήκες λειτουργίας της μονάδας υπό μοντελοποίησης (Leithner et al., 1993). Για κάθε τριπλέτα, μετά την επίλυση του συστήματος μπορεί εύκολα να υπολογιστεί ο συντελεστής ετερογένειας (H_d).

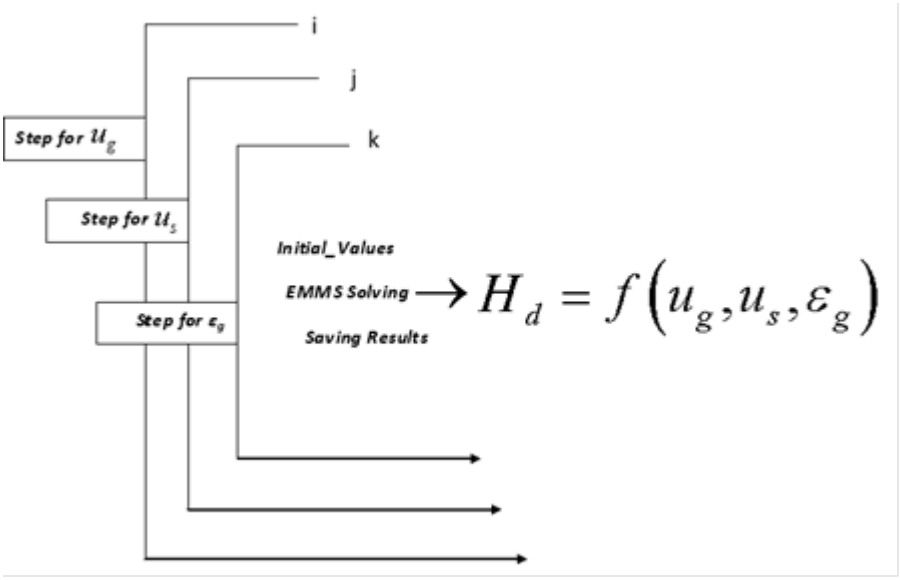

Σχήμα 4.2 Διαδικασία επίλυσης

Η διαδικασία επίλυσης του προβλήματος απεικονίζεται στο σχήμα 4.2. Αν και ο συντελεστής ετερογένειας είναι συνάρτηση τριών ποσοτήτων, η ανάλυση των αποτελεσμάτων του μοντέλου ανέδειξε πως ο συντελεστής είναι συνάρτηση του κλάσματος αερίου (ε_g) και της απόλυτης ταχύτητας ολίσθησης ($|(u_g-u_s)|$), συμπέρασμα που επιβεβαιώνεται και από τους Zhang et al., 2008.

Το σχήμα 4.3 απεικονίζει το συντελεστή ετερογένειας ως συνάρτηση του κλάσματος αερίου για συγκεκριμένη ταχύτητα ολίσθησης (u_{slip}=1.5 m/sec). Παρόμοια διαγράμματα μπορούν να φτιαχτούν και για άλλες ταχύτητες ολίσθησης. Κάθε κατανομή μπορεί να χωριστεί σε τρεις βασικές περιοχές, τις A, B και C. Η περιοχή A αναφέρεται σε αραιές συνθήκες ($0.95 \leq \varepsilon_g < \varepsilon^*$), ενώ η περιοχή B σε σχετικά πυκνότερες ($0.82 \leq \varepsilon_g < 0.95$). Στη περιοχή C, όπου ο όγκος ελέγχου είναι ιδιαιτέρως πυκνός σε σωματίδια η αισθητή πυκνότητα (που αντιπροσωπεύεται από το ε_c) των συμπλεγμάτων σταματά να αυξάνεται και παραμένει σταθερή.

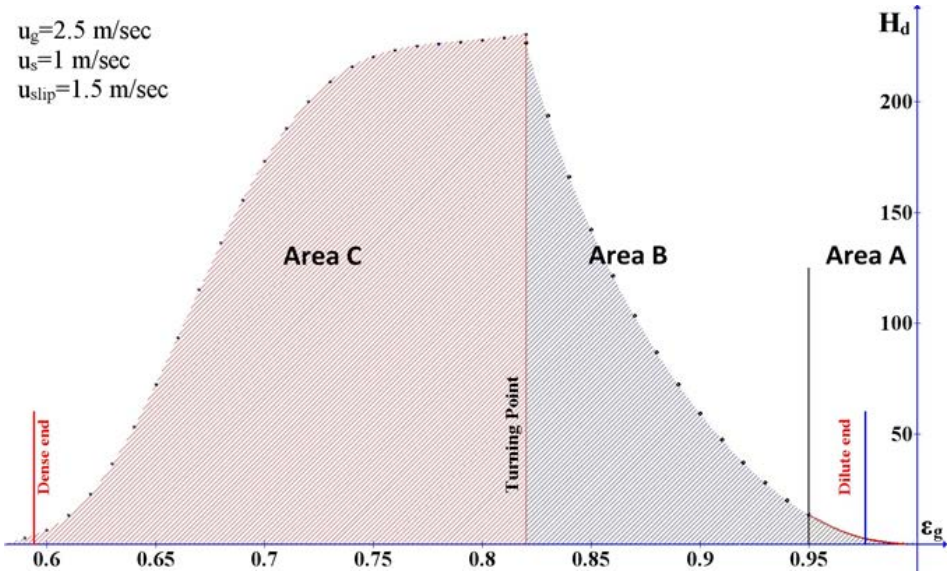

Σχήμα 4.3 Η συνάρτηση $H_d(\varepsilon_g)$ για u_{slip}=1.5m/sec.

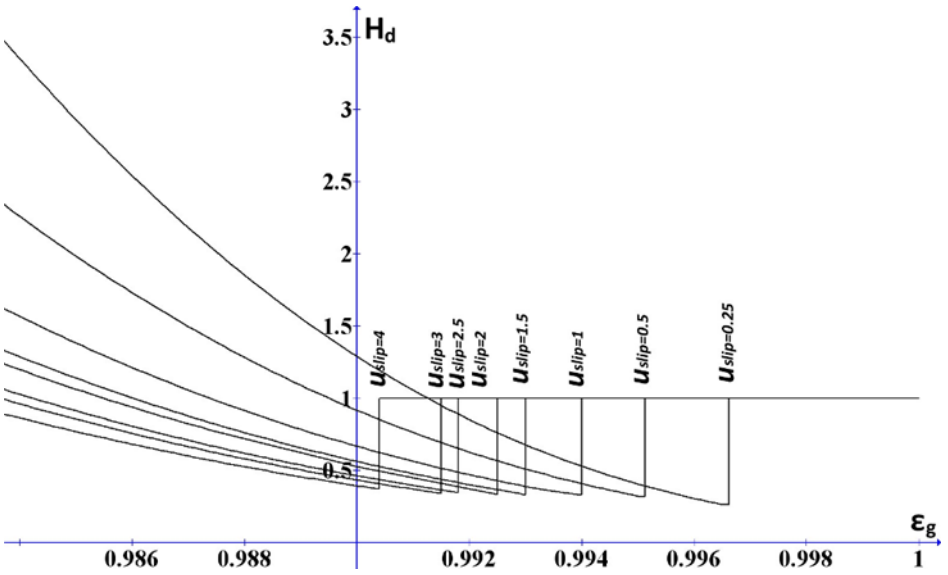

Σχήμα 4.4 Η συνάρτηση $H_d(\varepsilon_g)$ για u_{slip} = 1.5 m/sec (μεγέθυνση στο αραιό άκρο).

Για κάθε περιοχή (A, B και C), διαφορετικά πολυώνυμα της μορφής $H_d = f\left(|u_{slip}|, \varepsilon_g\right)$ κατασκευάστηκαν για λόγους παρεμβολής των αποτελεσμάτων. Επίσης το άνω όριο της περιοχής A είναι το ε^* και για μεγαλύτερα κλάσματα αερίου ο συντελεστής ισούται με τη μονάδα. Σε αυτή την διατριβή η τιμή αυτού του ορίου δε θεωρείται σταθερή όπως στην εργασία του Wang and Li, 2007, αλλά συνάρτηση της ταχύτητας ολίσθησης (Nikolopoulos et al., 2010[b]; Papafotiou, 2009) όπως φαίνεται και στο σχήμα 4.4. Αυτός ο νεοτερισμός είναι σημαντικός καθώς αυξάνει την ακρίβεια του μοντέλου στην αραιή περιοχή η οποία είναι και η επικρατέστερη εντός του αγωγού ανόδου (Atsonios, 2010). Για την περιοχή A το παρακάτω πολυώνυμο χρησιμοποιήθηκε για την παρεμβολή του H_d:

$$H_d = \sum_{i=1}^{4} 10^{\alpha_i \cdot \left[1000 \cdot \left(\varepsilon_g - 0.95\right)\right]^i} \qquad \text{Εξ. 4.1}$$

Για την περιοχή B αντίστοιχα:

$$H_d = \sum_{i=1}^{4} a_i {\varepsilon_g}^i \qquad \text{Εξ. 4.2}$$

Για την περιοχή C, με όρια $\varepsilon_{mf}(=0.55) \le \varepsilon_g \le 0.82$:

$$H_d = \sum_{i=1}^{6} a_i {\varepsilon_g}^i \qquad \text{Εξ. 4.3}$$

Θα πρέπει να τονιστεί πως επειδή το πρόβλημα επιλύθηκε για συγκεκριμένες ταχύτητες ολίσθησης, για τις ενδιάμεσες ταχύτητες χρησιμοποιήθηκε η ακόλουθη γραμμική παρεμβολή:

$$w = \frac{u_{slip}^{+} - u_{slip}}{u_{slip}^{+} - u_{slip}^{-}} \qquad \text{Εξ. 4.4}$$

$$H_d\left(u_{slip}\right) = \left(1-w\right) \cdot H_d\left(u_{slip}^{+}\right) + w \cdot H_d\left(u_{slip}^{-}\right) \qquad \text{Εξ. 4.5}$$

4.2.2 Περιγραφή αποτελεσμάτων του EMMS

Τα αποτελέσματα που παρουσιάζονται στις ακόλουθες ενότητες είναι αντιπροσωπευτικά για τις συνθήκες λειτουργίας της μονάδας των 1.2 MW_{th} και δεν πρέπει να θεωρηθούν καθολικά και εφαρμόσιμα σε οποιαδήποτε μονάδα.

Εν γένει ο σχηματισμός της πυκνής δομής πηγάζει από δύο μηχανισμούς. Ο πρώτος σχετίζεται με την μεγέθυνση των συμπλεγμάτων λόγω της αύξησης του όγκου τους, και ο δεύτερος λόγω της πύκνωσης τους σε σωματίδια. Οι δύο αυτοί μηχανισμοί αυξάνουν τη μάζα στην πυκνή δομή. Στις περιοχές A και B ο δεύτερος μηχανισμός είναι πιο ισχυρός ενώ στην περιοχή C επιδρά μόνο ο πρώτος μηχανισμός.

4.2.2.1 Χαρακτηριστικά της περιοχής A.

Εντός της περιοχής A ο συντελεστής ετερογένειας ποικίλει σημαντικά, ενώ για εξαιρετικά αραιές συνθήκες ισούται με τη μονάδα. Σε αυτή την περιοχή όπου f=0. (Σχήμα 4.5, $\varepsilon_g \geq \varepsilon^*$), η εξίσωση των Wen and Yu, 1966 ταυτίζεται με το μοντέλο EMMS.

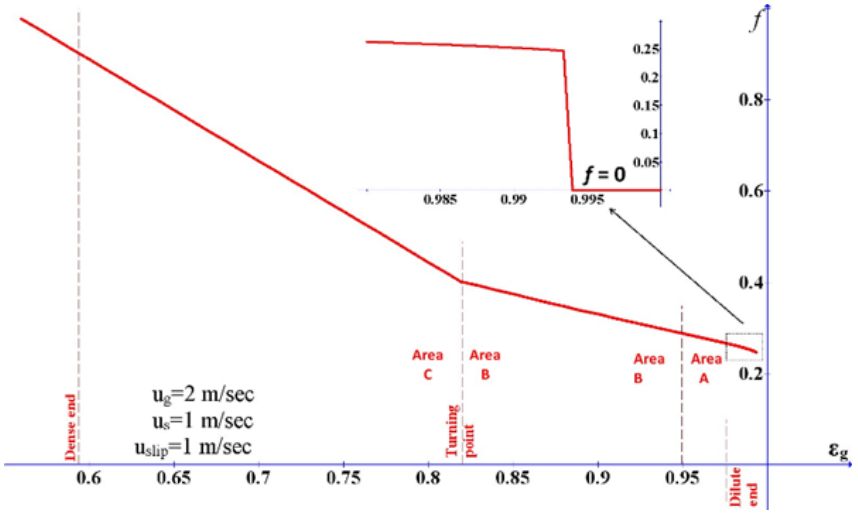

Σχήμα 4.5 Ποσοστό όγκου της πυκνής δομής (f).

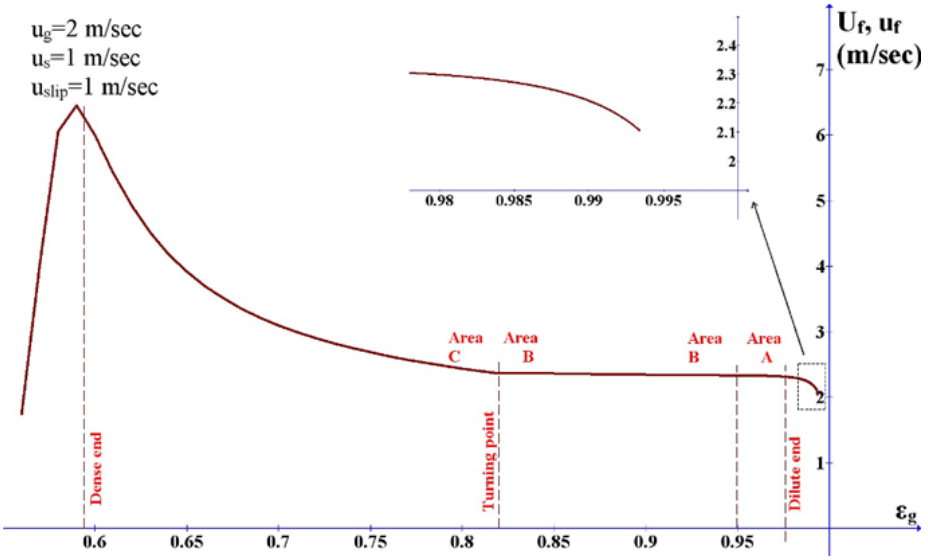

Σχήμα 4.6 Ταχύτητα αερίου εντός της αραιής δομής

Εντός της περιοχής A και καθώς ο όγκος ελέγχου πυκνώνει σε σωματίδια, το ποσοστό όγκου των συμπλεγμάτων αυξάνεται σταθερά (σχήμα 4.5). Οι μεγάλες τιμές αυτού του μεγέθους (f) που προελέχθησαν και από τους Wang and Li, 2007) μπορεί να μην είναι ρεαλιστικές για τόσο αραιές συνθήκες. Ωστόσο, όπως σωστά αναφέρουν και οι Wang and Li, 2007, σε αυτή την περιοχή η ετερογένεια της ροής δεν αποδίδεται μόνο με τα συμπλέγματα σωματιδίων καθώς ακόμα και η απλή γειτνίαση κάποιων σωματιδίων επηρεάζει σημαντικά

την επαγόμενη οπισθέλκουσα. Οι εξισώσεις του EMMS λαμβάνουν υπ' όψη τους τέτοια φαινόμενα αλλά τα μοντελοποιούν ως συμπλέγματα

Όσο μεγαλώνουν σε μάζα τα συμπλέγματα σωματιδίων τόσο το αέριο "αποφεύγει" να εισέλθει σε αυτά και λόγω αυτού του φαινομένου αυξάνεται η ταχύτητα του αέρα στην αραιή δομή (σχήμα 4.6) και μειώνεται στην πυκνή δομή (σχήμα 4.7). Αξίζει να σημειωθεί πως στο αραιό άκρο και οι δύο ταχύτητες τείνουν στη μέση ταχύτητα του όγκου ελέγχου (u_g = 2 m/sec).

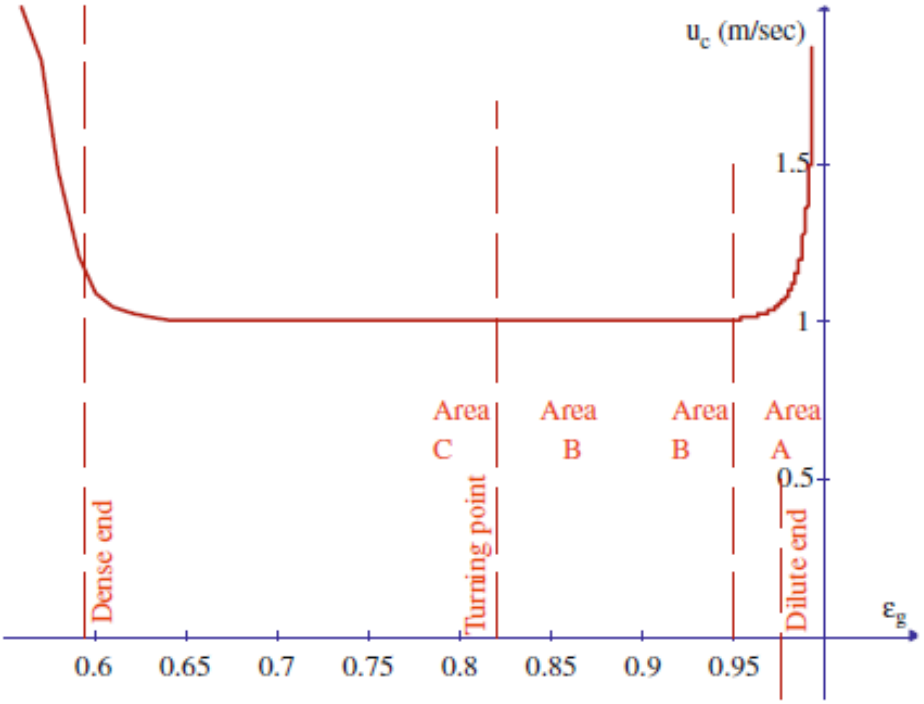

Σχήμα 4.7 Ταχύτητα του αερίου εντός της πυκνής δομής

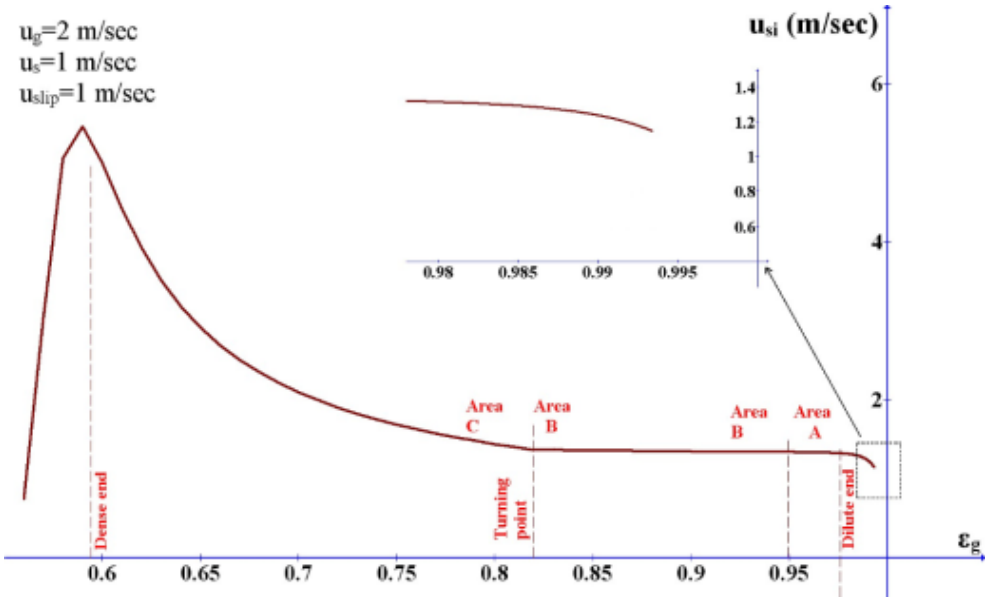

Σχήμα 4.8 Ταχύτητα ολίσθησης των συμπλεγμάτων u_{si}.

Η ταχύτητα ολίσθησης των συμπλεγμάτων (u_{si}) αυξάνεται απότομα κοντά στο αραιό άκρο και παραμένει σχετικά σταθερή και 20% μεγαλύτερη από τη μέση ταχύτητα ολίσθησης (u_{slip})

όπως φαίνεται και στο σχήμα 4.8). Το αποτέλεσμα αυτό είναι λογικό καθώς τα συμπλέγματα σωματιδίων, ως δομές μεγαλύτερου μεγέθους μπορούν να αναπτύσσουν μεγαλύτερες ταχύτητες ολίσθησης.

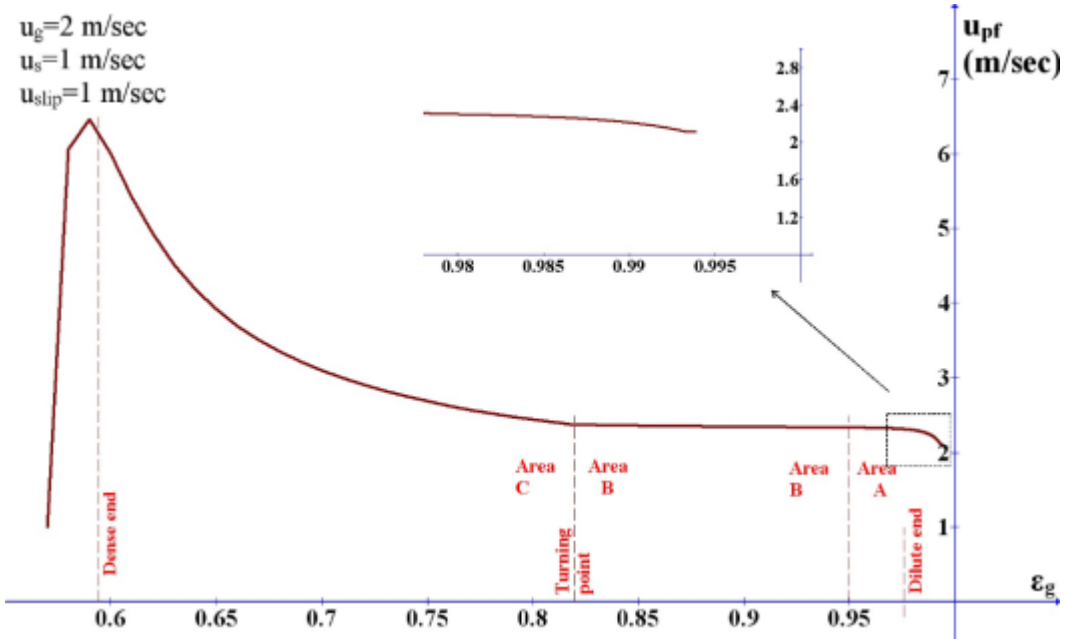

Σχήμα 4.9 Ταχύτητα σωματιδίων εντός της αραιής περιοχής.

Η ταχύτητα των σωματιδίων στην αραιή δομή είναι περίπου ίση με τη u_f, αφού το αέριο παρασύρει εύκολα τα διασκορπισμένα σωματίδια (σχήμα 4.9). Η ταχύτητα των σωματιδίων εντός των συμπλεγμάτων (u_{pc}), παραμένει σταθερή και ίση με u_s = 1 m/sec και στο σχήμα 4.10 που απεικονίζει την ταχύτητα ολίσθησης εντός των συμπλεγμάτων παρατηρείται η ίδια τάση όπως στο σχήμα 4.7. Συμπερασματικά εντός των συμπλεγμάτων, τα σωματίδια επιβραδύνουν το αέριο όσο αυξάνεται ο αριθμός τους.

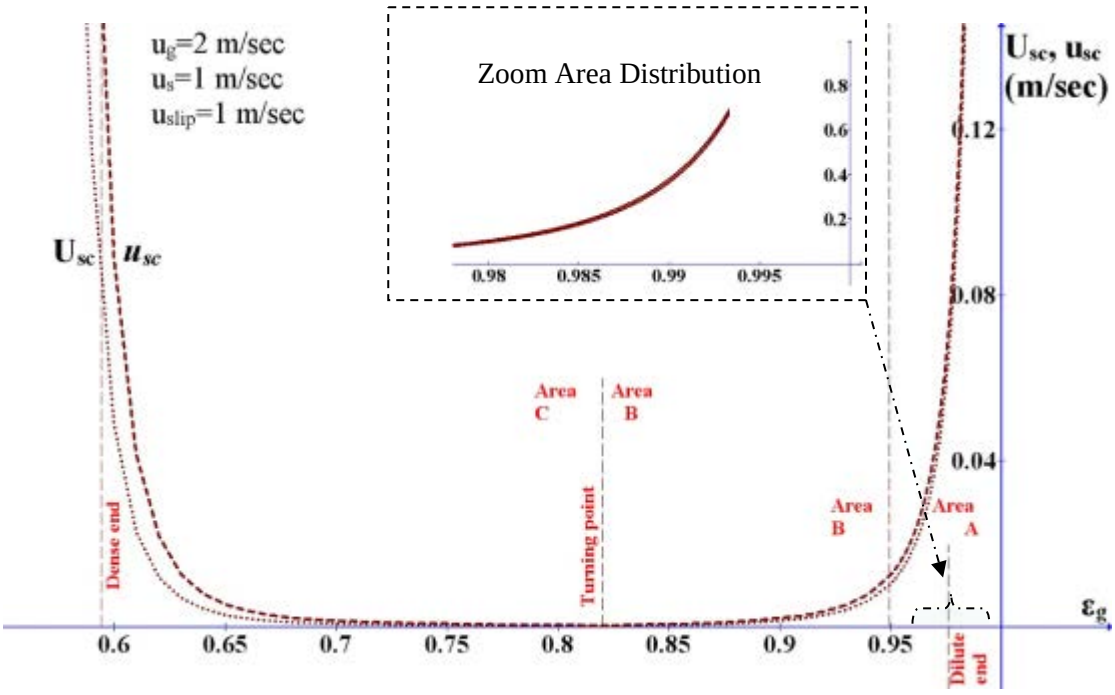

Σχήμα 4.10 Πραγματική και φαινόμενη ταχύτητα ολίσθησης εντός της πυκνής δομής

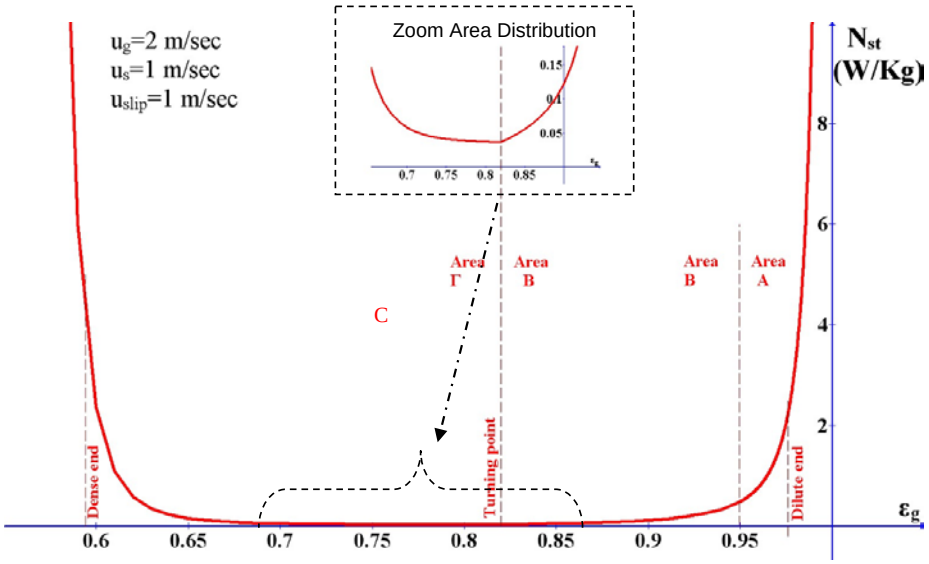

Σχήμα 4.11 Συναλλασσόμενη ενέργεια (N_{st}).

Οι συμπλεγματικές δομές δεν είναι τόσο κυρίαρχες στην περιοχή Α, με αποτέλεσμα η ενέργεια ανά μονάδα μάζας (N_{st}) να είναι αρκετά μεγάλη, ειδικά κοντά στο αραιό άκρο ε^* όπως φαίνεται και στο σχήμα 4.11. Φυσικά όσο αυξάνονται τα συμπλέγματα η ενέργεια αυτή μειώνεται αισθητά. Επιπρόσθετα, η επιτάχυνση της αραιής δομής $(a_f + g)$ είναι σχεδόν μηδενική όπως προβλέπει και το μοντέλο των Wang and Li, 2007. Αντιθέτως η επιτάχυνση εντός της πυκνής δομής ακολουθεί την συμπεριφορά της συναλλασσόμενης ενέργειας λόγω της μείωσης της ταχύτητας ολίσθησης που παρατηρείται στο σχήμα 4.10. Είναι σημαντικό ότι το μοντέλο EMMS, που αναπτύχθηκε σε αυτή τη διατριβή, προβλέπει ρεαλιστικές τιμές για το α_c (σχήμα 4.12) σε αντίθεση με τις προβλέψεις των Wang and Li, 2007.

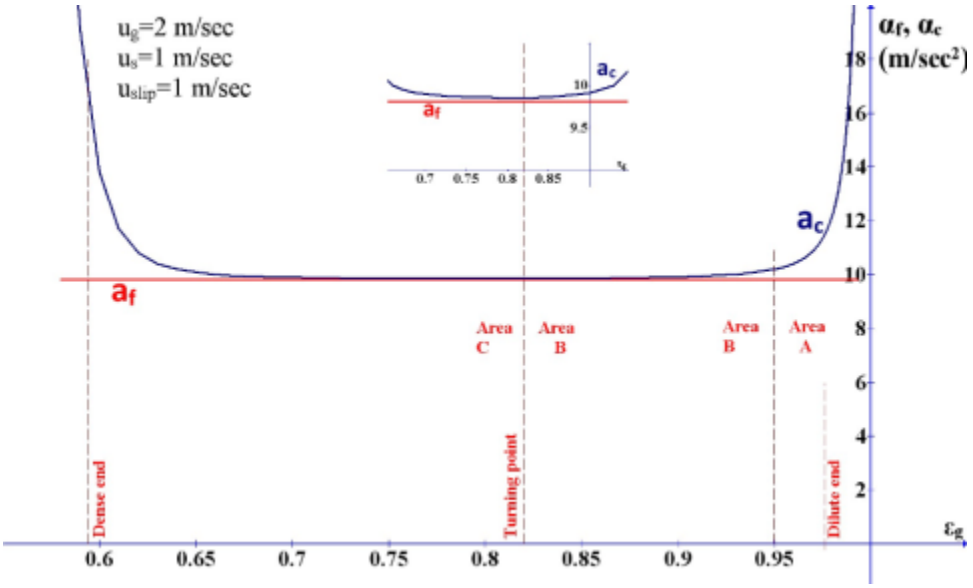

Σχήμα 4.12 Επιτάχυνση της αραιής και της πυκνής δομής.

4.2.2.2 Χαρακτηριστικά της περιοχής Β.

Στην περιοχή Β, επιδρούν οι ίδιοι μηχανισμοί που αναφέρθηκαν για την περιοχή Α. Όμως, καθώς τα φαινόμενα συμπλεγμάτωσης είναι πιο έντονα η συναλλασσόμενη ενέργεια

είναι πολύ χαμηλή, όπως φαίνεται και στο σχήμα 4.11. Η αύξηση του πληθυσμού των σωματιδίων αυξάνει σημαντικά την αισθητή πυκνότητα των συμπλεγμάτων εφόσον η αντίστοιχη αύξηση στο μέγεθος των συμπλεγμάτων δεν είναι πολύ μεγάλη (σχήμα 4.13).

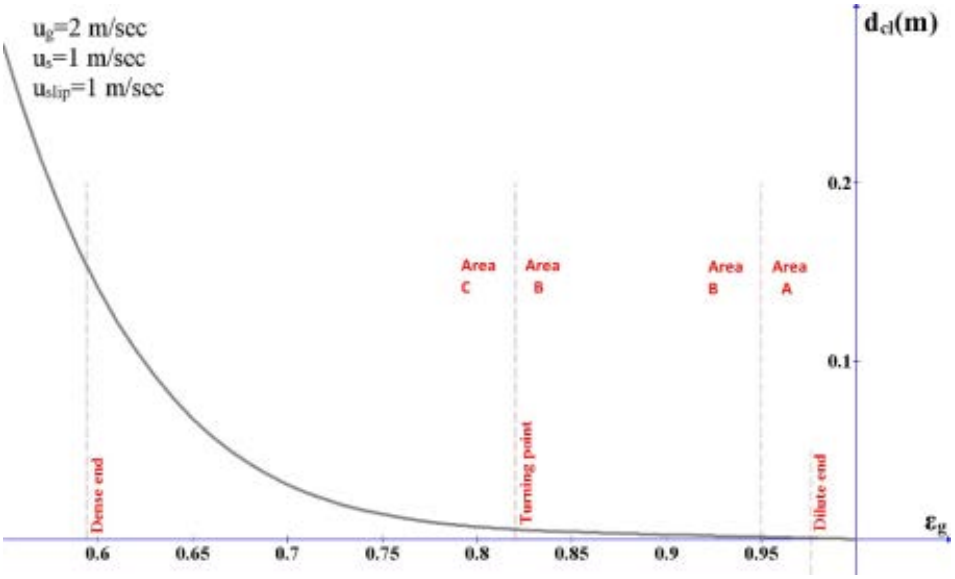

Σχήμα 4.13 Διάμετρος συμπλεγμάτων.

4.2.2.3 Χαρακτηριστικά της περιοχής C.

Εντός της περιοχής C ο περιορισμός 3.11 ενεργοποιείται. Η σημασία αυτού του περιορισμού είναι μεγάλη καθώς αποτρέπει την περαιτέρω πύκνωση των συμπλεγμάτων και επιτρέπει μόνο την αύξηση του μεγέθους τους. Το ποσοστό όγκου της πυκνής δομής (σχήμα 4.5), αυξάνει τον ρυθμό αύξησής του στο σημείο μετάβασης από την περιοχή B στη C (turning point), όπως υποδεικνύουν και τα αποτελέσματα των Wang and Li, 2007. Η μέγιστη τιμή του συντελεστή ετερογένειας και η ελάχιστη ενέργεια για κάθε ταχύτητα ολίσθησης βρίσκεται στο σημείο μετάβασης.

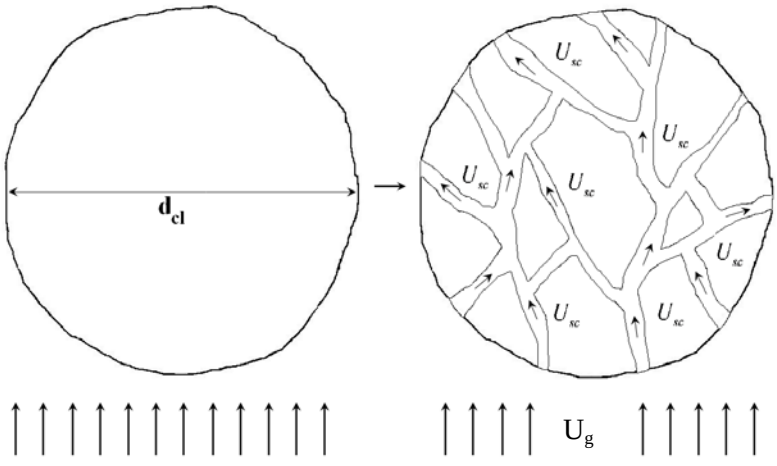

Σχήμα 4.14 Κατάρρευση των συμπλεγμάτων ως ενιαίας δομής.

Για μεγαλύτερες συγκεντρώσεις σωματιδίων (ε_g<0.59), η ροή θα έπρεπε να προσομοιάζει τη ρευστοποίηση φυσαλίδων (bubbling fluidization) όπως αναφέρουν οι Yang et al., 2003. Το μοντέλο EMMS προβλέπει αυτή την τάση, παρ' όλο που μια εμπειρική σχέση χρησιμοποιήθηκε για τον προσδιορισμό της διαμέτρου των συμπλεγμάτων, που προβλέπει πολύ μεγάλες τιμές. Λόγω τις αύξησης της διαμέτρου, το αέριο αναγκάζεται να εισχωρήσει

εντός των συμπλεγμάτων αυξάνοντας την ταχύτητα ολίσθησης u_{sc}, (σχήμα 4.10). Σαν αποτέλεσμα τα συμπλέγματα ως ενιαία δομή καταρρέουν (σχήμα 4.14) και η ταχύτητα ολίσθησής τους μειώνεται (σχήμα 4.8). Παράλληλα λόγω αυτής της κατάρρευσης η ενέργεια και η επιτάχυνση των σωματιδίων αυξάνονται.

Στην πολύ πυκνή περιοχή, θα πρέπει να τονιστεί ότι το μοντέλο EMMS προβλέπει ομοιογενείς συνθήκες και H_d ίσο με τη μονάδα όπως προέλεξαν και οι Wang and Li, 2007.

4.2.2.4 Η επίδραση της ταχύτητας ολίσθησης

Η ταχύτητα ολίσθησης μεταξύ του αερίου και των στερεών επηρεάζει τα αποτελέσματα του EMMS. Στο σχήμα 4.15 απεικονίζεται η συναλλασσόμενη ενέργεια (N_{st}) για διάφορες ταχύτητες ολίσθησης u_{slip}. Παρατηρείται ότι τα δύο μεγέθη είναι ανάλογα. Συμπερασματικά η ταχύτητα ολίσθησης και ο συντελεστής ετερογένειας είναι αντιστρόφως ανάλογα μεγέθη. Αυτή η επίδραση της ταχύτητας στις δομές μεσο-κλίμακας μπορεί έμμεσα να αναδειχθεί και από τα αποτελέσματα των Zhang and VanderHeyden, 2001.

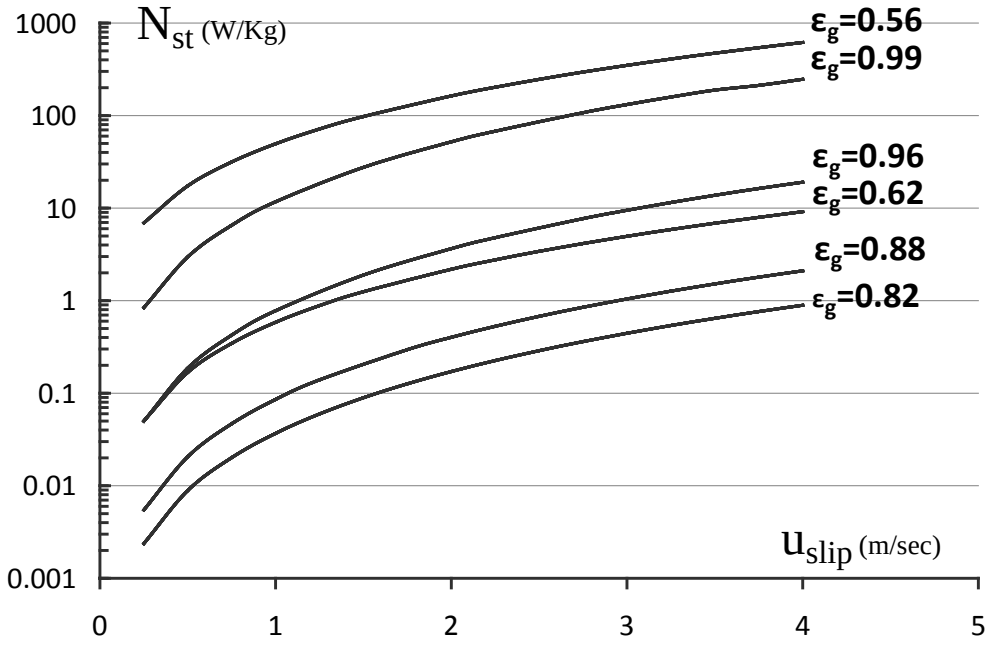

Σχήμα 0.15 Η συνάρτηση κόστους

4.3 Μοντελοποίηση του αγωγού ανόδου

Για την μοντελοποίηση του αγωγού ανόδου τέσσερα διαφορετικά μοντέλα εφαρμόστηκαν, τα οποία απαριθμούνται στον πίνακα 4.5.Εξετάσθηκε η επίδραση και της μοντελοποίησης του συντελεστή εναλλαγής ορμής καθώς και της πυκνότητας πλέγματος (αραιό - πυκνό). Όσον αφορά το συντελεστή ορμής εξετάστηκε το μοντέλο EMMS και το συμβατικό μοντέλο του Gidaspow.

Οπισθέλκουσα / Πλέγμα	Gidaspow	EMMS
Αραιό	Μοντέλο I	Μοντέλο II
Πυκνό	Μοντέλο III	Μοντέλο IV

Πίνακας 4.5 Μοντέλα που εφαρμόστηκαν

Επειδή το πεδίο ροής είναι μη μόνιμο, για την εξαγωγή αντιπροσωπευτικών μεγεθών υπολογίστηκαν μέσες τιμές για χρονική περίοδο 20 δευτερολέπτων (Kallio, 2006; Rampidis et al., 2007). Το μοντέλο EMMS, εν γένει, μείωσε την εφαρμοζόμενη οπισθέλκουσα δύναμη με αποτέλεσμα την αύξηση της μάζας εντός της κλίνης από 110 kg (μοντέλο I) που προέλεξε το μοντέλο του Gidaspow, σε 170 kg (μοντέλο II), για το αραιό πλέγμα. Αντίστοιχα στην περίπτωση του πυκνού πλέγματος, το μοντέλο του Gidaspow προέλεξε 270 kg (μοντέλο III), ενώ το EMMS 310 kg (μοντέλο IV). Αυτή η αύξηση αντικατοπτρίζεται και στο σχήμα 4.16.Σε αυτό το σχήμα παρουσιάζεται το προφίλ της χρονικά μέσης πίεσης καθ' ύψος μαζί με τα αντίστοιχα πειραματικά δεδομένα.

Όσον αφορά την επίδραση της πυκνότητας πλέγματος, τα αριθμητικά αποτελέσματα αναδεικνύουν πως και για τα δυο μοντέλα οπισθέλκουσας το πυκνό πλέγμα αυξάνει την ακρίβεια των υπολογισμών.

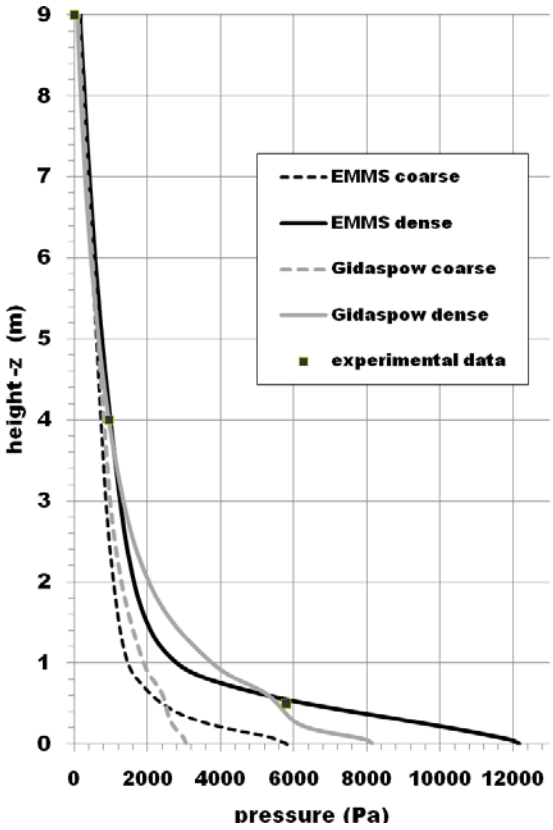

Σχήμα 4.16 Πίεση καθ' ύψος της κλίνης.

Τα σχήματα 4.17 και 4.18 παρουσιάζουν την μέση χρονικά συγκέντρωση των σωματιδίων και τη μέση ταχύτητα ολίσθησης για την κεντρογραμμή του αγωγού αντίστοιχα. Τα σχήματα αυτά, αναδεικνύουν πως οι μεγαλύτερες διαφορές στα αποτελέσματα των μοντέλων παρατηρούνται στην πυκνή κάτω περιοχή (bottom zone) που χαρακτηρίζεται από πολύπλοκη υδροδυναμική. Το μοντέλο EMMS υπερέχει καθαρά έναντι του συμβατικού σε αυτή την περιοχή, και για τα δύο πλέγματα. Επίσης, το EMMS μοντελοποιεί καλλίτερα το ροϊκό φαινόμενο S-shape (Kunii and Levenspiel, 1991).

Αυτή η επιτυχία μπορεί να αποδοθεί στην ορθότερη μοντελοποίηση της οπισθέλκουσας στη κάτω περιοχή αλλά και στην ορθότερη μοντελοποίηση της εσωτερικής ανακυκλοφορίας που οφείλεται στο ροϊκό φαινόμενο πυρήνα - δακτυλίου (core-annulus flow). Επίσης, τα μοντέλα με το πυκνό πλέγμα, ανεξαρτήτως μοντέλου οπισθέλκουσας προλέγουν μεγαλύτερη κάτω περιοχή (σχήμα 4.17).

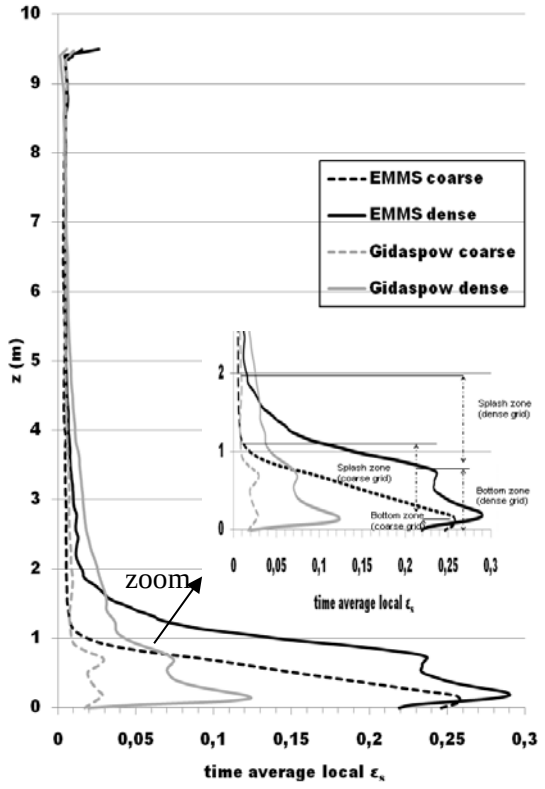

Σχήμα 4.17 Χρονικά μέση τοπική συγκέντρωση σωματιδίων καθ' ύψος της κλίνης.

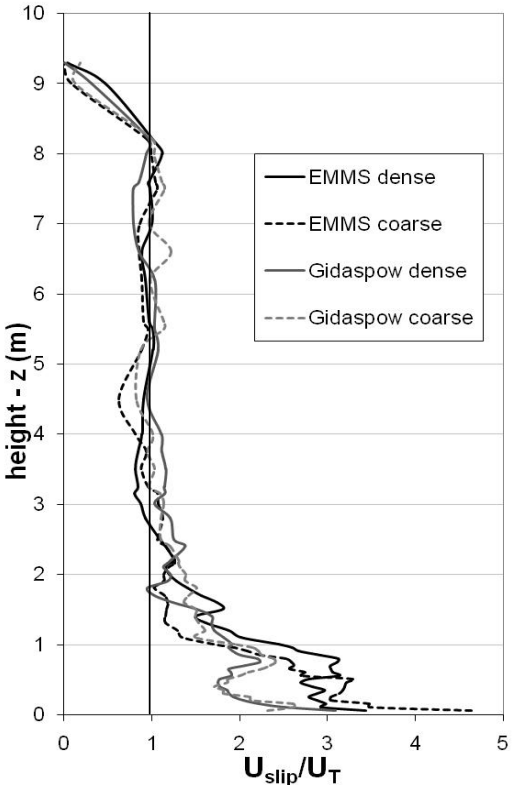

Σχήμα 0.18 Χωρικά (για κάθε διατομή) και χρονικά μέση ταχύτητας ολίσθησης

Στην κάτω περιοχή, η εφαρμογή του μοντέλου EMMS αυξάνει την ταχύτητα ολίσθησης λόγω της μείωσης της ελεύθερης διατομής (σχήμα 4.18). Ωστόσο στην άνω περιοχή (freeboard), το μοντέλο του Gidapow προβλέπει αισθητά μεγαλύτερη ταχύτητα ολίσθησης λόγω των χαμηλών τιμών του συντελεστή ετερογένειας. Η συγκέντρωση των σωματιδίων στην άνω περιοχή της κλίνης κυμαίνεται κοντά στο αραιό άκρο ε^* σε μια περιοχή που το μοντέλο EMMS προβλέπει ότι $F_{EMMS} > F_{WEN,YU}$.

Στην άνω περιοχή (freeboard) η ροή είναι αρκετά αραιή και η αδυναμία σχηματισμού μεγάλων συμπλεγμάτων, (δομές που αυξάνουν την επιτρεπόμενη ταχύτητα ολίσθησης) θα έπρεπε να περιορίσει την ανάπτυξη ταχυτήτων ολίσθησης μεγαλύτερων της οριακής (U_t). Αυτό τον περιορισμό τον σέβονται τα αποτελέσματα του EMMS αλλά όχι και του Gidapspow αναδεικνύοντας την υπεροχή του μοντέλου που αναπτύχθηκε.

Η πυκνότητα πλέγματος επίσης επηρεάζει σημαντικά τα χαρακτηριστικά της ροής. Το πυκνό πλέγμα έχει μεγαλύτερη ακρίβεια καθώς έχει τη δυνατότητα της ρητής μοντελοποίησης μικρότερων σωματιδιακών δομών (σχήμα 4.19). Στο σχήμα 4.20 διαφαίνεται πως το μοντέλο EMMS προβλέπει αυξημένη συγκέντρωση σωματιδίων στα τοιχώματα και ιδιαίτερα στις τέσσερις γωνίες της διατομής του αντιδραστήρα. Μια τέτοια πρόλεξη είναι λογική, καθώς σε αυτές τις περιοχές η ταχύτητα του αέρα είναι μικρή και δεν μπορεί να διασκορπίσει τα σωματίδια. Επίσης, το μοντέλο του Gidapsow, ιδιαίτερα για το αραιό πλέγμα, προβλέπει πολύ χαμηλές τιμές για το ε_s στην κάτω περιοχή (bottom zone), σχήμα 4.20.

Στην παρούσα μελέτη δεν επετεύχθη πλεγματική ανεξαρτησία για κανένα από τα μοντέλα οπισθέλκουσας (EMMS ή Gidaspow). Όπως αναφέρουν οι Wang et al., 2008 η πλεγματική ανεξαρτησία για το μοντέλο του Gidaspow υποτίθεται πως απαιτεί $l_r \sim 20$, πέντε φορές δηλαδή πυκνότερο πλέγμα από το πλέγμα που εφαρμόστηκε σε αυτή τη διερεύνηση.

Όσον αφορά το μοντέλο EMMS, η εξάρτηση πλέγματος μπορεί να αποδοθεί στη θεώρηση ομοιόμορφων συνθηκών εντός των υποπλεγματικών δομών.

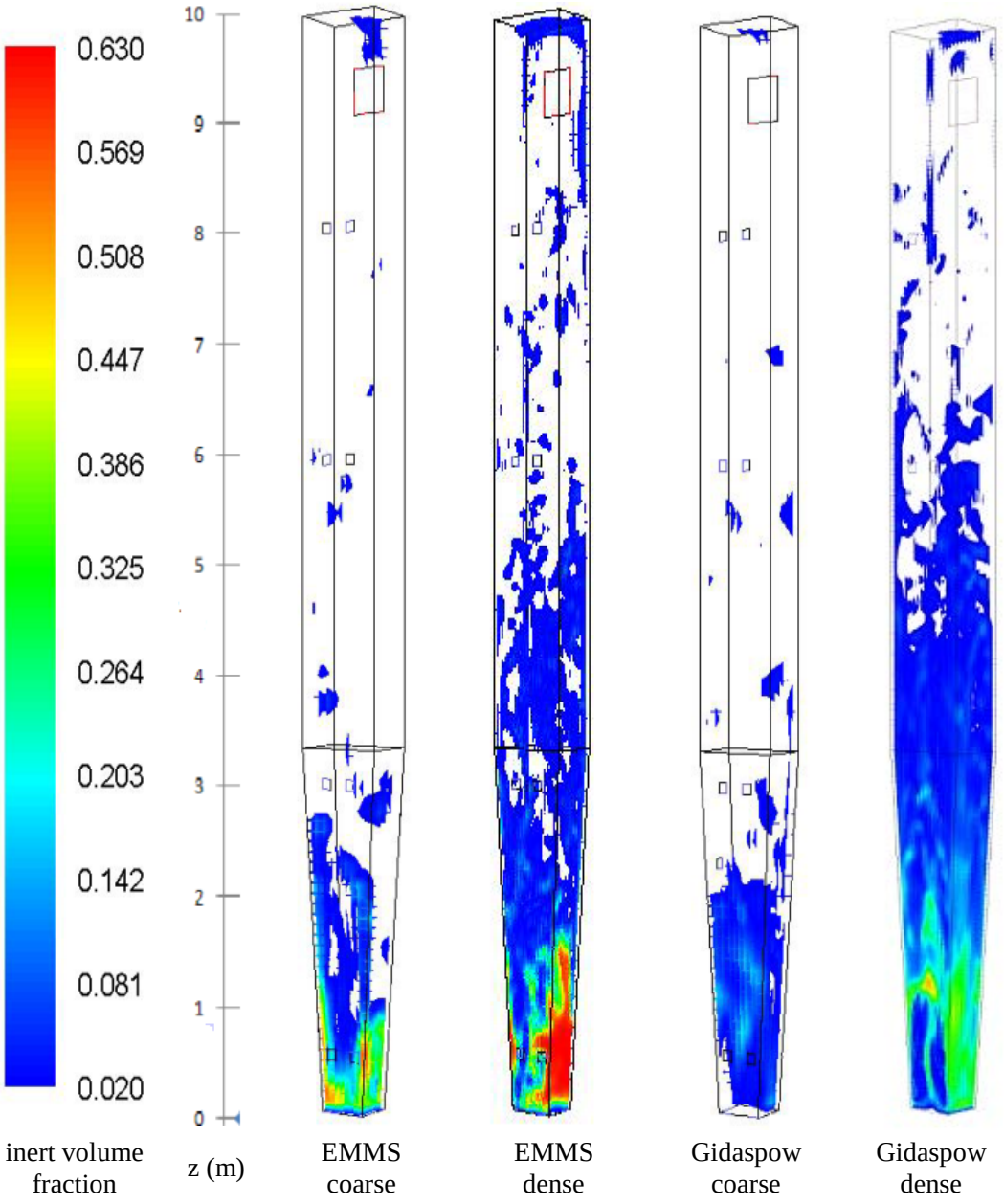

Σχήμα 4.19 Στιγμιαίο ποσοστό όγκου σωματιδίων (0.02-0.63)

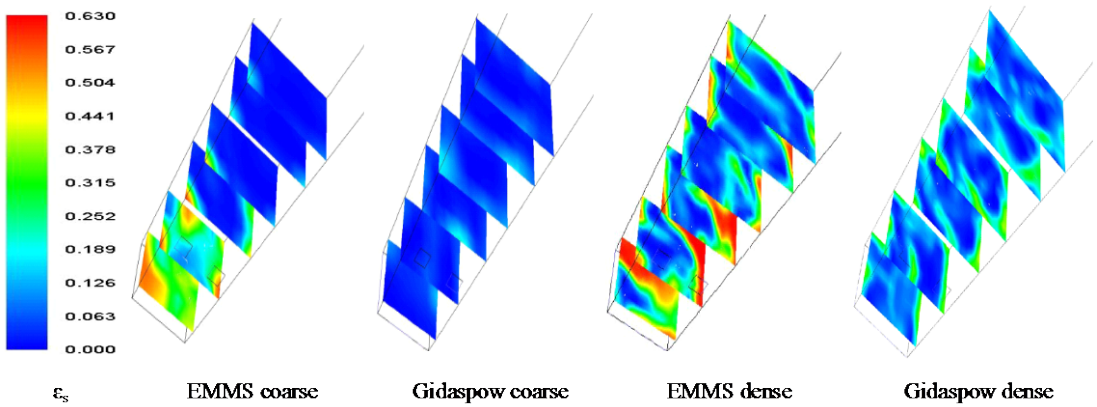

Σχήμα 4.20 Στιγμιαίο ποσοστό όγκου σωματιδίων για διαφορετικά ύψη στην πυκνή κάτω περιοχή για τα τέσσερα μοντέλα που εξετάστηκαν (I-IV).

5. ΜΟΝΤΕΛΟΠΟΙΣΗ ΚΑΥΣΗΣ ΣΤΕΡΕΟΥ ΚΑΥΣΙΜΟΥ ΚΑΙ ΕΚΠΟΜΠΩΝ NO_X / N_2O ΣΕ ΡΕΥΣΤΟΠΟΙΗΜΕΝΗ ΚΛΙΝΗ

Για την υπολογιστική ρευστοδυναμική μοντελοποίηση ροών με αντιδράσεις εντός ρευστοποιημένων κλινών ανακυκλοφορίας δεν υπάρχουν πολλές δημοσιευμένες εργασίες , και η πλειονότητα τέτοιων δημοσιεύσεων (Gungor, 2008[b]; Gungor and Eskin, 2008[b]) μοντελοποιούν τη ροή ως διδιάστατη. Αυτό το κεφάλαιο επικεντρώνεται στην τρισδιάστατη μοντελοποίηση της καύσης στερεού καυσίμου σε αγωγό ανόδου ενσωματώνοντας κατάλληλα μοντέλα για τη μεταφορά θερμότητας και τις χημικές αντιδράσεις. Για την μοντελοποίηση της υδροδυναμικής, το συμβατικό μοντέλο χρησιμοποιήθηκε (Rampidis et al., 2007). Επίσης, μελετήθηκε η υπολογιστική προσομοίωση των οξειδίων του αζώτου με ένα απεπλεγμένο μοντέλο. Εκτός από τα NO_x, μελετήθηκε και το N_2O τα οποία σχηματίζονται σε συνθήκες καύσης ρευστοποιημένης κλίνης λόγω χαμηλής θερμοκρασίας. Το παρών κεφάλαιο, χωρίζεται σε δύο μέρη: α) τη μοντελοποίηση της καύσης, και β) την αποζευγμένη μοντελοποίηση του NO_x και του N_2O.

5.1 Μοντελοποίηση της καύσης εντός CFBC 1.2 MW_{th}

Αυτή η ενότητα παρουσιάζει τη μεθοδολογία που ακολουθήθηκε για την μοντελοποίηση της καύσης σε ρευστοποιημένη κλίνη ανακυκλοφορίας και λαμβάνει υπ' όψη την αλληλεπίδραση υδροδυναμικής, μεταφοράς θερμότητας και χημικών αντιδράσεων.

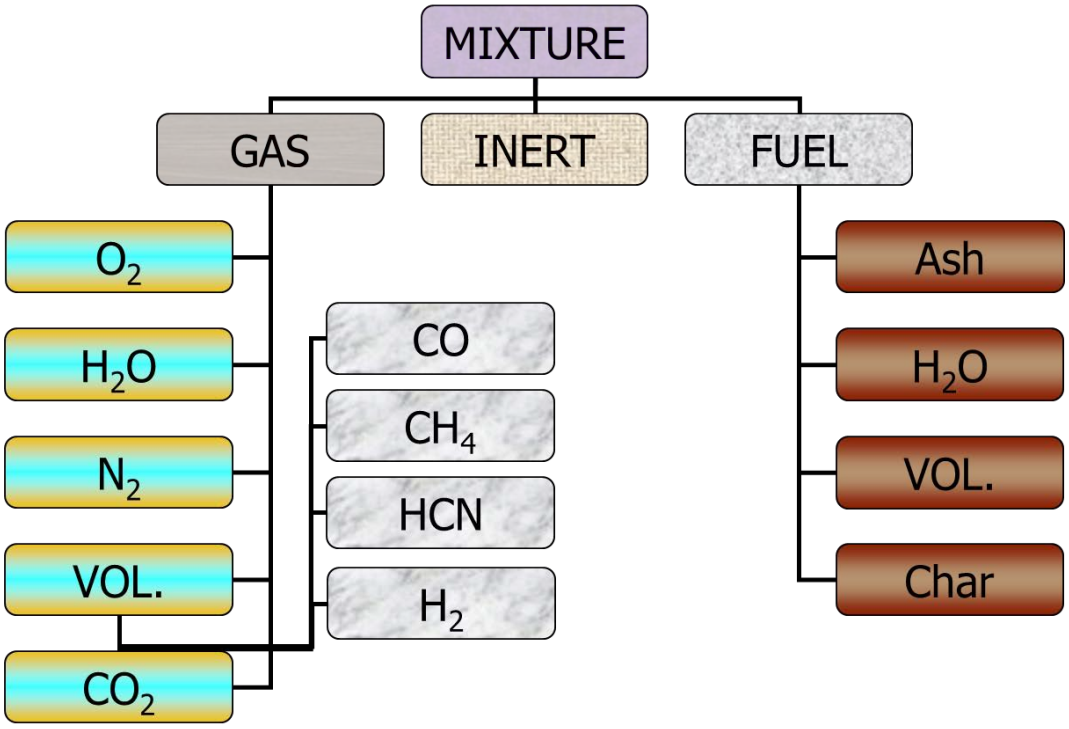

Σχήμα 5.1 Οι τρεις Euler φάσεις και οι συστατικές τους ενώσεις

Το υπολογιστικό κόστος είναι ένα σημαντικό μειονέκτημα της υπολογιστικής ρευστοδυναμικής μοντελοποίησης των ρευστοποιημένων κλινών ανακυκλοφορίας καύσης. Για αυτό, δεν ενδιαφέρει μόνο η ακρίβεια του μοντέλου αλλά και το όσο δυνατό μικρότερο υπολογιστικό κόστος.

Το μοντέλο καύσης για τη μονάδα των 1.2 MW_{th} μοντελοποιεί τη πολυφασική ροή μέσω τριών φάσεων που περιγράφονται αριθμητικά κατά Euler, την αέρια φάση, τη φάση του

καυσίμου και του αδρανούς υλικού, σχήμα 5.1. Εντός των φάσεων, ορίζονται συστατικά. Για το αέριο αυτά είναι τα εξής: O_2, CO_2. H_2O, N_2, πτητικά, CO, CH_4, H_2 και για τη μοντελοποίηση των οξειδίων του αζώτου HCN. Για το καύσιμο τα αντίστοιχα συστατικά είναι: η στάχτη, η υγρασία, τα πτητικά και το εξανθράκωμα.

5.1.1 Περιγραφή της μονάδας και της μεθόδου μοντελοποίησης

Η μονάδα που μοντελοποιήθηκε στο κεφάλαιο 4 μοντελοποιείται και σε αυτό το κεφάλαιο αλλά αυτή τη φορά δεν εξετάζεται μόνο η υδροδυναμικής της αλλά και οι αντιδράσεις που λαμβάνουν χώρα κατά τη διάρκεια της καύσης του ορυκτού καυσίμου. Το πείραμα που διερευνήθηκε αναφέρεται στην καύση λιγνίτη. Τα στοιχεία για αυτό το πείραμα βρέθηκαν στην εργασία των Leithner et al., 1993. Ο αέρας καύσης τροφοδοτείται κυρίως μέσω του διασκορπιστή αλλά και μέσω του ανοίγματος ανακυκλοφορίας. Ο δευτερεύων αέρας τροφοδοτείται μέσω πέντε εισόδων καθ' ύψος της κλίνης. Ο λόγος πρωτεύοντος με δευτερεύοντα αέρα είναι 86% προς 14%, πίνακας 5.1.

Ανοίγματα	παροχή [m^3/h]	Ύψος θύρας (z)
Διασκορπιστής	828 @ 501K	0
Άνοιγμα ανακυκλοφορίας	202 @ 501K	0.7
Δευτερεύων 1	199 @ 501K	0.5
Καυστήρας εκκίνησης	121 @ 501K	2.15
Δευτερεύων 2	32 @ 501K	2.8
Δευτερεύων 3	34 @ 501K	5.6
Δευτερεύων 4	36 @ 501K	7.6

Πίνακας 5.1 Διαβάθμιση αέρα

Το υπολογιστικό πλέγμα είναι το "αραιό" που χρησιμοποιήθηκε και στο κεφάλαιο 4. Επιλέχτηκε έναντι του πυκνού πλέγματος λόγω του μεγάλου υπολογιστικού κόστους της μοντελοποίησης της καύσης. Ο κάναβος αποτελείται από 5,724 εξαεδρικά, οριόδετα, δομημένα και ομοιόμορφα κελιά με μέση ανάλυση 9 εκατοστά ανά κελί.

Άμεση ανάλυση		Στοιχειακή ανάλυση	
υγρασία	57.00w%	C	27.1
πτητικά	21.63w%	H	1.92
εξανθράκωμα	19.07w%	O	11.18
στάχτη	2.30w%	N	0.33
Μέση διάμετρο καυσίμου	1500μm	S	0.17
Κατ. Θερμογόνος δύναμη	8560 MJ/Kg	Στάχτη	2.3
Πυκνότητα καυσίμου (a.r.)	2400 kg/m^3	Υγρασία	57

Πίνακας 5.2 Ιδιότητες του λιγνίτη

Όσον αφορά το καύσιμο του οποίου οι ιδιότητες παρατίθενται στον πίνακα 5.2, για τη μοντελοποίηση της καύσης του εφαρμόστηκε το μοντέλο μειούμενης διαμέτρου (shrinking

core). Ο λόγος αέρα – καύσιμου είναι 1.15, ενώ η παροχή του καυσίμου είναι 0.14 kg/s σε θερμοκρασία 373 K. Επιπλέον οι εξισώσεις που χρησιμοποιήθηκαν για τη μοντελοποίηση της καύσης εντός της ρευστοποιημένης κλίνης ανακυκλοφορίας είναι οι 3.52 έως 3.80 που περιγράφουν τους μηχανισμούς μετάδοσης θερμότητας και τις χημικές αντιδράσεις.

Αξίζει να σημειωθεί πως για τις μετρήσεις της συγκέντρωσης των αερίων υπάρχουν θύρες καθ' ύψος του αγωγού ανόδου. Οι τέσσερις θύρες βρίσκονται σε ύψος 1.15, 2.15, 5.2 και 8.3 m.

5.1.2 Αποτελέσματα μοντέλου καύσης

Το σύστημα των 25 μερικών διαφορικών εξισώσεων που διέπουν την καύση του στερεού παρουσιάζει αριθμητικές δυσκολίες στην επίλυσή του. Επιπλέον το υπολογιστικό κόστος σε σύγκριση με το ισοθερμοκρασιακό μοντέλο αυξάνει δραματικά, αλλά δεν είναι απαγορευτικό για μονάδες μικρού ή μεσαίου μεγέθους. Ο βασικός λόγος των δύο αυτών προβλημάτων είναι η τρίτη φάση του καυσίμου και η επίλυση του πεδίου ταχυτήτων της που είναι ισχυρά πεπλεγμένο με των άλλων δύο. Το ροϊκό πεδίο αρχικοποιήθηκε με βάση το αντίστοιχο ισοθερμοκρασιακό πεδίο.

Το υπολογιστικό μοντέλο επαληθεύτηκε μέσω πειραματικών δεδομένων των Leithner et al., 1993, οι οποίοι μέτρησαν τις συγκεντρώσεις του CO_2 και του O_2 στα τέσσερα ύψη που αναφέρθηκαν προηγουμένως. Αυτές οι μετρήσεις μαζί με τις προλέξεις του μοντέλου παρουσιάζονται στα διαγράμματα 5.2 και 5.3 για το O_2 και το CO_2 αντίστοιχα.

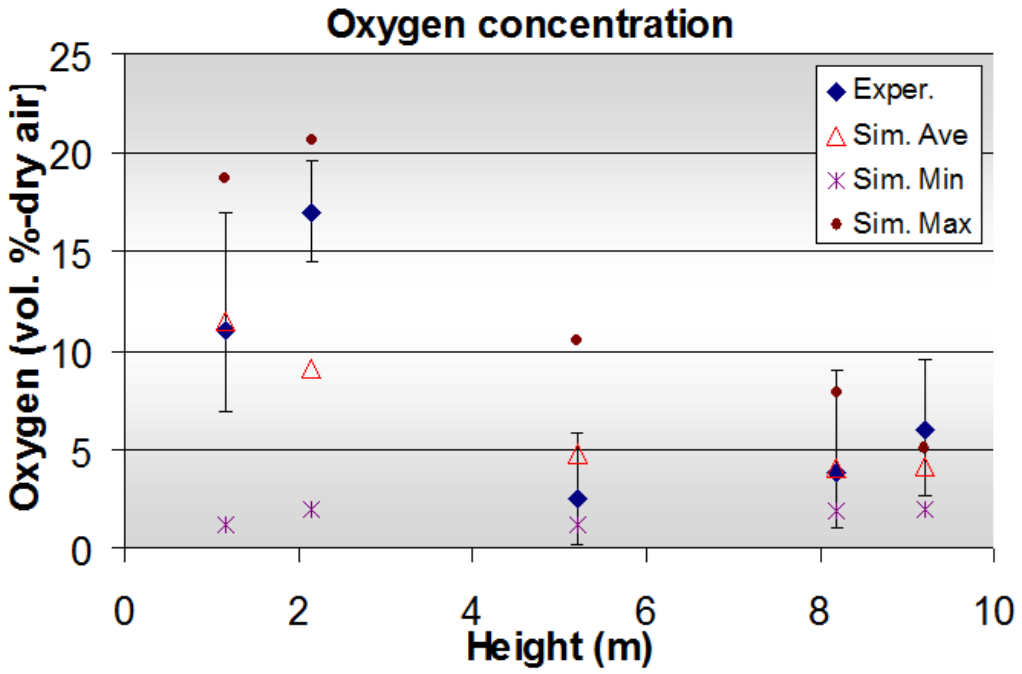

Σχήμα 5.2 Μέση χρονικά κατ' όγκων συγκέντρωση (% ξηρού) O_2 καθ' ύψος της κλίνης (αριθμητικά αποτελέσματα και πειραματικά δεδομένα).

Οι ελάχιστες, οι μέγιστες και οι μέσες πειραματικές τιμές παρουσιάζονται για κάθε ύψος. Σε κάθε ύψος 9 μετρήσεις σε διαφορετικά σημεία του κάθε επιπέδου είναι διαθέσιμες. Εξαίρεση είναι οι μετρήσεις στο ύψος 2.15 m όπου έγιναν μόνο 2. Δυστυχώς, στην εργασία των Leithner et al., 1993, δεν αναφέρεται σε ποιά συγκεκριμένα σημεία (συντεταγμένες X,Y) έγιναν οι μετρήσεις και για αυτό συγκρίσιμες με τα αποτελέσματα του μοντέλου είναι μόνο ελάχιστες, οι μέγιστες και οι μέσες τιμές. Από την εξέταση των διαγραμμάτων 5.2 και 5.3 αναδεικνύεται η καλή συμφωνία των αποτελεσμάτων του αριθμητικού μοντέλου και των

πειραματικών δεδομένων, πλην του ύψους 2.15. Όσον αφορά αυτή τη διατομή η οποία απεικονίζεται στο σχήμα 5.4, το μοντέλο αναπαράγει τιμές του O_2 και του CO_2 αντίστοιχες των πειραματικών δεδομένων σε μερικά σημεία του επιπέδου.

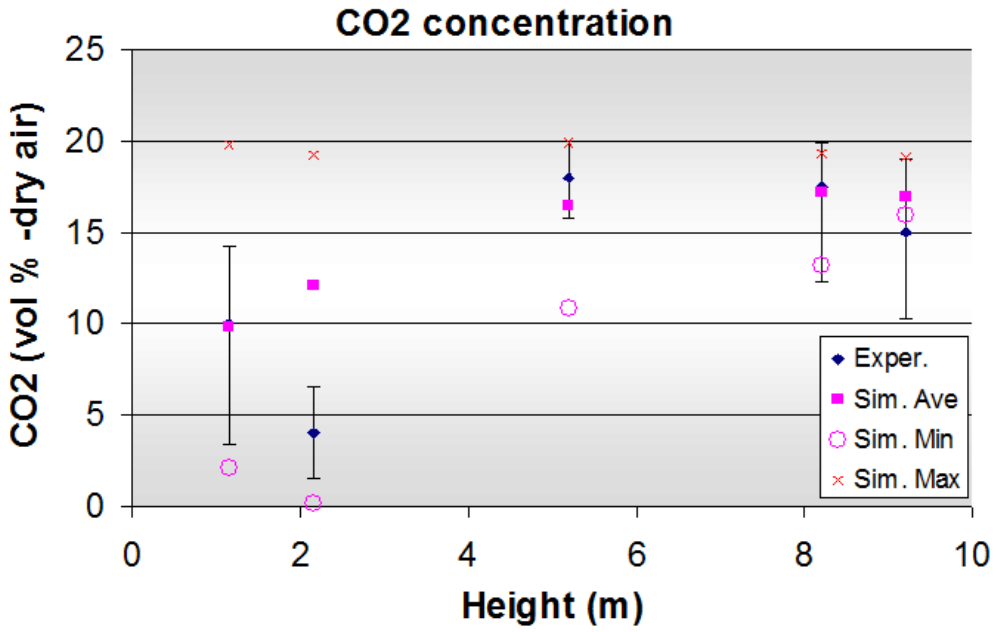

Σχήμα 5.3 Μέση χρονικά κατ' όγκον συγκέντρωση (% ξηρού) CO_2 καθ' ύψος της κλίνης (αριθμητικά αποτελέσματα και πειραματικά δεδομένα).

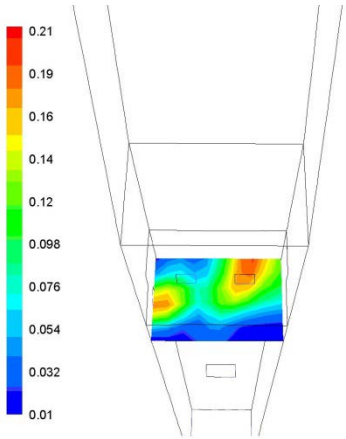

Σχήμα 5.4 Μέση χρονικά κατ' όγκον συγκέντρωση (% ξηρού) CO_2 για το ύψος 2.15m.

Θα πρέπει να σημειωθεί ότι η αντίστοιχη μέση τιμή απέχει αρκετά από τα πειραματικά δεδομένα. Ωστόσο, η αύξηση της συγκέντρωσης του οξυγόνου μεταξύ των επιφανειών Z=1.1m και Z=2.15m, που υποδεικνύουν τα πειραματικά δεδομένα, δεν συνάδει με το γεγονός πως δεν υπάρχει είσοδος δευτερεύοντος αέρα μεταξύ των δύο επιφανειών. Για αυτό, είναι εξαιρετικά απίθανο να αυξάνεται το οξυγόνο μεταξύ των δύο αυτών επιφανειών εφόσον δεν υπάρχει καμία αντίδραση στην καύση του λιγνίτη που να παράγει οξυγόνο. Υπό αυτό το πρίσμα, θεωρήθηκε πως είτε οι δύο μετρήσεις για την επίμαχη επιφάνεια δεν είναι αντιπροσωπευτικές ή οι δύο αυτές μετρήσεις δεν διεξήχθησαν σωστά.

Εν γένει, το μοντέλο που αναπτύχθηκε προβλέπει ότι το οξυγόνο καταναλώνεται ταχύτερα κοντά στα τοιχώματα που υπάρχει περισσότερο καύσιμο συγκριτικά με το κέντρο του αντιδραστήρα όπου το καύσιμο έχει μικρότερη συγκέντρωση (σχήμα 5.5). Αυτή η συμπεριφορά είναι σε συμφωνία με την εργασία των Zhao et al., 1997.

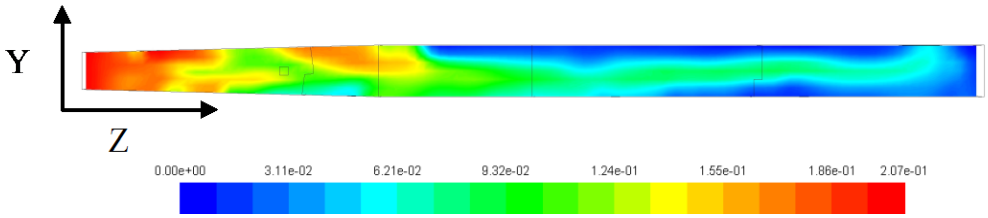

Σχήμα 5.5 Μέση χρονικά κατ' όγκον συγκέντρωση (% ξηρού) CO_2 για X=0.405m.

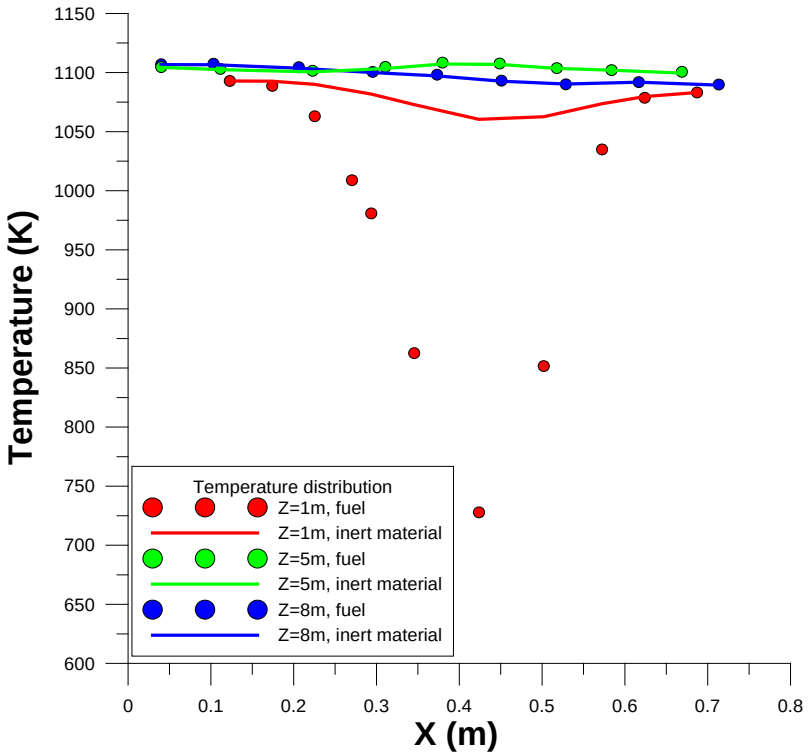

Σχήμα 5.6 Κατανομή θερμοκρασίας κατά την πλευρική διεύθυνση X (Y=0.27), για το καύσιμο και το αδρανές υλικό για διάφορα ύψη

Η μέση θερμοκρασία εντός του αγωγού ανόδου μοντελοποιήθηκε με ακρίβεια. Το υπολογιστικό μοντέλο προέλεξε 1095 K έναντι της πειραματικής τιμής 1100 K. (Leithner et al., 1993). Εν γένει, το θερμοκρασιακό επίπεδο είναι ομοιόμορφο. Οι διαφορές στη θερμοκρασία του αερίου, του αδρανούς και του καυσίμου είναι πολύ μικρές, όπως αναμενόταν λόγω του μεγάλου συντελεστή μετάδοσης θερμότητας εντός των κλινών. Το σχήμα 5.6 παρουσιάζει την κατανομή θερμοκρασίας σε διάφορα σημεία της κλίνης για το αδρανές υλικό και το καύσιμο. Το καύσιμο έχει ελαφρώς μεγαλύτερη θερμοκρασία κατά 5K. Ωστόσο, για το ύψος Z=1m που το καύσιμο εισάγεται στην κλίνη, η θερμοκρασιακές διαφορές είναι μεγάλες λόγω της υψηλής υγρασίας του καυσίμου (57%). Επιπροσθέτως, κοντά στην έξοδο του αγωγού ανόδου παρατηρείται μια θερμοκρασιακή διαφορά της τάξης των 80K, η οποία οφείλεται στην έντονη καύση του εξανθρακώματος σε αυτό το σημείο, η οποία παρατηρήθηκε και πειραματικά (Leithner et al., 1993). Σε αυτό το σημείο αναμειγνύεται το οξυγόνο από την κεντρική περιοχή του αντιδραστήρα με το καύσιμο που

υπάρχει κοντά στα τοιχώματα και αυξάνεται αρκετά ο ρυθμός καύσης. Επίσης, σε αυτό το μεγάλο ύψος το κλάσμα όγκου του αδρανούς υλικού δεν είναι τόσο μεγάλο για να προσλάβει την εκλυόμενη ενέργεια.

5.2 Μοντελοποίηση $NO_x - N_2O$

Σε αυτή την ενότητα, το μοντέλο για τα οξείδια του αζώτου που αναπτύχθηκε σε αυτή την διατριβή εφαρμόστηκε στη μονάδα CFBC 1.2 MW_{th}, και τα αποτελέσματά του συγκρίθηκαν με τις αντίστοιχες πειραματικές τιμές. Με σκοπό την ελαχιστοποίηση του υπολογιστικού κόστους ακολουθήθηκε η απεπλεγμένη προσέγγιση, που χρησιμοποιεί τα δεδομένα της καύσης αμετάβλητα και επιλύει μόνο τις αντιδράσεις και τις συγκεντρώσεις των στοιχείων που εμπλέκονται στο σχηματισμό / καταστροφή των NO_x και N_2O. Οι κινητικές των αντιδράσεων αντλήθηκαν από τη βιβλιογραφία. Επίσης, διεξήχθη ανασκόπηση της διεθνούς βιβλιογραφίας όσον αφορά το δίκτυο αντιδράσεων που εμπλέκονται στο σχηματισμό / καταστροφή των NO_x και N_2O.

5.2.1 Διερεύνηση του δικτύου αντιδράσεων των NO_x / N_2O

Η καύση του άνθρακα χωρίζεται σε δύο στάδια. Το πρώτο είναι η απελευθέρωση των πτητικών ενώ το δεύτερο η καύση του εξανθρακώματος. Κατά τη διάρκεια της απελευθέρωσης των πτητικών απελευθερώνονται και ενώσεις του αζώτου όπως το HCN, NH_3, N_2 και δεσμευμένο στις πίσσες άζωτο (Blair et al., 1977 και Nelson et al., 1992). Επίσης, κατά τη διάρκεια καύσης του εξανθρακώματος οξειδώνονται και τα εναπομένοντα στο καύσιμο άτομα του αζώτου προς το σχηματισμό NO. Όπως πρότειναν οι Goel et al., 1996[a], η κατανομή του αρχικού αζώτου του καυσίμου στα πτητικά και στο εξανθράκωμα επηρεάζει σημαντικά τις τελικές εκπομπές οξειδίων του αζώτου. Σύμφωνα με την εξίσωση που ανέπτυξαν οι Fine et al., 1974, περίπου το 43% του αρχικού αζώτου απελευθερώνεται με τα πτητικά. Ο λόγος του αζώτου προς τον άνθρακα του καυσίμου, χωρίς να συνυπολογιστεί η στάχτη και η υγρασία (*N/C*), για το καύσιμο υπό εξέταση, μετρήθηκε ίσος με 0.84584%.

Επίσης ο λόγος HCN προς NH_3 που απελευθερώνεται στα πτητικά είναι πολύ σημαντικός (Kilpinen et al., 2002). Εν γένει αυτή η παράμετρος εξαρτάται από το είδος του καυσίμου και στην παρούσα εργασία θεωρήθηκε πως το άζωτο απελευθερώνεται στα πτητικά αποκλειστικά στη μορφή του υδροκυανίου καθώς οι πειραματικές μετρήσεις έδειξαν πάρα πολύ μικρές συγκεντρώσεις αμμωνίας (Leithner et al., 1993).

Όλες οι αντιδράσεις που λαμβάνουν χώρα κατά το σχηματισμό / καταστροφή των οξειδίων του αζώτου συνοψίζονται στο σχήμα 5.7 και χωρίζονται σε τέσσερις κατηγορίες:

- ✓ ομογενής σχηματισμός NO/N_2O
- ✓ ομογενής καταστροφή NO/N_2O
- ✓ ετερογενής σχηματισμός NO/N_2O
- ✓ ετερογενής καταστροφή NO/N_2O

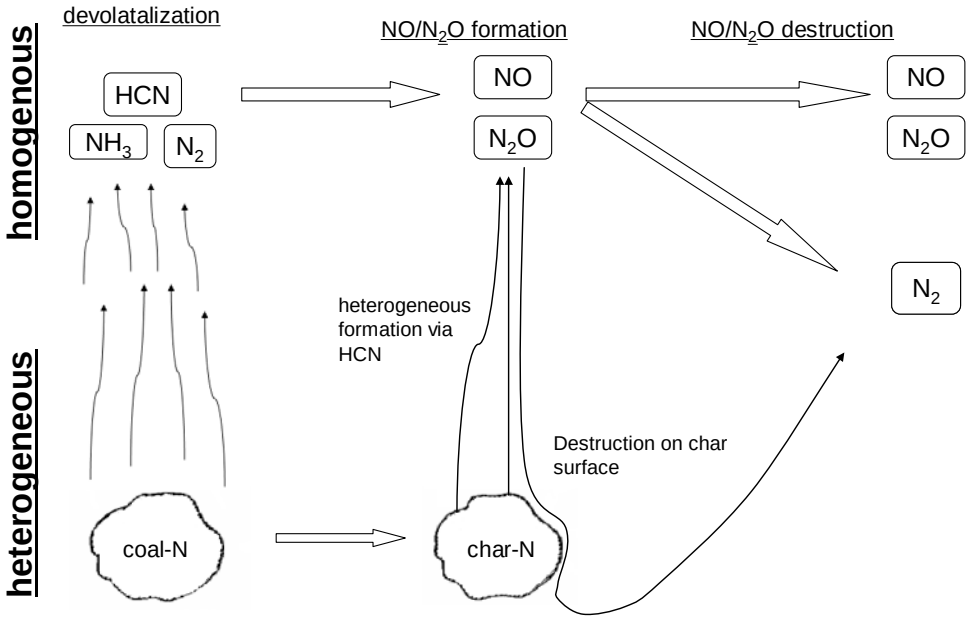

Σχήμα 5.7 Μηχανισμοί δημιουργίας / καταστροφής NO / N_2O

5.2.2 Δίκτυο αντιδράσεων

Στον πίνακα 5.3 παραθέτονται οι βασικές αντιδράσεις που περιγράφουν το μηχανισμό που απεικονίζεται στο σχήμα 5.7, και οι αντίστοιχες εξισώσεις για το ρυθμό τους. Δύο δίκτυα αντιδράσεων εξετάστηκαν στην παρούσα διατριβή (μοντέλα 1 και 2). Οι διαφοροποιήσεις των δύο μοντέλων θα αναλυθούν παρακάτω.

No.	Αντίδραση	Παράμετροι	Ρυθμός αντίδρ. (mol/m^3_{gas}*s)	Παραπομπή		
					Μοντ. 1	Μοντ. 2
			Ομογενής σχηματισμός			
I	$HCN + \frac{1}{2}O_2 \rightarrow CNO + H$	$k^{I} = 2{,}14 \cdot 10^{5} \cdot \exp(-10000/T)$	$k^{I} \cdot C_{O_2} \cdot C_{HCN}$	¥, £, ç	Ναι	Ναι
II	$CNO + \frac{1}{2}O_2 \rightarrow NO + CO$	$\frac{k_2^{II}}{k_1^{II}} = 1{,}02 \cdot 10^{9} \cdot \exp(-25460/T)$	$k^{I} \cdot C_{O_2} \cdot C_{HCN} \cdot (\frac{k_1^{II}}{k_1^{II} + k_2^{II} \cdot C_{NO}})$	¥, £, ç	Ναι	Ναι
III	$CNO + NO \rightarrow N_2O + CO$		$k^{I} \cdot C_{O_2} \cdot C_{HCN} \cdot (\frac{k_2^{II} \cdot C_{NO}}{k_1^{II} + k_2^{II} \cdot C_{NO}})$	¥, £, ç	Ναι	Ναι
IV	$NH_3 + \frac{5}{4}O_2 \rightarrow NO + \frac{3}{2}H_2O$	$k^{IV} = 2{,}73 \cdot 10^{14} \cdot \exp(-38160/T)$	$k^{IV} \cdot C_{NH_3} \cdot C_{O_2}$	£, ç, ß	Όχι	Όχι
			Ομογενής καταστροφή			
V	$NH_3 + \frac{3}{4}O_2 \rightarrow \frac{1}{2}N_2 + \frac{3}{2}H_2O$	$k^{V} = 3{,}38 \cdot 10^{7} \cdot \exp(-10000/T)$	$k^{V} \cdot \frac{C_{NH_3} \cdot C_{O_2}}{C_{O_2} + 0.054}$	¥, £	Όχι	Όχι
VI	$NO + NH_3 + \frac{1}{2}O_2 \rightarrow N_2 + \frac{3}{2}H_2O$	$k^{VI} = 1{,}11 \cdot 10^{12} \cdot \exp(-29400/T)$	$k^{VI} \cdot (C_{O_2} \cdot C_{NH_3} \cdot C_{NO})^{0,5}$	¥ , £, ç, Б	Όχι	Όχι
VII	$N_2O + \frac{1}{2}O_2 \rightarrow N_2 + O_2$	$k^{VII} = 1{,}75 \cdot 10^{8} \cdot \exp(-23800/T)$	$k^{VII} \cdot C_{N_2O}$	Þ	Ναι	Όχι
		$k^{VII}\ 5{,}7 \cdot 10^{9} \cdot \exp(-27000/T)$	$k^{VII} \cdot C_{N_2O}$	ç	Όχι	Ναι
VIII	$N_2O + CO \rightarrow 2N_2 + CO_2$	$k^{VIII} = 2{,}51 \cdot 10^{11} \cdot \exp(-23180/T)$	$k^{VIII} \cdot C_{N_2O} \cdot C_{CO}$	Þ	Όχι	Όχι
		$k^{VIII} = 50{,}1 \cdot \exp(-5292/T)$	$k^{VIII} \cdot C_{N_2O} \cdot C_{CO}$	£	Όχι	Ναι

No.	Αντίδραση	Παράμετροι	Ρυθμός αντίδρ. (mol/m$^3_{gas}$*s)	Παραπομπή		
					Μοντ. 1	Μοντ. 2
		Ετερογενής σχηματισμός				
IX	$\text{char} - \text{N} + \frac{1}{2}\text{O}_2 \rightarrow (-\text{CNO})$				Ναι	Ναι
X	$(-\text{CNO}) + \frac{1}{2}\text{O}_2 \rightarrow \text{NO} + (-\text{CO})$	$\frac{k_2^X}{k_1^X} = 4{,}86 \cdot 10^{-5} \cdot \exp(14999/T)$	$f_c \frac{N}{C} \cdot R_C \cdot (\frac{k_1^X}{k_1^X + k_2^X \cdot C_{NO}})$	¿	Ναι	Ναι
XI	$(-\text{CNO}) + \text{NO} \rightarrow \text{N}_2\text{O} + (-\text{CO})$		$f_c \frac{N}{C} \cdot R_C \cdot (\frac{k_2^X \cdot C_{NO}}{k_1^X + k_2^X \cdot C_{NO}})$	¿	Ναι	Ναι
		Ετερογενής καταστροφή				
XII	$\text{NO} + (-\text{C}) \rightarrow \frac{1}{2}\text{N}_2 + \text{CO}$	$k_a^{XII} = 1{,}3 \cdot 10^5 \cdot \exp(17111/T)$	$k_a^{XII} \cdot N_p \cdot \pi \cdot d_c^2 \cdot C_{NO}$ (mol/s)	£	Ναι	Όχι
		$k_b^{XII} = 1{,}17 \cdot 10^8 \cdot \exp(-13221/T)$	$k_b^{XII} \cdot C_{NO}$ (mol/m^3-fuel*s)	¿	Όχι	Ναι
XIII	$NO + (-CO) \rightarrow \frac{1}{2} N_2 + CO_2$	$k^{XIII} = 9{,}6 \cdot 10^4 \cdot \exp(-10000/T)$	$k^{XIII} \cdot C_{NO} \cdot C_{CO}$	¥	Ναι	Ναι
XIV	$\text{N}_2\text{O} + (-\text{C}) \rightarrow \text{N}_2 + \text{CO}$	$k^{XIV} = 2{,}9 \cdot 10^9 \cdot \exp(-16983/T)$	$k^{XIV} \cdot N_p \cdot \pi \cdot d_c^2 \cdot C_{N_2O}$ (mol/s)	£	Όχι	Όχι
			$k^{XIV} \cdot C_{N_2O}$ (mol/m^3-fuel*s)	¥	Όχι	Ναι

No.	Αντίδραση	Παράμετροι	Ρυθμός αντίδρ. (mol/m^3_{gas}*s)	Παραπομπή		
					Μοντ. 1	Μοντ. 2
			Θερμικά NO_x			
XV	$N_2 + O_2 \rightarrow 2NO$		βάσει του Ω	ø	Ναι	Ναι
			Άζωτο του καυσίμου			
XVI	$N - volatiles \xrightarrow{devol} HCN$		R_{vol}		Ναι	Ναι
XVII	$N - char \rightarrow HCN$		$(1 - f_c)\frac{N}{C} \cdot R_c$		Ναι	Όχι

Πίνακας 5.3 Δίκτυο αντιδράσεων NO / N_2O

Οι συγκεντρώσεις είναι σε mol ανά κυβικό μέτρο αερίου και η σταθερά των αερίων (R_u) σε KJ[mol K]$^{-1}$.

Παραπομπές του πίνακα 5.3:

- ¥ (Desroches-Ducarne et al., 1998)
- £ (Gungor and Eskin, 2008[b])
- ¿ (Kilpinen et al., 2002)
- Þ (Chen et al., 2001)
- ß (Afacan et al., 2007)
- ø (FLUENT, 2006)
- ç (Liu and Gibbs, 2002)
- Б (Jensen et al., 1995)
- Ω Zeldovich mechanism (FLUENT, 2010)

Σύμφωνα με τη βιβλιογραφία, τα οξείδια του αζώτου σχηματίζονται ετερογενώς με δύο τρόπους: α) άμεση οξείδωση του αζώτου και β) απελευθέρωση και εν συνεχεία οξείδωση του HCN (Αντίδραση XVII).

- Όσον αφορά στον πρώτο τρόπο, που προτάθηκε από τους Chen et al., 2001; Goel et al., 1996[a, b], και υιοθετήθηκε και από άλλους ερευνητές (Kilpinen et al., 2002; Liu and Gibbs, 2002) το οξυγόνο σπάει τους αρωματικούς δεσμούς στην επιφάνεια του εξανθρακώματος και ύστερα αντιδρά με το ελεύθερο άζωτο προς σχηματισμό –CNO, το οποίο είναι ενδιάμεση ένωση και παράγει NO και N_2O (αντιδράσεις IX, X, XI).
- Όσον αφορά στον δεύτερο τρόπο, παρατηρήθηκε πως παράγεται HCN κατά τη διάρκεια της καύσης του εξανθρακώματος (Kilpinen and Hupa, 1991 και Winter et al., 1996). Ωστόσο, οι Goel et al., 1996[b] έδειξαν πως για το καύσιμο που εξέτασαν δεν παρατήρησαν την ίδιο συμπεριφορά, γεγονός που υποδεικνύει ότι η απελευθέρωση HCN κατά τη διάρκεια της καύσης του εξανθρακώματος μπορεί να εξαρτάται από το καύσιμο.

Σε αυτή τη διατριβή, εξετάστηκαν δύο διαφορετικά δίκτυα αντιδράσεων (πίνακας 5.3). Στο μοντέλο 1, υιοθετήθηκε η υπόθεση πως το 30% του αζώτου του εξανθρακώματος οξειδώνεται απ' ευθείας προς NO ή N_2O, όπως εκτίμησαν οι Leithner et al., 1993, ενώ το υπόλοιπο 70% απελευθερώνεται ως HCN. Στο μοντέλο 2, υιοθετείται η υπόθεση των Goel et al., 1996[b] ότι το 100% του αζώτου του εξανθρακώματος οξειδώνεται προς NO και N_2O.

5.2.3 Μεθοδολογία μοντελοποίησης NO_x/N_2O

Για την αρχικοποίηση του προβλήματος, όλες οι συγκεντρώσεις των υπό επίλυση ενώσεων τέθηκαν ίσες με μηδέν πλην του CO. Η αρχική συγκέντρωση του CO εξισώθηκε με την αντίστοιχη τιμή που προέκυψε από την επίλυση του μοντέλου καύσης. Επίσης στην εξίσωση μεταφοράς του CO, ο όρος συναγωγής απαλείφθηκε, με σκοπό τη διατήρηση του προφίλ του CO που προέκυψε από την επίλυση της καύσης. Όλες οι εξισώσεις μεταφοράς των ρυπαντών επιλύθηκαν με άρρητο σχήμα και χρονικό βήμα $\Delta t = 10$ μs. Ο συντελεστής διάχυσης (D_{iff}) τέθηκε ίσος με $6.8\ 10^{-6}\ m^2s^{-1}$ για όλες τις ενώσεις (Kilpinen et al., 2002).

Η απεπλεγμένη προσέγγιση ακολουθήθηκε για αυτή την μοντελοποίηση και οι κατανομές της θερμοκρασίας (T), του ρυθμού οξείδωσης του εξανθρακώματος (R_c), του ρυθμού της απελευθέρωσης πτητικών (R_{vol}), της διαμέτρου του εξανθρακώματος (d_c) και της συγκέντρωσης O_2 ελήφθησαν από τα αποτελέσματα της μοντελοποίησης της καύσης (ενότητα 5.1).

5.2.4 Αποτελέσματα της μοντελοποίησης NO_x/N_2O

Τα αποτελέσματα της μοντελοποίησης παρουσιάζονται στα διαγράμματα που ακολουθούν και συγκρίνονται με τα αντίστοιχα πειραματικά δεδομένα. Στο σχήμα 5.8 απεικονίζεται η μέση, μέγιστη και ελάχιστη συγκέντρωση των NO_x καθ' ύψος. Τα αποτελέσματα συμφωνούν σε ικανοποιητικό βαθμό με τα πειραματικά δεδομένα και για τα δύο μοντέλα που εξετάστηκαν (1, 2). Ωστόσο, τα αποτελέσματα του μοντέλου 2 είναι μεγαλύτερης ακρίβειας. Λόγω αυτής της υπεροχής τα αποτελέσματα αυτού του μοντέλου θα παρουσιαστούν στα διαγράμματα που ακολουθούν.

Η μέση συγκέντρωση του υδροκυανίου (μοντέλο 2) καθ' ύψος της κλίνης απεικονίζεται στο σχήμα 5.9. Στο κάτω μέρος της κλίνης η συγκέντρωσή του είναι μεγάλη εξαιτίας της απελευθέρωσης των πτητικών του καυσίμου, αλλά γρήγορα καταναλώνεται στο ανώτερο κομμάτι της κλίνης. Όπως αναμενόταν η συγκέντρωσή του στην έξοδο είναι ιδιαίτερα μικρή.

Αντίθετα το μοντέλο 1 προβλέπει πολύ μεγάλες συγκεντρώσεις HCN στην έξοδο και αντίστοιχα πολύ χαμηλή συγκέντρωση N_2O. Αυτή η αστοχία του μοντέλου υποδεικνύει πως

η θεώρηση της απελευθέρωση HCN κατά τη διάρκεια της καύσης του εξανθρακώματος δεν επαληθεύεται.

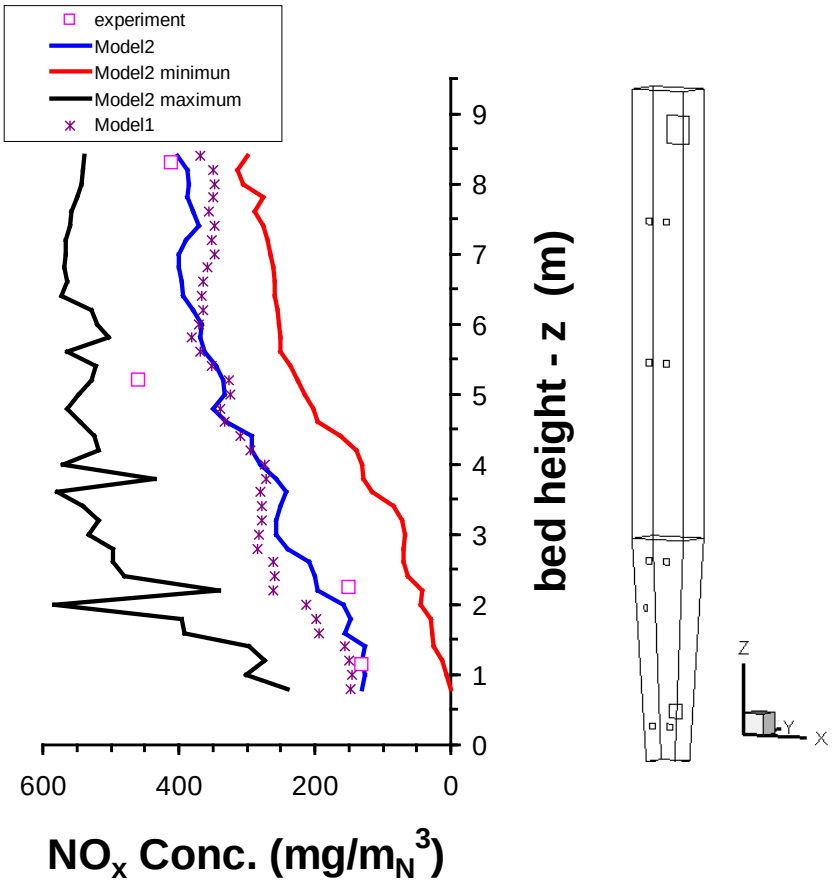

Σχήμα 5.8 Συγκέντρωση NO_x καθ' ύψος της κλίνης

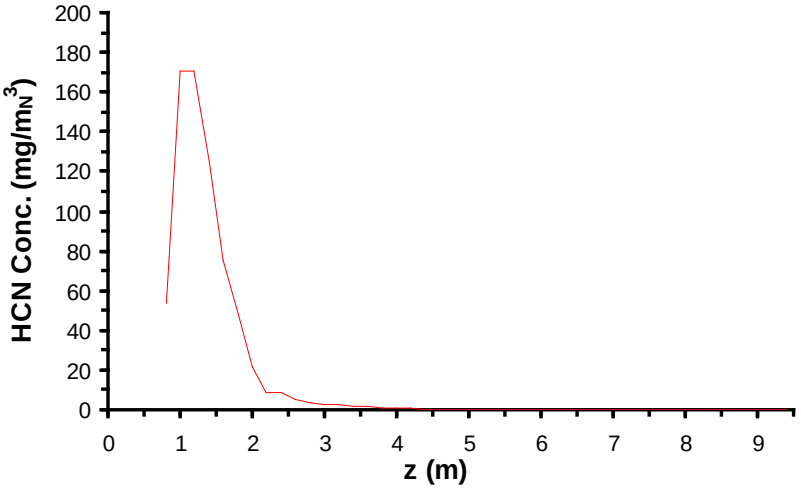

Σχήμα 5.9 Συγκέντρωση HCN καθ' 'ύψος του αντιδραστήρα (μοντέλο 2)

Στο σχήμα 5.10, παρουσιάζονται τα αποτελέσματα των δύο μοντέλων όσον αφορά τη συγκέντρωση του N_2O. Τα αποτελέσματα του μοντέλου 1 υποεκτιμούν αισθητά τη συγκέντρωση του N_2O και με βεβαιότητα υπολείπονται σε ακρίβεια έναντι των αποτελεσμάτων του μοντέλου 2. Θα πρέπει να τονιστεί πως το μοντέλο 1 υποεκτιμά τις εκπομπές N_2O αν και δεν ενσωματώνει καμία αντίδραση καταστροφής του (αντιδράσεις VII, VIII and XIV), που σημαίνει πως υποεκτιμά αισθητά τη δημιουργία του.

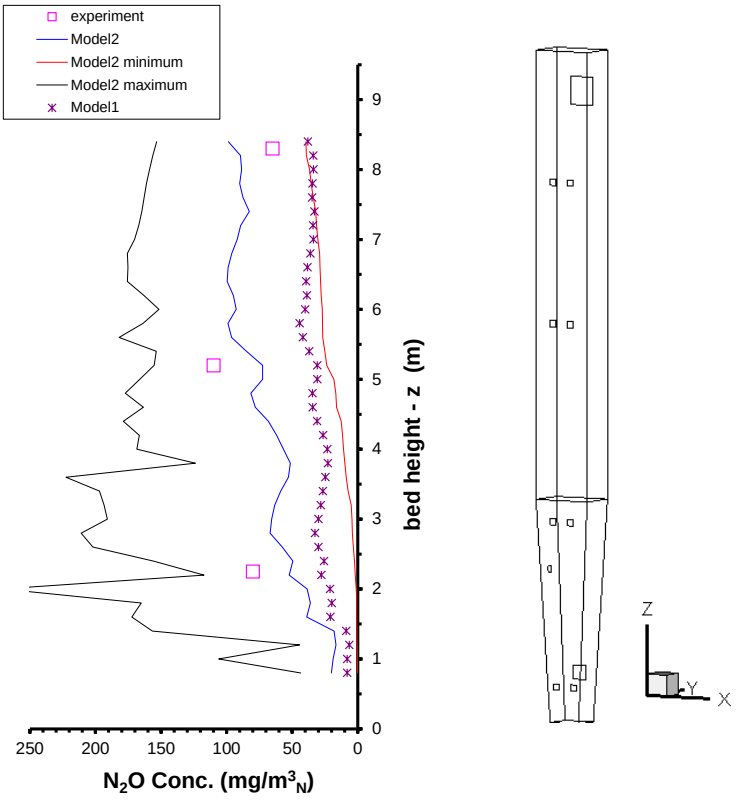

Σχήμα 5.10 Συγκέντρωση του N_2O καθ' ύψος της κλίνης.

Τα αποτελέσματα του μοντέλου 2 συμφωνούν με αρκετά καλή ακρίβεια με τα πειραματικά δεδομένα ιδιαίτερα όσον αφορά τη συγκέντρωση του N_2O στην έξοδο της μονάδας. Ωστόσο, θα πρέπει να σημειωθεί ότι για το ύψος z=1.15, η συγκέντρωση του N_2O μετρήθηκε 350 mg ανά κανονικό κυβικό (Leithner et al., 1993). Αυτή η τιμή δεν παρουσιάζεται στο σχήμα 5.14 γιατί θεωρήθηκε μη ρεαλιστική, και πιθανότατα δεν μετρήθηκε σωστά.

6. ΠΛΗΡΗΣ ΙΣΟΘΕΡΜΟΚΡΑΣΙΑΚΗ ΜΟΝΤΕΛΟΠΟΙΗΣΗ ΚΡΥΟΥ ΜΟΝΤΕΛΟΥ ΕΝΑΝΑΘΡΑΚΩΤΗ

Η δέσμευση του CO_2 με κύκλους ενανθράκωσης / ασβεστοποίησης (calcium looping, CaL) θεωρείται μια υποσχόμενη τεχνολογία που μπορεί να εφαρμοσθεί και σε παλιές και σε καινούργιες μονάδες ηλεκτροπαραγωγής. Προτάθηκε από τους Shimizu et al., 1999, και χρησιμοποιεί ένα σύστημα συζυγών κλινών (DFB) που αποτελείται από δύο αντιδραστήρες ρευστοποιημένης κλίνης, τον ενανθρακωτή και τον ασβεστοποιητή. Οι Charitos et al., 2010[b] ήταν οι πρώτοι που εξέτασαν τη διεργασία σε ρεαλιστικές συνθήκες στην πιλοτική μονάδα του IFK. Επίσης μέσω ενός κρύου μοντέλου αυτής της εγκατάστασης μελέτησαν την υδροδυναμική της εγκατάστασης. Το κρύο μοντέλο λειτουργεί σε ατμοσφαιρικές συνθήκες και σχεδιάστηκε βάσει των κανόνων ομοιότητας. Σε αυτό το κεφάλαιο της διδακτορικής διατριβής το κρύο μοντέλο του ενανθρακωτή μοντελοποιείται. Αυτή η μονάδα είναι μια ρευστοποιημένη κλίνη ανακυκλοφορίας.

Για την αριθμητική διερεύνηση της υδροδυναμικής της κλίνης χρησιμοποιήθηκε η μεθοδολογία TFM με το μοντέλο EMMS που δοκιμάστηκε επιτυχώς στο κεφάλαιο 4. Επίσης, σε αυτή τη μελέτη μοντελοποιήθηκε και το σύστημα ανακυκλοφορίας. Για την πλήρη μοντελοποίηση (αγωγός ανόδου, κυκλώνας, αγωγός καθόδου, πνευματική βαλβίδα) του κρύου μοντέλου του ενανθρακωτή, στο σύστημα ανακυκλοφορίας εφαρμόστηκε το νέο μοντέλο κοκκωδών τάσεων που αναπτύχθηκε και επαληθεύτηκε στο κεφάλαιο 3.

Κλείνοντας, θα πρέπει να τονιστεί πως εκτός από τα πειραματικά δεδομένα για την πίεση και την ανακυκλοφορία, διαθέσιμες για σύγκριση με τα αποτελέσματα του μοντέλου είναι και οπτικές παρατηρήσεις των πειραματιστών καθώς το κρύο μοντέλο είναι κατασκευασμένο από διαφανές υλικό (πλεξιγκλάς).

6.1 Μοντέλο EMMS

Όπως και στο τέταρτο κεφάλαιο, το σχήμα του EMMS εφαρμόστηκε για τις συνθήκες λειτουργίας της μονάδας υπό εξέταση. Θα πρέπει να τονιστεί ότι τα πολυώνυμα 4.1 έως 4.3 δεν μπορούν να χρησιμοποιηθούν γιατί οι συντελεστές τους εξαρτώνται από τις συνθήκες λειτουργίας. Για αυτό το λόγο, τα πολυώνυμα θα πρέπει να επαναϋπολογιστούν αφού πρώτα επιλυθεί το σύστημα ελαχιστοποίησης του EMMS. Τα χαρακτηριστικά της μονάδας υπό διερεύνηση, παρουσιάζονται στον πίνακα 6.1

d_p (διάμετρος σωματιδίων)	142 μm
ρ_s (πυκνότητα σωματιδίων)	5700 kg m^{-3}
ρ_g (πυκνότητα αέρα)	1.225 kg m^{-3}
μ_g (συνεκτικότητα αέρα)	1.7894 10^{-5} kg $[ms]^{-1}$

Πίνακας 6.1 Ιδιότητες σωματιδίων και αέρα για την εγκατάσταση του κρύου μοντέλου

Το σύστημα εξισώσεων του EMMS επιλύθηκε με το εμπορικό πακέτο GAMS® (http://www.gams.com/). Το σχήμα 6.1 παρουσιάζει τη συνάρτηση H_d για u_{slip} = 2 m/sec. Κατάλληλα πολυώνυμα παρεμβολής $H_d=f(|u_{slip}|, \varepsilon_g)$ αναπτύχθηκαν για την εύκολη ενσωμάτωση του μοντέλου στον κώδικα υπολογιστικής ρευστοδυναμικής

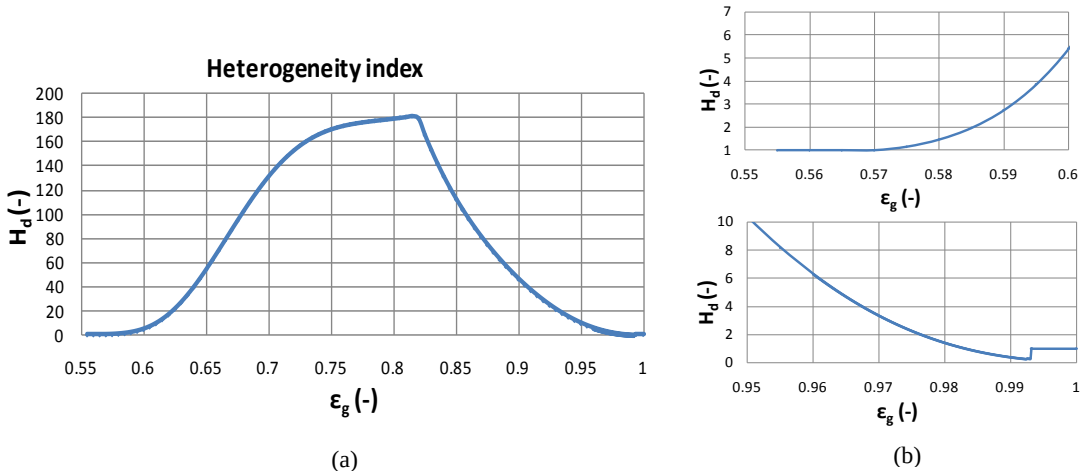

(a) (b)

Σχήμα 6.1 (a) Η συνάρτηση $H_d(\varepsilon_g)$ για u_{slip}=2 m/sec. (b) μεγεθύνσεις.

6.2 Δυνάμεις τριβής στο σύστημα ανακυκλοφορίας

Στην υπό εξέταση μονάδα, στο σύστημα ανακυκλοφοριάς χρησιμοποιείται ένας ανακυκλοφορητής στεγανοποίησης (Loop – Seal) ως μη μηχανική (πνευματική) βαλβίδα. Τα σωματίδια εντός αυτής της βαλβίδας ρευστοποιούνται με φυσαλίδες (bubbling regime, Basu and Cheng, 2000) αλλά στον αγωγό καθόδου το κλάσμα όγκου των σωματιδίων είναι αρκετά μεγαλύτερο και προσομοιάζει συνθήκες σταθερής κλίνης.

Όπως αναλύθηκε και στο κεφάλαιο 3, στις περιπτώσεις πολύ πυκνών ροών οι δυνάμεις τριβής μεταξύ των σωματιδίων είναι πολύ σημαντικές. Για αυτό, η μοντελοποίησή τους με εξελιγμένα μοντέλα, όπως αυτό που αναπτύχθηκε στην παρούσα διατριβή και βασίζεται στο κριτήριο διαρροής των Pitman- Schaeffer- Gray-Stiles, είναι *sine qua non* για την ακριβή μοντελοποίηση του συστήματος ανακυκλοφορίας ρευστοποιημένων κλινών ανακυκλοφορίας.

Για τον προσδιορισμό των τάσεων του αερίου και του στερεού χρησιμοποιείται η εξίσωση 2.7. Για τους αντίστοιχους συντελεστές συνεκτικότητας οι εξισώσεις που παρουσιάζονται στον πίνακα 6.3 χρησιμοποιούνται, ενώ για την κοκκώδη πίεση τριβής η εξίσωση των Johnson and Jackson, 1987 εφαρμόζεται. Επίσης, υιοθετείται η προσέγγιση του Makkawi et al., 2006 για την ενσωμάτωση των τριβικών συνεκτικών όρων για αραιές ροές. Οι παράμετροι του μοντέλου παρουσιάζονται στον πίνακα 6.2. Θα πρέπει να τονιστεί, πως το μοντέλο των τάσεων που εφαρμόστηκε στο σύστημα ανακυκλοφορίας είναι το ίδιο με αυτό που επαληθεύτηκε στο κεφάλαιο 3 μέσω της προσομοίωσης του πειράματος απόθεσης κοκκώδους υλικού.

e_{ss}	0.9 (Ding and Gidaspow, 1990; Hartge et al., 2009)
ε_s^{max}	0.65
ε_s^{fr}	0.5 (Gidaspow et al., 1992)

Πίνακας 6.2 Παράμετροι του μοντέλου

Μεταβλητή	Συμβατικό μοντέλο (αγωγός ανόδου)	Νέο μοντέλο (σύστημα ανακυκλοφορίας)
μ_{kin}	$\frac{10\rho_s d_s\sqrt{\Theta_s\pi}}{96\varepsilon_s(1+e_{ss})g_o} \times [1+\frac{4}{5}g_o\varepsilon_s(1+e_{ss})]^2$ (Gidaspow et al., 1992)	$\frac{\sqrt{\pi\Theta_s}\frac{d_s\rho_s}{24\varepsilon_s g_o}\frac{\left(5+2\varepsilon_s g_o(1+e_{ss})(3e_{ss}-1)\right)}{(1+e_{ss})(3-e_{ss})}}{\left(1+\frac{45\mu_g}{6\varepsilon_s g_o d_s\rho_s\sqrt{\frac{\Theta_s}{\pi}}(1+e_{ss})(3e_{ss}-1)}\right)}$ (Boelle et al., 1995), (Gevrin et al., 2008)
μ_{col}	$\frac{4}{5}\varepsilon_s\rho_s d_s g_o(1+e_{ss})\sqrt{\left(\frac{\Theta_s}{\pi}\right)}$ (Gidaspow et al., 1992)	$\frac{4}{5}\varepsilon_s\rho_s g_o(1+e_{ss})\left(\frac{\mu_{kin}}{\rho_s}+d_s\sqrt{\frac{\Theta_s}{\pi}}\right)$ (Boelle et al., 1995), (Gevrin et al., 2008)
μ_{fr}	$\frac{P_{fr}\sin\phi}{2\varepsilon_s\sqrt{II_{dD}}}$ (Johnson and Jackson, 1987)	$\frac{P_s\sin^2\varphi}{\varepsilon_s\sqrt{4\sin^2\varphi\cdot\text{II}_{dD}+(\nabla\cdot\vec{u}_s)^2}}$ (Dartevelle, 2003)
λ_{fr}	0	$\frac{P_s}{\varepsilon_s\sqrt{4\sin^2\varphi\cdot II_{dD}+(\nabla\cdot\vec{u}_s)^2}}$ (Dartevelle, 2003)
μ	$\varepsilon_s<\varepsilon_s^{fr}\Rightarrow\mu_{kin}+\mu_{col}$ $\varepsilon_s\geq\varepsilon_s^{fr}\Rightarrow\mu_{kin}+\mu_{col}+\mu_{fr}$	$\mu=\mu_{\text{kin}}+\mu_{\text{col}}+\mu_{\text{fr}}$ (Makkawi et al., 2006)
P_s	$\varepsilon_s<\varepsilon_s^{\text{fr}}\Rightarrow P_{\text{kin}}$ $\varepsilon_s\geq\varepsilon_s^{\text{fr}}\Rightarrow P_{\text{fr}}$	$\varepsilon_s<\varepsilon_s^{\text{fr}}\Rightarrow P_{\text{kin}}$ $\varepsilon_s\geq\varepsilon_s^{\text{fr}}\Rightarrow P_{\text{kin}}+P_{\text{fr}}$
g_o	$\left[1-\left(\frac{\varepsilon_s}{\varepsilon_s^{\max}}\right)^{\frac{1}{3}}\right]^{-1}$ (Ogawa et al., 1980)	$\left[1-\left(\frac{\varepsilon_s}{\varepsilon_s^{\max}}\right)\right]^{-2.5\varepsilon_s^{\max}}$ (Lun et al., 1984)

Πίνακας 6.3 Εξισώσεις για τον υπολογισμό των κοκκωδών τάσεων για τον αγωγό ανόδου και το σύστημα ανακυκλοφορίας (Nikolopoulos et al., 2012[c])

6.3 Αριθμητικό πλέγμα

Για την πλήρη μοντελοποίηση της μονάδας του IFK, το πλέγμα που κατασκευάστηκε αποτελείται από 286.753 κελιά και l_r ίσο με 21. Το πλέγμα αποτελείται κυρίως από εξαεδρικά κελιά με εξαίρεση τον κυκλώνα που διακριτοποιήθηκε με τετραεδρικά στοιχεία. Το πλέγμα είναι ιδιαίτερα πυκνό, το πυκνότερο που έχει εφαρμοστεί για τρισδιάστατη μοντελοποίηση. Το σχήμα 6.2 περιγράφει τη γεωμετρία και βασικές διαστάσεις του πλήρους κύκλου αυτής της μικρής μονάδας ρευστοποιημένης κλίνης ανακυκλοφορίας.

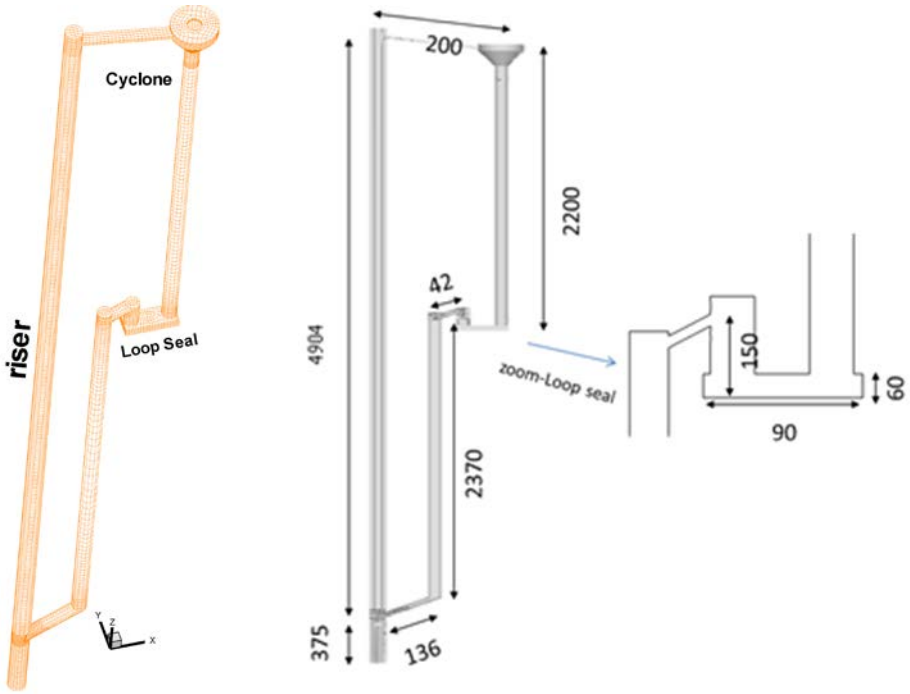

Σχήμα 6.2 Γεωμετρία και βασικές διαστάσεις της μονάδας.

6.4 Αποτελέσματα

Το χρονικό βήμα τέθηκε ίσο με 20 μs, και το πεδίο ροής αρχικοποιήθηκε με 1.5 kg στερεού ισόποσα διαμοιρασμένου στον αγωγό ανόδου και στο σύστημα ανακυκλοφορίας. Η παροχή αέρα μέσω του διασκορπιστή του αγωγού ανόδου και του Loop-seal ισούται με 8.95 και 1.5 kg/h αντίστοιχα.

Τα σχήματα 6.3 και 6.4 απεικονίζουν τη χρονικά μέση πίεση για τη μονάδα όπως αυτή μοντελοποιήθηκε από τα μοντέλα του EMMS και του Gidaspow, αντίστοιχα. Επίσης, στα ίδια διαγράμματα με κόκκινους σταυρούς αναπαριστούνται οι πειραματικές μετρήσεις του IFK. Ενώ το μοντέλο του Gidaspow αποτυγχάνει να μοντελοποιήσει με ακρίβεια την κάτω περιοχή (bottom zone) , ακόμη και για αυτό το πολύ πυκνό πλέγμα, το μοντέλο EMMS επιδεικνύει πολύ μεγάλη ακρίβεια. Το μέσο σφάλμα του EMMS, όσον αφορά τις προλέξεις πίεσης είναι μικρότερο του 10%. Η ακρίβεια του μοντέλου EMMS ειδικά για την κάτω περιοχή είναι πάρα πολύ μεγάλη, και όποιες μικρές αποκλίσεις από τα πειραματικά δεδομένα στην άνω περιοχή ενδέχεται να οφείλονται στη μονοδιαμετρική απλούστευση.

Όσων αφορά την περιοχή της πνευματικής βαλβίδας του ανακυκλοφορητή στεγανοποίησης (Loop – Seal) η συμφωνία με τα πειραματικά δεδομένα είναι καλή ανεξαρτήτως μοντέλου οπισθέλκουσας. Το γεγονός αυτό, υπογραμμίζει ότι σε αυτή την περιοχή οι δυνάμεις τριβής είναι κυρίαρχες και πως το μοντέλο που αναπτύχθηκε αναπαράγει επιτυχώς τη φυσική του προβλήματος. Θα πρέπει να τονιστεί, πως αυτή είναι η πρώτη φορά που τα αποτελέσματα ενός μοντέλου υπολογιστικής ρευστοδυναμικής συγκρίνονται με πειραματικά δεδομένα πίεσης για την πνευματική βαλβίδα του συστήματος ανακυκλοφορίας. Επίσης, είναι άξιο αναφοράς πως όταν εφαρμόστηκε το συμβατικό μοντέλο κοκκωδών τάσεων η υποεκτίμηση των δυνάμεων τριβής ήταν τόσο μεγάλη που η στεγανοποίηση της βαλβίδας παύει.

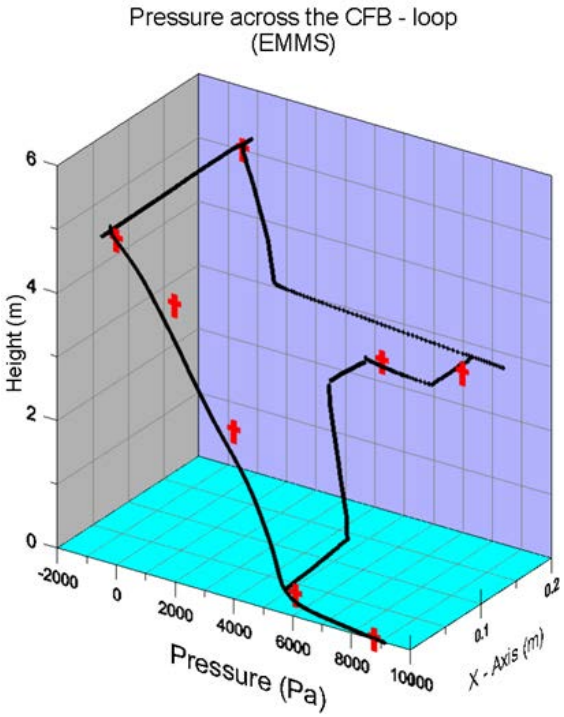

Σχήμα 6.3 Σύγκριση πειραματικών (κόκκινοι σταυροί) και αριθμητικών δεδομένων (συνεχής μαύρη γραμμή) για το μοντέλο του EMMS

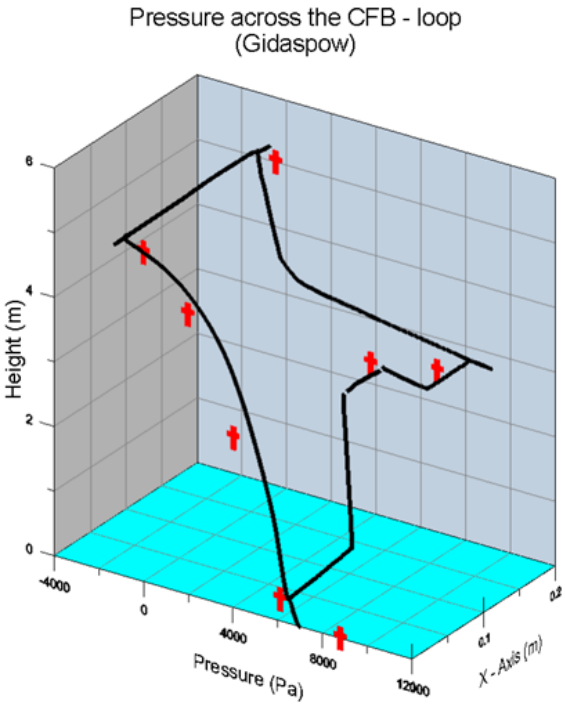

Σχήμα 6.4 Σύγκριση πειραματικών (κόκκινοι σταυροί) και αριθμητικών δεδομένων (συνεχής μαύρη γραμμή) για το μοντέλο του Gidaspow.

Μια άλλη σημαντική παράμετρος λειτουργίας, που επηρεάζεται από τη μοντελοποίηση του συντελεστή εναλλαγής ορμής, είναι η ανακυκλοφορία μάζας στη μονάδα. Κατά τη διάρκεια των πειραμάτων στο IFK αυτή η παροχή μετρήθηκε ίση με 63 kg/h. Οι προλέξεις του μοντέλου EMMS για την παροχή μάζας που μπαίνει και βγαίνει από τον αγωγό ανόδου απεικονίζεται στο σχήμα 6.5.

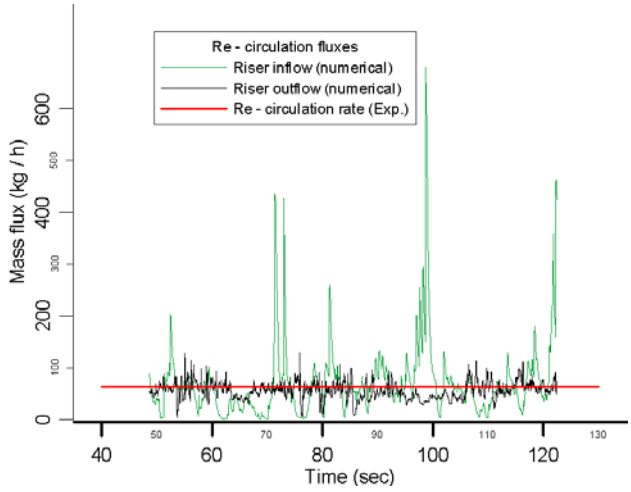

Σχήμα 6.5 Χρονοσειρές της ανακυκλοφορίας που εισέρχεται και εξέρχεται από τον αγωγό ανόδου.

Οι δύο χρονοσειρές διαφέρουν αρκετά, αλλά η μέση τιμή τους ταυτίζεται. Επίσης η μέση τους τιμή συμφωνεί με πολύ μεγάλη ακρίβεια με την πειραματική τιμή (σφάλμα < 2%). Το μοντέλο του Gidaspow υπερεκτίμησε την ανακυκλοφορία κατά περίπου 10%. Επίσης, τα αποτελέσματα του μοντέλου μπορούν να συγκριθούν και με τις οπτικές παρατηρήσεις των

πειραματιστών. Το υπολογιστικό μοντέλο προβλέπει πως η πνευματική βαλβίδα τροφοδοτεί τον αγωγό ανόδου με παλμούς φαινόμενο που παρατηρήθηκε και οπτικά, επαληθεύοντας τουλάχιστον ποιοτικά το υπολογιστικό μοντέλο.

7. ΜΟΝΤΕΛΟΠΟΙΗΣΗ ΕΝΑΝΘΡΑΚΩΤΗ 10 KW_{th}

Η τεχνολογία δέσμευσης CO_2 με κύκλους ενανθράκωσης / ασβεστοποίησης, που προτάθηκε από τους Shimizu et al., 1999, χρησιμοποιεί ένα σύστημα συζυγών κλινών (DFB) που συνεχώς ανακυκλώνει σωματίδια CaO για τη δέσμευση του CO_2, στον αντιδραστήρα ενανθράκωσης, και το σχηματιζόμενο $CaCO_3$ μεταφέρεται στον αναγεννητή όπου ασβεστοποιείται και το παραγόμενο CO_2 μπορεί να οδηγηθεί προς αποθήκευση σε κατάλληλους υπόγειους γεωλογικούς σχηματισμούς.

Οι Abanades et al., 2007 εξέτασαν την οικονομική βιωσιμότητα της διεργασίας ενώ οι Charitos et al., 2010[a, b], Charitos et al., 2011 εξέτασαν τη διεργασία σε ρεαλιστικές συνθήκες στην πιλοτική συζυγή μονάδα του IFK. Ο ενανθρακωτής αυτής της μονάδας ισχύος 10 kW, το όνομα του οποίου είναι DIVA, μοντελοποιείται σε αυτή την εργασία.

Το υδροδυναμικό μοντέλο που χρησιμοποιήθηκε στο έκτο κεφάλαιο της διατριβής χρησιμοποιήθηκε και στη μοντελοποίηση της DIVA. Επίσης στο μοντέλο ενσωματώθηκε η αντίδραση ενανθράκωσης. Δυστυχώς, μέχρι στιγμής δεν υπάρχουν πειραματικά δεδομένα για αυτή τη μονάδα που θα μπορούσαν να επαληθεύσουν το μοντέλο υπολογιστικής ρευστοδυναμικής. Ωστόσο, το μοντέλο που αναπτύχθηκε, εφαρμόστηκε στη γεωμετρία της DIVA, για τυπικές συνθήκες λειτουργίας που βρέθηκαν στη διεθνή βιβλιογραφία.

7.1 Περιγραφή της μονάδας

Η μονάδα των 10 KW_{th} DIVA είναι μια τυπική μονάδα ρευστοποιημένης κλίνης ανακυκλοφορίας ενανθράκωσης με την εξαίρεση πως συνδέεται με τη συζυγή της μονάδα ασβεστοποίησης. Το στερεό εντός της είναι ένα μείγμα CaO και $CaCO_3$ ενώ το αέριο ρευστοποίησης αποτελείται από άζωτο και διοξείδιο του άνθρακα σε αναλογία τυπικών καυσαερίων λιθάνθρακα. Το ασβεστοποιημένο υλικό εισέρχεται στη μονάδα μέσω θύρας που βρίσκεται σε ύψος 1.5 m. Επίσης, στην πνευματική βαλβίδα υπάρχει μια έξοδος που οδηγεί στον ασβεστοποιητή. Σε αυτή την έξοδο, η ροή μάζας ελέγχεται από μια κωνική μηχανική βαλβίδα.

Ύψος αντιδραστήρα	L	m	12.292
Διάμετρος αγωγού ανόδου	D	m	0.071
Μάζα στερεών στον ενανθρακωτή	TSI	kg	6.5
Παροχή καυσαερίων	F_{FG}	kmol/s	$2.802 \cdot 10^{-4}$
Συγκέντρωση CO_2 στα καυσαέρια	y_{CO2}	kmol/kmol	0.114
Λόγος ανακυκλοφορίας ασβεστίου	F_{Ca}/F_{CO2}	kmol/kmol	17.40
Θερμοκρασία εισόδου στερεών	T_R	^oC	900
Θερμοκρασία	T_g	^oC	650
Ασβεστοποίηση	X_{calc}	-	0.0294
Μέγιστη ενανθράκωση	X_{max}	-	0.0854

Πίνακας 7.1 Γεωμετρικά χαρακτηριστικά και συνθήκες λειτουργίας ενανθρακωτή (DIVA)

Σε αυτή τη μελέτη μοντελοποιείται μόνο ο ενανθρακωτής. Ο δεύτερος αντιδραστήρας δε συμπεριελήφθη στη μοντελοποίηση αλλά η επίδραση της λειτουργίας του λαμβάνεται υπ' όψη μέσω: α) της σύστασης (X_{calc}) της παροχής στερεών που τροφοδοτεί τον αγωγό ανόδου

του ενανθρακωτή, και β) τη μέγιστη ποσότητα CaO που μπορεί να δεσμεύσει CO_2 (X_{max}) και δεν έχει απενεργοποιηθεί λόγω της πυροσυσσωμάτωσης των κόκκων εντός των σωματιδίων (sintering) του ασβεστίου.

Ο πίνακας 7.1 συνοψίζει τα γεωμετρικά χαρακτηριστικά της DIVA και τις τυπικές συνθήκες λειτουργίας της διεργασίας, όπως αυτές αναφέρονται στη βιβλιογραφία (Charitos et al., 2010[b]). Θα πρέπει να τονιστεί πως το διαθέσιμο για τη δέσμευση του διοξειδίου του άνθρακα, CaO δίνεται από το γινόμενο του F_{Ca} με τον όρο (X_{max}- X_{calc}).

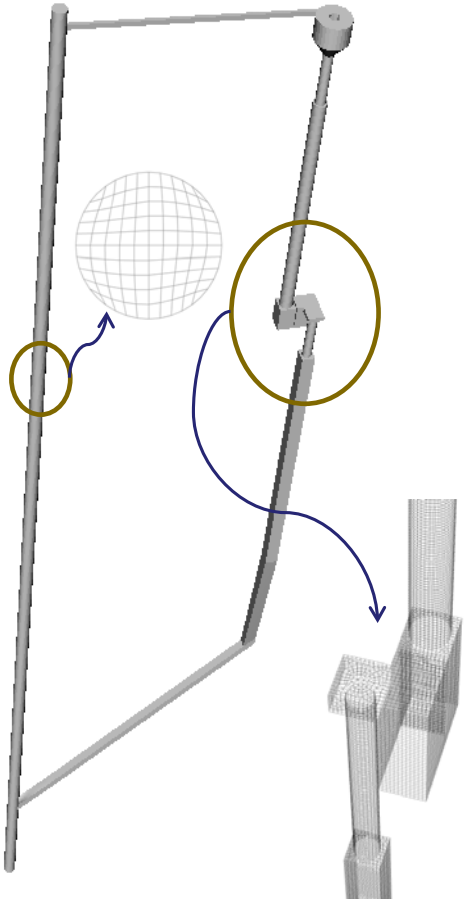

Σχήμα 7.1 Αριθμητικό πλέγμα και γεωμετρία της 10 KW_{th} DIVA

Το τρισδιάστατο αριθμητικό πλέγμα που εφαρμόστηκε αποτελείται από 392,130 εξαεδρικά κελιά με l_r ίσο με 21. Το πλέγμα κατασκευάστηκε χωρίς καμία απλούστευση στην πραγματική γεωμετρία (σχήμα 7.1).

7.2 Μεθοδολογία

Το μοντέλο που εφαρμόστηκε για τη μοντελοποίηση της μονάδας DIVA ενσωματώνει το υδροδυναμικό μοντέλο που παρουσιάστηκε στο κεφάλαιο 6, την επίλυση των συγκεντρώσεων χημικών συστατικών των φάσεων και μόνο μια ετερογενή αντίδραση. Οι εξισώσεις ενέργειας για τις δύο φάσεις (καυσαέρια και ασβέστιο) δεν επιλύθηκε και υιοθετήθηκε η απλούστευση τις ισοθερμοκρασιακής ροής, καθόσον η θερμοκρασία της μονάδας ελέγχεται με θερμικές αντιστάσεις. Ο ρυθμός αντίδρασης της ενανθράκωσης υπολογίσθηκε με βάση την εξίσωση 3.83. Τα χαρακτηριστικά του προσροφητικού υλικού δεν είναι γνωστά. Οι σταθερές, k_s, S_0 και e_0 που εμπλέκονται στην εξίσωση 3.83 βρέθηκαν στη βιβλιογραφία (Abanades et al., 2004, k_s = 5.95E^{-10} m^4 [mol s]$^{-1}$, S_0 = 40.E^{+6} m^2 m^{-3} and e_0 = 0.5). Για τα σωματίδια του ασβεστίου θεωρήθηκαν τυπικές ιδιότητες, d_p = 350 μm, ρ_s = 1800 kg m^{-3}

Οι οριακές συνθήκες για το αέριο και το στερεό προσδιορίστηκαν με βάση το μοντέλο του κεφαλαίου 6, με εξαίρεση την έξοδο του Loop – Seal που τροφοδοτεί τον ασβεστοποιητή. Σε αυτό το άνοιγμα η γραμμομοριακή ροή των στερεών ορίστηκε ρητά ίση με την αντίστοιχη ροή στην είσοδο όπου επιστρέφει μάζα από τον ασβεστοποιητή και βρίσκεται σε ύψος z=1.5 m στον αγωγό ανόδου του ενανθρακωτή. Η σύσταση του ρεύματος εξόδου καθορίστηκε με οριακή συνθήκη τύπου Neumann.

Όσον αφορά την αρχικοποίηση του πεδίου ροής, η μάζα του ασβεστίου ισομοιράστηκε μεταξύ αγωγού ανόδου και συστήματος ανακυκλοφορίας. Επίσης, το γραμμομοριακό κλάσμα του $CaCO_3$ αρχικοποιήθηκε ίσο με 5% (X_{carb} = 0.05). Το χρονικό βήμα που εφαρμόστηκε είναι 40 μs. Ωστόσο, δεν έγινε δειγματοληψία για την εξαγωγή μέσων τιμών καθώς δεν υπάρχουν ακόμη πειραματικά δεδομένα για σύγκριση και η διαδικασία της δειγματοληψίας είναι ιδιαιτέρως χρονοβόρα.

7.3 Αποτελέσματα

Τα αποτελέσματα του μοντέλου αναφέρονται σε στιγμιαίες τιμές των επιλύσιμων μεγεθών και μπορούν να αξιολογηθούν μόνο ποιοτικά εφόσον δεν αντιστοιχούν σε κάποιο συγκεκριμένο πείραμα. Όπως αναμενόταν η υδροδυναμική του φαινομένου και τυπικά ροϊκά φαινόμενα όπως η πυκνή κάτω περιοχή (dense bottom zone) και της ροής πυρήνα – δακτυλίου (core - annulus)μοντελοποιούνται ορθά, σχήμα 7.2α. Επίσης, το μοντέλο προβλέπει ότι ο ρυθμός της αντίδρασης ενανθράκωσης είναι μεγάλος στην πυκνή κάτω περιοχή όπως φαίνεται και στο σχήμα 7.2b, φαινόμενο που έχει επαληθευτεί και πειραματικά (Charitos et al., 2010[b]; Charitos et al., 2011).

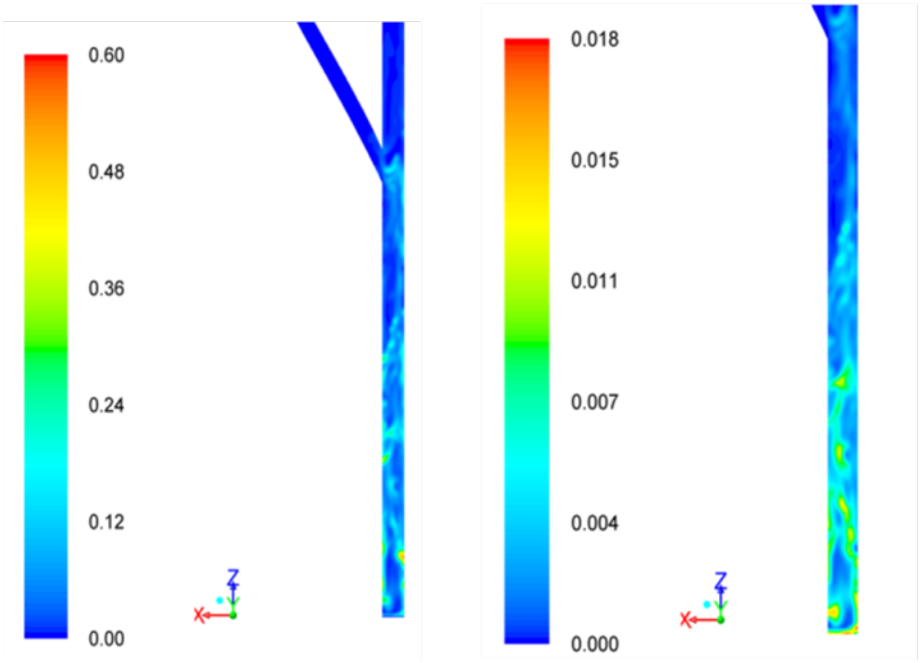

Σχήμα 7.2 α) Στιγμιαίο ποσοστό όγκου στερεών, β) ρυθμός ενανθράκωσης [kmol/(m^3 s)]

Η κατανομή της συγκέντρωσης του CO_2 καθ΄ ύψος του αγωγού ανόδου παρουσιάζεται στο σχήμα 7.3. Σε αυτό το σχήμα επιβεβαιώνεται πως η πλειονότητα του CO_2 δεσμεύεται στην κάτω πυκνή περιοχή, ενώ στην άνω περιοχή η δέσμευση συνεχίζεται με μικρότερους ρυθμούς (Nikolopoulos et al., 2012[a]). Η μείωση της συγκέντρωσης του CO_2 στο ύψος z = 1.5 m οφείλεται στις εισόδους που βρίσκονται σε αυτό το ύψος και τροφοδοτούν με άζωτο τον αγωγό ανόδου, αραιώνοντας έτσι τη ροή.

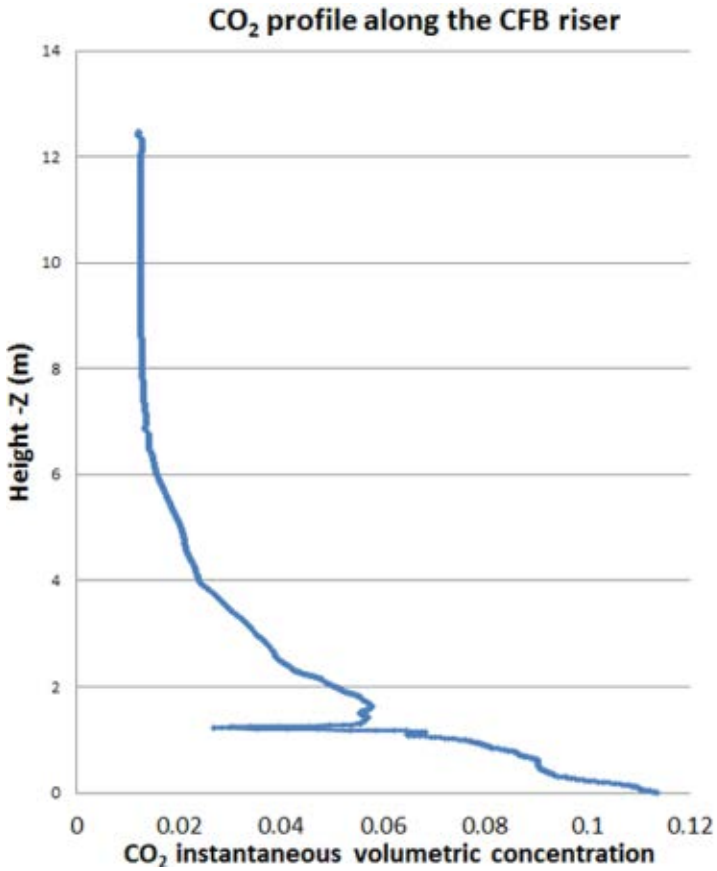

Σχήμα 7.3 Στιγμιαία συγκέντρωση CO_2 καθ' ύψος του αγωγού ανόδου

8. Συμπεράσματα

Σε αυτή την διδακτορική διατριβή, διερευνήθηκε η αριθμητική προσομοίωση των ρευστοποιημένων κλινών ανακυκλοφορίας. Η μοντελοποίηση των φαινομένων της ρευστοποίησης είναι εν γένει, δύσκολη και η πλειοψηφία των δημοσιευμένων εργασιών επικεντρώνεται σε αυτό το ζήτημα (Atsonios et al., 2011; Gidaspow et al., 1992; Ma et al., 2009; Nikolopoulos et al., 2010[a, b]; Nikolopoulos et al., 2012[b]; Vashisth and Grace, 2011; Wang and Li, 2007). Ωστόσο, υπάρχουν και κάποιες λίγες στον αριθμό δημοσιεύσεις για τη μοντελοποίηση αντιδράσεων εντός των κλινών (Gungor, 2008[b]; Gungor and Eskin, 2008[b]; Nikolopoulos et al., 2009; Wang et al., 2012[a]; Zhou et al., 2011).

Οι περισσότερες εργασίες που επικεντρώνουν στη μοντελοποίηση της υδροδυναμικής διερευνούν την επίδραση των φαινομένων μεσο-κλίμακας που έχουν μεγάλη επίδραση στην οπισθέλκουσα δύναμη (Ge et al., 2008), που επάγει το αέριο στο στερεό. Ένας αποδοτικός τρόπος ενσωμάτωσης αυτών των δομών, που απλουστευτικά αποκαλούνται συμπλέγματα, στα μοντέλα υπολογιστικής ρευστοδυναμικής, είναι μέσω κατάλληλων υποπλεγματικών μοντέλων. Σε αυτή τη διατριβή μελετήθηκαν αυτοί οι μηχανισμοί και αναπτύχθηκε μοντέλο EMMS που άρρητα ενσωματώνει την επίδραση αυτών των δομών στο συντελεστή εναλλαγής ορμής μεταξύ των φάσεων.

Το μοντέλο ΕΜΜΣ, αποτελείται από ένα σύνολο εξισώσεων και περιορισμών καθώς και από μια συνάρτηση κόστους που αναφέρεται στην ενέργεια που συναλλάσσεται μεταξύ αέριου και στερεών. Το μοντέλο EMMS που αναπτύχθηκε εμπεριέχει εξισώσεις και περιορισμούς διαθέσιμους στη βιβλιογραφία, καθώς και κάποιους νέους περιορισμούς. Το σύστημα των εξισώσεων αυτό του μη γραμμικού προβλήματος βελτιστοποίησης επιλύθηκε και τα αποτελέσματά του αναλύθηκαν διεξοδικά. Πλην του συντελεστή ετερογένειας H_d, η επιτάχυνση, η ταχύτητα ολίσθησης και το κλάσμα αερίου των συμπλεγμάτων εξετάστηκαν και αξιολογήθηκαν.

Το μοντέλο που αναπτύχθηκε, προέλεξε πιο ρεαλιστικές τιμές για το κλάσμα όγκου των συμπλεγμάτων σωματιδίων (f) εν συγκρίσει με τα αποτελέσματα των Wang and Li, 2007 όσον αφορά την αραιή περιοχή Α. Επίσης, συγκριτικά με τα αποτελέσματα των Wang and Li, 2007, το παρόν μοντέλο προέλεξε πιο ρεαλιστικές τιμές και για την επιτάχυνση των σωματιδίων. Ωστόσο, η ενσωμάτωση στο μοντέλο εμπειρικών και ήμι-εμπειρικών εξισώσεων εγείρει ερωτήματα για την καθολικότητα του μοντέλου.

Για την εφαρμογή του μοντέλου EMMS σε κώδικα υπολογιστικής ρευστοδυναμικής ο συντελεστής ετερογένειας με πολυώνυμα παρεμβολής και εφαρμόστηκε για τη μοντελοποίηση της ισοθερμοκρασιακής ροής εντός του αγωγού ανόδου μιας 1.2 MW_{th} ρευστοποιημένης κλίνης καύσης. Παράλληλα εξετάστηκε και το συμβατικό μοντέλο του Gidaspow καθώς και η επίδραση της πυκνότητας πλέγματος. Τα αποτελέσματα αυτής της μελέτης έδειξαν πως αυξανομένης της πυκνότητας πλέγματος, η ακρίβεια του μοντέλου αυξάνεται ανεξαρτήτως μοντέλου οπισθέλκουσας επειδή οι δομές μεσο-κλίμακας επιλύονται με ρητό τρόπο. Ωστόσο, για την ίδια πυκνότητα πλέγματος το μοντέλο EMMS είναι πιο ακριβές από το συμβατικό μοντέλο του Gidaspow. Επίσης το μοντέλο του EMMS μοντελοποίησε επιτυχώς τυπικά ροϊκά φαινόμενα όπως το S – Shape και το core – annulus και σεβάστηκε τον περιορισμό της οριακής ταχύτητας στην άνω περιοχή (freeboard), ακόμη και για το αραιό πλέγμα. Ωστόσο, τα αποτελέσματα του μοντέλου, EMMS αποδείχτηκαν πλεγματικώς εξαρτημένα. Αυτό το χαρακτηριστικό δεν έχει ακόμη μελετηθεί ενδελεχώς. Ίσως να πρέπει ν αποδοθεί πως το μοντέλο αυτό υποθέτει ομοιόμορφες συνθήκες εντός των υποπλεγματικών δομών. Αυτή η υπόθεση, πάντως, είναι σίγουρα περισσότερο αληθής από

την υπόθεση των συμβατικών μοντέλων που υποθέτουν ομοιόμορφες συνθήκες εντός ολόκληρου του όγκου ελέγχου.

Η μοντελοποίηση της καύσης ορυκτού καυσίμου εντός της ίδιας μονάδας 1.2 MW_{th} διερευνήθηκε επίσης. Το υπό εξέταση καύσιμο είναι λιγνίτης βόρειας Ρηνανίας - Βεστφαλίας. Οι τρεις φάσεις (αέριο, αδρανές υλικό και καύσιμο) προσεγγίστηκαν με τις εξισώσεις κατά Euler. Οι μηχανισμοί της καύσης και της μεταφοράς θερμότητας ενσωματώθηκαν στο υδροδυναμικό μοντέλο μαζί με ένα δίκτυο ομογενών και ετερογενών αντιδράσεων. Η μεταφορά θερμότητας μοντελοποιήθηκε με το μοντέλο του Gunn ενώ η καύση του εξανθρακώματος με το μοντέλο της μειούμενης διαμέτρου (shrinkig core model).

Τα χημικά στοιχεία που συμπεριελήφθησαν στη μοντελοποίηση ήταν τα O_2, CO_2. H_2O, N_2, πτητικά, CO, CH_4, H_2, HCN και εξανθράκωμα, υγρασία, πτητικά, στάχτη για το αέριο και το καύσιμο αντίστοιχα. Τα αποτελέσματα του μοντέλου για το οξυγόνο και το διοξείδιο του άνθρακα επαληθεύτηκαν με αντίστοιχα πειραματικά δεδομένα. Επίσης, όσον αφορά τη μέση θερμοκρασία της κλίνης, η πρόλεξη (1095 K) είναι πολύ κοντά στην πειραματική τιμή (1100 K, Leithner et al., 1993). Αν και το μοντέλο καύσης που αναπτύχθηκε επέδειξε ικανοποιητική ακρίβεια το υπολογιστικό του κόστος είναι αρκετά μεγάλο και η εφαρμογή του σε μεγάλης κλίμακας μονάδες ρευστοποιημένων κλινών ανακυκλοφορίας καύσης είναι δύσκολη αλλά όχι ακατόρθωτη. Η επίλυση του πεδίου θερμοκρασιών και της διασποράς των χημικών στοιχείων της καύσης επέτρεψε τη μοντελοποίηση και των εκπομπών NO_x-N_2O. Η μοντελοποίηση αυτών των ρυπαντών συντελεστή με ένα τριδιάστατο απεπλεγμένο μοντέλο. Είναι η πρώτη φορά που ένα τέτοιο μοντέλο εξετάζεται για μονάδα ρευστοποιημένης κλίνης.

Η απελευθέρωση HCN κατά τη διάρκεια της καύσης εξετάστηκε παραμετρικά μέσω δύο μοντέλων 1) HCN σχηματίζεται / απελευθερώνεται και κατά την απελευθέρωση πτητικών αλλά και κατά τη διάρκεια της καύσης του εξανθρακώματος, και β) το HCN απελευθερώνεται μόνο κατά την απελευθέρωση των πτητικών. Το μοντέλο 1 προέλεξε πολύ μεγάλες συγκεντρώσεις HCN στην έξοδο του αγωγού ανόδου. Επομένως, το μοντέλο 2 θεωρήθηκε ακριβέστερο, αποτέλεσμα που συμφωνεί με τη θεωρία των Goel et al., 1996[a, b]. Ωστόσο, οριστικά και καθολικά συμπεράσματα δεν μπορούν να εξαχθούν γιατί αυτή η συμπεριφορά μπορεί να εξαρτάται από τα χαρακτηριστικά του καυσίμου υπό εξέταση.

Η απεπλεγμένη μοντελοποίηση των NO_x-N_2O αναπαρήγαγε αποτελέσματα με καλή ακρίβεια, ιδίως για την έξοδο του αγωγού ανόδου. Συμπερασματικά, αυτό το επαληθευμένο και μικρού υπολογιστικού κόστους μοντέλο μπορεί να χρησιμοποιηθεί αποδοτικά για την μείωση των εκπομπών NO_x-N_2O, ακόμη και σε μεγάλης κλίμακας μονάδες. Βεβαίως, το μοντέλο αυτό πρέπει να τροφοδοτηθεί με στοιχεία για την καύση του καυσίμου εντός της κλίνης τα οποία μπορούν να καθοριστούν είτε μέσω υπολογιστικής ρευστομηχανικής μοντελοποίησης είτε με ήμι-εμπειρικά μοντέλα.

Οι εκπομπές NO_x-N_2O δεν ήταν οι μόνοι ρυπαντές που εξετάστηκαν σε αυτή τη διατριβή. Η δέσμευση του CO_2 διερευνήθηκε, επίσης. Συγκεκριμένα, αυτή η διατριβή επικεντρώθηκε στη μοντελοποίηση της ρευστοποιημένης κλίνης ενανθράκωσης της διεργασίας κύκλων ενανθράκωσης / ασβεστοποίησης (Calcium Looping process) που είναι μια ελκυστική καινούργια τεχνολογία για τη δραστική μείωση των εκπομπών διοξειδίου του άνθρακα στις ενεργοβόρες βιομηχανίες και κυρίως στην ηλεκτροπαραγωγή. Σε πρώτη φάση διερευνήθηκε η υδροδυναμική μοντελοποίηση του εν λόγω αντιδραστήρα μέσω της πλήρους μοντελοποίησης του κρύου μοντέλου του. Σε αυτή τη μοντελοποίηση, ένας νέος τανυστής για τη σωματιδιακή φάση εφαρμόστηκε στο σύστημα ανακυκλοφορίας για την ορθότερη μοντελοποίηση των ενδο-σωματιδιακών δυνάμεων τριβής. Το νέο μοντέλο βασίστηκε στο κριτήριο διαρροής των Pitman-Schaeffer-Stiles και επαληθεύτηκε μέσω της μοντελοποίησης ενός πειράματος για τον προσδιορισμό της γωνίας απόθεσης κοκκώδους υλικού.

Εκτός του νέου μοντέλου για τη σωματιδιακή συνεκτικότητα, το μοντέλο EMMS εφαρμόστηκε για τον υπολογισμό της οπισθέλκουσας. Το μοντέλο αναπαρήγαγε με επιτυχία το προφίλ πίεσης και την ανακυκλοφορία μάζας εντός της μονάδας. Το σφάλμα του μοντέλου για την πίεση είναι μικρότερο του 10% ενώ για την ανακυκλοφορία μικρότερο του 2%. Αξίζει να σημειωθεί πως σε αυτή τη διερεύνηση για πρώτη φορά συγκρίθηκαν αποτελέσματα μοντέλου υπολογιστικής ρευστοδυναμικής με δεδομένα πίεσης για την πνευματική βαλβίδα.

Η μοντελοποίηση της ισοθερμοκρασιακής ροής του ενανθρακωτή επεκτάθηκε καταλλήλως έτσι ώστε να συμπεριλάβει και την αντίδραση ενανθράκωσης. Η μοντελοποίηση της αντίδρασης έγινε μέσω της προσομοίωσης ενός 10 kW_{th} ενανθρακωτή ρευστοποιημένης κλίνης ανακυκλοφορίας. Αυτός ο αντιδραστήρας (DIVA), κατασκευάστηκε και λειτουργεί στο IFK, αλλά μέχρι σήμερα, δεν υπάρχουν κατάλληλα δεδομένα λειτουργίας για την προσομοίωση κάποιου πειράματος με τεχνικές υπολογιστικής ρευστοδυναμικής. Ως εκ τούτου, η μοντελοποίηση διεξήχθη για τυπικές συνθήκες λειτουργίας όπως αυτές βρέθηκαν στη βιβλιογραφία, αλλά για την πραγματική γεωμετρία της DIVA. Η αντίδραση της ενανθράκωσης μοντελοποιήθηκε μέσω δημοσιευμένων σχέσεων που μετασχηματίστηκαν, με την υπόθεση ότι κάθε όγκος ελέγχου είναι ένας ομοιογενής αντιδραστήρας (CSTR), έτσι ώστε να μπορούν να εφαρμοστούν σε μοντέλα υπολογιστικής ρευστοδυναμικής. Ελλείψει πειραματικών δεδομένων δεν μπορούν να εξαχθούν τελικά συμπεράσματα για αυτό το μοντέλο. Ωστόσο, τα αποτελέσματά του συμφωνούν ποιοτικά με πειραματικές παρατηρήσεις για τη λειτουργία τέτοιων μονάδων.

Η παρούσα διδακτορική διατριβή διερεύνησε μια γκάμα θεμάτων σχετιζόμενων με τη μοντελοποίηση της υδροδυναμικής των ρευστοποιημένων κλινών, αλλά και των εκπομπών της καύσης στερεών και της δέσμευσης του διοξειδίου του άνθρακα. Ωστόσο, υπάρχουν αρκετά ερευνητικά θέματα προς διερεύνηση και μελλοντική εργασία.

Ένα πολύ σημαντικό θέμα είναι ο προσδιορισμός της πυκνότητας πλέγματος για την αναπαραγωγή πλεγματικά ανεξάρτητων αποτελεσμάτων για τριδιάστατες μοντελοποιήσεις. Η αύξηση των διαθέσιμων υπολογιστικών πόρων θα βοηθήσει στην επίτευξη αυτού του στόχου και μπορεί παράλληλα να επιτρέψει την εφαρμογή του πολυδιαμετρικού μοντέλου που αναπτύχθηκε σε αυτή την εργασία. Επίσης, το μοντέλο EMMS που αναπτύχθηκε θα μπορούσε να βελτιωθεί μέσω της απεμπλοκής του από εμπειρικές και ήμι-εμπειρικές εξισώσεις που περιορίζουν τη καθολικότητά του. Επίσης, είναι πάρα πολύ σημαντικό να διερευνηθεί η επίδραση των συμπλεγμάτων στο ρυθμό αντίδρασης των συμπλεγμάτων (Wang et al., 2012[b]). Κλείνοντας, θα είχε μεγάλο ενδιαφέρον η εφαρμογή των υπομοντέλων που αναπτύχθηκαν σε αυτή τη διατριβή υπό την MP-PIC μεθοδολογία, καθώς αυτή η νέα μεθοδολογία φαίνεται να είναι μια πολλά υποσχόμενη εναλλακτική λύση έναντι της TFM (Chen and Wang, 2013).